

INMATEH -

**AGRICULTURAL
ENGINEERING**

JANUARY - APRIL

No liability is assumed by the editorial staff for the content of scientific papers and opinions published in this volume. They represent the author's point of view

Editorial

The National Institute of Research-Development for Machines and Installations designed to Agriculture and Food Industry - INMA Bucharest has the oldest and most prestigious research activity in the field of agricultural machinery and mechanizing technologies in Romania.

Short History

- ✓ *In 1927, the first research Center for Agricultural Machinery in Agricultural Research Institute of Romania - ICAR (Establishing Law was published in O.D. no. 97/05.05.1927) was established;*
- ✓ *In 1930, was founded The Testing Department of Agricultural Machinery and Tools by transforming Agricultural Research Centre of ICAR- that founded the science of methodologies and experimental techniques in the field (Decision no. 2000/1930 of ICAR Manager - GHEORGHE IONESCU ȘIȘEȘTI);*
- ✓ *In 1952, was established the Research Institute for Mechanization and Electrification of Agriculture - ICMA Băneasa, by transforming the Department of Agricultural Machines and Tools Testing;*
- ✓ *In 1979, the Research Institute of Scientific and Technological Engineering for Agricultural Machinery and Tools - ICSITMUA was founded - subordinated to Ministry of Machine Building Industry - MICM, by unifying ICMA subordinated to MAA with ICPMA subordinated to MICM;*
- ✓ *In 1996 the National Institute of Research-Development for Machines and Installations designed to Agriculture and Food Industry - INMA was founded - according to G.D. no.1308/25.11.1996, by reorganizing ICSITMUA, G.D no. 1308/1996 coordinated by the Ministry of Education and Research G.D. no. 823/2004;*
- ✓ *In 2008 INMA has been accredited to carry out research and developing activities financed from public funds under G.D. no. 551/2007, Decision of the National Authority for Scientific Research - ANCSno. 9634/2008.*

As a result of widening the spectrum of communication, dissemination and implementation of scientific research results, in 2000 was founded the institute magazine, issued under the name of SCIENTIFIC PAPERS (INMATEH), ISSN 1583 – 1019.

*Starting with volume 30, no. 1/2010, the magazine changed its name to INMATEH - *Agricultural Engineering*, appearing both in print format (ISSN 2068 - 4215), and online (ISSN online: 2068 - 2239). The magazine is bilingual, abstract being published in native language and English, with a rhythm of three issues / year: January-April, May-August, September-December and is recognized by CNCSIS – with B⁺ category. Published articles are from the field of AGRICULTURAL ENGINEERING: technologies and technical equipment for agriculture and food industry, renewable energy, machinery testing, environment, transport in agriculture etc. and are evaluated by specialists inside the country and abroad, in mentioned domains.*

*Technical level and performance processes, technology and machinery for agriculture and food industry increasing, according to national requirements and European and international regulations, as well as exploitation of renewable resources in terms of efficiency, life, health and environment protection represent referential elements for the magazine „INMATEH - *Agricultural Engineering*”.*

We are thankful to all readers, publishers and assessors.

Editor in chief,

Ph. D. Eng. Vladut Nicolae-Valentin

Managing Editorial Board - INMA Bucharest**Editor in Chief****Nicolae-Valentin VLADUȚ**

Ph.D.Eng, SR I

Executive Editor**Lucreția POPA**

Ph.D.Eng, SR I

Assistant Editor**Mihai-Gabriel MATACHE**

Ph.D.Eng, SR I

Logistic support, database**Virgil MURARU**

Ph.D.Eng, SR I

Scientific Secretary**Cârdei Petre, math.****Official translator****RADU Daniela-Cristina, English****Editorial Board**

- Prof.Ph.D.Eng. QUENDLER Elisabeth – Austria, Univ. of Natural Resources & Applied Life Sciences;
- Ir. HUYGHEBAERT Bruno – Belgia, Walloon Agricultural Research Center CRA-W;
- Prof.Ph.D.Eng. FABBRO Dal Inacio Maria - Brazil, Campinas State University;
- Prof.Ph.D.Eng. ATANASOV Atanas – Bulgaria, "Angel Kanchev" University of Rousse
- Prof.Ph.D.Eng. BILANDZIJA Nikola – Croatia, Zagreb University, Faculty of Agriculture;
- Prof.Ph.D.Eng. KOSUTIC Silvio – Croatia, Zagreb University, Faculty of Agriculture;
- Prof.Ph.D.Eng. GONZALEZ Omar - Cuba, Central University "Marta Abreu" de las Villas;
- Prof.Ph.D.Eng. KATHIJOTES Nicholas – Cyprus, University of Nicosia;
- Prof.Ph.D.Eng. HERAK David - Czech Republic, Czech University of Agriculture Prague;
- Prof.Ph.D.Eng. COZ Alberto – Spain, University of Cantabria, School of Nautical Studies;
- Prof.Ph.D.Eng. FENYVESI László – Hungary, Hungarian Institute of Agricultural Engineering Godolo;
- Ph.D.Eng. ALIZADEH Mohammad Reza– Iran, Rice Research Institute of Iran (RRII);
- Prof.Ph.D.Eng. DE WRACHIEN Daniele - Italy, State University of Milan;
- Ph.D.Eng. BIOCCA Marcello - Italy, Agricultural Research Council;
- Prof.Ph.D.Eng. SARAUSKIS Egidijus – Lithuania, Vytautas Magnus University, Faculty of Agricultural Engineering;
- Prof.Ph.D.Eng. EKIELSKI Adam - Poland, Warsaw University of Life Sciences;
- Prof.Ph.D.Eng. SAVIN Lazar– Serbia, Univ.of Novi Sad,
- Prof.Ph.D.Eng. SIMIKIC Mirko– Serbia, Univ.of Novi Sad;
- Prof.Ph.D.Eng. ERTEKIN Can - Turkey, Akdeniz University Antalya;
- Prof.Ph.D.Eng. KABAŞ Önder –Turkey, Akdeniz University;
- Prof.Ph.D.Eng. SELVİ Kemal Çağatay - Turkey, Ondokuz Mayıs University;
- Prof.Ph.D.Eng. BULGAKOV Volodymyr – Ukraine, National University of Life and Environmental Sciences of Ukraine
- Prof.Ph.D.Eng. HEVKO Roman Bohdanovich - Ternopil National Economic University, Faculty of Agricultural Economics and Management
- Prof. Ph.D. Eng. PARASCHIV Gigel - Romania, Politehnica University of Bucharest;
- Prof. Ph.D. Eng. VOICU Gheorghe - Romania, P.U. Bucharest;
- Prof. Ph.D.Eng. BIRIŞ Sorin - Romania, P.U. Bucharest;
- Prof.Ph.D.Eng. MAICAN Edmond - Romania, Politehnica University of Bucharest;
- Prof. Ph.D.Eng. TEODORESCU Răzvan-Ionuț - Romania, USAMV Bucharest;
- Prof.Ph.D. Eng. VLASE Sorin - Romania, "Transilvania" University of Braşov;
- Prof.Ph.D.Eng. FILIP Nicolae - Romania, Technical University Cluj Napoca;
- Prof.Ph.D. Eng. COZAR Onuc-Romania, „Babes-Bolyai” University of Cluj-Napoca;
- Prof. Ph.D. Eng. ȚENU Ioan - Romania, USAMV Iași;
- Prof.Ph.D. Eng. HERIȘANU Nicolae - Romania, Politehnica University of Timisoara
- Prof.Ph.D.Eng. GERGEN Iosif - Romania, USAMVB Timișoara;
- Prof.Ph.D.Eng. BORDEAN Despina-Maria - Romania, USAMVB Timișoara;
- Prof.Ph.D.Eng. BUNGESCU Sorin - Romania, USAMVB Timișoara;
- Ph.D.Eng. VOICEA Iulian - Romania, INMA Bucharest
- Ph.D.Eng. DEAK Gyorgy - Romania, INCDPM;
- Prof. Ph.D.Eng. BELC Nastasia - Romania, IBA Bucharest;
- Ph.D. Eng. BUȚU Alina - Romania, INCDSB Bucharest

INMATEH - Agricultural Engineering journal is indexed in the next international databases:

ELSEVIER /SciVerse SCOPUS, CLARIVATE ANALYTICS - WEB of SCIENCE- Emerging Sources Citation Index (ESCI),

ULRICHS Web: Global Serials Directory, CABI, SCIPPO, Index COPERNICUS International, EBSCO Publishing,

Elektronische Zeitschriftenbibliothek

INMATEH - Agricultural Engineering**vol. 60, no.1 / 2020**

e-ISSN: 2068 – 2239; p: ISSN: 2068 – 4215

<https://inmateh.eu/>E-mail: inmatehjournal@gmail.comEdited by: **INMA Bucharest****Copyright: INMA Bucharest / Romania**National Institute for Research-Development of Machines and Installations
Designed for Agriculture and Food Industry - INMA Bucharest
6, Ion Ionescu de la Brad Bvd., sector 1, Bucharest, ROMANIA

CONTENT

	Page(s)
1. DESIGN AND TEST OF VARIABLE DIAMETER PNEUMATIC DRUM TYPE BEAN SEED METERING DEVICE / <i>变粒径气力滚筒式豆类种子精量排种器的设计与实验</i> Kaixing Zhang ^{1,3} , Yuanyuan Sun ¹ , Lei Liu ² , Xianxi Liu ^{1,3} , Xiuyan Zhao ¹ ¹ College of Mechanical and Electronic Engineering, ShanDong Agricultural University, Taian / China ² College of Vehicle Engineering, China Agricultural University, Beijing / China ³ Shandong Provincial Engineering Laboratory of Agricultural Equipment Intelligence. China	9
2. MATHEMATICAL MODELING AND STUDY OF THE GRAIN CLEANING MACHINE SIEVE FRAME OPERATION / <i>МАТЕМАТИЧЕСКОЕ МОДЕЛИРОВАНИЕ И ИССЛЕДОВАНИЕ РАБОТЫ РЕШЕТНОГО СТАНА ЗЕРНООЧИСТИТЕЛЬНОЙ МАШИНЫ</i> Ildar Badretdinov [*] , Salavat Mudarisov, Ramil Lukmanov, Radik Ibragimov, Valeri Permyakov, Marat Tuktarov Federal State Budgetary Educational Establishment of Higher Education "Bashkir State Agrarian Univ.", Ufa / Russia	19
3. RESEARCH ON RESONANT OSCILLATIONS OF THE TELESCOPIC SCREW – GRANULAR MEDIA SYSTEM CAUSED BY EXTERNAL PERIODIC FORCES / <i>ДОСЛІДЖЕННЯ РЕЗОНАНСНИХ КОЛИВАНЬ СИСТЕМИ ТЕЛЕСКОПІЧНИЙ ГВИНТ – СИПКЕ СЕРЕДОВИЩЕ ЗУМОВЛЕНИХ ЗОВНІШНІМИ ПЕРІОДИЧНИМИ СИЛАМИ</i> Victor Hud, Roman Rogatynsky, Ivan Hevko, Oleg Lyashuk, Andriy Pik, Oleg Huryk Ternopil Ivan Puluj National Technical University / Ukraine	29
4. JUSTIFICATION OF AIR FLOW SPEED IN THE OXIDATION AREA OF A GASIFIER IN CASE OF STRAW PELLETS USING / ОБҐРУНТУВАННЯ ШВИДКОСТІ РУХУ ПОТОКУ ПОВІТРЯ В ЗОНІ ОКИСЛЕННЯ ГАЗОГЕНЕРАТОРА У ВИПАДКУ ВИКОРИСТАННЯ СОЛОМ'ЯНИХ ГРАНУЛ Savelii Kukharets ¹ , Gennadii Golub ² , Oleh Skydan ¹ , Yaroslav Yarosh ¹ , Mikolai Kukharets ¹ ¹ Zhytomyr National Agroecological University / Ukraine ² National University of Life and Environmental Sciences of Ukraine / Ukraine	37
5. ENGINEERING MANAGEMENT OF TILLAGE EQUIPMENT WITH CONCAVE DISK SPRING SHANKS / <i>ІНЖЕНЕРНИЙ МЕНЕДЖМЕНТ ҐРУНТООБРОБНИХ АГРЕГАТІВ З ПРУЖНИМИ СТОЯКАМИ СФЕРИЧНИХ ДИСКІВ</i> Ivan Rogovskii ¹ , Luidmyla Titova ¹ , Viktor Trokhaniak V.I., Oleksandr Haponenko ^{1,2} , Mykola Ohienko ¹ , Vasyli Kulik ¹ ¹ National University of Life and Environmental Sciences of Ukraine / Ukraine; ² Scientific Organization "Leonid Pogorilyy Ukrainian Scientific Research Institute of Forecasting and Testing of Machinery and Technologies for Agricultural Production" / Ukraine	45
6. OPTIMIZATION OF THE DECORTICATION PROCESS OF INDUSTRIAL HEMP STEMS BY MATHEMATICAL PLANNING METHOD / <i>ОПТИМІЗАЦІЯ ТЕХНОЛОГІЧНОГО ПРОЦЕСУ ДЕКОРТИКАЦІЇ СТЕБЕЛ ТЕХНІЧНИХ КОНОПЕЛЬ МЕТОДОМ МАТЕМАТИЧНОГО ПЛАНУВАННЯ</i> Galina Boyko ¹ , Hanna Tikhosova ¹ , Tatiana Ternova, ² ¹ Kherson National Technical University, Department of Commodity Studies, Standardization and Certification, Kherson / Ukraine; ² Kherson National Technical University, Department of Information Technology, Kherson / Ukraine	53
7. EFFECTS OF MOISTURE CONTENT ON SOME ENGINEERING PROPERTIES OF ARECANUT (ARECA CATECHU L.) FRUIT WHICH ARE RELEVANT TO THE DESIGN OF PROCESSING EQUIPMENT / <i>PENGARUH KADAR AIR TERHADAP BEBERAPA SIFAT KETEKNIKAN BUAH PINANG (ARECA CATECHU L.) YANG RELEVAN UNTUK PERANCANGAN PERALATAN PENGOLAHANNYA</i> Ramayanty Bulan ¹ , Devianti ¹ , Ega Septi Ayu ¹ , Agustami Sitorus ² ¹ Department of Agriculture Engineering, Faculty of Agriculture, Syiah Kuala University / Indonesia ² Research Centre for Appropriate Technology, Indonesian Institute of Sciences (LIPI), Subang / Indonesia	61
8. RESEARCH ON COMPOSITE RICE STRAW-CEMENT BRICK FOR HIGH-RISE BUILDING / <i>适用于高层建筑的稻草秸秆-水泥复合墙砖研究</i> Liang X.C. [*] , Zhang M., Tian S. C. Southwest University, College of Engineering and Technology, Chongqing Key Laboratory of Agricultural Equipment for Hilly and Mountainous Regions / P. R. China	71
9. DEVELOPMENT AND EVALUATION OF DRUM COFFEE ROASTING MACHINE FOR SMALL-SCALE ENTERPRISES / PENGEMBANGAN DAN EVALUASI MESIN PENYANGRAI KOPI TIPE DRUM UNTUK USAHA SKALA KECIL Dadang Dayat Hidayat ¹ , Arie Sudaryanto ¹ , Yose Rizal Kurniawan ¹ , Ashri Indriati ¹ , Diang Sagita ¹ ¹ Research Centre for Appropriate Technology, Indonesian Institute of Sciences	79

		Page(s)
10.	DESIGN AND EXPERIMENT OF ECCENTRIC SWING COMBING DEVICE FOR <i>CERASUS HUMILIS</i> / 钙果偏心摆动梳脱装置的设计与试验 Xiaobin Du, Junlin He ^{*)} , Yongqiang He, Dawei Fang College of Engineering, Shanxi Agriculture University, Taigu/China	89
11.	EXPERIMENTAL INVESTIGATION OF BIONIC SOIL-ENGAGING BLADES FOR SOIL ADHESION REDUCTION BY SIMULATING <i>ARMADILLIDIUM VULGARE</i> BODY SURFACE / <i>ARMADILLIDIUM VULGARE</i> بررسی تجربی تیغه‌های خاک‌ورز بایونیک به منظور کاهش چسبندگی خاک با شبیه‌سازی سطح بدن Jafar Massah ^{*)} , Fatemeh Hassanpour Roubdeneh ²⁾ , Zeinab Hassanpour Roubdeneh ³⁾ , Keyvan Asefpour Vakilian ¹ ¹⁾ Department of Agrotechnology, College of Abouraihan, University of Tehran, Tehran, Iran ²⁾ Department of Mechanical Engineering, Tarbiat Modares University, Tehran, Iran ³⁾ National Institute of Genetic Engineering and Biotechnology (NIGEB), Tehran, Iran	99
12.	JUSTIFICATION OF DESIGN AND TECHNOLOGICAL PARAMETERS OF THE ONION HARVESTER BED-SHAPING ROLLER SPIRAL DRUM / ОБОСНОВАНИЕ КОНСТРУКТИВНЫХ И ТЕХНОЛОГИЧЕСКИХ ПАРАМЕТРОВ СПИРАЛЬНОГО ВАЛЬЦА КАТКА-ЛОЖЕОБРАЗОВАТЕЛЯ МАШИНЫ ДЛЯ УБОРКИ ЛУКА Dorokhov A.S., Aksenov A.G., Sibirev A.V., Sazonov N.V. FSBSI "Federal Scientific Agronomic and Engineering Centre VIM" / Russian	107
13.	RESEARCH ON THE IMPACT OF THE AIR-LIQUID JET MIXER UPON RING BIOREACTOR OPERATION / ДОСЛІДЖЕННЯ ВПЛИВУ ПОВІТРЯНО-РІДИННОГО СТРУМІНЕВОГО ЗМІШУВАЧА НА РОБОТУ КІЛЬЦЕВОГО БІОРЕАКТОРА Yaroshevsky V. ¹⁾ , Bulgakov V. ²⁾ , Ivanovs S. ³⁾ , Krutyakova V. ¹⁾ , Belchenko V. ¹⁾ , Olt J. ⁴⁾ ¹⁾ Engineering and Technology Institute "Biotechnica", National Academy of Agrarian Sciences of Ukraine, Ukraine, ²⁾ National University of Life and Environmental Sciences of Ukraine, Ukraine; ³⁾ Latvia University of Life Sciences and Technologies, Latvia; ⁴⁾ Estonian University of Life Sciences, Institute of Technology, Estonia	115
14.	SMALL POWER ELECTRIC TRACTOR PERFORMANCE DURING PLOUGHING WORKS / PERFORMANȚELE UNUI TRACTOR ELECTRIC DE PUTERE MICĂ, ÎN TIMPUL LUCRĂRILOR DE ARAT Matache M.G. ¹⁾ , Cristea M. ¹⁾ , Găgeanu I. ¹⁾ , Zapciu A. ²⁾ , Tudor E. ³⁾ , Carpus E. ⁴⁾ , Popa L.D. ⁵⁾ ¹⁾ INMA Bucharest / Romania; ²⁾ INCDMTM / Romania; ³⁾ INCDIE ICPE-CA / Romania; ⁴⁾ INCDTP / Romania, SCDA Secuieni / Romania	123
15.	PERFORMANCE TEST OF THE 2BDE-2 TYPE MILLET FINE AND SMALL-AMOUNT ELECTRIC SEEDER / 2BDE-2 型谷子精少量电动播种机性能试验 Deng Sun, Qingliang Cui [*] , Yanqing Zhang, Huaming Hou College of Engineering, Shanxi Agriculture University, Taigu/China	129
16.	TECHNICAL AND TECHNOLOGICAL SOLUTIONS FOR PRODUCING FIBRE FROM BAST CROPS / ТЕХНІКО-ТЕХНОЛОГІЧНІ РІШЕННЯ ПРОЦЕСУ ОДЕРЖАННЯ ВОЛОКНА З ЛУБ'ЯНИХ КУЛЬТУР Berezovsky Yu. ¹⁾ , Kuzmina T. ¹⁾ , Lialina N. ²⁾ , Yedynovych M. ¹⁾ , Lobov O. ¹⁾ ¹⁾ Kherson National Technical University, Kherson / Ukraine; ²⁾ Kyiv National University of Construction and Architecture, Kyiv / Ukraine	137
17.	OPTIMIZATION OF PROCESS PARAMETERS OF PELLETIZER FOR AGROPYRON SEEDS UNDER VIBRATION FORCE FIELD / 振动力场作用下冰草种子丸粒化包衣机工艺参数优化 Zhanfeng Hou, Yi Qiu, Zhi Chen ^{*)} , Haiyang Liu, Fang Guo, Longkai Mi Inner Mongolia Agricultural University, College of Mechanical and Electrical Engineering, Inner Mongolia, China	147
18.	EVALUATION OF AN AUTOMATIC CONTROL SYSTEM WITH DRIP IRRIGATION SYSTEM SHOWING POOR HYDRAULIC PERFORMANCE تقييم نظام تحكم أوتوماتيكي مع نظام ري بالتنقيط ذو أداء هيدروليكي ضعيف Moataz Elnemr Department of Agricultural Engineering, Faculty of Agriculture, Damietta University/ Egypt	155
19.	RESEARCH ON THE CONTRIBUTION RATIO OF APPLE PEEL PUNCTURE BEHAVIOR TO FRUIT FIRMNESS / 苹果果皮穿刺质地对果实硬度贡献率的研究 Juxia Wang ^{*)} , Bingyao Jiang ¹⁾ , Shuanghua Xu ²⁾ , Qingliang Cui ¹⁾ , Decong Zheng ¹⁾ College of Engineering, Shanxi Agriculture University, ¹⁾ College of Engineering, Shanxi Agriculture University, Taigu/China ²⁾ Organization Department, Shanxi Agricultural University, Taigu/China	163

		Page(s)
20.	<p>DESIGN AND THRESHING OUTPUTS STUDY OF INTERNAL AND EXTERNAL ROTARY ROLLER BUCKWHEAT THRESHER / 内外滚筒旋转式荞麦脱粒装置设计与脱出物研究 Jiawei Wang, Zhiwei Li*, Saddam Hussain, Qi Lu, Haiyan Song, Decong Zheng College of Engineering, Shanxi Agriculture University, Taigu/China</p>	173
21.	<p>VIBRATION AND IMPACT DETECTION OF AXIAL- FLOW THRESHING UNIT UNDER DYNAMIC THRESHING CONDITIONS / 动态脱粒工况下轴流脱粒装置的振动与冲击检测 Ji Jiangtao^{1,2}, Hu Jingpeng¹, Wang Shengsheng^{1,2}, Zhang Ruihong¹, Pang Jing¹ ¹ Henan University of Science and Technology, College of Agricultural Equipment Engineering/ China; ² Collaborative Innovation Centre of Machinery Equipment Advanced Manufacturing of Henan Province/ China</p>	183
22.	<p>ASSESSMENT INDICES FOR THE EFFICIENCY OF THE SEPARATION PROCESS ON A SIEVE WITH CONICAL SEPARATION SURFACE / INDICI DE APRECIERE A EFICIENȚEI PROCESULUI DE SEPARARE PE O SITĂ CU SUPRAFAȚA DE SEPARARE CONICĂ Stoica Dorel¹, Voicu Gh.¹, Popa L.², Constantin G.A.¹, Tudor P.¹ ¹ POLITEHNICA University of Bucharest, Faculty of Biotechnical Systems Engineering / Romania; ² INMA Bucharest / Romania</p>	193
23.	<p>SHADOW PROCESSING TECHNOLOGY OF AGRICULTURAL PLANT VIDEO IMAGE BASED ON PROBABLE LEARNING PIXEL CLASSIFICATION / 基于概率学习像素分类法的农业植物视频图像阴影处理技术研究 Cheng Yang¹, Ping Wang¹, Yan Bao¹ ¹ College of Electronic Information and Electrical Engineering, Changsha University, Changsha / China</p>	201
24.	<p>CONTROL METHOD FOR PARAMETERS COORDINATE MATCH OF FLUTED ROLLER FERTILIZER APPARATUS / 外槽轮施肥参数协调匹配控制方法 Huimin Feng^{1,2}, Nana Gao², You Li², Weiqiang Fu³, Yuming Guo^{*1} ¹ College of Engineering, Shanxi Agricultural University, Taigu /China; ² Beijing Research Centre for Information Technology in Agriculture, Beijing /China; ³ Beijing Research Centre of Intelligent Equipment for Agriculture, Beijing / China</p>	211
25.	<p>IMPROVING THE OPERATING COMFORT OF THE ELECTRIC MINI-TILLER BASED ON SIMULATION ANALYSIS AND FIELD TEST / 基于仿真分析和田间试验的电动微耕机操作舒适性提高 Po Niu, Jian Chen, Chenjun Hu, Jindou Zhao Southwest University, College of Engineering and Technology / P.R China</p>	221
26.	<p>NEAR-INFRARED SPECTROSCOPY AS A RAPID AND SIMULTANEOUS ASSESSMENT OF AGRICULTURAL GROUNDWATER QUALITY PARAMETERS / NEAR INFRARED SPECTROSCOPY SEBAGAI METODE CEPAT DAN SIMULTAN UNTUK PREDIKSI KUALITAS AIR TANAH LAHAN PERTANIAN Ichwana¹, Zulkifli Nasution², Agus Arip Munawar^{*1} ¹ Syiah Kuala University, Department of Agricultural Engineering / Indonesia; ² North Sumatera University, Faculty of Agriculture / Indonesia</p>	233
27.	<p>FAULT ANALYSIS METHOD FOR LIQUID LEVEL CONTROL CIRCUIT OF A WATER SUPPLY SYSTEM / 某型供水系统液位控制电路的故障分析方法 Wang Ling ¹ Shaanxi Vocational & Technical College, Shaanxi, Xi'an / China</p>	241
28.	<p>DESIGN AND TEST OF HYDRAULIC DEVICE FOR ELECTRO-HYDRAULIC CONTROLLED HITCH SYSTEM OF A HORTICULTURAL TRACTOR / 园艺电液控制系统液压装置的设计与试验 Qiang Gao, Zhixiong Lu, Jinlin Xue *, Huisong Gao College of Engineering, Nanjing Agricultural University, Nanjing / China</p>	253
29.	<p>RESEARCH OF THE OF BULK MATERIAL MOVEMENT PROCESS IN THE INACTIVE ZONE BETWEEN SCREW SECTIONS / ДОСЛІДЖЕННЯ ПРОЦЕСУ ПЕРЕМІЩЕННЯ СИПКОГО МАТЕРІАЛУ В НЕАКТИВНІЙ ЗОНІ МІЖ ГВИНТОВИМИ СЕКЦІЯМИ Trokhaniak O.M.*¹, Hevko R.B.², Lyashuk O.L.², Dovbush T.A.², Pohrishchuk B.V.³, Dobizha N.V.³ ¹National University of Life and Environmental Sciences of Ukraine / Ukraine; ²Ternopil Ivan Puluj National Technical University / Ukraine; ³Ternopil National Economical University / Ukraine</p>	261

		Page(s)
30.	<p>RESULTS OF THE NUTRITIONAL PRESERVATION RESEARCH OF THE ALFALFA LAYING ON STORAGE WITH TWO-PHASE COMPACTION / РЕЗУЛЬТАТИ ДОСЛІДЖЕННЯ ЗБЕРЕЖЕНОСТІ ПОЖИВНИХ РЕЧОВИН ЛЮЦЕРНИ ПРИ ЗАКЛАДЦІ НА ЗБЕРІГАННЯ МЕТОДОМ ДВОСТАДІЙНОГО УЩІЛЬНЕННЯ Milko D.O.¹⁾, Sclyar O.H.¹⁾, Sclyar R.V.¹⁾, Pedchenko G.P.¹⁾, Zhuravel D.P.¹⁾, Bratishko V.V.²⁾ ¹⁾ Dmytro Motornyi Tavria State Agrotechnological University / Ukraine ²⁾ National University of Life and Environmental Sciences of Ukraine / Ukraine</p>	269
31.	<p>OPTIMIZATION RESEARCH OF FERTILIZER GUIDING MECHANISM BASED ON THE DISCRETE ELEMENT METHOD / 基于离散元法的导肥装置优化研究 HongJian Zhang¹⁾, YuFeng Li¹⁾, ChunBao Xu¹⁾, ShuangXi Liu^{1,2)}, ZeKun Quan¹⁾, JinXing Wang^{*1,2)} ¹⁾ College of Mechanical and Electronic Engineering, Shandong Agricultural University, Taian / China; ²⁾ Shandong Provincial Key Laboratory of Horticultural Machinery and Equipment, Taian / China</p>	275
32.	<p>EXPERIMENTAL MODEL OF A COMBINED THERMAL SYSTEM FOR EFFICIENT USE OF RENEWABLE ENERGIES / MODEL EXPERIMENTAL DE SISTEM TERMIC COMBINAT PENTRU UTILIZAREA EFICIENTĂ A ENERGIILOR REGENERABILE Dumitrescu C.¹⁾, Rădoi R.*¹⁾, Cristescu C.¹⁾, Dumitrescu L.¹⁾ ¹⁾ Hydraulics and Pneumatics Research Institute INOE 2000-IHP, Bucharest / Romania</p>	287
33.	<p>KINETOSTATIC ANALYSIS OF THE PRECOMPACTION MECHANISM IN MUNICIPAL SOLID WASTE COLLECTING EQUIPMENT / ANALIZA CINETOSTATICĂ A MECANISMULUI DE PRECOMPACTARE LA MAȘINILE DE COLECTAT DEȘURI MENAJERE Moise V.¹⁾, Voicu Gh.*¹⁾, Lazea M.²⁾, Stoica D.¹⁾, Popa L.³⁾, Tudor P.¹⁾, Ungureanu L.¹⁾ ¹⁾ University Politehnica of Bucharest / Romania; ²⁾ CCR Romania; ³⁾ INMA Bucharest / Romania</p>	295
34.	<p>MODELING HERBICIDE INSTALLATION FOR THE TREATMENT OF PEACH PLANTATIONS / МОДЕЛИРАНЕ НА ХЕРБИЦИДНА УРЕДБА ЗА ТРЕТИРАНЕ НА НАСАЖДЕНИЯ ОТ ПРАСКОВИ Dimitar Kehayov^{*1)}; Atanas Atanasov²⁾ Agricultural University, Plovdiv, University of Ruse / Bulgaria</p>	303
35.	<p>EFFECTS OF DOUBLE V-SHAPED OPENERS WITH FURROW COMPACTION FUNCTION ON SEEDBED CHARACTERISTICS AND SOYBEAN EMERGENCE UNDER DOUBLE ROW RIDGE CULTIVATION TECHNIQUE / 垄上双行种植技术下具有种沟镇压功能的双V型筑沟器对种床特性和大豆出苗的影响 Jiaxin Zheng, Jiameng Fang, Yuqing Zhao, Yong Zhao, Zhi Yang, Rong Chen[*] School of Mechanical and Electrical Engineering, Yunnan Agricultural University, Kunming 650201, China</p>	311

DESIGN AND TEST OF VARIABLE DIAMETER PNEUMATIC DRUM TYPE BEAN SEED METERING DEVICE

变粒径气力滚筒式豆类种子精量排种器的设计与实验

Kaixing Zhang^{1,3}, Yuanyuan Sun¹, Lei Liu², Xianxi Liu^{1,3}, Xiuyan Zhao^{*1} ¹

¹) College of Mechanical and Electronic Engineering, ShanDong Agricultural University, Taian 271018, China

²) College of Vehicle Engineering, China Agricultural University, Beijing 100083, China

³) Shandong Provincial Engineering Laboratory of Agricultural Equipment Intelligence

^{*}) Corresponding author, E-mail address: sdauzhaoxiuyan@163.com

First author E-mail address: kaixingzhang@sda.u.edu.cn

DOI: <https://doi.org/10.35633/inmateh-60-01>

Keywords: variable particle size, metering device, pneumatic drum type, orthogonal experiment

ABSTRACT

The roller for seeds of different sizes, a variable-size pneumatic cylinder precision seed metering device was designed, which could realize the precision seeding of different diameter seeds without changing the roller. The structure and working principle of seed metering device were explained, and the structural parameters of the main components of the seed meter were determined. The ANSYS was used to analyse the influence of the size of the negative pressure inlet pipe and the shape of the eyelet on the airflow velocity in a negative pressure chamber. Based on the above optimal structure, the orthogonal experiment of seed metering device was carried out. Testing results showed: under the negative pressure of 4 kPa, roller speed of 16.93r/min and the wind speed of 11.48m/s, the seed metering device had the best seeding effect. The qualification rate of the seed metering device was 92.37%, the miss-seeding rate was 3.74% and the over-seeding rate was 3.88%.

摘要

针对豆类种子排种器对不同粒径种子进行排种时需要更换滚筒等问题,设计了一种变粒径气力滚筒式豆类种子精量排种器,无需更换滚筒便可实现不同径粒种子的精量播种。首先,阐释了排种器的结构以及工作原理,确定了排种器主要部件的结构参数。其次,通过 ANSYS 流体仿真分析了负压进气管结构尺寸和窝眼孔形状对负压腔内气流流速的影响。最后,基于上述优选结构对排种器进行正交实验。结果表明:滚筒转速为 16.93r/min,负压为 4.97kPa,清种风速为 11.48m/s 时为最佳参数组合,排种器的合格率为 92.37%,漏播率为 3.74%,重播率为 3.88%。

INTRODUCTION

In China, bean is one of the important food crops. The performance of the seed metering device directly affects the quality and effect of the seeding (Karayel D, 2009). The efficient, versatile, and qualified seed metering device provide strong support for the survival and development of beans. Owing to the adaptability of the air-suction metering device and the ability to achieve high speed and precision seeding, the air-suction metering device has gradually developed into the mainstream (Gaikwad B. B. and Sirohi N. P. S, 2008; Yang et al., 2016). Negative pressure, seed speed and suction hole shape have a great influence on the performance of the seeding device (Zeliha Bereket and Aziz, 2004; Singh R.C. et al., 2005; Jack St. Dylan et al., 2013; Dizaji H.Z et al., 2010). Singh et al. monitored the seed metering process in real time through an electronically controlled metering system, reducing the miss-seeding rate and improving seeding quality (Singh T. and Mane D., 2011). Qi Bing et al designed a circumferential cleaning device suitable for the seed metering device, which solved the serious problem of reseeded (Qi Bing et al., 2015).

The working parameters have a great influence on the seeding effect (Rajaiah. P et al, 2016; Yazgi A and Degirmencioglu A, 2014). Kumar Devesh et al. designed the seed metering device that overcomes the

¹ Kaixing Zhang, A/Prof. Ph.D. Eng.; Yuanyuan Sun, As. M.S. Stud. Eng.; Lei Liu, M.S. Stud. Eng.; Xianxi Liu, Prof. Ph.D. Eng.; Xiuyan Zhao, A/Prof. Ph.D. Eng.

uneven distribution of seeds (Kumar Devesh et al., 2017). Jia Honglei et al improved the seed filling effect by increasing the type of seed churning device and filling power (Jia H et al., 2018).

The above research did not realize the seeding of multi-size seeds. Therefore, this paper designed a seed meter that converts different pore diameters by double drum rotation combination, which can realize seeding of different particle sizes.

MATERIALS AND METHODS

• Overall scheme design

Structure and working principle

The seed metering device mainly consists of inner and outer roller, rotating handle, seed box, pressure releasing device and others, as shown in Fig.1

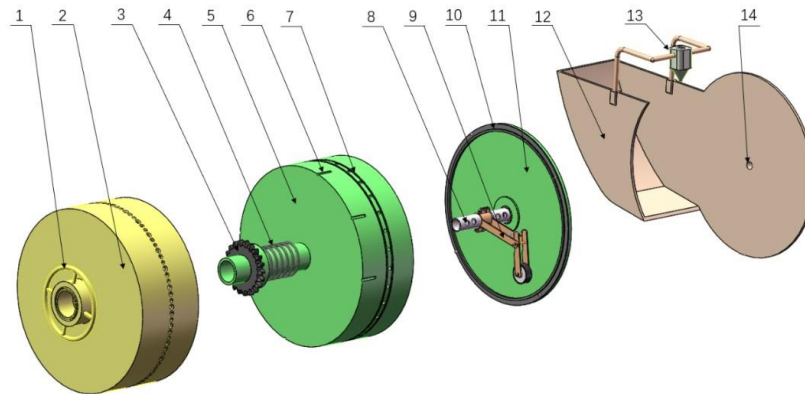


Fig.1 - Schematic diagram of seed metering device

1 -Rotating handle; 2 - Outer roller; 3 – Driving chain wheel; 4 – Spring; 5 - Inner roller; 6 - Groove;
7 - Seal ring; 8 – Intake manifold; 9 - Pressure releasing device; 10 - Seal ring; 11 - Rear cover; 12 - Seed box;
13 - Blow nozzle; 14 - Air inlet

With main seed metering disc rotated, the seeds are adsorbed on the holes by gas chamber negative pressure. When the seeds pass through the seed cleaner, the excess seeds are removed by the weight and the airflow produced by the blow nozzle. The seed rotates away from the zone of negative pressure with the disc, and the adsorption force of the seed disappears. The hole loses the adsorption force to the seed. Under the action of gravity and centrifugal force, the seed falls into the seed bed at a certain speed to complete the seeding process.

• Determination of main parameters

The diameter of the seeding drum is the basic characteristic parameter of the seed metering device, and its size affects the linear velocity of the seed metering device, the number of holes and other parameters. According to agricultural machinery design manual, the diameter range of the roller is 80~200mm. Therefore, the diameter of the outer roller is 200mm and the diameter of the inner roller is 196mm. Both materials are made of stainless steel with a thickness of 2mm.

$$\begin{cases} Q = \frac{V_s}{S} = \frac{v_l}{P} \\ 60v_l = \pi Dn \\ ZT = \pi D \\ 2d_{max} \leq T \end{cases} \quad (1)$$

Where:

Z is the number of holes; Q is the dropping frequency, [s⁻¹]; T is the distance of the holes, [m]; S is the plant spacing, [m]; v_l is the line speed of the metering device, [m/s]. P is the power, [W]; d_{max} is the maximum particle size of seeds, [m].

Each seed of Zhong Wan no.6, Qing Feng no.4 and Lin Fan no.6 was measured several times to obtain their respective triaxial dimensions. The equivalent diameter (D_s) was calculated according to the obtained average value.

$$D_s = \sqrt[3]{LWH} \tag{2}$$

Where:

- D_s is equivalent diameter, [mm];
- L is length, [mm]; W is width, [mm];
- H is thickness, [mm].

The results of the number of holes and equivalent particle size are shown in Table 1.

Table 1

Equivalent diameter size of beans and the number of holes			
Varieties of beans	plant spacing (m)	Number of holes	equivalent diameter (mm)
Zhong Wan no.6	0.25~0.40	18~27	6.70
Qing Feng no.4	0.40~0.55	20~35	8.80
Lin Fan no. 6	0.12~0.20	15~23	12.52

According to Table 1, the number of holes in the three types of beans is 20, all of which are uniformly placed on the drum. The combination of the holes is shown in Fig 2. From the empirical formula $d = (0.64\sim0.66) D_s$, it can be concluded that the diameter of class A hole is 8mm, that of class B hole is 5.8mm, and that of class C hole is 4.4mm.

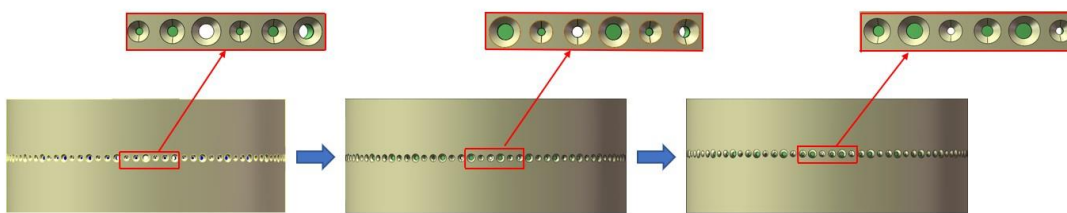


Fig. 2 - Combination diagram of three kinds of eyelet

• **Simulation analysis of planter based on ANSYS**

The model of seed metering device was imported into Geometry, and the seed metering device was meshed and simulated. The inlet pressure was set to 0 kPa, the outlet pressure was set to -5 kPa, the convergence accuracy was set to 0.001, and the number of iteration steps was set to 100 steps.

• **Influence of pipe diameter on flow velocity**

The diameter of the air outlet on the intake pipe was set to 6mm, and the arrangement was set to 6x6. The FLUENT was used to simulate the flow field in the negative pressure inlet pipe when the diameter was 15mm, 24mm, 30mm and 40mm, as shown in Fig.3 and Fig.4.

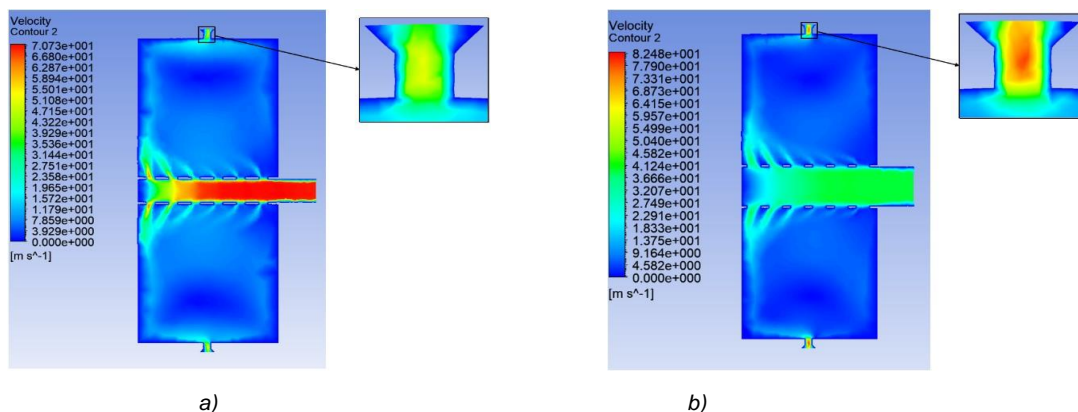


Fig. 3 - Velocity cloud diagram of negative pressure cavity with different tube diameters
 a) Diameter of 15 mm b) Diameter of 24 mm

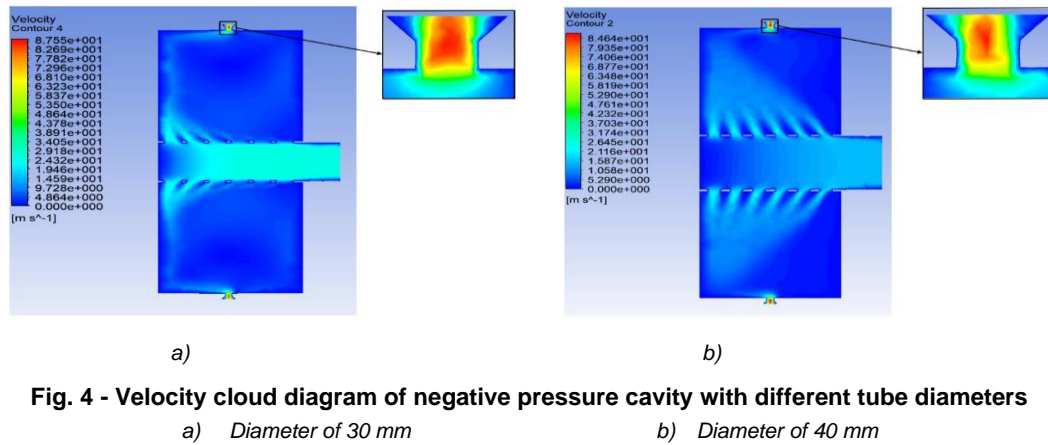


Fig. 4 - Velocity cloud diagram of negative pressure cavity with different tube diameters

When the diameter of the inlet pipe was 15 mm, the overall flow velocity in the intake pipe was large, and the flow velocity of each discharge port varied greatly, causing large reflux and eddy current. When the diameter of the inlet pipe was 24 mm, the flow velocity of each discharge port varied greatly, resulting in uneven flow field, large backflow and eddy current. When the diameter of the intake pipe was 30 mm, the overall flow velocity in the intake pipe did not change much, there was a gap in the flow velocity of each discharge port, and the phenomenon of reflux and eddy current was light. When the diameter of the intake pipe was 40mm, the overall flow velocity in the intake pipe did not change much, but the airflow had interference intersection.

Through the above analysis, it could be concluded that the effect was the best when the diameter of the intake pipe was 30 mm, so the diameter of the intake pipe was selected to be 30 mm.

• Influence of vent layout on Flow Speed

The diameter of the negative pressure intake pipe was set to 30mm, and the mode of arrangement was 4 × 4, 6 × 6, and 8 × 9. Flow field in negative pressure cavity were shown in Fig. 5. When the vent layout was 6 × 6, the red part of the velocity cloud at the hole of the seeder was full of the main suction area, and the overall flow field speed was better than the other two cases, so the vent layout was selected to be 6×6.

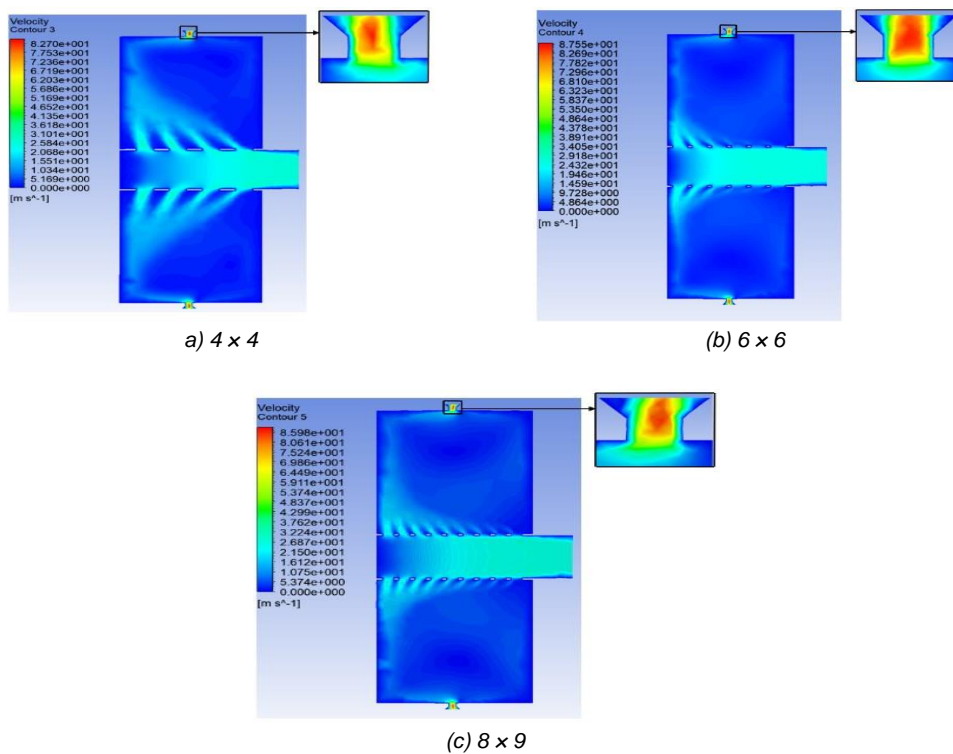


Fig. 5 - Velocity cloud diagram of negative pressure cavity with different vent layout

• **Influence of hole shape on Flow Speed**

The shape of the socket hole is also the key to affect the suction process and the carrying process. The straight type, the tapered hole type, the countersunk head shape and chamfering type were selected as the variables for simulation analysis, and the meshing result were shown in Fig. 6.

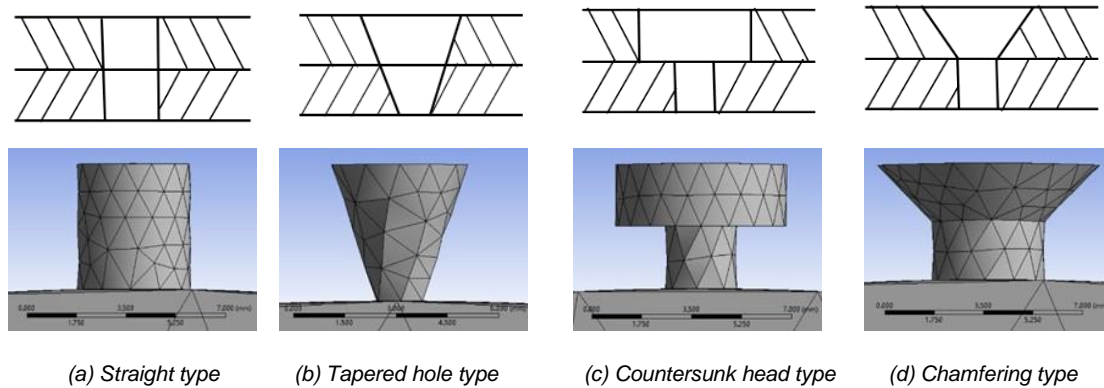


Fig. 6 - Shape and mesh of socket hole

The airflow velocity of the negative pressure cavity under different socket holes is shown in Fig. 7.

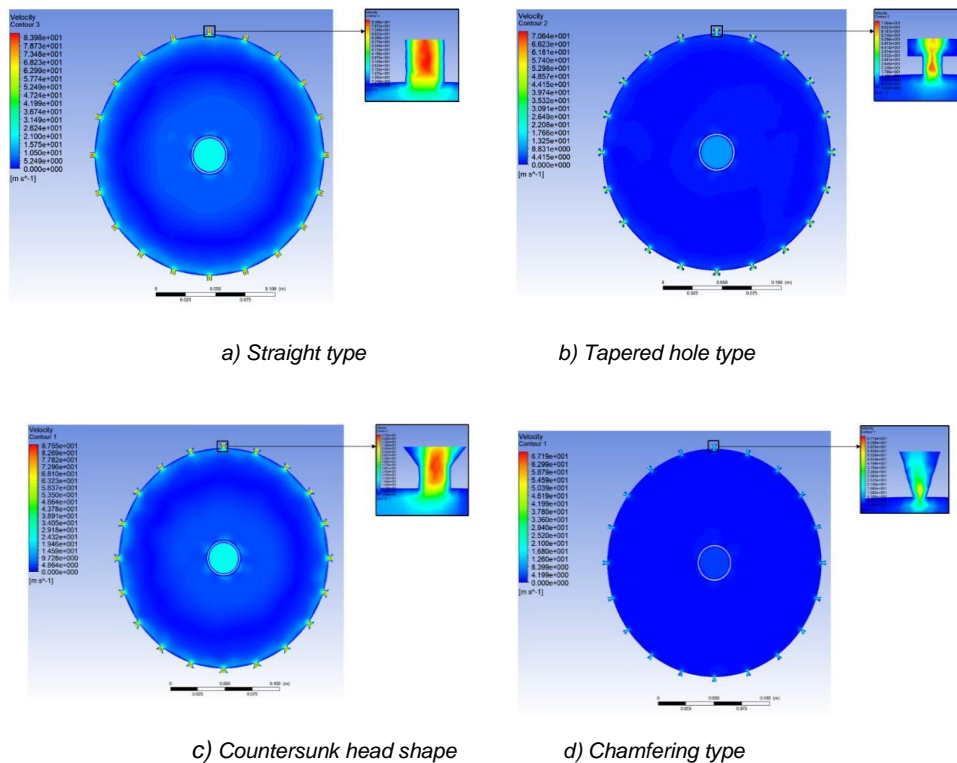


Fig. 7 - Airflow velocity map under different socket hole

Because the gas flow channel did not change, the gas velocity inside the whole straight cylindrical hole was evenly distributed and relatively large. The maximum gas velocity of the cone hole occurred at the minimum diameter of the socket hole. The gas velocity gradually decreased along the bus of the hole to the outer end, and the gas velocity at the outermost edge of the hole was only 5m/s.

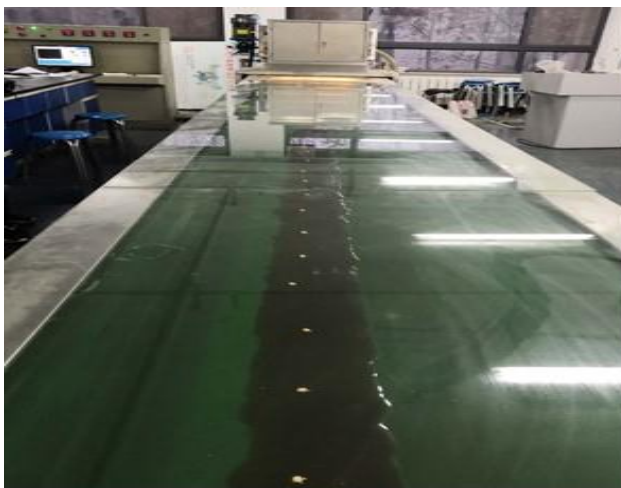
Owing to the sudden change of the circular section of the countersunk head, the gas flow velocity in the straight section was disturbed, and the maximum flow velocity of the centre strip was divergent outward, and the lowest velocity of the gas flow appeared on the wall surface. The gas flow velocity at the chamfered hole was gradually increased from the wall toward the centre of the hole, reaching a maximum at the centre.

Considering the rationality of the structure of the socket hole and the flow velocity, the socket hole was selected as chamfering type.

• Test materials and methods



a) Control console



b) Test bench

Fig. 8 - JSP-12 type seed meter performance test bench

This experiment was carried out on the JSP-12 type seed meter performance test bench. Qing Feng no.4 was selected as the test object. According to the theoretical analysis and pre-test, the cylinder speed range was 15~20 r/min, the negative pressure range was 4~6 kPa, and the air blowing speed range was 10~12m/s. Cylinder speed X_1 , negative pressure X_2 and air blowing speed X_3 were selected as test factors, and the qualification rate A, miss-seeding rate D and over-seeding rate M were selected as seed metering performance indicators.

• Test plan design

According to the design principle of Central Composite Design, the paper made response surface test analysis on the Cylinder speed X_1 , negative pressure X_2 and air blowing speed X_3 in three factors and five levels. These factors were marked as $X_1 - X_3$. The test factor codes and level are shown in Table 2.

Table 2

Encoding of test factors			
Coding	Cylinder speed $X_1/(r \cdot \text{min}^{-1})$	Negative pressure X_2/kPa	air blowing speed $X_3/(m \cdot s^{-1})$
1.682	21.70	6.68	12.68
1	20.00	6.00	12.00
0	17.50	5.00	11.00
-1	15.00	4.00	10.00
-1.682	13.29	3.32	9.32

RESULTS

• Results of experimental schemes

Each group of experiments was repeated three times, and the design and results of experimental schemes were shown in Table 3.

Table 3

Design and results of experimental schemes						
Test groups	X_1	X_2	X_3	Response values		
				A	D	W
1	-1	1	1	90.35	5.78	3.87
2	0	0	-1.682	85.13	9.93	4.94
3	0	0	0	91.61	4.78	3.61

Test groups	X ₁	X ₂	X ₃	Response values		
				A	D	W
4	0	0	0	91.91	4.33	3.75
5	0	0	1	90.77	3.84	5.39
6	0	0	0	91.47	4.31	4.22
7	-1	-1	-1	88.85	6.57	4.58
8	-1	0	0	89.54	5.82	4.64
9	0	1.682	0	89.63	5.74	4.64
10	0	0	0	92.35	3.72	3.93
11	1	1	1	89.71	3.15	7.14
12	1.682	0	0	87.92	4.13	7.95
13	-1	1	-1	86.38	8.99	4.62
14	0	0	0	91.87	4.35	3.78
15	-1	-1	1	90.12	4.95	4.93
16	0	0	0	92.34	3.44	4.22
17	0	-1.682	0	90.72	3.83	6.35
18	1	1	-1	85.58	8.35	6.07
19	1	-1	1	91.4	2.19	6.41
20	1	-1	-1	87.92	6.07	6.01

- **Picking performance test analysis and the establishment of regression equations**

Design-Expert was used to obtain the response surface model of comprehensive index Y through multiple regressions fitting for the test results, and made variance analysis on the quadratic equation of the response surface model. It also made significant testing to the terms of regression equations. The significance test results are shown in Table 4.

Table 4

Regression coefficient Y and its significant test

Source of variation	Qualification rate				Miss-seeding rate				Over-seeding rate			
	Square sum	Degree of freedom	Value of F	Value of P	Square sum	Degree of freedom	Value of F	Value of P	Square sum	Degree of freedom	Value of F	Value of P
X1	1.07	1	4.63	0.0469	6.43	1	36.11	0.0001	12.75	1	71.84	<0.0001
X2	4.81	1	20.90	0.0010	6.89	1	38.70	<0.0001	0.71	1	3.98	0.0440
X3	36.53	1	158.78	<0.0001	42.71	1	239.79	<0.0001	0.24	1	1.38	0.0279
X1X2	0.40	1	1.74	0.2164	1.25	1	0.70	0.9935	0.41	1	2.31	0.1597
X1X3	0.70	1	3.05	0.1112	2.26	1	12.68	0.0052	0.44	1	2.46	0.1477
X2X3	1.40	1	6.10	0.0331	1.06	1	5.94	0.0350	0.02	1	0.13	0.7257
X12	18.27	1	79.41	<0.0001	1.44	1	8.08	0.0175	8.69	1	48.93	<0.0001
X22	5.45	1	23.69	0.0007	0.89	1	5.01	0.0492	3.51	1	19.77	0.0012
X32	28.31	1	123.07	<0.0001	14.16	1	79.50	<0.0001	2.05	1	11.53	0.0048
Model	89.59	9	43.27	<0.0001	74.45	9	46.44	<0.0001	26.79	9	16.77	<0.0001
Residual	2.30	10			1.78	10			1.77	10		
Lack of fit	1.64	5	2.47	0.1714	0.60	5	0.50	0.7645	1.45	5	4.47	0.0631
Error	0.66	5			1.18	5			0.32	5		
Sum	91.89	19			76.23	19			28.56	19		

Note: $p < 0.5$ (significant)

In the qualification rate model of the metering device, the P was less than 0.0001, and the effect was significant. The P in the missed term was equal to 0.1714, and the effect was not significant. It was shown that within a certain range of parameters, the regression model of the qualification rate had a high degree of fit. The P of $X_1, X_2, X_3, X_2X_3, X_{12}, X_{22}$ and X_{32} was less than 0.05, and the effect was significant. The P of X_1X_2 and X_1X_3 was greater than 0.1, and the effect was not significant. In the miss-seeding rate model of the seed metering device, the P was less than 0.0001, and the effect was significant. The P in the missed term was equal to 0.7645, and the effect was not significant.

It was shown that within a certain range of parameters, the regression model of the miss-seeding rate had a high degree of fit. The P of $X_1, X_2, X_3, X_1X_3, X_2X_3, X_{12}, X_{22}$ and X_{32} was less than 0.05, and the effect was significant. The P of X_1X_2 was greater than 0.05, and the effect was not significant. In the over-seeding rate model of the metering device, the P was less than 0.0001, and the effect was significant.

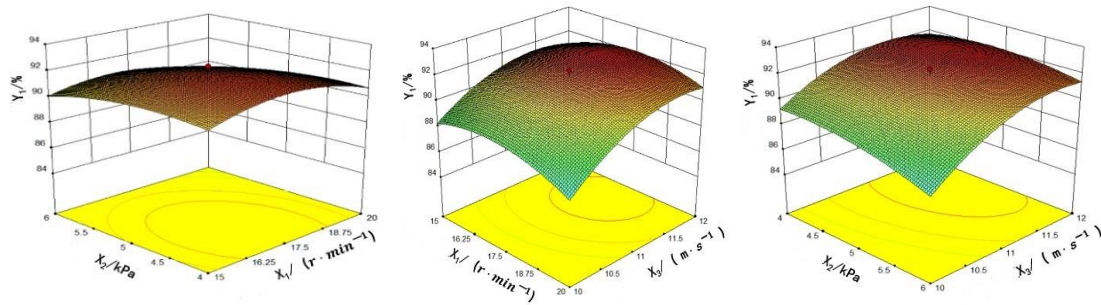
The P in the missed term was equal to 0.0631, and the effect was not significant. It was shown that within a certain range of parameters, the regression model of the over-seeding rate had a high degree of fit. The P of $X_1, X_2, X_3, X_{12}, X_{22}$ and X_{32} was less than 0.05, and the effect was significant. The P of X_1X_2, X_1X_3 and X_2X_3 was greater than 0.05, and the effect was not significant.

The models excluding the insignificant regression term are specific to:

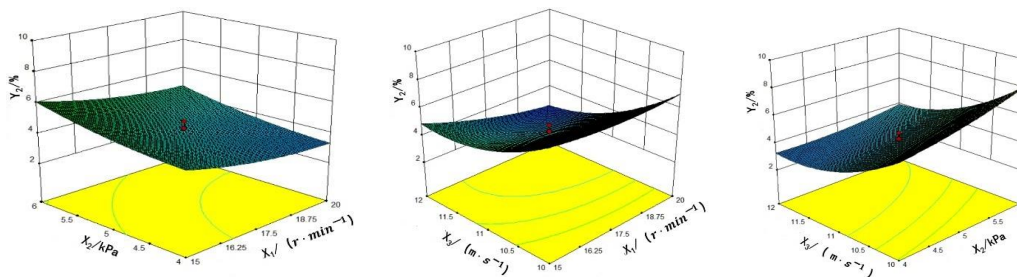
$$\begin{cases} Y_1 = 91.92 - 0.28 X_1 - 0.59 X_2 + 1.64 X_3 - 0.22 X_1 X_2 + 0.30 X_1 X_3 + 0.42 X_2 X_3 - 1.13 X_1^2 - 0.62 X_2^2 - 1.40 X_3^2 \\ Y_2 = 4.15 - 0.69 X_1 + 0.71 X_2 - 1.77 X_3 - 0.00125 X_1 X_2 - 0.53 X_1 X_3 - 0.36 X_2 X_3 + 0.32 X_1^2 + 0.25 X_2^2 + 0.99 X_3^2 \\ Y_3 = 3.93 + 0.97 X_1 - 0.23 X_2 + 0.13 X_3 + 0.23 X_1 X_2 + 0.23 X_1 X_3 - 0.054 X_2 X_3 + 0.78 X_1^2 + 0.49 X_2^2 + 0.38 X_3^2 \end{cases} \quad (3)$$

• Analysis on the impact of test factors

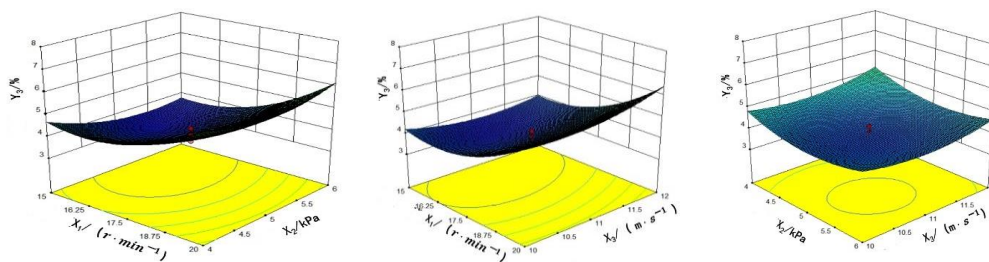
In order to more intuitively analyse the relationship between various influencing factors and the performance of seed metering device, the response surface graph was obtained by processing the data of orthogonal test, as shown in Fig. 9.



a) the influence of various factors on the qualification rate



b) the influence of various factors on the miss-seeding rate



c) the influence of various factors on the over-seeding rate

Fig. 9 - Influences of various factors on evaluation indexes

With the increase of cylinder speed, qualification rate increased first and then decreased, and the miss-seeding rate and over-seeding rate decreased first and then increased. With the increase of negative pressure, the qualification rate increased first and then decreased, and the miss-seeding rate and over-seeding rate decreased first and then increased. With the increase of the air blowing speed, the qualification rate increased first and then decreased, and the miss-seeding rate and over-seeding rate decreased first and then increased.

- **Optimization of the picking condition and test of the regression model**

From the above experiments and analysis, the optimal parameter combination is that the cylinder speed is 16.93 r/min, the negative pressure is 4.97 kPa and the air blowing speed is 11.48 m/s. At this moment, the qualification rate of seed metering device is 92.37%, the miss-seeding rate is 3.74%, and the over-seeding rate is 3.88%.

The optimized theoretical results were tested and verified on the test bench. The cylinder speed of the drum was set at 16.9 r/min, the negative pressure was set at 5.0 kPa, vent layout was selected to be 6×6, and the air blowing speed was set at 11.5m/s. Three repeated tests were carried out.

The average qualification rate was 92.15%, the average miss-seeding rate was 3.82%, and the average over-seeding rate was 4.03%. The experimental results were basically consistent with the theoretical results.

CONCLUSIONS

(1) To solve the problem of changing the drum for seeds with different grain sizes, a double-drum structure with different grain sizes combined by rotating the drum was designed. The precision sowing of seeds with different sizes could be realized without changing the drum, which improved the generality of the seed metering device and saved the cost.

(2) Under the negative pressure of 4 kPa, roller speed of 16.93 r/min and the wind speed of 11.48 m/s, the seed metering device has the best seeding effect; The qualification rate of the seed metering device was 92.37%, the miss-seeding rate was 3.74%. The over-seeding rate was 3.88%.

(3) The seed meter meets the sowing requirements, and the performance of the seed metering device is significantly improved compared with the traditional seed metering device, providing good conditions for seed growth.

ACKNOWLEDGEMENT

The study was supported by the Key research and development project in Shandong province (2017NC212008).

REFERENCES

- [1] Dizaji H.Z., Aheram R.Y., Minaei S., (2010), Air-jet seed knockout device for pneumatic precision planters. *AMA-Agricultural Mechanization in Asia, Africa and Latin America*, vol. 41, issue 1, pp. 45-50;
- [2] Gaikwad B. B., Sirohi N. P. S., (2008), Design of a low-cost pneumatic seeder for nursery plug trays. *Biosystems Engineering*, vol. 99, issue 3, pp. 322-329;
- [3] Jack D., Hesterman D., Guzzomi A., (2013), Precision metering of Santalum spicatum (Australian Sandalwood) seeds. *Biosystems Engineering*, vol. 115, issue 2, pp. 171-183;
- [4] Jia H., Chen Y., Zhao J. et al., (2018), Design and key parameter optimization of an agitated soybean seed metering device with horizontal seed filling. *International Journal of Agricultural & Biological Engineering*, vol. 11, issue 2, pp. 76-87;
- [5] Karayel D., (2009), Performance of a modified precision vacuum seeder for no-till sowing of maize and soybean. *Soil and Tillage Research*, vol. 104, issue 1, pp. 121-125;
- [6] Kumar Devesh, Tripathi Ashok, Kant Kam et al., (2017). Design and laboratory test of a seed metering device of sowing soybean seeds. *Asian Journal of Multidimensional Research (AJMR)*, vol. 6, issue 2, pp. 57-66;
- [7] Qi Bing, Zhang Dongxing, Liu Quanwei et al., (2015), Design and experiment of cleaning performance in a centralized pneumatic metering device for maize. *Transactions of the Chinese Society of Agricultural Engineering (Transactions of the CSAE)*, vol. 31, issue 1, pp. 20-27;

- [8] Rajaiah P.I. Mani A. Kumar et al., (2016), Development and evaluation of electronically controlled precision seed-metering device for direct-seed paddy planter. *Indian Journal of Agricultural Sciences*, vol. 86, issue 5, pp. 598-604;
- [9] Singh R. C., Singh G., Saraswat D. C., (2005), Optimization of Design and Operational Parameters. of a Pneumatic Seed Metering Device for planting Cottonseeds, *Biosystems Engineering*, vol. 92, issue 4, pp. 429-438;
- [10] Singh T., Mane D., (2011), Development and laboratory performance of an electronically controlled metering mechanism for okra seed. *Agricultural Mechanization in Asia, Africa and Latin America*, vol. 42, issue 2, pp. 63-69;
- [11] Yazgi A., Degirmencioglu A., (2014), Measurement of seed spacing uniformity performance of a precision metering unit as function of the number of holes on vacuum plate. *Measurement* vol. 56, issue10, pp. 128-135;
- [12] Yang L., Yan B. X., Cui T., Yu Y.H. He X.T., Liu Q. W., Liang Z. J, Yin X.W., Zhang D. X., (2016), Global overview of research progress and development of precision maize planter. *International Journal of Agricultural & Biological Engineering*. vol. 9, issue 1, pp. 9-26;
- [13] Zeliha Bereket Aziz, (2004), Effect of Different Operating Parameters on Seed Holding in the Single Seed Metering Unit of a Pneumatic Planter. *Turkish Journal of Agricultural and Forestry*, vol.28, issue 6, pp. 435-441.

MATHEMATICAL MODELING AND STUDY OF THE GRAIN CLEANING MACHINE SIEVE FRAME OPERATION

МАТЕМАТИЧЕСКОЕ МОДЕЛИРОВАНИЕ И ИССЛЕДОВАНИЕ РАБОТЫ РЕШЕТНОГО СТАНА ЗЕРНООЧИСТИТЕЛЬНОЙ МАШИНЫ

Ildar Badretdinov ^{*}), Salavat Mudarisov, Ramil Lukmanov, Radik Ibragimov, Valeri Permyakov, Marat Tuktarov

Federal State Budgetary Educational Establishment of Higher Education "Bashkir State Agrarian University", Ufa / Russia

Tel: 7(347)2283213; E-mail: badretdinovil@rambler.ru

DOI: <https://doi.org/10.35633/inmateh-60-02>

Keywords: grain cleaning machine, kinematic scheme, mathematical model, modeling, sieve frame, technological process.

ABSTRACT

The purpose of this work is a mathematical description of sieve frame structural and technological parameters necessary for the implementation of the technological process model of a grain cleaning machine operation. The paper presents the results of the study of the grain cleaning machine sieve frame operation. A kinematic study of a flat swivel multi-link mechanism of the grain cleaning machine sieve frame was made. The method of determining the coordinates of the sieve frame nodal points was developed to calculate their speed. Structural and technological parameters of the mechanism were also studied.

АННОТАЦИЯ

Цель данной работы – математическое описание структурных и технологических параметров решетного стана, необходимых для реализации модели технологического процесса работы зерноочистительной машины. В статье представлены результаты исследования работы решетного стана зерноочистительной машины. Проведено кинематическое исследование плоского шарнирного многозвенного механизма решетного стана зерноочистительной машины, для которого известны все геометрические размеры и закон движения ведущего звена. Приведена методика определения координат узловых точек решетного стана для расчета скорости их движения, а также исследование конструктивно-технологических параметров механизма.

INTRODUCTION

Today, grain cleaning machines with a sieve cleaning system are dominant means of removing impurities from food and seed grain (Dorokhov et al., 2018; Ma et al., 2018; Okunola et al., 2018; Vasylykovskiy et al., 2019). Design of grain cleaning machines with such a working body is rather simple, easy to use, the most universal and popular in agricultural production (Ma et al., 2018; Okunola et al., 2018; Popov et al., 2015; Shevtsov and Beznosov, 2014; Vasylykovskiy et al., 2019). The separation of grain heap on sieves occurs according to geometric parameters, i.e. according to seed thickness and width. Thickness is the smallest geometric size of a single seed (of an ellipsoid shape), and the width is the average grain size (Steponavičius et al., 2008; Vasylykovskiy et al., 2019). Grain material is split by width on sieves with round holes: grains, the width of which is less than the diameter of the sieve holes, pass through them (passage), and large grains are thrown out from the sieve (descent). By thickness, grain material is split on the sieve with oblong holes. Sieve frames are usually sprung (with flexible springs). The springs make oscillatory motion provided by crank gear. Sieve frame oscillation frequency varies from 420 to 500 min⁻¹, oscillations amplitude $A = 7.5...15$ mm, canting angle is equal to 5...8 degrees (Okunola et al., 2018; Popov et al., 2015; Shevtsov and Beznosov, 2014; Singh et al., 2017). The sieves are mainly installed as follows: first sieves for large impurities separation are installed, and then sieves for small impurities separation are placed (i.e. for feeble and crushed grain). To increase productivity sieves are arranged by parallel tiers. Grain crops have an ellipsoidal shape (Fominykh, 2006; Kornev, 2015; Kundu and Gupta, 2014; Voicu et al., 2008).

Most of crop production area of the Russian Federation is used for small grains and pulse crops (about 60%). The most common crops are wheat, barley, rye and oats. According to statistical data of the Ministry of Agriculture of the Russian Federation the record bulk yield of wheat during the last three years was in 2017 and made 85 Mt (the weight of wheat after cleaning).

To improve the efficiency of grain separation process carried out using sieve frames, it is necessary to know the laws of sieve frame drive system operation, as well as structural and technological parameters of the links of a sieve mechanism. Service properties of sieve system grain cleaning machines do not fully meet the increasing requirements of modern agricultural production. Imperfect design results in vibration and bad separation of grain heap (Popov et al., 2015; Singh et al., 2017; Steponavičius et al., 2008). Vibration in its turn negatively affects the design of the grain cleaning machine and destroys its driving gear. There are many difficulties during the technological process of grain sieving connected with a wide range of cultures, various geometrical sizes and physical and mechanical parameters of seeds, on which the sieve selection depends. The interaction process of separated materials' components with the working bodies of the machine is also rather complicated.

Another difficulty of the grain sieving process is insufficient development of its theoretical framework as well as of the justification methods of machines parameters and their operating modes (Fominykh, 2006; Giyevskiy et al., 2018; Kornev, 2015; Singh et al., 2017; Tarasenko et al., 2012; Vasylykovskiy et al., 2019). In this regard, there is a need to improve both the theory of separation and the design of grain cleaning machines' sieve frames (Dorokhov et al., 2018; Fominykh, 2006; Kornev, 2015; Mudarisov and Badretdinov, 2008; Steponavičius et al., 2008; Tarasenko et al., 2012).

The purpose of this study is to develop a mathematical model of the functioning of kinematic mechanism of the grain cleaning machine sieve frame, to determine the coordinates of the sieve mechanism node points, as well as the links velocity and acceleration, to establish a scientific rational for the kinematic parameters of a sieve frame and a grain heap to implement a mathematical model for the technological process of the grain cleaning machine sieve frame operation taking into account its structural and technological parameters.

MATERIALS AND METHODS

The Froude number is one of the most important functional parameters for estimating grain material movement on the sieve surface. It reflects the ratio of forces acting on a single seed lying on the sieve, the sieve oscillations amplitude and gravity (Savinyh et al., 2018; Steponavičius et al., 2008).

Let us consider a design model used to determine the coordinates of the sieve frame nodal points of the grain cleaning machine ZVS-20 (The constructive parameters of the mechanism, m: $OA = OA_1 = 0.01$, $AB = 0.45$, $A_1B_1 = 0.5$, $O_1B = O_2C = O_3B_1 = O_4C_1 = 0.355$, $BC = 1.758$, $B_1C_1 = 1.764$) necessary to calculate their speed and inertia forces acting on grain heat components on the sieve (Figure 1).

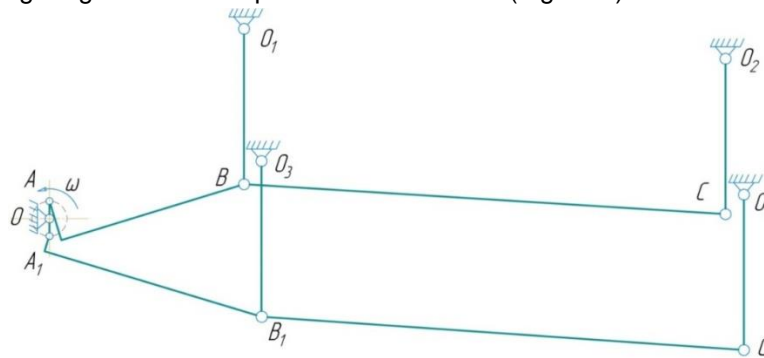


Fig. 1 - Design model of the grain cleaning machine sieve frame

Let h_k and l_k be the coordinates of anchor poles O_k , $k = 1, 2, 3, 4$. Right-handed Cartesian coordinate system will be taken as the reference frame. The origin of the coordinate system is located in the sieve frame drive shaft marked as point O . We plot the sieve frame nodal points to compose the equations of geometric relations, trajectories of which are known: A, B, C, A_1, B_1, C_1 . These points move round radii circles $OA, O_1B, O_2C, OA_1, O_3B_1, O_4C_1$ respectively. Point A simultaneously belongs to the crank OA and to the connecting rod AB . The crank OA of radius r ($r = OA = OA_1$) makes a rotational motion and accordingly the motion law of point A is known. Point A at time t , depending on the rotation angle value of the driving link $\varphi(t)$ has coordinates:

$$x_A = r \cdot \cos \omega_0 t, \quad y_A = r \cdot \sin \omega_0 t \quad (1)$$

The motion law of the driving link of the mechanism:

$$\varphi(t) = \omega_0 t,$$

Point *B* belongs simultaneously to the connecting rod *AB* and the crank *O₁B*. Point *C* belongs to the connecting rod *BC* and to the crank *O₂C*. Three independent parameters are necessary to describe plane motion of the sieve frame nodal points. They are: the *x*, *y* coordinates of the point and the rotation angle φ around this pole. The position of a planar figure in its plane at any given time can be completely determined by the time functions. It is called the equations of the planar figure motion:

$$x_A = x_A(t), \quad y_A = y_A(t), \quad \varphi = \varphi(t) \quad (2)$$

The position of a planar figure (sieve frame) in its plane is determined by the position of its two points. As base points in the equations of geometric relations we take points *B* and *C* (Figures 2, 3).

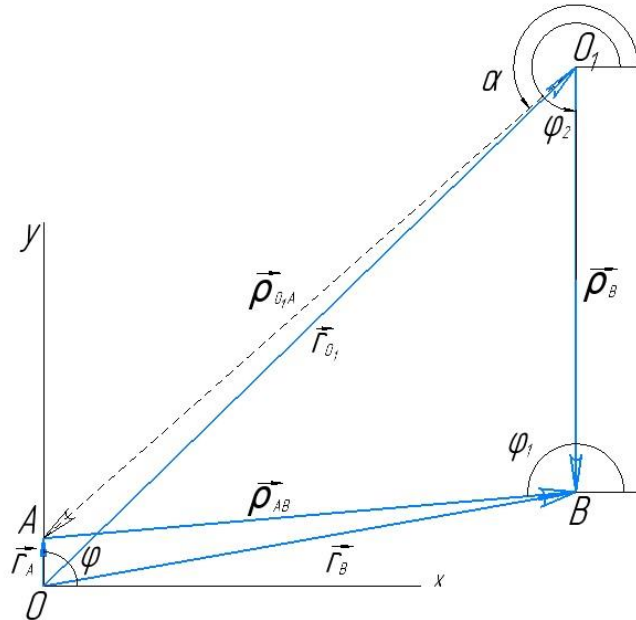


Fig. 2 - Vector paths for finding point B

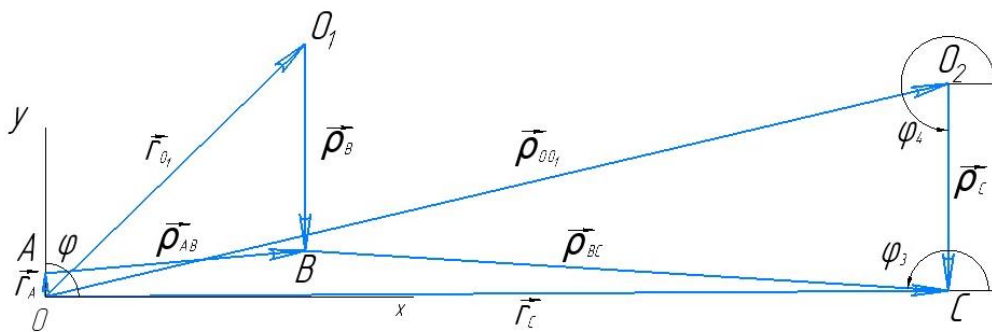


Fig. 3 - Vector paths for finding point C

We project vectors on the coordinate axes *Ox* and *Oy* to obtain the equations of geometric relations of the links of the sieve mechanism.

$$\begin{aligned} OA \cos(\varphi) + AB \cos(\varphi_1) &= l_1 + O_1B \cos(\varphi_2) \\ OA \sin(\varphi) + AB \sin(\varphi_1) &= h_1 + O_1B \sin(\varphi_2) \\ l_1 + O_1B \cos(\varphi_2) + BC \cos(\varphi_3) &= l_2 + O_2C \cos(\varphi_4) \\ h_1 + O_1B \sin(\varphi_2) + BC \sin(\varphi_3) &= h_2 + O_2C \sin(\varphi_4) \end{aligned} \quad (3)$$

To obtain the equation of geometric relations in a coordinate form we transfer the summands with unknown functions to one side:

$$\begin{aligned} AB \cos(\varphi_1) - O_1B \cos(\varphi_2) &= l_1 - OA \cos(\varphi), \\ AB \sin(\varphi_1) - O_1B \sin(\varphi_2) &= h_1 - OA \sin(\varphi) \end{aligned} \quad (4)$$

In equations (3) the given function is the law of a driving link $\varphi(t)$.

The calculated functions of time are: $\varphi_1(t)$, $\varphi_2(t)$, $\varphi_3(t)$, $\varphi_4(t)$.

We solve the system of nonlinear equations (3) using the analytical method, and thus obtain expressions for the required functions in parametric form.

To determine the movement of the links of the sieve frame mechanism we write down the equations for point B:

$$\begin{aligned} AB \cos(\varphi_1) - O_1B \cos(\varphi_2) &= l_1 - OA \cos(\varphi) = -O_1A \cos \alpha \\ AB \sin(\varphi_1) - O_1B \sin(\varphi_2) &= h_1 - OA \sin(\varphi) = -O_1A \sin \alpha. \end{aligned} \quad (5)$$

where $O_1A \cos \alpha$ and $O_1A \sin \alpha$ is a projection of the vector p_{O_1A} onto a coordinate axis.

$$O_1A = \sqrt{(O_1A \cos \alpha)^2 + (O_1A \sin \alpha)^2} = \sqrt{OO_1^2 + OA^2 - 2 \cdot OA \cdot OO_1 \cos(\varphi - \beta)} \quad (6)$$

$$OO_1 = \sqrt{h_1^2 + l_1^2}, \quad \beta = \arctg\left(\frac{h_1}{l_1}\right) \text{ module and direction of the vector } r_{O_1}$$

$$\begin{aligned} AB \cos(\varphi_1) &= O_1B \cos(\varphi_2) - O_1A \cos \alpha, \\ AB \sin(\varphi_1) &= O_1B \sin(\varphi_2) - O_1A \sin \alpha. \end{aligned} \quad (7)$$

We square both sides of the equation and sum the first with the second, using trigonometric formulas, we get:

$$\begin{aligned} AB^2 &= O_1B^2 + O_1A^2 - 2 \cdot O_1B \cdot O_1A \cdot \cos(\varphi_2 - \alpha) \\ \varphi_2 &= \alpha + \arccos\left(\frac{O_1B^2 + O_1A^2 - AB^2}{2 \cdot O_1B \cdot O_1A}\right) \end{aligned} \quad (8)$$

We rewrite equation (4) to find the angular coordinate φ_1 :

$$\begin{aligned} O_1B \cos(\varphi_2) &= AB \cos(\varphi_1) + O_1A \cos \alpha, \\ O_1B \sin(\varphi_2) &= AB \sin(\varphi_1) + O_1A \sin \alpha. \\ O_1B^2 &= AB^2 + O_1A^2 + 2 \cdot AB \cdot O_1A \cdot \cos(\varphi_2 - \alpha), \end{aligned}$$

The final form of the angular coordinate φ_1 is:

$$\varphi_1 = \alpha + \arccos\left(\frac{O_1B^2 - O_1A^2 - AB^2}{2 \cdot AB \cdot O_1A}\right) \quad (9)$$

Since the links of the sieve mechanism are suspended in parallel, the angular coordinate $\varphi_2 = \varphi_4$.

The remaining unknown values of the equation system (3) are found on the same model.

$$\begin{aligned} l_1 + O_1B \cos(\varphi_2) + BC \cos(\varphi_3) &= l_2 + O_2C \cos(\varphi_4) \\ h_1 + O_1B \sin(\varphi_2) + BC \sin(\varphi_3) &= h_2 + O_2C \sin(\varphi_4) \\ \varphi_3 &= -\arccos\left(\frac{l_2 - l_1 + O_2C \cos(\varphi_4) - O_1B \cos(\varphi_2)}{BC}\right) \end{aligned} \quad (10)$$

We differentiate with respect to time the equations of geometric connections (3) to determine the angular velocities of the links of the sieve frame mechanism.

$$\begin{aligned} -AB \cdot \sin(\varphi_1)\omega_1 \quad O_1B \cdot \sin(\varphi_2)\omega_2 \quad 0 \quad 0 &= OA \cdot \sin(\varphi)\omega_0, \\ AB \cdot \cos(\varphi_1)\omega_1 \quad -O_1B \cdot \cos(\varphi_2)\omega_2 \quad 0 \quad 0 &= -OA \cdot \cos(\varphi)\omega_0, \\ 0 \quad -O_1B \cdot \sin(\varphi_2)\omega_2 - BC \cdot \sin(\varphi_3)\omega_3 \quad O_2C \cdot \sin(\varphi_4)\omega_4 &= 0, \\ 0 \quad O_1B \cdot \cos(\varphi_2)\omega_2 \quad BC \cdot \cos(\varphi_3)\omega_3 - O_2C \cdot \cos(\varphi_4)\omega_4 &= 0. \end{aligned} \quad (11)$$

The system of equations (8) is represented in matrix form:

$$A \cdot X_\omega = B, \quad (12)$$

where A is the matrix of coefficients of the left parts of the equations; X_ω is the vector of unknown angular velocities of the links; B is the vector of the right parts of the equations.

$$\begin{aligned} A &= \begin{pmatrix} -AB \cdot \sin(\varphi_1) & O_1B \cdot \sin(\varphi_2) & 0 & 0 \\ AB \cdot \cos(\varphi_1) & -O_1B \cdot \cos(\varphi_2) & 0 & 0 \\ 0 & -O_1B \cdot \sin(\varphi_2) & -BC \cdot \sin(\varphi_3) & O_2C \cdot \sin(\varphi_4) \\ 0 & O_1B \cdot \cos(\varphi_2) & BC \cdot \cos(\varphi_3) & -O_2C \cdot \cos(\varphi_4) \end{pmatrix} \\ X_\omega &= \begin{bmatrix} \omega_1 \\ \omega_2 \\ \omega_3 \\ \omega_4 \end{bmatrix}, \quad B = \begin{bmatrix} OA \cdot \sin(\varphi)\omega_0 \\ -OA \cdot \cos(\varphi)\omega_0 \\ 0 \\ 0 \end{bmatrix} \end{aligned}$$

The solution of the equations (9) has the following form:

$$X_\omega = A^{-1} \cdot B \quad (13)$$

To determine the angular accelerations of the links of the sieve frame mechanism we will differentiate with respect to time equation (8) and obtain a system of equations in matrix form:

$$A \cdot X_a = C \tag{14}$$

where C is the vector of the right parts of the equations.

Solution of the equations (11) allows us to determine the angular acceleration of the links of the sieve frame mechanism. It has the following form:

$$X_a = A^{-1} \cdot C \tag{15}$$

$$C = \begin{pmatrix} OA \cos(\varphi)\omega_0^2 + AB \cos(\varphi_1)\omega_1^2 - O_1B \cos(\varphi_2)\omega_2^2 \\ OA \sin(\varphi)\omega_0^2 + AB \sin(\varphi_1)\omega_1^2 - O_1B \sin(\varphi_2)\omega_2^2 \\ -O_1B \cos(\varphi_2)\omega_2^2 - BC \cos(\varphi_3)\omega_3^2 + O_2C \cos(\varphi_4)\omega_4^2 \\ -O_1B \sin(\varphi_2)\omega_2^2 - BC \sin(\varphi_3)\omega_3^2 + O_2C \sin(\varphi_4)\omega_4^2 \end{pmatrix}$$

We determine velocities and accelerations of the nodal points of the sieve frame mechanism using Figures 2, 3, and taking into account that the vector modules are constant and their derivatives with time can be determined using Euler formula:

$$\dot{\vec{r}} = \vec{\omega} \times \vec{r} \tag{16}$$

We find the velocities of the nodal points of the sieve frame mechanism:

$$\vec{v}_A = \vec{\omega}_0 \times \vec{r}_A, \quad \vec{v}_B = \vec{\omega}_2 \times \vec{\rho}_B, \quad \vec{v}_C = \vec{\omega}_4 \times \vec{\rho}_C. \tag{17}$$

Having differentiated with respect to time expression (14), we find the acceleration of these points:

$$\begin{aligned} \vec{a}_A &= \dot{\vec{\omega}}_0 \times \vec{r}_A + \vec{\omega}_0 \times (\vec{\omega}_0 \times \vec{r}_A), & \vec{a}_B &= \dot{\vec{\omega}}_2 \times \vec{\rho}_B + \vec{\omega}_2 \times (\vec{\omega}_2 \times \vec{\rho}_B), \\ \vec{a}_C &= \dot{\vec{\omega}}_4 \times \vec{\rho}_C + \vec{\omega}_4 \times (\vec{\omega}_4 \times \vec{\rho}_C). \end{aligned} \tag{18}$$

Equations (8-10, 13, 15, 17, 18) are a mathematical model of a kinematic mechanism of the grain cleaning machine scalping frame. This model allows determining the coordinates of the nodal points, their speed and acceleration. A similar method is used to determine the coordinates of the nodal points, their speed and acceleration for the lower sieve, which works in the opposite direction of the upper sieve. (*Badretdinov et al., 2017; Bertiaev, 2005*).

RESULTS

Included in Tables 1, 2 are basic physical and mechanical properties and statistical analysis of geometric parameters of grain heap before cleaning. To analyse the physical and mechanical properties of the grain material, certain fresh crop samples harvested at a normal amount of moisture were taken. Geometric parameters were measured using a micrometre MK 0-25, the inherent error of the device being ±0.01 mm. The amount of sampling of the grain heap components was 100 pieces. The mass of a single seed-beetle was determined using electronic jewellery scale A 03 with accuracy class of ±0.001 g.

Table 1

Statistical analysis of geometric parameters of grain heap (“Vatan” wheat variety)

Parameter	Minimal	Maximal	Average value, X	Dispersion, σ ²	Squared error distance, σ	Variation, v
<i>Grain heap (before cleaning)</i>						
Length l, mm	1.11	28.1	10.77	39.8	6.31	58.59
Thickness a, mm	0.30	9.5	2.11	1.80	1.34	63.57
Width e, mm	1.40	5.7	3.53	1.02	1.01	28.64
Equivalent diameter, d _e , mm	0.72	5.41	2.59	-	-	-

Table 2

Statistical analysis of the mass of a single seed beetle (“Salavat lulaev” wheat variety)

Parameter	Minimal	Maximal	Average value, X	Dispersion, σ ²	Squared error distance, σ	Variation, v	Standard error of the mean
Weight [g]	0.012	0.08	0.036	0.0001	0.0105	29.32	0.0011

Experimental studies of the grain heap show (Tables 1, 2) that grain heap is inhomogeneous and has a wide range of both physical and mechanical and geometric parameters (*Casandriou et al., 2009; Ermolev, 2010; Fominykh, 2006; Saitov et al., 2016*).

Variation coefficient v in respect to thickness is 63.57%, and 28.64% in respect to width. This greatly complicates the process of a proper sieve selection. The mass of a single grain is taken into account when determining the inertial force, judging by the coefficient of variation $v = 29.32\%$ varying in a wide range.

Conditions for moving the components of the grain heap downward the oscillating sieve frame. If the components of the grain material move downward the sieve, inertial force, acting on the individual seeds, will be directed downwards, the force of friction on the sieve will be directed upwards along the sieve surface, the force of gravity - downward, and the normal sieve reaction - upward and perpendicular to the sieve surface. By the direction of the forces acting on the grain heap components, the nature of their movement trajectory by the oscillating sieve surface can be defined. The mode of movement of the grain components by the sieve is selected in the following way: the time of the heap component particles contact with the sieve should be maximum, which ensures more efficient separation. At the same time, to improve the performance of the grain cleaning machine, the speed of the grain material movement by the sieve should also be maximum. Apparently, these requirements contradict each other. Thus, optimization problem should be solved.

One of the most important functional parameters of a layer on the surface of the sieve is the Froude number expressing the ratio of the forces acting on a particle lying on the sieve, oscillation amplitude of the sieve and gravity. This number can be expressed as follows

$$F_r = \frac{r\omega^2}{g}, \tag{19}$$

where r is the radius of the crank ($r = 0.01$ m); ω is the angular velocity of the crank drive shaft ($\omega = 425...475$ min⁻¹); g is the acceleration of free fall, m/s².

Visualization of trajectories of speed and acceleration movement of the links, which were received according to the results of modeling and calculation performed with the use of Mathcad program, is presented in Figures 4, 5.

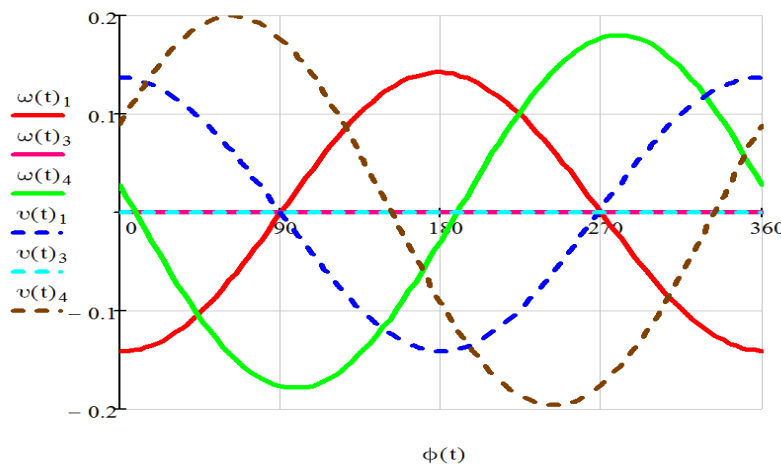


Fig. 4 - Graph of changes in speed (rad/s) of the links of the grain cleaning machine sieve frame

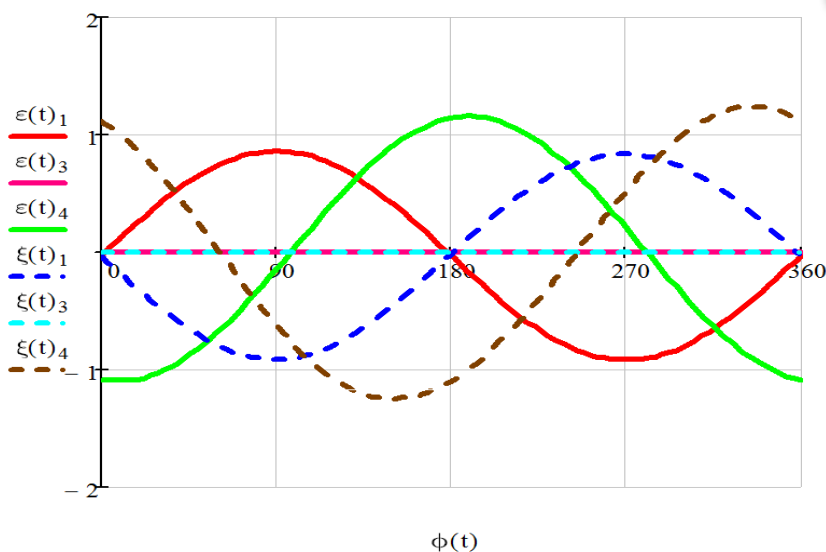


Fig. 5 - Graph of changes in the acceleration (rad/s²) of the links of the grain cleaning machine sieve frame

In Figure 4 acceleration of the scalping frame links are marked by unbroken lines. Acceleration of the bottom frame links are marked by dotted lines. As one can see, they work in inversed manner. There are also small deviations: the speed of the bottom sieve frame link is slightly higher than the speed of the scalping frame link. Due to that, the technological operation process is accompanied by vibration.

The analysis of Figure 5 is similar to the graph of changes in speed of the sieve frame mechanism links. There are also small deviations: the acceleration of the bottom sieve frame link is slightly higher than the acceleration of the scalping frame link. That can be a possible cause of vibration.

Figure 6 shows a kinematic diagram of the sieve frame mechanism and a scaled illustration of speed and acceleration vectors at nodal points. When the scalping frame moves to the right, the bottom frame moves to the left. This is proved by the calculation results and shown by vectors directions.

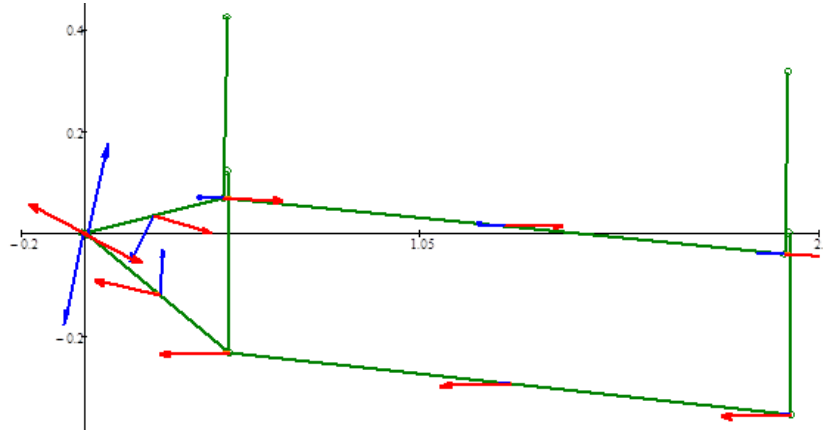


Fig. 6 - Plotting of a sieve frame mechanism, speed and acceleration vectors

Figure 7 shows that speed vectors are perpendicular to the crank and directed down the mechanism rotation. Acceleration vectors are directed down the crank.

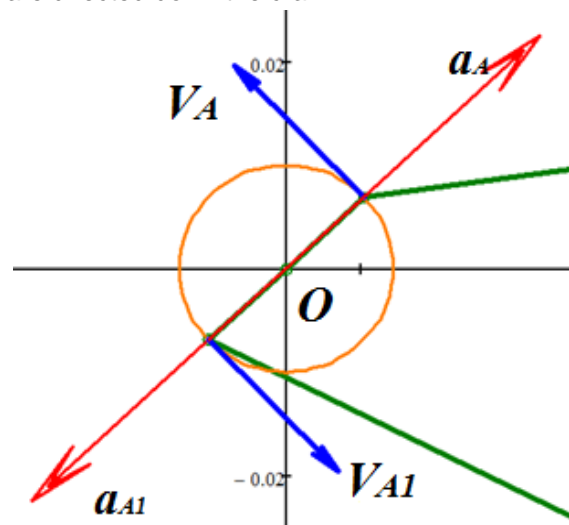


Fig. 7 - Visualization of the sieve frame crank (drive) trajectory, speed and acceleration vectors

Figures 8 and 9 show the plans of speeds and accelerations, respectively, at arbitrary values of the angle of rotation of the crank drive. Depending on the time, you can build such plans of speeds and accelerations for any position (angle of rotation) of the crank. The velocity (acceleration) diagram is a diagram which in real time captures vectors representing a module and a direction of motion of multiple links in the mechanism. The velocity diagram has the following properties: the segment connecting the tips of the velocity vectors of any two points of the body, perpendicular to the line connecting corresponding points of the body; the lengths of segments connecting the ends of the velocity vectors of body points, the proportional length of the segments connecting corresponding points.

The plan of speeds (accelerations) allows solving graphically the problems of determination of body points' speeds (accelerations), and is the most widespread graph-analytical method of research. In this case, the larger the selected scale, in which the vectors of velocities (accelerations) of body points are constructed, the more accurately the problem is solved.

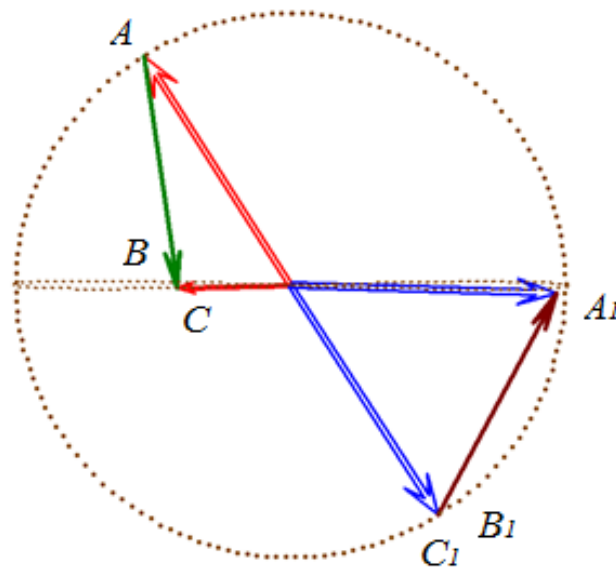


Fig. 8 - Plotting of velocity diagram at a selected value of the crank angle

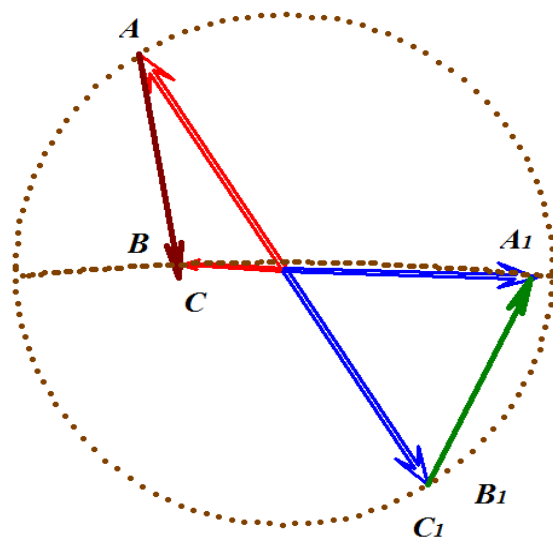


Fig. 9 - Plotting of the acceleration diagram at a selected value of the crank rotation angle

Experimental data got during the study of the grain heap components to be cleaned show the distribution of physical-mechanical and geometric parameters, which vary sufficiently over a wide range. This is proved by their variation coefficients (table 1 and 2). This primarily affects the sieving process, makes the correct selection of sieves difficult, reduces productivity, and affects grain cleaning efficiency.

Other scientists note the same in their studies (Dorokhov *et al.*, 2018; Ma *et al.*, 2018; Okunola *et al.*, 2018; Singh *et al.*, 2017; Vasytkovskyi *et al.*, 2019). In addition to geometric parameters, separation efficiency is also affected by other properties (clogging, humidity) (Kornev, 2015; Mudarisov *et al.*, 2009, 2017; Okunola *et al.*, 2018; Vasytkovskyi *et al.*, 2019).

Modeling and study of the sieve frame kinematic mechanism makes it possible to determine the coordinates of the nodal points, links speed and acceleration, as well as to identify and optimize the problem areas, choose the right design and technological parameters.

Using this method after simulating and calculating the model of a real grain cleaning machine sieve frame on the example of ZVS-20, problem areas were identified, which is confirmed by vibration. These problems can be solved by changing the design parameters.

Using this modeling method makes it possible to improve the design and technological parameters of grain cleaning machines with a sieve cleaning system without significant effort and cost.

CONCLUSIONS

A mathematical model of the kinematic scheme of the grain cleaning machine sieve frame was developed. During the study, coordinates of the nodal points of the grain cleaning machine sieve frame were developed, their movement speed and acceleration plans were plotted. A mathematical model of the kinematic operation scheme of the grain cleaning machine sieve frame was designed. Froude number for a sieve frame $Fr = 0,05 \text{ } 0,062\dots$ was determined. This value characterizes the ratio between inertial forces and gravity, in the field of which the components of a cleaned culture move. According to generally accepted classification, $Fr < 1$ means a quiet fluency. According to the results of modeling and calculation made on the example of the most common grain cleaning machine ZVS-20, its problem areas and imperfections of structural and technological parameters were identified. The proposed method of simulation of grain cleaning machines with a sieve cleaning system makes it possible to study the drive mechanism kinematics and the process of separation by flat oscillating working bodies, to analyse the contact degree of particles of grain heap components with the sieve, to identify problem areas and improve the design and technological parameters of the sieve frame of any grain cleaning machine. The model can be used many times, without requiring investment for its manufacturing and laboratory tests. Correct operation modes of the separation process can be chosen for different crops.

REFERENCES

- [1] Badretdinov I., Mudarisov S., Lukmanov R., Permyakov V., Ibragimov R., Nasyrov R., (2017), Mathematical modeling and research of the work of the grain combine harvester cleaning system. *Computers and Electronics in Agriculture*, Vol.165, No.104966;
- [2] Bertiaev V.D., (2005), *Theoretical mechanics on the basis of Mathcad. Practicum: Textbook (Теоретическая механика на базе Mathcad. Практикум)*. St. Petersburg. BHV pbl., St. Petersburg, (in Russian);
- [3] Casandroiu T., Popescu M., Voicu G., (2009), Developing a mathematical model for simulating the seeds separation process on the plane sieves. *Scientific Bulletin-University Politehnica of Bucharest, Series D*, Vol.71, No.3, pp.17-28;
- [4] Dorokhov A., Khamyev V., Lepeshkin K., (2018), Modernization of grinding machines of grain cleaning machines. *MATEC Web of Conferences*, Vol.224, No.05009;
- [5] Ermolev Yu.I., (2010), Modeling of air-screen grain cleaning machine (Моделирование зерноочистительной машины с воздушным ситом). *Bulletin of Dagestan State Technical University*, Vol.10, No.8, pp.1245-1254;
- [6] Fominykh A.V., (2006), *Increase in the efficiency of grain and soy separation on the basis of improvement of fractional technologies and machines (Повышение эффективности сепарирования зерна и сои на основе совершенствования фракционных технологий и машин)*. Ph.D. thesis in Technical Sciences. Cheliabinsk;
- [7] Giyevskiy A.M., Orobinsky V.I., Tarasenko A.P., Chernyshov A.V., Kurilov D.O., (2018), Substantiation of basic scheme of grain cleaning machine for preparation of agricultural crops seeds. *IOP Conference Series Materials Science and Engineering*, Vol.327, No.042035.
- [8] Kornev A.S., (2015), *Improving the efficiency of grain separation using flat screens of grain cleaning machines (Повышение эффективности сепарации зерна на плоских решетках зерноочистительных машин)*. Ph.D. thesis in Technical Sciences. Voronezh;
- [9] Kundu D., Gupta A.K., (2014), On bivariate Weibull-geometric distribution. *Journal of Multivariate Statistics*, Vol.123, pp.19-29;
- [10] Ma L., Song X., Wang H., Xu X., Han T., Guo H., (2018), Screening Kinematics Analysis of Cleaning Organs and Extractives. *IOP Conference Series Materials Science and Engineering*, Vol.452, No.042123;
- [11] Mudarisov S., Khasanov E., Rakhimov Z., Gabitov I., Badretdinov I., Farchutdinov I., Galliamov F., Davletshin M., Aipov R., Jarullin R., (2017), Specifying Two-Phase Flow in Modeling Pneumatic Systems Performance of Farm Machines. *Journal of Mechanical Engineering Research and Developments*, Vol.40, No.4, pp.706-715;
- [12] Mudarisov S.G., Badretdinov I.D., (2008), Improvement of technological lines for post-harvest processing of grain in farms (Оптимизация параметров пневматической системы зерноочистительной машины). *Proceedings of the XLVII International Scientific and Technical conference dedicated to the 100th birth anniversary of I. E. Ullman*, pp.28-33;

- [13] Mudarisov S.G., Rakhimov Z.S., Badretdinov I.D., Akbatyrov A.V., Farkhutdinov I.M., (2009), Modernization of technological lines of grain processing taking into account economic conditions (Модернизация технологических линий переработки зерна с учетом хозяйственных условий). In the collection of articles: Scientific support of sustainable functioning and development of agriculture. *Proceedings of All-Russian Scientific and Practical conference with international participation (in the framework of the 19th International Specialized exhibition “AgroComplex-2009”)*, pp.122–126;
- [14] Okunola A.A., Isaac-Bamgboye A., Olayanju A., Osueke Ch.O., Alhassan E.A., (2018), Development of a rice cleaner cum grader for cottage industry processors in Nigeria. *International Journal of Mechanical Engineering and Technology*, Vol.9, No.11, pp.2339-2351;
- [15] Popov I.P., Chumakov V.G., Terentev A.D., (2015), Reduction of drive power of sieve frame grain cleaning machines. *Scientific and technical Bulletin of St. Petersburg State Polytechnic University*, Vol.2, No.219, pp.175-181;
- [16] Saitov V.E., Kurbanov R.F., Suvorov A.N., (2016), Assessing the Adequacy of Mathematical Models of Light Impurity Fractionation in Sedimentary Chambers of Grain Cleaning Machines. *Procedia Engineering*, Vol.150, pp.107–110;
- [17] Savinyh P., Sychugov Y., Kazakov V., Ivanovs S., (2018), Development and theoretical studies of grain cleaning machine for fractional technology of flattening forage grain. *17th International Scientific Conference Engineering for Rural Development*, pp.124-130;
- [18] Shevtsov I.B., Beznosov, V.A., (2014), Drive unit of the sieve frame of grain cleaning machines (Приводное устройство решетных станков зерноочистительных машин). *Agrarian Bulletin of the Urals*, Vol.2, No.120, pp.43-45;
- [19] Singh K.P., Agrawal K.N., Hota S., Potdar R.R., Tiwari P.S., (2017), Effect of moisture content on physical properties of finger millet (*eleusine coracana*). *Agricultural Mechanization in Asia, Africa and Latin America*, Vol.48, No.4, pp.24-32;
- [20] Steponavičius D., Špokas L., Petkevičius S., (2008), The influence of position of the first straw walkers section on grain separation. *Agronomy Research*, Vol.6, pp.377-385;
- [21] Tarasenko A.P., Orobinsky V.I., Gievsky A.M., Merchalova M.E., (2012), Improvement of mechanization means for receiving qualitative grain (Совершенствование средств механизации для получения качественного зерна). *Bulletin of the Voronezh State Agrarian University*, Vol.3, No.34, pp.109-115;
- [22] Vasytkovskyi O., Vasytkovska K., Moroz S., Sviren M., Storozhyk L., (2019), The influence of basic parameters of separating conveyor operation on grain cleaning quality (Вплив основних параметрів роботи транспортера-сепаратора на якість очищення зерна). *INMATEH - Agricultural Engineering*, Vol.57, No.1, pp.63-70;
- [23] Voicu G., Casandroi T., Tarcolea C., (2008), Testing stochastic models for simulating the seeds separation process on the sieves of a cleaning system and a comparison with experimental data. *Agriculturae Conspectus Scientificus*, Vol.73, No.2, pp.95-101.

RESEARCH ON RESONANT OSCILLATIONS OF THE TELESCOPIC SCREW – GRANULAR MEDIA SYSTEM CAUSED BY EXTERNAL PERIODIC FORCES

ДОСЛІДЖЕННЯ РЕЗОНАНСНИХ КОЛИВАНЬ СИСТЕМИ ТЕЛЕСКОПІЧНИЙ ГВИНТ – СИПКЕ СЕРЕДОВИЩЕ ЗУМОВЛЕНИХ ЗОВНІШНІМИ ПЕРІОДИЧНИМИ СИЛАМИ

Victor Hud, Roman Rogatynsky, Ivan Hevko, Oleg Lyashuk, Andriy Pik, Oleg Huryk ¹

Terнопil Ivan Puluj National Technical University / Ukraine;

E-mail: vic_g@ukr.net

DOI: <https://doi.org/10.35633/inmateh-60-03>

Keywords: screws, conveyor, telescopic, elastic body, amplitude, frequency

ABSTRACT

The article presents the results of resonant oscillations theoretical research of the telescopic screw - granular material system caused by external periodic forces. In the theoretical part a mathematical model of bending vibrations of an elastic body is described, which rotates along a fixed axis with a constant angular velocity, provided that it moves with a constant relative linear velocity along the elastic body. In the experimental part, according to the obtained equations, it has been established for the various kinematic characteristics of the system, a telescopic screw-granular media of amplitude passing through resonance at the frequency of external periodic perturbation. The results of experimental research and recommendations for the selection of constructive kinematic for telescopic screw conveyor have been presented.

РЕЗЮМЕ

У статті наведено теоретичні дослідження резонансних коливань системи телескопічний гвинт – сипкий матеріал зумовлених зовнішніми періодичними силами. В теоретичній частині описано математичну модель згинальних коливань пружного тіла, яке обертається вздовж нерухомої осі із сталою кутковою швидкістю за умови, що вздовж нього рухається зі сталою відносною лінійною швидкістю. В експериментальній частині відповідно до отриманих рівнянь, представлено для різних кінематичних характеристик системи телескопічний гвинт – сипке середовище амплітуду проходження через резонанс на частоті зовнішнього періодичного збурення. Представлені результати експериментальних досліджень та наведені рекомендації для вибору конструктивно-кінематичних телескопічних гвинтових транспортерів.

INTRODUCTION

One of the premises for the high efficiency of machine-building enterprises is to improve the existing and to introduce new competitive products, which can fully meet the needs of consumers. Screw transport mechanisms are one of the most commonly used mechanical means in agricultural production and other sectors of the economy as individual elements, as well as in other machines. According to various data, their specific gravity in loading and unloading operations of different types is 40-45%.

They are especially widely used as elements of agricultural machines when overloading agricultural loads in the field conditions. Often, the universal units for loading seeders, hoppers, reloaders and combine harvesters are complicated (the term is used for composition and decomposition) in order to obtain a significant material overload path. To achieve the required overload distance, they are decomposed - composed with the use of hydraulic or pneumatic equipment. This makes their constructions too complicated and expensive. The examples are the universal hoppers-reloaders of the companies "EGRITECH", "Liliani MBA", combine harvesters CASE 8120 AXIAL FLOW, New Holland CR10.90 and others. Therefore, using the telescope principle will have widespread use in the design of agricultural machinery equipped with screw conveyors.

Despite a large number of scientific works devoted to the development and research of the features of screw conveyors operation, there is a wide range of unexplored issues related to their constructive and

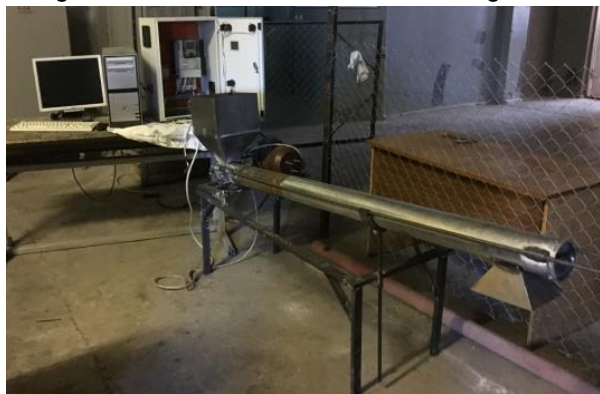
¹ Hud V.Z., Assoc. Prof. PhD. Eng.; Rogatynskyi R.M., Prof. PhD. Eng.; Hevko I.B., Prof.PhD.Eng.; Lyashuk O.L., Prof.PhD.Eng.; Pik A.I., Assoc. Prof. PhD. Eng.; Huryk O.Y., Assoc. Prof. PhD. Eng.

functional characteristics. Therefore, the development of telescopic screw conveyors makes it possible to improve the efficiency of the overload of loose materials. However, due to the significant angular velocities of the screw rotation in telescopic screw conveyors, the asymmetry of the telescopic screw and external perturbations, fluctuations often occur, which result in significant dynamic loads in the screw (Hevko I.B., 2013; Lyashuk O.L., et al., 2016), especially in resonant cases. The works of Lyashuk O.L. et al. (2018) show the movement of the grain mixture along the working body of the loader. Differential equations are obtained that describe the bending fluctuations of the horizontal screw of the mixer loader.

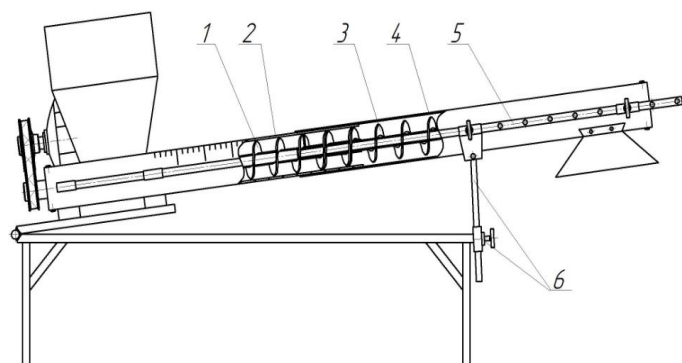
The results of theoretical and experimental studies of simultaneous transportation and mixing of feed mixtures components on the curved lines of tubular conveyors are presented. A mathematical model is constructed that characterizes the dependence of the change of elementary work, which is performed when the elemental mass of loose material moves along the curvilinear region (Hevko R.B., et al., 2018). The method of carrying out researches on determining the power indicators of different movement types of loose materials is presented. Therefore, the study of dynamic loads in the screw of a telescopic conveyor during the movement of loose material enables to choose the rational modes of operation of the conveyor, which minimize these negative phenomena and increase the life of exploitation of telescopic screw conveyor.

MATERIALS AND METHODS

To study the principle of telescopes in screw conveyors based on a patent search and analysis of scientific literature and synthesis (Rogatynsky R.M., et al., 2014), a pilot installation has been developed, designed, manufactured and shown in Figures 1 - 3.



a)



b)

Fig. 1 - Stand to study the characteristics of telescopic screw conveyors: a) general view; b) structural scheme

- 1) screw axial motion in the axial direction of the screw section;
- 2) part of the casing is fixed in the axial direction;
- 3) screw moving in the axial direction of the screw section;
- 4) part of the casing moving in the axial direction;
- 5) guides;
- 6) support for adjusting the height of the material

The outer diameter of the auger in the pilot installation is 97 mm, internal diameter of the fixed pipe is 100 mm, the outer one is 107 mm, the inner diameter of the movable branch pipe is 109 mm. The movable nozzle is made of galvanized sheet, and therefore it contains a connecting seam and ovals and has uneven shapes along the entire length, which affect the speed of twisting and unwinding of the telescopic part of the screw conveyor.

Studies have shown that the biggest problem in telescopic screw conveyors is to maintain the same clearance between the casing and the spiral in different sections of the telescope, which significantly affects the time of rolling in and rolling out of the axially moving part of the auger fixed and the appearance and magnitude of the rotational bending oscillations. It has also been found that the overload performance of agricultural goods by telescopic screw conveyor does not differ from the overload performance of these materials with traditional screw conveyors.

It is established by Sokil B.I. et al. (2010; 2011; 2012; 2017) that there is an effect of the motion of a continuous stream of granular media on the longitudinal or bending vibrations of elastic bodies. Consequently, it can be assumed that even the movement velocity of a granular media has changed the main dynamic characteristics of bending or longitudinal oscillations, and the magnitude of the action of this media increases significantly with an increase in the relative amount of its motion.

Therefore, at a significant angular velocity of rotation of telescopic screws, even small transverse deformations at a certain moment result in significant tension.



Fig. 2 - Scale of the stand screw to study the characteristics of telescopic screw conveyors



Fig. 3 - A stand for the study of telescopic screw conveyors in a disassembled state

In study of Fedoseev V.I. (1951), a mathematical model of flexural oscillations of an elastic body rotating along a fixed axis with a constant angular velocity Ω was presented. This action was provided when a continuous flow of a homogeneous medium moves along it at a constant relative linear velocity V . The proposed model of the dynamic process was presented in the form of zero rigidity, where a system of differential equations is used.

$$\begin{aligned}
 &(\rho_1 + \rho_2) \frac{\partial^2 u}{\partial t^2} + 2\rho_2 V \frac{\partial^2 u}{\partial t \partial z} - 2(\rho_1 + \rho_2) \Omega \frac{\partial w}{\partial t} + \rho_2 V^2 \frac{\partial^2 u}{\partial z^2} - \\
 &- 2(\rho_1 + \rho_2) I \Omega \frac{\partial^3 w}{\partial t \partial x^2} + EI \frac{\partial^4 u}{\partial z^4} - (\rho_1 + \rho_2) \Omega^2 u = \varepsilon f \left(u, w, \frac{\partial u}{\partial t}, \frac{\partial w}{\partial t}, \frac{\partial u}{\partial z}, \frac{\partial w}{\partial z}, \dots, \frac{\partial^3 u}{\partial z^3}, \frac{\partial^3 w}{\partial z^3}, \gamma \right) \\
 &(\rho_1 + \rho_2) \frac{\partial^2 w}{\partial t^2} + 2\rho_2 V \frac{\partial^2 w}{\partial t \partial z} + 2(\rho_1 + \rho_2) \Omega \frac{\partial u}{\partial t} + \rho_2 V^2 \frac{\partial^2 w}{\partial z^2} + \\
 &+ 2(\rho_1 + \rho_2) I \Omega \frac{\partial^3 u}{\partial t \partial x^2} + EI \frac{\partial^4 w}{\partial z^4} - (\rho_1 + \rho_2) \Omega^2 w = \varepsilon g \left(u, w, \frac{\partial u}{\partial t}, \frac{\partial w}{\partial t}, \frac{\partial u}{\partial z}, \frac{\partial w}{\partial z}, \dots, \frac{\partial^3 u}{\partial z^3}, \frac{\partial^3 w}{\partial z^3}, \gamma \right)
 \end{aligned} \tag{1}$$

In Eq.(1) $u(t, z), w(t, z)$ - projection of the vector of moving the point of the central axis with the coordinate z of the telescopic screw at an arbitrary time t in the projections on the axis of the fixed coordinate system $OXYZ$. The axis OZ of the reference system coincides with the undrained straight line of the auger screw Ω , - the angular velocity of the screw rotation around the axis, ρ_1, ρ_2 - respectively the mass of the unit of body length and moving medium, EI - its rigidity to the screw's bend,

$$f \left(u, w, \frac{\partial u}{\partial t}, \frac{\partial w}{\partial t}, \frac{\partial u}{\partial z}, \frac{\partial w}{\partial z}, \dots, \frac{\partial^3 u}{\partial z^3}, \frac{\partial^3 w}{\partial z^3}, \gamma \right) \text{ and } g \left(u, w, \frac{\partial u}{\partial t}, \frac{\partial w}{\partial t}, \frac{\partial u}{\partial z}, \frac{\partial w}{\partial z}, \dots, \frac{\partial^3 u}{\partial z^3}, \frac{\partial^3 w}{\partial z^3}, \gamma \right) - 2\pi -$$

periodic by $\gamma = vt + \gamma_0$ functions that describe the nonlinear components of the restoring force, the strength of the resistance, and other forces the maximum values of which are significantly lower than the value of the restoring force, as indicated by the small parameter ε . Below, for simplicity, we assume that these functions are polynomials in the set of variables, and from the physical content of them it results that they must be bound by the relation

$$f \left(u, w, \frac{\partial u}{\partial t}, \frac{\partial w}{\partial t}, \frac{\partial u}{\partial z}, \frac{\partial w}{\partial z}, \dots, \frac{\partial^3 u}{\partial z^3}, \frac{\partial^3 w}{\partial z^3}, \gamma \right) = g \left(w, u, \frac{\partial w}{\partial t}, \frac{\partial u}{\partial t}, \frac{\partial w}{\partial z}, \frac{\partial u}{\partial z}, \dots, \frac{\partial^3 w}{\partial z^3}, \frac{\partial^3 u}{\partial z^3}, \gamma \right)$$

In the case of complex oscillations of the screw (a combination of bending and twisting), provided that the latter are described by a known law $\mathcal{G}(z, t)$ (the torsion below is considered to be the simplest of their mathematical models), the system of equations (1) is transformed into a form:

$$\begin{aligned}
 & (\rho_1 + \rho_2) \frac{\partial^2 u}{\partial t^2} + 2\rho_2 V \frac{\partial^2 u}{\partial t \partial z} - 2(\rho_1 + \rho_2) \left(\Omega + \frac{\partial \mathcal{G}(z, t)}{\partial t} \right) \frac{\partial w}{\partial t} + \rho_2 V^2 \frac{\partial^2 u}{\partial z^2} - \\
 & - 2(\rho_1 + \rho_2) I \left(\Omega + \frac{\partial \mathcal{G}(z, t)}{\partial t} \right) \frac{\partial^3 w}{\partial t \partial x^2} + EI \frac{\partial^4 u}{\partial z^4} - (\rho_1 + \rho_2) \left(\Omega + \frac{\partial \mathcal{G}(z, t)}{\partial t} \right)^2 u - (\rho_1 + \rho_2) \frac{\partial^2 \mathcal{G}(z, t)}{\partial t^2} w = \\
 & = \varepsilon f_1 \left(u, w, \frac{\partial u}{\partial t}, \dots, \frac{\partial^3 w}{\partial z^3}, \gamma \right) \\
 & (\rho_1 + \rho_2) \frac{\partial^2 w}{\partial t^2} + 2\rho_2 V \frac{\partial^2 w}{\partial t \partial z} + 2(\rho_1 + \rho_2) \left(\Omega + \frac{\partial \mathcal{G}(z, t)}{\partial t} \right) \frac{\partial u}{\partial t} + \rho_2 V^2 \frac{\partial^2 w}{\partial z^2} + \\
 & + (\rho_1 + \rho_2) \frac{\partial^2 \mathcal{G}(z, t)}{\partial t^2} u = \varepsilon f_2 \left(u, w, \frac{\partial u}{\partial t}, \dots, \frac{\partial^3 w}{\partial z^3}, \gamma \right) \tag{2}
 \end{aligned}$$

From the form of the right-hand side of the differential equation (2) it results that in the system under consideration, resonant phenomena are possible due to external periodic forces or torsional oscillations of the telescopic screw itself. The second case will be called internal resonance, and - the first - external. Simpler resonant oscillations have been caused by external periodic forces, so let's consider them first.

The condition for the existence of a given type of resonance is the existence of a rational connection between the frequencies of the internal oscillations of the telescopic screw system and the granular media and the frequency of the external periodic perturbation, i.e. $m\nu \neq n\omega_k$

The dispersion ratio determines the intrinsic frequency of bending vibrations of the body as a function of the angular and linear velocity of the medium along the elastic body in the form:

$$\omega_k = \Omega(I\kappa_k - 1) \pm \kappa_k \sqrt{\Omega^2 I(\kappa_k^2 I - 2) - \frac{\rho_2 V^2 - EI\kappa_k^2}{\rho_1 + \rho_2}} \tag{3}$$

Simultaneously, the obtained ratio serves as the basis for solving a more complex problem - the determination of the influence of nonlinear forces on the dynamic process, as well as the whole set of external and internal factors on bending fluctuations of a screw. Dependence (3) indicates at the same time the simplest way to avoid external resonance: for the given magnitude of the external periodic perturbation, the rotation frequency of the screw propeller should be chosen from the condition:

$$m \left[\Omega(I\kappa_k - 1) \pm \kappa_k \sqrt{\Omega^2 I(\kappa_k^2 I - 2) - \frac{\rho_2 V^2 - EI\kappa_k^2}{\rho_1 + \rho_2}} \right] \neq m\nu.$$

The ratios that determine the laws of amplitude variation and frequency of the wave process are as follows:

$$\begin{aligned}
 \frac{da}{dt} &= -\frac{1}{2\pi\omega l(\rho_1 + \rho_2)} \int_0^l \int_0^{2\pi} \tilde{f}(a, z, \psi, \gamma, \mathcal{G})(\cos(\kappa z + \psi) - \cos(\kappa z - \psi)) d\psi dz, \\
 \frac{d\theta}{dt} &= \omega + \frac{1}{2a\pi\omega l(\rho_1 + \rho_2)} \int_0^l \int_0^{2\pi} \tilde{f}(a, z, \psi, \gamma, \mathcal{G})(\sin(\kappa z + \psi) + \sin(\kappa z - \psi)) d\psi dz, \tag{4}
 \end{aligned}$$

In the system of differential equations (4), the integral functions, and therefore the right parts of it are periodic in terms of arguments $\psi, \gamma, \mathcal{G}$, which means that non-resonant and resonant oscillations may occur in the screw auger. As for the former, they have in the conditions $\omega \neq \nu$ and $\omega \neq \Theta$ ratios between which there is no rational connection between their own frequency ω and frequency of external perturbation ν or frequency of torsional oscillations Θ . For the first approximation of non-resonant oscillations, the amplitude and frequency of flexural oscillations of a telescopic screw have been described by dependencies:

$$\frac{da}{dt} = \frac{-\varepsilon}{8\omega\pi^2 l} \int_0^l \int_0^{2\pi} \int_0^{2\pi} \int_0^{2\pi} \tilde{f}(a, z, \psi, \gamma, \vartheta) \sin \frac{\pi}{l} z \cos \psi dz d\psi d\gamma d\vartheta, \tag{5}$$

$$\frac{d\psi_1}{dt} = \omega - \frac{\varepsilon}{8\omega\pi^2 a l} \int_0^l \int_0^{2\pi} \int_0^{2\pi} \int_0^{2\pi} \tilde{f}(a, z, \psi, \gamma, \vartheta) \sin \frac{\pi}{l} z \sin \psi dz d\psi d\gamma d\vartheta$$

RESULTS

To study the process of resonance passage for the base, we adopt the system of differential equations (5) and the property of the resonant oscillations, which is as follows: the amplitude of the resonance passage essentially depends on the phase difference between the proper and forced oscillations. For the case under consideration this is $\phi = \psi - \gamma$ (here and below for simplicity only the case of the main resonance is considered). Entering the given parameter in the system of differential equations (4), after averaging over the phases of forced and torsional oscillations we obtain:

$$\frac{da}{dt} = -\frac{1}{8\pi\omega l(\rho_1 + \rho_2)} \int_0^l \int_0^{2\pi} \int_0^{2\pi} \tilde{f}(a, z, \phi + \gamma, \gamma, \vartheta) (\cos(\kappa z + \phi + \gamma) - \cos(\kappa z - \phi + \gamma)) d\gamma d\vartheta dz,$$

$$\frac{d\gamma}{dt} = \omega - \nu + \frac{1}{8a\pi\omega l(\rho_1 + \rho_2)} \int_0^l \int_0^{2\pi} \int_0^{2\pi} \tilde{f}(a, z, \phi + \gamma, \gamma, \vartheta) (\sin(\kappa z + \phi + \gamma) + \sin(\kappa z - \phi + \gamma)) d\gamma d\vartheta dz. \tag{6}$$

The system of equations (6) for the case of the above nonlinearly elastic law of the telescopic screw material and the viscoelastic forces of resistance and mono-harmonic periodic perturbation is transformed into a form:

$$\frac{da}{dt} = -\frac{k_1(\omega)^{s-1}}{(\rho_1 + \rho_2)\pi} a^s + \frac{h}{\pi\omega} \cos \gamma; \tag{7}$$

$$\frac{d\gamma}{dt} = \omega - \nu - \frac{\bar{k}_1 EI}{(\rho_1 + \rho_2)} a^2 - \left(\frac{\pi}{l}\right)^2 \frac{\rho_2}{8\omega(\rho_1 + \rho_2)} V^2 + \frac{h}{\pi a \omega} \sin \gamma$$

Below, in accordance with the obtained equations, a telescopic screw is shown for various kinematic characteristics of the system - the granular media of amplitude passing through resonance at the frequency of external periodic perturbation. Figure 4.

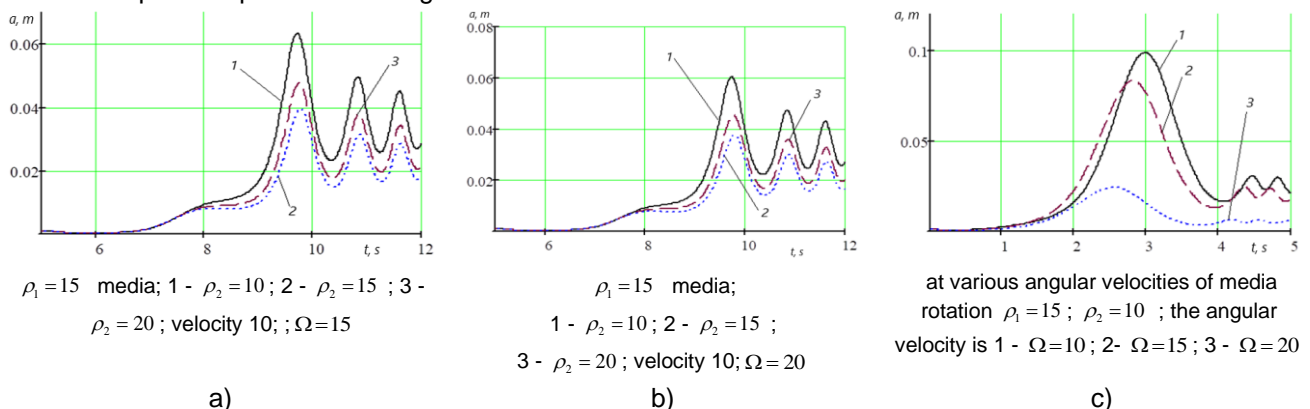


Fig. 4 - Changing the amplitude of the telescopic screw system is a granular media at the transition through the resonance due to external periodic perturbation

The obtained dependences show that for: a) the larger values of the particle mass of the media, the amplitude of the transition through the resonance is less; b) for larger values of the angular velocity of the body, the actual frequency of bending vibrations is smaller while the amplitude of the transition through the resonance is smaller; c) the amplitude is less at a higher speed of transition.

According to the research results, the graphical dependences of engine power N on the rotation speed of the working body n , the angle of the conveyor α and the length of transportation are constructed. It is established that the power N has a fairly clearly expressed linear nature of the growth of N with increasing n .

On the basis of the multivariate experiment, a regression dependence has been obtained to determine the effect of n , α and L on the magnitude of the power N during grain transportation of corn, barley and mixed fodder: $300 \leq n \leq 700$ (rpm); $1,33 \leq l \leq 1,61$ (m); $5 \leq \gamma \leq 45$ (deg.).

- during corn transportation:

$$N_{(n,l,\gamma)} = -2.22 \cdot 10^{-2} - 4.94 \cdot 10^{-4} n - 2.76 \cdot 10^{-2} l + 9.25 \cdot 10^{-4} \gamma + 9.29 \cdot 10^{-4} n l + 1.58 \cdot 10^{-6} n \gamma + 9.25 \cdot 10^{-7} n^2 + 3.37 \cdot 10^{-2} l^2 - 1.83 \cdot 10^{-5} \gamma^2; \quad (8)$$

- during wheat transportation:

$$N_{(n,l,\gamma)} = -2.13 \cdot 10^{-2} - 5.09 \cdot 10^{-4} n - 2.85 \cdot 10^{-2} l + 9.38 \cdot 10^{-4} \gamma + 9.64 \cdot 10^{-4} n l + 1.65 \cdot 10^{-6} n \gamma + 9.75 \cdot 10^{-7} n^2 + 3.52 \cdot 10^{-2} l^2 - 1.93 \cdot 10^{-5} \gamma^2; \quad (9)$$

- during mixed fodder transportation:

$$N_{(n,l,\gamma)} = -2.68 \cdot 10^{-2} - 4.18 \cdot 10^{-4} n - 2.06 \cdot 10^{-2} l + 8.25 \cdot 10^{-4} \gamma + 8.21 \cdot 10^{-4} n l + 1.4 \cdot 10^{-6} n \gamma + 8.25 \cdot 10^{-7} n^2 + 3.01 \cdot 10^{-2} l^2 - 1.65 \cdot 10^{-5} \gamma^2. \quad (10)$$

Using Statistica-6.0 software for PCs, we constructed a graphical reproduction of common regression models in the form of quadratic response surfaces and their two-dimensional power sections N as a function of two variable factors $x_{i(1,2)}$ with a constant unchangeable level taking into account the third factor $x_{i(3)} = const$.

The analysis of the given regression equations shows that the main factors affecting the increase in drive power are: factors x_1 , x_2 , (n , l) and combinations of these factors. An increase in the value of factor x_3 (γ) leads to an increase in power by 4.2% (Fig. 5). Moreover, an increase in the value of factor x_2 (l) leads to an increase in power by 9.8%.

In general, to reduce power, it is necessary to reduce the speed of the screw and the angle of the conveyor inclination. The graphical values of the power dependence results obtained using Mathcad 2000 Professional based on the analysis of regression equations are shown in Fig. 5.

Figure 5 shows the response surfaces of the change in the values of n from the simultaneous change of two factors: a) $N = f(n, \alpha)$; b) $N = f(n, l)$; c- $N = f(\alpha, l)$.

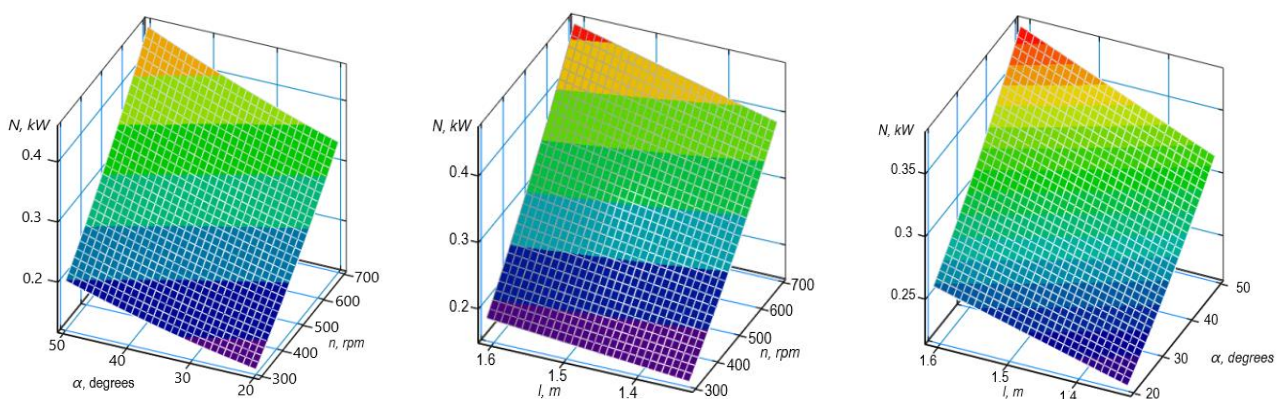


Fig. 5 - Response surfaces of the change in the values of n from the simultaneous change of two factors: a - $N = f(n, \alpha)$; b - $N = f(n, l)$; c- $N = f(\alpha, l)$

It can be seen from the figures that with an increase in the screw speed, length, extension of the screw and the angle of inclination of the screw conveyor, the power on the screw drive increases, and the maximum power of 1.29 kW is achieved when transporting wheat.

The maximum power on the screw drive of the telescopic screw conveyor for transporting corn and mixed fodder is 1.23 kW and 1.10 kW, respectively, and the minimum is 0.31 kW and 0.28 kW, respectively. Increase in screw speed $n_{ш}$, from 300 rpm. to 700 rpm leads to an increase in power on the auger drive by 3.14 times.

Studies have shown that the biggest problem in telescopic screw conveyors is to maintain the same clearance between the casing and the spiral in different sections of the telescope, which significantly affects the time of rolling in and rolling out of the axially moving part of the auger fixed and the appearance and magnitude of the rotational bending oscillations.

CONCLUSIONS

In order to improve the performance of screw conveyors, which are to ensure the transport of loose materials, increase the load capacity, as well as improve their serviceability, the telescopic screw conveyor is developed.

The theoretical calculations of the resonance phenomenon are caused by external periodic forces or torsional vibrations of the telescopic screw itself. The differential equations of the bending oscillations of an elastic body rotating along a fixed axis with a constant angular velocity Ω are deduced, provided that a continuous flow of a homogeneous capacity is used along it with a constant relative linear velocity V .

A telescopic screw- granular media of the amplitude passing through resonance at the frequency of external periodic perturbation is presented for various kinematic characteristics of the system:

a) As a result of the conducted research it has been established that for higher values of the granular media, the amplitude of the transition through the resonance is lower;

b) It has been established that for higher values of the angular velocity of the body, the natural frequency of bending oscillations is smaller. At the same time, the amplitude of the transition through the resonance is smaller;

c) It has been established that at a higher speed of transition through resonance the amplitude is smaller.

On the basis of the multivariate experiment, a regression dependence has been obtained to determine the influence of the rotation speed of the working body n , the angle of the conveyor α and the length of transportation l on the power N when transporting grain material, from the analysis of which it is found that the dominant factor affecting the value of N is the angle of inclination $\alpha = 30$ degrees, hereinafter the values $n = 500$ rpm and lengths of transportation $l = 1.47$ m.

REFERENCES

- [1] Babakov I.M., (1965), The theory of oscillations (Теория колебаний), *Textbook (Підручник)*, 560 p., Moscow / USSR;
- [2] Fedoseev V.I., (1951), About oscillations and stability of a pipe when liquid goes through it. (О колебаниях и устойчивости трубы при протекании через нее жидкости), *Engineering compilation (Инженерный сборник)*, vol.10, pp.251–257, Moscow / USSR;
- [3] Невко І.В., (2013), Scientific and applied foundations of creation of screw transport and technological mechanisms (Науково-прикладні основи створення гвинтових транспортно-технологічних механізмів), *The author's dissertation abstract for the degree of doctor of technical sciences (Автореферат дисертації на здобуття наукового ступеня доктора технічних наук)*, 42 p., Lviv / Ukraine;
- [4] Невко І.В., Hud V.Z., Shust I.M. et al., (2016), Synthesis of telescopic screw conveyors (Синтез телескопічних гвинтових конвеєрів), *Bulletin of the KhNTUSG named after Peter Vasilenko. "Resource-saving technologies, materials and equipment in repairing" (Вісник ХНТУСГ імені Петра Василенка. «Ресурсозберігаючі технології, матеріали та обладнання у ремонтному виробництві»)*, vol.168, pp.85-91, Lutsk / Ukraine;
- [5] Невко R.B., Liubin M.V., Tokarchuk O.A., Lyashuk O.L., Pohrishchuk B.V., Klendii O.M., (2018), Determination of the parameters of transporting and mixing feed mixtures along the curvilinear paths of tubular conveyors, *INMATEH-Agricultural Engineering*, vol.55, no.2, 2018, pp.97-104, Bucharest / Romania;
- [6] Lyashuk O.L., (2016), The study on nonlinear model of dynamics of a system 'extruder elastic auger working body', *Acta technologica agriculturae*, no. 4, pp. 102-107, Nitra / Slovak Republic;

- [7] Lyashuk O.L., Sokil M.B., Klendiy V.M., Skyba O.P., Tretiakov O.L., Slobodian L.M., Slobodian N.O. (2018) Mathematical model of bending vibrations of a horizontal feeder-mixer along the flow of grain mixture, *INMATEH-Agricultural Engineering*, vol. 55, no. 2, pp. 35-45, Bucharest / Romania;
- [8] Lyashuk O.L., Pyndus T.B., Marunych O.P., Sokil M.B., (2016), Longitudinal-angular oscillation of wheeled vehicles with non-linear power characteristics of absorber system (Дослідження поздовжньо-кутових коливань колісних транспортних засобів), *Scientific Journal of the Ternopil National Technical University (Вісник Тернопільського національного технічного університету)*, vol.84, no.2, pp.82-89, Ternopil / Ukraine;
- [9] Rogatynsky R.M., Hevko I.B., Dyachun, A.E. et al., (2014), Scientific and applied foundations of creation of screw transport and technological mechanisms, (Науково-прикладні основи створення гвинтових транспортно-технологічних механізмів), *Textbook (Підручник)*, 280 p., Ternopil / Ukraine;
- [10] Sokil B.I., Sokil M.B., (2017), Forced oscillations of flexible tubular bodies, along which a continuous flow of medium moves (Вимушені коливання гнучких трубчастих тіл, вздовж яких рухається суцільний потік середовища). *Bulletin of the National University "Lviv Polytechnic" Dynamics, strength and design of machines and instruments (Вісник національного університету "Львівська політехніка" Динаміка, міцність та проектування машин і приладів)*, vol.866, pp.60-65, Lviv / Ukraine;
- [11] Sokil B.I., Hutrak O.I., (2011), Influence of the velocity of the longitudinal motion on the stresses in the flexible elements of the drive systems for resonance (Вплив швидкості поздовжнього руху на напруження у гнучких елементах систем приводів за резонансу), *Bulletin of the National University "Lviv Polytechnic". Optimization of production processes and technical control in machine building and instrument making (Вісник національного університету "Львівська політехніка". Оптимізація виробничих процесів і технічний контроль у машинобудуванні і приладобудуванні)*, vol.702. pp.76-83, Lviv / Ukraine;
- [12] Sokil M.B., Andruhiv A.I., Hutrak O.I., (2012), Application of the wave theory of motion and the asymptotic method for studying the dynamics of some classes of longitudinal and moving systems (Застосування хвильової теорії руху та асимптотичного методу для дослідження динаміки деяких класів поздовжньо-рухомих систем) *Bulletin of the National University "Lviv Polytechnic". Dynamics, durability and design of machines and devices (Вісник національного університету "Львівська політехніка". Динаміка, міцність та проектування машин і приладів)*, vol.730. pp.114-118, Lviv / Ukraine;
- [13] Sokil M.B., (2010), Flexible nonlinear oscillations of one-dimensional bodies that are characterized by longitudinal velocity and approximate their study (Згинні нелінійні коливання одновимірних тіл, які характеризуються поздовжньою швидкістю руху, і наближене їх дослідження) *Bulletin of the National University "Lviv Polytechnic". Dynamics, durability and design of machines and devices (Вісник національного університету "Львівська політехніка". Динаміка, міцність та проектування машин і приладів)* vol.678, pp.97-102, Lviv / Ukraine;
- [14] Sokil M.B., (2010), Definition on the basis of motion of optimal nonlinear characteristics of systems, which are described by the Klein-Gordon equation (Визначення на основі руху оптимальних нелінійних характеристик систем, які описуються рівнянням Клейна-Гордона), *Automation of production processes for machine building and instrument making (Автоматизація виробничих процесів к машинобудуванні і приладобудуванні)*, vol. 44, pp.57-61, Lviv / Ukraine

JUSTIFICATION OF AIR FLOW SPEED IN THE OXIDATION AREA OF A GASIFIER IN CASE OF STRAW PELLETS USING

ОБҐРУНТУВАННЯ ШВИДКОСТІ РУХУ ПОТОКУ ПОВІТРЯ В ЗОНІ ОКИСЛЕННЯ ГАЗОГЕНЕРАТОРА У ВИПАДКУ ВИКОРИСТАННЯ СОЛОМ'ЯНИХ ГРАНУЛ

Savelii Kukharets ¹⁾, Gennadii Golub ²⁾, Oleh Skydan ¹⁾, Yaroslav Yarosh ¹⁾, Mikolai Kukharets ¹⁾ ¹

¹⁾ Zhytomyr National Agroecological University / Ukraine

²⁾ National University of Life and Environmental Sciences of Ukraine / Ukraine,

Tel: +380676653548, E-mail: saveliy_76@ukr.net

DOI: <https://doi.org/10.35633/inmateh-60-04>

Keywords: tuyere belt, flow diameter, flow length, flow rate loss coefficient, Reynolds number

ABSTRACT

On the basis of the Bernoulli equation the dependence for determining the air flow rate in the oxidation zone of the gasifier was obtained. The obtained dependence makes it possible to theoretically establish the average speed and diameter of the air flow depending on the flow length. To check and clarify the obtained dependence for determining the air flow rate in the oxidation zone, the value of the total loss coefficient of the air flow rate in the volume of straw pellets, which are used as fuel for the gasifier, is experimentally established.

АБСТРАКТ

На основі рівняння Бернуллі отримано залежність для визначення швидкості потоку повітря в зоні окислення газогенератора. Отримана залежність дозволяє теоретично встановити середню швидкість та діаметр потоку повітря в залежності від довжини потоку. Для перевірки та уточнення отриманої залежності для визначення швидкості потоку повітря в зоні окислення, експериментально встановлено значення загального коефіцієнту втрат швидкості потоку повітря в об'ємі солом'яних гранул, що використовуються в якості палива для газогенератора.

INTRODUCTION

One of the promising ways to reduce greenhouse gas emissions is the use of biological fuels (Golub et al, 2017). The equipment in which straw is used to produce heat and electricity is widely used (Barmina et al, 2017). However, when burning straw there are difficulties associated with heterogeneity, high humidity, low specific energy and low melting point of ash (Golub et al, 2018a). Therefore, to obtain a stable supply of energy to the consumer during the burning of straw, it will be appropriate to use gasifiers (Sarker et al, 2015; Wu et al, 2017). The experience of exploitation of gas-producing installations on various biofuel types shows that for the production of gas from straw and straw containing fuels there should be used straight flow gasifiers of the converted gasification process (Sheth et al, 2009; Basu, 2013; Gai et al, 2014). They ensure the stability of the gas formation process, a high degree of decomposition of resins, simplification of technological schemes for cleaning the wood gas from moisture and impurities (Mysak et al, 2017; Goleb et al., 2018b).

In scientific studies considerable attention is paid to the theoretical study on the influence of structural (Susastriawan et al, 2017) or technological (Sheth et al, 2009) parameters of the gasifiers on the quality of the resulting gas. The influence of such parameters as the operating temperature in the oxidation and reduction zones (Sharma, 2011), as well as the humidity of biomass (Channiwala, Ratnadhariya, 2007) on the qualitative composition of the obtained gas is substantiated. Analysis of scientific research allows us to conclude that the gasification of biomass is a complex process based on the equations of thermochemical equilibrium, kinetics, heat transfer and mass transfer, which are based on the rate of gasification of biomass. However, the speed of gasification and the efficiency of the gasification process depend on the modes of air supply to the oxidation zone of the gasifier (Zainal et al, 2001; Melgar et al, 2007; De La Hoz et al, 2017). The experience of gasification of fuels with different straw content shows that insufficient air flow rate can lead to the formation of areas with

¹ Savelii Kukharets, Prof., Doc of Eng.; Gennadii Golub, Prof., Doc of Eng.; Oleh Skydan, Prof., Doc of Econ.; Yaroslav Yarosh, Ph.D. Eng.; Mikolai Kukharets, As.

a lack of air in the field of fuel oxidation, which can significantly reduce the efficiency of the gasification process and cause the phenomenon of ash and slag agglomeration (Sarker et al, 2015; Wu et al, 2017).

Nevertheless, the establishment of real air flow rates in the working areas of the gasifier is difficult for theoretical research due to the complexity of the interaction, diversity and transience of the processes taking place during the gasification of straw and other biomass types (Ali et al, 2016; Yan et al, 2018). This complexity prevents theoretical models from achieving the necessary accuracy to adequately determine the air flow velocity and the geometric shape of the air flow (Gu et al, 2018; Mazaheri et al, 2019). The mathematical models of air movement in the working zones of the gasifier presented in the analysed scientific studies have uncertain boundary conditions. Therefore, it is necessary to accumulate experimental data in the real range of parameters of gas generators and create simple mathematical models that adequately describe the speed of air flow in the oxidation zone of the gasifier.

MATERIALS AND METHODS

To establish the velocity of air flow in the oxidation zone of the gasifier, consider the jet (flow) of air between sections 1-1 and 2-2 (fig. 1) that flows out from the hole of the gasifier tuyere belt (tuyere hole).

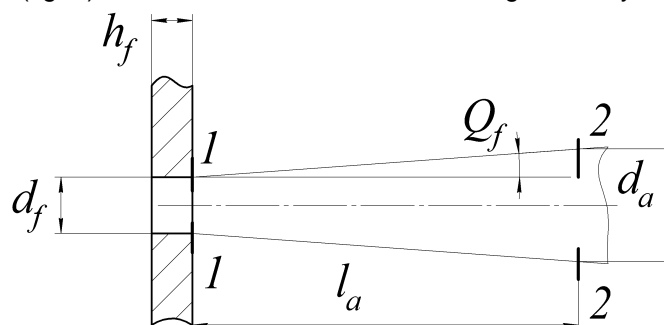


Fig. 1 - Scheme of air flow in the fuel oxidation zone

h_f – tuyere belt depth, m; d_f – the diameter of the flow at the outlet of the tuyere, m; Q_f – polycut expansion of gas stream, deg.; l_a – flow length, m; d_a – diameter of the expanded flow, m

According to Bernoulli's equation (Dayev, 2018; Yeon, Tu, 2019) for real flow it can be written:

$$p_1 + \frac{\rho_1 u_1^2}{2} = p_2 + \frac{\rho_2 u_2^2}{2} + \Delta p_{1-2}, \quad (1)$$

where:

p_1, p_2 – pressure at the beginning and end of the flow, PA; ρ_1, ρ_2 – air density at the beginning and end of the flow, kg/m³; u_1, u_2 – air flow rate at the beginning and at the end, m/sec; Δp_{1-2} – flow pressure loss, PA.

The equation of gas flow continuity (Yeon, Tu, 2019) is as follows:

$$\rho_1 u_1 \frac{\pi d_f^2}{4} = \rho_2 u_2 \frac{\pi d_a^2}{4} = const, \quad (2)$$

where:

d_f – the diameter of the flow at the outlet of the tuyere, m; d_a – diameter of the expanded flow, m.

Pressure loss Δp_{1-2} in the air stream consist of two components, the first is pressure loss along the flow length due to friction between the airflow and the side surface elements (particles) of fuel in the fuel oxidation zone of the gasifier and a pressure loss that is similar to the local loss, which delve into the process of interaction of the flow with a frontal (anterior) surface of the fuel particles.

Based on the above, we can write:

$$\Delta p_{1-2} = \frac{\lambda l_a u_{1-2}^2 \rho_{1-2}}{8 r_{1-2}} + \frac{\xi u_{1-2}^2 \rho_{1-2}}{2} = \frac{u_{1-2}^2 \rho_{1-2}}{2} \left(\frac{\lambda l_a}{d_{1-2}} + \xi \right), \quad (3)$$

where:

ρ_{1-2} – average air flow density, kg/m³; u_{1-2} – average air flow rate, m/sec; d_{1-2} – average flow diameter, m; l_a – flow length, m; λ – coefficient of pressure loss in the flow, which depends on the area of the lateral surface of the fuel elements; ξ - coefficient of pressure loss in the flow, which depends on the density of the fuel elements in the oxidation zone of the gasifier.

On the basis of equations 1-3, the equation of air flow velocity in the section 2-2 is obtained:

$$v_2 = \sqrt{\left(2p_1 - 2p_2 + \rho_1 v_1^2 - v_{1-2}^2 \rho_{1-2} \left(\frac{\lambda l_a}{d_{1-2}} + \xi\right)\right) / \rho_2} \tag{4}$$

If we assume that the hydrostatic pressure in the air flow and the air density are stable, and the hydrodynamic pressure is formed by the velocity head, and express the total coefficient of the flow rate loss in the form of:

$$k_a = \frac{\lambda l_a}{d_{1-2}} + \xi, \tag{5}$$

equation 4 can be written as follows:

$$v_2^2 (4 + k_a) + 2v_1 k_a v_2 + v_1^2 (k_a - 4) = 0, \tag{6}$$

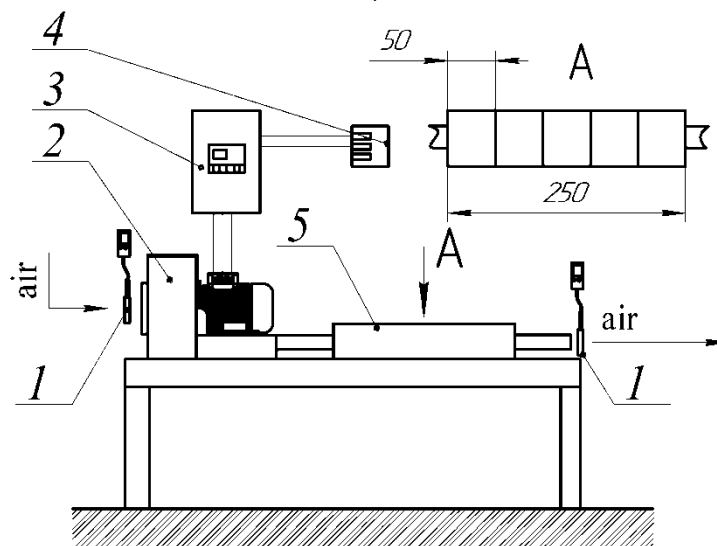
The solution of this equation is as follows:

$$v_2 = \frac{v_1 (4 - k_a)}{4 + k_a}. \tag{7}$$

Given that $d_{1-2} = \sqrt{2v_1 d_f^2 / (v_1 + v_2)}$, the numerical solution of equation (4) allows us to theoretically set the average air flow rate depending on the length of the flow, as well as according to equation (2) continuity of the flow to determine the diameter of the flow. However, to test the theoretical solution, it is necessary to experimentally establish the value of the total coefficient of the flow rate loss and solve the equation (7). For the experimental finding of the coefficient of rate loss of the air flow passing through straw pellets, it was used a pilot plant (fig. 2).



a)



b)

Fig. 2 - The plant for the study of air flow rate losses

a – appearance; b – scheme; 1 – anemometer Tenmars TM-402; 2 – blower Goorui GHBH-0D5-34-1R2; 3 – frequency converter Hitachi-3G3JX-A4075-EF; 4 – socket 0.4 kW; 5 – vessel for simulation of air flow length

The plant consisted of the following main components: a blower 2 and a vessel 5 to simulate the length of the air flow. The air flow rate at the outlet of the blower varied from 6.7 m/sec to 22.2 m/sec. Control of the speed of the blower impeller was carried out using the frequency converter. Vessel 5 was made in the form of a parallelepiped with a width of 100 mm and a height of 80 mm. Inside, the vessel was divided into 5 sections with a length of 50 mm by means of breathable partitions. The inlet and outlet pipes of the vessel were 40 mm in diameter, and were equal to the diameter of the inlet pipe of the blower. During the experiment, each section was consistently unloaded with fuel pellets made of straw. Thus, the length of the air flow in the oxidation zone of the gasifier (from 50 mm to 250 mm) was simulated. Using the anemometer 1, the air rate at the inlet to the blower 2 and the outlet of vessel 5 was determined. The difference in rates made it possible to establish the pressure drop as a result of energy losses of the air flow and to find, according to the methods that are described in the works (Baltussen et al, 2018; Berk, 2018), the k_a loss coefficient.

RESULTS

Experimental studies have allowed to establish the values of the coefficient k_a (table 1) depending on the length of the air flow l_a and the average air flow rate u_{1-2} .

Table 1

Results of experimental studies of air flow losses

Air flow length, mm	Air rate at the inlet to the air-blower, m/sec	Air rate at the outlet of the air-blower, m/sec	Air flow rate losses, m/sec	Air flow pressure loss, PA	Average air flow rate, m/sec	Flow rate loss coefficient
50	22.2	17.5	4.7	3.3	19.9	0.056
50	18.7	15.0	3.7	2.1	16.9	0.048
50	15.8	13.0	2.8	1.2	14.4	0.038
50	10.8	9.6	1.2	0.2	10.2	0.014
100	21.5	15.5	6.0	5.4	18.5	0.105
100	18.5	13.5	5.0	3.8	16.0	0.098
100	13.2	10.1	3.2	1.5	11.6	0.073
100	9.3	7.5	1.8	0.5	8.4	0.046
150	21.0	14.2	6.8	6.9	17.6	0.149
150	15.5	10.7	4.8	3.5	13.1	0.134
150	12.4	8.8	3.6	1.9	10.6	0.115
150	8.1	6.1	2.0	0.6	7.1	0.079
200	20.5	13.0	7.5	8.4	16.8	0.200
200	17.1	11.0	6.2	5.7	14.0	0.192
200	14.1	9.2	4.9	3.6	11.7	0.177
200	7.2	5.0	2.2	0.7	6.1	0.130
250	20.0	12.0	8.0	9.6	16.0	0.250
250	16.6	10.1	6.6	6.4	13.3	0.242
250	13.6	8.4	5.2	4.1	11.0	0.227
250	6.7	4.3	2.4	0.9	5.5	0.190

The analysis of the data in table 1 allowed us to obtain an empirical equation of the dependence of the k_a coefficient on the air flow length l_a and the average air flow rate u_{1-2} , which is valid for the values of the air flow length more than 50 mm and the average air flow rate more than 6.7 m/sec.

$$k_a = -0.3412 + 0.002l_a + 0.0337u_{1-2} - 0.0008u_{1-2}^2 \quad (8)$$

The dependence 8 is graphically shown in fig. 3.

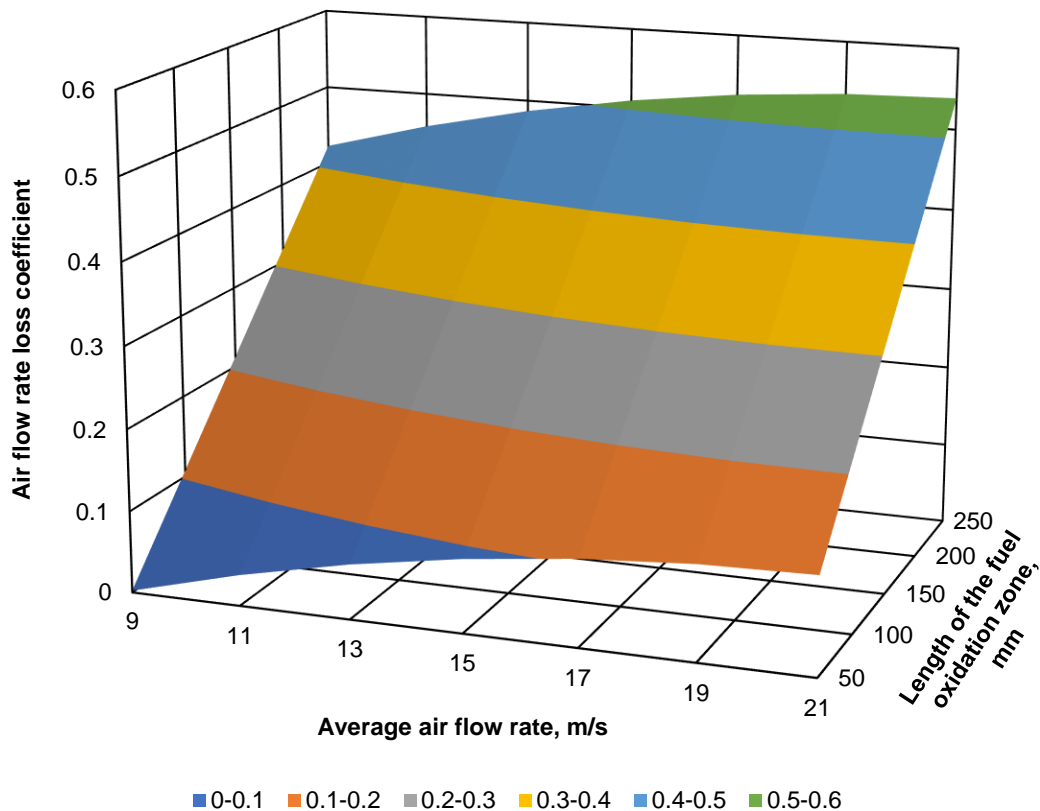


Fig. 3 - Dependence of the air flow rate loss coefficient on the length of the fuel oxidation zone and the average air flow rate

If we compare the dependence of the average air flow rate on its length calculated by numerical method according to equation (4) (theoretical values) and the dependence calculated by equation (7) using the empirical coefficient of loss of air flow rate k_a (experimental values), we can observe almost complete identity of the obtained theoretical and experimental values of the average air flow rate (fig. 4).

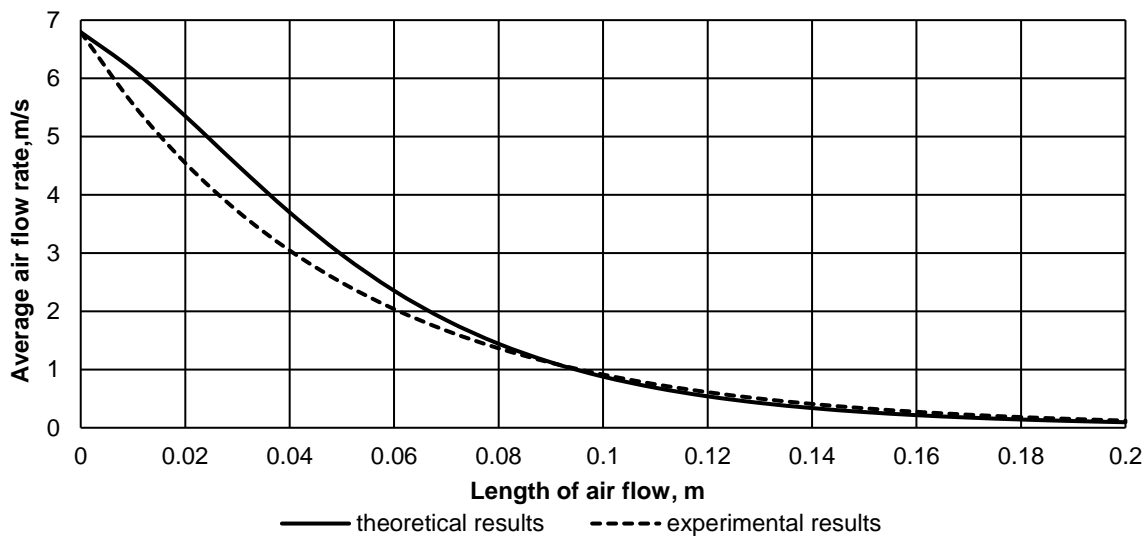


Fig. 4 - Comparison of the dependence of the average air flow rate on its length calculated by the numerical method (theoretical values at loss coefficients $\lambda=0,08$, $\xi=0,2$) and calculated using the empirical loss coefficient k_a (experimental values). The air supply to tuyere belt $0.012 \text{ m}^3/\text{sec}$, the diameter of the tuyere holes – 0.01 m , the number of holes – 24

We assume that the effective air flow rate in the oxidation zone of the gasifier can be estimated by the Reynolds similarity criterion (Berk, 2018; West, Photiou, 2018) and must conform to turbulent regime movement ($Re > 2000$). Such air movement in the oxidation zone in the gasifier provides fuel oxidation without forming low-temperature areas with a lack of air. In particular, the air supply to the tuyere belt of $0.012 \text{ m}^3/\text{sec}$, the diameter of the tuyere holes of 0.01 m , the number of holes of 24 , the effective air movement is terminated at a distance of 0.2 m from tuyere belt, as the Reynolds criterion takes on values smaller than 2000 (Fig. 5). The air flow regime becomes laminar, low-temperature areas appear, the efficiency of the fuel oxidation process decreases, the quality of the gasifier deteriorates.

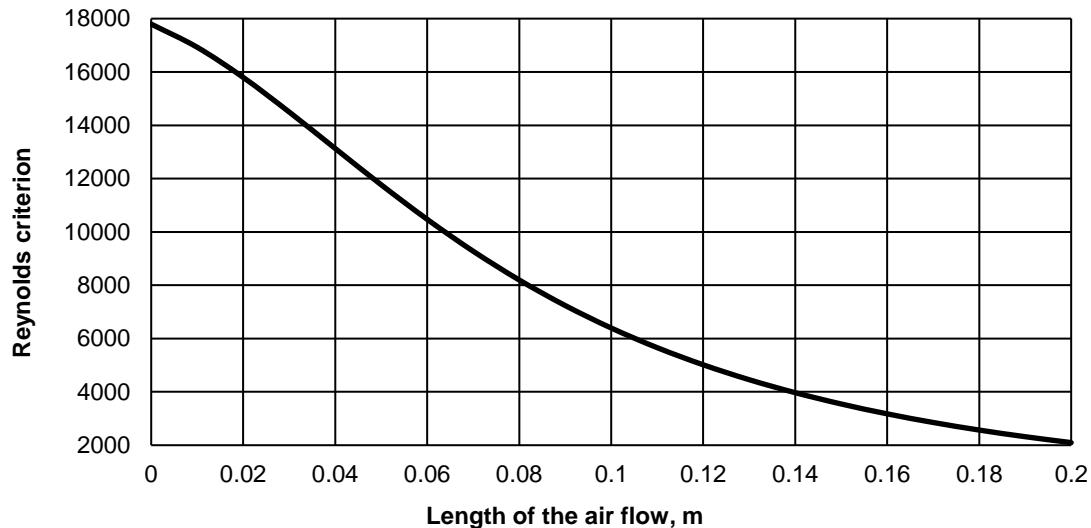


Fig. 5 - The dependence of the Reynolds criterion on the length of the air flow (air supply to the tuyere belt $0.012 \text{ m}^3/\text{sec}$, the diameter of the tuyere holes – 0.01 m , the number of holes – 24)

The flow diameter determined according to equation (2) and reflected in fig.6, in our opinion, will correspond to the effective height of the oxidation zone of the gasifier.

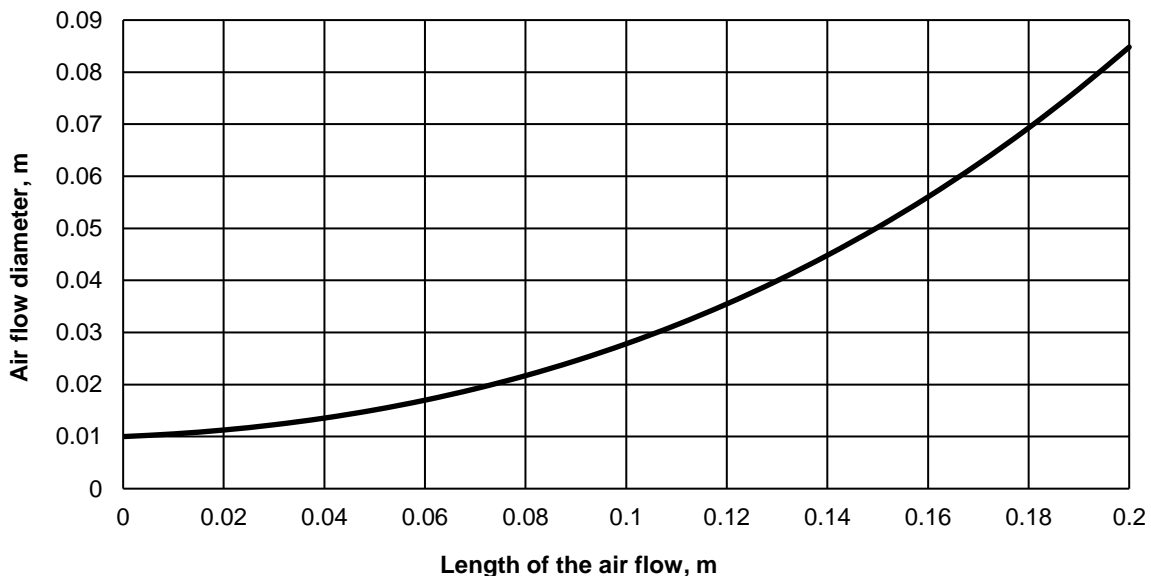


Fig. 6 - Dependence of the air flow diameter on its length (loss coefficients $\lambda=0,08$, $\xi=0,2$, the air supply to tuyere belt - $0.012 \text{ m}^3/\text{sec}$, the diameter of the tuyere holes – 0.01 m , the number of holes – 24)

Thus, when air is supplied to the tuyere belt of $0.012 \text{ m}^3/\text{sec}$, the diameter of the tuyere holes – 0.01 m , the number of holes – 24 , the effective length of the flow l_a in the fuel oxidation zone in the gasifier will be 0.2 m , height h_a of the fuel oxidation zone will be 0.085 m . If the air supply to the tuyere belt of the gasifier is changed, the effective flow length changes accordingly.

For example, when air is supplied to the tuyere belt of 0.006 m³/sec, the diameter of the tuyere holes of 0.01 m, the number of holes of 24, the effective length of the oxidation zone l_a in the gasifier will be 0.15 m, and the height h_a of the fuel oxidation zone – 0.05 m.

As a result of the analysis of theoretical and experimental studies, the influence of the air flow rate from the tuyere hole on the air flow length (linear length of the oxidation zone of the gasifier) was determined:

$$l_a = 0.089 \ln(v_1) + 0.0394 \quad (9)$$

as well as the influence of the air flow rate from the tuyere hole on the air flow diameter (the effective height of the oxidation zone of the gasifier):

$$h_a = (0.0144v_1 - 0.0036) + h_f \quad (10)$$

where:

h_f – tuyere hole height, m

With the help of equations 9 and 10, it is possible to calculate the geometric parameters of the oxidation zone in the gas generator, which ensure the oxidation of the fuel without the formation of low-temperature regions with a lack of air.

CONCLUSIONS

The dependence of the air flow rate in the oxidation zone (gas generator), obtained on the basis of the Bernoulli equation allows us to theoretically set the average air flow rate depending on the flow length, as well as according to the continuity equation to determine the air flow diameter. To verify and clarify the theoretical equation, the value of the total loss coefficient of the flow rate in the volume of straw pellets, which are used as fuel for the gas generator, is experimentally established.

The effective air flow rate in the oxidation zone of the gasifier can be estimated by the Reynolds similarity criterion and must correspond to the turbulent regime ($Re > 2000$). Such air movement in the oxidation zone of the gasifier provides fuel oxidation without forming low-temperature areas with a lack of air. In particular, the air supply to the tuyere belt of 0.012 m³/sec, the diameter of the tuyere holes of 0.01 m, and the number of holes of 24, the efficient air movement stops at a distance of 0.2 m from the tuyere belt, since the Reynolds criterion acquires values less than 2000. The air flow regime becomes laminar, low-temperature areas appear, the efficiency of the fuel oxidation process decreases, the quality of the gasifier deteriorates.

In terms of air supply to the tuyere belt of 0.012 m³/sec, the diameter of the tuyere holes of 0.01 m, the number of holes of 24, the efficient length of the flow in the fuel oxidation zone of the gasifier will be 0.2 m, the height of the fuel oxidation zone will be of 0.085 m. These geometric parameters of the oxidation zone in the gasifier provide straw pellets oxidation without the formation of low-temperature areas with lack of air.

When changing the air supply to the tuyere belt of the gasifier, the effective length of the air flow changes. Thus, when air is supplied to the tuyere belt of 0.006 m³/sec, the diameter of the tuyere holes of 0.01 m, the number of holes of 24, the effective length of the oxidation zone l_a in the gasifier is 0.15 m, and the height of the fuel oxidation zone is 0.050 m.

REFERENCES

- [1] Ali D.A., Gadalla M.A., Abdelaziz O.Y. et al., (2016), Co-gasification of coal and biomass wastes in an entrained flow gasifier: Modelling, simulation and integration opportunities, *Journal of Natural Gas Science & Engineering*, Vol.37, pp.126-137, Netherlands;
- [2] Baltussen M.W., Buist K.A. Peters E.A.J.F., Kuipers, J.A.M., (2018), Multiscale Modelling of Dense Gas-Particle Flows, *Advances in Chemical Engineering*, pp.1–52, Cambridge/U.S.A
- [3] Barmina I., Valdmanis R., Zake M. et al., (2017), Development of gasification/combustion characteristics at thermochemical conversion of biomass mixtures, *Proceedings of 16th International Scientific Conference “Engineering for rural development”*, pp.725-729, Jelgava/Latvia;
- [4] Basu P., (2013), Biomass gasification, pyrolysis and torrefaction: practical design and theory, *Elsevier Science Publishing Co Inc*, 548 p., San Diego/USA;
- [5] Berk Z., (2018), Fluid flow, *Food Process Engineering and Technology*, pp.31–78. London/U.K.;
- [6] Channiwala S.A., Ratnadhariya J.K., (2007), Three zone equilibrium and kinetic free modeling of biomass gasifier – a novel approach, *Renewable Energy*, Vol.34, Issue 4, pp.1050–1058, London/U.K.;
- [7] Dayev Z.A., (2018), Theoretical modelling of natural gas unsteady flow rate measurement using variable differential pressure method, *Flow Measurement and Instrumentation*, Vol.62, pp.33–36, London/U.K.;

- [8] De La Hoz C.K., Pérez J.F., Chica Arrieta E.L., (2017), Design of a Top-Lit Up-Draft Micro-gasifier Biomass Cookstove by Thermodynamic Analysis and Fluent Modeling, *International Journal of Renewable Energy Research*, Vol.7, No.4, pp.2172-2187, Ankara/Turkey;
- [9] Gai C., Dong Y.P., Zhang T.H., (2014), Downdraft gasification of corn straw as a non-woody biomass: Effects of operating conditions on chlorides distribution, *Energy*, Vol.71, pp.638–644, Vol. 50, pp. 583–593, London/U.K.;
- [10] Golub G., Kukharets S., Tsyvenkova N. et al., (2018), Experimental study into the influence of straw content in fuel on parameters of generator gas, *Eastern-European Journal of Enterprise Technologies*, Vol.5/8(95), pp.76-86, United Arab Emirates
- [11] Golub G.A., Kukharets S.M., Tsyvenkova N.M., Golubenko A.A., Kalenichenko P.S., (2018), Research on a boiler furnace module effectiveness working on small fracture wastes, *INMATEH – Agricultural Engineering*, Vol.55, Issue 2, pp.7–16, Bucharest/Romania;
- [12] Golub G.A., Kukharets S.M., Yarosh Y.D, Kukharets V.V., (2017), Integrated use of bioenergy conversion technologies in agroecosystems, *INMATEH – Agricultural Engineering*, Vol.51, Issue 1, pp.93–100, Bucharest/Romania;
- [13] Gu H., Tang Y., Yao J., Chen F., (2018), Study on biomass gasification under various operating conditions”, *Journal of the Energy Institute*, Vol.92, Issue 5, pp.1329-1336, U.K.;
- [14] Mac an Bhaird, S., Walsh, E., Hemmingway, P. et al., (2014), Analysis of bed agglomeration during gasification of wheat straw in a bubbling fluidised bed gasifier using mullite as bed material, *Powder Technology*, Vol.254, pp.448–459, Netherlands;
- [15] Mazaheri N., Akbarzadeh A.H., Madadian E., Lefsrud M., (2019), Systematic review of research guidelines for numerical simulation of biomass gasification for bioenergy production, *Energy Conversion and Management*, Vol.183, pp.671-688, London/U.K.;
- [16] Melgar A., Perez J., Laget H., Horillo A., (2007), Thermochemical equilibrium modelling of a gasifying process, *Energy Conversion and Management*, Vol.48, Issue 1, pp.56–67, London/U.K.;
- [17] Mysak J., Lys St., Martynyak-Andrushko M., (2017), Research on gasification of low-grade fuels in a continuous layer, *Eastern-European Journal of Enterprise Technologies*, Vol.2/8(86), pp.16-23, United Arab Emirates;
- [18] Sarker S., Arauzo J., Nielsen H.K., (2015), Semi-continuous feeding and gasification of alfalfa and wheat straw pellets in a lab-scale fluidized bed reactor, *Energy Conversion and Management*, Vol.99, pp.50–61, London/U.K.;
- [19] Sharma A.K., (2011), Modeling and simulation of a downdraft biomass gasifier 1. Model development and validation, *Energy Conversion and Management*, Vol.52, pp.1386–1396, London/U.K.;
- [20] Sheth P.N., Babu B.V., (2009), Experimental studies on producer gas generation from wood waste in a downdraft biomass gasifier, *Bioresource Technology*, Vol.100, Issue 12, pp.3127–3133, Netherlands;
- [21] Susastriawan A.A.P., Saptoad H., Purnomo, (2017), Small-scale downdraft gasifiers for biomass gasification: A review, *Renewable and Sustainable Energy Reviews*, Vol.76, pp.989–1003, Netherlands;
- [22] West T., Photiou A., (2018). Measurement of gas volume and gas flow, *Anaesthesia & Intensive Care Medicine*, Vol.19(4), pp.183–188, London/U.K.
- [23] Wu Z., Meng H., Luo Z., et al., (2017), Performance evaluation on co-gasification of bituminous coal and wheat straw in entrained flow gasification system, *International Journal of Hydrogen Energy*, Vol.42, Issue 30, pp.18884–18893, London/U.K.;
- [24] Yan W.-C., Shen Y., You S., and et al., (2018), Model-Based Downdraft Biomass Gasifier Operation and Design for Synthetic Gas Production, *Journal of Cleaner Production*, Vol.178, pp.476-493, Netherlands;
- [25] Yeoh G.H., Tu J., (2019), Gas-Particle and Liquid-Particle Flows, *Computational Techniques for Multiphase Flows*, pp.227–319, London/U.K.;
- [26] Zainal Z., Ali R., Lean C., Seetharamu K.N., (2001), Prediction of performance of a downdraft gasifier using equilibrium modeling for different biomass materials, *Energy Conversion and Management*, Vol.42, Issue 12, pp.1499-1515, London/U.K.

ENGINEERING MANAGEMENT OF TILLAGE EQUIPMENT WITH CONCAVE DISK SPRING SHANKS

/

ІНЖЕНЕРНИЙ МЕНЕДЖМЕНТ ҐРУНТОБРОБНИХ АГРЕГАТІВ З ПРУЖНИМИ СТОЯКАМИ СФЕРИЧНИХ ДИСКІВ

Ivan Rogovskii ¹⁾, Luidmyla Titova ¹⁾, Viktor Trokhaniak V.I.¹⁾, Oleksandr Haponenko ^{1,2)},
Mykola Ohienko ¹⁾, Vasyi Kulik ¹⁾

¹⁾ National University of Life and Environmental Sciences of Ukraine / Ukraine;

²⁾ Scientific Organization "Leonid Pogorilyy Ukrainian Scientific Research Institute of Forecasting and Testing of Machinery and Technologies for Agricultural Production" / Ukraine

Tel: +380673513082; E-mail: Trohaniak.v@gmail.com

DOI: <https://doi.org/10.35633/inmateh-60-05>

Keywords: disk, spring shank, soil medium, dynamic characteristics, deflections.

ABSTRACT

The programme and the procedure of the experimental laboratory and field investigations of the shank parameters and the interaction process of a concave disk spring shank and a soil medium under ballast operating element loading, if there is a change in the travelling speed of a unit, have been developed. Estimation of the measurement results has been conducted based on the uncertainty concept. Under ballast loading (optimal reduced mass), the influence of the random components of a draft force on the process of interaction of a concave disk on a spring shank and the soil is at least one and a half times less. According to the results of the experimental studies, the dependences that show the influence of a unit speed and an operating element reduced mass on the drag force (energy indicator) and the elastic deflections of a shank (an agro-technical indicator) have been determined. Technical and economic assessment of the operating efficiency of tillage equipment according to the operating cost structure and based on practical implementation has been conducted.

РЕЗЮМЕ

В статті обґрунтовано програму і методику експериментальних досліджень з визначення параметрів пружного стояка сферичного диска і режимів процесу його взаємодії з ґрунтовим середовищем при використанні баластного довантаження при зміні поступальної швидкості мобільного енергетичного засобу. Адекватність результатів вимірювань виконано за концепції невизначеності. Встановлено, що з баластним довантаженням за оптимальної зведеної маси, безпосередній вплив випадкових складових тягового опору на процес взаємодії сферичного диска на пружному стояку з ґрунтом, щонайменше в півтора рази, менший. За даними експериментальних досліджень встановлено залежності з визначення впливу швидкості мобільного енергетичного засобу та зведеної маси на робочому органі на енергетичний показник, а саме тяговий опір, та агротехнічний показник, а саме пружні відхилення стояка. Представлено результати техніко-економічної оцінки ефективності експлуатації дискового ґрунтообробного агрегату за структурою експлуатаційних витрат і на основі виробничого застосування.

INTRODUCTION

There are significant quality changes taking place in modern agricultural production engineering caused by intensification of production processes together with efficient use of resources (Viāduŝ D.I. et al, 2018). According to these changes, it is necessary to improve agricultural equipment in order to provide their optimum process conditions with minimum energy consumption and improve reliability of individual parts and units (Xiong P. et al, 2018). The accomplishment of these tasks is of great importance for soil-tilling equipment, namely for disk headers, since they provide 60–80% of soil pre-treatment and basic cultivation (Razzaghi E. & Sohrabi Y., 2016; Srivastava A.K. et al, 2016).

¹ Rogovskii I.L., Prof. Ph.D. Eng.; Titova L.L., Assoc. Prof. Ph.D. Eng.; Trokhaniak V.I., Assoc. Prof. Ph.D. Eng.; Haponenko O.I., Ph.D. Eng.; Ohienko M.M., Assoc. Prof. Ph.D. Eng.; Kulik V.P., Ph.D. Eng.

The non-market harvest part left on the surface of a field is the determining factor for further performance of technological operations and developing requirements for operational devices, namely, for the development of disk tillage equipment with new design and technical characteristics in order to provide quality stubble cleaning, the decrease of energy consumption and the increase of operational reliability (Viăduț V. et al, 2018). The experience of using spring shanks of cultivator operating elements and their positive assessment opens up fresh opportunities for the improvement of disk tillage equipment reliability (Dewangan A. et al, 2017).

Operating elements arranged on spring shanks oscillate due to the irregularity of soil drag forces (Gheorghiuță N.E. et al, 2018; Badegaonkar U.R. et al, 2010). As a result, soil breakdown takes place with less energy consumption that decreases the rate of fuel consumption by tillage equipment (Klendii M.B. & Klendii O.M., 2016). A disk header with spring shanks can be better adjusted to a field surface texture and, thus, can provide the required quality of soil cultivation (David A. et al, 2014).

Thus, a relevant applied scientific task is the substantiation of the dynamic characteristics and the design parameters of the spring shanks of the disk operating elements of soil-tilling equipment (Hevko B.M. et al, 2018; Hevko R.B. et al, 2017).

The aim of the research – is to improve the operating efficiency of disk tillage equipment by means of substantiating their design parameters and the dynamic characteristics of operating element spring shanks.

MATERIALS AND METHODS

The general research technique provided the use of modern methods of theoretical and experimental investigations, the theoretical substantiation was conducted with the help of the methods of mathematics, theoretical mechanics, oscillation theory, differential and integrated calculation (Asejeva A. et al, 2013). The experimental research was conducted in the field environment based on standard practices and the specific techniques developed by the author. The procedure of measuring elastic deflections of the operating elements provided for the use of the information and measurement system and the method of strain measurement (Tutunaru L.F. et al, 2014). The research data processing was conducted with the help of mathematical methods of statistics. The method of regression analysis was applied.

The design and engineering characteristics of disk tillage equipment are improved in case of the arrangement of disk operating elements on spring shanks due to their oscillations. Substantiation of the design parameters and the dynamic characteristics of shanks as a system “soil – disk – spring shank” allows for improving the efficiency of equipment operation in terms of operational reliability and energy consumption.

The analysis of the existing scientific research suggests that the significant influence on the operation process of a tillage unit on a spring shank is characterized by the models that take into account the influence of empirical factors and design parameters with coefficient matrices. The application of complex models makes it almost impossible to solve the problem of the description of a spring shank with a concave disk movement (Barwicki J. et al, 2012).

Thus, it is necessary to solve the applied scientific task – substantiate the dynamic characteristics and the design parameters of a spring shank of disk tillage equipment (Constantin N. & Cojocaru I., et al, 2012).

The programme of the experimental investigation on spring shanks of concave disks allowed for:

- substantiating the measuring diagram and estimating the dynamic characteristics of a concave disk spring shank;
- determining the design parameters and the dynamic characteristics of a spring shank;
- investigating the influence of the dynamic characteristics of an operating element spring shank on the efficiency of equipment, taking into account the randomness of soil reaction (field research);
- comparing the theoretical and the experimental data and their compliance.

The scheme of the measuring system, taking into account the information flow of the changes in soil properties, was substantiated (Galat U.N. & Ingale A.N. et al, 2016). There were KF-5P1 full-bridge strain gauge sensors arranged on a shank and they were connected through SPIDER-8 analog-to-digital converter with CatMan Express 4.5 software (Trokhaniak V.I., et al, 2019). The converter performed scanning with a frequency of 250 Hz, analog-to-digital signal conversion and digital array generation as a *.xls file (Gheres M.I., 2014). The sensors were cable connected to the equipment and protected from the effect of inferences (Rogovskii I.L. et al, 2019). In order to conduct experimental research (testing and assessment of spring shank performance), an experimental plant was developed (Fig. 1).

The information obtained as a result of the laboratory experiments was presented in the form of calibration curves of “deflection” and “loading” (Rogovskii I.L. et al, 2019). Simulation of the change in spring shank dynamic characteristics was performed by applying lumped mass to an operating element mounting and bearing unit (impact factor at the following levels: reduced mass and mass plus added weight) (Rogovskii I.L. et al, 2019). The investigation was conducted with the use of a multilevel experiment (Constantin N. & Cojocaru I., 2008). The peculiarity and the advantage of this pattern is the most complete estimation of the investigation process (Table 1). The increase in the level of external impact (by means of increasing travelling speed) determines the level of influence on a spring shank and ballast loading determines the sublevel.

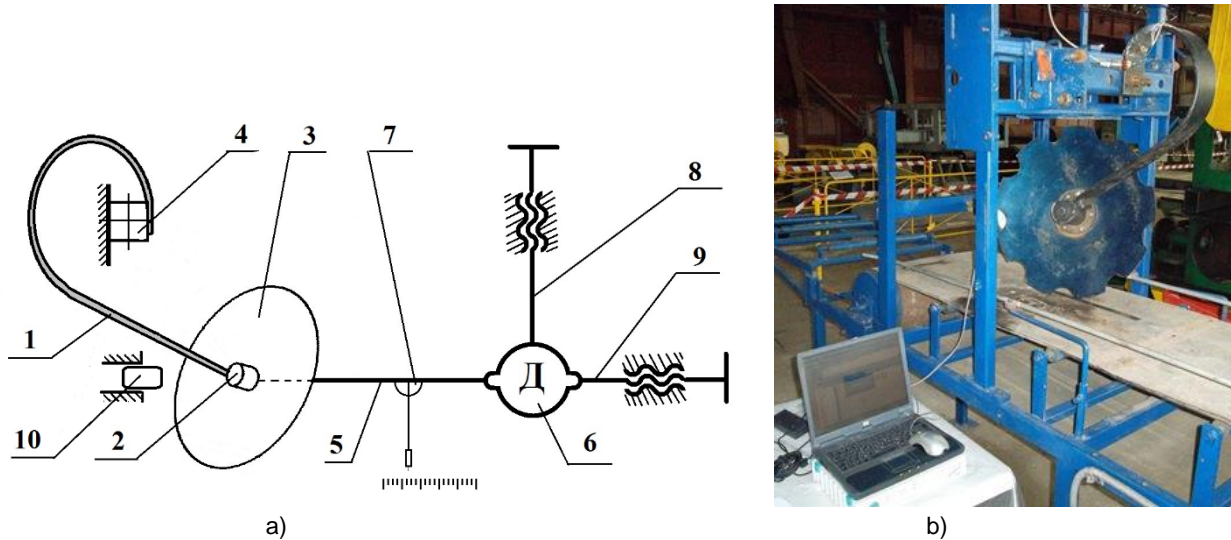


Fig. 1 - An experimental plant (technical equipment) for testing and evaluation of spring shank operation efficiency

a – structural diagram; b – general view; 1 – spring shank of a concave disk; 2 – bearing unit; 3 – operating element (concave disk); 4 – fixed base; 5 – wire rope; 6 – dynamometer; 7 – level; 8 – screw-type vertical regulator; 9 – screw-type horizontal regulator; 10 – percussive mechanism for disturbing shank equilibrium.

Table 1

Investigation Pattern									
Impact factors		Optimization Parameters							
Travelling speed, v [km/h]		Reduced mass, m [kg]		External impact / draft force [N]		Deflection [mm]		Generalized coordinate [deg.]	
Level (total levels)	Variability interval	Level (total levels)	Variability interval	Average value	Mean square deviation	Average value	Mean square deviation	Average value	Mean square deviation
1 (5)	2	30	0.5 (2)	F	F_{MSD}	δ	δ_{MSD}	λ	λ_{MSD}

Process parameters were recorded in real time in the course of unit operation rounds with the predefined sampling period. Recording areas under steady-state loading conditions were considered. The defined digital array obtained from the analog-digital converter contained several thousand values of the variable under study. If there are many observations, the “n” testing error is less than 0.5–1%. According to “loading” calibration curves, the digital array of the external impact values was processed and statistical process parameters were determined.

In order to process the experimental data, the methods of mathematical planning and mathematical statistics were used. The estimation of the research findings was performed on the basis of the uncertainty conception describing the dispersion of the values, which could be reasonably assigned to the variable to be measured.

RESULTS

The procedure of determining the design parameters and the dynamic characteristics of spring shanks was investigated using the suggested fabricated and approved design of the experimental plant, the values of the reduced mass (Fig. 2, a) were determined, a load-deflection curve was defined and free spring shank oscillations were observed (Fig. 2, b).

Field experiments were conducted in the process of breaking grain crop fallen seeds germination (second de-husking). The experimental spring shank was attached to the frame of DL-2.5 unit (Fig. 3).

It was determined that the interaction process of a disk operating element on a spring shank and the soil is unsteady and its statistic performance varies with time (Fig. 4). Process unsteadiness is caused by quick changing conditions of operation in a soil medium and the influence of meso- and micro-relief of a field surface.

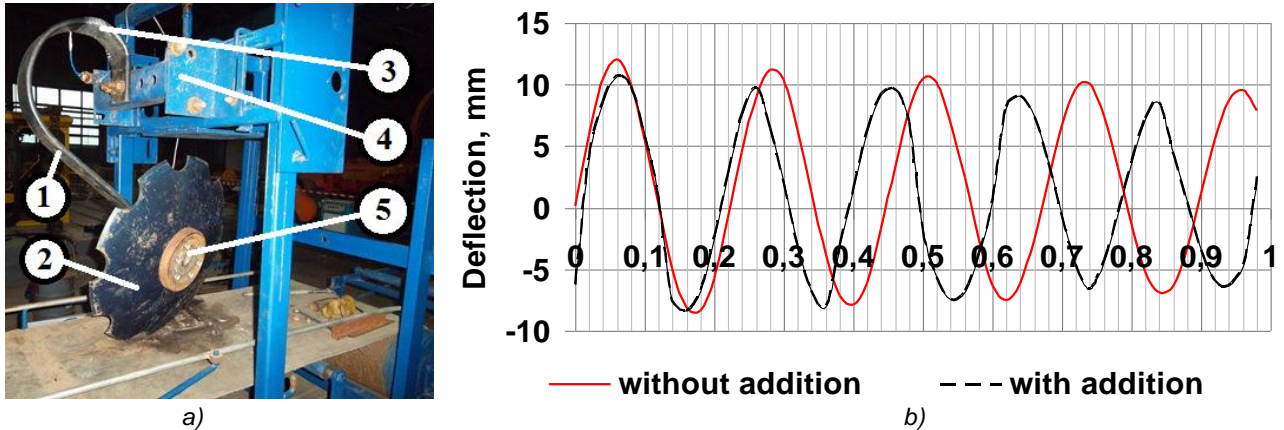


Fig. 2 - Realization of laboratory investigations: a – exterior of a spring shank with ballast loading while determining the reduced mass; b – free spring shank oscillations

1 – a spring shank of a concave disk; 2 – an operating element (a concave disk);
3 – resistive strain gauges on the surface of a spring shank; 4 – a fixed base; 5 – ballast loading



a)

b)



Fig. 3 - General view of a disk header with spring shanks

a – general view of the unit; b – spring shanks under study; 1 – roller; 2 – unit frame; 3 – hitch linkage; 4 – operating element (a concave disk); 5 – spring shank; 6 – resistive strain gauges on the surface of a spring shank.

The probability laws of the instantaneous indicator values of the interaction process of the soil and an operating element on a spring shank (Fig. 4, b) show two vertices in the distribution series, which proves the unsteadiness of the phenomenon under study, the degree of the distribution asymmetry is within the range from 0.1 to -0.1. The shape of the correlation function (Fig. 4, c) meets a zero value that corresponds to the cycle of latent periodical vibrations; however, since the influence of random noise is significant, if there are considerable shifts, the value of the correlation coefficient tends to zero.

The conducted spectral analysis (Fig. 4, d) shows that shank oscillations is a mixed random process with a polyharmonic deterministic component.

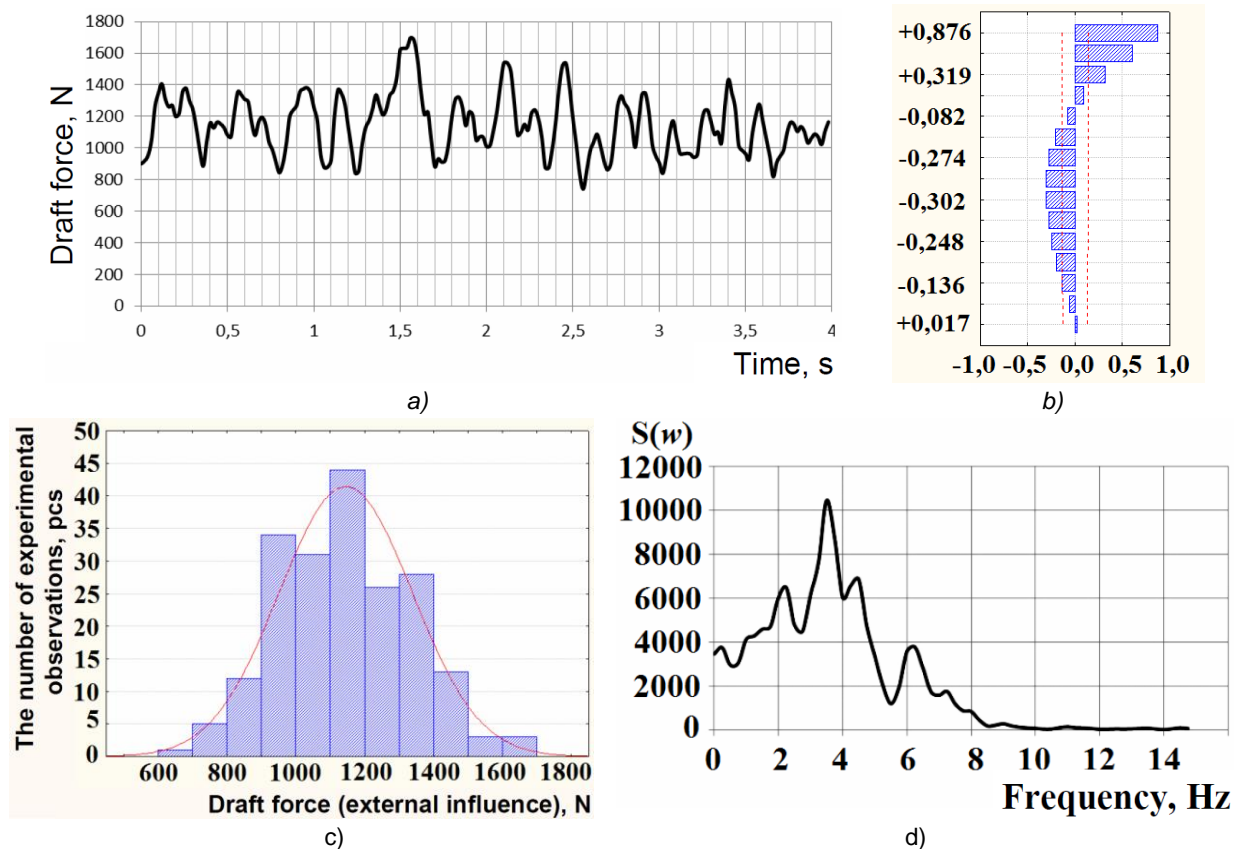


Fig. 4 - Statistical characteristics of the interaction process of an operating element on a spring shank and the soil

a – behaviour of spring shank response to the external impacts; b – autocorrelation function; c – density of distribution; d – spectral analysis.

The investigation results prove that there is a change of spring shank response to a soil medium under additional operating element loading. The increase of the draft force was $F = 1180 \dots 1300$ N of the device speed without additional operating element loading, which was equal to 17%, and under additional loading it was $F_{load} = 1170 \dots 1240$ N or 11%. If a unit travelling speed is 4 m/s, the difference between additional loading options is equal to 10% (Fig. 5, Fig. 6).

Vibroactivity $F_{MSD} = 180 \dots 290$ N of a spring shank without additional loading increases almost linearly and within the speed range from 1.9 to 4 m/s it increases for 78%, and under additional loading it increases for 136% – in 2.36 times. The increase of operating element vibroactivity influences a soil medium and decreases its resistance to breaking down, which explains the decrease of the drag force under additional loading.

Estimation of the process-dependent parameters of a disk header with spring shanks was conducted according to the statistical characteristics of elastic deflections in the process of interaction of an operating element and the soil (Fig. 7, Fig. 8).

Mean-square spring shank deflection describes the uniformity of tillage depth provided by an operating element, according to the reference conditions the non-uniformity is $\sigma = 15$ mm. That is to say, the increase of a unit's energy efficiency (draft force decrease) is limited by the qualitative process flow indicator at the speed value of 4 m/s.

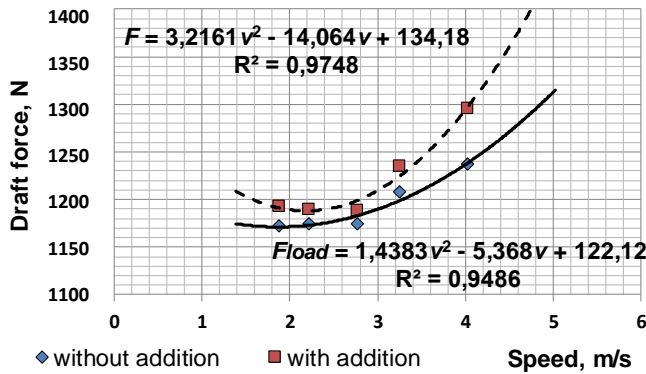


Fig. 5 - Draft force-vs-unit travelling speed characteristic curve (according to calibration curves)

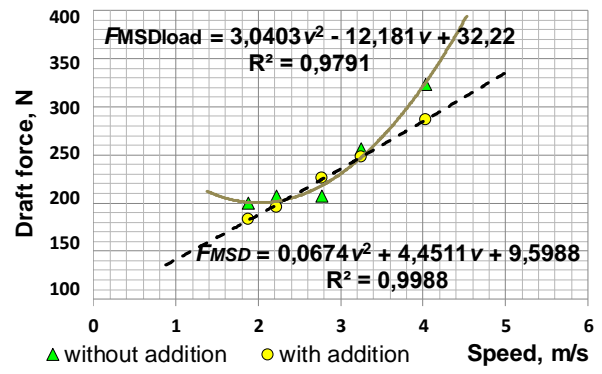


Fig. 6 - Mean-square draft force deviation-vs-unit travelling speed curve

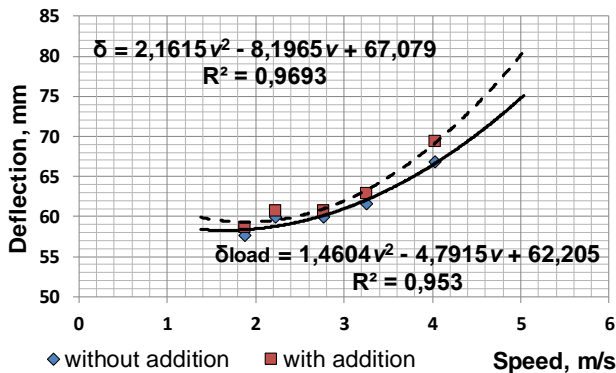


Fig. 7 - Average deflection value-vs-unit travelling speed curve (according to calibration curves)

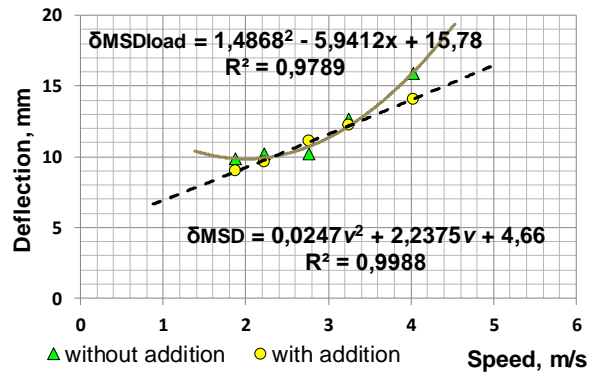


Fig. 8 - Mean-square value of shank deflections-vs-unit travelling speed characteristic curve $\sigma = f(\delta)$

Based on the minimum draft force criterion, the aimed speed rate is 10 km/h, and the value of draft force is equal to approximately 12 kg per one shank.

When comparing the uncertainties of the measurements, it can be concluded that, if there is ballast additional operating element loading, the influence of random components on the interaction process of a concave disk on a spring shank and the soil is at least one and a half times less.

The theoretical and the experimental investigation results on the change of the generalized coordinate during process performance were compared (Fig. 9), the difference in the values under various unit speed rates increases with speed gain, the decrease rate at the speed of 4 m/s is by 1.33% greater compared to the theoretical dependence. The average deviation of the experimental data (rate 2.77 m/s) from the theoretical ones is equal to 0.164 deg., which does not exceed the expanded measurement uncertainty.

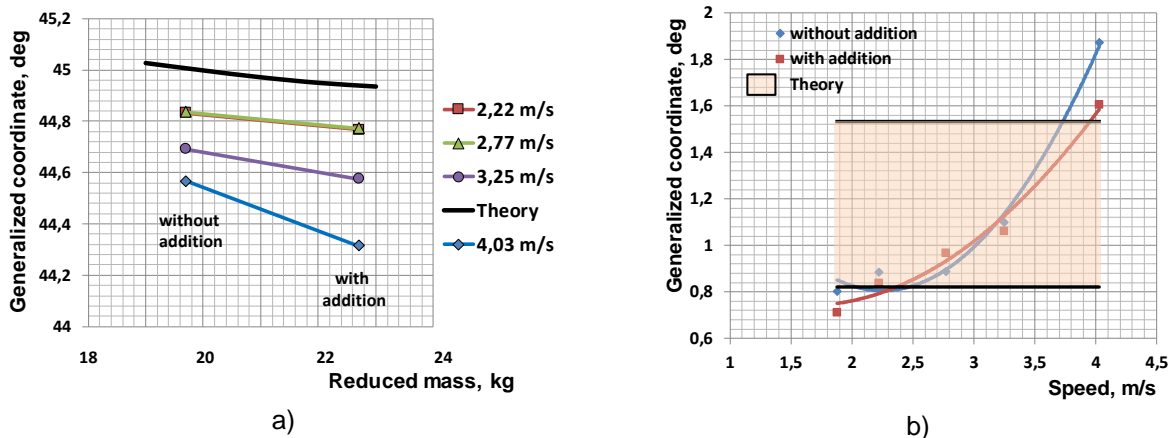


Fig. 9 - Comparison of the theoretical dependences and the experimental data
 a – generalized coordinate value in dynamic equilibrium;
 b – generalized coordinate value as a mean-square deviation from dynamic equilibrium

When comparing the theoretically obtained dependences of the generalized coordinate deviations and the mean-square values from the experimental data, it is obvious that there is their significant compliance according to the range of values. The lower limit to the range of values obtained theoretically (Fig. 9, b) approximates the experimental data at the rate of 2.22 m/s, the upper limit approximates at the rate of 3.25 m/s, here, the value deviations exceed the uncertainty of measurements by 4.3 and 1.7 times, respectively. Thus, it can be concluded that deviations from the dynamic equilibrium are determined by the influence of a soil medium, however, if the reduced mass is increased, the uncertainty decreases – the interaction process of a concave disk on a spring shank and the soil acquires 2.5 times better controllability.

CONCLUSIONS

1. The dependences obtained from the experimental investigations prove that there is a change in the interaction characteristics of an operating element on a spring shank and a soil medium on condition of the reduced mass change. While in operation, the increase of the draft force produced by the change of the speed from 2 to 4 m/s is equal to 17% for a unit equipped with typical spring shanks and it is equal to 11% in case of the shanks with the substantiated reduced mass indicators, which proves the weightage of the reduced mass influence on process performance. If a unit speed is 4 m/s, the advantage of the spring shanks with the substantiated parameters makes the difference of 5%, or 60 N per each shank.

2. Due to the use of the improved procedure of estimating measurement results it has been determined that the influence of random components on the interaction process of the system “soil – disk – spring shank” is at least one and a half times less in case of the operating elements with the substantiated reduced mass. The mean difference of the experimental and the theoretical data according to a shank deflection parameter is equal to 0,164 deg. (speed rate 2.77 m/s), which does not exceed the permissible measurement uncertainty.

3. The recommended rational parameters of spring shanks, which have been determined according to the investigation results, are the following: the rigidity (20 – 40 kN/m), the reduced mass (10 – 30 kg), the frequency (1.6 – 4 Hz and 3.5 – 7 Hz) and the amplitude (1 – 9 deg. and 2.5 deg.) of oscillations. It has been determined that the use of spring shanks with the defined parameters allows for decreasing energy consumption in the process of soil tillage by a disk operating element by 7% without degrading the quality of process performance, compared to a typical spring shank with the parameters that are substantiated only in terms of the functional need to protect an operating element from overloading.

REFERENCES

- [1] Asejeva A., Kopiks N., Viesturs D., (2013), Optimal distribution of the amount of work among the tractor aggregates considering set agrotechnical terms. *Proceedings of the International scientific conference "Economic science for rural development": Production and cooperation in agriculture. Finance and taxes*, no. 30, pp. 38-42, Jelgava / Latvia;
- [2] Badegaonkar U.R., Dixit G. Pathak K.K., (2010), An experimental investigation of cultivator shank shape on draft requirement. *Archives of Applied Science Research*, no. 2, issue 6, pp. 246-255, Chhattisgarh / India;
- [3] Barwicki J., Gach St., Ivanovs S., (2012), Proper utilization of soil structure for crops today and conservation for future generations. *Proceedings of 11th International Scientific Conference "Engineering for Rural Development"*, vol. 11, pp. 10-15, Jelgava / Latvia;
- [4] Constantin N., Irimia D., Persu C., (2012), Testing the multifunctional aggregate for soil tillage works – MATINA, *INMATEH Agricultural Engineering*, vol. 36, issue 1, pp. 5-12, Bucharest / Romania;
- [5] Constantin N., Cojocaru I., (2008), Large working capacity technical equipment for overturning the stubble field and preparing the germinating bed in all types of soil designed to tractors of 120-220 HP, *Scientific Papers INMATEH*, no. 26, pp. 102-108, Bucharest / Romania;
- [6] David A., Voicu Gh., Persu C., Gheorghe G., (2014), The Determination of the Resistant Forces for Deep Loosening of Soil Machines with Active Organs. *INMATEH Agricultural Engineering*, vol. 42, issue 1, pp. 5-12, Bucharest / Romania;
- [7] Dewangan A., Singh Rajput N., (2017), Stress Analysis of Cultivator: A Survey Approach. Crop cultivation. *International Research Journal of Engineering and Technology*. vol. 04, issue 01, pp. 692-696, Delhi / India;
- [8] Galat U.N., Ingale A.N., (2016), Failure Investigation & Analysis of Agricultural 9 Tyne Cultivator Used In Various Soil Condition. *International Journal on Recent and Innovation Trends in Computing and Communication*. vol. 4, issue 1, pp. 173–179, Delhi / India;

- [9] Gheorghiuță N.E., Biriș S.Șt., Ungureanu N., Ionescu M., (2018), Contributions to the analysis of the vibratory working tools by FEM. *International Symposium ISB INMA TEH Agricultural and Mechanical Engineering*, 01-03 November, pp. 579-582, Bucharest / Romania;
- [10] Gheres M.I., (2014), Mathematical model for studying the influence of tillage tool geometry on energy consumption. *INMATEH Agricultural Engineering*, vol. 42, issue 1, pp. 5-12, Bucharest / Romania;
- [11] Hevko B.M., Hevko R.B., Klendii O.M., Buriak M.V., Dzyadykevych Y.V., Rozum R.I., (2018), Improvement of machine safety devices. *Acta Polytechnica*, vol. 58, no. 1, pp. 17-25, Prague / Czech Republic.
- [12] Hevko R.B., Yazlyuk B.O., Liubin M.V., Tokarchuk O.A., Klendii O.M., Pankiv V.R., (2017), Feasibility study of the process of transportation and stirring of mixture in continuous-flow conveyers. *INMATEH: Agricultural engineering*, vol. 51, issue 1, pp. 49-58. Bucharest / Romania;
- [13] Klendii M.B., Klendii O.M., (2016), Interrelation between incidence angle and roll angle of concave disks of soil tillage implements. *INMATEH: Agricultural engineering*, vol. 49, issue 2, pp. 13-20, Bucharest / Romania;
- [14] Razzaghi E., Sohrabi Y., (2016), Vibratory soil cutting a new approach for the mathematical analysis. *Soil and Tillage Research*. vol. 159, pp. 33-40, Kiel / Germany;
- [15] Rogovskii I., Titova L., Trokhaniak V., Trokhaniak O., Stepanenko S., (2019), Experimental study on the process of grain cleaning in a pneumatic microbiocature separator with apparatus camera. *Bulletin of the Transilvania University of Brasov, Series II: Forestry, Wood Industry, Agricultural Food Engineering*, vol. 12 (61), issue 1, pp. 117-128, Brasov / Romania;
- [16] Rogovskii I.L., Titova L.L., Trokhaniak V.I., Rosamaha Yu.O., Blesnyuk O.V., Ohienko A.V., (2019), Engineering management of two-phase coulter systems of seeding machines for implementing precision farming technologies. *INMATEH Agricultural Engineering*, vol. 58, issue 2, pp. 137-146, Bucharest / Romania;
- [17] Rogovskii I.L., Titova L.L., Trokhaniak V.I., Solomka O.V., Popyk P.S., Shvidia V.O., Stepanenko S.P. (2019), Experimental studies of drying conditions of grain crops with high moisture content in low-pressure environment. *INMATEH Agricultural Engineering*, vol. 57, issue 1, pp. 141-146, Bucharest / Romania;
- [18] Srivastava A.K., Goering C.E., Rohrbach R.P., Buckmaster D.R., (2016), Soil tillage. Chapter 8, Engineering Principles of Agricultural Machines, *Monography*, 2nd ed., St. Joseph, Michigan: ASABE. Copyright American Society of Agricultural and Biological Engineers, pp. 169-230, Michigan / USA;
- [19] Trokhaniak V.I., Rutylo M.I., Rogovskii I.L., Titova L.L., Luzan O.R., Bannyi O.O., (2019), Experimental studies and numerical simulation of speed modes of air environment in a poultry house. *INMATEH Agricultural Engineering*, vol. 59, issue 3, pp. 9-18, Bucharest / Romania;
- [20] Tutunaru L.F., Nagy E.M., Coța C., (2014), Influence of tillage tools cutting edge wear over technical and economic indicators. *INMATEH Agricultural Engineering*, vol. 44, issue 3, pp. 5-12, Bucharest / Romania;
- [21] Vlăduț D.I., Biriș S., Vlăduț V., Cujbescu D., Ungureanu N., Găgeanu I., (2018), Experimental researches on the working process of a seedbed preparation equipment for heavy soils. *INMATEH Agricultural Engineering*, vol. 55, issue 2, pp. 27-34, Bucharest / Romania;
- [22] Vlăduț V., Gheorghe G., Marin E., Biriș S. Șt., Paraschiv G. Cujbescu D., Ungureanu N., Găgeanu I., Moise V., Boruz S., (2017), Kinetostatic analysis of the mechanism of deep loosening system of arable soil. *45th International Symposium "Actual tasks on agricultural engineering"*, 21-24 February, ISSN 1848-4425. pp. 217-227, Opatija / Croatia;
- [23] Xiong P., Yang Z., Sun Z., Zhang Q., Huang Y., Zhang Z., (2018), Simulation analysis and experiment for three-axis working resistances of rotary blade based on discrete element method. *Nongye Gongcheng Xuebao, Transactions of the Chinese Society of Agricultural Engineering*, vol. 34, issue 18, pp. 113-121, Beijing / Chine.

OPTIMIZATION OF THE DECORTICATION PROCESS OF INDUSTRIAL HEMP STEMS BY MATHEMATICAL PLANNING METHOD

/

ОПТИМІЗАЦІЯ ТЕХНОЛОГІЧНОГО ПРОЦЕСУ ДЕКОРТИКАЦІЇ СТЕБЕЛ ТЕХНІЧНИХ КОНОПЕЛЬ МЕТОДОМ МАТЕМАТИЧНОГО ПЛАНУВАННЯ

Galina Boyko¹⁾, **Hanna Tikhosova**¹⁾ **Tatiana Ternova**²⁾ ¹

¹⁾ Kherson National Technical University, Department of Commodity Studies, Standardization and Certification, Kherson / Ukraine

²⁾ Kherson National Technical University, Department of Information Technology, Kherson / Ukraine

Tel: +3(08)0508274885; E-mail: galina_boyko_86@ukr.net

DOI: <https://doi.org/10.35633/inmateh-60-06>

Keywords: industrial hemp, diameter, decortication, mathematical planning

ABSTRACT

The paper presents the results of theoretical and experimental studies aimed at optimizing the decortication process of industrial hemp stems. In order to achieve this goal, physical and mechanical properties of industrial hemp straw stems were investigated, with the choice of the main quality indicator - diameter, which directly influences the bast output. Also, with the help of mathematical planning of the experiment, the optimal treatment mode for the stems of industrial hemp with clearing of wood of 5-6% was calculated.

РЕЗЮМЕ

Представлена робота містить результати теоретичних та експериментальних досліджень, спрямованих на оптимізацію процесів декортикації стебел соломи технічних конопель. Для досягнення поставленої мети проводили дослідження фізико-механічних властивостей стебел технічних конопель з вибором основного показника якості – діаметра, який безпосередньо впливає на вихід лубу, та проведенням математичного планування експерименту, який дозволив отримати оптимальні режими переробки стебел з очищенням лубу від костриці 5-6 %.

INTRODUCTION

Hemp is a highly productive agricultural crop, the cultivation and processing of which allows to obtain income that is ten times higher than the cost of its cultivation and processing. However, the cultivation and processing of industrial hemp is currently declining significantly in Ukraine (Boyko G. A., et al., 2018). This is due to a number of reasons - lack of capacity for primary processing, outdated regulatory documentation for determining the quality of raw materials, and the lack of modern lean processes, which leads to obtaining low quality products.

The main stage in processing industrial hemp straw stems in the field is decortication, which results in the destruction of stem structure and the separation of bast. During decortication, the connections between the fibrous layer and the wood must be broken and, at the same time, the strength of the bast should be maintained when fully released from shives (Boyko G. A., et al., 2017). Thus, the influence of physical and mechanical properties on the process of decortication plays an important role in the output of high-quality bast. Therefore, in order to regulate the decortication process itself and determine the optimum breaking parameters, it is necessary to examine in detail all the qualitative properties of straw to determine the basic quality indicators that directly affect the fibre output.

At present, obtaining high-quality bast from stems of industrial hemp on decortication machines is an urgent task for experts in the hemp industry in many European countries. Many foreign and domestic scientists devoted their scientific works to the problem of studying the influence of physical and mechanical characteristics of hemp stems on the operation modes of decorticators: Hiliyazetdinov R.N., Ipatov O.M., Novikov Ye.V., Hobson R.N., Amaduccis D.I., Igathinathane C.A., Kovur S.K., Munder F. (Boyko G. A., et al., 2017).

¹ Boyko G., Ph.D. doctoral student; Tikhosova H., Prof. Ph.D. Eng.; Ternova T., Ph.D. doctoral student

In these works, it is stated that the main parameters for establishing the optimal decortication mode are the roller set, the depth of the grooves, the pressure of the roller springs and the feed rate of the stems in the processing area.

Taking into account previous researches of physical and mechanical indicators of the stems of industrial hemp straw, in this paper the optimal parameters of the decortication mode and their influence on qualitative indicators of initial production were established by means of mathematical planning.

MATERIALS AND METHODS

Materials

For conducting the research, new varieties of industrial hemp have been selected, bred by the Institute of Bast Crops of NAASU and harvested at different maturity periods (green, full maturity), which are most often sown by agrarians in Ukraine: Viktoria, Gliana, and Nika.

Hemp fibre was obtained on a decorticator developed by «CannaSystems» (Canada). The modern decorticator simultaneously collects and processes the stems of industrial hemp, both on the field and in a stationary environment.

Raw material is fed to the unit through the front conveyor system. Straw is collected and fed by conveyor to the grinding rolls, and the wood is sent through the back holes to the second conveyor. As a result of this process, fibre is obtained with a purification of up to 8% in just one pass.

For the research on the industrial hemp stems a decorticator developed by CannaSystems was used. Currently, this technology is used in North American countries, China and Australia. According to this technology, the stems of hemp straw, after mowing in the field, come to the mobile decorticator, which in the process of processing the stems in the rollers are separated by the bast and wood, which are directed separately to different conveyor belts of the decorticator (Boyko G. A., et al., 2017). This technology is shown in Figures 1, 2.

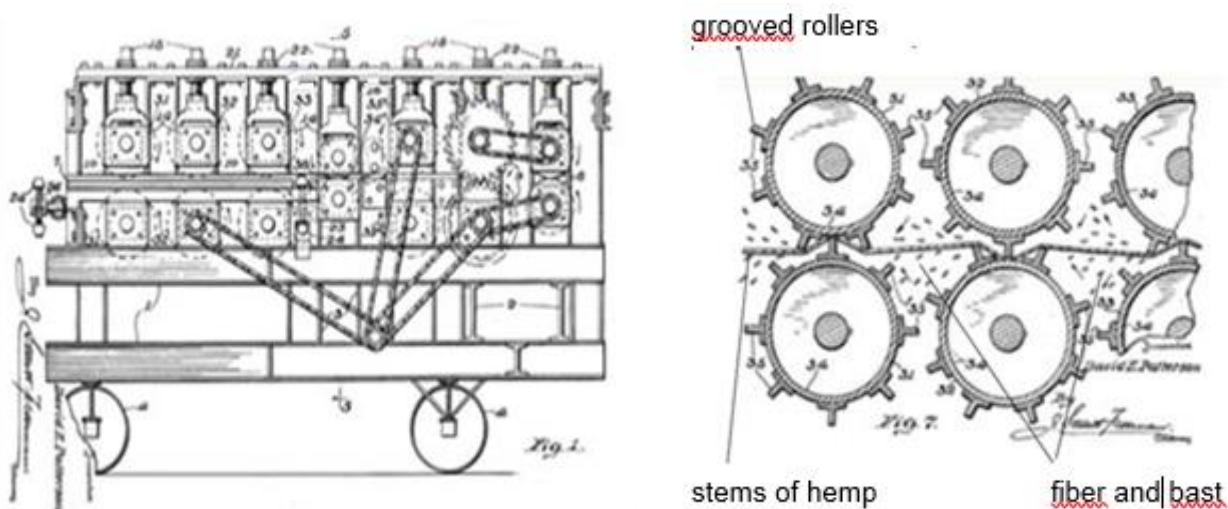


Fig. 1 - Decorticator for processing stems of hemp straw in the field and stationary conditions



Fig. 2 - Working elements of the decorticator

A - a pair of smooth rollers; B - three pairs of grooved rollers
C - decortication field; D - power rotor; E - the main fixed rotor

The main stage in the technological process of processing the stems of hemp straw in the field is decortication, which results in the destruction of the stem structure and the separation of the bast. During decortication, the bonding between the fibrous layer and the wood must be broken and, at the same time, the strength of the bark should be maintained when fully released from the wood.

The main working bodies of the decorticator are horizontal grooved rollers shown in Fig. 3.

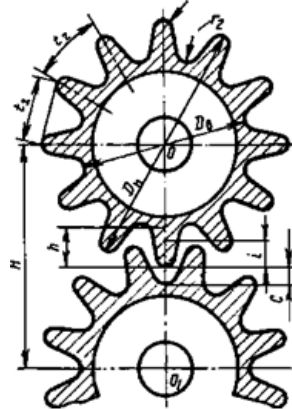


Fig. 3 - The main dimensions of the rollers in the decorticators

The decorticator, depending on the physical properties of hemp straw stems, changes the set of rollers, the depth of the grooves, the amount of pressure on the permeable material, the density of loading of the decorticator raw material, the speed of rotation of the rollers and the location of the stems relative to the grooves.

When decorticating large diameter hemp stems, a set of small diameter rollers are used and, conversely, large diameter rollers are used to decorticate small diameter hemp stems.

To increase the efficiency of the passage of hemp straw stems increase the depth of the grooves. When it is necessary to soften the passage mode, which is important in the case of processing weakened and easily processed stems, the depth of the grooves must decrease.

Unit specifications:

- Processing speed: varies according to the feed rate of the wood from 2 t/h. up to 5 t/h.
- Hydraulic flow of 100-150 litres/min., liquid/cooling 30 hp.
- The basis of the unit is a power unit with a capacity of 15 hp, a feed conveyor 5 l.s.
- Conveyors weight 2000 kg, conveyor systems 5500 kg.
- Working surface 900 mm, length 1.8 m wide 2.43 m
- Conveyor length 3.65 m, height 2.74 m
- The unit is equipped with a rail and a cut-off switch for safety.
- The unit must be serviced by two people.
- Front and rear clearance for straw 3 m., 300 mm lateral clearance for collecting raw material / cleaning.
- The input tray is installed for fast straw feed systems.
- AC 220V motor, PTO14 hydraulic drive.
- It processes from 4,000 to 16,000 tons/year.

Methods

In order to ensure the validity of the conclusions based on the experimental data, the results of the experiments were statistically processed for the case of small samples from the general population with normal distribution (*Ternova T.I. et al., 2018*). The following statistical characteristics were determined: arithmetic mean; deviation from the arithmetic mean; variance; mean square deviation; coefficient of variation; the confidence interval in which the mean of the measurement results is likely; relative error; absolute error.

Selection of decortication parameters by rotatable design

In Ukraine, the stems of industrial hemp are processed generally by traditional technology - the technology of dry processing of wood. Traditional technologies are aimed only at obtaining the most valuable long parallelized hemp fibre - raw materials whose physical and mechanical properties are only able to satisfy the needs of twine and rope factories. The low percentage of long fibre hemp yield (15-20%) compared to its high content in stems (more than 35%) and a significant amount of fibrous waste

(approximately 75-80% by weight of recycled wood) is evidence of the imperfection of existing technologies of primary treatment of this bast hemp culture and the irrational use of hemp.

In order to obtain greater fibre yield and high quality, Kherson National Technical University scientists are constantly researching the improvement of both traditional and modern technologies for processing industrial hemp straw.

The scientists of Kherson National Technical University carried out a number of studies on the development of an effective decortication process for the processing of industrial hemp. Initially, to determine the optimum modes of decortication, the physical and mechanical characteristics of industrial hemp stems were investigated and the main input quality index of stems - diameter (x_1) was selected, which has the greatest influence on the process of their breaking in decorticators (Tihosova A.A., et al., 2018). The content of shives in the bast after breaking the stems (y) was selected as the output characteristic, which can be used to evaluate the quality of the separation of bast from hurds. The quality of breaking in the decorticator rollers depends mainly on the depth of the grooves (x_2).

Thus, on the basis of the obtained data, mathematical models of the process of industrial hemp stems decortication of different harvesting periods for all three studied varieties were obtained in order to produce bast suitable for widespread use, that is, as much as possible cleaned from shives (Ternova T.I., et al., 2018). Rotatable second-order experiment design optimized the setting of groove depth (x_2) depending on the diameter of industrial hemp stems (x_1) for three varieties - Gliana, Nika and Viktoria - to obtain bast with predetermined content values of shives (y) under different periods of harvesting. All indicators of the experimental calculations are shown in table 1.

Table 1

Matrices of rotatable design of the second-order experiment

Variety and harvesting period	Design Matrix of experiment	Diameter of stems, mm	Dependence of the shive content in the bast on the grooves depth and the diameter of hemp straw stems
Gliana (green harvesting of industrial hemp straw stems)	maximum diameter at $x_1 = +1$	7.4 mm	
	minimum diameter at $x_1 = -1$	5.8 mm	
	optimum grooves depth x_2	6.0 mm	
Nika (green harvesting of industrial hemp straw stems)	maximum diameter at $x_1 = +1$	9.3 mm	
	minimum diameter at $x_1 = -1$	7.7 mm	
	optimum grooves depth x_2	6.0 mm	
Viktoria (green harvesting of industrial hemp straw stems)	maximum diameter at $x_1 = +1$	8.1 mm	
	minimum diameter at $x_1 = -1$	6.5 mm	
	optimum grooves depth x_2	6.0 mm	

Variety and harvesting period	Design Matrix of experiment	Diameter of stems, mm	Dependence of the shive content in the bast on the grooves depth and the diameter of hemp straw stems
Gliana (harvesting for seeds upon full maturity of stems)	maximum diameter at $x_1 = +1$	7.8 mm	
	minimum diameter at $x_1 = -1$	6.2 mm	
	optimum grooves depth x_2	6.0 mm	
Nika (harvesting for seeds upon full maturity of stems)	maximum diameter at $x_1 = +1$	9.5 mm	
	minimum diameter at $x_1 = -1$	7.9 mm	
	optimum grooves depth x_2	6.0 mm	
Viktoria (harvesting for seeds upon full maturity of stems)	maximum diameter at $x_1 = +1$	9.8 mm	
	minimum diameter at $x_1 = -1$	8.2 mm	
	optimum grooves depth x_2	6.0 mm	

The mathematical models of the process of industrial hemp stems decortication of different harvesting periods for all three studied varieties were obtained in order to produce bast suitable for widespread use, that is, as much as possible cleaned from shives. Thus, as a result of a full factorial experiment, the dependence of the quality of decortication of hemp stems of three varieties - Gliana, Nika, Viktoria - on the depth of the grooves of decorticator rolls and the diameter of the stems after green harvesting and harvesting for seeds upon full maturity was obtained.

Determination of coefficients and absolute errors

In further studies of rotatable experiment design, using known ratios to obtain the coefficients of equation, the coefficients for the three studied varieties and two harvesting periods were determined, that is, for six dependencies, as well as absolute errors in calculating their values (Ternova T.I., et al., 2016). The calculated dependence coefficients and the values of their absolute errors are given in Table. 2.

Table 2

Dependence coefficients and the values of their absolute errors

i	y ₁ Gliana, full maturity		y ₂ Nika, full maturity		y ₃ Viktoria, full maturity		y ₄ Gliana, green harvesting		y ₅ Nika, green harvesting		y ₆ Viktoria, green harvesting	
	b _i	Δb _i	b _i	Δb _i	b _i	Δb _i	b _i	Δb _i	b _i	Δb _i	b _i	Δb _i
0	11.96	0.53	12.50	0.34	13.96	0.36	10.16	0.19	11.46	0.27	10.98	0.15
1	2.68	0.42	2.70	0.27	2.88	0.28	2.82	0.15	2.70	0.22	2.11	0.12
2	-5.53	0.42	-5.82	0.27	-6.26	0.28	-5.24	0.15	-5.71	0.22	-5.92	0.12
12	-0.35	0.59	-0.58	0.38	0.21	0.40	-0.53	0.21	-0.45	0.31	0.70	0.16
11	0.13	0.45	0.15	0.29	0.35	0.30	0.12	0.16	0.12	0.23	0.06	0.13
22	0.55	0.45	0.75	0.29	1.70	0.30	1.02	0.16	0.92	0.23	2.11	0.13

The adequacy of the obtained models was determined according to the Fisher criterion. For the 95% confidence probability, the number of degrees of freedom of the greater variance - 3 and less - 4, the critical value of the Fisher criterion is $F_{cr.} = 6.59$. The values of the Fisher criterion, which were determined in the study of each of the designed models, are shown in table 2. It is obvious that all $F_{observatin.} < F_{cr.}$, therefore designed models are adequate (table 3). The significance of the coefficients of each model was estimated by the magnitude of their errors, the values of which are given in Table 2. As it is known, if the absolute value of the coefficient is less than the value of its absolute error, such coefficient is considered insignificant and can be excluded from the equation.

Table 3

Determining the Fisher criterion value $F_{observatio}$ for the dependencies $y_1 - y_6$

y ₁	y ₂	y ₃	y ₄	y ₅	y ₆
6.075	5.981	6.580	4.578	6.198	5.687

According to the experimental data, the following analytical dependencies were eventually obtained (1-6):

$$y_1 = 11.96 + 2.68x_1 - 5.53x_2 + 0.55x_2^2, \quad (1)$$

$$y_2 = 12.50 + 2.70x_1 - 5.82x_2 - 0.58x_1x_2 + 0.75x_2^2, \quad (2)$$

$$y_3 = 13.96 + 2.88x_1 - 6.26x_2 + 0.35x_1^2 + 1.70x_2^2, \quad (3)$$

$$y_4 = 10.16 + 2.82x_1 - 5.24x_2 - 0.53x_1x_2 + 1.02x_2^2, \quad (4)$$

$$y_5 = 11.46 + 2.70x_1 - 5.71x_2 - 0.45x_1x_2 + 0.92x_2^2, \quad (5)$$

$$y_6 = 10.98 + 2.11x_1 - 5.92x_2 + 0.70x_1x_2 + 2.11x_2^2. \quad (6)$$

The obtained analytical dependences were used in the paper to determine the influence of the diameter of industrial hemp straw stems of different varieties on the quality of bast cleaning from shives in the process of decortication.

RESULTS AND DISCUSSION

According to the results of the tests, the mathematical dependences of the wood content in the fiber on the diameter of the hemp straw stalks and the mathematical dependences of the wood content in the fiber on the depth of the grooves of the decorticator rollers were obtained.

According to the experimental design matrices shown in Table 1, the stems of industrial hemp straw of three varieties - Gliana, Nika, Viktoria - were decorticated after green harvesting and harvesting upon full maturity. As a result of processing the experimental data, mathematical dependences of the shives content in the bast on the diameter of hemp straw stems were obtained, and the mathematical dependences of the shives content in the bast on the depth of the decorticator rollers' grooves, which are presented in Table 4.

Table 4

Mathematical dependences of the shives content in the bast on the depth of the decorticator rollers' grooves

Harvesting technology	yg1, yn1, yv1 – shives content in bast depending on the influence of basic indicators of the decortication of hemp straw stems under green harvesting (g -Gliana, n – Nika, v – Viktoria)	Graphical representation of the dependencies: 1-Gliana, 2- Nika, 3- Viktoria.	The highest degree of bast cleaning, depending on the optimal modes, %
The influence of diameter on the quality of bast cleaning			
Green harvesting technology	$y_{g1} = -12.97 + 2.87d$ $y_{n1} = -17.21 + 2.81d$ $y_{v1} = -18.77 + 3.50d$		4,5-6,0
Full stem maturity	$y_{g2} = -16.43 - 3.35d$ $y_{n2} = -17.01 + 2.81d$ $y_{v2} = 21.00 - 6.18d + 0.54d^2$		5,0-6,5
The influence of grooves depth on the quality of bast cleaning			
Green harvesting technology	$y_{g3} = 61.76 - 15.41h + 1.02h^2$ $y_{n3} = 63.06 - 14.93h + 0.92h^2$ $y_{v3} = 93.05 - 27.04h + 2.11h^2$		4,0-5,0
Full stem maturity	$y_{g4} = 53.48 - 11.07h + 0.55h^2$ $y_{n4} = 60.27 - 13.28h + 0.75h^2$ $y_{v4} = 87.72 - 23.24h + 1.70h^2$		5,5-7,0

Analyzing the data from table 4, it can be noted that the thinner the stems of industrial hemp straw, the lower the content of shives in the bast after the processing of stems on the decorticator at the optimum depth of the grooves (Ternova T.I., 2018). Also, it should be noted that at the optimum depth of the grooves in the bast of Victoria hemp variety, the content of shives is 9.41% at an average diameter of 9.0 mm, and the lowest content of shives is 6.98% which is characteristic of the bast of Gliana hemp variety with an average diameter of 7.0 mm.

In view of the above, in order to obtain high quality raw materials, it is necessary to regulate the parameters of decorticator adjustment depending on the diameter of stems and the hemp harvesting period, taking into account their varietal differences.

Nika, Gliana and Victoria varieties can be processed using all existing industrial hemp processing technologies. The results of fibre output and wood cleaning may be different. But at this stage of work, the optimal technology of processing stems of industrial hemp of these varieties for Ukraine was selected.

CannaSystems' decorticator processes hemp stems on the field, which saves on the cost of additional space. But the quality indicators of fibre in their parameters satisfy the domestic entrepreneurs with the further processing of the obtained fibre.

CONCLUSIONS

The analysis of regression models and graphical dependences of the quality indicators of bast quality on the harvesting period of industrial hemp straw stems of different varieties showed that hemp stems upon full maturity require more intensive actions during the processing on the decorticator to clean bast from shives than the hemp stems of green harvesting (Boyko G. A., et al., 2019). Also, the direct dependence of the output of high-quality raw material on the diameter of stems of industrial hemp straw was proved. Thus, for better bast cleaning from shives when decorticating hemp stems, the grooves depth should be set up depending on the diameter of stems, the harvesting period and the varietal differences of hemp.

ACKNOWLEDGEMENT

Boiko Halyna conducted the research of physical and mechanical properties of industrial hemp and carried out the compilation of literature; Ternova Tetiana conducted mathematical calculations and experiment design; Anna Tikhosova supervised the research project.

REFERENCES

- [1] Boyko G. A., Tihosova A.A., Kynasov A.V., (2018), Influence of harvesting methods on processing technology and further use of hemp fibre, *Vestnik Kherson National Technical University*, pp. 75-81.
- [2] Boyko G. A., Chursina L.A., Kynasov A.V., (2017), Comparative analysis of domestic, European and north American technologies of industrial hemp, *Vestnik Khmelnytsky National University*, pp. 76-79.
- [3] Boyko G. A., Chursina L.A., Kynasov A.V., (2017), Development of Ukrainian light industry through the use of hemp raw materials, *The scientific heritage, Budapest/ Hungary*, pp. 68-71.
- [4] Tihosova A.A., Boyko G. A., Kynasov A.V., (2018), Classification of a system for processing industrial hemp stems according to collection methods, *International scientific-practical Internet-conference «Entrepreneurship, trade, marketing: strategies, technologies, innovations»*. Kyiv, pp. 101-106.
- [5] Ternova T.I., Kashtalyan P.V., Rozhkov S.A., (2018), Detection and assessment of changes in the state of an object in information management systems, *Vestnik Kherson National Technical University*, pp. 311-318
- [6] Ternova T.I., Kashtalyan P.V., Rozhkov S.A., (2018), Problems of object recognition in information management systems, *XIX International Conference on Mathematical Modeling - Kherson KNTU*, pp. 91-105.
- [7] Ternova T.I., Gorach O.O., Bogdanova O.F., (2016), Modeling the technological process of obtaining cellulose through the method of production of technology and industrial designation, *Vestnik Khmelnytsky National University*, pp. 120-124.
- [8] Boyko G. A., Chursina L.A., Kynasov A.V., (2017), Development of Ukrainian light industry by using raw hemp, *The scientific heritage (Budapest, Hungary)*, pp. 68-71.
- [9] Ternova T.I., (2018), Assessment of the change in the state of the object in the information management complexes, *Proceedings of the 4th International Scientific and Practical Conference «Modern Technologies of Industrial Complex»*- 2018, pp. 298.
- [10] Boyko G. A., Chursina L.A., Tihosova A.A., (2019), Quality evaluation of industrial hemp stems by an optimized technique, *Materials of International Scientific-Practical Conference «New approaches to state quality control under European principles*, pp.149-152.

EFFECTS OF MOISTURE CONTENT ON SOME ENGINEERING PROPERTIES OF ARECANUT (*ARECA CATECHU L.*) FRUIT WHICH ARE RELEVANT TO THE DESIGN OF PROCESSING EQUIPMENT

PENGARUH KADAR AIR TERHADAP BEBERAPA SIFAT KETEKNIKAN BUAH PINANG (*ARECA CATECHU L.*) YANG RELEVAN UNTUK PERANCANGAN PERALATAN PENGOLAHANNYA

Ramayanty Bulan¹, Devianti¹, Ega Septi Ayu¹, Agustami Sitorus² ¹

¹Department of Agriculture Engineering, Faculty of Agriculture, Syiah Kuala University / Indonesia

²Research Centre for Appropriate Technology, Indonesian Institute of Sciences (LIPI), Subang / Indonesia

E-mail: rama_bulan@unsyiah.ac.id

DOI: <https://doi.org/10.35633/inmateh-60-07>

Keywords: *machinery, local product crops, precision machine, water content*

ABSTRACT

The physical and mechanical properties of fresh arecanut fruit have not been comprehensively and thoroughly investigated scientifically yet. This made the researchers and engineers not to be precise in designing the fresh arecanut handling machine. Thus, the present study was aimed to investigate some engineering properties of arecanut fruit in three moisture viz. 67.66%, w.b. (underripe stages), 64.86%, w.b. (ripe stages), and 33.90%, w.b. (overripe stages). In general, the results of the study show that the geometric and arithmetic mean diameter, surface area, bulk and true density, porosity, angle of repose, compression force and static coefficient of friction at different surfaces (stainless steel, plywood, and glass) of arecanut fruit were found to increase 2.16%, 2.70%, 4.26%, 0.02%, 42.16%, 42.41%, 9.97%, 17.04%, 20.30%, and 22.04% respectively at decrease of moisture content from 67.66%, w.b. to 33.90%, w.b. However, sphericity, aspect ratio, thousand fruit mass, and bulk density of the arecanut fruit were found to decrease 2.31%, 3.31%, 34.54%, and, 50.24%, respectively at a decrease of moisture content from 67.66% (w.b.) to 33.90% (w.b.). Some engineering properties of arecanut fruit indicate something slightly different from the arecanut kernels so that this data can help the researcher or engineer to design the fresh arecanut fruit handling machine more precisely.

ABSTRAK

Sifat fisik dan mekanik buah pinang belum komprehensif dan mendalam diselidiki secara ilmiah. Hal ini menyebabkan banyak para peneliti dan perekayasa kurang presisi dalam merancang mesin penanganan buah pinang. Oleh karena itu, penelitian ini bertujuan untuk menyelidiki beberapa sifat keteknikan dari buah pinang dalam tiga kandungan kadar air yaitu 67,66%, b.b. (tahap kurang matang), 64,86%, b.b. (tahap matang), dan 33,90%, b.b. (tahap lewat matang). Secara umum, hasil penelitian menunjukkan bahwa diameter rata-rata geometris dan aritmatika, luas permukaan, massa dan kepadatan sebenarnya, porositas, angle of repose, gaya kompresi dan koefisien gesekan statis pada permukaan yang berbeda (stainless steel, kayu lapis, dan kaca) buah pinang ditemukan masing-masing meningkat 2,16%, 2,70%, 4,26%, 0,02%, 42,16%, 42,41%, 9,97%, 17,04%, 20,30%, dan 22,04% seiring dengan penurunan kadar airnya dari 67,66%, b.b. hingga 33,90%, b.b. Namun, sphericity, aspect ratio, massa seribu buah pinang, dan kepadatan massa buah pinang ditemukan menurun masing-masing adalah 2,31%, 3,31%, 34,54%, dan, 50,24%, seiring dengan penurunan kadar airnya dari 67,66% (b.b.) menjadi 33,90% (b.b.). Beberapa sifat rekayasa dari buah pinang menunjukkan hal berbeda dari biji pinang itu sendiri sehingga data ini dapat membantu peneliti atau perekayasa untuk merancang mesin penanganan buah pinang segar lebih presisi.

INTRODUCTION

Arecanut (*Areca catechu L.*) is a large-scale plantation plant in Aceh Province, Indonesia. The availability of post-harvest handling of arecanut is still not widely investigated scientifically, which results in the inefficiency of the arecanut fruit processing chain from harvest in the field to the product that can be used. Meanwhile, the level of need for the use of betel nuts as a mixture of medicines and cosmetics from areca products continues to increase.

¹ Ramayanty Bulan, Ph.D. Eng.; Devianti, Ph.D. Eng.; Ega Septi Ayu, B.Eng.; Agustami Sitorus, M.Sc.

Therefore, some engineering properties are importantly related to the design of machines and the analysis of the behaviour of the product during agricultural process operations such as handling, planting, harvesting, threshing, cleaning, sorting, drying, and packaging [Moradi et al., 2019].

According to several studies (Moradi et al., 2019; Pandiselvam et al., 2019; Singh and Meghwal, 2019; Bajpai et al., 2019) the design of machines handling agricultural products is determined by the physical and mechanical properties of the product itself. Therefore, many researchers and engineers made the determination of physical properties of agriculture products such as us Kaleemullah and Gunasekar (2002), Sarajeh et al. (2014), Ahmed et al. (2019), determined physical properties of arecanut kernels, grass peas, smany and zaghoul date fruit, respectively.

The lack of published articles on moisture dependent physical properties of arecanut is only about the measurement of physical properties from kernels (Kaleemullah and Gunasekar, 2002). Therefore, the present study is envisaged to investigate some engineering properties of arecanut fruit such as mean diameters (geometric and arithmetic), sphericity, aspect ratio, surface area, thousand fruit mass, true density and bulk density, porosity, angle of repose, compression force, and static coefficient of friction at different surfaces (stainless steel, plywood, and glass) over moisture content range from 67.66%, (w.b.) to 33.90%, (w.b.).

Three stages of arecanut fruit that were commonly harvested in arecanut farmers in Aceh Province were investigated, namely underripe phase (67.66%, w.b.), ripe phase (64.86%, w.b.), and overripe phase (33.90%, w.b.) (Figure 1). The effects of arecanut fruit (*Areca catechu* L.) age on some engineering properties relevant to the design of processing equipment was investigated and modelled too. We hope, measurement of some engineering properties of arecanut fruit will be helpful for researchers and engineers in machine designing for industrial processing and fabrication of preharvest and postharvest handling equipment like planting, harvesting, sorting, grading, collecting, drying, pulper, grinding, packaging machines, and storage structures more precisely.

MATERIALS AND METHODS

Three stages of arecanut fruit maturation are used as samples to be measured in this study. These three samples are based on the habits of arecanut farmers in Aceh Province in harvesting arecanut. The three samples are included in the category underripe phase, ripe phase, overripe phase whose moisture content is 67.66% (w.b.), 64.86% (w.b.), and 33.90% (w.b.), respectively (Figure 1). The moisture content of each sample was determined using the AOAC (1995) method and calculated using Equation 1.

$$M_c = \left(\frac{W_i - W_d}{W_i} \right) \times 100\% \quad (1)$$



Fig. 1 - Three stages of arecanut fruit which are commonly harvested by farmers in Aceh Province

The arecanut fruit size was determined by picking one hundred arecanut fruit (underripe stages (67.66%, w.b.), ripe stages (64.86%, w.b.), and overripe stages (33.90%, w.b.)) randomly and measuring their three main dimensions (major, medium and minor diameters). After that, the geometric mean diameter is determined using Equations 2 and arithmetic mean diameter using Equation 3.

$$D_g = \sqrt[3]{LWT} \quad (2)$$

$$D_a = \frac{LWT}{3} \quad (3)$$

After that, sphericity, aspect ratio, and surface area of arecanut fruit were determined by the following relationship Equation 4 to Equation 6 (Mohsenin, 1986).

$$s = \frac{(LWT)^{1/3}}{L} \quad (4)$$

$$A_R = \frac{L}{W} \quad (5)$$

$$A_S = \pi \times D_G^2 \quad (6)$$

The bulk density was calculated by filling a one-litre glass measuring cup with arecanut fruit and then weighing the fruits. The fruit density was researched by the water displacement method as recommended by *Kaleemullah and Gunasekar (2002)*, *Yahya et al. (2013)* and *Sacilik et al. (2003)*. After that, porosity could be determined using Equation 1.

$$\varepsilon = \left(1 - \frac{\rho_{BD}}{\rho_{TD}} \right) \times 100\% \quad (7)$$

To measure the angle of repose, a container with a diameter of 30 cm was chosen with a ceramic base. This is following the method used by *Amin et al. (2004)*. The height, minor and major width in the surface after shedding was measured, and the angle of repose was calculated using the tangent rule according to Equation 8.

$$\theta = \tan^{-1} \left(\frac{2H}{D_1 + D_2} \right) \quad (8)$$

To determine the compression force of arecanut fruit, a Universal Testing Machine (UTM) unit was used (Force maximum 500 N, the accuracy of 0.5N). The fruits were placed between two iron plates and pressed at the 0.01 mm/s speed until they arrive at to rupture point. Simultaneity force vs. deformation curves were recorded by a personal computer (Figure 2).

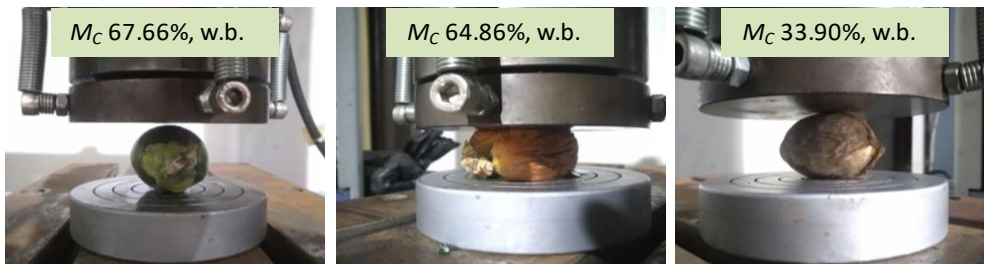


Fig. 2 -Compression force testing from arecanut fruit using UTM

To calculate the static coefficient of friction that occurs in arecanut fruit, it is computed using Equation 9. Three types of surfaces that are potentially used in the design of the arecanut models are used in this study, namely stainless steel, plywood, and glass (*Mollazade et al., 2009*).

$$\mu = \tan(\alpha) \quad (9)$$

RESULTS AND DISCUSSION

Arecanut fruit size

The dimensions of arecanut fruit were determined in three basic sizes. The geometric mean diameter of arecanut increased from 37.05 mm to 39.81 mm as the moisture content decreased from the underripe arecanut stages (67.66%, w.b.) to ripe arecanut stages (64.86%, w.b.). In the next steps, the geometric mean diameter of the overripe arecanut stages (33.90%, w.b.) decreased to 37.86 mm. The arithmetic mean diameter of arecanut increased from 38.04 mm to 40.05 mm as the moisture content decreased from the underripe arecanut stages (67.66%, w.b.) to arecanut ripe stages (64.86%, w.b.). Furthermore, the arithmetic mean diameter of the arecanut decreases again from 40.05 mm to 39.10 mm as the moisture content falls from the ripe arecanut stages (64.86%, w.b.) to overripe arecanut stages (33.90%, w.b.) (Figure 3). This phenomenon is thought to be caused by the biological factors of the arecanut fruit, which keep growing until the arecanut is in the ripe phase and decreases when the betel nut is in the overripe stages. The variations of bulk and true densities were found to be polynomial equations for both with the moisture content and can be represented by the following regression Equation 10 and Equation 11.

$$D_A = -0.022M_C^2 + 2.22M_C - 10.66 \quad (10)$$

$$D_G = -0.031M_C^2 + 3.14M_C - 32.70 \quad (11)$$

both with a value for the coefficient of determination R^2 of 1.0.

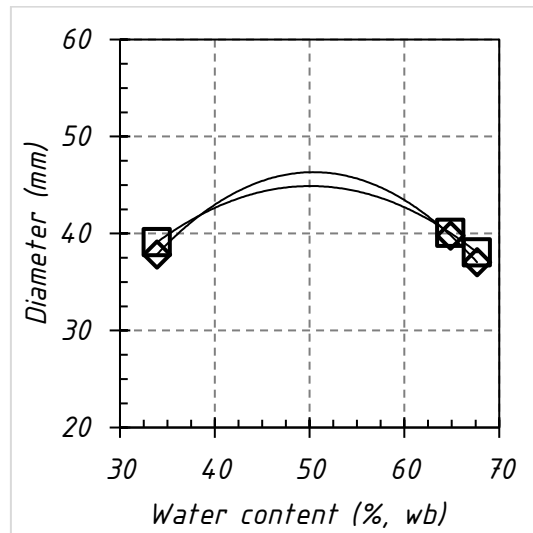


Fig. 3 - Arecanut fruit geometric (◇) and arithmetic (◻) mean diameter at different moisture content

The geometric equation model for mean diameter and arithmetic one for mean diameter are different from Opeaburoo and Abontem maize as reported by *Hayford et al. (2019)*. However, the results of *Singh et al. (2010)* for barnyard millet grain and kernel found a relationship model that is in line with arecanut fruit that is following the polynomial equation. This indicates that arecanut fruit tend to have dimensions (geometric and arithmetic) more similar to millet grain millets and kernels than Opeaburoo and Abontem maize.

Sphericity and aspect ratio

The sphericity of arecanut fruit was found to increase from 0.73 to 0.86 with a decrease in moisture content from 67.66% (w.b.) to 64.86% (w.b.) and subsequently decreased to 0.71 in the moisture content of 33.90% (w.b.) (Figure 4). The relationship model increase and decrease between sphericity and moisture content was polynomial, too. This increase and decrease can be described by the following Equation 12 and Equation 13. This behaviour has been in line with those reported by *Hayford et al. (2019)* for Opeaburoo and Abontem maize, *Zewdu and Solomon (2008)* for grass pea seeds.

$$s = -0.002M_c^2 + 0.16M_c - 2.87 \tag{12}$$

$$A_R = -0.002M_c^2 + 0.21M_c - 4.18 \tag{13}$$

with a value for R² of 1.

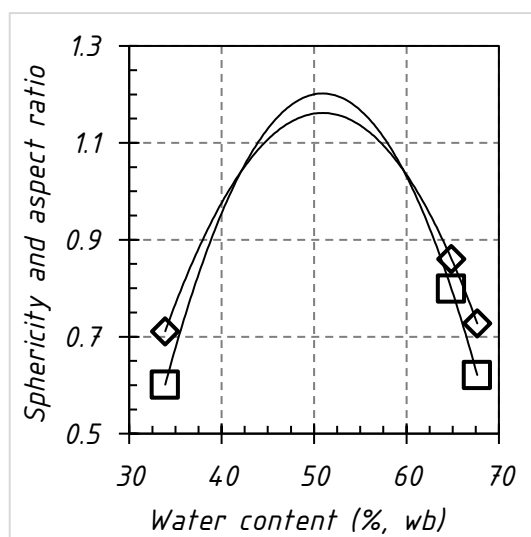


Fig. 4 - Effect of moisture content on sphericity (◇) and aspect ratio (◻)

Surface area

The surface area of arecanut fruit was found to increase from 4334.78 mm² to 5004.53 mm² with a decrease in moisture content from 67.66% (w.b.) to 64.86% (w.b.) (Figure 5). Furthermore, the reduction in

moisture content from 64.86% (w.b.) to 33.90% (w.b.) was found to decrease the surface area of arecanut fruit from 5004.53 mm² to 4527.53 mm². The relationship existing between surface area and moisture content is non-linear and can be expressed by the regression Equation 14. The connection of model surface area with a moisture content of arecanut fruit has been in line with research results reported by *Ganjloo et al. (2018)* for green peas, *Singh et al. (2010)* for barnyard millet grain and kernel and *Mollazade et al. (2009)* for cumin seed.

$$A_s = -7.55M_c^2 + 760.99M_c - 12594 \quad (14)$$

With a value for R² of 1.0.

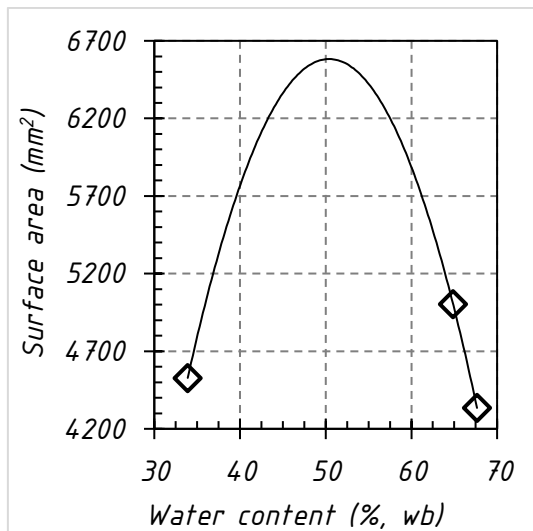


Fig. 5 - Effect of moisture content on surface area

Thousand fruit mass

Thousand fruit mass for arecanut fruit with an increase in moisture content from 33.90% (w.b.) to 67.66% (w.b.), was found to tend to increase from 2620.50 g to 3525.70 g (Figure 6). The linear equation for the description of this behaviour was found in the following relation to Equation 15. The linear increase of thousand arecanut fruit mass is in line with the results of the research of *Ganjloo et al. (2018)* for green peas, *Aviara et al. (2013)* for *Moringa oleifera* seed, *Hayford et al. (2019)* for Opeaburoo and Abontem maize and *Iyilade et al. (2019)* for bush mango nut.

$$M_{1000} = 0.29M_c + 16.40 \quad (15)$$

with a value for R² of 0.973.

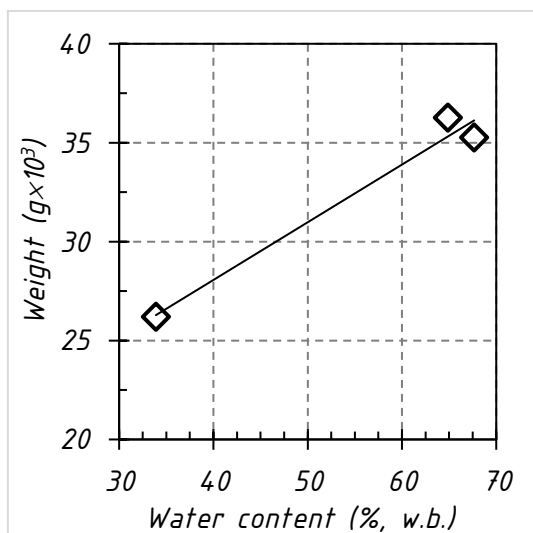


Fig. 6 - Effect of moisture content on thousand fruits weight

Bulk and true densities

As arecanut fruit moisture content increases, the bulk density and true density were found to increase. This increase was linear. The range of change with increase in moisture content from 33.90% (w.b.) to 67.66% (w.b.) for the bulk density and true density was, 395.90 kg/m³ to 594.80 kg/m³, and 866.50 kg/m³ to 866.31

kg/m³, respectively (Figure 7). The relationship existing between bulk and true densities and moisture content is linear and can be expressed by the regression Equation 16 and Equation 17. The linear increase of bulk and true densities of arecanut fruit is in line with the results of the research of Ganjloo et al. (2018) for green peas, Aviara et al. (2013) for Moringa oleifera seed, Hayford et al. (2019) for Opeaburoo and Abontem maize, Iyilade et al. (2019) for bush mango nut and Pradhan et al. (2008) for Karanja kernel.

$$\rho_{BD} = 5.35M_C + 212.83 \tag{16}$$

$$\rho_{TD} = 0.0053M_C + 866.69 \tag{17}$$

with a value for R² of 0.957.

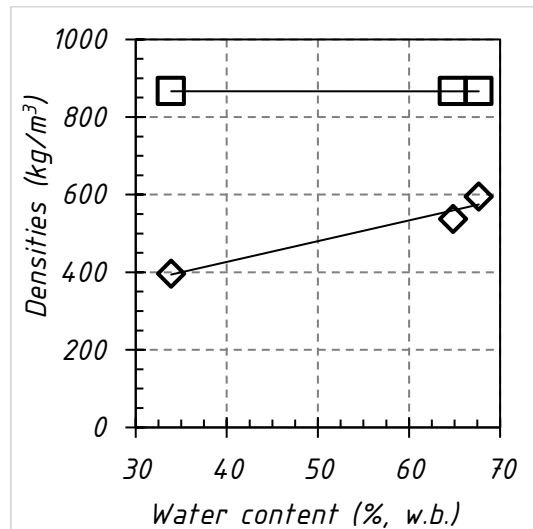


Fig. 7 - Effect of moisture content on bulk density (□) and true density (◇)

Porosity

Porosity of arecanut fruit decreases with increasing moisture content (Figure 8). Its decrease was linear. The range of change with an increase in moisture content from 33.90% (w.b.) to 67.66% (w.b.) for porosity was, 54.35% to 31.43%. The relationship existing between porosity and moisture content is linear and can be expressed by regression Equation 18. The linear decrease of arecanut fruit porosity is in line with the results of Mollazade et al. (2009) for cumin seed, Tavakoli et al. (2009) for soybean grains, Sessiz et al. (2007) for caper fruit and Garnayak et al. (2008) for jatropha seed.

$$\varepsilon = -0.62M_C + 75.45 \tag{18}$$

with a value for R² of 0.957.

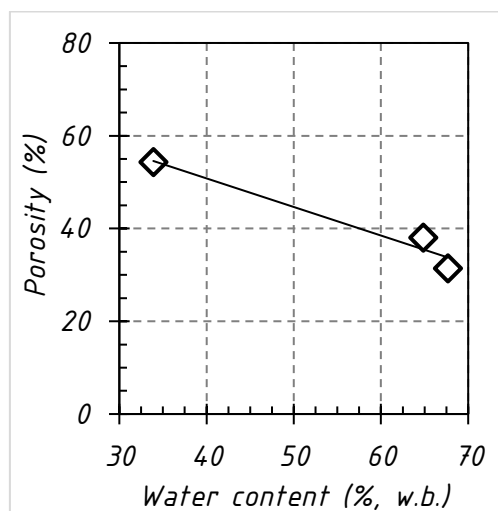


Fig. 8 - Effect of moisture content on porosity

Angle of repose

Experimentally determined values of angle of repose are plotted against moisture content, as shown in Figure 9. From this, it can be observed that the angle of repose decreased from 22.60° to 13.01° as the fruit

moisture content decreased from 67.66% (w.b.) to 33.90% (w.b.). Hayford et al. (2019) and Iyilade et al. (2019) reported a similar type of result in the case of Opeaburoo and Abontem maize, bush mango nut, respectively.

The relationship existing between the angle of repose and moisture content is linear and can be expressed as Equation 19.

$$\theta = -0.26M_c + 31.52 \quad (19)$$

With a value for R^2 of 0.968.

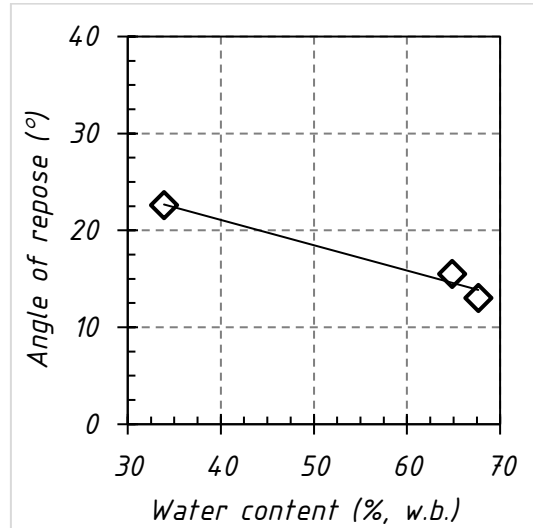


Fig. 9 - Effect of moisture content on angle of repose

Compression force

The compression force of arecanut fruit in moisture content from 33.90% (w.b.) to 67.66% (w.b.) was deeply scrutinized. Compression force of arecanut fruit in moisture content from 33.90% (w.b.) to 64.86% (w.b.) tends to increase from 79.50 kgf to 104.74 kgf and in moisture content from 64.86% (w.b.) to 67.66% (w.b.) tends to decrease from 104.74 kgf to 71.57 kgf (Figure 10). It is thought to be caused by the biological factors of the arecanut, which tends to harden in the ripe stages and tends to soften again in the overripe stages. The relationship existing between compression force and moisture content is represented by polynomial equations and can be expressed by the regression Equation 20. This model is in line with the results of Singh et al. (2010), who discovered that the compression force on a millet grain and kernel barnyot follows the polynomial equation.

$$C_F = -0.376M_c^2 + 37.90M_c - 773.73 \quad (20)$$

with a value for R^2 of 1.0.

Static coefficients of friction

The coefficient of static friction between the arecanut fruit and three surfaces, namely stainless steel, plywood and glass, was determined. On all these surfaces a polynomial increase of the static coefficient of friction has been found.

With an increase in moisture content from 33.90% (w.b.) to 67.66 (w.b.), this decrease for stainless steel, plywood and glass was found from 0.25 to 0.21, 0.18 to 0.19 and 0.18 to 0.14, respectively (Figure 11). Kudos and Solanki (2018) and Hayford et al. (2019) quoted similar types of results in the case of amaranth grain, Opeaburoo and Abontem maize, respectively. The polynomial equation for the description of this behaviour for stainless steel, plywood, and glass was found in the relations (Equation 21 to 23), respectively.

$$\mu_{SS} = -0.0004M_c^2 + 0.0358M_c - 0.54 \quad (21)$$

$$\mu_W = -0.0004M_c^2 + 0.0379M_c - 0.63 \quad (22)$$

$$\mu_G = -0.0004M_c^2 + 0.0358M_c - 0.54 \quad (23)$$

with a value for R^2 of 1.0.

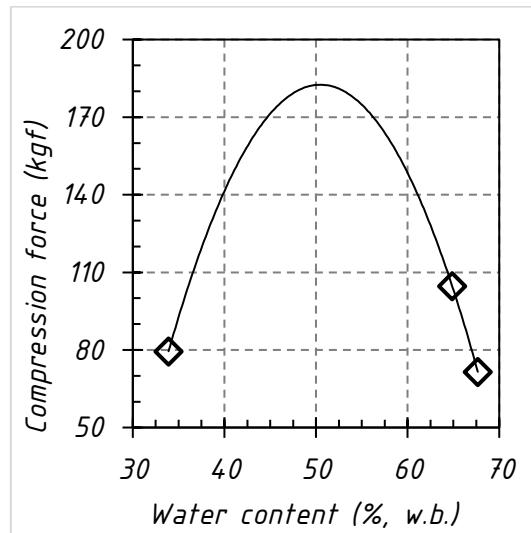


Fig. 10 - Effect of moisture content on compression force

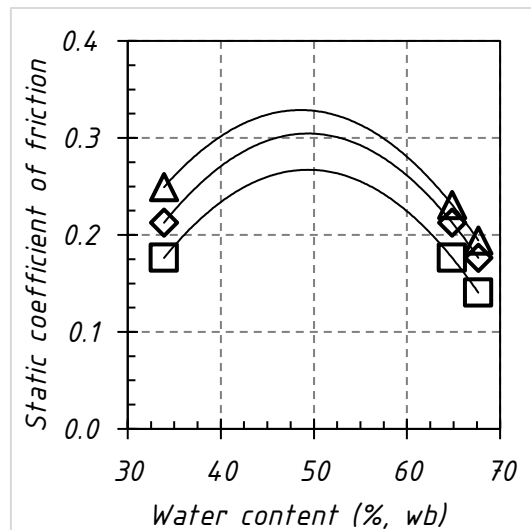


Fig. 11 - Effect of moisture content on static coefficients of friction at some material (Δstainless steel, ◇ plywood, ◻ glass)

CONCLUSIONS

Three phases of common types of arecanut fruit that farmers harvested were identified, namely underripe, ripe and overripe, with their moisture content of 67.66% (w.b.), 64.86% (w.b.), 33.90% (w.b.), respectively. The relationship between water content in the three phases of betel nut with seven characteristic physical parameters and two mechanical properties was modelled in a linear and non-linear equations.

Engineering properties geometric mean diameter, arithmetic mean diameter, sphericity, aspect ratio, surface area compression force, and static coefficient of friction follow the polynomial equation model.

Engineering properties such as porosity and angle of repose follow the decreasing linear equation model, and a thousand mass of fruits bulk density and true density follow the increasing linear equation model. The next work of this research is to investigate the model of the relationship of rupture force to the physical properties of arecanut fruits in various stages.

It is crucial for researchers and engineers of pre-harvest and post-harvest agricultural machinery to estimate the force limits that can be applied in handling arecanut fruit without damaging the product itself.

ACKNOWLEDGEMENT

The authors would also like to thank anonymous reviewers for their valuable comments. The author is particularly thankful to the technical staff of the chair for their helpful assistance. The first to third authors are the main contributors to this paper.

REFERENCES

- [1] Ahmed AE-RAE-R, Hassan HE-S, HAM Lotfy, (2019), Mathematical Model for Some Physical Characteristics of Yellow and Red Date Fruits Varieties, *Agricultural Engineering International: CIGR Journal*, Vol.21(3), pp.234-241.
- [2] Amin M., Hossain M, Roy K., (2004), Effects of moisture content on some physical properties of lentil seeds, *Journal of Food Engineering*, Vol.65(1), pp.83-87.
- [3] Aviara N.A., Power P.P., Abbas T., (2013), Moisture-dependent physical properties of Moringa oleifera seed relevant in bulk handling and mechanical processing, *Industrial Crops and Products*, Vol.42, pp.96-104.
- [4] Bajpai A., Kumar Y., Singh H., Prabhakar P.K., Meghwal M., (2019), Effect of moisture content on the engineering properties of Jamun (*Syzgium cuminii*) seed, *Journal of Food Process Engineering*, Vol. pp.e13325.
- [5] Ganjloo A., Bimakr M., Zarringhalami S., Safaryan J.M., Ghorbani M., (2018), Moisture-dependent physical properties of green peas (*Pisum sativum* L.), *International Food Research Journal*, Vol.25(3), pp.1246-1252.
- [6] Garnayak D.K., Pradhan R.C., Naik S.N., Bhatnagar N., (2008), Moisture-dependent physical properties of jatropha seed (*Jatropha curcas* L.), *Industrial Crops and Products*, Vol.27(1), pp.123-129.
- [7] Hayford O, Francis A., Isaac A.K., Albert A.I., Nathan O.T., (2019), Moisture-dependent physical properties of Opeaburoo and Abontem maize varieties during drying, *International Food Research Journal*, Vol.23(11), pp.109-115.
- [8] Iyilade I.A., Aviara N.A., Aremu A.K., Oyeniyi S.K., (2019), Effect of moisture content on physical properties of bush mango (*Irvingia gabonensis*) nut, *Agricultural Engineering International: CIGR Journal*, Vol.20(4), pp.221-226.
- [9] Kaleemullah S., Gunasekar J.J., (2002), PH—Postharvest Technology: Moisture-dependent Physical Properties of Arecanut Kernels, *Biosystems engineering*, Vol.82(3), pp.331-338.
- [10] Kudos S., Solanki C., (2018), Evaluation of physical properties of amaranth grain (*Amaranthus paniculatus*), *International Journal of Chemical Studies*, Vol.6(2), pp.2197-2201.
- [11] Mohsenin N.N, (1986), "Physical properties of plant and animal materials." **In.**
- [12] Mollazade K., Ahmadi H., Khorshidi J., Rajabipour A., Mohtasebi S.S, (2009), Moisture-dependent physical and mechanical properties of cumin (*Cuminum cyminum* L.) seed, *International Journal of Agricultural and Biological Engineering*, Vol.2(2), pp.49-56.
- [13] Moradi M., Balanian H., Taherian A., Mousavi Khaneghah A., (2019), Physical and mechanical properties of three varieties of cucumber: A mathematical modeling, *Journal of Food Process Engineering*, Vol.pp.e13323.
- [14] Pandiselvam R., Manikantan M., Balasubramanian D., Beegum P.S., Mathew A., Ramesh S., Hebbar K., Niral V., (2019), Mechanical properties of tender coconut (*Cocos nucifera* L.): Implications for the design of processing machineries, *Journal of Food Process Engineering*, Vol.pp.e13349.
- [15] Pradhan RC, SN Naik, N Bhatnagar, SK Swain, (2008), Moisture-dependent physical properties of Karanja (*Pongamia pinnata*) kernel, *Industrial Crops and Products*, Vol.28(2), pp.155-161.
- [16] Sacilik K, R Öztürk, R Keskin, (2003), Some physical properties of hemp seed, *Biosystems engineering*, Vol.86(2), pp.191-198.
- [17] Sarajeh H, E M.A., K M., B O., M K., (2014), Effect of moisture content on some physical properties of Grass pea (*Lathyrussativus* L.), *Agricultural Engineering International: CIGR Journal*, Vol.16(4), pp.216-267.
- [18] Sessiz A., Esgici R., Kızıl S., (2007), Moisture-dependent physical properties of caper (*Capparis* ssp.) fruit, *Journal of Food Engineering*, Vol.79(4), pp.1426-1431.
- [19] Singh H., Meghwal M., (2019), Physical and thermal properties of various ajwain (*Trachyspermum ammi* L.) seed varieties as a function of moisture content, *Journal of Food Process Engineering*, Vol.pp.e13310.
- [20] Singh K.P., Mishra H.N., Saha S., (2010), Moisture-dependent properties of barnyard millet grain and kernel, *Journal of Food Engineering*, Vol.96(4), pp.598-606.
- [21] Tavakoli H., Rajabipour A., Mohtasebi SS, (2009), Moisture-dependent some engineering properties of soybean grains, *Agricultural Engineering International: CIGR Journal*, Vol.11(1), pp.1-14.

- [22] Yahya A., Hamdan, K.Ishola T.A., Suryanto H., (2013), Physical and Mechanical Properties of *Jatropha Curcas*. L Fruits from Different Planting Densities, *Journal of Applied Sciences*, Vol.13(7), pp.1004-1012.
- [23] Zewdu A., Solomon W., (2008), Moisture-dependent physical properties of grass pea (*Lathyrus sativus* L.) seeds, *Agricultural Engineering International: CIGR Journal*, Vol.10(1), pp.1-14.

RESEARCH ON COMPOSITE RICE STRAW-CEMENT BRICK FOR HIGH-RISE BUILDING

适用于高层建筑的稻草秸秆-水泥复合墙砖研究

Liang X.C. ^{*)}, Zhang M., Tian S.C. ¹

Southwest University, College of Engineering and Technology, Chongqing Key Laboratory of Agricultural Equipment for Hilly and Mountainous Regions / P. R. China
Tel: 86-023-68251265; E-mail: dylb1978@swu.edu.cn
DOI: <https://doi.org/10.35633/inmateh-60-08>

Keywords: Rice straw-cement brick, heat retaining property, fire resistance

ABSTRACT

The composite rice straw-cement brick is analysed with simulations and experiments using mechanical and heat transfer theory, and data demonstrate excellent characteristic of such brick including heat retaining, light weight and fire resistance, which is beneficial to save the precious clay resource, reduce energy consumption during production and enhance the safety and comfort of high-rise building. In the future, the processing of such brick should be optimized, and this new type of manufacturing apparatus is expected to be designed to satisfy the requirements of commercial application.

摘要

利用力学和热学的相关知识对秸秆-水泥复合墙砖的特性进行了仿真和实验研究，数据表明其既能节约宝贵的黏土资源和降低生产中的能量消耗，又在保温性、轻量化和耐火性方面具有突出的优点，显著提升了建筑物的舒适性和安全性。未来还应该在复合砖的生产工艺方面进行优化，以便设计出面向工业化生产的制造装备，使其能够大范围推广应用。

INTRODUCTION

It is well known that the traditional brick is the crucial material for the urban construction, but it has obvious drawbacks such as high rate of energy consumption, pollution and ruining the environment. Rice straw has been applied widely for thousands of years in China and other countries as shown in Figure 1, and it is proved to be eminent construction stuff for heat retention, sound insulation and light weight.



Fig. 1 – Straw house in foreign countries and in China

In China, rice straw yields 0.2 billion tons yearly, while it is always considered agricultural waste, lacking of effective processing technology. Considering the strong market demand for brick generated by urbanization, it is crucial to develop eco-friendly brick based on rice straw.

There are many studies on straw-brick published. A sort of rice straw-wood particle composite board with different parameters was researched for sound absorbing, and the most suitable specific gravity of the board could be determined (Yang H.S. *et al*, 2003). In order to reinforce performance such as sound absorption, electrical insulation, erosion-resisting for a type of rice straw composite board, waste tire particles were added (Yang H.S. *et al*, 2004). In Thailand, a light wall is designed using rice straw and maize husk, and its good properties are demonstrated (Padkho N., 2012).

¹ Liang X.C., Ph.D. Eng.; Zhang M., Ms. Stud. Eng.; Eng. Tian S. C., B.A. Stud.

Similarly, an ECO-MDF board is manufactured with rice straw in Egypt, which can be used in furniture or hardscape (Shehata S.M., 2016). Obtaining morphological and mechanical performance about rice straw, wood and potato tuber, relevant tests are conducted to show that inherent characteristics of all the cellulose microfibrils exhibit the same characteristics in the dry state regardless of tissue functions (Hiroyuki Y.K.A., 2009). Rice straw contains high content of lignocellulose, and it is vital to be disposed through dilute acid and alkali enzymatic hydrolysis (Li Y. et al, 2016; Hsu T.C., 2010). Nowadays, two types of the most problematic wastes — rice straw, expanded polystyrene foam must be dealt with pressingly, and hard wood-composite can be made of them to replace the natural wood in many daily applications (Tawfik M. E., 2017). There are several published papers on mechanical investigation of bundled rice straw. Stephen conducted a vibration test of straw brick house in the University of Nevada, Pakistan, and it could resist 0.8g horizontal acceleration without collapse (Yuan B., et al, 2014). Heat retaining is critical to the building, and studies of this type were also done. A theoretical model of concrete block wall filled with compressed straw was created, and heat transfer coefficient was only 0.446 W/(m²·k), which is far smaller than that of concrete wall (1.5 W/(m²·k)) (Hou S. D. et al, 2017). Homogeneously, a type of cement-straw composite brick is manufactured in Southwest University, China and mechanical and heat transfer tests demonstrate that it satisfies requirements of residential building regulation (Wang D., 2016). Fire resistance is significant to the house as well, and the straw material is of excellent performance. Silicon and wax content are so high in straw that it is tough to be burnt in the sealed environment, and wiring inside straw walls can prevent fires effectively. In addition, poisonous gas hardly releases from straw even burning. (Lin Y. T. et al, 2010).

Briefly, researching on straw can be divided into mechanical, heat retaining, sound insulation and fire resistance fields. But several application problems regarding straw—whether such brick can be used in the high-rise building or not, and how to innovate the manufacture process achieved by the automatic equipment—are still unsolved. Hence, concerned researches should be conducted.

MATERIALS AND METHODS

Generally, the rice straw is applied in the construction domain under two forms: bundling and gelatinization. When the rice straw is used in bundling mode, the durability may be influenced by the insects. Besides, the challenge is to build the wall with a uniform density. Evidently, straw gelatinization can avoid these shortcomings (insects will be eliminated entirely by the chemical reagent). Instead, chemical reagent such as NaOH and quicklime must be used to decompose straw cellulose, rising the manufacturing cost. For the sake of reliability and safety of straw buildings, it is wise to adopt the gelatinization mode for straw, which is also beneficial to make brick through automatic apparatus.

It must be pointed out that rice straw-brick cannot sustain the weight alone for high-rise building, and it should be combined with other stuff when using. Compared with other materials, the concrete hollow block has the following advantages: abundant raw stuff, low price, high compressive strength, good durability and simple production process, so it has been used as the main building material for the urban and rural houses (Hou S. D. et al, 2017). However, the high energy consumption for concrete hollow block cannot be neglected when it comes to its poor heat retention, which conflicts the increasingly strict construction code. As a result, rice straw-concrete composite brick may be a practicable way to improve the energy-saving effect of cement hollow block. Apparently, such a composite brick is eligible to be used in the high-rise building, particularly for the separating walls. The rice straw-cement compound brick is showed in Figure 2.

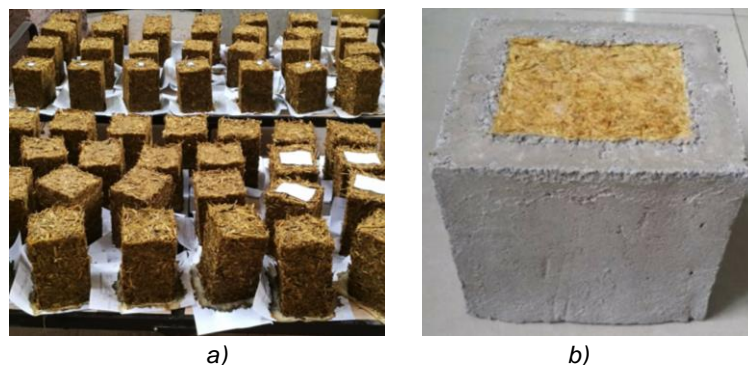


Fig. 2 – Rice straw–cement compound brick

The manufacturing process of rice straw brick is described here. Firstly, the rice straw collected from the countryside in Chongqing is cut into small sections of a certain length. Secondly, the chemical reagent such as NaOH or quicklime and the cut straw are stirred together for some minutes, which is useful to make the compound uniform. Thirdly, the mixture is put in a mould and then the mould is compressed by a press machine. Fourthly, the straw brick is maintained for some days to get uniform size, minimizing the bounce-back. After the assembling of rice-straw brick and hollow cement brick, the composite production can be obtained.

After manufacturing the composite brick, it is natural to research its properties such as thermal performance, mechanical performance and fire resistance, which are crucial to indicate its reliability. In this study moisture content, compressive strength and heat transfer coefficient or thermal conductivity of the composite brick will be illustrated gradually.

Moisture content will lead to mildew, so it is closely related to the brick life span—the higher the moisture content, the shorter the life span of brick is. Besides, moisture content can exert a negative impact on the heat transfer coefficient — the higher the moisture content, the higher the energy consumption is (Kong F.H. et al, 2010). Hence, the moisture content must be controlled within a certain range. Generally, it is can be denoted applying formula 1 below

$$h = \frac{m_w - m_d}{m_w} \quad (1)$$

where:

m_w is the mass of brick in the wet state, [g];

m_d - mass of the brick in the dry state, [g];

h - moisture content of the brick.

When the composite brick is used in the building construction, it must sustain the weight of upper stuff. This is the reason why the compressive strength of brick is compulsorily required to satisfy the corresponding norm. In engineering, it is always showed as formula 2. Of course, in most of the cases the compressive strength of the material can be predicted with formula 3 (GB 25003-2011) bellow.

$$f = \frac{P}{A} \quad (2)$$

where: f is the compressive strength, [MPa];

P - ultimate load, [N];

A - contact area, [mm²].

$$f_m = k_1 f_1^\alpha (1 + 0.07 f_2) k_2 \quad (3)$$

where:

f_m is the average compressive strength of the brick, [MPa];

f_1 - strength level of the brick, [MPa];

f_2 - compressive strength of the mortar, [MPa];

α - constant, $\alpha=0.9$;

k_1 - constant, $k_1=0.46$;

k_2 - constant, $k_2=1.0$.

Apart from the moisture content, heat transfer coefficient has decisive influence on the energy efficiency of the building. In theory, heat transfer coefficient is expressed by formula 4 (Qiu S.J., 2012; Li A.J. et al, 2018)

$$k = \frac{1}{\frac{1}{\alpha_{in}} + \sum \frac{\delta_i}{\lambda_i} + \frac{1}{\alpha_{out}}} \quad (4)$$

where: α_{in} is the indoor convective heat transfer coefficient, [$W \cdot m^{-2} \cdot K^{-1}$];

α_{out} is the outdoor convective heat transfer coefficient, [$W \cdot m^{-2} \cdot K^{-1}$];

λ_i - heat conductivity coefficient of the i^{th} layer material, [$W \cdot m^{-1} \cdot K^{-1}$];

δ_i - thickness of the i^{th} layer material, [m].

If some parameters are difficult to measure when using formula 4, the heat transfer coefficient can be calculated in practice by formula 5 and 6 (Hou S. D. et al, 2016). In essence, formula 6 can be viewed as a rewrite of formula 4, using different parameters.

$$R = \frac{\sum_{i=1}^n (T_{1i} - T_{2i})}{\sum_{i=1}^n q_i} \tag{5}$$

$$k = \frac{1}{R + R_i + R_o} \tag{6}$$

where:

R is the average heat resistance of material after multiple measurements, [$m^2 \cdot k \cdot W^{-1}$];

R_i - inner surface heat resistance, [$m^2 \cdot k \cdot W^{-1}$];

R_o - outer surface heat resistance, [$m^2 \cdot k \cdot W^{-1}$];

T_1 - inner surface temperature of material, [K];

T_2 - outer surface temperature of material, [K];

q - heat flux, [$W \cdot m^{-2}$].

RESULTS

Actually, the closed thin-walled hollow structure of rice straw can enable it to sustain pressure, and that is the reason why it has super sound insulation character — when the sound wave propagates, the air in the fibre gap inside the straw will vibrate, but the air near the surface will not be activated under the action of the viscous resistance of the fibre. Indicating the fine pressure resistance, stress experiments shown in Figure 3 have been accomplished based on the rice straw (shown in Figure 3a) and composite brick (shown in Figure 3b).

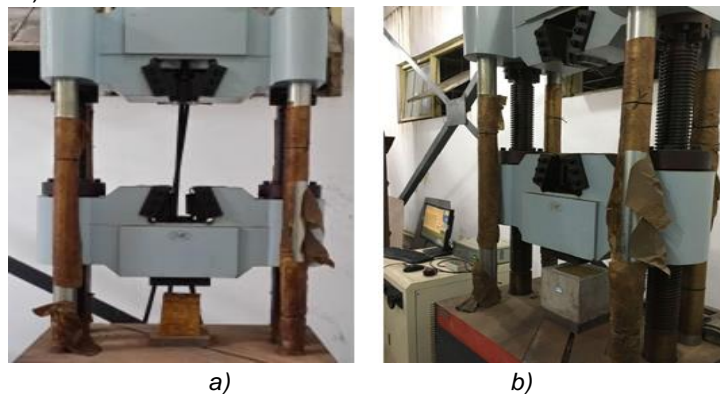


Fig. 3 – Stress experiment of straw and composite bricks

In the experiment, the pressure machine is WAW-1000, produced by the Kexin Test Instrument Co. LTD, Changchun, China. The test data demonstrate that straw brick only has slight deformation if the stress is less than 15kN; the deformation will be more and more obvious with the stress increasing. Once the pressure disappears, the shape of straw brick will recover gradually. It is also indispensable to point out that the stress is an average value of different concentrations of NaOH solution—2%, 3%, 4%, 5%, which is used in disposing the rice straw. Meanwhile, in order to verify the validity of formula 3, simulations have also been listed in Table 1 (f_i is the test strength result of the brick, and f_m is the simulation result).

Table 1

Test data of rice-straw composite brick				
Number	Load [kN]	f_i [MPa]	f_m [MPa]	f_i/f_m
1	218.55	5.95	6.21	0.96
2	220.70	6.01	6.21	0.97
3	223.06	6.04	6.21	0.97

According to the relevant construction regulation, this composite brick is allowed to be used in the bearing wall of village and town constructions, and it can be used in the separating wall of high-rise building incontrovertibly.

The experiment on the heat transfer of rice-straw brick is described here. The main instrument is DRCD-3030 intelligent thermal conductivity tester shown in Figure 4, made by Tianjin MEITESI Co., China, and the temperature of hot plate is set at 35°C, while the temperature of cold plate is controlled at 15°C. According to the operation manual of the instrument, heat transfer coefficient can be obtained. Similarly, the heat transfer coefficient of compound brick can be measured with such apparatus.

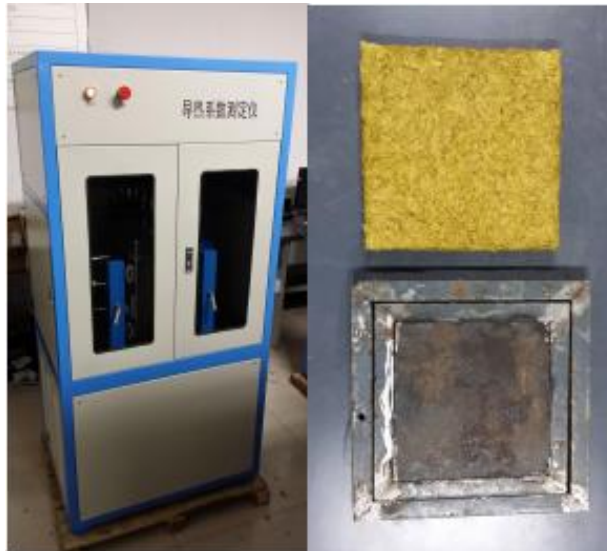
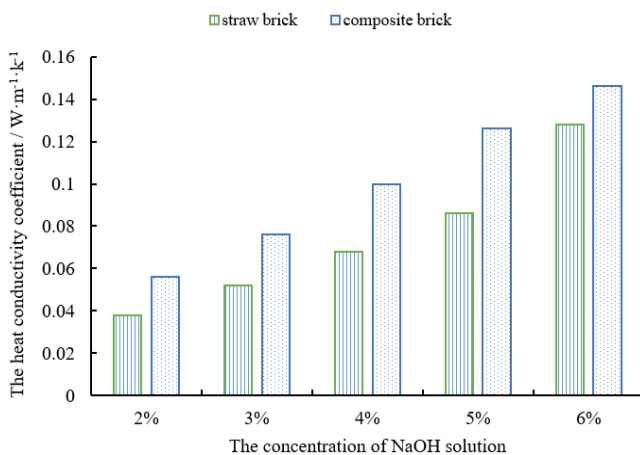


Fig. 4 – The instrument of heat transfer experiment

The NaOH solution plays a final role in disposing the rice straw fibre, and different concentrations of the solution have obvious impact on the density and heat conductivity of rice-straw and composite brick. Test data are illustrated in Figure 5 and Figure 6. It is not difficult to draw two conclusions —the heat conductivity coefficient of compound brick is higher than that of rice-straw brick, and high concentration of solution would give rise to large heat conductivity coefficient. For the straw brick, heat is transferred mainly by the air, so it indicates small heat conductivity coefficient, determined by the air property. But for the composite brick, the voidage of concrete stuff can be neglected and heat is transferred easily, so its heat conductivity coefficient keeps big. The moisture content is decisive to heat conductivity coefficient as well (Huang J. E. et al, 2015; Bao Y. et al, 2018). The bigger concentration of solution is, the higher moisture content keeps. Moreover, the heat conductivity of water is much bigger than that of the air, and this is the cause why the heat conductivity coefficient of brick becomes bigger with the moisture content increasing.



Fi g. 5– The comparison of two types of bricks

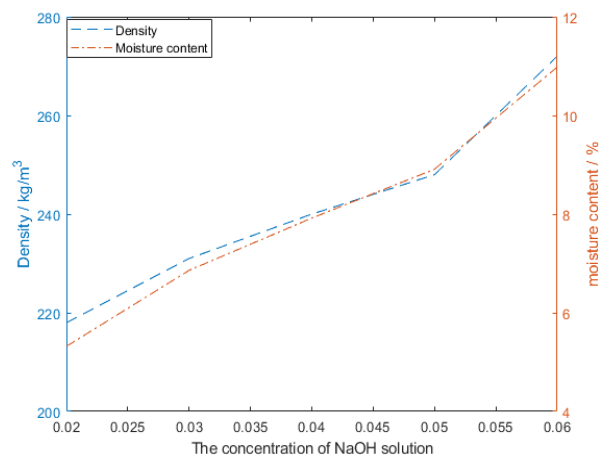


Fig. 6– The property of straw brick

Except for the moisture content, the concentrations of the NaOH solution are also crucial to the shrinkage rate of rice straw brick, influencing on the assembling of two sorts of bricks and the uniformity of composite brick. Test data have been list in Table 2, and it is not hard to find some rules. The concentration of NaOH solution is in direct proportion to the shrinkage rate of rice brick, similarly to the moisture content rate of rice brick. The conclusion can be explained as follow. The lignin and hemicellulose of rice straw may be degraded by the NaOH solution, and the resilience force of compressed rice straw will lose, so the rice brick disposed by high concentration NaOH solution has big shrinkage rate.

Simultaneously, the moisture content rate of rice brick is affected as well. The bigger the shrinkage rate is, the harder the moisture evaporates, which is stated that the air circulation is blocked in a compact structure obviously. In a word, the concentration of NaOH solution exerts a vital impact on the physical performance of rice brick, and thus selecting the most appropriate concentration of NaOH solution is a challenging task, obtaining the satisfying the properties of rice brick.

Table 2

The physical properties of rice brick regarding different concentrations of NaOH solution

The concentration of NaOH solution	The shrinkage rate of rice brick	The moisture content rate of rice brick
2%	2.84%	5.32%
3%	3.76%	6.86%
4%	4.48%	7.92%
5%	5.34%	8.91%
6%	7.41%	10.98%
7%	9.45%	12.13%

When heat transfer coefficient is not convenient to calculate, it is wise to use another terminology — heat conductivity coefficient. Although there is a small difference between the two parameters such as unit (heat transfer coefficient is generally for the convective case, while heat conductivity coefficient is invariably for heat conduction), they can both give expression to the heat retention capacity of the material. Compared with other material, the composite brick is still an excellent construction stuff as shown in Table 3. Remarkably, the mechanical property of rice-straw brick has been improved greatly so that it can be used for high-rise building.

Table 3

Comparison of heat properties of different materials

Material	Density [kg·m ⁻³]	Heat conductivity coefficient [W·m ⁻¹ ·k ⁻¹]
Clay brick	800~1000	0.45~0.81
Rice straw brick	218~248	0.038~0.08
Concrete	1413~1900	1.51
Expanded perlite	2200~2400	0.021~0.062
Composite brick	1142~1413	0.056~0.126

It is important to underline two points resulting from the Table 2. Firstly, the heat conductivity coefficient of rice straw brick is the smallest, determined by the closed thin-walled hollow structure, which is a poor heat conductor. Although the heat transfer factor of expanded perlite is similar to the rice straw, its density is far larger than that of rice straw brick, which is crucial to the safety of high-rise building. Secondly, the density of composite brick is a little different compared to concrete density, while the heat transfer coefficient is very different due to the unique structure of rice straw.

Fire resistance of material is vital to the urban construction, particularly to the skyscraper (Wu W. *et al*, 2015). It is well known that the yield strength and ultimate strength of the steel structure are degenerated sharply with temperature rising. If the temperature is above 600 °C, the steel structure will even lose bearing capacity, as demonstrated by the collapse of New York World Trade Centre Towers. The compressive strength of brick applied in the separating wall is expected to be larger than 5MPa, the composite brick fits the bill definitely. In addition, the density of composite brick is about 24%-35% smaller than that of concrete as shown in Table 2, which is beneficial to satisfy the requirement of structure's light weight. If a good fire resistance can be demonstrated in the case of the composite brick, it will be an excellent stuff for building skyscrapers. Just like it is used, the top surface of composite brick shown in Figure 2b is sealed with cement at first. Then the sealed brick is put into a test stove.

After burning for three hours, the fire resistance test has been completed. The experimental scene is shown in Figure 7.



Fig. 7 – Fire resistance of composite brick

As it can be seen in Figure 7a, it is hard to find distinct change on the surface of compound brick after burning for three hours, while some variation appeared inside the compound brick in Figure 7b—merely the top of rice straw has become carbonized, but the other parts remained unchanged. There are two reasons for this. One is that the rice straw has a high content of silicon, which is an excellent material of fire resistance; The other is the lack of oxygen in such environment, which makes the fire stops inevitably. Moreover, the rice straw cannot give off any poisonous gas even if it can be ignited, and there is no fireproofing agent added except for the reagent. Briefly, the safety of high-rise building has been enhanced greatly after using concrete-rice brick.

CONCLUSIONS

- Test data indicate eminent advantages of compound brick including heat retention, mechanical performance and fire resistance, and it is feasible to be used in the high-rise building.
- The composite brick is made by hand in this study, and efforts are made to optimize this process and develop new apparatus to implement industrial production of the brick.

ACKNOWLEDGEMENTS

This paper was financially supported by the Fundamental Research Funds for the Central Universities (No. XDJK2016B025) and the Doctoral Fund of Southwest University (No. SWU115022).

REFERENCES

- [1] Bao Y., Chen Y. M., Liu X. W., Dong W. Q., Fang A. M., (2018), Simulation model of coupled heat and moisture transfer in porous building elements and its verification (多孔介质墙体热湿耦合传递模拟计算模型及其验证), *Building Science*, vol. 34, issue 10, pp.66-75;
- [2] GB50003-2011, (2011), GB 50003-2001, *Code for design of masonry structures (砌体结构设计规范)*, Beijing;
- [3] Hiroyuki Y. K. A., (2009), Comparison of the characteristics of cellulose microfibril aggregates of wood, rice straw and potato tuber, *Cellulose*, vol.16, pp.1017-1023;
- [4] Hou S. D., Liu F.S., Wang S.J., Bian H. B., (2017), Coupled heat and moisture transfer in hollow concrete block wall filled with compressed straw bricks, *Energy and Building*, vol.135, pp.74-84;
- [5] Hou S. D., Liu F. S., Fan J., Zhou T., (2016), Experimental study on the heat and moisture transfer of concrete block wall filled with compressed blocks of straw(混凝土夹心秸秆砌块墙体热湿传递试验研究), *Concrete*, issue 12, pp.114-117;
- [6] Hou S. D., Zhang H. J., Liu F. S., Fan J., (2017), Study on insulation and energy saving performance of sandwich straw concrete block building(夹芯秸秆混凝土砌块试点建筑保温节能性能研究), *New Building Materials*, issue 3, pp. 56-59;
- [7] Huang J. E., Lv H. L., Feng W., (2015), Mathematical model and its validation of coupled heat and moisture transfer for multilayer wall (多层墙体热湿耦合传递模型及验证), *Journal of civil, architectural & environmental engineering*, vol.37, issue 1, pp.18-22;

- [8] Hsu T. C., Guo G. L., Chen W. H., Hwang W. S., (2010), Effect of dilute acid pre-treatment of rice straw on structural properties and enzymatic hydrolysis, *Bioresource Technology*, vol.101, pp.4907-4913;
- [9] Kong F. H., Liao S. M., Zheng M. Y., (2010), Study on the change of envelope heat transfer coefficient for new completed building (新建建筑围护结构的传热系数变化研究), *Acta Energiæ Solaris Sinica*, vol. 31, issue 6, pp. 717-722;
- [10] Li A. J., Bao A. H., Rao K., Luo Q., (2018), On thermal performance of self-insulation concrete-straw composite block (自保温混凝土-秸秆复合砌块热工性能研究), *Journal of Southwest China Normal University (Natural Science Edition)*, vol. 43, issue 12, pp. 85-90;
- [11] Li Y., Qi B. K., Luo J. Q., Wan Y. H., (2016), Effect of alkali lignins with different molecular weights from alkali pre-treated rice straw hydrolysate on enzymatic hydrolysis, *Bioresource Technology*, vol.200, pp.272-278;
- [12] Padkho N., (2012), A new design recycle agricultural waste materials for profitable use rice straw and maize husk in wall, *Procedia Engineering*, vol.32, pp.1113-1118;
- [13] Qiu S., (2012), *Type optimization of concrete sandwich straw block and thermal performance research of the wall (混凝土夹心秸秆砌块型优化及墙体热工性能研究)*, Master dissertation, Shandong Agricultural University, Shandong/China;
- [14] Shehata S. M., (2016), Straw wastes from an environmental disaster to ECO-Board towards a sustainable urban environment, *Procedia Environmental Sciences*, vol.34, pp.539-546;
- [15] Tawfik M. E., Eskander S. B., Nawwar G.A., (2017), Hard wood-composites made of rice straw and recycled polystyrene foam wastes, *Journal of Applied Polymer Science*, vol.134, issue 18, pp.1-9;
- [16] Wu W., Tian L. J., Han C. W., Guo Y, Xue C. M, Zhang Y. H., (2015), Study on technique of using modification and fire retardant to enhance straw brick in northern China(北方民居改性阻燃防腐强化稻草砖工业探究), *Journal of Anhui Agri. Sci.*, vol. 43, issue 3, pp.206-208;
- [17] Yang H. S., Kim D. J., Kim H. J., (2003), Rice straw-wood particle composite for sound absorbing wooden construction materials, *Bioresource Technology*, vol.86, pp.117-121;
- [18] Tang D., (2016), *Study on the composite block of straw and concrete brick (稻草砖-混凝土复合砌块研究)*, Master dissertation, Southwest University, Chongqing/China;
- [19] Yang H. S., Kim D. J., Lee Y. K., Kim H. J., Jeon J. Y., Kang C.W., (2004), Possibility of using waste tire composite reinforced with rice straw as construction material, *Bioresource Technology*, vol.95, pp.61-65;
- [20] Yuan B., Cao B. Z., Duan W. F., (2014), The application of straw bale in building and the analysis of present research situation (秸秆草砖在建筑中的应用与研究现状分析), *Journal of Jilin Institute of Architecture & Civil Engineering*, vol.31, issue 3, pp.19-22.

DEVELOPMENT AND EVALUATION OF DRUM COFFEE ROASTING MACHINE FOR SMALL-SCALE ENTERPRISES

/

PENGEMBANGAN DAN EVALUASI MESIN PENYANGRAI KOPI TIPE DRUM UNTUK USAHA SKALA KECIL

Dadang Dayat Hidayat¹⁾, Arie Sudaryanto¹⁾, Yose Rizal Kurniawan¹⁾, Ashri Indriati¹⁾, Diang Sagita*¹⁾ ¹

¹⁾Research Centre for Appropriate Technology, Indonesian Institute of Sciences

Tel: 6285719002251; E-mail: diang.sagita@lipi.go.id

DOI: <https://doi.org/10.35633/inmateh-60-09>

Keywords: coffee roaster, design, drum roaster, small enterprises

ABSTRACT

The design, manufacture and evaluation of a drum coffee roasting machine had been carried out. The aimed of the study was to develop a small-scale drum roaster to meet the demand of the small enterprises at design and function. The development stage consisted of sizing of the main components, creating technical drawings, determination of component materials, manufacture and performance test. The dimension of the roaster drum was 168.28 mm in diameter and 250 mm in length; the capacity of the roaster was 750 gram/batch. Results of the test determined that the coffee roasting machine had worked well as expected. The preheating time was 15-22 minutes at a drum speed of 67.5 rpm. The initial loading temperature was 180°C. The test using arabica coffee bean reveals that the average crack time was 8.78 minutes, development time was 2.35 minutes, decreasing mass and increasing volume ranged from 19.80 – 20.30 % and 49.97 – 54.85 % respectively. The average crack time of Robusta coffee bean was 10 minutes; development time was 3 minutes, decreasing mass and increasing volume ranged from 10.87 – 14.90 % and 44.93 – 56.20 %, respectively. The required time to roast Arabica green coffee bean to the light-medium and medium-dark level was 11.3 and 12.38 minutes respectively, besides for Robusta green coffee beans was 13.00 and 14.00 minutes respectively.

ABSTRAK

Desain, manufaktur, dan evaluasi mesin penyangrai kopi tipe drum telah dilakukan. Tujuan dari penelitian ini adalah untuk mengembangkan drum roaster skala kecil untuk memenuhi permintaan usaha kecil dalam desain dan fungsi. Tahap pengembangan terdiri dari penyesuaian komponen utama, pembuatan gambar teknis, penentuan bahan komponen, pembuatan prototipe dan uji kinerja. Diameter drum roaster adalah 168.28 mm dan panjang 250 mm; kapasitas drum adalah 750 gram/batch. Hasil tes menentukan bahwa mesin penyangrai kopi telah bekerja dengan memuaskan seperti yang diharapkan. Waktu pemanasan awal adalah 15-22 menit pada kecepatan drum 67.5 rpm. Suhu pemuatan awal adalah 180°C. Tes menggunakan biji kopi Arabika mengungkapkan waktu retak rata-rata adalah 8.78 menit, waktu pengembangan adalah 2.35 menit, penurunan massa dan peningkatan volume berturut-turut berkisar antara 19.80 – 20.30% dan 49.97 – 54.85%. Rata-rata waktu retak biji kopi Robusta adalah 10 menit, waktu pengembangan adalah 3 menit, penurunan massa dan peningkatan volume berturut-turut berkisar antara 10.87 – 14.90 dan 44.93 – 56.20%. Waktu yang diperlukan untuk menyangrai biji kopi Arabika ke tingkat light-medium dan medium-dark berturut-turut adalah 11.3 dan 12.38 menit, sementara untuk biji kopi Robusta berturut-turut adalah 13.00 dan 14.00 menit.

INTRODUCTION

The heat in a rotating drum is transferred by conduction, as the beans come into direct contact with hot metal surfaces, and convection, as the hot air flows through the drum. As the drum rotates above a heat source, the coffee beans continuously move during the process, effectively aiding in even more roast (Hoffmann, 2014; Rao, 2014). The roasting process of rotating drum needs high temperature and a long time (HTLT).

¹ Dadang Dayat Hidayat, M.Eng.Sc.; Arie Sudaryanto, M.Agr.; Yose Rizal Kurniawan, M.Sc.; Ashri Indriati, M.Sc.; Diang Sagita M.Sc.

The drum roaster is one of the most commonly used roasters today, especially by craft roasters and small-scale enterprises, because it allows them to roast at relatively slower speeds. The drum roaster consists of a roasting drum which rotates horizontally with a spiral flight running along the inside of the drum to axially mix the beans (Hoffmann, 2014; Schwartzberg, 2002).

A small roaster usually uses drum roasters, where beans rotate in a drum heated beneath either with direct or indirect flame. Roasting with this type of machines is very stable; they have high durability and are easier to construct. Nevertheless, there are some disadvantage of this type of roaster such as the need for high temperatures during roasting, roasting time takes up to 18 minutes which can cause some beans to scorch and often leave oil and char deposits on the chamber walls (Eggers and Pietsch, 2008; Nagaraju et al., 1997; Putranto and Chen, 2012).

A coffee roasting drum can be manufactured from different types of metal. Some alternative materials for roasting drum are chromium stainless steel, alloy steel, stainless steel and carbon steel. Material compatibility for the roasting drum can be seen from the amount of thermal coefficient expansion; the less amount of expansion due to temperature change the better. Mild steel is more used than stainless steel because the amount of thermal coefficient expansion of mild steel $11.7 \times 10^{-6} (\text{°C})^{-1}$ is smaller than that of stainless steel, $17.3 \times 10^{-6} (\text{°C})^{-1}$. Furthermore, the use of stainless steel can cause hot spots, resulting in scorching of the coffee beans (ASTM, 2000; Bolay et al., 2010; Paulig, 2017).

Besides materials, some other essential parameters in designing roasting drum are volume, the ratio between length and diameter (L/D ratio) and drum speed. The typical roaster has an optimum load that works the best. One of the previously published paper reported that for small scale drum roaster its optimum volume is 600-750 grams (Coffee Navigated, 2019). Most of the commercial drums have an equal ratio of diameter to length. Disproportionate L/D ratio will affect the quality of the roasted coffee produced if at the same time having an inconsistent heat down the length of the drum and poor bean recirculation in the drum (Coffee Navigated, 2019). Some previously published papers report that L/D ratio for small scale roaster, which has a capacity less than 1 kg, ranges between 1-1.5 (Coffee Navigated, 2019) and for medium scale roaster, which has a capacity up to 10 kg, the length of the drum has to be no higher than 25% of diameter (Home Roasting Coffee Community, 2006). The minimum percentage of headspace in the drum is 55% of drum volume. It is needed to allow an efficient roasting process and facilitating an optimum expansion of the beans (Bolay et al., 2010).

Drum speed is also an essential parameter in designing the roaster. If the drum speed is plodding, then the beans will be in touch with the drum longer; as a result, the coffee beans will get burnt. On the other hand, if the drum speed is very high, the coffee beans will stick to the drum wall all the time due to centrifugal forces and they will also get burnt. To prevent the centrifugal force from counterbalancing gravity and causing coffee beans to stay at the drum wall without falling, then the roasting drum has to rotate with an RPM smaller than $(30/\pi)(g/r)^{0.5}$, where g is gravitational acceleration, and r is the drum radius (Coffee Navigated, 2019).

Most of the small-scale coffee entrepreneurs in Indonesia still use relatively simple equipment; so that their processed products are less competitive. This study aimed to develop a small-scale drum roaster that is safe and reliable having the ability to be easily reproduced and being able to meet the demand from the small enterprises in terms of design and functioning, so that they produce standard quality coffee.

MATERIALS AND METHODS

The development stage of the drum coffee roasting machine consisted of a general description of the roasting machine, sizing of the main components, creating technical drawings, determination of component materials, manufacture, and performance test of the constructed prototype. Before the design stage, the measurement of physical properties of green and roasted coffee bean was conducted.

Physical properties of the green and roasted bean

Physical properties of green and roasted coffee bean are required to calculate the capacity of a roaster, primarily to determine the dimension of the roasting drum, cooling tray, motor power to drive the roasting drum and agitator of the cooling plate. Table 1 shows the physical properties of Arabica and Robusta green and roasted coffee bean as a result of the preliminary study.

Table 1

Physical properties of Arabica and Robusta coffee bean

Physical properties	Arabica			Robusta		
	Green Bean	Light to Medium	Medium to Dark	Green Bean	Light to Medium	Medium to Dark
Moisture content (%)	13.08	6.54	6.24	11.22	7.56	6.12
Weight (g)	0.22	0.17	0.17	0.16	0.14	0.13
Bulk density (g/cm ³)	0.69	0.35	0.31	0.72	0.40	0.32
Mass decrease (%)	-	19.80	20.30	-	10.87	14.90
Volume increase (%)	-	49.97	54.85	-	44.93	56.20

Description of coffee roasting machine design

The roasting machine consists of at least five essential components, i.e. rotating drums, electric motor, the heat source, exhaust fan and cooling tray. Rotating drum has a function as a roasting chamber, in which the bean kept inside will be turned horizontally and mixed axially by spiral fins along the inside of the drum. There are two motors used in this roaster; one used to drive the roaster drum, and the other used to drive the agitator of the cooling tray.

The gearbox was used to couple the electromotor to the roaster drum. Another gearbox was used to couple the electromotor to the propeller of the agitator. The heat source used was a ceramic infrared heater (*Gasolec*) that use liquified petroleum gas as fuel. The exhaust fan has a double function, i.e. to suck hot air from the inside of drum chamber and to suck the chaff and dust from the cooling tray. The cooling bin has a function to collect the hot roasted bean from the roaster drum and to cool it. As an illustration, the drum roaster to be manufactured is presented in figures 1 and 2.

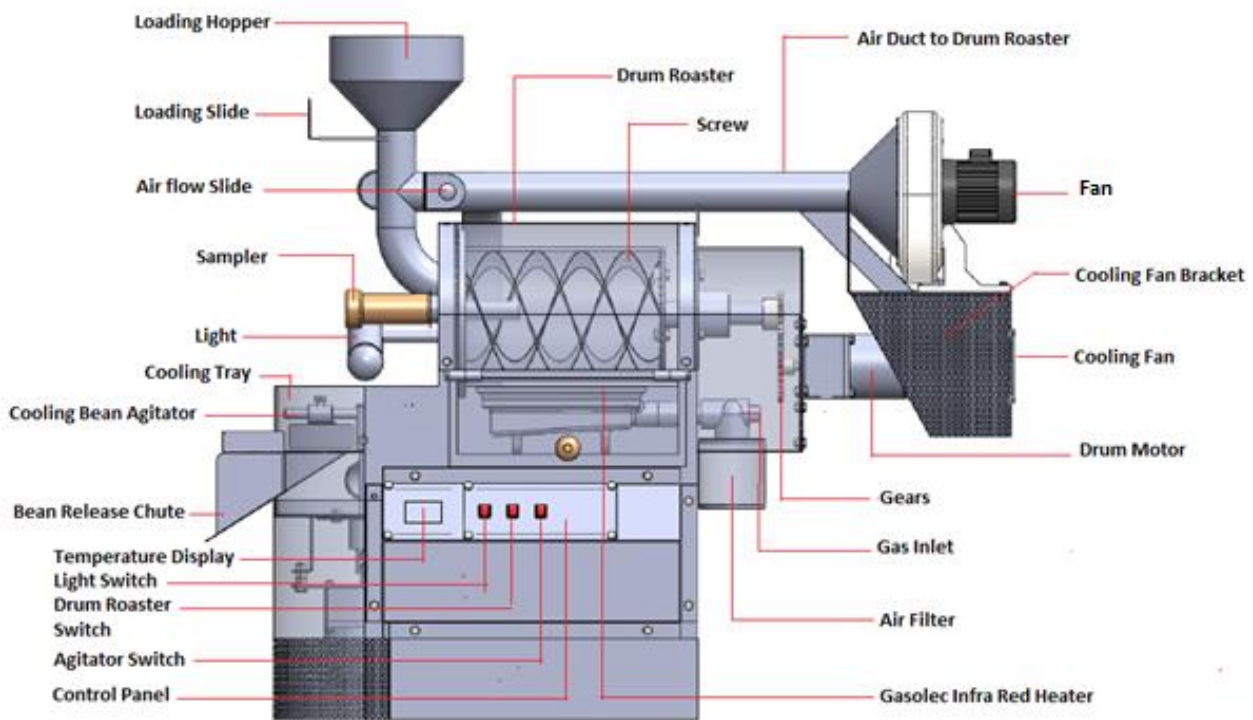


Fig. 1 - Front view of a drum roaster design

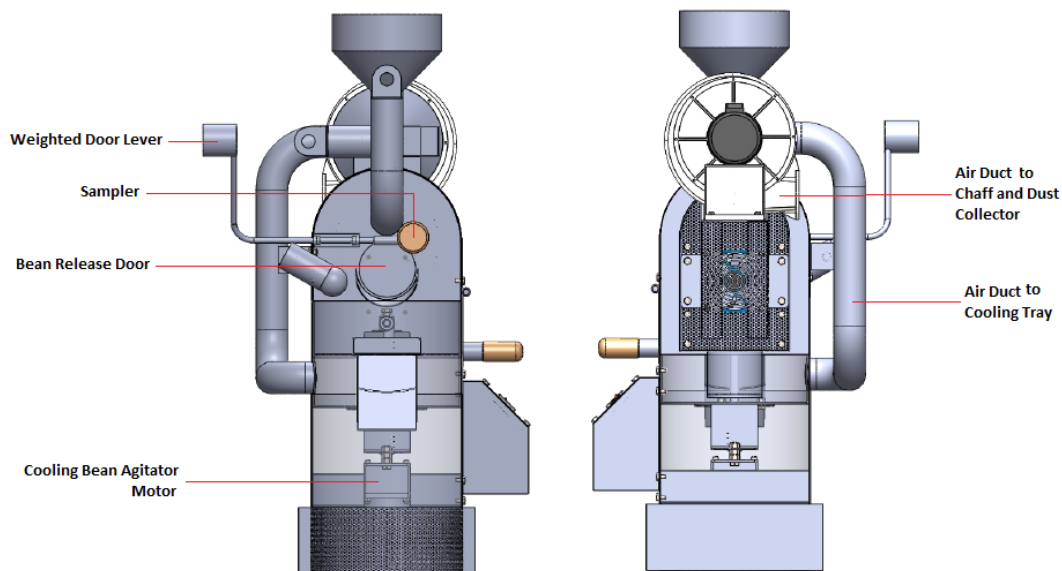


Fig. 2 - Left and right-side views of a drum roaster design

Sizing of the main components

Main components sizing was based on the engineering of Arabica coffee beans. The capacity of a roasting machine to be designed was 750 grams, and the temperature was set up to 500 °C.

Drum roaster

- Dimension

The volume of a drum roasting machine was determined using the following equation formula (Bolay et al., 2010; Mohsenin, 1986).

$$V = \frac{m}{\rho} \quad (1)$$

Where, V is the volume of green beans (cm^3);

m is mass of green beans (kg); and ρ is bulk density of green beans (kg/cm^3).

The volume of green beans to be roasted is 1.09 litres. Volume increasing from green bean to roasted bean (light to medium) was 1.5; thus, the net amount of green bean was 1.635 litres. To anticipate the different range of green bean density, the safety factor considered was 2, and the correction factor was 1.4. The calculated drum roaster volume was 4.58 litres, and rounded to be 5 litres. The drum roaster dimensions for 5 litres of green beans were: length (L) = 25 cm, outer diameter (Φ_{od}) = 16.83 cm, inner diameter (Φ_{id}) = 16.15 cm.

- Drum speed

The optimum drum speed was determined by using the following formula (Coffee Navigated, 2019). The optimum drum speed ranges between 10-25%, less than $30/\pi (g/r)^{0.5}$.

$$D_s = \frac{30}{\pi} \times \sqrt{\frac{g}{r}} \quad (2)$$

Where, D_s is drum speed (rpm); g is gravitation (9.81 m/s^2); and r is inner radius of roaster drum (0.08 m).

The calculated drum speed using equation (2) was 105.7 rpm, but most of the home roaster design used the optimum speed 25% less than D_s . Based on the calculation, the optimum speed chosen was 79.3 rpm. The available gear ratio in the market was 1:10, 1:20, 1:30 and 1:40; with the electromotor rpm of 1350, then the rpm of every gearbox would be 135, 67.5, 45, and 33.75 respectively. Referring to the calculation, the gearbox used for the roaster that would be designed was 1:20, then the drum speed was 67.50 rpm.

- Power requirement

The power requirement was determined using the following equation (Khurmi and Gupta, 2005).

$$P = \frac{2 \times \pi \times n \times T}{60} \quad (3)$$

$$T = m_d \times g \times r \quad (4)$$

Where:

P is power requirement (J/s);

T - Torsion (N.m);

m_d - total mass of roaster drum and coffee bean (kg);

r - the radius of roaster drum (m).

The result of calculation determined that the required power was 24.74 J/s. The electromotor type used to drive the drum roaster was M425-402, 25 W, 220 V, 50/60 Hz, 4-pole, 1400 rpm, Gear Ratio 1:20.

Loading hopper

The dimension of loading hopper, as shown in figure 3, was determined using the following equations (Zegarelli, 2007).

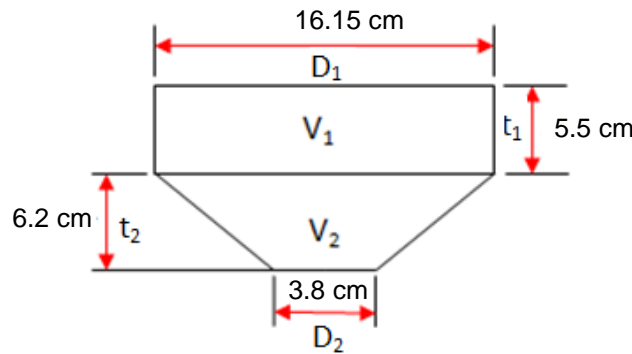


Fig. 3 - Cross-section of the loading hopper

$$V_1 = \pi \times \frac{D_1^2}{4} \times t_1 \quad (5)$$

$$V_2 = \frac{1}{3} \pi \times t_2 \left[\left(\frac{D_1}{2} \right)^2 + \left(\frac{D_2}{2} \right)^2 + \left(\frac{D_1}{2} \right) \left(\frac{D_2}{2} \right) \right] \quad (6)$$

$$\sum V = V_1 + V_2 \quad (7)$$

Results of calculation show that the volume of loading hopper ($\sum V$) was 1672.4 cm³ or 1.67 litres while the loading volume target of the coffee bean was 750 gram or 1087 cm³ or 1.09 litres. This means that the hopper capacity exceeded the volume target of the coffee to be roasted so that the coffee bean could be entirely placed in the hopper.

Cooling tray

Table 1 showed that the mass decrease of Arabica bean from green bean to light-medium and medium-dark roasted bean ranged from 19.8-20.3 % and the volume increase of that was between 49.97-54.85 %. The average mass decrease and volume increase of arabica green bean after roasting was 20.05 % and 52.41 % respectively. Cooling tray parameters to be calculated were dimension and power requirement.

- Dimension

The volume of 1.087 litres of green arabica bean after roasting would become 1.65 litres. Results of calculation found that the diameter and height of the cooling tray were 21.74 cm and 7.8 cm, respectively. The volume of the cooling plate was determined as follows (Mohsenin, 1986; Zegarelli, 2007).

$$V_{ct} = \frac{\pi \times D^2}{4} \times t \quad (8)$$

Where, V_{ct} is the volume of the cooling tray (cm^3); D is the diameter of the cooling tray (cm); and t is the height of the cooling tray (cm).

- Power requirement

The mass of 750 grams arabica green bean after roasting would become 607.15 grams. The power requirement of the cooling tray to drive the agitator was determined using equation (3-4) (*Khurmi and Gupta, 2005*). Mass of agitator propeller and green coffee bean was 1.16 kg; the radius of agitator propeller was 0.112 m. Results of calculation determined that the required power of the agitator motor was 8.98 J/s. The electromotor type chosen to drive the agitator propeller of the cooling tray was M315-402, 15 J/s, 220 V, 50/60 Hz, 4-pole, 1400 rpm.

Energy consumption

The energy required to heat the drum roaster and the green bean was determined by the following equation (*Gupta, 1999*). The temperature was designed up to 500°C , and the ambient temperature was 30°C .

$$\Delta Q = m_{dr} \times C_{st} \times \Delta T + m_{gb} \times C_{gb} \times \Delta T \quad (9)$$

where:

- ΔQ is the energy consumption (Joule);
- m_{dr} - mass of the roaster drum (3.5 kg);
- m_{gb} - mass of green bean (0.75 kg);
- C_{st} - heat capacity of stainless steel ($500 \text{ J/kg}^\circ\text{C}$);
- C_{gb} - heat capacity of green bean coffee ($330 \text{ J/kg}^\circ\text{C}$).

Results of calculation showed that the energy needed to roast the green coffee bean was around 224 Kcal/hr. The burner used to roast the coffee bean was ceramic burner plate S8 $\varnothing 1.30$ mm of Gasolec infrared heater with the capacity of 3000 Kcal/hr, and fuel consumption of 270 grams liquefied petroleum gas per hour.

Airflow

Drum roasters require a fan; otherwise, it will produce an extremely uneven roasted bean, since it relies only on conductive heat and a little of radiant heat to roast. Too high airflow will risk the coffee bean get roasted quicker on the outside than in the core, on the other hand, too low airflow will risk an uneven heat distribution and as a result, will produce an uneven roasted bean (*Home barista, 2013*). The specification of the fan used was: power 150 J/s, voltage 220 V, frequency 50 Hz, flow rate $2.5 \text{ m}^3/\text{min}$.

Evaluation of the coffee roasting machine

The constructed coffee roasting machine was performed with and without loads. At the unload performance, the roaster was operated with the fan off and on. The temperature was set up to 180°C , and after the set temperature was reached, the fuel-gas was stopped. The machine performance with loads of 750- grams was conducted against two varieties of coffee beans, i.e. Arabica and Robusta green coffee beans. The parameters evaluated consist of processing temperature in the drum, time to achieve a light-medium colour qualification, time to achieve a medium-dark colour qualification, crack time and development time. Crack time is the time it takes for the coffee beans to crack. Development time is the duration from the first crack to the unloading of roasted coffee (*Coffee Navigated, 2019*). The sample of the green coffee bean was taken from coffee farmers located in Cupunagara village (Latitude $6^\circ 46' 57.71''\text{S}$, Longitude $107^\circ 41' 37.15''\text{E}$, and elevation 1153 MAMSL), Cisalak sub-district, Subang district, West Java province. The green coffee bean samples were roasted up to reach light-medium and medium-dark degrees.

RESULTS

The prototype of the coffee roasting machine

Figure 4 shows the designed coffee roasting machine that was manufactured. Table 2 shows the specifications of the roasting machine.



Fig. 4 - The prototype of a coffee roasting machine

Table 2

Specifications of a coffee roasting machine prototype

Parameter	Specification
Overall dimension	1040 × 530 × 810 mm
Weight	50 kg
Roaster drum	Ø 168 mm, length 250 mm
Roaster drum motor	M425-402, 25 J/s, 220 V, 50/60 Hz, 4-pole, 1400 rpm, gear ratio 1:20
Fan	150 J/s, Ø 2", 2.5 m ³ / min
Cooling tray	Ø220 mm, height 78 mm
- Net volume	750- gram green coffee bean
- Motor	M315-402, 15 J/s, 220 V, 50/60 Hz, 4-pole, 1400 rpm
Temperature display	TC 4 series, max 500°C
Thermocouple Sensor	MAX6675 Module + K Type, 12-Bit, 0.25°C Resolution, Temperature Ranging 0°-700°C, App. For Arduino, Raspberry
Burner	Gasolec infrared heater, ceramic burner plate S8 Ø1.30mm
Fuel consumption	270 g/h, liquefied petroleum gas

Performance test of coffee roasting machine

The roasting device was heated up to 180°C, then the gas was stopped. After stopping the gas, the temperature still increased. Figure 5 shows that at the position of the fan ON, the temperature was 186°C, and at the state of the fan OFF, the temperature reached 196°C.

At the position of the fan ON the temperature increased and decreased faster than that of the fan OFF. The average time required to reach the temperature 180°C of the fan ON and OFF was 15 and 22 minutes respectively.

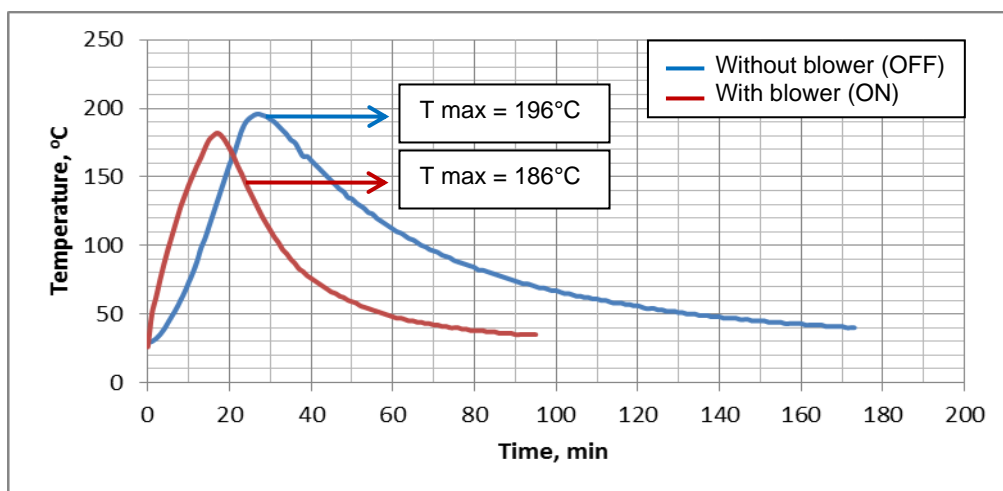


Fig. 5 - Unloaded performance of the roaster with blower ON and OFF

Heating beans is not only relying on power-setting during the roasting but also on the temperature of roaster before the coffee beans are charged. Preheating time is not only relying on a type of roaster design but also on operator habits and experience to get a certain quality of the roasted coffee bean product (*Coffee Navigated, 2019*).

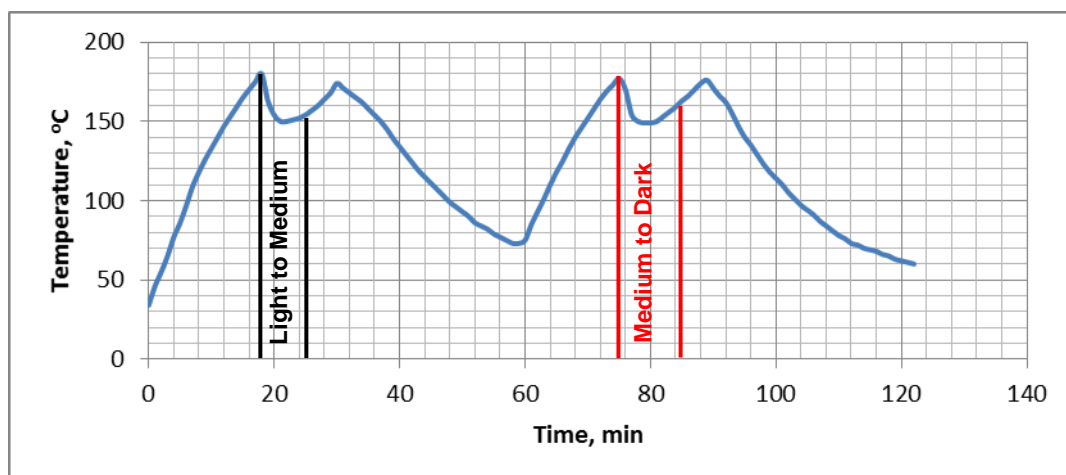


Fig. 6 - Roaster performance of Arabica coffee bean roasting process

Figure 6 shows that the changes from green coffee beans (moisture content of 13.08 ± 0.13 %) to light-medium levels of roasted Arabica coffee beans (moisture content of 6.54 ± 0.26 %) required 11.3 minutes. The crack and development times were 8.78 and 2.35 minutes, respectively.

The ratio between development time and total roast time was 21.14%. The decrease in mass and increase in volume were 19.80 and 49.97%, respectively. It was required 12.38 minutes to produce medium-dark levels of roasted Arabica coffee beans. The crack and development times were 9.08 and 3.30 minutes, respectively; the development time of medium-dark roasted coffee bean was 23.08 %.

The decrease in mass and increase in volume were 20.30 and 54.85%, respectively. One of the previously published paper reported that the weight loss of a light roast is around 11-13%, and of real dark is 20-22% (*Coffee Navigated, 2019*).

The different results of this study and those of the previous report (*Coffee Navigated, 2019*) were suspected due to the difference in moisture content before roasting, the treatment before roasting, e.g. preheating and also the different geographical areas where the green coffee bean yielded. First crack and development time as a finding of this study was below that of the previous study (*Fadai et al., 2017; Rao, 2014*).

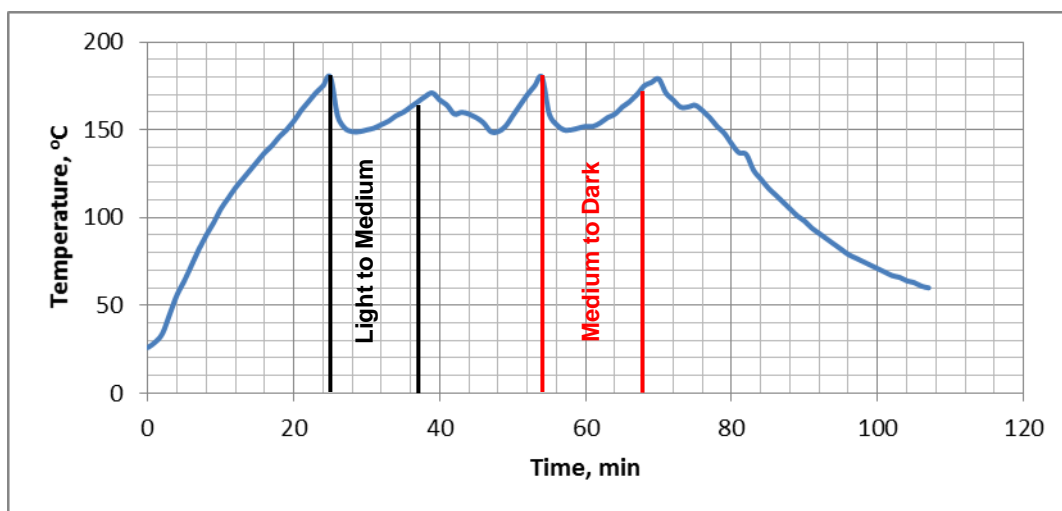


Fig. 7 - Roaster performance of Robusta coffee bean roasting process

Figure 7 shows the time requirement for green coffee beans (moisture content of 11.22 ± 0.11 %) to reach light-medium levels of roasted Robusta coffee beans (moisture content of 7.56 ± 0.52 %). It was 13 minutes (more than the roasting time of Arabica coffee beans). The crack and development times were 10.00 and 3.00 minutes, respectively; the ratio between development time and total roasting time was 26.66%. The decrease in mass and increase in volume were 10.87 and 44.93 %, respectively. 14.00 minutes were necessary to produce medium-dark levels of roasted Robusta coffee beans. The crack and development times were 10.00 and 4.00 minutes, respectively; the development time of medium-dark roasted coffee bean was 28.57%. The decrease in mass and increase in volume were 14.90 and 56.20% respectively.

The crack time, development time and total time of roasting of Arabica coffee bean were relatively shorter than that of Robusta coffee bean; this happened because of the difference in hardness. The results of the preliminary study showed that the green Robusta bean was harder than the green Arabica bean; the hardness value of green Robusta and Arabica coffee beans was 17.70 ± 5.91 kgf and 17.67 ± 2.83 kgf, respectively. The drum speed of the designed roaster was operated at rpm of 67.5 rpm. The speed was within the range of mostly small roaster drum speed, i.e. 50-77 rpm (*Coffee Navigated*, 2019).

CONCLUSIONS

A prototype of small drum roasting machine was designed, manufactured and evaluated successively for different varieties of green coffee bean. The roaster capacity was 750 gram per batch. The overall dimension of length, width and height were 1040 mm, 530 mm and 810 mm respectively. The size of the roaster drum was 152 mm of diameter, 250 mm of length, and 50 kg of weight. The motor of 25 J/s drove the drum roaster while motor 15 J/s drove the agitator of the cooling tray. Both of the roaster drum and agitator motor was coupled to a gearbox with the ratio of 1:20 and 1:40 respectively. The rotation of roaster drum and cooling tray agitator was 67.5 and 35 rpm respectively. The temperature of the roaster was set up to 500°C, and the type of burner used was a ceramic burner plate of infrared heater. The heat source was liquefied natural gas with the fuel consumption of 270 gram per hour.

The prototype has technically worked well based on the results of the performance test. The preheating time ranged from 15-22 minutes. The test using arabica coffee bean reveals that the average crack time was 8.78 minutes, development time was 2.35 minutes, decreasing mass and increasing volume ranged from 19.80 - 20.30 % and 49.97 - 54.85 % respectively. The average crack time of Robusta coffee bean was 10 minutes; development time was 3 minutes, decreasing mass and increasing volume ranged from 10.87 - 14.90 and 44.93 - 56.20 %, respectively. The required time to roast Arabica green coffee bean to the light-medium and medium-dark level was 11.3 and 12.38 minutes respectively, besides for Robusta green coffee beans was 13.00 and 14.00 minutes respectively.

ACKNOWLEDGEMENT

The authors would like to thank everyone from the Research Center for Appropriate Technology, Indonesian Institute of Sciences, which provided us with assistance throughout our works.

REFERENCES

- [1] ASTM. (2000), *Standard Test Method for Linear Thermal Expansion of Solid Materials by Thermomechanical Analysis*, American Society for Testing and Materials.
- [2] Bolay K., Hubbard K., Looke B., Marshall M. and Moyer N., (2010), *Design of 300 Kg Coffee Roaster. Roasting Innovation*, Oklahoma, available at: <https://bae.okstate.edu/wp-content/uploads/2017/09/SD-2010-2011-US-Rosters-Fall-Report.pdf>.
- [3] Coffee Navigated, (2019), “Roasting basics”, available at: <http://coffeenavigated.net/roasting-coffee/> (accessed 15 April 2019).
- [4] Eggers R. and Pietsch A., (2008), *Technology I: Roasting*, pp. 90–107.
- [5] Fadai N.T., Melrose J., Please C.P., Schulman A. and Van Gorder R.. (2017), A heat and mass transfer study of coffee bean roasting, *International Journal of Heat and Mass Transfer*, Vol. 104, pp. 787–799.
- [6] Gupta C.P., (1999), *Engineering Heat Transfer*, Nem Chand & Bros., India.
- [7] Hoffmann J., (2014), *The World Atlas of Coffee: From Beans to Brewing – Coffees Explored, Explained and Enjoyed*, Octopus Publishing Group Ltd, London.
- [8] Home barista, (2013), “What are the functions of airflow in a drum roaster”, available at: <https://www.home-barista.com/home-roasting/what-are-functions-of-air-flow-in-drum-roaster-t25943.html> (accessed 20 March 2019).
- [9] Home Roasting Coffee Community, (2006), Building a roaster: drum size and capacity, available at: https://forum.homeroasters.org/forum/viewthread.php?thread_id=127.
- [10] Kelly C., (2018), *The Art of Coffee Roasting: Investigations into Sensor Development for the Application of Controlling Coffee Roasting*, The University of Waikato, available at: <https://researchcommons.waikato.ac.nz/handle/10289/11614>.
- [11] Khurmi R.S. and Gupta, J.K., (2005), *Machine Design (S.I. Units)*., Eurasia Publishing House (Pvt.) Ltd., New Delhi.
- [12] Mohsenin, N.N., (1986), *Physical Properties of Plant and Animal Materials*, Gordon and., New York.
- [13] Nagaraju V.D., Murthy, C.T., Ramalakshmi, K. and Rao, P.N.S. (1997), Studies on roasting of coffee beans in a spouted bed, *Journal of Food Engineering*, Vol. 31 No. 2, pp. 263–270.
- [14] Paulig G., (2017), “Coffee Roasting Basics: Developing Flavour by Roasting Paulig Barista Institute”, available at: <https://www.baristainstitute.com/blog/sampo-latvakangas/may-2017/coffee-roasting-basics-developing-flavour-roasting>.
- [15] Putranto A. and Chen, X.D., (2012), Roasting of Barley and Coffee Modeled Using the Lumped-Reaction Engineering Approach (L-REA), *Drying Technology*, Taylor & Francis, Vol. 30 No. 5, pp. 475–483.
- [16] Rao S., (2014), *The Coffee Roaster’s Companion*, 1st ed., Canada.
- [17] Schwartzberg H.G., (2002), Modeling Bean Heating during Batch Roasting of Coffee Beans, *Engineering and Food for the 21st Century*, 1st ed., CRC Press, Boca Raton, p. 1104.
- [18] Zegarelli M., (2007), *Basic Math & Pre-Algebra For Dummies*, Wiley Publishing Inc, Indianapolis.

DESIGN AND EXPERIMENT OF ECCENTRIC SWING COMBING DEVICE FOR *CERASUS HUMILIS*

/

钙果偏心摆动梳脱装置的设计与试验

Xiaobin Du, Junlin He*, Yongqiang He, Dawei Fang¹

College of Engineering, Shanxi Agriculture University, Taigu/China

Tel: +86-0354-6288400; E-mail: hejunlin26@126.com

DOI: <https://doi.org/10.35633/inmateh-60-10>

Keywords: eccentric; swing; feeding; combing; parameter optimization; experiment; *Cerasus humilis*

ABSTRACT

An eccentric swing combing device was designed on the basis of the growth characteristics of *Cerasus humilis* in mature stage in this work to improve the removal rate and reduce the damage rate. The device adopted a swing mechanism to realize comb rod entry from the roots of branches and an eccentric mechanism to realize horizontal combing. The kinematic equation and the main affecting factors of the combing effect were obtained through the kinematic and dynamic analyses of the combing device. Rotation speed, feeding speed, and comb swing angle were considered the influencing factors, and removal and damage rates were taken as the evaluation indexes. We conducted an experiment of quadratic orthogonal rotation centre combination with three factors and five levels on the combing device. Results showed that the contribution rate of each factor to the removal and damage rates was in the order of feeding speed, rotation speed and comb swing angle. The best combination of parameters was obtained as follows: rotating speed of 11.26 r/min, feeding speed of 0.227 m/s, and comb swing angle of 5°. The removal and damage rates were 95.21% and 4.56%, respectively, under this parameter combination. The relative error with the predicted result was less than 5%. This study can effectively improve the effect of *C. humilis* fruit removal and provide reference for further design of *C. humilis* harvesting machinery.

摘要

针对钙果机械化采收难以脱果的问题, 本文为提高钙果脱净率, 降低破损率, 结合其生长特性, 设计了钙果偏心摆动梳脱装置。该装置采用摆动机构实现枝条根部喂入, 利用偏心机构实现水平梳脱, 完成脱果作业。在钙果梳脱状态动力学分析的基础上, 利用该装置选择以脱净率和破损率为评价指标, 以梳齿轮转速、喂入速度和梳齿摆角为试验因素, 实施三因素五水平二次正交旋转中心组合优化试验。结果表明, 各因素对脱净率和破损率的贡献率由大到小依次是喂入速度、梳齿轮转速和梳齿摆角; 得到最佳参数组合为梳齿轮转速 11.26 r/min, 喂入速度 0.227 m/s, 梳齿摆角 5°, 在此参数组合下钙果偏心摆动梳脱装置的脱净率为 95.21%, 破损率为 4.56%, 与预测结果相对误差小于 5%。该研究有效提高钙果脱果效果, 可为提高钙果机械化收获提供参考。

INTRODUCTION

Cerasus humilis pulp is rich in calcium citrate malate pentahydrate, which is easy to be absorbed (Chang et al., 2011). In recent years, the planting area has increased rapidly year by year with the promotion and recognition of the market. *C. humilis* species have a large number of fruits, which can be produced from the root to the top of the branch (He et al., 2018; He et al., 2019). *C. humilis* branches are soft, and they will lodge under the gravity of fruits when they are mature. Lodging is good for fruit to receive light and ensure good colour and quality (Du et al., 1992). However, the characteristics of dense fruit and lodging branches bring difficulty in harvesting the *C. humilis* near the root. At present, the mechanized harvesting equipment of *C. humilis* is yet to be perfected. Thus, the development of the *C. humilis* industry should be promoted to strengthen the research of *C. humilis* harvesting machinery.

Traditional *C. humilis* harvest mainly depends on manual picking, which has high labour intensity and cost (Sanders., 2005). Extensive research has been conducted on picking small berries. The use of high-power fan to produce intermittent air flow and make branches swing can achieve fruit removal (Whitney et al., 1972). Pneumatic harvester has no rigid connection with fruit trees and can thus reduce the mechanical damage of fruit trees (Chen et al., 2011).

¹ Xiaobin Du, As. Ph.D. Stud. Eng.; Junlin He, Prof. Ph.D. Eng.; Yongqiang He, M.S. Stud. Eng.; Dawei Fang, M.S. Stud. Eng.

A close relationship exists between fruit removal rate and connection force (Coppock et al., 1981). *C. humilis* has a strong connection force, and the cost of air flow for fruit removal is high (Sun et al., 2016). Vibration harvester uses vibrating rods to knock fruits off or vibrate the trunk of the plant to cause fruit swing and fall-off (Peterson et al., 1997). However, *C. humilis* branches are soft, and the vibration transmission is difficult. Fruit removal equipment suitable for *C. humilis* growth characteristics should be developed. Our research group has performed a series of research on the way and equipment of *C. humilis* fruit removal. Double-roller stripping harvester simulates the mechanism of artificial harvesting and achieves staged harvesting (Liu et al., 2013). However, this harvester requires cutting off branches to reduce the yield in the next year. Comb-type *C. humilis* harvester can achieve high fruit removal rate and low damage rate but has difficulty harvesting the *C. humilis* near the root (Zhang et al., 2018).

On the basis of the feasibility of combing verified by previous research (Du et al., 2019), an eccentric swing combing device was designed in accordance with the growth characteristics of *C. humilis*. In this work, the key parameters of the device were studied by experiment of quadratic orthogonal rotation centre combination. The best working parameters were obtained using the removal and damage rates as evaluation indexes. This study can provide technical support for further research and development of *C. humilis* harvester.

MATERIALS AND METHODS

Materials and growth characteristics

Sampling was conducted in early September, 2018. The sampling site was Juxin Modern Agriculture Base in Taigu County, Shanxi Province, China (112°29'E, 37°23'N), and the variety was "Nongda 4." The branches with uniform length and no damage were selected and cut from the place close to the ground. The number of fruits on each branch was 40–60, the moisture content of branch was 56.74%, and the moisture content of grape was 78.2%. The experiment was performed immediately after sampling.

C. humilis is an oblate fruit. Fig. 1 presents the mature *C. humilis* plants. These plants are characterized by a large and dense number of fruits. Table 1 exhibits the measurement data of shape parameters and connecting force of fruit stalk in the mature stage. The average diameter of *C. humilis* is 24.65 mm, the connection force is 8.20 N, the number of fruits is 48.84, and the root diameter is only 6.56 mm, which hardly supports its weight and upright position. Mechanical fruit removal requires overcoming the difficulty in fruit removal near the root caused by the lodging of branches and reducing the damage caused by the large connecting force of fruit stalk.



Fig. 1 – Growth characteristics of *C. humilis* at maturity

Table 1

Measured data of *C. humilis*

Parameters	Range	Average	Standard deviation
Fruit diameter/ mm	20.64~30.3	24.65	2.65
Connection force/ N	3.55~13.65	8.20	2.19
Branch length/ cm	24~80	46.72	10.35
Root diameter/ mm	4.60~8.28	6.56	1.00
Number of fruits	30~65	48.84	10.74
Fruit bearing interval length/ cm	18~61	39.24	11.09

Device and process

The fruit removing device was the key part of *C. humilis* harvester. In this work, an eccentric swing combing device was designed on the basis of the growth characteristics of *C. humilis*. The device was mainly composed of the gantry, swing mechanism, eccentric combing mechanism, and transmission system. The swinging mechanism was composed of a rocker, a rocker shaft, a connecting rod and a crankshaft to feed the comb rods from the root of the plant. The eccentric combing mechanism was composed of the comb wheel, comb rods, comb rack, comb wheel rocker, and eccentric wheel. Six rows of comb rods were present to realize the horizontal combing of the comb rods rotating with the comb wheel. The transmission system included motor and synchronous pulley and belt. Fig. 2 shows the system structure. The comb clearance was larger than the branch diameter but smaller than the fruit diameter. Thus, the fruits could be removed by combing (Zhang *et al.*, 2014). With the advance of the device, the transmission system drove the combing device to rotate clockwise for realizing combing from bottom to top.

Before the experiment, the crankshaft was changed to adjust the swing angle, and the feeding speed control system was adjusted to set the feeding speed. The number of fruits on branches was counted, and then, the fruits were fixed in the branch fixture. During the experiment, the electromagnetic speed regulating motor was started, and the eccentric swing combing device was operated. Then, the electromagnetic speed regulating controller was adjusted. The digital tachometer was used to measure the speed of the combing wheel. When the device ran stably, the feeding speed control system was started. Branch feeding was realized by track traction. At the end of experiment, the abscission fruits were collected and counted.



Fig. 2 – Eccentric swing combing mechanism

1- Track; 2- Branch fixture; 3- Feeding speed control system; 4- Comb rods; 5- Gantry; 6- Synchronous belt; 7- Crank rocker mechanism; 8- Crankshaft; 9- Electromagnetic speed regulating motor; 10- Electromagnetic speed regulating controller

Design of key structural parameters

Design of the swing mechanism

The swing mechanism, which was actually a crank rocker mechanism, was designed to make the comb rods enter from the root of branches and increase the combing range. The mechanism was mainly composed of a crankshaft, a connecting rod, and a rocker. The comb wheel was connected to the rocker. As the rocker swung back and forth, the comb angle was changed to form elevation and depression angles. The average speed of the process and the return of the rocker should be close to reduce the impact damage caused by the swinging comb rods. Thus, the travel speed ratio coefficient $k = 1.05$. The polar angle θ was obtained from the polar angle formula. The dimension of each member was obtained from the limit position relationship, as shown in Fig. 3. The crank length was changed by changing the crankshaft to adjust the swing angle.

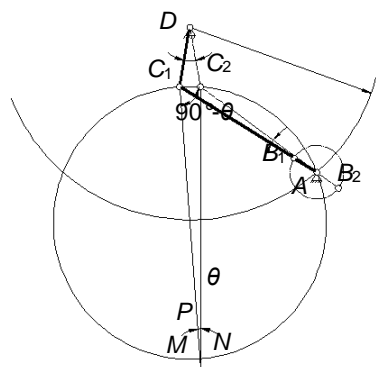


Fig. 3 – Design principle of the swing mechanism

Design of the eccentric mechanism

The eccentric mechanism was composed of the comb wheel M , comb rod AK , comb rack $A-A$, comb wheel rocker $O-O_1$, and eccentric wheel M_1 . Fig. 4 shows the eccentric mechanism structure. Six rows of comb rod AK were present. The length of the comb wheel rocker and the other end of the comb rack are equal ($O-O_1=A-a$) because the outer diameters of the comb and eccentric wheels were equal ($A-O=a-O_1$). Thus, the whole eccentric comb wheel was composed of six groups of parallelogram mechanism OO_1aA . The maximum length of the branch was 800 mm, and the comb wheel radius R was 450 mm in design.

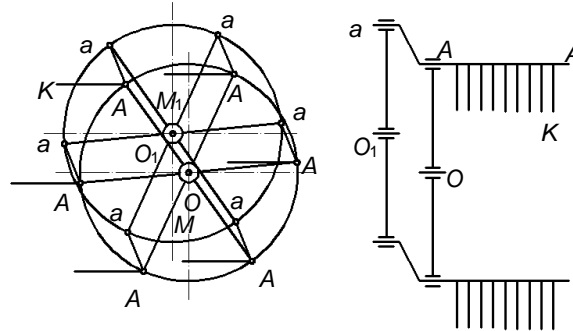


Fig. 4 – Schematic of the eccentric mechanism

Experimental factor analysis and simulation

Kinematic analysis of comb rods

During the device operation, the comb rods were involved in three movements. The comb rods moved along the straight-line direction with the device, the root of comb rods rotated around the comb wheel, and the comb swings up and down. Fig. 5 shows the movement principle.

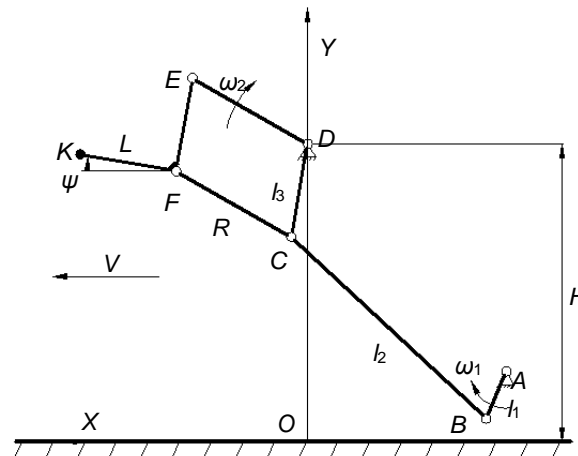


Fig. 5 – Motion principle

After time t , the motion equation of the comb tip (shown as point K in fig. 5) was

$$\begin{cases} x_1 = Vt + L\cos\psi + R\cos\omega_2t + l_3\sin\psi \\ y_1 = H + L\sin\psi + R\sin\omega_2t - l_3\cos\psi \end{cases} \quad (1)$$

The motion equation of the root of comb rods (shown as point F in fig. 5) was

$$\begin{cases} x_2 = Vt + R\cos\omega_2t + l_3\sin\psi \\ y_2 = H + R\sin\omega_2t - l_3\cos\psi \end{cases} \quad (2)$$

- where V is the feeding speed, [mm/s];
- t is the rotation time interval of comb wheel, [s];
- L is the length of comb rod, [mm];
- ψ is the swing angle, [°];
- R is the radius of comb wheel, [mm];
- ω_2 is the angular velocity of comb wheel, [rad/s];
- l_3 is the length of rocker, [mm];
- H is the height of eccentric from the ground, [mm].

A key factor affecting the combing effect was the number of times that the comb rods brush the branches. The more the branches were brushed, the more fruits were removed. However, the damage of comb rods to branches and leaves was great. The number of times of each branch was brushed was

$$Q = 6 \cdot \frac{n}{60} \cdot \frac{L + 2R}{V} = \frac{n}{10V} \cdot (L + 2R), \quad (3)$$

where Q is the number of times the branches were combed, [times];

n is the rotation speed, [r/min].

Therefore, feeding and rotation speeds were the two factors that must be considered in the combing of *C. humilis*.

Dynamics analysis of comb rods

In the process of combing, the collision and squeezing forces between fruits are mainly produced by the comb teeth. These forces simultaneously make the fruit fall off but cause different degrees of damage (Li et al., 2017). In this work, comb up and down were selected for analysis, as shown in Fig. 6.

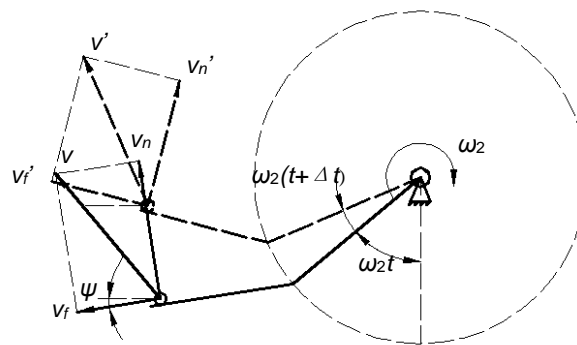


Fig. 6 – Sketches of combing *C. humilis*

Let the comb be located directly below the rotation centre of the comb wheel as the starting point. After time t , the rotation angle of the comb was $\omega_2 t$. At this time, the movement speed of the comb relative to the fruit was v , which can be divided into v_n and v_t , as shown in Fig. 6.

When the comb rods first contacted with the plant, the comb rods were in a downward state, and the comb started from the root of the plant. At this time,

$$\begin{cases} v_n = v \sin(\omega_2 t + \psi) \\ v_t = v \cos(\omega_2 t + \psi) \end{cases} \quad (4)$$

The normal velocity v_n of the comb increased due to the swing angle ψ of the comb rods, and this condition improved the combing ability of the comb.

After time Δt , the comb went up. At this time,

$$\begin{cases} v'_n = v' \sin[\omega_2(t - \Delta t) - \psi] \\ v'_t = v' \cos[\omega_2(t - \Delta t) - \psi] \end{cases} \quad (5)$$

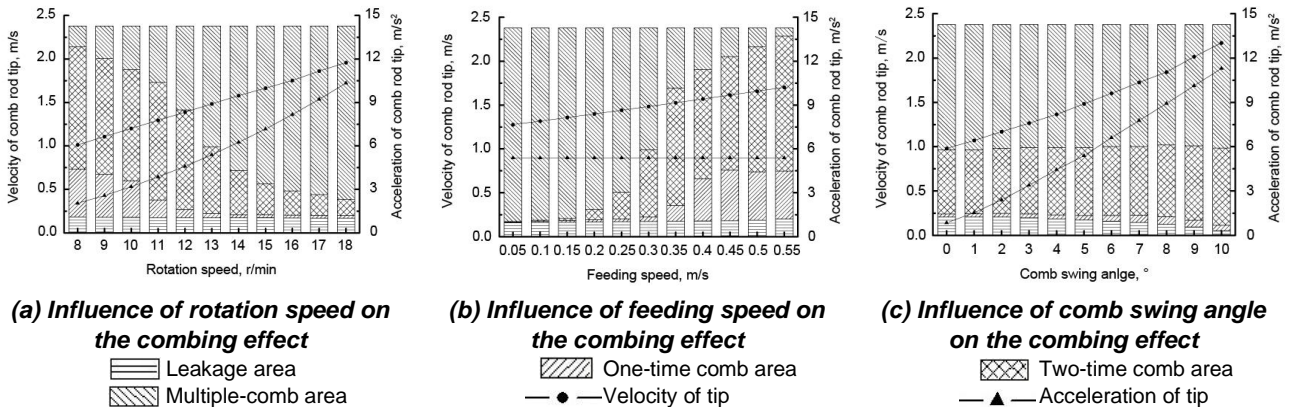
The comb swing angle ψ could reduce the normal velocity v_n , increase the tangential velocity v_t , improve the movement ability of fruits along the comb surface, reduce the accumulation above the comb surface, and decrease the extrusion and collision between fruits. Therefore, the proper comb swing angle was beneficial to increase the combing range and reduce the damage of *C. humilis*.

Combing simulation

The previous experiment and research manifested that the fruit removal result was related to the movement track of the comb rod, and the reasonable movement track could improve the removal rate (Zhang et al., 2018). Therefore, this work used rotation speed, feeding speed, and swing angle as factors to analyse the absolute movement track of the comb rod (Xiang et al., 2015; Shi et al., 2017). The motion trace of the comb tip and root and the velocity and acceleration of the comb tip were obtained using ADAMS simulation software. The area ratios of leakage under one-time combing, two-time combing, and multiple-time combing were calculated using the inclusion–exclusion principle. Fig. 7 shows the results.

Fig. 7(a) indicates that, as the rotation speed increased, the speed of combing off became fast, the area of multiple-time combing significantly increased, and the speed and acceleration of tooth tip rose. Fig. 7(b) reveals that the comb rods repeatedly brushed the same part when the feeding speed was small. As a result, the combing efficiency was low.

When the feeding speed was large, the area of multiple-time combing decreased. Fig. 7(c) shows that the leakage area decreased gradually with the increase in the swing angle, but the velocity and acceleration of tip increased.



Note: In Fig. 7(a), the feeding speed was 0.3 m/s and the comb swing angle was 5°; in Fig. 7(b), the rotation speed was 13 rad/min and the comb swing angle was 5°; in Fig. 7(c), the rotation speed was 13 rad/min and the feeding speed was 0.3 m/s.

Fig. 7 – Simulation results of the influence of various factors on the combing effect

Experiment design

The theoretical analysis showed that the main affecting factors of the combing effect were rotation speed, feeding speed and comb swing angle. In this experiment, quadratic orthogonal rotation centre combination was designed to study the influence of rotation speed X_1 , feeding speed X_2 and comb swing angle X_3 on the combing effect. The multi-objective parameter optimization was completed. The level range of each factor was determined by the simulation results and pre-experiments. The experiment had three factors and five levels. Table 2 presents the factor codes.

Table 2

Coding schedule of experimental factors

Coded	Rotation speed	Feeding speed	Comb swing angle
	[r/min]	[m/s]	[°]
	X_1	X_2	X_3
1.682	16.70	0.47	8.36
1	15.00	0.40	7.00
0	12.50	0.30	5.00
-1	10.00	0.20	3.00
-1.682	8.30	0.13	1.64

The combing effect was evaluated by fruit removal and damage rates. Fruit removal rate Y_1 was the percentage of the numbers of *C. humilis* to be combed off in the total number of *C. humilis* on branches. Damage rate Y_2 was the percentage of the number of *C. humilis* damaged in the number of *C. humilis* to be combed off. The drop damage can be ignored because of the low drop height (He et al., 2019).

$$Y_1 = \frac{N_1}{N}, \tag{6}$$

$$Y_2 = \frac{N_2}{N_1}, \tag{7}$$

where N is the total number of *C. humilis* on the branches before experiment;
 N_1 is the number of *C. humilis* removed from experiment;
 N_2 is the number of damaged *C. humilis* after experiment.

RESULTS

Experimental results and establishment of the regression model

The experiments of the quadratic orthogonal rotation centre combination were conducted in accordance with the code of the experimental factors. A total of 23 groups of experiment were considered, and each group was repeated five times. The results were taken as the average value. The experiment scheme design and result analysis were completed with Design Expert software, as shown in Table 3.

Table 3

Experimental results

No.	Comb distance X_1	Combing speed X_2	Comb rod radius X_3	Fruit removal rate Y_1	Damage rate Y_2
	[mm]	[mm/s]	[mm]	[%]	[%]
1	-1	-1	-1	90.20	4.79
2	1	-1	-1	93.07	7.90
3	-1	1	-1	85.02	6.23
4	1	1	-1	91.42	8.61
5	-1	-1	1	95.28	5.45
6	1	-1	1	96.77	9.13
7	-1	1	1	87.60	6.52
8	1	1	1	92.62	8.12
9	-1.6818	0	0	88.57	3.97
10	1.6818	0	0	94.27	9.31
11	0	-1.6818	0	93.87	6.25
12	0	1.6818	0	87.65	7.81
13	0	0	-1.6818	89.57	5.81
14	0	0	1.6818	91.85	6.96
15	0	0	0	92.77	4.56
16	0	0	0	94.09	5.00
17	0	0	0	91.65	4.68
18	0	0	0	94.04	5.19
19	0	0	0	93.27	4.61
20	0	0	0	95.25	4.58
21	0	0	0	92.82	5.26
22	0	0	0	94.32	4.89
23	0	0	0	93.88	4.53

Table 4

ANOVA

Sources	SS	DF	F Value	P Value	Sources	SS	DF	F Value	P Value
Model 1	168.18	9	17.17	<0.0001**	Model 2	57.82	9	55.23	<0.0001**
X_1	47.12	1	43.29	<0.0001**	X_1	28.56	1	245.54	<0.0001**
X_2	62.09	1	57.05	<0.0001**	X_2	1.71	1	14.71	0.0021**
X_3	19.68	1	18.08	0.0009**	X_3	0.96	1	8.27	0.0130*
$X_1 X_2$	6.23	1	5.72	0.0325*	$X_1 X_2$	0.99	1	8.48	0.0121*
$X_1 X_3$	0.95	1	0.87	0.3667	$X_1 X_3$	0.01	1	0.05	0.8311
$X_2 X_3$	3.13	1	2.87	0.1140	$X_2 X_3$	0.55	1	4.69	0.0494*
X_1^2	6.01	1	5.52	0.0352*	X_1^2	7.96	1	68.43	<0.0001**
X_2^2	11.44	1	10.51	0.0064**	X_2^2	11.36	1	97.69	<0.0001**
X_3^2	11.92	1	10.95	0.0056**	X_3^2	6.06	1	52.11	<0.0001**
Residual	14.15	13			Residual	1.51	13		
Lack of Fit	5.20	5	0.93	0.5097	Lack of Fit	0.87	5	2.18	0.1564
Pure Error	8.95	8			Pure Error	0.64	8		
Total	182.33	22			Total	59.33	22		

Note: $P < 0.01$ (extremely significant, **), $P < 0.05$ (significant, *);

Model 1 is variance analysis of fruit removal rate;

Model 2 is variance analysis of damage rate.

Multiple regression analysis was performed on the test results in Table 3. The quadratic polynomial regression models among the rotation speed X_1 , feeding speed X_2 , comb swing angle X_3 , fruit removal rate Y_1 , and damage rate Y_2 were established. The following regression equations were obtained after the insignificant factors were eliminated:

$$Y_1 = 93.55 + 1.86X_1 - 2.13X_2 + 1.20X_3 + 0.88X_1X_2 - 0.62X_1^2 - 0.85X_2^2 - 0.87X_3^2 \quad (8)$$

$$Y_2 = 4.80 + 1.45X_1 + 0.35X_2 + 0.27X_3 - 0.35X_1X_2 - 0.26X_2X_3 + 0.71X_1^2 + 0.85X_2^2 + 0.62X_3^2 \quad (9)$$

where X_1 , X_2 , and X_3 were the coding values of rotation speed, feeding speed, and comb swing angle, respectively.

ANOVA was conducted to verify the applicability of the regression model, as shown in Table 4. The P values of the regression models of removal rate Y_1 and damage rate Y_2 were less than 0.0001, which indicates that the models were extremely significant. The P values of the regression models were larger than 0.05, which indicates that the regression models effectively fit with the actual situation within the scope of the experiment. The coefficient determination R^2 of regression models Y_1 and Y_2 were 0.8687 and 0.9569, respectively. A high correlation was observed between the predicted and actual values, and the experiment error was small. Therefore, the models could be used to analyse and predict the effect of fruit removal.

Analysis of influencing factors

Analysis of the effect of experimental factors on the performance indexes

By referring to the calculation method of the contribution rate of each factor to the index in multiple quadratic regression (Zhou et al., 2009), the influence degree of each factor on each index was determined. Table 5 shows the results.

Table 5

Contribution rate of each factor

Factors	Contribution rate			Ranking contribution rate from large to small
	X_1	X_2	X_3	
Y_1	2.208	2.626	2.179	$X_2 > X_1 > X_3$
Y_2	2.422	2.756	2.253	$X_2 > X_1 > X_3$

Analysis of the effect of interaction of experimental factors on the performance indexes

This work studied the influence rule of interaction of factors on the performance indexes by using ANOVA. The interaction of rotation and feeding speeds significantly affected the fruit removal rate ($P < 0.05$). The fruit removal rate increased with the increase in rotation speed and decreased with the increase in feeding speed when the comb swing angle was at 0 level ($X_3 = 5^\circ$), as shown in Fig. 8a. The branches were combed frequently when the feeding speed was low. The fruits that were not combed off in the previous row or leaked from the comb clearance were combed again by the next row of comb rods. As a result, the fruit removal rate was high. At least one row of comb rods could not be guaranteed to enter from the root of branches when the feeding speed was large. The branches were partially combed. Consequently, the fruit removal rate was low.

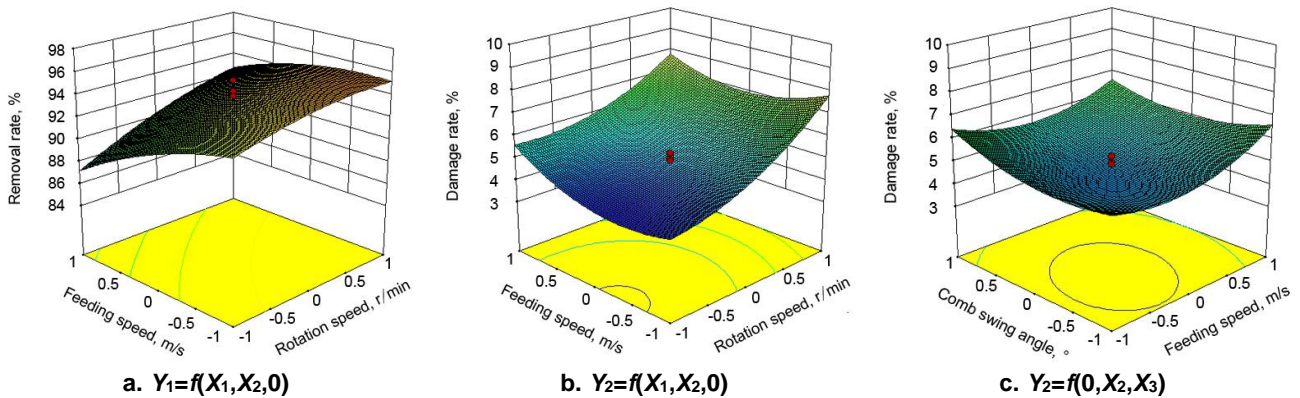


Fig. 8 – Response surfaces of the interaction of test factors on the performance indexes

The interaction of rotation and feeding speeds significantly affected the damage rate ($P < 0.05$). When the comb swing angle was at the 0 level ($X_3 = 5^\circ$), the damage rate increased with the increase in rotation speed and initially decreased before increasing with the increase in the feeding speed, as shown in Fig. 8b. When the rotation speed increased, the velocity and acceleration of comb rods increased, and the collision effect between fruits increased. This phenomenon resulted in the increase in damage rate. When the feeding speed was increased properly, the fruit accumulation on the comb rod surface, the extrusion effect between fruits, and the damage of fruits could be reduced. However, if the feeding speed was too high, then the feeding amount would be large. The fruits would also accumulate at the joint of the root of comb rods and would thus block the comb rods. Ultimately, the damage rate would increase.

The interaction of feeding speed and comb swing angle significantly affected the damage rate ($P < 0.05$). When the rotation speed was at 0 level ($X_1 = 12.5$ r/min), the damage rate initially decreased before increasing with the increase in feeding speed and comb swing angle, as shown in Fig. 8c. The swing of the comb surface caused by the swing angle was conducive to the fruit movement.

This situation decreased the accumulation of fruits on the comb surface and avoided the damage of fruits stuck in the clearance of comb rods. Accordingly, the damage rate decreased. However, the excessive comb swing angle increased the velocity and acceleration of comb rods simultaneously. The collision effect of the comb rods on the fruits increased, which resulted in the increase in the damage rate. This finding was consistent with the results of the dynamic analysis and simulation.

Parameter optimization and validation

This work aimed to achieve high fruit removal and low damage rates to ensure enhanced performance of the eccentric swing combing device. The numerical optimization module in Design Expert software was used to solve the optimization problem. The objective function and constraints were as follows:

$$\begin{cases} X_1 \in [-1,1] \\ X_2 \in [-1,1] \\ X_3 \in [-1,1] \\ \max Y_1 \\ \min Y_2 \end{cases} \quad (10)$$

After optimization, the optimum combination of parameters was obtained as follows: rotation speed of 11.26 r/min, feeding speed of 0.227 mm/s, and comb swing angle of 5.185°. The predicted value of the fruit removal rate was 94.01%, and the damage rate was 4.38%.

The validation test was performed on the eccentric swing combing device with the following parameter combination: rotation speed of 11.26 r/min, feeding speed of 0.227 mm/s and comb swing angle of 5°. The experiment was repeated five times to obtain the average value, as shown in Table 6. The results showed that the fruit removal rate was 95.21%, and the relative error with the predicted result was 1.28%. The damage rate was 4.56%, and the relative error with the predicted result was 4.20%. These values were consistent with the result of optimization parameters and meet the operation requirements of *C. humilis* combing.

Verification result

Table 6

Test number	Rotation speed (r·min ⁻¹)	Feeding speed (m·s ⁻¹)	Comb swing angle / (°)	Fruit removal rate / %			Damage rate / %		
				Predictive value/ %	Actual value/ %	Relative error/ %	Predictive value/ %	Actual value/ %	Relative error/ %
1	11.26	0.227	5	94.01	96.28	1.28	4.38	4.73	4.20
2					96.53			3.98	
3					93.76			4.91	
4					95.45			4.77	
5					94.04			4.43	

CONCLUSIONS

(1) An eccentric swing combing device of *C. humilis* was designed. This device adopted a swing mechanism to feed the comb rods from the root of *C. humilis* plant and an eccentric mechanism to realize horizontal combing of *C. humilis* for improving the combing effect.

(2) The kinematic equation of the combing device and the main affecting factors of the combing effect were obtained through the kinematic and dynamic analyses of the combing device. The times that the *C. humilis* plants were combed was calculated by simulation analysis of the absolute movement track of the comb rod combined with the inclusion–exclusion principle, and the influence rule of each factor on the combing effect was obtained.

(3) The bench tests showed that the contribution rate of the test factors to the fruit removal and damage rates was in the order of feeding speed, rotation speed, and comb swing angle. The best working parameter combination of the device was as follows: rotation speed of 11.26 r/min, feeding speed of 0.227 m/s, and comb swing angle of 5°. Under this condition, the fruit removal rate was 95.21%, and the damage rate was 4.56%. These findings were consistent with the results of the optimized parameters and meet the operation requirement of the *C. humilis* combing. This work provides a reference for the further design of *C. humilis* harvesting machinery.

ACKNOWLEDGEMENTS

This research titled 'Parameter optimization and experiment on the combing of *Cerasus humilis*' was funded by the Key Research and Development Plan of Shanxi Province, China (201703D221029-1).

The authors are grateful and honoured to have obtained support from the Laboratory of Key Technology and Equipment for Dry Farming Machinery.

REFERENCES

- [1] Chao Li, Jiejie Xing, Liming Xu, et al., (2017), Design and experiment of wine grape trellis traveling stripping platform, *Transactions of the Chinese Society for Agricultural Machinery*, Vol.48, issue 2, pp.98–103, Beijing / P.R.C.
- [2] Du Chen, Xiaoqiang Du, Shumao Wang, et al., (2011), Mechanism of vibratory fruit harvest and review of current advance, *Transactions of the Chinese Society of Agricultural Engineering (Transactions of the CSAE)*, Vol.27, issue 8, pp.195–200, Beijing / P.R.C.
- [3] Hong Chang, Yanping Lan, Jiahua Zhou, et al., (2011), Isolation and Identification of Anthocyanins in the Fruits of *Prunus humilis* Bunge, *Food Science*, Vol.32, issue 9, pp.59–63, Ontario / Canada. Peterson D.L., Wolford S.D., Timm E.J., et al., (1997), Fresh market quality blueberry harvester, *Transactions of the ASAE*, Vol.40, Issue 3, pp.535–540, MI / U.S.A.
- [4] Coppock G.E., Donhaiser J.R., (1981), Conical scan air shaker for removing citrus fruit, *Transactions of the ASAE*, Vol.24, issue 6, pp.1456–1458, MI / U.S.A.
- [5] Haifeng Liu, Junlin He, Junjie Min, et al., (2013), Experimental study on technical parameters of *Cerasus Humilis* picking device, *Journal of Shanxi Agricultural University (Natural Science Edition)*, Vol.33, issue 4, pp.342–345, Jinzhong / P.R.C.
- [6] Junjie Du, Huaiyi Yang, Qin Cao, et al., (1992), Studies on the bionomics of Chinese dwarf cherry, *Journal of Shanxi Agricultural University (Natural Science Edition)*, Vol.12, issue 4, pp.311–314, Jinzhong / P.R.C.
- [7] Sanders K.F., (2005), Orange harvesting systems review, *Biosystems Engineering*, Vol.90, issue 2, pp.115–125, England / UK.
- [8] Weijing Zhou, Zhida Sun, Bijun Xie, et al., (2009), Technology optimization for extracting procyanidins from litchi pericarp, *Transactions of the Chinese Society of Agricultural Engineering (Transactions of the CSAE)*, Vol.25, issue S1, pp.175–179, Beijing / P.R.C.
- [9] Wei Zhang, Xiaobin Du, Junlin He, et al., (2018), Simulation analysis and experiment of combing pluck of *Cerasus humilis*, *Agriculture Engineering*, Vol.8, issue 5, pp.89–94, Beijing / P.R.C.
- [10] Whitney J.D, Patterson J.M., (1972), Development of a citrus removal device using oscillating forced air, *Transactions of the ASAE*, Vol.15, issue 5, pp.849–855, MI / U.S.A.
- [11] Xiaobin Du, Junlin He, Yongqiang He, et al., (2019), Parameter optimisation and experiment on the combing of *Cerasus humilis*, *INMATEH-Agricultural Engineering*, Vol.57, issue 1, pp.103–114, Bucharest / Romania.
- [12] Yang Xiang, Xiwen Luo, Shan Zeng et al., (2015), Operation performance analysis of reciprocating cutter based on visual programming, *Transactions of the Chinese Society of Agricultural Engineering (Transactions of the CSAE)*, Vol.31, issue 18, pp.11–16, Beijing / P.R.C.
- [13] Yinyan Shi, Man Chen, Xiaochan Wang, et al., (2017), Dynamic simulation and experiments on *Artemisia selengensis* orderly harvester cutter, *Transactions of the Chinese Society for Agricultural Machinery*, Vol.48, issue 2, pp.110–116, Beijing / P.R.C.
- [14] Yongqiang He, Junlin He, Xiaobin Du et al., (2018), Design and experimental study of the finger-type lifter test bench for *Cerasus humilis* branches, *INMATEH- Agricultural Engineering*, Vol.56, issue 3, pp.147–154, Bucharest / Romania.
- [15] Yongqiang He, Junlin He, Dawei Fang, et al., (2019), Experimental design and evaluation of the finger-type lifter bench for *Cerasus humilis* branches, *Journal of Shanxi Agricultural University (Natural Science Edition)*, Vol.39, issue.2, pp.105–112, Jinzhong / P.R.C.
- [16] Yongqiang He, Junlin He, Dawei Fang, et al., (2019), Collision injury assessment of mechanical harvesting *Cerasus humilis* fruit based on deformation energy, *Agriculture Engineering*, Vol.9, issue 3, pp.67–72, Beijing / P.R.C.
- [17] Zhibin Sun, Junlin He, Junjie Du, et al., (2016), Experiment on physical parameter and biomechanical properties of *Cerasus humilis* 5. *Agriculture Engineering*, Vol.6, Issue 2, pp. 1–4, Beijing / P.R.C.
- [18] Zhilong Zhang, Dongxing Zhang, Tao Cui, et al., (2014), Design and experiment of corn stripping monomer mechanism, *Transactions of the Chinese Society of Agricultural Engineering (Transactions of the CSAE)*, Vol.30, issue 20, pp.1–9, Beijing / P.R.C.

EXPERIMENTAL INVESTIGATION OF BIONIC SOIL-ENGAGING BLADES FOR SOIL ADHESION REDUCTION BY SIMULATING ARMADILLIDIUM VULGARE BODY SURFACE

بررسی تجربی تیغه‌های خاک‌ورز بایونیک به منظور کاهش چسبندگی خاک با شبیه‌سازی سطح بدن ARMADILLIDIUM VULGARE

Jafar Massah ^{*1)}, Fatemeh Hassanpour Roubeneh ²⁾, Zeinab Hassanpour Roubeneh ³⁾, Keyvan Asefpour Vakilian ¹⁾ ¹

¹⁾ Department of Agrotechnology, College of Abouraihan, University of Tehran, Tehran, Iran

²⁾ Department of Mechanical Engineering, Tarbiat Modares University, Tehran, Iran

³⁾ National Institute of Genetic Engineering and Biotechnology (NIGEB), Tehran, Iran

Tel: +982 136041058; E-mail: jmassah@ut.ac.ir

DOI: <https://doi.org/10.35633/inmateh-60-11>

Keywords: soil adhesion, bionic blades, energy consumption, drag force

ABSTRACT

Soil adhesion is a physical phenomenon which results in undesirable effects including increment in drag force and energy consumption of cutting or tillage tools. One method to reduce the soil adhesion is biomimetics, i.e., focusing on the technique soil-burrowing animals' benefit. In this study, three types of blade were designed and built: flat blade, corrugated blade and a combination of flat and corrugated blades. The corrugated blade was simulated from *Armadillidium vulgare* body surface geometrical shape. Experimental results showed that in dry soil, flat and corrugated blades required similar drag force while the combined blade showed higher drag force requirements. In wet soil, the corrugated blade resulted in the lowest drag force, which was due to faster movement of soil layer on the blade surface. Drag force of the corrugated blade was lower than the half of the drag force of two other blades at travel speed of 0.04 m/s. Besides, the drag force of corrugated blade decreased by increasing the blade travel speed. Furthermore, in wet soil, the energy consumption of the corrugated blade at the travel speeds of 0.02 and 0.04 m/s was 66% and 83% lower than the flat blade, respectively.

ABSTRACT

چسبندگی خاک یک پدیده فیزیکی است که منجر به اثرات نامطلوب از جمله افزایش نیروی کششی و مصرف انرژی ابزار برش یا خاک‌ورز می‌شود. یکی از روش‌های کاهش چسبندگی خاک، بایومیمتیک است، یعنی تمرکز بر روی تکنیکی که حیوانات حرکت‌کننده در خاک از آن بهره می‌گیرند. در این مطالعه سه نوع تیغه طراحی و ساخته شد: تیغه مسطح، تیغه کنگره‌ای و ترکیبی از این دو تیغه. تیغه کنگره‌ای از شکل هندسی سطح بدن *Armadillidium vulgare* شبیه‌سازی شد. نتایج آزمایشات تجربی نشان داد که در خاک خشک، تیغه‌های مسطح و کنگره‌ای نیاز به نیروی کششی مشابه دارند، در حالی که تیغه ترکیبی نیروی کشش مورد نیاز بیشتری را نشان داد. در خاک مرطوب، تیغه کنگره‌ای منجر به کمترین نیروی کششی شد که دلیل آن، حرکت سریع‌تر لایه خاک بر روی سطح تیغه بود. نیروی کشش تیغه کنگره‌ای کمتر از نیمی از نیروی کششی دو تیغه دیگر در سرعت پیشروی 0/04 متر بر ثانیه بود. علاوه بر این، با افزایش سرعت پیشروی تیغه، نیروی کششی تیغه کنگره‌ای کاهش یافت. همچنین، در خاک مرطوب، مصرف انرژی تیغه کنگره‌ای در سرعت‌های پیشروی 0/02 و 0/04 متر در ثانیه به ترتیب 66٪ و 83٪ کمتر از تیغه مسطح بود.

INTRODUCTION

The phenomenon of soil adhesion takes place frequently when soil cutting or tillage machines interact with soil. Soil adhesion increases the working resistance and energy consumption of cutting or tillage tools and often reduces the working quality (Soni and Salokhe, 2016). Soil adhesion, working resistance and abrasive wear are the three major problems of soil-engaging tools. Wang et al. (1998) found that soil adhesion can be reduced using vibration of the machines' parts contacted with soil. Furthermore, Tong et al. (2005) described that soil adhesion can be decreased using methods such as lubrication, electro-osmosis and vibration.

¹ Massah J., Prof.; Hassanpour Roubeneh F., Ms.; Hassanpour Roubeneh Z., Ms.; Asefpour Vakilian K., Dr. Eng.

They also found that phosphorus has the ability of decreasing adhesion between two surfaces. *Zhang (1985)* analyzed the influence of moisture contents and soil bulk density on adhesive properties. The moist compressed soils are more adhesive than loose dry soils. Results demonstrated that the undisturbed soils are 2 to 3 times more adhesive than disturbed soils.

Many approaches, such as surface coating, surface shape modification, materials modification, lubrication, heating, vibration, a flexible structure, electro-osmosis and magnetization have been considered in order to decrease soil adhesion forces between soil and tool surfaces (*Ren et al., 2006; Soni et al., 2007; Saha and Celata, 2011; Sun et al., 2018*).

The problem of soil adhesion has been resolved by some soil-burrowing animals, such as the dung beetle, ant, and pangolin which make a hole or tunnel in soil (*Sun et al., 2008*).

Studies have shown that some external parts of soil-burrowing animals have geometrical rough structures, which is one of the causes why soil-burrowing animals do not stick to the soil (*Ren et al., 2002; Ren, 2009; Zhang et al., 2016*). These structures have corrugated, concave, wavy and scaly shapes etc. The size of structural parts on these rough surfaces differs from 0.075 to 0.20 mm, and they are useful for the reduction of adhesion and surface frictional shear resistance against soil. The rough shapes on soil-burrowing animals' body surfaces were analyzed by scanning electron-microscopy and visual stereomicroscopy (*Qian et al., 1999; Cheng et al., 2002*).

As a pioneering research, *Qian and Zhang (1984)* reported that the energy consumed by adhesion and friction between soil and tillage implements is 30-50% of the gross energy required for the tillage procedure. The surface structures of the soil-engaging implements play an important role in decreasing soil adhesion and friction (*Zhu et al., 1992*). *Salokhe and Gee-Clough (1989)* studied decreasing adhesion by coating lug surfaces with different materials containing silicon lubricant oil, lead oxide paint, gloss paint and varnish, chromium painting, Teflon tape, Teflon sheet, ceramic tile and enamel coating. They showed that lug coating can reduce soil adhesion noticeably. However, there were practical problems such as cost and low durability in using silicon lubricant oil, Teflon tape, ceramic tile and enamel coating.

Chen et al. (1990) reported that soil animals prevent adhesion of soil to their bodies because of their exterior structure, presence of anti-adhesive parts and biological electrical system in their body surfaces, and secretion of some special substances. *Ren et al. (2001)* demonstrated that bodies of soil animals have low soil adhesion resistance because of the evolution of their biological systems.

Zu et al. (2006) showed that earthworms decrease adhesion of soil to their bodies due to electro-osmotic flow of lubricating fluid at the body and soil interface. *Gao et al. (2010)* reviewed some of these methods useful in adhesion preventing mechanism related to soil animals on the surfaces of soil engaging parts of various devices.

In this paper, several blades for use in soil tillage implements were made by modeling the body surface of a soil-animal called *Armadillidium vulgare* (the common pill bug). Then, the effects of these blades on drag force of simulated surfaces were investigated. The objective of this research is to reduce soil adhesion of soil tillage implements such as ditcher machines and bulldozers using the simulation of geometric shape of organism body, which can result in a reduction in energy consumption.

SOIL-BURROWING ANIMALS AND BIONIC TILLAGE TOOLS

Human being has benefited the nature not only as the source of life but also as a model to improve living conditions. This improvement was done by paying attention to surrounding living world consisting of plants and animals. A group of animals which can be considered as living models to improve lifestyle are soil-burrowing animals. These animals prepare the soil for plant growth by their movements (*Wang et al., 2018*).

These characteristics of soil organisms make them a suitable pattern for designing and manufacturing soil preparation tools in agriculture and industry.

The simulation of the pattern of soil organisms' geometrics would result in tremendous innovation in the field of soil preparation tool (*Zhang et al., 2017; Li et al., 2019*).

During the evolution, the body surface structure of soil-burrowing animals has been mutated to adapt to their environment.

The surface morphology features related to a kind of *Armadillidiidae* family called *Armadillidium vulgare* – the common pill bug is investigated in this study as a method to reduce soil adhesion (Fig. 1).

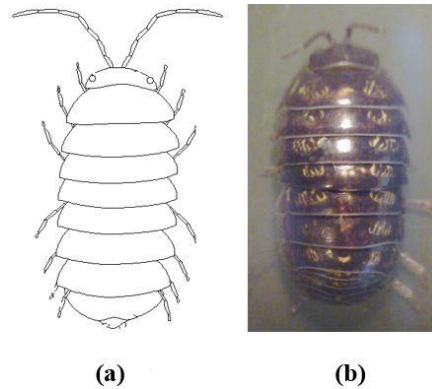


Fig. 1 - The *Armadillidium vulgare* body surface, (a) schematic image, (b) real image

Armadillidiidae is a family of woodlice, also known by many common names is an isopod crustacean. *Armadillidium vulgare* may reach a length of 18 mm and is capable of rolling into a ball when disturbed; this ability, along with its general appearance, gives it the name pill bug. Fig. 1 depicts a schematic of this organism's body surface. As seen in Fig. 1, pill bug has a laminated body which help it to burrow in soil. The laminated body of pill bug was simulated to construct soil preparation tool.

MATERIAL AND METHODS

Construction of the simulated blades

After studying the shape of soil-burrowing bodies and their ability of soil tunnelling, the pill bug *Armadillidium vulgare* was selected for simulation and construction of an efficient tillage blade. To study the shape of the soil-engaging blades, three types of blade were designed and built namely flat blade, corrugated blade and a combination of flat and corrugated blades (Fig. 2). The corrugated blade was simulated from *Armadillidium vulgare* body surface geometrical shape. All the three blades had a dimension of 100×308 mm² and the corrugated and combined blades had bumps with a diameter of 22 mm and a length of 100 mm. The number of these bumps was 7 and 14 in combined and corrugated blades, respectively. The weight of corrugated blade was 24% and 48% more than that of combined and flat blades, respectively.

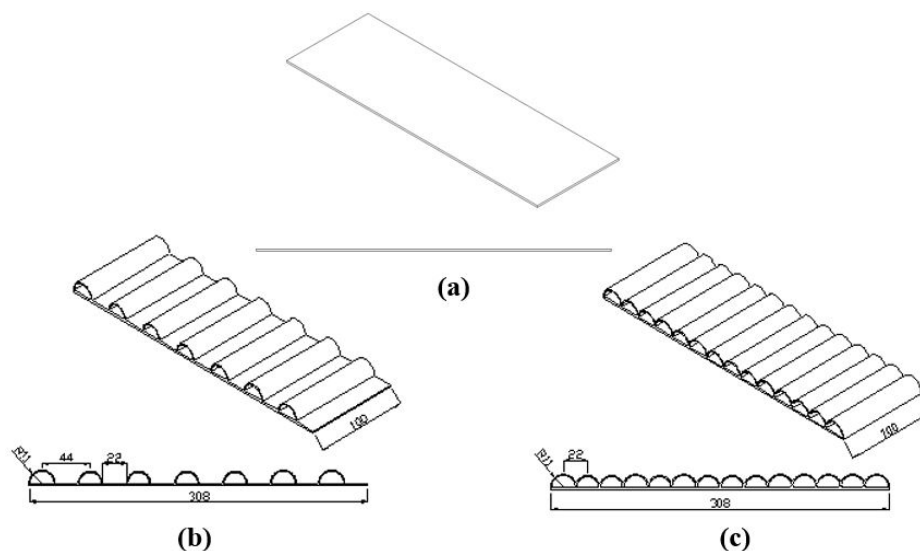


Fig. 2 - The designed blades, (a) flat blade, (b) combined blade and (c) corrugated blade

After the blade modeling by SolidWorks software, distributed force was applied by soil to the blades (Fig. 3). The amount of distributed loading was considered as 15 N/cm^2 . The bending resistance of the corrugated and combined blades under distributed loading were equal and 25% more than the flat blade, respectively.

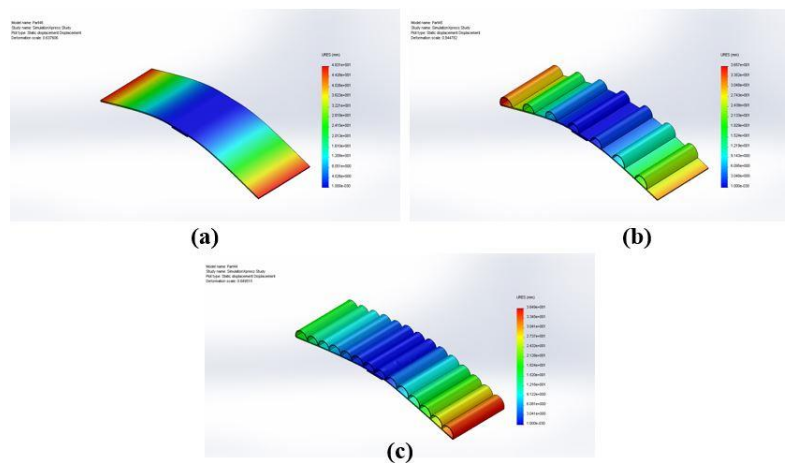


Fig. 3 - Stress distribution in the blades obtained by SolidWorks software, (a) flat blade, (b) combined blade, and (c) corrugated blade

Experiment equipment

Experiments were conducted at the Laboratory of Soil Dynamics, College of Abouraihan, University of Tehran using a soil bin (Fig. 4). As seen in this figure, the soil bin contained five main parts: bin, carriage, power transmission unit, soil processing unit and control unit.

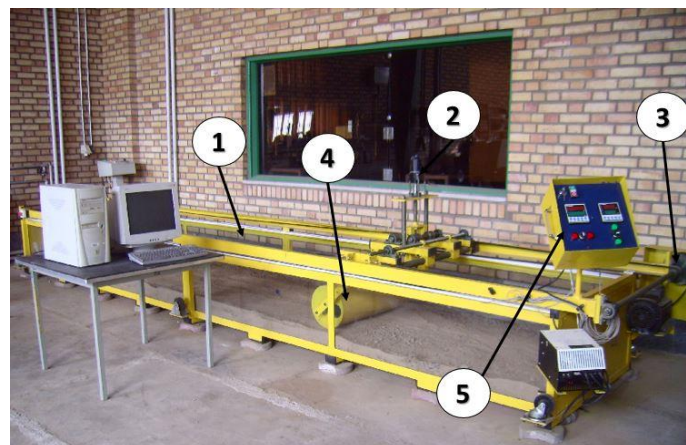


Fig. 4 - The soil bin used in this study

Part 1: The soil bin operative dimensions were: length - 6 m, width - 1 m and height - 0.5 m and filled up by soil to a depth of 0.3 m.

Part 2: The moving carriage had an overall dimension of 0.9 m wide and 0.5 m in high, with total weight of 50 kgf. The rails supported the carriage by four rigid wheels installed at four corners of the carriage.

Part 3: The power transmission unit consisted of two electromotors. A 2 kW 380V- AC electromotor moved the carriage along with the tool-tester through the length of soil bin using chain system, and a 1.5 kW 24V- DC electromotor moved an inner frame of carriage at vertical direction.

Part 4: The soil processing unit included one roller to compact the soil. The soil in the tank was manually prepared for each experiment.

Part 5: A control unit was used to control the direction and travel speed of carriage movement as well as the soil processing roller.

Experiment conditions

Two types of soil were used in the experiments, dry soil and wet soil with 34.3g (100g)^{-1} moisture content (Fig. 5). The soil was classified as a loam, with a texture analysis of 24.6% clay, 40.8% silt and 34.6% sand. After filling the soil tank by dry soil and carrying out the required experiments on dry soil, the wet soil was prepared by adding water to obtain desirable wet soil. Then, the wet soil surface was coated by a nylon cover for 24 h to homogenize the soil moisture.



Fig. 5 - Two types of soil; (a) dry soil, and (b) wet soil.

To conduct the experiments, the blades traversed a distance of 1.5 meters in each soil type with a minimum depth of 150 mm at three speed levels (0.01, 0.02 and 0.04 m/s) similar to the travel speed of a soil-burrowing animal in soil. The experiments were carried out with three replications.

Throughout the procedure, the interface received the analog signals from the S-shape load cell. Then, the signals were transferred to the monitoring software in a computer to record the force–time graph for each experiment. The control software was developed using a graphical user interface (GUI) in Microsoft Visual C. The control system software acquired the output data from the interface and produced a force-displacement graph based on the data for further analysis.

RESULTS AND DISCUSSION

Performance of the simulated surfaces in dry soil

Comparison of Fig. 6 and Fig. 7 shows the flat surface in wet soil required more drag force than dry soil. To reduce the surface drag force in wet soil, the body surface of *Armadillidium vulgare* was modeled as two types of blade: corrugated and combined blades.

The force-time curves at three travel speeds of 0.01, 0.02 and 0.04 m/s are drawn for each type of the blades in Fig. 6. As seen in the figure, flat and corrugated blades had almost the same performance in drag force, but the curves belonging to combined blade showed an irregularity in drag force. The reason of this irregularity may be the soil pass from non-uniform surface.

As shown in Fig. 6, in dry soil, the drag force of combined blade was higher than that of the other blades by increasing the travel speed which could result from its uneven surface. The combined blade consisted of semi-circular bumps and smooth surfaces among them (Fig. 2) and this alternative surface geometry shape caused the non-monotonic movement of soil layer on blade surface.

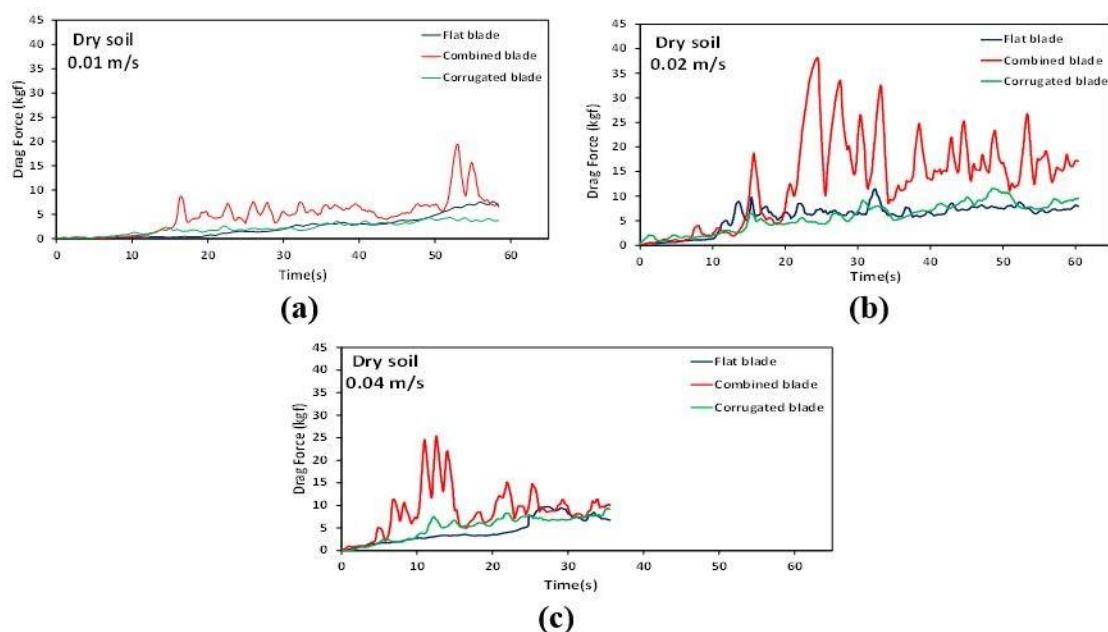


Fig. 6 - The drag force-time curves of the blades in dry soil at three travel speed of (a) 0.01, (b) 0.02, and (c) 0.04 m/s

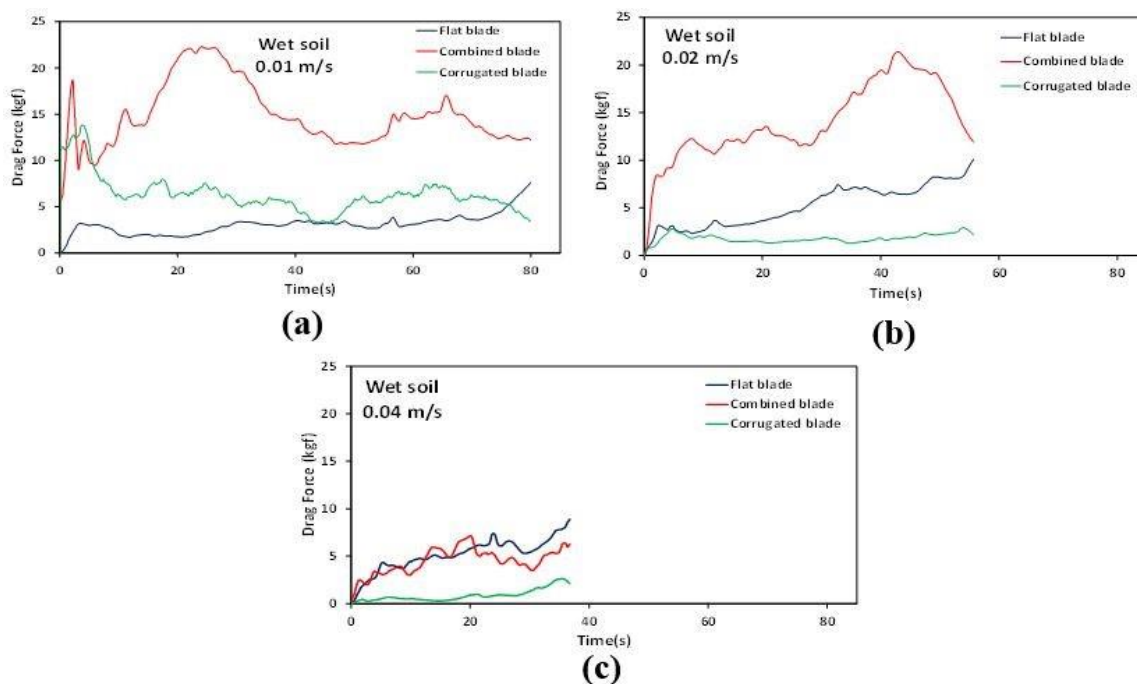


Fig. 7 - The drag force-time curves of the blades in wet soil at three travel speed of (a) 0.01, (b) 0.02, and (c) 0.04 m/s

Performance of the simulated surfaces in wet soil

As can be seen in Fig. 7(a), drag force belonging to the combined, corrugated and flat blades had decreasing trend, respectively. As shown in Figs. 7(b) and 7(c), the corrugated blade had the lowest drag force, which was due to faster movement of soil layer on corrugated blade surface. So, the soil layer could not be inserted into the grooves between the bumps, and it was only in contact with the outer surface of bumps. This event reduced the contact surface of soil layer with the metal surface and therefore decreased the soil adhesion to metal. This finding can be used in construction of the off-road vehicles side surfaces.

As illustrated in Fig. 7, in wet soil, the combined blade had the most drag force at travel speeds of 0.01 and 0.02 m/s, which resulted from the non-uniform surface shape of this blade. However, at travel speed of 0.04 m/s, the drag force of combined blade was similar to flat blade. It was found from Fig. 7 that the drag force of corrugated blade decreased by increasing the travel speed, for example; the drag force of corrugated blade was lower than those of the two other blades at travel speed of 0.04 m/s (1/3 less than others). These findings about reducing the drag force are in good agreement with the results of *Ren et al. (2006)* who investigated soil adhesion on a soil-burrowing animal.

Energy consumption of the simulated surfaces in dry and wet soils

The energy consumption for the blades was calculated using the area below the drag force-time curve at three constant travel speeds (0.01, 0.02 and 0.04 m/s) which is shown in Figs. 8 and 9 for dry and wet soils, respectively.

As shown in Fig. 8, the corrugated blade had a proper performance compared to other blades at the travel speed of 0.01 m/s. However, at the travel speed of 0.02 m/s, the corrugated blade performance was similar to the flat blade, and at the travel speed of 0.04 m/s it had a poor performance compared to the flat blade. The combined blade had a poorer performance than the others at all three travel speeds, which can be due to non-uniform motion of the soil on this blade.

Fig. 9 shows the energy consumption of blades in wet soil. Obviously, the corrugated blade had a favourable performance in reducing the energy consumption compared to the flat and combined blades. It is notable that the energy consumption of corrugated blade decreases in wet soil. The energy consumption ratio of this blade at 0.04 m/s was about a quarter lower than its rate at 0.01 m/s, which could be attributed to a more fluid motion of the soil at higher travel speeds on the corrugated blade. This indicates that the outer surface of *Armadillidium vulgare* is compatible with its living environment, which is mostly wet soil.

Therefore, using the corrugated blade in cutting or tillage tools in contact with wet soil will not only increase their strength, but also significantly reduce energy consumption.

Although the combined blade had a poor performance compared to the other blades at the travel speed of 0.01 and 0.02 m/s; it had a good performance in reducing the energy consumption compared to the flat blade at the travel speed of 0.04 m/s. The poor performance of the combined blade may be due to non-uniform motion of the soil on this blade causing the soil to move with more resistance.

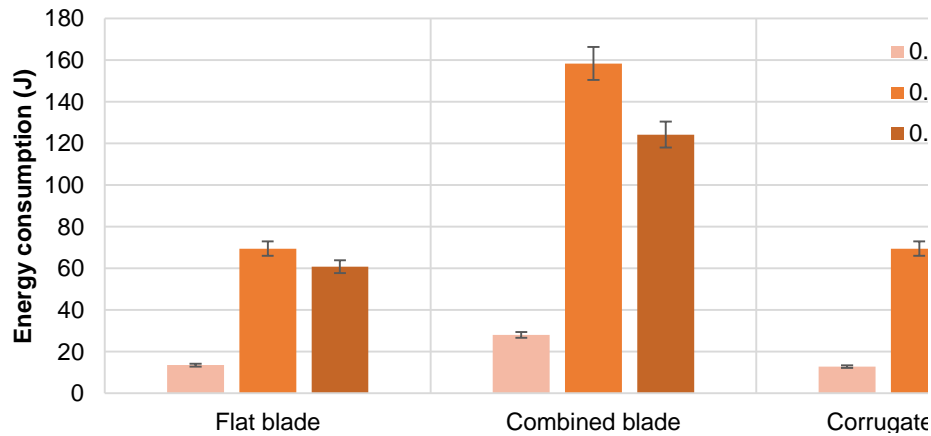


Fig. 8 - The energy consumption of the blades in dry soil.

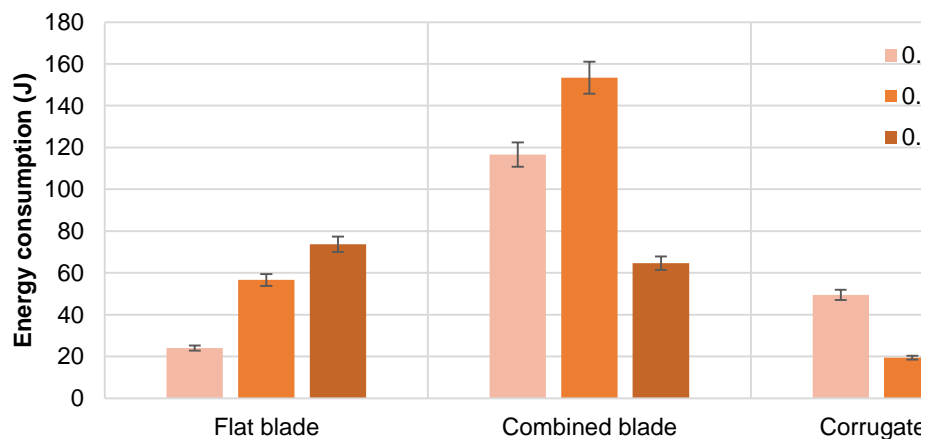


Fig. 9 - The energy consumption of the blades in wet soil

CONCLUSIONS

In this research, it has been tried to design and construct a blade for utilizing in soil tillage implements such as the ditcher machine and bulldozer using the simulation of geometric shape of *Armadillidium vulgare* surface body (corrugated blade). The drag force of this blade was compared with the flat and combined blades. Results showed that the corrugated blade had better performance in wet soil and its drag force was lower than two other blades' drag force. The energy consumption of the corrugated blade at the travel speed of 0.02 and 0.04 m/s in wet soil was 66% and 83% lower than the flat blade, respectively. This simulated blade with such desirable characteristics can be used in agricultural machines and construction equipment, which can result in a decrease in drag force and energy consumption.

REFERENCES

- [1] Chen B.C., Ren L.Q., Cui X.X., Wang Y.M., (1990). Preliminary research on reducing soil adhesion and resistance of claw shapes of typical soil animals. *Proceedings of the international agricultural engineering conference and exhibition*, Bangkok, Thailand. pp. 309-315.
- [2] Cheng H., Sun J., Li J., Ren L., (2002). Structure of the integumentary surface of the dung beetle *Copris ochus* Motschulsky and its relation to non-adherence of substrate particles. *Kun chong xue bao. Acta Entomologica Sinica*, Vol.45, Issue 2, pp. 175-181.

- [3] Gao F., Baraka-Kamali E., Shirtcliffe N., Terrell-Nield C., (2010). A preliminary study of the surface properties of earthworms and their relations to non-stain behaviour. *Journal of Bionic Engineering*, Vol.7, Issue 1, pp. 13-18.
- [4] Li B., Wang X., Xia R., Yang Z., Liu Y., Li T., (2019). Research on the bionic design of the middle trough of a scraper conveyor based on the finite element method. *Proceedings of the Institution of Mechanical Engineers, Part C: Journal of Mechanical Engineering Science*, Vol.233, Issue 9, pp. 3286-3301.
- [5] Qian C., Luquan R., Bingcong C., Beizhan Y., (1999). Using characteristics of burrowing animals to reduce soil-tool adhesion. *Transactions of the ASAE*, Vol.42, Issue 6, pp. 1549.
- [6] Qian D.H., Zhang J.X., (1984). Research on adhesion and friction of soil against metallic materials. *Acta Agromecanica*, Vol.15, Issue 1, pp. 70-78.
- [7] Ren L., (2009). Progress in the bionic study on anti-adhesion and resistance reduction of terrain machines. *Science in China Series E-Technological Sciences*, Vol.52, Issue 2, pp. 273-284.
- [8] Ren L.Q., Tong J., Li J.Q., Chen, B.C., (2001). SW—soil and water: soil adhesion and biomimetics of soil-engaging components: a review. *Journal of Agricultural Engineering Research*, Vol.79, Issue 3, pp. 239-263.
- [9] Ren L., Han Z., Li J., Tong J., (2002). Effects of non-smooth characteristics on bionic bulldozer blades in resistance reduction against soil. *Journal of Terramechanics*, Vol.39, Issue 4, pp. 221-230.
- [10] Ren L.Q., Han Z.W., Li J.Q., Tong J., (2006). Experimental investigation of bionic rough curved soil cutting blade surface to reduce soil adhesion and friction. *Soil and Tillage Research*, Vol.85, Issue 1-2, pp. 1-12.
- [11] Saha S.K., Celata, G.P., (2011). Advances in modelling of biomimetic fluid flow at different scales. *Nanoscale Research Letters*, Vol.6, Issue 1, pp. 344.
- [12] Salokhe, V.M., Gee-Clough, D., (1989). Technology showcase applications of enamel coating in agriculture. *Journal of Terramechanics*, Vol.26, Issue 3-4, pp. 275-286.
- [13] Soni, P., Salokhe V.M., (2016). Bio-Inspired Macro-Morphologic Surface Modifications to Reduce Soil–Tool Adhesion. In: Yuehao L., Yin-kwee N.E. (eds.). *Bio-Inspired Surfaces and Applications*. UK: World Scientific Publishing. pp. 421-484.
- [14] Soni P., Salokhe V.M., Nakashima H. (2007). Modification of a mouldboard plough surface using arrays of polyethylene protuberances. *Journal of Terramechanics*, Vol.44, Issue 6, pp. 411-422.
- [15] Sun J.Y., Tong J., Ma Y.H., (2008). Nanomechanical behaviours of cuticle of three kinds of beetle. *Journal of Bionic Engineering*, Vol.5, pp. 152–157.
- [16] Sun J., Wang Y., Ma Y., Tong J., Zhang Z., (2018). DEM simulation of bionic subsoilers (tillage depth > 40 cm) with drag reduction and lower soil disturbance characteristics. *Advances in Engineering Software*, Vol.119, pp. 30-37.
- [17] Tong J., Sun J., Chen D., Zhang S., (2005). Geometrical features and wettability of dung beetles and potential biomimetic engineering applications in tillage implements. *Soil and Tillage Research*, Vol.80, Issue 1-2, pp. 1-12.
- [18] Wang X.L., Ito N., Kito K., Garcia P.P., (1998). Study on use of vibration to reduce soil adhesion1. *Journal of Terramechanics*, Vol.35, Issue 2, pp. 87-101.
- [19] Wang P., Ni H., Wang R., (2018). A new drilling method—Earthworm-like vibration drilling. *PLoS one*, Vol.13, Issue 4, e0194582.
- [20] Zhang J.G., (1985). Studies on the adhesion and friction of soil to solid materials, Doctoral dissertation, Ph.D. Dissertation, Jiangsu Technical College, China.
- [21] Zhang D., Chen Y., Ma Y., Guo L., Sun J., Tong J., (2016). Earthworm epidermal mucus: Rheological behaviour reveals drag-reducing characteristics in soil. *Soil and Tillage Research*, Vol.158, pp. 57–66.
- [22] Zhang Z., Shao F., Liang Y., Lin P., Tong X., Ren L., (2017). Wear Behaviour of Medium Carbon Steel with Biomimetic Surface Under Starved Lubricated Conditions. *Journal of Materials Engineering and Performance*, Vol. 26, Issue 7, pp. 3420-3430.
- [23] Zhu H., Tan L., Wu S., (1992). An experimental study on the “comet-type passage-holes” plough of reducing resistance. *Transactions of the Chinese Society for Agricultural Machinery*, Vol.23, Issue 4, pp. 20.
- [24] Zu Y.Q., Yan Y.Y., (2006). Numerical simulation of electro-osmotic flow near earthworm surface. *Journal of Bionic Engineering*, Vol.3, pp. 179–186.

JUSTIFICATION OF DESIGN AND TECHNOLOGICAL PARAMETERS OF THE ONION HARVESTER BED-SHAPING ROLLER SPIRAL DRUM

ОБОСНОВАНИЕ КОНСТРУКТИВНЫХ И ТЕХНОЛОГИЧЕСКИХ ПАРАМЕТРОВ СПИРАЛЬНОГО ВАЛЬЦА КАТКА-ЛОЖЕОБРАЗОВАТЕЛЯ МАШИНЫ ДЛЯ УБОРКИ ЛУКА

Dorokhov A.S., Aksenov A.G., Sibirev A.V., Sazonov N.V. ¹

FSBSI "Federal Scientific Agronomic and Engineering Centre VIM" / Russian

Telephone: 89645843518; E-mail: sibirev2011@yandex.ru

DOI: <https://doi.org/10.35633/inmateh-60-12>

Keywords: onion sets, cleaning, repair work, finishing working bodies, design and technological parameters, roller-forming agent

ABSTRACT

One feature of harvesting seed onions is that the impurities of the onion-soil pile coming from the digging executive devices to the separating executive devices contain soil lumps that are similar in size with the seed onion bulbs and hard to separate at the slotted (bar elevators, screens) executive devices (M. Tauseef Asghar, 2014). This problem is most urgent when collecting seed onions from the rolls, because together with the bulbs the separating executive devices receive the soil layer loosened by the digging executive devices during the first phase of harvesting seed onions, the fractional composition core of which is soil lumps similar to bulbs and hardly separable on slotted executive devices. This circumstance is explained by the fact that after the soil layer is undercut together with the saleable produce, a significant amount of soil lumps, hardly separable on the separating executive devices and causing damage to root crops and bulbs during their interaction, arrives to the separating executive device. In addition, separation of soil lumps on slotted executive devices (bar conveyors and screens) occurs according to dimensional properties and this does not solve the existing problem – separation of soil lumps comparable in size with seed onion bulbs. Consequently, to ensure qualitative indicators of harvesting seed onions, namely, the separation completeness of the bulbs from soil impurities, it is necessary to ensure a reduction or complete elimination of the flow of soil lumps to the separating executive devices at the second harvesting phase.

РЕЗЮМЕ

Особенностью уборки лука-севка является то, что состав примесей луко-почвенного вороха, поступающего с выкапывающих на сепарирующие рабочие органы, составляют почвенные комки, соизмеримые по размерам с луковицами лука-севка, которые являются трудноотделимыми на щелевых (прутковые элеваторы, грохоты) рабочих органах. Данная проблема является наиболее актуальной при подборе лука-севка из валков, так как совместно с луковицами на сепарирующие рабочие органы поступает почвенный слой, взрыхленный подкапывающими рабочими органами в первой фазе уборки лука-севка, основу фракционного состава которого составляют почвенные комки соизмеримые с луковицами и являющиеся трудноотделимыми на щелевых рабочих органах. Данное обстоятельство объясняется тем, что после подкапывания пласта почвы совместно с товарной продукцией, на сепарирующие рабочие органы поступает значительное количество почвенных комков, которые являются трудноотделимыми на сепарирующих рабочих органах и приводят к повреждению корнеплодов и луковиц при их взаимодействии. Кроме того, выделение почвенных комков на щелевых рабочих органах (прутковые транспортеры и грохоты) происходит по размерным признакам и это не приводит к решению существующей проблемы – сепарации почвенных комков, соизмеримых по размерам с луковицами лука-севка. Следовательно, для обеспечения качественных показателей уборки лука-севка, а именно – полноты отделения луковиц от почвенных примесей необходимо обеспечить снижение или полнейшее исключение поступления на сепарирующие рабочие органы почвенных комков во второй фазе уборки, что и интенсифицирует предлагаемый каток-ложеобразователь машины для уборки лука.

¹ Dorokhov. A.S., Prof. PhD. Eng.Sc.; Aksenov A.G., PhD. Eng.Sc.; Sibirev A.V., PhD. Eng.Sc.; Sazonov N.V., Eng.Sc.

INTRODUCTION

Analysis of the current state of methods and technical means to reduce the content of soil impurities in commercial products of seed onions showed that the development of science-based technical solutions facilitating the reduction in the content of soil impurities during onion harvesting requires, first of all, additional theoretical and practical research on the effects of executive devices and factors affecting the separation completeness of soil lumps when harvesting seed onions during both the first and the second phases (Aksenov A.G., Sibirev A.V., Emelianov P.A., 2018).

Based on the technological process of harvesting seed onions, it is known that formation of a high-quality prepared bed for laying bulbs in a roll is the final operation in a complex chain of industrial production. Therefore, qualitative indicators of harvesting are determined by how well the previous process operations have been performed (Lobachevsky Ya.P., Emelyanov P.A., Aksenov A.G., Sibirev A.V., 2016). Bearing this in mind, in order to increase the efficiency of harvesting machines, the search for structural and technological solutions shall be aimed at restricting the supply of over-compacted particles by levelling the surface of a dense bed (Natenadze N., 2016).

Eventually, the next operation of harvesting seed onions, which is collection of bulbs from the rolls after post-ripening *in vivo*, depends on the quality of the prepared bed. Most onion harvesters, by foreign ("Simon", France, "Krukowiak", Poland) and domestic manufacturers of agricultural machinery, currently use passive press wheels (fig. 1) made of various materials to form the bed-forming area, and some even have none whatsoever (Lobachevsky Ya.P., Emelyanov P.A., Aksenov A.G., Sibirev A.V., 2016).



Fig. 1 – Bed-forming device of the Z-653/1 onion harvester, "Krukowiak", Poland

The roller of the onion harvester prepares the surface before laying the roll, which facilitates faster drying of the onions. The increased diameter and plastic surface ensure smooth rotation and keep wet soil from sticking.

The disadvantage of this bed-forming device is the inability to prepare an optimally flat ridge for efficient collection of seed onions, because of the insufficient functionality to level the surface of the bed being formed (Kurdyumov V.I., Zykin E.S., Lazutkina S.A., 2016).

The bed-forming device of the onion harvester manufactured by "Samon" and "IMAC" Holland, is a passive cylindrical roller with wave-shaped protrusions along the shell, in parallel with the roller axis (fig. 2).



Fig. 2 – Bed-forming device of the disk onion harvester «Samon» (A) and «IMAC» (B) (Holland)

A serious disadvantage of the known bed-forming device is that a dimple-shaped profile is formed on the surface of the created bed, where bulbs are accumulated in the indentations that formed, and when collection is performed, more soil is lifted to the separating executive devices, and more bulbs are lost, due to the inability to collect the bulbs efficiently.

There is also a known bed-forming device of a root lifter.

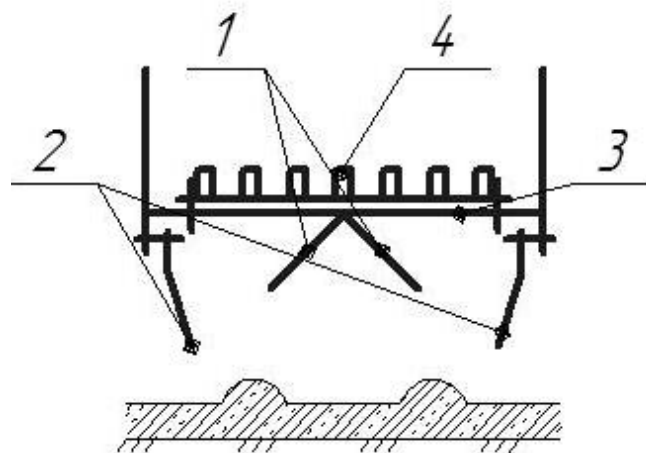


Fig. 3 – Bed-forming device:

1 – tray; 2 – deflector shields; 3 – separating device; 4 – sieves

This device (fig. 3) is made in the form of a duo-pitch tray 1 and deflector shields 2, where the top of the duo-pitch tray 2 faces the separating surface 3, with the pitches made as wedges, with tops aimed at the raising executive device, and the deflector shields are attached to the sides of the separating executive device, leaned towards one another.

The disadvantage of the said bed-forming device is the complexity and metal consumption of the structure, and the bed formed by the device contributes to the bulbs rolling away across the field and, as a consequence, increased loss when collecting the seed onions from the rolls.

MATERIALS AND METHODS

In this regard, to reduce the flow of soil lumps to the separating executive devices together with seed onion bulbs during the second harvesting phase, i.e. when collecting from the rollers, as well as to intensify separation of seed onions from comparable soil lumps, a bed-shaping roller (RF patent № 2601060) for an onion harvester has been developed, which facilitates the reduction of the flow of soil lumps to the separating executive devices during the second harvesting phase of seed onions (Aksenov A.G., Pryamov S.A., Sibirev A.V., 2016).

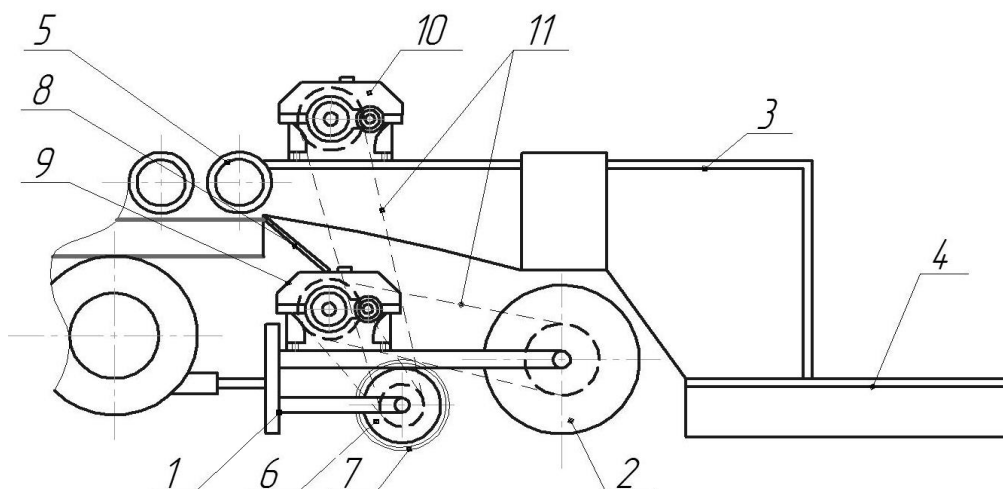


Fig. 4 – Structure diagram of an onion harvester bed-shaping roller

1 – frame; 2 – spiral drum; 3 – narrowing tray; 4 – roller shaper; 5 – roller separator; 6 – spiral drum; 7 – segment; 8 – impurity discharge tray; 9, 10 – gear units; 11 – chain transmission

A bed-shaping roller (figure 4) consists of frame 1, cylindrical drum 2, narrowing tray 3 and roller shaper 4, separating elevator 5, under which spiral drum 6 is mounted on frame 1 with a peripheral cross-section shaped along its entire length in the form of segment 7, impurity discharge tray 8, gearbox 9 and 10 adjusting the rotation speed of the rollers and chain transmission 11.

Bed-shaping roller operates as follows.

Along with progressive rotation of spiral roller 6 across the field, it compresses the soil to the optimal value with its cylindrical surface, while its protrusions located on the surface of spiral roller 6 in the form of segment 7 symmetrically relative to the transverse axis create a wavy terrain on the soil surface. Spirals 7 of roller 6 form a depression on the surface of the field, and due to the fact that the beginning and the end of each protrusion of segment 7 are on the same shaping line of spiral roller 6 and coincide with the middle of the next protrusion, the roller's movement is uniform, it does not displace the soil and produces no shock impact. Smooth cylindrical drum 2 mounted behind spiral roller 6 solidifies and forms restrictive ridges located along the edges of the harvested field surface.

Thus, the bed shaped by the bed-shaping roller prevents the bulbs from rolling away and is formed from loose, separated, fine-grained soil without compaction, which eliminates or reduces to the minimum the subsequent flow of soil lumps to the machine separating devices when collecting the bulbs from the swath, and, as a result, reduces the content of soil and plant impurities, as well as injury to the seed onions when they are collected from the rollers, by forming a bed of adjustable density for the swath, ensuring product bletting on its surface.

One of the main parameters, along with the structural composition of the lumps of soil in the onion roll, which determine the quality of the roller-bed forger of the onion harvesting machine, is the degree of loosening of the soil (*Sojka R.E., Horne D.J, Ross C.W, Baker C.J., 1997*).

An increase in the rotational speed of the rollers of the bed-forming machine leads to an increase in the peripheral speed of the spiral v_0 and cylindrical v_{CF} rollers, which positively affects the quality of soil grinding, i.e. increase the degree of soil loosening (*Farhadi R., Sakenian N., Azizi P., 2012*).

RESULTS AND DISCUSSION

To ensure a well-prepared bed for a seed onion swath, it is necessary for the spiral drum of the bed-shaping roller to grind soil lumps to sizes smaller than the minimum diameter of a standard onion fraction, so that the bulbs on the separating executive devices get cleaned from small soil impurities (since the receiving-undercutting part of the onion harvesting machine, together with the bulbs, collects soil clumps that are hard to separate, due to their size comparable with standard bulbs) (*Hevko R.B., Tkachenko I.G., Synii S.V., 2016*).

Based on the foregoing, it follows that the maximum diameter d_{Kmax} of a soil lump should be less than the minimum diameter D_{Lmin} of a standard seed onion fraction, i.e.:

$$d_{Kmax} \leq D_{Lmin} \quad (1)$$

where:

d_{Kmax} – is the maximum diameter of a soil lump, m.

The minimum diameter of the d_{CP} bed-shaping roller spiral drum is determined based on the maximum size d_{Kmax} of the soil lump formed after the plough of the onion harvester undercuts the soil layer, to ensure that the soil clump is caught between the spiral and the drum of the bed-shaping roller:

$$d_{CPB} \geq \frac{d_{Kmax} \cdot \cos \varphi}{(1 - \cos \varphi)} \quad (2)$$

This condition is met when the soil lumps, after passing the spiral drum of the bed-shaping roller, compose a single fraction, since according to agrotechnical requirements, the quality of soil grinding is estimated by its fractional composition (*Kamaletdinov R.R., 2012*)

We shall consider the geometrical dimensions of soil lumps ground by the bed-shaping roller spiral drum (figure 5).

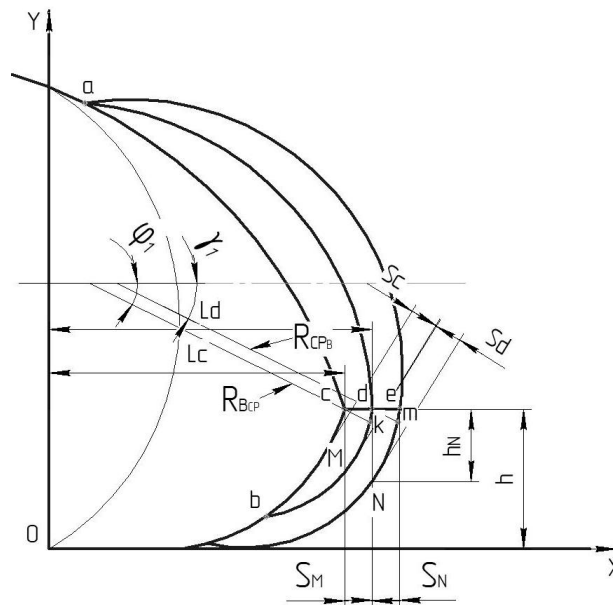


Fig. 5 – Diagram for determining the diameter of the onion harvester bed-shaping roller spiral drum

The width and height of soil lumps M and N depend on the thickness of the inverted soil layer and coverage B_{CP_B} of the bed-shaping roller spiral drum.

Therefore, in order for soil lumps M and N to constitute one fraction, it is necessary to ensure uniformity of their maximum thickness.

For this, the soil clump (M + N) limited by two trajectories — the spiral and the drum of the spiral roller, must be divided in the longitudinal section of the spiral path in such a way that the maximum soil clump thickness $F - (\delta_{MAX}^M)$ in the inverted soil layer is equal to the maximum thickness of soil clump $G - (\delta_{MAX}^N)$.

Let's assume that the equality

$$\delta_{MAX}^M = \delta_{MAX}^N \quad (3)$$

is valid when the roller spiral path $\delta_{MAX}^{(M+N)}$ is divided in half.

The value $R_{C_{P_B}}$ should be such that the points of contact $R_{B_{CP}}$ and $R_{C_{P_B}}$ with the surface of the inverted soil layer in the longitudinal-vertical plane are located at a distance

$$S_M = S_N = \frac{2\pi \cdot R_{B_{CP}}}{\varrho \lambda} \quad (4)$$

where:

ϱ – is the angle between the turns of the bed-shaping roller drum spiral, degrees;

λ – kinematic indicator of the bed-shaping roller spiral drum.

$$\lambda = \frac{v_0}{v_D} \quad (5)$$

where:

v_0 – is the circumferential speed of a bed-shaping roller drum spiral, m/s;

v_D – is the progressive speed of the harvester movement, m/s.

In coordinates XOY segment S_F is parallel to the abscissa axis, therefore the distance from the ordinate axis to point d must be greater than the distance from the ordinate axis to point c by the value S_M :

$$L_d = L_c + \frac{2\pi \cdot R_{B_{CP}}}{\varrho \lambda} \quad (6)$$

Value L_c is determined by the sum of projection of segment $R_{B_{CP}}$ on the abscissa axis and the progressive movement of the bed-shaping roller spiral drum during turn $R_{B_{CP}}$ until contact with the soil, i.e. at angle φ_1 :

$$L_c = \frac{\varphi_1 \cdot R_{B_{CP}}}{\lambda} + R_{B_{CP}} \cdot \cos \varphi_1 \quad (7)$$

Angle φ_1 of turn $R_{C_{P_B}}$ until contact with the surface of the inverted layer:

$$\varphi_1 = (\alpha + \gamma_1) \quad (8)$$

where:

γ_1 – is the angle at which the bed-shaping roller spiral drum enters the soil, deg.

Therefore, value L_d is determined by the sum of projection of segment R_{CP_B} on the abscissa axis and the progressive movement of the bed-shaping roller spiral drum for the period t during the turn at angle φ_1 :

$$\varphi_1 = (\alpha + \gamma_1) \tag{9}$$

$$L_d = \frac{(\alpha + \gamma_1) \cdot R_{B_{CP}}}{\lambda} + R_{CP_B} \cdot \cos \gamma_1 \tag{10}$$

By inserting (7) and (10) into equation (6) we obtain:

$$\frac{(\alpha + \gamma_1) \cdot R_{B_{CP}}}{\lambda} + R_{CP_B} \cdot \cos \gamma_1 = \frac{\varphi_1 \cdot R_{B_{CP}}}{\lambda} + R_{B_{CP}} \cdot \cos \varphi_1 + \frac{2\pi \cdot R_{B_{CP}}}{\varrho \lambda} \tag{11}$$

Using expression (11) we shall express angle γ_1 , for which we shall determine the distance from the abscissa axis to points d and c , and also equate them, thus.

$$\gamma_1 = \arcsin \left(\frac{\sin \varphi_1}{R_{CP_B} / R_{B_{CP}}} \right) \tag{12}$$

By inserting (12) into formula (11) we have:

$$\frac{\pi / \varrho - \varphi_1 + \arcsin \left(\frac{\sin \varphi_1}{R_{CP_B} / R_{B_{CP}}} \right)}{\cos \varphi_1 - \sqrt{\left(R_{CP_B} / R_{B_{CP}} \right)^2 - \sin^2 \varphi_1}} = \lambda \tag{13}$$

Expression (13) makes sense when:

$$R_{CP_B} / R_{B_{CP}} > \sin \varphi_1. \tag{14}$$

Coverage B_{CP_B} of the bed-shaping roller spiral drum (figure 6) is determined by the technological width of the undercutting device B_K , which in turn depends on the technological pattern of sowing onions, the width of the screening conveyor B_T and the distance S_K between the guards narrowing the pile which leaves the executive device of the harvester.

Since the last factor affecting the width of the formed swath based on the technological process of harvesting onions is distance S_K between the narrowing guards 1, coverage B_{CP_B} of bed-shaping roller spiral drum 2 should meet the inequality:

$$B_{CP_B} \geq S_K \tag{15}$$

The loose soil layer is formed as a result of crumbling and grinding soil lumps after the bulbs are removed from the soil by the plowshares of the onion harvester (V. Mayer, D. Vejchar, L. Pastorková, 2017). The spiral winding on the roller contributes to intensification of the process of crushing soil lumps by the harvester bed-shaping roller.

To determine winding pitch t_{CP} of the spiral and angle Σ of its inclination to horizontal axis OO of the roller, we shall consider the forces affecting a soil clump. Soil clump K is affected by the impact force of spiral F_{CP} (figure 7), which can be split in two components – normal F_N and tangential F_T .

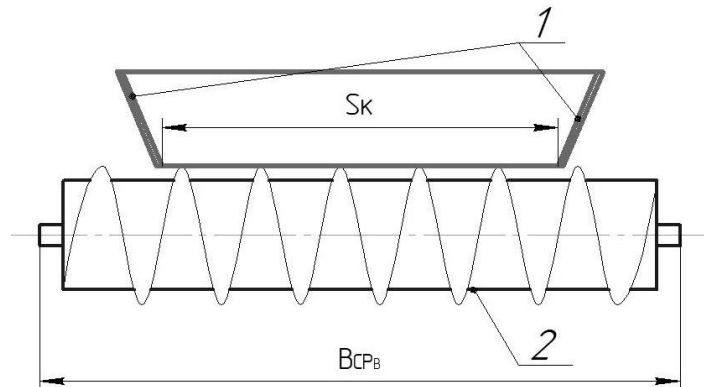


Fig. 6 – Diagram for determining the spiral drum width:
1 – narrowing guards; 2 – spiral drum

A soil clump is moved along the surface of the spiral on condition that:

$$F_T \geq F_{TP} \tag{16}$$

where:

F_{TP} – is the friction force of the soil against the surface of the spiral, N.

Determining the friction force (figure 7):

$$F_{TP} = F_N \cdot \operatorname{tg} \varphi_P \tag{17}$$

where:

φ_P – is the friction angle of soil clumps against the surface of the spiral, deg.

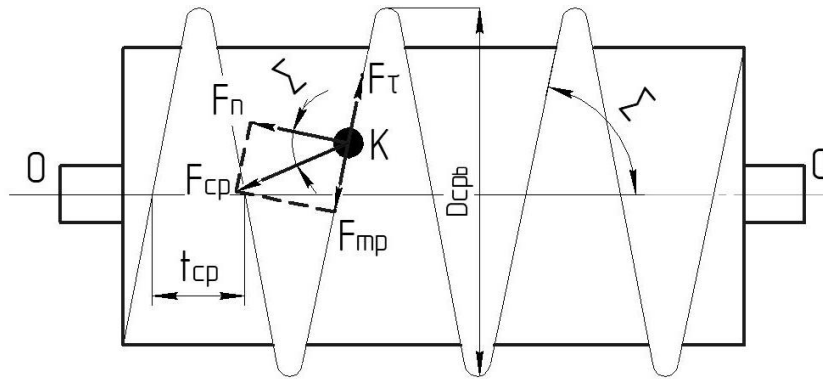


Fig. 7 – Diagram of the forces affecting a soil clump through the drum spiral

Determining F_T the tangential component of the force F_{CP} :

$$F_T = F_N \cdot \operatorname{tg}\Sigma \quad (18)$$

Taking into account formulae (17) and (18), condition (16) will be written as:

$$\operatorname{tg}\Sigma \geq \operatorname{tg}\varphi_P \quad (19)$$

Thus, angle Σ of inclination of the spiral to horizontal axis OO should be greater than angle φ_P of friction of soil lumps on the surface of the spiral.

Based on the theory for calculation of the design parameters of screw machines, we have:

$$t_{CP} = \operatorname{tg}\Sigma \cdot \pi \cdot D_{CP_B} \quad (20)$$

where:

D_{CP_B} – is the diameter of the spiral drum, m.

Besides, it is known that in order to prevent soil loading by the bed-shaping roller spiral drum, diameter D_{CP_B} of the drum should be determined:

$$D_{CP_B} = d_{K_{\max}} \cdot \operatorname{ctg}^2(\varphi_1 + \varphi_P) \quad (21)$$

where:

$d_{K_{\max}}$ – is the maximum diameter of a soil clump, m;

φ_1 – is the angle of internal friction between soil lumps, deg.

Taking into account formula (21), the expression determining the pitch of the spiral shall be written as follows:

$$t_{CP} = \operatorname{tg}\Sigma \cdot \pi \cdot [d_{K_{\max}} \cdot \operatorname{ctg}^2(\varphi_1 + \varphi_P)] \quad (22)$$

Due to the fact that the onion harvester bed-shaping roller spiral drum performs the technological process of working in line with the onion harvesting machine with the progressive v_D movement speed within 2.8...5.6 km/h, then with a known range $\lambda = 6 \dots 9$ of the spiral drum kinematic indicator, based on the results of earlier studies related to operation of rotary soil tillage machines for tilled crops (Sun D.X, Zhang A.M, Gong J.X., 2016), providing high-quality grinding of the inverted soil layer, we shall determine rotational speed n_{CP_B} of the bed-shaping roller spiral drum.

It is known that

$$\lambda = \frac{v_0}{v_D} = \frac{\omega_{CP_B} \cdot R_{CP_B}}{v_D} \quad (23)$$

Due to the fact that

$$\omega_{CP_B} = \frac{\pi \cdot n_{CP_B}}{30} \quad (24)$$

where:

n_{CP_B} – is the rotation speed of the bed-shaping roller spiral drum, rpm.

By inserting expression (24) into expression (23) we get:

$$n_{CP_B} = \frac{30 \cdot v_D \cdot \lambda}{\pi \cdot R_{CP_B}} \quad (25)$$

CONCLUSIONS

Theoretical studies of the bed-shaping roller of an onion harvester made it possible to obtain dependencies for determining diameter (2) and pitch (22) of the spiral, as well as width (15) of coverage, kinematic indicator (23) and rotation frequency (25) of the bed-shaping roller spiral drum.

Based on the theoretical studies performed, a bed-shaping roller was made, which was subjected to laboratory and field tests to justify the optimal design and technological parameters.

REFERENCES

- [1] Aksenov A.G., Sibirev A.V., Emelianov P.A., (2018), Oriented Bulbs Planting with Forked-Roller Planting Apparatus, *Vestnik of Mordovia University*, Issue number 1, pp. 20-24, Saransk / Russia;
- [2] Farhadi R., Sakenian N., Azizi P., (2012), Design and construction of rotary potato grader, *Bulgarian Journal of Agricultural Science*. Issue number 2, pp. 304-314, Sofia / Bulgaria;
- [3] Hevko R.B., Tkachenko I.G., Synii S.V., (2016), Development of design and investigation of operation processes of small-scale root crop and potato harvesters, *INMATEH-agricultural engineering*. Vol. 49 (2). pp. 53 – 60, Bucharest / Romania;
- [4] Kamaletdinov R.R., (2012), Object-oriented simulation modeling in the information theory environment (information modeling), *News of the International Academy of Agrarian Education*, Issue number 14, pp. 186–194, Moscow / Russia;
- [5] Kurdyumov V.I., Zykin E.S., Lazutkina S.A. (2016), Justification of the distance between flat disks of inter-row cultivator, *Herald of Ulyanovsk State Agricultural Academy*, Issue number 3, pp. 174 – 178, Ulyanovsk / Russia;
- [6] Lobachevsky Ya. P., Emelyanov P.A., Aksenov A.G., Sibirev A.V., (2016), *Onion production machine technology*, M.: Federal State Budgetary Scientific Institution Federal Scientific Agroengineering Centre, 168 p., Moscow / Russia;
- [7] Mayer V., Vejchar D., Pastorková L., (2017), Measurement of potato tubers resistance against mechanical loading, *Research in Agricultural Engineering*, Issue number 2, pp. 22-31, Prague / Czech Republic;
- [8] Natenadze N., (2016), The design and theoretical justification of a vibratory digger shovel, *Scientific technical union of mechanical engineering Bulgarian association of mechanization in agriculture*. Issue number 5, pp. 9–12;
- [9] Sun D.X, Zhang A.M, Gong J.X., (2016), Design and experiment on 1SZL-250A type subsoiling rotary tillage fertilizer combined soil working machine, *Journal of Chinese Agricultural Mechanization*, Issue number 37(4), pp. 1 – 6, Beijing / China;
- [10] Sojka R.E, Horne D.J, Ross C.W, Baker C.J., (1997), Subsoiling and surface tillage effects on soil physical properties and forage oat stand and yield, *Soil and Tillage Research*, Issue number 40 (3-4), pp. 25–144, Amsterdam / Netherlands;
- [11] Tauseef Asghar M., Ghafoor Abdul, Munir Anjum, Iqbal Muhammad, Ahmad Manzoor., (2014). Design modification and field testing of groundnut digger, *Asian Journal of Science and Technology*, Issue number 5. pp. 389–394, Delhi / India;
- [12] ***Patent №. 2585481 Russia, IPC A01 D17/00. Seed onions harvester / A.G. Aksyonov, S.A. Pryamov, A.V. Sibirev. – №. 2585481; Appl. 24.06.2015; Publ. 27.05.2016, Bull. №. 15.

RESEARCH ON THE IMPACT OF THE AIR-LIQUID JET MIXER UPON RING BIOREACTOR OPERATION

/

ДОСЛІДЖЕННЯ ВПЛИВУ ПОВІТРЯНО-РІДИННОГО СТРУМІНЕВОГО ЗМІШУВАЧА НА РОБОТУ КІЛЬЦЕВОГО БІОРЕАКТОРА

Yaroshevsky V.¹⁾, Bulgakov V.²⁾, Ivanovs S.³⁾, Krutyakova V.¹⁾, Belchenko V.¹⁾, Olt J.⁴⁾ ¹

¹⁾Engineering and Technology Institute "Biotechnica", National Academy of Agrarian Sciences of Ukraine, Ukraine,

²⁾National University of Life and Environmental Sciences of Ukraine, Ukraine;

³⁾Latvia University of Life Sciences and Technologies, Latvia;

⁴⁾Estonian University of Life Sciences, Institute of Technology, Estonia

*Correspondence: Tel.+37129403708, e-mail: semjons@apollo.lv

DOI: <https://doi.org/10.35633/inmateh-60-13>

Keywords: aeration, jet bioreactor, jet mixer, fermentation medium, circulation ring

ABSTRACT

In the production of biological preparations for agriculture there are promising jet bioreactors with an external circulation ring, providing intense mixing of the medium along with a high degree of aeration. However, application of these bioreactors is limited by large shear loads on the microorganisms (microorganism cells) arising in the circulation pump. The article deals with one of the ways for solving this problem by using a low-capacity pump for the circulation of the fermentation medium according to a non-standard scheme of medium jet aeration in order to intensify the mass exchange processes. There are presented results of physical simulation of the mixing parameters of flows in an aerator-jet mixer and their impact upon the intensity of metabolic processes in the circulation ring of a bioreactor.

АНОТАЦІЯ

Застосування струменевих біореакторів із зовнішнім циркуляційним кільцем лімітується великими зрізовими навантаженнями на мікроорганізми (клітини мікроорганізмів), що виникають в циркуляційному насосі. У статті розглядається один із шляхів вирішення даної проблеми за рахунок застосування малопотужного насоса для циркуляції ферментаційного середовища з використанням нестандартної схеми струменевої аерації середовища для інтенсифікації масообмінних процесів. Наводяться результати фізичного моделювання параметрів зміщення потоків в аераторі – струменевому змішувачі та їх вплив на інтенсивність обмінних процесів в циркуляційному кільці біореактора.

INTRODUCTION

Mixing and aeration of the fermentation medium play one of the important roles in the deep cultivation of microorganisms. These processes directly affect the supply of nutrients and oxygen to the cells, as well as the removal of metabolic products. The technical and technological design both of mixing and aeration includes many engineering solutions. However, intensification of the metabolic processes between the liquid and the gaseous phases still remains an urgent task for most types of bioreactors. Among the devices providing intense mixing of the fermentation medium along with a high degree of aeration, it is worth highlighting jet bioreactors with an external circulation ring (Stanbury P. et al., 2016). Mixing in devices of such a type is based on the pump circulation of the medium along an external ring (Warmeling H. et al., 2016). Additional intensification of the mass exchange processes is achieved due to jet aeration of the fermentation medium (Weber S. et al., 2018). Such an organisation scheme of mixing and aeration also allows one to avoid using additional devices inside the device immersed into the fermentation medium (impellers, bubblers, etc.), which helps to improve the aseptic fermentation conditions.

¹ Yaroshevsky V., Dr.; Bulgakov V., Prof.Ph.D. Eng.; Ivanovs S., Dr.; Krutyakova V., Dr.; Belchenko V., Dr.; Olt J., Prof. Ph.D.Eng.

Despite the fact that general schemes for mixing and fermentation of the medium with the use of pump circulation have been known for quite a long time they have not found wide application in biotechnology since it is believed that cells in the impeller of the pump experience large shear loads. Therefore, jet reactors are now used mainly in chemical technology (Warmeling H. *et al.*, 2016; Pangarkar V., 2015). Analysis of the studies made in the recent years on the inhibition of the biomass growth because it gets into the pump impeller during circulation (Weber S. *et al.*, 2018; Ughetti M., 2018) showed that the shear loads have a much less pronounced negative effect on the cells than it was previously assumed. At the same time, it is noted that the intensity of the mass exchange processes in the jet bioreactors significantly exceeds a similar indicator for the most common devices equipped with mechanical impellers (Dierendonck L., 1998; Weber S. *et al.*, 2019). It was also pointed out that the technological design of mixing and aeration of the fermentation medium in the jet bioreactors was more energy-efficient compared to the use of the bubble columns or fermenters with mixers (Ughetti M., 2018; Weber S. *et al.*, 2018; Besspalov I. & Hodorchuk V., 2017; Botton R. *et al.*, 2009).

The main technological obstacle limiting the application of jet reactors in biological processes remains the need to reduce the shear loads on the cells, which translates into a requirement to reduce the number of the pump impeller revolutions with a corresponding decrease in the mixing intensity of the medium. For the small-scale production of biological products this task is most acute since the application of the approach developed for industrial fermenters (with a volume of 40 m³, or more), involving the use of multiphase pumps pumping the air-liquid mixtures along the circulation ring (Stanbury P. *et al.*, 2016), seems very costly and nonpurposeful. There are technical solutions (Besspalov I. & Hodorchuk V., 2017; Krutyakova V. *et al.*, 2019) that look much more attractive, suggesting reduction in the shear loads by using low-capacity pumps and intensification of medium mixing by aeration in small bioreactors (100 l). Numerous studies were devoted to jet mixing of the fermentation medium and air in reactors with an external circulation ring (Pangarkar V., 2015; Botton R. *et al.*, 2009; Fadavi A. & Chisti Y., 2005). One of the most common flow mixing schemes is implemented by means of a jet apparatus (JA) – an ejector (Stanbury P. *et al.*, 2016; Sharma D. *et al.*, 2015; Fadavi A. & Chisti Y., 2005). As a rule, a medium flow is supplied to the nozzle of such an ejector, but air is injected. The ready-made air-liquid mixture can be supplied under the level of the medium in the apparatus, or sprayed above the surface of this medium.

We have developed a new scheme of jet aeration of the fermentation medium in the bioreactor (Fig. 1), taking into account the advantages and disadvantages of the existing technical solutions.

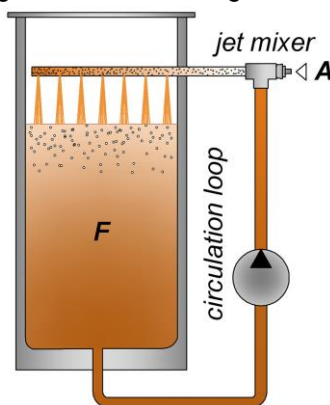


Fig. 1 - A scheme of mixing and aeration of the fermentation medium in a jet bioreactor

F – fermentation medium, *A* – air

The basis of this development is also the use of a JA – a mixer. The organisation of the working process in a jet mixer (JM) has two essential differences: 1) not the fermentation medium but air is supplied to the JM nozzle; 2) both flows (the air and the medium) are under pressure, i.e. the amount of the mixed air does not depend on the formation of negative pressures in the JA, and it allows one adjustment of the conditions of mixing. To improve mixing, the flows are supplied at right angles to each other, and the mixture flows into the bioreactor in thin jets through the air gap. The movement of the fermentation medium along the bioreactor ring is carried out using a low-capacity circulation pump. Analysis of the references to the JA (Dutta N. & Raghavan K., 1987) shows that the proposed scheme of organisation of the workflow is atypical not only for the jet bioreactors but also for the JA used in other areas. Therefore, the purpose of this study is qualitative assessment of the impact of the JM on the main characteristics of the bioreactor.

MATERIALS AND METHODS

Jet mixer (JM) is a simplified design of the mixer (JA) without additional compression of the mixed flow (Fig. 2), i.e. without a diffuser. The design is based on a standard equal-bore profiled T-joint 2 with a diameter of 15 mm, in one of the branches of which a steel nozzle 1 with a 1.8 mm flow section is installed. The nozzle is centred relative to the longitudinal axis of the T-joint and fixed with a gasket 4 inserted into the standard pipe reducer 3.

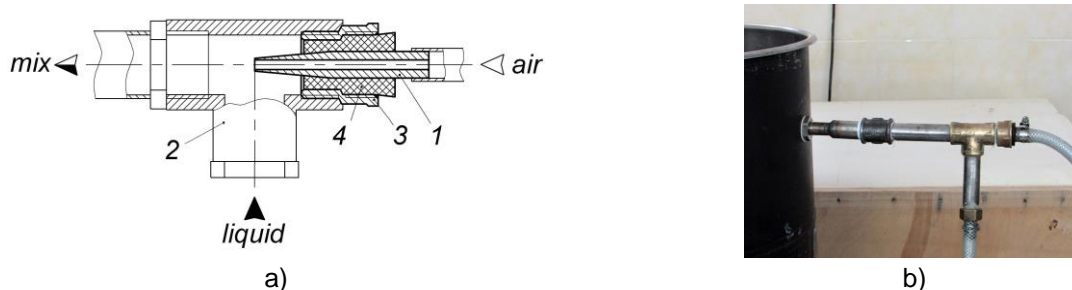


Fig. 2 - A jet mixer scheme (a) and a photo of the JM installed before the inlet of the bioreactor internal capacity (b)

1 – nozzle; 2 – T-joint; 3 – pipe reducer; 4 – gasket

During the operation of the JM, the active flow (the compressed air) flows out of the nozzle 1 and admixes the passive flow (the liquid). The function of the mixing chamber in this case is performed by the flow part of the T-joint 2. Final mixing of the flows takes place in the area between the JM and the sprayer installed inside the bioreactor. The experimental plant (Fig. 3) is designed to simulate the jet aeration process of the fermentation medium pumped by a pump along the external circulation ring of the bioreactor. The aeration conditions of the fermentation medium were simulated by using the JM 1 installed before the inlet of the bioreactor internal capacity 2 (ETI "Biotechnica", 100 l). The mixture obtained at the outlet of the JM was distributed over the surface of the liquid inside the container 2 using a sprayer 3. In the experiments purified tap water was used as a working fluid.

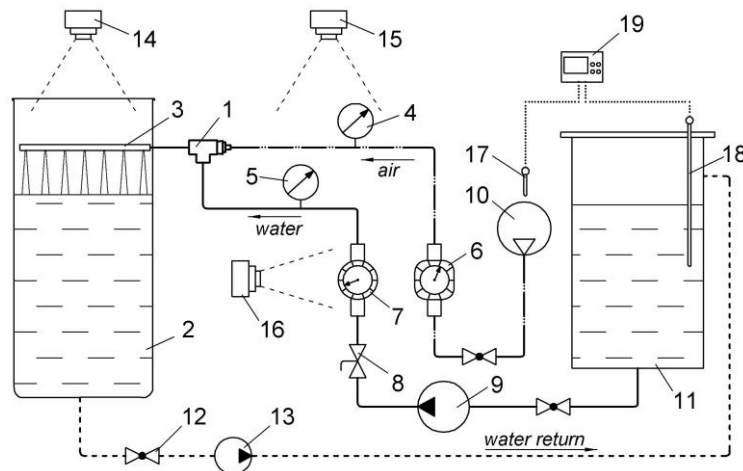


Fig. 3 - A diagram of the experimental plant

1 – jet mixer; 2 – the internal capacity (100 l); 3 – sprayer; 4, 5 – pressure gauges; 6 – gas meter; 7 – water meter; 8 – manual control valve; 9 – circulation pump; 10 – air compressor; 11 – auxiliary container with water (180 l); 12 – locking ball valve; 13 – pump for the returning water; 14, 15, 16 – digital cameras; 17, 18 – temperature sensors; 19 – temperature controller

The operation of the fermentation medium circulation line was simulated using an auxiliary container 11 (ETI "Biotechnica", 180 l) from which water was supplied by the pump 9 (Wilo Star RS 15 / 5-3P) to the suction pipe JM 1. The flow rate of the pump 9 was controlled by the throttling method using a manual control valve 8. The return of water from the working container 2 was carried out using a pump 13 (Aquario AC 254-180). Besides, only the pump 9 was working during the experiments but the valve 12 on the water return line was closed. The aeration air is supplied to the nozzle JM 1 using a compressor 10 (ABAC FC2 / 50 CM2). The parameters of the water and the air flows were measured by means of pressure gauges 4 (MTI –1... + 3 bar) and 5 (MTI 0...0.6 bar), the gas meter 6 (Arsenal G 2.5), the water meter 7 (Novator LK-

15C). In order to record the readings of devices 4, 5 and 6, 7, as well as the process of the mixture outflow into the container 2, digital cameras 14-16 (Canon) were used. The air and the water temperatures were measured using the remote temperature sensors 17 and 18 (TERA RTD), the data of which were transmitted to the temperature controller 19 (RPC "ANT Electronics", TRC-2200-T).

Water from the container 11 (Fig. 3) was supplied to the JM 1 by means of the circulation pump 9. The water flow was controlled by the tap 8. Alongside with the water supply to the nozzle of JM 1, compressed air was supplied using the compressor 10. The flows were mixed in the JM and an air-water mixture entered the container 2 through the sprayer 3. The outflow process of the mixture into the container 2, as well as the readings of the pressure gauges 4, 5 and the flow meters 8, 9 were video captured using stationary cameras 14-16. Before the beginning of experiments measurements were made of the air temperature at the inlet of the compressor 10 and of the water temperature in the container 11 by means of a temperature controller 19 with remote sensors 17 and 18. The experiments were carried out for three modes of operation of the circulation pump, corresponding to three frequencies of rotation of the impeller (2350, 2630, 2720 rpm). In each operation mode of the pump, tests were conducted for four fixed values of the air pressure at the compressor outlet (1.0, 1.5, 2.0, 2.5 bar). Separate measurements were also performed for the parameters of the pump and compressor separate operations. At the beginning of each experiment the water level in the container 2 was 50 litres. The excess water, accumulated during the experiment, at the end of the tests was pumped into the auxiliary container 11 by means of the pump 13.

The readings of the pressure gauges and flow meters were determined by processing the video recordings captured by cameras 15 and 16 (Fig. 3) in the software environment of the Sony Vegas Pro video editor. The video recordings of the instrument readings were previously synchronised according to characteristic peaks of the sound tracks, which made it possible to compare the parameters of the hydrodynamic processes taking place in the experiment simultaneously. In a frame-by-frame analysis of the video recordings instantaneous values of volumes and static pressures of water and air were determined. The time values for the corresponding frames of the videos were determined by the timeline scale of the Sony Vegas Pro. The flow rates of water and air were calculated on the basis of the measured values as a ratio of the volume passed through the flow meter during a period of time to the duration of this time period. Statistical processing of measurements was performed using the MS Excel spreadsheet according to a standard method (Bulgakov V. et al., 2018). During the data processing the arithmetic mean values of the measured magnitudes, the mean root square deviation, were determined; the relative and absolute measurement errors were calculated for a confidence level of 95%. During the experiments the temperature of air and water, measured with the help of remote sensors 17, 18 (Fig. 3), remained unchanged, and it was 27°C. Based on the values measured by the standard dependences, the average cross-sectional flow velocities, the dynamic and total pressures in the cross-sections were calculated before each of the flows entered the JM. The analysis of the flowing process of the mixture into the bioreactor container was carried out by processing the videos and photos obtained from the camera 14.

RESULTS

To determine the performance parameters of the JA it is convenient to use dimensionless hydraulic characteristics, which are ratios of the corresponding flow parameters of the mixed media (Lyamaev B., 1988). The basic characteristics of the JA of any type are the relative flow rate (the injection coefficient) and the relative pressure. The mathematical models of processes occurring in the classical JAs often consider the flow mixing as an auxiliary process accompanying the transfer of energy from the active flow to a passive one. In our case, mixing is the main result of the jet mixer operation, the processes of energy redistribution in the structural parts of the apparatus being secondary. Owing to such a change in the approach to the study of the jet processes, a need for strict attachment to classical dependencies in order to determine the relative flow rate and pressure of the JA becomes unnecessary.

The relative flow rate of the JM can be conveniently determined using the ratio of the volumetric flow rates:

$$q = \frac{Q_w}{Q_a}, \quad (1)$$

where q – the relative flow rate; Q_w, Q_a – the relative flow rates of water and air, [l/min⁻¹].

The use in dependence (1) of volumetric flow rates, rather than the mass ones, as in the classical JA, is determined by the fact that the passive flow is not sucked up due to the created vacuum but is pumped by

a separate pump. Therefore, the process is not based on inertia, the measure of which is mass, but on friction that occurs when the flows are mixed. Second, it is accepted in practice that the degree of aeration of the fermentation medium is estimated by the amount of air supplied per 1 litre of the medium. The relative flow rate, determined by formula (1), is a value inverse to the aeration degree. To determine the relative pressure, it is convenient to use the ratio of the total pressure of the water and air flows before the inlet of the plant:

$$h = \frac{H_a^t}{H_w^t}, \quad (3)$$

where: h – the relative pressure; H_a^t , H_w^t – full pressures of the air and water flows at the jet mixer inlet, bar.

The characteristics of the jet mixer without adjusting the parameters of the water flow are shown in Fig. 4. Analysis of the graphs shows that an increase in air pressure at a constant rotational speed of the impeller leads to a decrease in the relative flow rate of the JM q , respectively, an increase in the proportion of air in the mixture. At the same time, an increase in the impeller speed at a constant air pressure, on the contrary, significantly increases q .

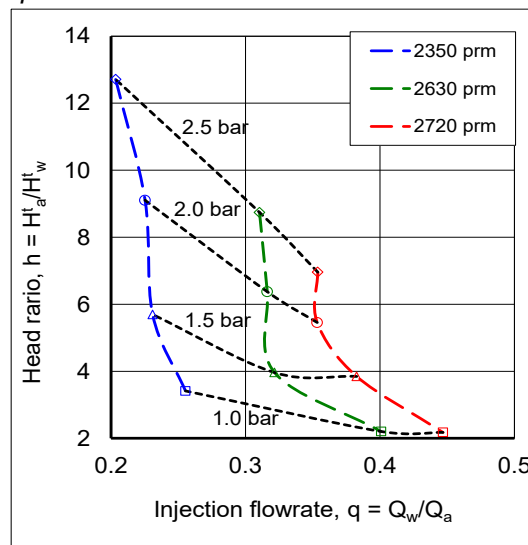


Fig. 4 - The dimensionless characteristics of the JM in the absence of the parameter adjustment of the water flow at the air pressures (1.0- 2.5 bar) and the revolution frequencies of the pump impeller (2350, 2630, 2720 rpm)

The parameter adjustment of the water flow allows one a slight expansion of the range of values of the relative flow rates ($q = 0.05...0.45$) and relative pressures ($h = 2...25$). Throttling of the passive flow leads to a pronounced decrease in the relative JM flow rate with a simultaneous increase in the relative pressure, which is observed in all the tested conditions. The aeration degree of the fermentation medium is inversely proportional to the relative flow rate of the JM q . Analysis of the experiments shows that even the use of the simplest JM design allows mixing the media in a wide range of volume ratios: 2.2...18.5 litres of air per 1 litre of water. Consequently, even in the case of a significant difference in the viscosity of the fermentation medium from the viscosity of water in the experiment and a corresponding reduction in the obtained range of the air-medium ratios, this jet aeration scheme can be used in the production of a sufficiently large range of biological products. Separately it is worth noting the advantage of the air supply through the JM nozzle in the proposed aeration diagram, which allows one the adjustment of the amount of the air supplied without changing the pump performance parameters. In the standard jet aeration schemes, air is injected with the fermentation medium. An increase in the viscosity of the medium during fermentation, caused by an increase in the concentration of microorganisms in the bioreactor capacity, leads to a decrease in the pump flow rate and a corresponding decrease in the amount of the injected air. Therefore, in order to maintain the required degree of aeration, it is necessary to increase the number of revolutions of the pump impeller, which means that the power consumption will increase. The use of the JM makes it possible to maintain the desired degree of aeration while increasing the viscosity of the medium by increasing the air pressure, i.e. without affecting the pump. Mixing of the fermentation medium is one of the key processes responsible for a mass exchange during the deep cultivation of microorganisms. In the jet bioreactors the most intense mixing of the fermentation medium takes place in the circulation ring (Weber S. *et al.*, 2019).

Therefore, it is necessary, first of all, to evaluate the impact of the JM upon the medium mixing intensity exactly in the circulation ring of the bioreactor. The mixing intensity is usually estimated applying the dimensionless criteria of hydrodynamic similarity, in particular, the Reynolds number (Pangarkar V., 2015). Intense mixing is achieved at the Re values corresponding to the turbulent flow regime, i.e. at $Re > 3000$. In order to perform the calculations, the pressure section of the water supply line of the experimental plant (Fig. 3), simulating the bioreactor circulation ring, was divided into two sections: before the JM (the first section) and after the JM (the second section), respectively. In the first section water moves through the pipeline, and in the second – the air-water mixture. Calculations of the Reynolds number for the first section (Table 1) indicated that in all the pump operation modes a mode of a turbulent flow took place. At the same time, it was pointed out that the change in the parameters of the air supplied to the JM nozzle did not have any significant impact upon the mode of the water flow in this section. Mixing of the fermentation medium in the circulation ring before the JM will occur sufficiently intensely with a minimal impact of the jet processes proceeding in the mixer itself.

Table 1

The Reynolds number for the first section of the water supply line (before the JM)

Air pressure, bar	The Reynolds number, Re		
2.5	4461	6702	7749
2.0	4830	6704	7681
1.5	4800	6703	7877
1.0	4800	6980	8267
	Velocity of the pump impeller, rpm		
	2350	2630	2720

A more complicated task is how to determine the flow conditions of the air-water mixture flow in the second section. The standard dependence for the calculation of the Reynolds number, in addition to the diameter of the JM outlet cross section and the flow velocity in it, determined on the basis of experimental data, includes density and the dynamic viscosity of the mixture. If the density of the air-water mixture can be calculated analytically as a ratio of the sum of the mass flow rates to the sum of the volumetric flow rates, it is not possible to calculate the exact value of the viscosity without conducting separate experiments. However, for a qualitative assessment of the mode of motion, it is possible to determine the boundaries of the interval into which the Re value of the mixture falls. For this it is sufficient to calculate the boundary values of the Reynolds numbers based on the boundary values of the dynamic viscosity of water and air. Based on the fact that the dynamic viscosity of the mixture should be less than the viscosity of water but more than the viscosity of compressed air, the desired value of the Reynolds number will fall into the range:

$$\mu_a < \mu_{mix} < \mu_w, Re_a > Re_{mix} > Re_w \tag{4}$$

where μ_a, μ_w, μ_{mix} – the dynamic viscosity of compressed air, water and mixture

Re_a, Re_w, Re_{mix} – the Reynolds number for compressed air, water and mixture

The results of calculation of the boundaries of the interval Re_a and Re_w for the second section of the circulation ring are given in Table 2.

Table 2

The Reynolds number of the air-water mixture for the second section water supply line (after the JM)

Air pressure, bar	The Reynolds number of the air-water mixture, Re_{mix}		
2.5	$3.8 \cdot 10^4 \dots 2.2 \cdot 10^5$	$5.8 \cdot 10^4 \dots 3.2 \cdot 10^5$	$6.7 \cdot 10^4 \dots 3.7 \cdot 10^5$
2.0	$4.2 \cdot 10^4 \dots 2.3 \cdot 10^5$	$5.8 \cdot 10^4 \dots 3.2 \cdot 10^5$	$6.6 \cdot 10^4 \dots 3.7 \cdot 10^5$
1.5	$4.1 \cdot 10^4 \dots 2.3 \cdot 10^5$	$5.8 \cdot 10^4 \dots 3.2 \cdot 10^5$	$6.8 \cdot 10^4 \dots 3.8 \cdot 10^5$
1.0	$4.1 \cdot 10^4 \dots 2.3 \cdot 10^5$	$5.9 \cdot 10^4 \dots 3.3 \cdot 10^5$	$7.1 \cdot 10^4 \dots 3.9 \cdot 10^5$
	Velocity of the pump impeller, rpm		
	2350	2630	2720

It is evident from the data in Table 2 that the air-water mixture at the outlet of the JM moves in a developed turbulence mode in all tested modes. Comparison of the data in Table 1 and Table 2 shows that the JM plant allows increasing the Reynolds number by more than an order of magnitude, which indicates a significantly intensified medium mixing in the circulation ring of the bioreactor. During the JM operation there is an increase in the water pressure before the apparatus, observed by 10...34%, in contrast to the movement of water through the JM without mixing with air. Consequently, the flow of air flowing out of the nozzle will throttle the flow of the fermentation medium in the circulation ring. The throttling process is generally accompanied by a reduction in the flow rate. However, the decrease in the water flow rate was not observed in all the modes studied. So, at the frequencies of the pump impeller revolutions 2630 rpm and 2720 rpm the water flow rate decreased 7...13% but at a frequency of 2350 rpm, contrary to the increase in the water pressure, an increase was observed rather than a decrease in the water flow rate by 3...11%. The obtained increase in the water flow rate, when mixed with air, at minimum pump revolutions of the impeller exceeds the measurement error. Therefore, it is logical to assume that this effect is caused by a change in the nature of the jet processes occurring in the JM. In jet mixing the injection processes generally take place: a part of the energy of the active stream is spent on the injection of the passive stream. In the first two operating modes of the pump (at frequencies of 2630 rpm and 2720 rpm), the losses of the water pressure during mixing exceeds the injection pressure created by the air stream. As a result of this, the flow of water is throttled (propped) by the flow of air, and the water flow rate is accordingly reduced. In the third mode (at a frequency of 2350 rpm), the injection pressure exceeds the losses during mixing. Accordingly, a part of the energy of the nozzle stream is spent on the injection of an additional water flow. Thus, even in the case of mixing in the JM, the pressure flows induced by various compressors a possibility arises of useful application of the injection effects in a certain range of the flow parameter ratios. The impact of the jet mixer upon spraying of the medium was analysed by using the videos obtained during the experiments and the photos of the outflow of the air-water mixture into the bioreactor container, and by comparison of these data with the parameters of the air and water flows before the JM. This analysis shows that the intensification effect of the mass exchange processes during jet aeration, obtained on the basis of calculations, is confirmed by the results of visual observations of spraying the mixture in the bioreactor (Fig. 7). The pressure and the opening angle of the jets flowing from the sprayer increases with increasing the air pressure, and, at the same time, it little depends on the change in the number of pump impeller revolutions. Analysis of the photos also revealed that the process of the foam formation on medium surface in the bioreactor during the aeration of the medium is less intense than without aeration.



Fig. 5 - The outflow of the air-water mixture into the bioreactor at a frequency of the pump impeller revolutions of 2720 rpm with aeration at an air pressure of 1.5 bar and (a) and without aeration (b)

The study of video recordings confirmed that in case the jets pass through the intermediary air layer in the bioreactor container, excess air is removed from the mixture. In a maximum operating mode of the plant (2.5 bar – 2720 rpm) this process is accompanied by intense emission of the water dust that settles on the inner surfaces of the bioreactor container and the sprayer. Analysis of the photos indicates that the formation of the water dust is caused by a decreased size of the droplets suspended in the air flow and arising as a result of an increased air pressure. Consequently, at the maximum performance parameters of compressors it becomes possible to spray the liquid, circulating along the ring, onto the surfaces located above the sprayer. This effect can be used when sterilizing the internal capacity of the bioreactor by means of liquid disinfectants. At the stage of microorganism cultivation, the formation of dust is not desirable. To prevent its occurrence, the air pressure before the JM nozzle should not exceed 2 bar.

CONCLUSIONS

The plant JM on the circulation ring of a jet bioreactor allows intensification of the mass exchange processes, improvement of the aeration conditions of the medium, and reduced foaming at the fermentation stage. The obtained data correlate with the results of studies conducted by other authors on jet aerators in which a liquid, circulating along the reactor ring, is used as an active flow, the passive flow being air. Taking into account the low coefficient of efficiency of the JA, we proposed a concept of the organisation of the working process, focused on the improvement of the quality of mixing, and not on the injection of the secondary stream. That is why air was chosen as the active flow but the passive flow – the liquid – was made the pressure flow. This makes it possible to use a low-capacity circulation pump that not only lowers the cost of the electric power but also significantly reduces the shear loads on the cultural fluid, entering the impeller. The scheme of mixing the flows in the JM assumes useful application of the injection effects (an increased fluid flow rate) in a certain range of the flow parameters. Absence of a diffuser in the JM design contributes to great hydraulic losses during mixing, which limits the range of useful application of injection with a minimum number of revolutions of the pump impeller. Consequently, further research in this area will be aimed at developing a more advanced design of the JM.

REFERENCES

- [1] Bepalov I, Hodorchuk V., (2017), Economic fermentative unit for production of microbiological means of protections of plants. *Vesntik Agrarnoi Nauki*,1, Moscow/Russia, pp.38–42;
- [2] Botton R, Cosserat D, Poncin S, Wild G., (2009), A simple gas-liquid mass transfer jet system. *8th World Congress of Chem. Eng.*, Montréal/Canada, pp. 513;
- [3] Bulgakov V., Pascuzzi S., Ivanovs S., Kaletnik H., Yanovich V., (2018), Angular oscillation model to predict the performance of a vibratory ball mill for the fine grinding of grain. *Biosystems Engineering*, Vol. 171, pp.155.-164;
- [4] Degermenci N., Cengiz I, Yildiz E, Nuhoglu A., (2016), Performance investigation of a jet loop membrane bioreactor for the treatment of an actual olive mill wastewater, *J Environ Manage.*, 184 (2), pp.441–447;
- [5] Dierendonck L., Zahradník J, Linek V., (1998), Loop Venturi reactor a feasible alternative to stirred tank reactors? *Ind. Eng. Chem. Res.*, 37(3), pp.734–738;
- [6] Dutta N, Raghavan K., (1987), Mass transfer and hydrodynamic characteristics of loop reactors with reversed flow liquid jet ejector. *Chem. Eng. J.*, 36(2), pp.111–121;
- [7] Fadavi A., Chisti Y., (2005), Gas–liquid mass transfer in a novel forced circulation loop reactor. *Chem. Eng. J.*, 112, pp.73–80;
- [8] Kim Y., Lee D., Kim H., Ahn J., Kim K., (2012), An experimental and numerical study on hydrodynamic characteristics of horizontal annular type water-air ejector. *J. Mech. Sci. Technol.*, 26(9), pp. 2773–81;
- [9] Krutyakova V., Bulgakov V., Belchenko V., Rucins A. (2018). Investigation of mechanical method of trichogram dispersal. “*Engineering for rural development*”, Vol. 18, Jelgava/Latvia, pp. 247–255;
- [10] Lyamaev B., (1988), Liquid-Jet Pumps and Facilities. Mashinostroenie, Leningrad/Russia, 256 p;
- [11] Pangarkar V., (2015), Design of Multiphase Reactors. John Wiley&Sons, Inc, New Jersey/USA, 535 p;
- [12] Sharma D., Patwardhan A., Ranade V., (2017), Estimation of gas induction in jet loop reactors: Influence of nozzle designs. *Chem. Eng. Res. Des.*, 125: pp.24–34;
- [13] Stanbury P, Whitaker A, Hall S., (2016), *Principles of fermentation technology*. 3rd ed. Butterworth-Heinemann Ltd, Oxford/UK, 824 p;
- [14] Ughetti M, Jussen D, Riedlberger P., (2018), The ejector loop reactor: Application for microbial fermentation and comparison with a stirred – tank bioreactor. *Eng. Life Sci.*, 18(5), pp. 281–286;
- [15] Warmeling H, Behr A, Vorholt A., (2016), Jet loop reactors as a versatile reactor set up – Intensifying catalytic reactions: A review. *Chem. Eng. Sci.* 149, pp. 229–248;
- [16] Weber S, Schaepe S, Freyer S, Kopf M., Dietzsch C. (2018). Jet aeration as alternative to overcome mass transfer limitation of stirred bioreactors. *Eng. Life Sci.*, 18(4): pp.244–253;
- [17] Weber S, Schaepe S, Freyer S, Kopf M., Dietzsch C. (2019). Monitoring gradient formation in a jet aerated bioreactor. *Eng. Life Sci.*, 19(3): pp.159–167.

SMALL POWER ELECTRIC TRACTOR PERFORMANCE DURING PLOUGHING WORKS

/

PERFORMANȚELE UNUI TRACTOR ELECTRIC DE PUTERE MICĂ ÎN TIMPUL LUCRĂRILOR DE ARAT

Matache M.G.¹⁾, Cristea M.¹⁾, Găgeanu I.¹⁾, Zapciu A.²⁾, Tudor E.³⁾, Carpus E.⁴⁾, Popa L.D.⁵⁾ ¹

¹⁾INMA Bucharest / Romania; ²⁾INCDMTM / Romania; ³⁾INC DIE ICPE-CA / Romania; ⁴⁾INCDTP / Romania; ⁵⁾SCDA Secuieni / Romania

E-mail: dy.hemp420@gmail.com

DOI: <https://doi.org/10.35633/inmateh-60-14>

Keywords: *electric tractor, draft force, efficiency*

ABSTRACT

Taking into consideration the current trend to mitigate the agriculture's negative impact on the environment, this implies using new technologies and equipment for performing agricultural works. Currently, the most used equipment in agriculture is the agricultural tractor with heat engine. One alternative is represented by electric motors, usually powered by batteries. The main advantage for the environment is that zero emissions are released into the atmosphere during agricultural works. Another advantage consists of the nominal torque which could be sustained from almost zero revolutions of the electric motors resulting in lower loads on the batteries with a proper mechanical transmission. Ploughing represents the agricultural work which exploits most of the performances of an agricultural tractor, in terms of fuel consumption and engine wear. Within this paper are presented the tests performed on an electric tractor during ploughing works, at different depths and with different working speeds, in order to assess its autonomy and efficiency with a single battery charge. The electrical parameters of the tractor were recorded during tests, as well as the tractor draft force. The results were used to establish the optimal working regime of the electric tractor during ploughing works.

REZUMAT

Luând în considerare tendința actuală de atenuare a impactului negativ al agriculturii asupra mediului, aceasta implică utilizarea de noi tehnologii și echipamente pentru efectuarea lucrărilor agricole. În prezent, cel mai utilizat echipament în agricultură este tractorul agricol cu motor termic. O alternativă este reprezentată de motoarele electrice, de obicei alimentate cu baterii electrice. Principalul avantaj pentru mediu este că zero emisii sunt eliberate în atmosferă în timpul lucrărilor agricole. Un alt avantaj constă în cuplul nominal care ar putea fi susținut de la rotații aproape de zero ale motoarelor electrice, ceea ce duce la sarcini mai mici pe baterii cu o transmisie mecanică adecvată. Aratul reprezintă munca agricolă care exploatează cea mai mare parte a performanțelor unui tractor agricol, în ceea ce privește consumul de combustibil și uzura motorului. În cadrul acestei lucrări sunt prezentate testele efectuate pe un tractor electric în timpul lucrărilor de arat, la adâncimi diferite și cu viteze diferite de lucru, pentru a evalua autonomia și eficiența acestuia cu o singură încărcare a bateriei. Parametrii electrici ai tractorului au fost înregistrați în timpul încercărilor, precum și forța de tragere susținută de tractor. Rezultatele au fost utilizate la stabilirea regimurilor optime de funcționare a tractorului electric la lucrarea de arat.

INTRODUCTION

Research and innovation in the bioresources production domain using renewable and clean energy sources will allow digital agriculture to respond to the increasing nutrition needs at international level while mitigating the negative impact on the environment produced by anthropic actions. Thus, worldwide the agricultural machinery producers, especially tractors developers, started designing agricultural tractors which are using hybrid or entirely electric drive systems instead of classic heat engines (Moreda G.P. et al., 2016). The use of non-polluting energy has risen as a necessity to the international effort to reduce air, soil and water pollution. Developers of electric tractors are consecrated large firms, with many years of experience in the field (John Deere, Fendt, Escorts Group, etc.), but also start-ups having the main purpose to develop electric vehicles (Soletrac, etc.). According to <https://www.fwi.co.uk/arable/analysis-electric-technology-set-kill-off->

¹ Matache M.G., Ph.D. Eng.; Cristea M., Ph.D. Stud. Eng.; Găgeanu I., Ph.D. Stud. Eng.; Zapciu A., Ph.D. Eng.; Tudor E., Ph.D. Eng.; Carpus E., Prof. Ph.D. Eng.; Popa L.D., Ph.D. Eng.

diesel-tractors, electric tractors provide three key advantages: increased efficiency (a diesel engine converts thermal to mechanical energy with approximately 35% efficiency while electric motors have an efficiency of 90%), many more opportunities for optimal control and automation given by usage of electric power and finally, the possibility to use renewable energy. Especially for isolated farms, producing electric energy directly on site, using wind, photovoltaic solar or biodigestion energy sources and storing it (Maican A. *et al*, 2019), could be a real source for electric tractors' batteries recharge so that the diesel fuel transportation problems is avoided.

The advantages of using electric engines for tractor propulsion are multiple: zero emissions, possibility of batteries recharge from mobile stations which are using renewable energy (from wind power or photovoltaic panels), reduced noise and vibrations in exploitation, high torque for a wide range of rotating speeds, costs consumption optimization for an agricultural farm. The major disadvantage consists of the reduced autonomy together with the relatively long recharging time for classic batteries and high costs for battery replacement. Taking into consideration these aspects, the issue regarding the autonomy and efficiency of such an electric tractor used for high energy consuming agricultural works like ploughing has to be approached.

During ploughing or tilling the soil characteristics are not homogenous, fact that leads to changing soil resistance which affects the necessary torque at the wheel, forcing the driver to accelerate in order to compensate the traction power loss (Guo H. *et al.*, 2017). The amount of travel reduction ratio or slippage has to be measured in order to obtain the actual drawbar power needed for the work (Vladut D.I. *et al.*, 2018).

Xie, Zhang, Chen, Mao and Du (2015) constructed an agricultural machine endowed with an industrial DC motor and performed ploughing tests in different types of soils. The obtained results concluded that as the working depth of the plough increased, the electric motor torque oscillated with great amplitudes correlated with the soil resistance heterogeneity (Xie B. *et al.*, 2015). Thus, the research led to finding various ways to design and optimize the drive train system of such electric tractors (Xiaofei Z., 2017; We Z. *et al*, 2019).

This paper presents the results obtained during various tests performed with an experimental model electric tractor during ploughing for different working conditions. The results regarding the tractor's autonomy and transmission efficiency allowed for an optimal choice of the working regime. The paper highlights the fact that tractor with electric propulsion could achieve the same performance, if not better, than the heat engine tractor, having less negative impact on the environment.

MATERIALS AND METHODS

The experiments were conducted on a 28.8 kW experimental model of agricultural electric tractor developed by INMA Bucharest with rear wheels traction. The 17.28 kWh electric battery powering the tractor was fitted with an ORION battery management system (BMS) with possibility of recording the instantaneous power consumption during works. The advantage of the electric motor used for propelling the tractor compared to the diesel one comes from the maximum output torque, even at very low revolutions per minute. The tractor was also endowed with a mechanical transmission with 8 forward gears or reverse shift which allowed for a minimum travel speed of 1.71 km/h and maximum of 26 km/h for a nominal rotational speed of the electric motor of 2350 s⁻¹. The weight of the tractor was 1210 kg. For experiments a 2-coulter reversible plough was chosen, which was set for a working width of 0.5 m and a maximum working depth of 0.2 m.



Fig. 1 - Experimental model of electric tractor with plough mounted on

In order to measure the draft force during ploughing, several strain gauges were placed on the plough frame. The data acquisition system used during the tests for draft force recording was a QuantumX 1615 amplifier. In view of calibrating the strain gauges for draft force measurement, a calibration test was performed in laboratory using a 10 kN hydraulic cylinder which loaded the plough in longitudinal direction while fixed to a test rig which simulated the tractor three-point linkage system.

The values recorded by strain gauges for 2÷10 kN excitation forces were used to calculate the gain and offset factors which should be used in order to measure in real time the draft force necessary for the ploughing process.

We used the 3^k factorial design to prepare the experiments, a factorial arrangement with k factors, each at three levels. (Montgomery D.C., 2013). We took into consideration 2 factors: working depth and speed, each at three levels: low, intermediate, and high. So, we imposed 3 mean depths for the plough combined with three mean working speeds (calculated from the gear ratios), each experiment being replicated 3 times, resulting a number of 27 tests. In table 1 are presented the values used as the inputs of the factorial experiment.

Table 1

Factorial experiment – factor levels		
Factor Level	Working depth – a, m	Theoretical working speed – v_T , m/s
low	0.1	0.55
intermediate	0.15	1.1
high	0.2	1.6

During the experiments we measured the draft force and the real travel speed, computing afterwards the travel reduction ratio (TRR) also called slippage which is a reduction in speed due to several factors like slip between surfaces (rubber and soil), shear within soil (due to soil structure and humidity) or flexing of the tractive device (Zoz F.M., Grisso R.D., 2003).

$$TRR = 1 - \frac{v_a}{v_T}, [\%] \quad (1)$$

where: TRR – travel reduction ratio, %;
 v_a – actual working speed, m/s;
 v_T – theoretical working speed, m/s;

The drawbar power P_d necessary to drag the plough through the soil was computed as in formulae (2), while the electric power input P_e used by the motor was computed using formulae (2).

$$P_d = F_d v_a, [W] \quad (2)$$

where P_d – drawbar power, W;
 F_d – mean draft force, N;
 v_a – actual working speed, m/s.

$$P_e = UI, [W] \quad (3)$$

where P_e – electric power input, W;
 U – battery voltage, V;
 I – battery current, A.

The power delivery efficiency (PDE) of the system during ploughing was calculated as the ratio between drawbar power and electric power input used for ploughing and was used to identify an optimal set up for the transmission gear in order to optimize the ploughing work.

The ploughing testing was performed on a 16-meter-wide field with a total length of 100 meters, totalizing 0.16 ha surface.

RESULTS

During the tests were obtained draft force curves which converged to a mean value of approximately 7 kN, not taking into consideration the start and stop of the test, for the maximum ploughing depth. In Fig. 2 is presented the draft force evolution in time for a test corresponding to a maximum ploughing depth of 0.2 m and an imposed working speed of 1.1 m/s. Because of the slip ratio, the actual working speeds were lower than the theoretical ones.



Fig. 2 - Draft force evolution for 1.1 m/s and 0.2 m depth ploughing test

In table 2 are presented the mean results obtained during the tests, for each set of 3 replicas of the experiments. The soil humidity in the tests area was 16%, which is considered to be within the optimal values for ploughing.

Table 2

Experimental results obtained for draft force

Experiment no.	Working depth a, m	Actual working speed v_a , m/s	Mean draft force F_d , N	Travel reduction ratio TRR, %
1	0.10	0.50545	3822	8.1
2	0.15	0.48895	5728	11.1
3	0.2	0.4719	7527	14.2
4	0.10	0.9988	3884	9.2
5	0.15	0.9526	5801	13.4
6	0.2	0.8954	7644	16.6
7	0.10	1.4032	3926	12.3
8	0.15	1.3392	5844	16.3
9	0.2	1.2608	7789	23.2

By analysing data obtained for the travel reduction ratio and the mean draft force mean value from table 2 we observe that they are strongly correlated, with a correlation coefficient $R=0.844$, which means that the slip increases as the pull of the tractor increases up to the maximum net traction ratio of the tractor.

In fig. 3 is presented the evolution of the tractor traction ratio (draft force/tractor weight) versus travel reduction ratio obtained for the ploughing tests.

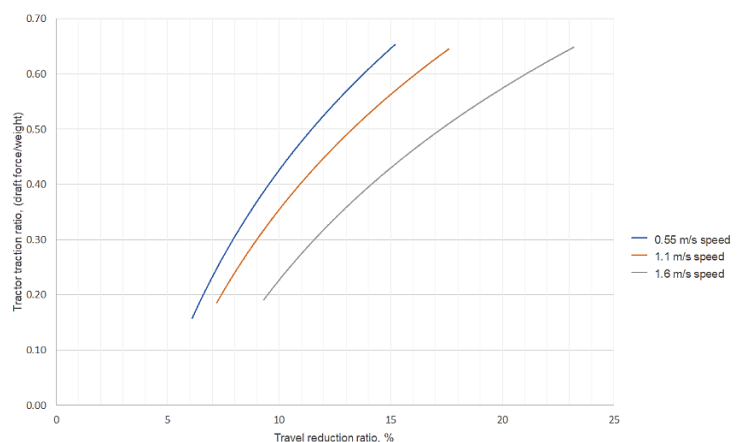


Fig. 3 - Tractor traction ratio versus travel reduction for different theoretical speeds

Looking at the diagrams in figure 3, we can notice a slight difference between the values for the first two theoretical speeds. The slip increases as the working theoretical speed increases correlated with the tractor

traction ratio. From the diagram we observe that the tractor loses traction faster at higher ploughing speeds. The maximum pull to weight ratio obtained for ploughing was 0.64, in the case corresponding to maximum working depth of 0.2 m. This value is in the same range as the one obtained for diesel engine tractors, validating the fact that the ploughing performances are similar for both types of tractors. Thus, the advantages of using electric tractors are given by the zero emissions in the atmosphere during works and a much lower costs with the fuel used, such as electricity, being much cheaper than diesel fuel, at the same tractive performances.

In figure 4 is presented the theoretical drawbar power (theoretical working speed multiplied by mean draft force) versus actual drawbar power (computed as actual working speed multiplied by mean draft force).

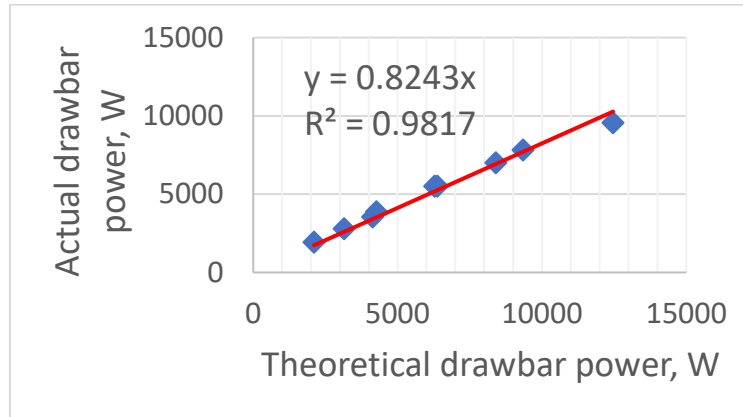


Fig. 4 - Mechanical power loss due to travel reduction ratio

In fig. 4 we observe that the power loss due to slip during ploughing is around 18%, at the same electric power consumption, fact which affects the autonomy of the electric tractor for the same ploughed surface. Thus, the purpose of this paper was to identify the working regime which minimized the losses for this particular experimental model of electric tractor. In order to do this, the power delivery efficiency was chosen as an indicator.

In table 3 are presented the results obtained by computing the experimental data corresponding to each working depth – working speed combination, previously presented in table 2, for obtaining the drawbar power and electric power input, as well as also the power delivery efficiency values. The power needed for the self-propelling of the tractor was measured separately and it was subtracted from the total electric power, so that the electric power input represents only the value used for the ploughing work.

Table 3

Power delivery efficiency for ploughing works

Experiment no.	Drawbar power P_d , W	Electric power input P_e , W	Power delivery efficiency PDE
1	1932	3454	0.55930
2	2801	4594	0.60964
3	3552	7354	0.48300
4	3879	7940	0.48858
5	5526	9702	0.56958
6	7013	12602	0.55647
7	5509	11487	0.47958
8	7826	14435	0.54217
9	9571	19147	0.49988

As shown, the power delivery efficiency values are in the same range for all the studied cases, with a slightly better situation for experiments conducted at the working depth of 0.15 m for all the working speeds and 0.2 m (maximum working depth) for the intermediate working theoretical speed of 1.1 m/s.

Table 4 shows data corresponding to the autonomy of the tractor with a single charge of the 17.28 kWh battery for each experimental case taken into consideration, based on the electric power consumption. The ploughing productivity was computed using the actual working speeds measured during experiments and the working width of 0.5 m of the plough. Also, total ploughed surface was computed as ploughing productivity multiplied by the tractor autonomy, making the hypothesis of working in a straight line, not taking into consideration the time needed to turn over the tractor at the end of the field.

Table 4

Electric tractor autonomy for ploughing works

Experiment no.	Electric power input P_e , W	Tractor autonomy, h	Ploughing productivity, ha/h	Total ploughed surface, ha
1	3454	5.00	0.09	0.46
2	4594	3.76	0.09	0.33
3	7354	2.35	0.08	0.20
4	7940	2.18	0.18	0.39
5	9702	1.78	0.17	0.31
6	12602	1.37	0.17	0.23
7	11487	1.50	0.25	0.38
8	14435	1.20	0.24	0.29
9	19147	0.90	0.22	0.20

CONCLUSIONS

The purpose of the experiments was to identify optimal working regime for a small power experimental model of agricultural tractor during ploughing works. The tractive performances measured during experiments showed that the best power delivery efficiency values bigger than 0.54 were recorded for the intermediate working depth of 0.15 m for all the working speeds, fact that suggests this is an optimum working regime. The tractor autonomy is strongly correlated with the drawbar power which affects the electric power consumption. Thus, even though the draft force is quasi-constant for the imposed working depth, having a very small deviation due to the imposed working speed, the latter has a big influence on the electric tractor behaviour. The increase in speed causes an increase in the travel reduction ratio and for this particular experimental model an exponential increase in electric power consumption.

The maximum pull to weight ratio obtained during experiments was 0.64, value similar to diesel engine tractors fact which confers feasibility to the future development of the experimental model to a prototype.

ACKNOWLEDGEMENT

This work was supported by a grant of the Romanian Research and Innovation Ministry, through Sectoral Plan, contract no. 1PS/2019 and through Programme 1 – Development of the national research-development system, subprogramme 1.2 – Institutional performance – Projects for financing excellence in RDI, contract no. 16PFE.

REFERENCES

- [1] Guo, H., Jia, T., Liu, Z. J., & Wu, M. (2017), Research on handling behaviour of tractor driver in field work. *Tractor & Farm Transporter*, 44(4), pp. 6-10;
- [2] Montgomery D.C., (2013), *Design and analysis of experiments. Eighth edition.* John Wiley & Sons Publishing House, ISBN-13: 9781118097939;
- [3] Moreda G.P., Muñoz-García M.A., Barreiro P., (2016), High voltage electrification of tractor and agricultural machinery – A review, *Energy Conversion and Management* 115, pp. 117–131;
- [4] Maican E., Vlăduț V., Vlăduț C., Sorică C., Dorian M., Mirea D.P., Bogățeanu R., (2019), Hybrid renewable energy systems for isolated farms - A review, *INMATEH – Agricultural Engineering* 59(3), pp. 77-92
- [5] Vlăduț D.I., Biriș S., Vlăduț V., Cujbescu D., Ungureanu N., Găgeanu I., (2018), Experimental researches on the working process of a seedbed preparation equipment for heavy soils, *INMATEH – Agricultural Engineering* 55(2), pp. 27-34
- [6] Wu Z., Xie B., Li Z., Chi R., Ren Z., Du Y., Inoue E., Mitsuoka M., Okayasu T., Hirai Y., (2019), Modelling and verification of driving torque management for electric tractor: Dual-mode driving intention interpretation with torque demand restriction, *Biosystems Engineering Volume* 182, pp.65 -83;
- [7] Xiaofei Z., (2017), Design Theory and Performance Analysis of Electric Tractor Drive System, *International Journal of Engineering Research & Technology (IJERT)*, pp 235–238;
- [8] Xie, B., Zhang, C., Chen, S., Mao, E. R., & Du, Y. F. (2015), Transmission performance of two-wheel drive electric tractor. *Transactions of the Chinese Society for Agricultural Machinery*, 46(6), pp. 8-13;
- [9] Zoz F.M, Grisso R.D., (2003), Traction and Tractor Performance, *Tractor Design No. 27*, Published by ASAE – the Society for engineering in agricultural, food, and biological systems 2950 Niles Road, St. Joseph, MI 49085-9659 USA;
- [10] ***<https://www.fwi.co.uk/arable/analysis-electric-technology-set-kill-off-diesel-tractors>

PERFORMANCE TEST OF THE 2BDE-2 TYPE MILLET FINE AND SMALL-AMOUNT ELECTRIC SEEDER

/ 2BDE-2 型谷子精少量电动播种机性能试验

Deng Sun, Qingliang Cui*, Yanqing Zhang, Huaming Hou¹
College of Engineering, Shanxi Agriculture University, Taigu/China
Tel: +86-0354-6288254; E-mail: qlcui@126.com
DOI: <https://doi.org/10.35633/inmateh-60-15>

Keywords: electric, seeder, millet, fine and small-amount

ABSTRACT

This work designed a 2BDE-2 type millet fine and small-amount electric seeder to solve certain problems, such as difficult cultivation and large workload of millet in hilly and mountainous areas. This seeder can finish the sowing operations, such as ditching, fine and small-amount of seed discharging, covering soil and suppressing at one time. The central composite design method was used to test the seeding performance of the seeder along with the factors of the seed metering plate amplitude and operating speed. This task was undertaken to determine the optimal working parameters of the seeder. The mathematical model of the average number of seeds in each 100 mm section and the variation coefficient of seeding uniformity were established. The influence of single factor effects and interaction on the seeding performance was also analysed. The optimum combination after parameter optimisation was determined as follows: seed metering plate amplitude of 109 μm and seeder operating speed of 0.76 m/s. The field sowing experiment was conducted according to the parameter combination. Results showed that the average number of seeds in each 100 mm section was 7.8, and the variation coefficient of seeding uniformity was 19.64%. The relative errors with the predicted values were 1.28% and 4.98%. The research can be used for sowing a small amount of millet in the hilly mountain area.

摘要

针对丘陵山区谷子播种难、间苗工作量大等问题, 本文设计了 2BDE-2 型电磁振动式谷子精少量播种机, 该机可一次性完成开沟、精少量排种、覆土和镇压等播种作业。为确定播种机最佳工作参数, 采用中心组合试验的方法, 以排种盘振幅和作业速度为因素, 对播种机进行了播种性能试验, 建立了每 100mm 区段内种子的平均粒数、播种均匀性变异系数的数学模型, 分析了单因素效应和交互作用对播种性能的影响规律。经参数优化, 确定最优组合为排种盘振幅 109 μm 、播种机作业速度 0.76m/s, 根据该参数组合进行田间播种试验验证, 得到每 100mm 区段内种子的平均粒数为 7.8 粒, 播种均匀性变异系数为 19.64%, 与预测值相对误差分别为 1.28%、4.98%。该研究可用于丘陵山区谷子精少量播种。

INTRODUCTION

Millet is a traditional food crop that originated in China. Such food crop is rich in nutrients and has high edible and medicinal value. Millet is widely planted in the arid and semi-arid hills and mountains of Asia and Africa, with small and scattered planting plots (Saleh et al., 2013; Li et al., 2018). Millet seeds are small in size and mostly sown traditionally with large sowing amount, thereby resulting in seed waste. Artificial thinning of seedlings is also required to reduce the competition amongst seedlings and ensure a stable yield; however, this process is time consuming and troublesome (Zhang et al., 2017; Zhang et al., 2014).

Many achievements have been attained in the research and development of millet seeders. Most domestic millet seeders use various mechanical seed metering devices, such as socket type, reciprocating and grooved wheel type seed metering devices. Majority of the foreign millet seeders use pneumatic seed metering devices, such as SN series air suction seeders (MFC Company, United States) and Aeromat II air blowing seeders (Baker Company, Germany). The majority of the above-mentioned seeders are large-scale machines that are unsuitable for operation in hilly and mountainous areas.

¹ Deng Sun, As. M.S. Stud. Eng.; Qingliang Cui*, Prof. Ph.D. Eng.; Yanqing Zhang, Lec.Ph.D.Eng.; Huaming Hou, Lec. Ph.D. Eng.

These seeders are also towed by fuel tractors, thereby causing large energy consumption and serious pollution (Tian et al., 2013; Tao et al., 2011). The mechanical seed metering device often experiences seed injury and jamming. Meanwhile, the pneumatic seed metering device has a complex structure and high requirements for air tightness (Li et al., 2007; Lv et al., 2018; Zheng et al., 2018). The electromagnetic vibration seed metering technology is used for seeding because of its low seed injury rate, simple structure and easy operation. A small electromagnetic vibrating wheat seeder was designed to solve the drawbacks of the traditional wheat seeder (Li et al., 2016). The influencing rule of the working performance of the electromagnetic vibration seeder for field seed raising of rice bud-seed was studied to determine the optimal working parameters (Yang et al., 2012). The use of electric agricultural machinery reduces carbon emission and noise pollution, labour intensity and field operation cost (Tao et al., 2011). Numerous scholars worldwide have also attained many achievements in the development of electric croppers for different crops. The Yazaki SYV series electric vegetable planter produced in Japan can realise multi-row sowing of various crops, such as rapeseed and Chinese cabbage. An electric planter for vegetables with small particle size was designed using the hollow-eye wheel seed metering device to reduce the labour intensity of farmers and save the production cost (Du et al., 2017). Moreover, an electric double-row carrot seeder was developed to realise mechanised carrot sowing (Wang et al., 2016). However, the electromagnetic vibration electric seeder used for sowing millet has not been reported.

Considering the difficulty in planting millet in hilly and mountainous areas, a millet fine and small-amount electric seeder was designed according to the agronomic requirements of a small amount of millet seeds, combined with the topographical features of the main production areas. Taking the seeder operating speed and the seed metering plate amplitude as factors and the average number of seeds in each 100 mm section and the variation coefficient of seeding uniformity as evaluation indices, the optimal parameter combination of the seeder is obtained by using the central combination test method. The test verification is also conducted to provide a reference for the design and parameter optimisation of the seeder with a small amount of millet.

MATERIALS AND METHODS

Test materials and equipment

The variety of millet used in the experiment is Jingu 21, with 1000 grain weight of 3.3 g and moisture content of 11.5%. Jingu 21 has a high yield and strong drought resistance. The test equipment includes 2BDE-2 type millet fine and small-amount electric seeder, hand-held vibration tester (accuracy of 1 μ m), ruler, steel tape and brush.

Overall structure and working principle

The entire machine mainly comprises various parts, such as electromagnetic vibration millet seed metering device, power transmission system, control system, battery pack (48 V/20 Ah), runner coulter, scraper type soil coverer, rack and ground and pressing wheels. The power transmission system comprises a one-stage reduction chain drive of DC reduction motor (48 V/600 W). The control system comprises two parts: speed and seed metering control systems. The speed control system mainly comprises a DC deceleration motor governor and digital display meter, whilst the seed metering control system is mainly composed of thyristor voltage regulator and inverter. Both systems are powered by a battery pack.

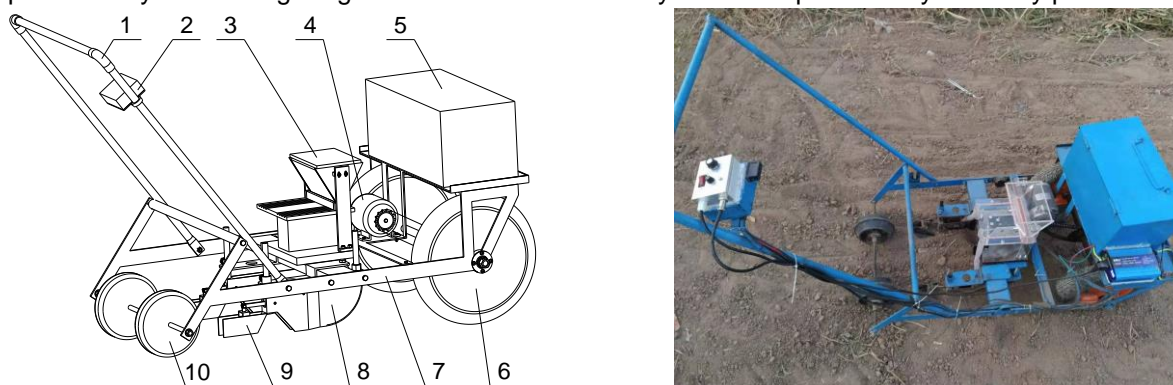


Fig. 1 - Overall structure of seeder

1 – Hand support bracket; 2 – Control system; 3 – Electromagnetic vibration type millet fine seed metering device; 4 – Power transmission system; 5 – Battery pack; 6 – Ground wheel; 7 – Rack; 8 – Runner coulter; 9 – Scraper type soil coverer; 10 – Pressing wheel

The 2BDE-2 type millet fine and small-amount electric seeder adjusts the motor speed through the speed control system and transmits the power to the ground wheel shaft to drive the planter through the first speed reduction chain drive. The seed metering plate amplitude is adjusted by the seed metering control system, and the metering device is used for metering. The seed falls into the seed ditch already opened by the opener through the seed guide tube. The soil coverer will cover the soil on both sides of the seed ditch evenly back to the original position. The pressing wheel will suppress the covered soil and complete the seeding operation. During operation, the ditch depth can be adjusted by changing the installation height of the opener thread support column in the range of 0 cm to 10 cm. The opener and coverer can be raised to the height of the bottom off the ground when transporting. The row spacing of the seeding can be adjusted by changing the distance between two sowing units. The operating speed can be adjusted to 0–1.2 m/s through the speed control system. The seed metering plate amplitude can be adjusted to 0–1 mm through the seed metering control system.

Experiment design

The preliminary test results showed that the operating speed is 0.4–1.2 m/s, and the seed metering plate amplitude is 60–140 μm . The central composite design (CCD) method was used to determine the optimal combination of the above-mentioned factors (Wang, 2012; Wang et al., 2019). The operating speed and the seed metering plate amplitude are regarded as the factors, whilst the average number of seeds in each 100 mm section and the variation coefficient of seeding uniformity are regarded as the indicators. The quadratic regression equation was established through the test, and the effects and interactive effects of every single factor were studied. Table 1 shows the corresponding relationship between the coded and the actual values of the two-factor centre combination test.

Table 1

Coding schedule of experimental factors		
Coding values	Operating speed	Seed plate amplitude
	A	B
	[m/s]	[μm]
-1.414	0.40	60
-1	0.52	72
0	0.8	80
1	1.08	128
1.414	1.2	140

Performance evaluation of seeding

The test was performed in accordance with the Chinese standard GB/T 9478-2005. The key factors affecting the seeder performance, including the operating speed and the seed metering plate amplitude, were selected in the experiment. Each row was divided lengthwise into several sections (100 mm each) during the test and the number of seeds measured in each section. Each row is continuously taken for 30 sections. The seeding performance can be evaluated by the average number of seeds in each 100 mm section and the variation coefficient of seeding uniformity. The calculation methods are presented in Formulas (1) and (2). Each group of tests is performed fivefold to reduce the test error, and the average value is considered (China National standardizing committee, 2005).

$$\bar{x} = \frac{1}{n} \sum_{i=1}^n x_i \quad (1)$$

$$a = \frac{100}{\bar{x}} \sqrt{\frac{1}{n} \sum x_i^2 - (\bar{x})^2} \quad [\%] \quad (2)$$

where: x_i is the number of seeds in section i ;

\bar{x} is the average number of seeds in each 100 mm section;

n is the total number of test sections, 30 sections;

a is the variation coefficient of seeding uniformity, [%].

RESULTS

Test results and analysis

The design requirements of the two-factor CCD method indicate that 13 groups of experiments were conducted, and each group was repeated fivefold. The mean value was taken as the test result, and the indices were calculated according to Equations (1) and (2). Table 2 shows the test results.

Table 2

The test results

NO.	Operating speed A	Seed plate amplitude B	the average number of seeds in each 100 mm section Y ₁	the variation coefficient of seeding uniformity Y ₂
	[m/s]	[μm]	/	[%]
1	0	0	6.6	19.69
2	-1	1	13.6	19.52
3	-1.414	0	12.5	22.05
4	1.414	0	4.1	25.55
5	0	0	6.7	19.07
6	-1	-1	5	26.80
7	1	1	7.5	21.34
8	1	-1	2.7	35.22
9	0	0	5.9	21.46
10	0	1.414	10.3	19.87
11	0	0	6.5	20.83
12	0	-1.414	2.6	32.66
13	0	0	6	19.16

Analysis of variance and regression model

The test results were analysed by variance, and the results are presented in Table 3. The regression models were obtained as Formulas (3) and (4). The variance analysis indicated that the quadratic regression models of the average number of seeds in each 100 mm section Y₁ and the variation coefficient of seeding uniformity Y₂ were extremely significant (P < 0.01), and the misfit terms of the regression model were insignificant (P > 0.05). The R² values of the quadratic regression equation were 0.978 and 0.969. The order of influence of the average number of seeds in each 100 mm section and the variation coefficient of seeding uniformity is as follows: the seed metering plate amplitude B > the operating speed A. The above-mentioned results show that a high correlation exists between the predicted and the actual values. Moreover, the model has a good fitting degree, which can be used to predict and analyse the effects of operating speed and seed metering plate amplitude on the average number of seeds in each 100 mm section and the variation coefficient of seeding uniformity.

$$Y_1 = 6.34 - 2.53A + 3.05B - 0.96AB + 0.94A^2 + 0.012B^2 \quad (3)$$

$$Y_2 = 20.05 + 1.9A - 4.93B - 1.67AB + 2.07A^2 + 3.3B^2 \quad (4)$$

Where:

A is the operating speed, [m/s]; B is the seed metering plate amplitude, [μm]

Y₁ is the average number of seeds in each 100mm section; Y₂ is the variation coefficient of seeding uniformity, [%].

Table3

The results of variance analysis

Item	Degree of freedom	Mean square	F Value	P Value	Item	Degree of freedom	Mean square	F Value	P Value
Model 1	5	26.97	63.51	<0.0001**	Model 2	5	65.11	43.62	<0.0001**
A	1	51.41	121.04	<0.0001**	A	1	28.84	19.32	0.0032**
B	1	73.67	173.45	<0.0001**	B	1	192.39	128.89	<0.0001**
AB	1	3.61	8.50	0.0225*	AB	1	10.89	7.30	0.0306*
A ²	1	6.09	14.34	0.0068**	A ²	1	29.68	19.88	0.0029**
B ²	1	0.001	0.002	0.9618	B ²	1	74.81	50.11	0.0002**

Note: P < 0.01 (extremely significant, **), P < 0.05 (very significant, *);
Model 1 is the average number of seeds in each 100mm section;
Model 2 is the variation coefficient of seeding uniformity.

Single factor effect analysis

1) Analysis of the influence of test factors on the average number of seeds in each 100 mm section

When the operating speed or the seed metering plate amplitude is fixed at zero level, the influencing model of every single factor can be obtained as follows:

Operating speed: $Y_{11} = 6.34 - 2.53A + 0.94A^2$

Seed metering plate amplitude: $Y_{12} = 6.34 + 3.05B + 0.012B^2$

The influencing curve of each factor is shown in Fig. 2. When other factors are fixed at the zero level, the single-factor effect curve of the operating speed is a parabola, and single factor effect of the seed metering plate amplitude is approximately a straight line. As shown in Fig. 2, the average number of seeds in each 100 mm section tends to gradually decrease with the increase in operating speed. The main reason is that the seed broadcasted in each section is thin and the number of particles is small when the operation speed is high. In the single-factor effect curve of seed metering plate amplitude, the average number of seeds in each 100 mm section increases with the seed metering plate amplitude. This phenomenon is attributed to the increase in the number of seeds falling in each section with the increase in the seed metering plate amplitude, seed rate and displacement.

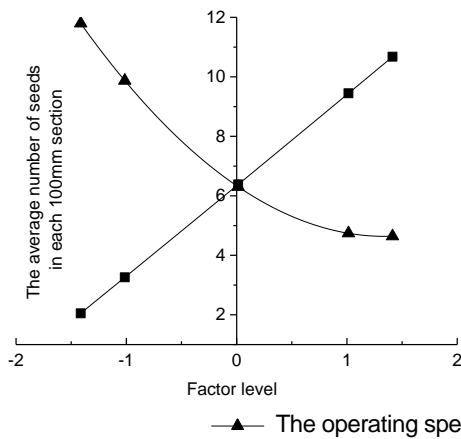


Fig. 2 - Effect of single factor on the average number of seeds in each 100mm section

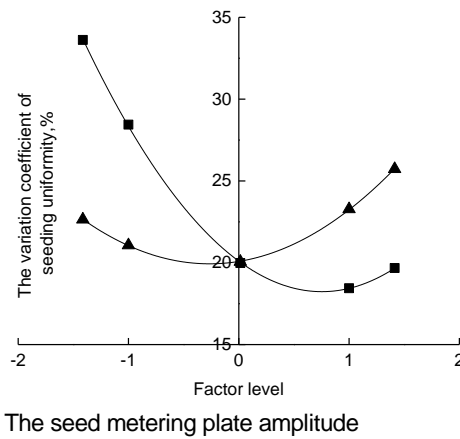


Fig. 3 - Effect of single factor on the variation coefficient of seeding uniformity

2) Analysis of the influence of experimental factors on the variation coefficient of seeding uniformity.

When the operating speed or the seed metering plate amplitude is fixed at zero level, the influence model of every single factor can be obtained as follows:

Operating speed: $Y_{21} = 20.05 + 1.9A + 2.07A^2$

Seed metering plate amplitude: $Y_{22} = 20.05 - 4.93B + 3.3B^2$

The influence curve of each factor is shown in Fig. 3. When the other factors are fixed at the zero level, the single-factor effect curves of the operating speed and the seed metering plate amplitude are parabolic. The figure shows that the parabolic extreme value of the operating speed curve is close to the zero-horizontal point, and the variation coefficient of seeding uniformity is small when the seeder operating speed is 0.8 m/s. The variation coefficient of seeding uniformity has an increasing trend when the speed is higher or lower than 0.8 m/s. This phenomenon is attributed to the easy accumulation of the planted seeds when the operating speed is <0.8 m/s. Accordingly, seeding uniformity is affected. When the operating speed is larger than 0.8 m/s, the sowing machine generates a certain degree of vibration during the operation, resulting in an increased variation coefficient of seeding uniformity. The extreme point for the one-factor effect curve of the seed metering plate amplitude is approximately near the +1 level, and the variation coefficient of seeding uniformity is firstly decreased and then increased. The main reason is that the seeding speed is small, the seed in the seed groove is sparse and the variation coefficient of seeding uniformity is large when the seed metering plate amplitude is small. When the seed metering plate amplitude is large, the seed movement mode changes from slip to throwing motion, the seeding speed increases. Such situations result in an increase in the variation coefficient of seeding uniformity.

Analysis of the influence of interaction factors on seeding performance

A 3D surface response surface map was generated according to the CCD method. The effects of operating speed A and seed metering plate amplitude B on the seeder performance were analysed according to the response surface results.

1) Analysis of the influence of test factors on the average number of seeds in each 100 mm section

The response surface of the operating speed A and the seed metering plate amplitude B to the average number of seeds in each 100 mm section is shown in Fig. 4a. The average number of seeds in each 100 mm section decreased with increased operating speed. Moreover, the average number of seeds in each 100 mm section increased with the seed metering plate amplitude.

The change of response value affected by test factors on the average number of seeds in each 100 mm section showed that the overall influence trend of test factors on the average number of seeds in each 100 mm section is as follows: the seed metering plate amplitude is relatively large, the operating speed of the seeder is comparatively small and the average number of seeds in each 100 mm section is increased. This phenomenon is attributed to the high seed metering speed and displacement when the seed metering plate amplitude is large. At this time, the seeding is concentrated, and the average number of seeds in each 100 mm section is high when the operating speed of the seeding machine is small. When the speed is high, the seeding is dispersed and the average number of seeds in each 100 mm section is reduced.

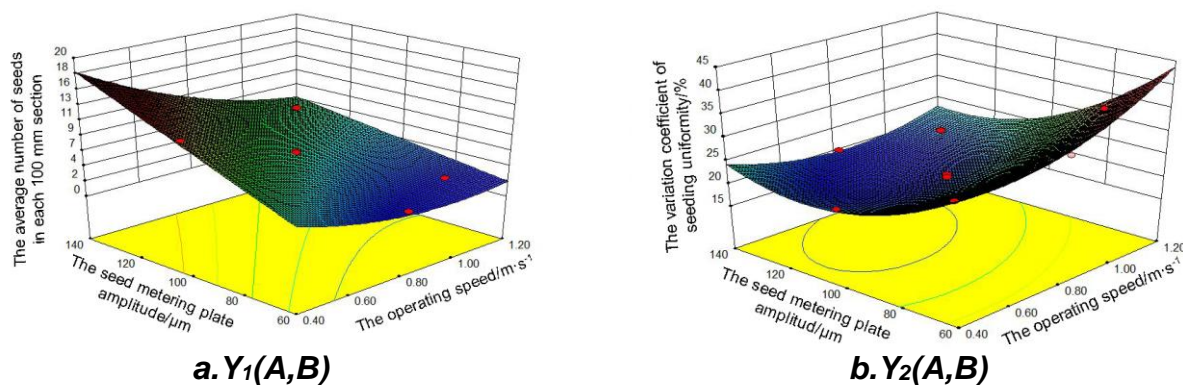


Fig. 4 - Response surface result

2) Analysis of the influence of experimental factors on the variation coefficient of seeding uniformity

The response surface of operating speed A and seed metering plate amplitude B to the variation coefficient of seeding uniformity is shown in Fig. 4b. The variation coefficient of seeding uniformity firstly decreased and then increased with the increase in operating speed. The variation coefficient of seeding uniformity gradually decreases with the increase in the seed metering plate amplitude.

The change of the response value of test factors on the variation coefficient of seeding uniformity demonstrated that the overall influence trend of the test factors on such variation coefficient is as follows: moderate operating speed, large seed metering plate amplitude, enhanced seeding uniformity and small variation coefficient. The main reasons were as follows: when the operating speed was low, seed accumulation easily occurs. The planting opportunity produces a certain degree of vibration when the operating speed is fast. Such a situation has a certain impact on seeding. When the operating speed is moderate, the planter runs smoothly, which is beneficial to planting. At this time, the seed metering plate amplitude is large, and the seeds in the planter are difficult to jam, easy to disperse and evenly distributed. Thus, the seeding uniformity is satisfactory.

Parameter optimization and validation

The agronomic requirements of millet sowing combined with those of the national standard grain planter Part 1: Technical conditions indicated that meeting the requirements of the average number of seeds (6–8) in each 100 mm section and the minimum variation coefficient of seeding uniformity is necessary to optimise the performance of the planter (Zhang et al., 2011; Ministry of Industry and Information Technology, 2013). The effect of interaction factors on the average number of seeds in each 100 mm section and the variation coefficient of seeding uniformity showed that the seeder must operate at a moderate speed and the seed metering plate amplitude must also remain moderate to attain the above-mentioned average number of seeds in each 100 mm.

The operation speed of the seeding machine is moderate and the seed metering plate amplitude is large to minimise the variation coefficient of seeding uniformity. In the range of 60–140 μm seed metering plate amplitude and 0.4–1.2 m/s seeder operating speed, the average number of seeds in each 100 mm section was set at 6–8 and the variation coefficient of seeding uniformity was also set as the minimum by using design-expert software to find the optimal parameter combination satisfying the above-mentioned objective function simultaneously. Combined with the actual situation, the optimal results are as follows: when the seed metering plate amplitude is 109 μm and the operating speed of the seeder is 0.76 m/s, the comprehensive response value of the model curved surface is optimal, the average number of seeds in each 100 mm section is 7.7 and the variation coefficient of seeding uniformity is 18.66%.

A field verification test is performed on the optimised parameter combination to test the prediction model accuracy. The seed metering plate amplitude t and the seeder operating speed are set to 109 μm and 0.76 m/s, respectively. The test is repeated fivefold, and the average value is obtained. The results showed that the average number of seeds in each 100 mm section was 7.8, and the variation coefficient of seeding uniformity was 19.64%. These findings *satisfied the technical requirements of the grain seeder in the national standard*. The relative errors of the predicted values were 1.28% and 4.98%.

CONCLUSIONS

1. The 2BDE-2 type millet fine and small-amount electric seeder designed in this work adopts the electromagnetic vibration type millet fine and small-amount seed metering device. Each parameter is easy to adjust, and its performance is stable. The seeder can be used for millet and other small seed crop fine and small-amount of sowing.

2. The quadratic regression equation of the operating speed, the seed metering plate amplitude and the average number of seeds in each 100 mm section and the variation coefficient of seeding uniformity were established through the CCD method. The variance of the test results was analysed to obtain the influence. The order of the average number of seeds in each 100 mm section and the variation coefficient of seeding uniformity is as follows: the seed metering plate amplitude $B >$ the operating speed A .

3. The CCD method is used to optimise the analysis. The optimal parameters of the planter operation are as follows: the seed metering plate amplitude is 109 μm , the operating speed is 0.76 m/s and the predicted result is the average number of seeds in each 100 mm section was 7.7 capsules. The variation coefficient of seeding uniformity was 18.66%. The field verification test was conducted under the condition that the seed metering plate amplitude was 109 μm and the operating speed was 0.76 m/s. The experimental results showed that the average number of seeds in each 100 mm section was 7.8, and the variation coefficient of seeding uniformity was 19.64%. The requirements of the national standard are met; the errors with the predicted value are 1.28% and 4.98%. This finding is consistent with the optimisation result, and the regression model is reliable.

ACKNOWLEDGEMENTS

This research titled 'Performance test of the 2BDE-2 type millet fine and small-amount electric seeder' was funded by the National Key Research and Development Plan of China(2016YFD0701801). The authors are grateful and honoured to have obtained support from the Laboratory of Key Technology and Equipment for Dry Farming Machinery.

REFERENCES

- [1] Du Z., (2017), Design and manufacture of seed planter for small grain vegetable (小粒径蔬菜电动播种机的研制), *Journal of Chinese Agricultural Mechanization*, Vol.38, Issue 11, pp.5-10, Jiangsu / P.R.C;
- [2] Li S.G., (2018), Technology Need and Prospect of Foxtail Millet Industry Development in China in the New Era(新时期中国谷子产业发展技术需求与展望), *Journal of Agriculture*, Vol.8, Issue 6, pp.96-100, Beijing / P.R.C;
- [3] Li B.J., (2003), *Agricultural Mechanics* (农业机械学), ISBN 978-7-109-08403-2, China Agriculture Press, pp.71-78, Beijing / P.R.C;
- [4] Li Y.P., (2016), Development of Small Electromagnetic Vibration Type Wheat Seeding Machine (小型电磁振动式小麦播种机的研制), *Journal of Agricultural Mechanization Research*, Vol.38, Issue 10, pp.114-117+122, Heilongjiang / P.R.C;

- [5] Lv X.R., (2018), Research and development of air-suction corn precision seed metering device. *INMATEH-Agricultural Engineering*, Vol. 56, No.3, pp.137-146, Bucharest / Romania;
- [6] Saleh A.S.M., (2013), Millet grains: nutritional quality, processing, and potential health benefits. *Comprehensive Reviews in Food Science and Food Safety*, Vol.12, Issue 3, pp. 281–295, Boston / U.S.A;
- [7] Tian C., (2013), Millet Precision Seeder Research and Development (谷子精量播种机的研究现状与开发设想), *Journal of Agricultural Mechanization Research*, Vol.35, Issue 1, pp.10-13, Heilongjiang / P.R.C;
- [8] Tao L.B., (2011), Research on Human and Electric Power Small Planter (电动播种机研究), *Journal of Hebei Institute of Architecture & Civil Engineering*, Vol.29, Issue 3, pp.42-44, Hebei, P.R.C;
- [9] Wang H., (2016), Design and test of the motor-driven double row carrot seeder(电动双行胡萝卜播种机的研制与试验), *Journal of Chinese Agricultural Mechanization*, Vol.37, Issue 6, pp.4-9, Jiangsu / P.R.C;
- [10] Wang Y.S., (2012), *Experimental design and statistical analysis*(试验设计与统计分析), ISBN 978-7-5606-2932-2, Xidian University Press, pp.47-56, Xi'an / P.R.C;
- [11] Wang S.S., (2019), Design and experimental optimization of cleaning system for peanut harvester. *INMATEH-Agricultural Engineering*, Vol. 57, No.1, pp.243-252, Bucharest / Romania;
- [12] Yang J., (2012), Optimization experiments on electromagnetic vibration seeder of rice bud-seed for field seedling raising (电磁振动式拌浆育秧水稻芽种播种机优化试验), *Transactions of the Chinese Society of Agricultural Engineering*, Vol.28, Issue 6, pp.32-38, Beijing / P.R.C;
- [13] Zhang Y.Q.,(2017), Design and test of fluid and small-amount seed metering device for foxtail millet.(谷子精少量流体排种装置的设计与试验), *Transactions of the Chinese Society of Agricultural Engineering*, Vol.33, Issue 12, pp.20-27, Beijing / P.R.C;
- [14] Zhang S.J., (2014), Analysis and Improvement of Millet Planter with Comparative (谷子播种机具的对比分析与改进) *Journal of Agricultural Mechanization Research*, Vol.36, Issue 2, pp.164-167+172, Heilongjiang / P.R.C;
- [15] Zhang D.G., (2011), Research on Mechanized Hill-drop Planting Processes for Millet (谷子机械化精少量种植工艺的研究), *Journal of Shanxi Agricultural University*, Vol.31, Issue 6, pp.563-567, Shanxi / P.R.C;
- [16] Zheng J.X., (2018), Design of shaped-hole volume-variable precision seeder. *INMATEH-Agricultural Engineering*, Vol. 56, No.3, pp.129-136, Bucharest / Romania;
- [17] ***China National standardizing committee, (2005), *Testing methods of sowing in lines*, GB/T 9478-2005, Chinese Standard Press, Beijing / P.R.C;
- [18] ***Ministry of Industry and Information Technology, (2013), *Grain drill. Part 1: Specifications*, JB/T 6274.1-2013, China Machine Press, Beijing / P.R.C.

**TECHNICAL AND TECHNOLOGICAL SOLUTIONS FOR PRODUCING FIBRE
FROM BAST CROPS**

/

**ТЕХНІКО-ТЕХНОЛОГІЧНІ РІШЕННЯ ПРОЦЕСУ ОДЕРЖАННЯ ВОЛОКНА З
ЛУБ'ЯНИХ КУЛЬТУР****Berezovsky Yu.¹⁾, Kuzmina T.¹⁾, Lialina N.,²⁾ Yedynovych M. ¹⁾, Lobov O., ¹⁾**¹⁾ Kherson National Technical University, Kherson / Ukraine;²⁾ Kyiv National University of Construction and Architecture, Kyiv / Ukraine;

Tel: +38 (099) 023-62-32; E-mail: berezov.sky.ua@gmail.com

DOI: <https://doi.org/10.35633/inmateh-60-16>**Keywords:** flax; bast raw material; cleaning; processing; method, processing device; production.**ABSTRACT**

The paper is devoted to solving problems related to developing scientific bases for resource-saving technologies in bast crops complex processing. The work contains theoretical and experimental research in processing flax and hemp raw materials.

The work objective is to find ways to improve the production conditions for processing bast fibre plants and to solve the problems of ameliorating the qualitative and quantitative bast fibre characteristics by improving the technological features of stem material processing and structural design application to the joint connections of the devices for processing bast-fibre raw materials. The paper also analyses current trends in the flax and hemp processing industry development, investigates the technical and technological features of processing bast-fibre crop stems and assesses the directions for increasing their processing efficiency.

РЕЗЮМЕ

Статтю присвячено вирішенню проблем розвитку наукових основ ресурсозберігаючих технологій комплексної переробки луб'яних культур. Стаття містить теоретичні та експериментальні дослідження в галузі переробки лляної і конопляної сировини.

Завданням роботи є пошук шляхів покращення виробничих умов переробки лубоволокнистих рослин та розв'язання питань підвищення якісних і кількісних характеристик луб'яних волокон за рахунок поліпшення технологічних особливостей обробки стеблового матеріалу і застосування конструкційних розробок вузлових з'єднань пристроїв з обробки лубоволокнистої сировини. У статті також проаналізовано сучасні тенденції розвитку переробної галузі льонарства та коноплярства, досліджено технічні і технологічні особливості процесу обробки стеблової частини лубоволокнистих культур та надано оцінку напрямкам підвищення ефективності їх переробки.

INTRODUCTION

The issue of the domestic agrarian market's modern development and functioning, which comprises both flax and hemp products market, now needs urgent consideration. Its importance is due to the significant destructive changes in the current light industry condition in Ukraine. Common flax, which in the second half of the nineteenth century was a strategic agricultural crop and the only natural fibre source in Ukraine, is now a technical plant that is little used in production. Rapid decrease in acreage from 169.4 thousand hectares in 1990 to 1.3 thousand hectares in 2018 (Ukraine's State Statistics Service), decline in flax products yield and quality, lack of effective market infrastructure, losing economic connections between different industries, as well as sales channels, significant dependence on energy resources was caused by the correspondent processes in the specified field, which resulted in losing Ukrainian raw materials base for light and textile industry with flax and hemp producers unable to provide the domestic market with the raw materials and high-quality fabrics and other necessary products from bast plants, and with leading positions in foreign markets lost (Prymachuk T.Yu. *at. al.*, 2017; Chekhova I.V. *at. al.*, 2017). The decline in domestic flax and hemp production industries came to Ukraine immediately after the decrease in textile production.

Among all agricultural crops, bast plants are most difficult to process, with seeds and straw or retted straw obtained after harvesting, further formed into bales or rolls.

The fibre production efficiency under modern conditions cannot be ensured without using machines with low metal and energy consumption (*Rudyk R.I. et al., 2015*). At the same time, the lack of specialized machines, produced in Ukraine, required for harvesting and post-harvest operations, equipment for the primary bast plant processing and the foreign equipment's high cost do not contribute to the industry's re-equipment to the latest technologies. The low processing enterprises efficiency now allows obtaining only 20-30% of scutched flax fibre from the total flax amount produced (*Prymachuk T.Yu. et al., 2017*), and lacking flax factories for processing raw materials into commodity products forced the flax producers to seek raw material consumers abroad.

The flax and hemp production industry still has sufficient potential and opportunities for stabilization and further development, first of all, due to favourable soil and climatic conditions, availability of, albeit outdated, material and technical processing base in possible bast crops growing areas, relevant local population's professional skills in bast production. Under certain investment attraction conditions and introducing innovative technologies the industry will acquire considerable potential, which will help to increase the domestic raw materials competitiveness, leading to flax and hemp production revival, stable Ukrainian economy development and the rural population's well-being.

Therefore, it should be noted that an important relevant issue for today is the revival and stabilization of domestic flax and hemp production, which can be achieved by introducing latest high-efficiency and energy-saving technologies, using modern scientific developments and design inventions, increasing the yield capacity, improving the quality which will ensure economic efficiency of domestic fibre-containing plants production and processing, developing with appropriate subsidies the undeveloped agricultural regions, improving economic relations between market agents.

MATERIALS AND METHODS

Theory and practice of enterprises' technical re-equipment, technological machinery modernization, applying modern effective equipment for processing bast raw materials, which are considered in scientific sources (*Helyazetdinov R.N., 2009; Tikhosova H.A., 2011*) give reason to state that nowadays, in order to overcome crisis phenomena in the Ukrainian light industry and to obtain positive results in processing flax and hemp stem material, it is necessary to use innovative solutions to the processing-related problems taking into account these industrial crops' specific physical and mechanical properties, changing consumer market demand for environmentally friendly and safe products, modern high-tech innovations, new mechanisms design specificity for processing bast raw materials.

Based on the conducted theoretical and experimental research, the inefficiency in using traditional processing technology for domestic bast crops with the use of heavy, metal-intensive and energy-consuming equipment, as well as the inappropriate use of existing technological machinery has been determined. The analysis of technical and technological directions for development, considered in scientific works (*Helyazetdinov R.N., 2009; Berezovsky Yu.V., 2014*), indicates that equipment of various functional purpose should be used to obtain high quality fibre mass.

Currently, relevant discussions are underway and scientific bases are being established to develop advanced technologies for processing stem bast material, to design high-performance technological equipment or its nodal components, and to work on the prospects for their industrial implementation, which in general can have a positive effect on improving the qualitative and quantitative values of performance indicators. So far, developing and implementing advanced bast processing technologies with the use of effective components and nodes of the breaking and scutching unit parts, which, due to innovations, can significantly improve separating and clearing the fibre from processed material non-fibrous part.

In the countries of the Eurasian continent there is a growing demand for bast plants constituents, which are increasingly demanded in various industries due to the development of advanced processing technologies for the respective industrial crops. Currently, EU plant producers are making extensive use of plant biological resources in the high-tech automotive, aviation and construction industries that serve as a driving power for other industries. Due to the increasing needs for flax and hemp plant components, the cultivation area is increasing, which creates the necessary prerequisites for preserving the environment and expanding the society greening by creating a clean safe product with a high natural component content. Therefore, the efficient and rational use of natural resources in the context of limited financial capacity and lacking wide raw material range is currently unsolved and urgent.

Previously, many specialists were involved in bast crop manufacturing and using their valuable properties, but so far, universal methods for obtaining natural fibre have not been invented, and equipment used at industrial enterprises requires modernization, as it is energy and metal-intensive and includes numerous components, which reduces its effectiveness and the flax and hemp production profitability (Helyazetdinov R.N., 2009; Berezovsky Yu.V., 2016).

In recent years, there are 3 areas in Ukraine where common flax cultivation continues in small areas – Zhytomyr, Sumy, and Chernihiv regions, whose farming enterprises harvest it at an average yield of 6.3 c/ha. The cultivation structure shows that common flax was cultivated in the forest-steppe zone and Polissia from 2012 to 2014, and oilseed flax was cultivated in all zones, with the Steppe zone prevailing (Rudyk R.I. et al., 2015; Prymachuk T. Yu. et al., 2017) (Fig. 1).

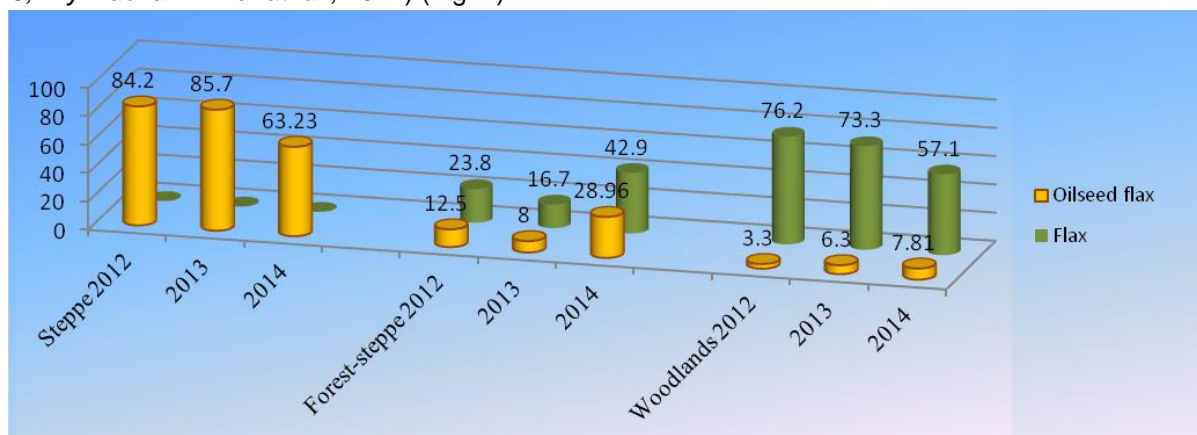


Fig. 1 – Flax cultivation structure within Ukrainian natural and climatic zones for the period 2012 - 2014 (constructed according to the Ukrainian State Statistics Service)

Over the last decade in Ukraine, areas under common flax have been gradually converted to the oilseed flax cultivation, the seeds containing 45-55% oil (Agronews.Ua, 2017). Comparing the oilseed flax production in Ukraine and in the world, the opposite trends can be noticed: the decline in Ukraine, the growth in the world. Flax production is not intensive, Ukraine's share in the world flax seeds production is only 2% with the amount of 40-60 thousand tons annually (Ilkiv L.A., 2018; Bakertilly.Ua, 2017; RosFlaxHemp.RU, 2017), and its share in the flax fibre production is negligible. As a consequence, flax is not an attractive crop for farmers and is sown inconsistently (Fig. 2).



Fig. 2 – Oilseed flax production in Ukraine, 2011-2019

Obviously, to increase the flax production profitability, it is necessary to use flax straw to produce at least fuel briquettes or pellets. The next step should be the fibre production from stem material, which requires larger long-term investments.

In the meantime, existing flax processing enterprises are idle due to the lack of raw materials while flax straw in the southern regions is either plowed or burned in the fields. World flax seed production is between 1.6 and 2 million tons annually.

Kazakhstan has become the world's leading oilseed flax producer in 2018, planting 1103 thousand hectares, Russia – 744 thousand hectares, and Canada – 358 thousand hectares, accounting for about 34% of the world's gross harvest (*AgroPortal.Ua., 2018*). The largest flax seed importers are the USA, China, Germany and the Netherlands.

In the import structure, the United States and China occupy 70% of the world market. Due to the globalization and economic growth in South and Southeast Asia countries, flax seed consumption in these regions is forecasted to increase significantly in the coming years.

In such a situation, the state's indifference towards the domestic fibre production and the absence of a realistic plan for the flax and hemp production development leads to further decline in the bast fibre crop primary processing, which increases the likelihood for this industry disappearance and increases the costs of light industry producers for the procurement of natural fibre raw materials.

As oilseed flax differs from common flax by anatomic and physico-technological properties, processing oilseed flax stem material by the technology used for common flax is not possible (*Holovenko T.M., 2013*), although its processing can use similar processing techniques – breaking, scutching, shaking with various features of the technological equipment structural design and its application procedure.

Due to this, oilseed flax processing is carried out by the technology for obtaining monotypic fibre. Various methods and devices are used for the monotypic fibre production, the characteristic feature being their designation for shives processing and not being adapted for retted straw direct processing. During the breaking process, the wood destruction is carried out, the connection between fibres and wood is broken, and shives are partially separated (*Valko P.M., 2011*). This operation is the preparation for the further fibre clearing from shives in the production line scutching part to obtain monotypic fibre.

In traditional production conditions, monotypic fibre is obtained by a method that includes drying retted straw to reach a 12% moisture content, forming a dried retted straw layer, its breaking and shaking on a shaking machine, re-breaking and batting a thinned layer of raw material, drying to a 6-8% moisture content and finishing on a tow preparing machine (*Tikhosova HA, 2011*). In this way, monotypic fibre is obtained, similar to the common short type, separated from shives. The disadvantage behind this method is the large number of operations performed and not sufficient line productivity; it also implies high equipment metal and energy-consumption. In some developed technological lines, disintegrator and advanced flax processing machines are used for the processing of oriented and entangled straw and retted straw stems of common flax and oilseed flax with different maturation degrees, crossed hemp stems, shives, short flax fibres, hemp, flax and hemp tow of high and low linear density. However, these innovations require the complete equipment replacement at existing plants, the line performance is quite low with limited differentiation of the impact on the fibre, which affects the finished product quality. In addition, the breaking and shive removing mechanism on the flax processing machine is not disclosed, so the problem related to choosing the equipment that can be used for machining bast raw materials remains unsolved.

At present, scanty raw materials volumes available at the bast crop primary processing plants, outdated equipment and stem material processing technologies, which no longer meet the modern production requirements, are still used. Domestic manufacturers are simply unable to buy high-performance overseas processing lines for bast fibre material. With the increase in demand for organic products for processing various domestic bast raw materials, new measures and technological equipment for its processing are to be developed (*Berezovsky Yu.V., 2013*). Under these conditions, the development of the flax and hemp production industry potential through introducing innovative technologies in agricultural, processing and industrial production should become a priority. The broad innovation involvement in this field should provide a comprehensive approach to solving industry problems. More efficient bast crop stem processing requires improved breaking and scutching processes.

In previous decades, the industrial capacity of domestic primary processing enterprises was mainly focused on processing common flax retted straw to produce a significant long fibre percentage. Nowadays, with the cottonization technology spreading, the production priorities in flax and hemp industry have changed significantly towards stem material processing in order to obtain monotypic fibre, which could be used to receive mixtures with fibres of different origin - natural, artificial, and synthetic. Monotypic fibre can be used not only for textile production by traditional technologies, but also for producing cellulose, cotton wool and the

like. The technological process for obtaining monotypic fibre made it possible to accelerate flax retted straw processing, to avoid the need for fibre distribution processes, which reduced production costs.

According to the results obtained due to the scientific, technical and patent sources analysis, experimental and theoretical studies at Kherson National Technical University, a method for obtaining monotypic fibre and a device for its implementation were developed (Berezovsky Yu.V., 2016), which allows to obtain flax and hemp fibre with low content of shives and non-fibrous impurities, improve processing equipment performance.

The results of experimental and theoretical studies of production processes for obtaining processing products show that the studied mechanical methods for processing bast raw materials are based on using different approaches to the fibre production. The most common foreign fibre producers' approaches are applying basic mechanical effects on the processed bast raw material to the processed material by the low-destructive action of breaking stem material and the maximum scutching process efficiency. The concept and practice of domestic bast fibre plant processing is to perform another significant mechanical impact on the processing material. The devices used cannot effectively break the connections between the wood and the fibre of bast raw materials, do not provide sufficient separation of the stem wood part from the fibrous one, will not allow to efficiently clean the fibre from wood and other non-fibrous impurities, which in general has a negative impact on the entire unit efficiency for processing bast crop stems.

In order to achieve higher productivity and effective separation of shives and other impurities from the fibre, researchers have often tried to apply techniques such as shaking, vibration, drawing, scraping and layer thinning (Helyazetdinov R.N., 2009; Valko P.M., 2011). Developments based on the technologies proposed to improve the conditions for the cleaning and separation of flax fibre and other bast crops have not been able to sufficiently ensure that the retted straw treatment is improved and that its versatility is guaranteed. The positive aspects in different approaches to the bast raw material processing should be fundamental in developing new construction elements, methods and processing technologies that can ensure the innovative products manufacturing.

Therefore, the basis for the new development was the task of creating a method for obtaining a monotypic fibre from domestic bast crops, in which due to technological features it would be possible to obtain a fibre with a high degree of cleaning from shives and other non-fibrous impurities.

The set task is solved in a way that involves unwinding rolls on unwinding machine, breaking with rollers with simultaneous drawing, scutching, and final cleaning the fibre from shives on tow shaker. During the breaking with rollers the raw flax is arranged, simultaneously carrying out the scraping, thinning of the raw material layer by the stripping rollers of bar, disk, comb type in complex interaction with the shaking-vibration device, which is placed between the breaking and scutching processes, carried out by simultaneous action of beater bars and scutching drum blades. Implementing complex interaction of the stripping rollers of bar, disk, and comb type within breaking process with shaking-vibration device of the shaking process, which is placed between the breaking and scutching processes after arrangement, breaking bast raw material layer allows for preliminary cleaning from shives and other non-fibrous impurities, which helps to remove free shives formed during the material passage through the breaking machine (Berezovsky Yu.V., 2016).

The essence of the presented development is explained in Fig. 3, which shows a flow diagram of a process for obtaining monotypic fibre from bast-fibre crops. The technological scheme uses the following equipment: an unwinding machine 1, if necessary, a drying machine 2, a spiked mechanism 3, a breaking machine 5 with a pair of rollers of enlarged diameter 4 and a set of rollers of various types, a shaker 6 for primary cleaning with a vibration device, scutching units 7 and shakers 8 equipped with a vibration device (Berezovsky Yu.V., 2016; Berezovsky Yu.V., 2017).

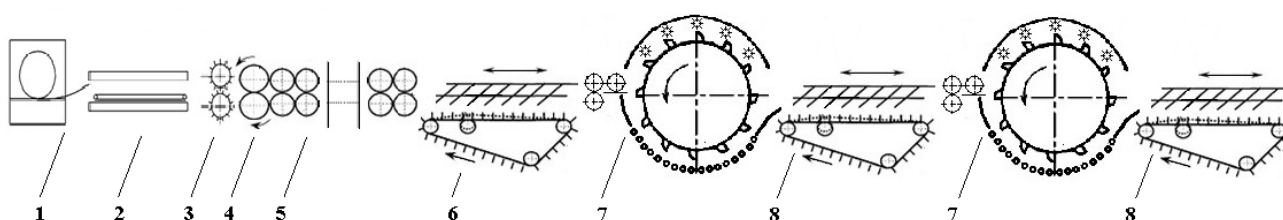


Fig. 3 – Process flow diagram for obtaining monotypic fibre from bast-fibre crops

1 – unwinding machine; 2 – drying machine; 3 – spiked mechanism; 4 – pair of rollers of enlarged diameter; 5 – breaking machine; 6 – shaker for primary cleaning with a vibration device; 7 – scutching units; 8 – shakers equipped with a vibration device

The process of producing monotypic fibre from bast-fibre crops is carried out as follows. Bast-fibre raw material after unwinding rolls on unwinding machine 1 is passed, if necessary, to a drying machine 2, then by means of a spiked mechanism 3 is fed to the first pair of rollers of enlarged diameter 4 of breaking machine 5, which provides efficient drawing of stems with different physical and mechanical properties and passes the raw material to the breaking machine 5 rollers of various types, where parallelization takes place, arranging raw flax stems, intensive breaking with simultaneous drawing, scraping, and thinning of the raw material layer which is sent to the shaker 6 for primary cleaning from shives and other non-fibrous impurities equipped with a vibration device. The raw material, beaten and partially cleaned from shives is fed to the scutching unit 7, where an intensive process of separating bulk containing shives and other non-fibrous impurities takes place. Depending on the bast raw material type, its condition and quality, it is possible to adjust the gaps between the beater bars and scutching blades and between the grid and the scutching drum at unit 7. For the final cleaning from shive residues and other non-fibrous impurities, the fibre mass from the scutching unit 7 goes to the vibration machine 8 equipped with a vibration device for the final cleaning of the fibre from shives and impurities.

RESULTS

The developed method for obtaining monotypic fibre from bast-fibre crops and the device for its implementation allows to provide versatility of bast crop stem processing through processing different types of domestic bast-fibre raw materials and to increase the processing equipment productivity. Using the above method for obtaining monotypic fibre from bast-fibre crops and the device for its implementation allows increasing the efficiency of destructing residual bonds between wood and beaten bast raw material fibre, separating fibre from shives and other non-fibrous impurities, increasing the productivity of processing bast raw materials.

The developed device's breaking part includes a number of breaking rollers of various designs (*Berezovsky Yu.V., 2014; Berezovsky Yu.V., 2016; Berezovsky Yu.V., 2017*), which, due to their structural features, provide improvement of conditions for separating shives from fibre mass and bast-fibre raw material contraction by 3-5% in comparison with traditional technological equipment used at domestic processing enterprises:

- flattening rollers, presenting a hollow cylinder, along the entire length of which, in a circle with constant pitch, one-sided set profile depressions are made, the lateral sides having a convex rather steep surface;
- corrugated breaking rollers of slope riffling with a larger curvature radius of the ruffle edge relative to the curvature radius of the ruffle edge of the steep riffling corrugated breaking rollers;
- rollers, presenting a shaft with fixed disks mounted on it, installed at an equal distance between them, with unilateral bends at the edges made in a circle with a constant pitch, and bushings placed between the disks, with unilateral bends across the entire bends' height having unilateral protrusions in the form of corrugations of a slope or steep set riffling profile with a constant pitch in a circle;
- stripping rollers of bar or rotor with rifles type, which are made with an increase in their diameters by 3-10% relative to the diameters of the breaking rollers between which they are located and are rotatable with angular velocity equal to other rollers, given by their kinematics;
- rollers, presenting a hollow cylinder, with generatrices lines having ruffles of slope and steep profile, while along the tops of the roller ruffles micro-ruffles of steep corrugation are placed, with tight brushes being placed above and below the pair formed by them;
- rollers of steep riffling having ridge profile contour of the ruffles and a relatively small ruffle height in comparison with their pitch;
- rollers of a bar type with a speed difference between them, the first pair of rollers having an enlarged diameter, providing a uniform gap between the roller profiles.

The design features specific for these breaking rollers allow to ensure the parallelization, retted straw stems ordering between themselves within the raw material layer being drawn, to improve the efficiency of the conditions of destruction and weakening the connection between the fibrous part of the stem and the wood due to the transverse compression processes in those stem parts that were not subjected to the effect of transverse compression when passing through the first pair of breaking part's flattening rollers.

These rollers make it possible to create conditions for numerous areas of shear force or shear stress, which facilitates the processes of bending-breaking and fibre separation from wood due to the occurrence of fracture to the lengths less than critical, increasing the roller surface adhesion coefficient with the bast crop stems. During their action, the fibre breaking and separation from the wood is improved due to simultaneous transverse compression processes, stem wood bending-breaking, sliding bending and shives shifting in relation to fibre, drawing, scraping and thinning of the material layer. Breaking process in the developed breaking unit is carried out more softly and effectively without considerable damage to fibre while providing the necessary load on the stem material.

To implement the developed method for obtaining monotypic fibre from the bast-fibre crops a scutching unit is used (Fig. 4), comprising a scutching drum, having beater bars on it, and scutching blades above them, and a grid, located under the scutching drum, the beater bars having wavy profile in cross-section, and their working edge made by cutting at a blunt angle in relation to the movement direction of the bars, with the profile of each bar offset relative to the profile of the adjacent bars by halfway of a wave, and on the top, on the surface of scutching blades a protrusion is made in the form of a ridge, while inside the scutching unit above the scutching drum, bar rollers, rotatable on axes, are mounted. The grid is designed to move in relation to the scutching drum to adjust the gap between the grid and the scutching drum, which breaks the residual bonds between the wood and the fibre, separating fibre from shives, allows providing more effective conditions for breaking the residual bonds between the wood and beaten bast raw material fibre, cleaning fibre from shives and other non-fibrous impurities. The presented scutching unit model allows improving the efficiency of the scutching process with the possibility for obtaining cleaner fibrous mass by 4-5% compared with the technological equipment currently used in domestic light industry.

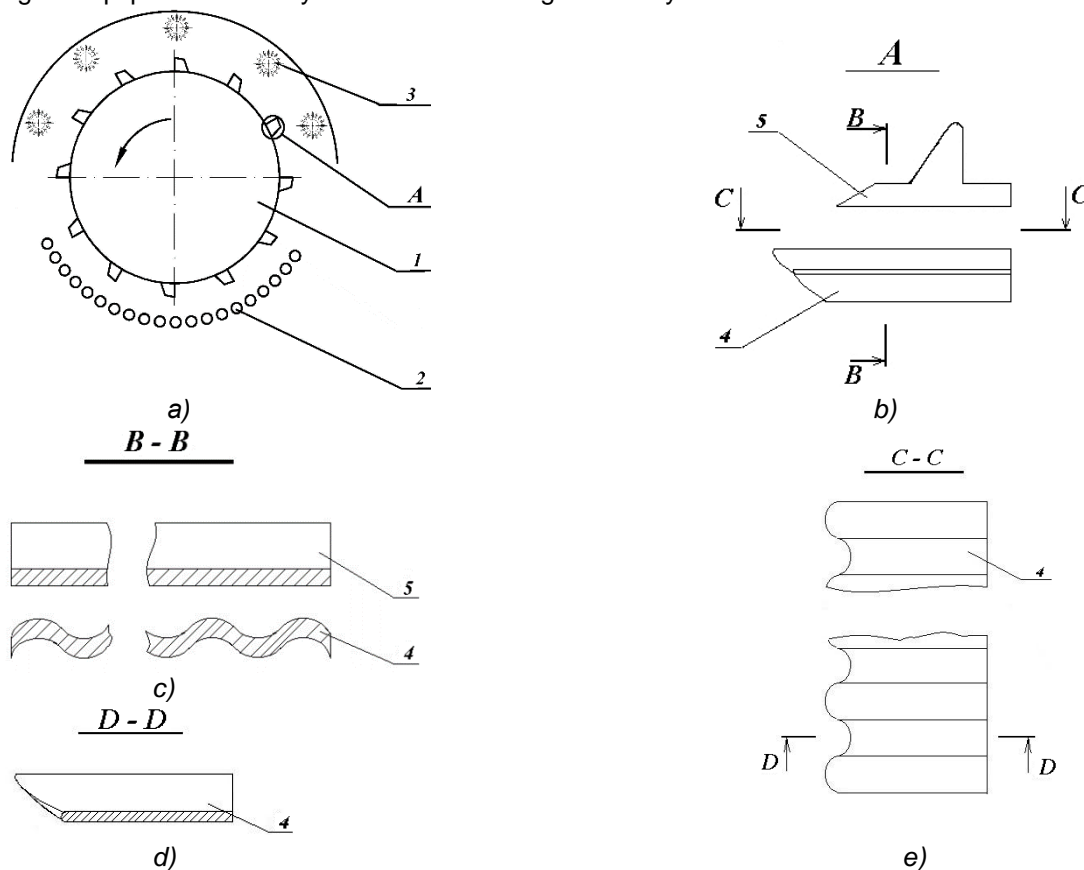


Fig. 4 – Scutching unit design

a – top view, b – section view of the beater bars and scutching blades; c – cross section of the beater bar and the scutching knife; d – beater bar top view; e – beater bar cross section; 1 – scutching drum; 2 – grid; 3 – bar roller; 4 – beater bar; 5 – scutching blade

The application after scutching beaten and pre-cleaned material on the shaking machine equipped with a vibration device allows additional shaking and cleaning of the fibre mass from shives and other non-fibrous impurities. Due to the oscillations of the needle feeder vibrating under the influence of the vibrating device, an intensive separation of the residual shives occurs, which significantly improves fibre purification.

The process of bast raw material double treatment with a scutching unit and shakers equipped with a vibrating device, provides the most effective cleaning of fibre mass from shives and other non-fibrous impurities.

The presented technical and technological solutions allow improving the efficiency of shives removal, obtaining high quality fibre with low content of non-fibrous impurities, which at the end of the manufacturing process gives the opportunity to obtain better fibre and in larger amount, and therefore the possibility for expanding its further application scope. This was confirmed by the conducted research on common flax and oilseed flax processing at the Starosambirskyi Flax Plant, and the research on hemp was carried out within the study samples. The developed device due to the structural features of its parts provides effective conditions for breaking the connections between wood and fibre of bast raw materials, sufficient separation of the stem wood part from the fibrous one and increase in the degree of fibre cleaning from foreign impurities, which in general has a positive effect on the efficiency of all technological equipment for processing bast crops stems. Using this device should provide greater processing capabilities for different types of domestic bast-fibre raw materials, which increases the versatility and productivity of processing equipment in general.

Taking into account the conditions of rapid increase in the cost of energy and other material resources, according to the above method for processing bast crop stems, fibre was produced not by increasing energy and material costs, but by improving and optimizing technological processes that would ensure high product quality. Under these conditions, production and procurement costs are significantly reduced, the costs associated with the fibre distribution in the production process, which have a positive effect on the economic component of processing bast material. This allows to significantly simplify the technological processes of harvesting flax retted straw by reducing the number of harvesting equipment and to increase its productivity in further primary processing, to comprehensively mechanize both harvesting and primary processing processes, as well as to increase the equipment productivity by 40÷50%, to reduce the shives content in fibre to 3-5%, reduce the equipment's metal consumption to 20%, energy consumption – up to 30%, improve working conditions and general production culture. These figures may vary depending on raw material type and its initial condition.

In order to ensure stable qualitative indicators of processing bast fibre raw materials, it is further necessary to investigate the change of the fibre's physical and mechanical properties in processing stem material, to determine the impact on it of equipment structural modifications to develop an adequate production process model for obtaining fibre products with forecasting its optimal parameters, which will provide appropriate recommendations for industrial applications.

The fibre obtained as a result of using the proposed innovative technical and technological solutions, allows to implement in-depth processing of domestic bast-fibre plants, to expand the product range based on them, to use it in various fields of application, to stimulate farmers to cultivate flax and hemp and to carry out their primary processing, to enhance their role as leading technical crops. All of the above can lead to improved living conditions in rural areas and a reduction in the dependence of the national economy on raw material import, which can save the country's foreign exchange reserves for relevant purposes. Prospects for using the presented technical and technological developments can contribute to the modernization of the light industry processing sector, its further development, and Ukrainian market expansion, increasing job opportunities and attracting highly qualified specialists to the correspondent sphere, improving the competitiveness of domestic products in the world market.

CONCLUSIONS

In order to increase the efficiency of fibrous material treatment processes, a method for processing oilseed flax has been developed, which allows to expand the product range from processing oilseed flax retted straw and to create waste-free technology. Also, a method for obtaining monotypic fibre from bast-fibre crops has been developed, which makes it possible to process all types of domestic bast crops, providing its versatility, reducing the equipment's metal and energy intensity. The device for its implementation allows to effectively separate fibre from wood and other non-fibrous impurities, and increases the processing equipment productivity.

The indicated developments are able to increase the flax and hemp product competitiveness by improving its quality and reducing production costs. The innovative component of the proposed technical and technological solutions for flax and hemp processing gives the opportunity to manufacture products with new consumer and functional properties, extending the application scope, increasing its attractiveness and

competitiveness due to decreasing the shives content in fibre to 3-5%, reducing equipment energy intensity to 30% and increasing its productivity by 40÷50%.

The presented methods for raw material processing and structural design of elements and units of the technological process for obtaining monotypic fibre from bast-fibre crops provide an opportunity to solve the problem of different domestic bast-fibre raw materials industrial processing, which increases the versatility of the technological processing scheme by improving the efficiency of the purification of bast raw materials due to improving the conditions of residual connections destruction between wood and fibre, cleaning fibre from shives and other non-fibrous impurities. Within industrial use, it can have a positive impact on the production and economic performance of flax and hemp processing enterprises by producing high quality natural fibre in larger amounts.

REFERENCES

- [1] Berezovsky Yu.V., (2013), Theoretical aspects in flax and flax-containing commodities eco-branding in Ukraine (Теоретичні аспекти розвитку екобрендингу лляних та льоновмісних товарів в Україні), *Commodity research and innovation*, Issue 5, pp. 24-33, Donetsk / Ukraine;
- [2] Berezovsky Yu.V., (2014), Applying new technical decisions in flax production (Застосування нових технічних рішень у виробництві лляної продукції), *Kherson National Technical University Bulletin*, № 4 (51), pp. 51-58, Kherson / Ukraine;
- [3] Berezovsky Yu.V., (2016), Applying new technical decisions in the industrial flax production (Використання нових технічних рішень у промисловому виробництві лляної продукції), *Science and innovation*, Vol. 12, № 4, pp. 53-70, Kiev / Ukraine;
- [4] Berezovsky Yu.V., (2016), *Method of producing monotypic bast crop fibre and device for its implementation (Спосіб одержання однотипного волокна з лубоволокнистих культур і пристрій для його здійснення)*, Ukraine's Patent № 113090;
- [5] Berezovsky Yu.V., (2017), Technical solution for processing flax raw materials (Технічні рішення процесу переробки лляної сировини), *Science and innovation*, Vol. 13, № 3, pp.25-37, Kyiv/Ukraine;
- [6] Chekhova I.V., Chekhov S.A., Shkurko M.P., (2017), Domestic flax market (Вітчизняний ринок льону), *Ukrainian Economy*, № 1 (662), pp. 52-63, Kyiv / Ukraine;
- [7] Flax cultivation: traditional crafts revival (Льонарство: відродження традиційного промислу). *Bakertilly.Ua*. URL: <http://www.bakertilly.ua/news/id1182>. Last accessed: 17.10.2019, Kyiv / Ukraine;
- [8] Helyazetdinov R.N., (2009), *Developing scientific bases for creating innovative technology of primary bast crops processing (Розвиток наукових основ створення інноваційних технологій первинної переробки луб'яних культур)*: diss. Doctor of Technical Sciences, 255 p., Kherson / Ukraine;
- [9] Holovenko T.M., (2013), *Processing technology development for oilseed flax retted straw to produce nonwoven materials (Розроблення технології переробки стебел трести льону олійного з метою одержання нетканих матеріалів)*: diss. PhD in Technical Sciences, 226 p., Kherson/Ukraine;
- [10] Ilkiv L.A., (2018), Flax production modern state and efficiency (Сучасний стан та ефективність виробництва льону), *Young Scientist*, № 12 (64), pp. 614-618, Kherson / Ukraine;
- [11] Prymachuk T.Yu., Shtanko T.A., Kovalov V.B., (2017), Flax Industry Development in Ukraine (Розвиток галузі льонарства в Україні), *Agrarian Science Bulletin*, №7, pp. 68-75, Kiev / Ukraine;
- [12] Rudyk R.I., Kovalov V.B., Prymachuk T.Yu., (2015), Prospects for flax cultivation in Zhytomyr region (Перспективи розвитку льонарства на Житомирщині), *Institute of Agriculture Polesie NAAS of Ukraine*, 25 p., Zhytomyr / Ukraine;
- [13] Tikhosova H.A., (2011), *Developing scientific basis for primary oil flax fibre processing (Розвиток наукових основ технологій первинної переробки волокон льону олійного)*: diss. Doctor of Technical Sciences, 358 p., Kherson / Ukraine;
- [14] Valko P.M., (2011), *Improving the scutching flax fibre technology using cleaning rolls (Удосконалення технології одержання тіпаного лляного волокна з використанням очищувальних валків)*: diss. PhD in Technical Sciences, 179 p., Kherson / Ukraine;
- [15] ***Features and prospects of flax growing (Особливості та перспективи вирощування льону), *Agronews.Ua*. URL: <https://agronews.ua/node/77788>. Last accessed: 19.09.2019, Kyiv / Ukraine;
- [16] ***Flax production in Ukraine (Производство льна на Украине), *RosFlaxHemp.RU* URL: <https://www.rosflaxhemp.ru/fakti-i-cifri/spravochne-materiali.html/id/1819>. Last accessed: 20.09.2019;

- [17] ***Opinion: Ukraine is dropping out the world flax market due to reduced production (Думка: Україна випадає зі світового ринку льону через скорочення виробництва), *AgroPortal.Ua*. URL: <http://agroportal.ua/ua/news/rastenievodstvo/mnenie-ukraina-vypadaet-iz-mirovogo-rynka-lna-izza-sokrashcheniya-proizvodstva/#>. Last accessed: 22.10.2019;
- [18] ***State Statistics Service of Ukraine, (2018), URL: <http://www.ukrstat.gov.ua>.

OPTIMIZATION OF PROCESS PARAMETERS OF PELLETIZER FOR AGROPYRON SEEDS UNDER VIBRATION FORCE FIELD

振动力场作用下冰草种子丸粒化包衣机工艺参数优化

Zhanfeng Hou, Yi Qiu, Zhi Chen¹⁾, Haiyang Liu, Fang Guo, Longkai Mi

Inner Mongolia Agricultural University, College of Mechanical and Electrical Engineering, Inner Mongolia, China

Tel: 04714309215; Corresponding author E-mail address: sgchenzhi@imau.edu.cn

DOI: <https://doi.org/10.35633/inmateh-60-17>

Keywords: Pelleting; Agropyron seed; Coating machine; Single seed rate; Design-Expert

ABSTRACT

In order to solve the poor pelleting quality of Agropyron seeds, this paper designs a novel pelleting experimental platform. A regression mathematical model of pelleting qualified rate and single seed rate was established and analysed by variance. The results showed that vibration had significant effect on pelleting quality. The order of influence is as follows: rotating speed > vibration frequency > tilt angle of coater. When the speed is 41.7 r/min, the vibration frequency is 20.28 Hz, and the tilt angle is 34.89°, the pelleting qualified rate and the single seed rate are the highest, 83.1% and 94.9% respectively.

摘要

针对冰草种子丸化包衣品质较差等问题, 该文设计了新型丸化包衣实验平台。建立冰草种子丸化合格率、单籽率的回归数学模型并进行方差分析。结果表明: 振动对冰草种子的丸化合格率和单籽率有显著效果, 影响冰草种子丸化合格率和单籽率的主次要因素为: 包衣锅转速 > 包衣锅振动频率 > 包衣锅倾角; 当包衣锅转速为 41.7 r/min、包衣锅振动频率 20.28 Hz、包衣锅倾角 34.89° 时, 丸化合格率和单籽率分别达到最高, 分别为 83.1% 和 94.9%。

INTRODUCTION

In recent years, the area of degraded grassland in the Inner Mongolia has accounted for 31.77% of the total grassland area. The degradation of grassland results in a significant reduction of production and ecological functions, which affects the normal growth of vegetation (Gui, 2012; Hang, 2012). Seed pelleting is the key technique to guarantee the germination rate and survival rate of the seeds after sowing (Andrew, 2016). Therefore, it is of great significance to study the pelleting equipment and technology for the restoration and reconstruction of degraded grassland vegetation (Shen, 2016). American scientists Thornton and Ganulee first put forward the problem of seed coating in 1926, until the 1980s, the technology of pelleted seed coating in developed countries was basically mature (Ge, 2016; Masoume, 2012). However, the research on pelleting technology in China started late. Since 1990s, the pelleting of tobacco seeds was studied (Han, 2018). Junhao Mei et al. studied pelleting of rice seeds in 2000 (Wu, 2017). Although China's pelleting technology has made some progress, there is still a big gap compared with developed countries, especially in forage grass seed pelleting technology where there are more problems. In this paper, the two-regression orthogonal test and response surface methodology are used to study the pelleting technology and optimize the parameters of the novel pelleting equipment. The results can provide technical reference for solving the problem of poor pelleting quality of Agropyron seeds.

MATERIALS AND METHODS

Pelleting machine and working principle

The pelletizer for Agropyron seed is shown in Fig. 1. When the machine is working, seeds and powder are lifted up to the seed hopper 18 and the powder hopper 1 respectively. The seed coating agent is mixed in a certain proportion, and is pumped to the atomizer by the high-pressure pump 8. When seeds pass through the seed diffuser plate 16, they are arranged in sequence. It is preliminarily mixed with seed coating agent to make the liquid film form on the surface of the seed. The seeds after film formation fall into the coater 14, and the powder is sprayed into the coater 14. The coater 14 starts to rotate under the drive of the motor 11. Meanwhile, the electric vibrator 13 changes the magnitude of the exciting force by adjusting the frequency of the converter, and applies the exciting force to the spindle of the coater 14, and then transfers the vibration to the coater 14. After pelleting, the seeds are poured into the discharge port 12 to complete the whole process.

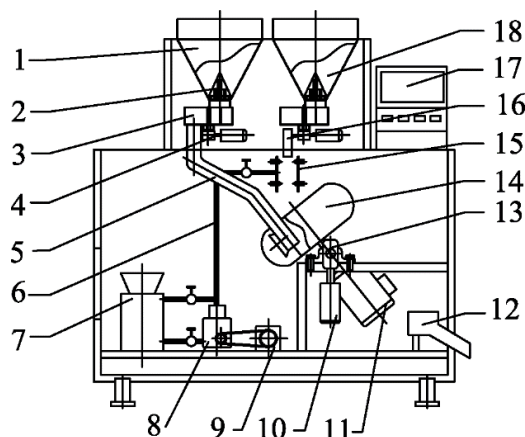


Fig. 1 - Schematic diagram of overall structure of pelletizer for Agropyron seeds

1. Powder feed inlet 2. Feed inlet valve 3. Weighing system 4. Step motor 5. Powder conveying pipeline 6. Liquid medicine pipe
7. Liquid medicine storage tank 8. High pressure pump 9. Motor 10. Rotary stepper motor 11. Coater motor 12. Outlet port
13. Electric vibration exciter 14. Coater 15. Nozzles 16. Seed diffuser plate 17. Controller 18. Seed feed inlet

Experiment materials

Agropyron seeds grown under natural conditions were selected as test objects. The shape is shuttle shape, the length is 6~7 mm and the 1000 grain mass was 2.4 g. Carboxymethyl cellulose and polyvinyl alcohol were used as seed coating agents. The blend of diatomite, bentonite and talcum powder were used as coating powder (Liu, 2020).

The Agropyron seed mass was 200 g and the powder mass was 1000 g (diatomite 400 g, bentonite 400 g, talcum powder 200 g). The adhesive mass was 60 g (Carboxymethyl cellulose 6 g, polyvinyl alcohol 3 g, water 51 g).

Test response parameters

According to People's Republic of China industry standard (JB/T 7730-2011) on seed coating machine test method (Wang, 2017). The percentage of seed coating agent completely covered on the surface of Agropyron seeds in the total number of pelleted seeds as pelleting qualified rate (J). The percentage of single pelleted seed in the total number of pelleted seeds is called single seed rate (P). The formula is as follows:

$$J = \frac{Z_h}{Z_b + Z_h} \times 100\% \quad (1)$$

$$P = \frac{D_d}{D_d + D_f} \times 100\% \quad (2)$$

where: J is the pelleting qualified rate, [%];

Z_h - the number of particles fully coated for Agropyron seeds, [-];

Z_b - the number of particles that are not fully coated on the seed surface, [-];

P - single seed rate, [%];

D_d - the number of single seed in the total of pelleted seeds, [-];

D_f - the number of Multi-seeds in the total of pelleted seeds, [-].

Single factor test results and discussion

Effect of vibration frequency on the pelleting quality

The coater speed is set at 30 r/min, the tilt angle of the coater is adjusted to 45° and the amplitude of the coater is 2 mm. The vibration frequencies are set at 10, 15, 20, 25, and 30 Hz, respectively, and pelleting experiment is performed. The relation between vibration frequency of coater and pelleting qualified rate and single seed rate was obtained, see Fig. 2.

In Fig. 2, when the vibration frequency is 10-30 Hz, the qualified rate and the single seed rate of the pelleting seeds are increased first and then decreased with the increase of vibration frequency. When the vibration frequency is 20 Hz, the qualified rate and the single seed rate of Agropyron seed pellets are the highest. Therefore, when the vibration frequency is 20Hz, it is the best frequency of the coating machine.

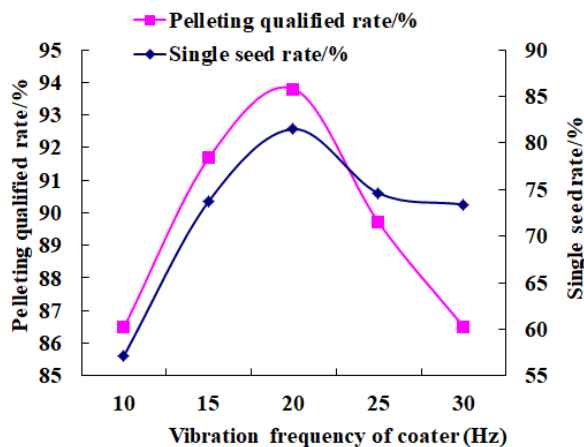


Fig. 2 - Effect of vibration frequency on the pelleting quality

The effect of coater rotating speed on the pelleting quality

When the vibration frequencies are set at 0 and 20 Hz, the angle of coater is 45°, the amplitude is 2 mm, the rotating speed is adjusted to 30, 35, 40, 45, 50 r/min respectively, the seed pelleting qualified rate and single seed rate test are conducted. The relation between rotating speed and pelleting qualified rate and single seed rate was obtained under the action of vibration or no vibration, see Fig. 3.

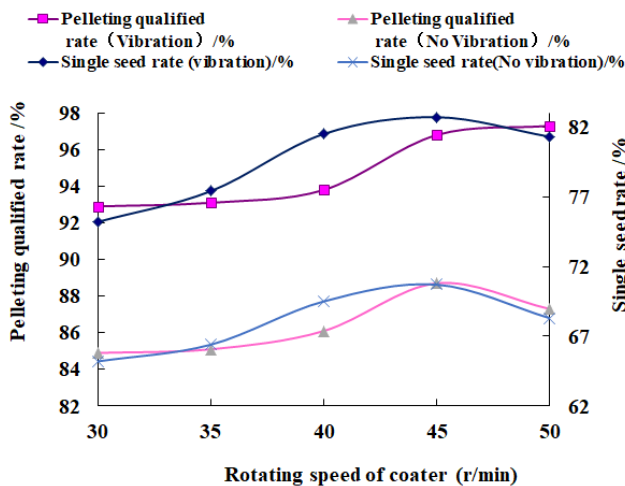


Fig. 3 - Effect of coater rotating speed on the quality of pelleting

The pelleting qualified rate and single seed rate under no vibration were significantly lower than with vibration. Therefore, this paper only discussed the pelleting qualified rate and single seed rate under vibration. When the rotating speed of the coater was 30~45 r/min, pelleting qualified rate and single seed rate gradually increased with the increase of rotating speed. As the rotating speed was 45~50 r/min, the pelleting qualified rate and single seed rate gradually decreased with the increase of rotating speed. It can be concluded that when the rotating speed of the coater is 45 r/min, the single seed rate and the qualified rate of pelleting were the highest.

The effect of coater tilt angle on the pelleting quality

The vibration frequency was set at 0 and 20 Hz respectively, the speed was 40 r/min, the amplitude was 2 mm, and the tilt angle was adjusted to 25, 30, 35, 40 and 45 ° respectively. Experimental study on pelletization of Agropyron seeds was conducted. The relation between coater tilt angle and the pelleting qualified rate and the single seed rate was obtained under the action of vibration or no vibration (Fig. 4).

In Fig.4, the pelleting qualified rate and single seed rate without vibration are significantly lower than with vibration. When the tilt angle is 25~35°, the single seed rate increases with the increase of the tilt angle. When the coater tilt angle is 35~45°, the single seed rate decreases with the increase of the tilt angle. When the coater tilt angle is 25~40°, with the increase of the tilt angle, the qualified rate increases. When the tilt angle of coater is 40~45°, with the increase of the tilt angle, the qualified rate increases. It can be concluded that the best single seed rate can be obtained when the tilt angle of the coater is 35°, and the best pelleting qualified rate can be obtained when the tilt angle of the coater is 40° under vibration.

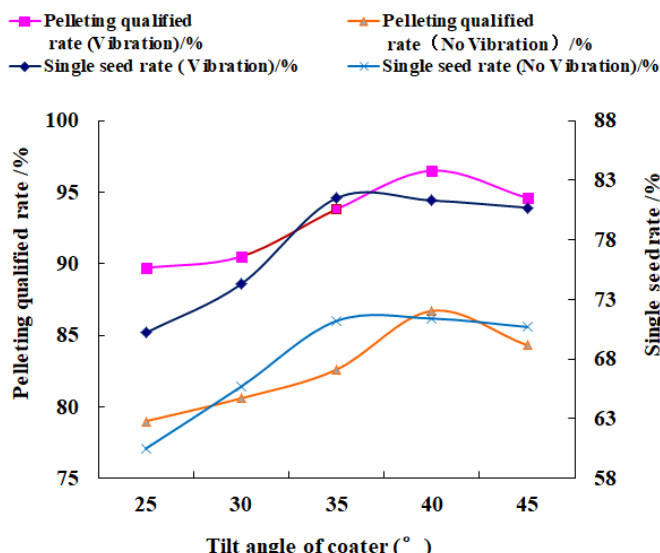


Fig. 4 - Effect of coater tilt angle on the pelleting quality

Orthogonal test results and discussion

The pelleting qualified rate and single seed rate were taken as the test performance index. Taking rotating speed, vibration frequency and coater tilt angle as experimental factors, 3 factors and 3 level orthogonal experiments were conducted (Chi, 2015). According to the single factor test results, the best parameter was selected by two-regression orthogonal test coding, and the factor level encoding was shown in Table 1. Two-regression orthogonal statistical results were shown in Table 2.

Factors and levels encoding table

Table 1

Level	Coater rotating speed	Coater vibration frequency	Coater tilt angle
	A [$r \cdot \text{min}^{-1}$]	B [Hz]	C [°]
1	30	15	30
0	40	20	35
-1	50	25	40

Two-regression orthogonal test scheme and experimental results

Table 2

Test No.	Coater rotating speed	Coater vibration frequency	Coater tilt angle	Single seed rate	Pelleting qualified rate
	A [$r \cdot \text{min}^{-1}$]	B [Hz]	C [°]	[%]	[%]
1	1	-1	0	73.9	93.4
2	0	1	1	83.2	95.8
3	1	0	1	74.1	93.5
4	-1	0	-1	72.1	92.3
5	0	0	0	84.1	96.1
6	1	0	-1	74.2	92.2
7	0	0	0	78.5	93.1
8	0	-1	1	77.2	92.5
9	-1	-1	0	82.5	95.1
10	0	1	-1	72.4	92.4
11	0	-1	-1	83.6	96.5
12	0	0	0	72.6	92.5
13	-1	1	0	74.8	92.8
14	0	0	0	82.8	95.8
15	0	0	0	72.2	92.3
16	1	1	0	74.1	92.1
17	-1	0	1	73.1	92.1

Analysis of pelleting qualified rate

Variance analysis of pelleting qualified rate

According to table 2, two-regression method was applied to analyse pelleting qualified rate. At the same time, Design-Expert was used to analyse variance (see Table 3), and regression mathematical model was established.

$$J = 95.86 + 0.43A + 0.16B - 0.14C + 0.075AB - 0.025AC - 0.05BC - 1.43A^2 - 1.91B^2 - 1.55C^2 \quad (3)$$

where: A is the coater rotating speed, [r/min]; B is coater vibrational frequency, [Hz];

C is the coater tilt angle, [°].

The absolute value of each factor in the model determines the influence degree on the pelleting qualified rate. Therefore, the influence of each factor on the pelleting qualified rate is: A , B , C , that is, the coater rotating speed > the coater vibration frequency > the coater tilt angle.

Table 3

Variance analysis of test result of pelleting qualified rate

Origin	Squares	Df	SD	F Value	P Value
Mode	39.837	9	4.426	22.70	0.0002
A	1.445	1	1.445	7.413	0.0297
B	0.211	1	0.211	1.084	0.3325
C	0.151	1	0.151	0.776	0.4076
A•B	0.022	1	0.022	0.115	0.7440
A•C	0.002	1	0.002	0.013	0.9130
B•C	0.010	1	0.010	0.051	0.8273
A ²	8.610	1	8.610	44.17	0.0003
B ²	15.280	1	15.280	78.38	< 0.0001
C ²	10.181	1	10.181	52.23	0.0002
Residual	1.365	7	0.195		
Lack of Fit	0.313	3	0.104	0.396	0.7636
Pure Error	1.052	4	0.263		
R ²	0.9669				
Adequate Precision	11.362				

Note: DF is degree of freedom. SD is standard deviation. F value is the statistical verification value. P value is a parameter used to determine the result of hypothesis test.

From table 3, it can be seen that the F value of the model is 22.71 and the P value is less than 0.01. The P value of the model is very significant and the Lack of fit is not obvious. It is proved that the regression equation (3) has high accuracy with the actual results. Therefore, this model can be used to analyse and predict pelleting qualified rate.

Surface analysis of pelleting qualified rate

According to the regression mathematical model (3), the response surface of the rotating speed, the tilt angle and the vibration frequency of the coater to pelleting qualified rate is obtained (Fig. 5).

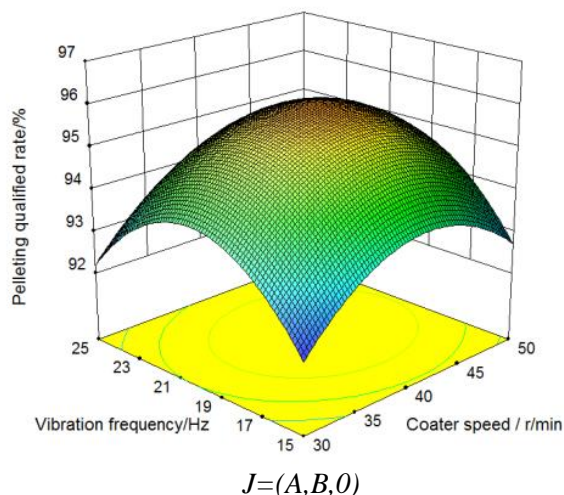


Fig. 5 - Response surface of coater rotating speed to pelleting qualified rate

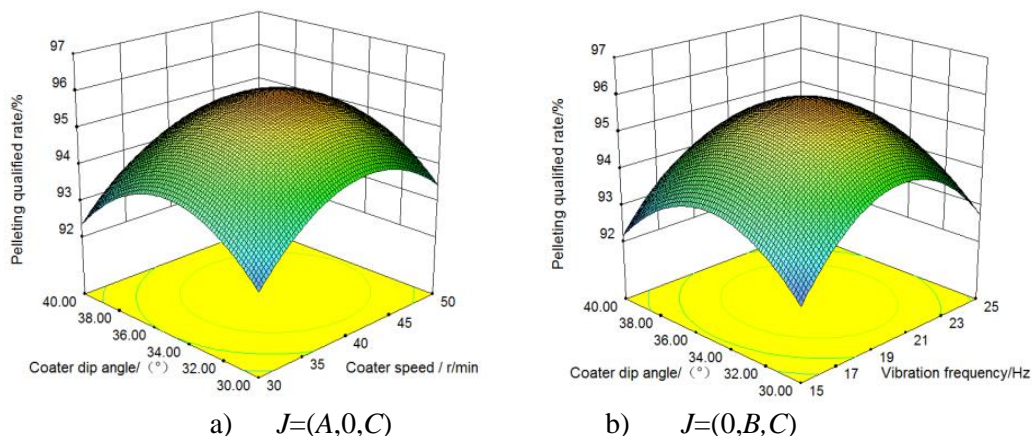


Fig. 6 - Response surface of vibration frequency and coater tilt angle to pelleting qualified rate

Fig. 5 and fig. 6 show that with the increase of each factor, the pelleting qualified rate increases first and then decreases. As the rotating speed increases, seed peristalsis in coater increases. When the speed increases to a certain extent, the seed is stationary with respect to the coater under the action of friction, thereby affecting the pelleting qualified rate. However, when the coater tilt angle is too large, the seed rotates with the coater, resulting in poor pelleting quality. Because the coater tilt angle is too large, most of the seeds basically fall at the bottom of the coater. The seed peristalsis effect is not good, resulting in a low pelleting qualified rate. In addition, vibration can increase the peristalsis of the seed in the coater, but the vibration intensity is too large, and the impact between the seeds is too large, resulting in a decrease in the pelleting qualified rate.

Single seed rate analysis

Analysis of single seed rate variance

According to the two-regression orthogonal test scheme and experimental data in Table 2, the single seed rate was analysed by two-regression methods (see Table 4) and the regression mathematical model was established simultaneously.

$$P = 83.24 + 1.61A + 0.36B - 0.025C + 0.75AB - 0.075AC - 0.27BC - 4.14A^2 - 3.55B^2 - 6.02C^2 \quad (4)$$

where: *A* is the coater rotating speed, [r/min]; *B* is the vibrational frequency of coater, [Hz]; *C* is the tilt angle of coater, [°].

Table 4

Variance analysis of test results of single seed rate

Origin	Squares	Df	SD	F Value	P Value
Mode	332.613	9.000	36.9570	36.41	< 0.0001
A	20.801	1.000	20.801	20.49	0.0027
B	1.051	1.000	1.051	1.036	0.3427
C	0.005	1.000	0.005	0.005	0.9460
A*B	2.250	1.000	2.250	2.217	0.1801
A*C	0.022	1	0.022	0.022	0.8858
B*C	0.303	1	0.303	0.298	0.6021
A ²	72.341	1	72.341	71.27	< 0.0001
B ²	52.914	1	52.914	52.13	0.0002
C ²	152.591	1	152.591	150.3	< 0.0001
Residual	7.1045	7	1.01492		
Lack of Fit	5.493	3	1.831	4.543	0.0889
Pure Error	1.612	4	0.403		
R ²	0.9791				
Adequate Precision	15.307				

The absolute value of each factor in the model determines the influence degree on the single seed rate. Therefore, the influence of each factor on the pelleting qualified rate is: *A*, *B*, *C*, that is, coater rotating speed > coater vibration frequency > coater tilt angle.

Single seed rate surface analysis

According to the regression mathematical model (4), the response surface of rotating speed, tilt angle and vibration frequency of the coater to the single seed rate can be obtained, as shown in Fig. 7.

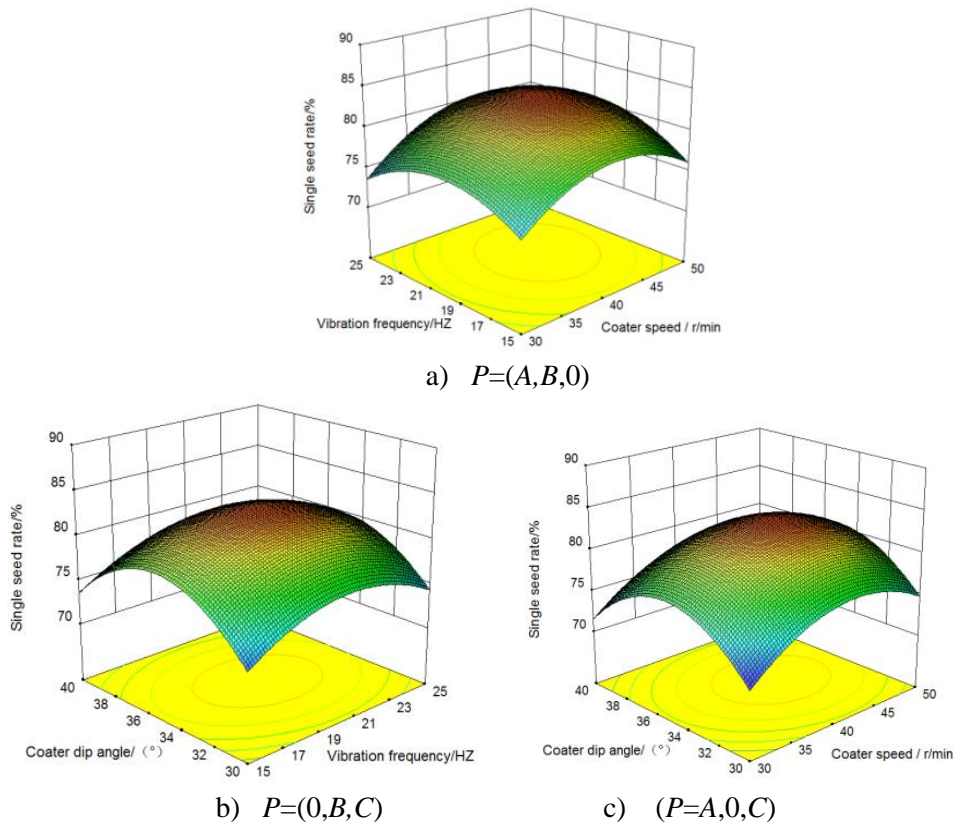


Fig. 7 - Response surface of coater rotating speed, vibration frequency and tilt angle to single seed rate

Fig. 7 shows the response surface of each of the two factors to the single seed rate. The analysis shows that with the increase of each factor, the single seed rate increases first and then decreases. As the coater rotating speed increases, the peristalsis of the seed in the coater increases, so the probability of mixing the multi-seeds is reduced. When the rotating speed continues to increase, the peristaltic effect of the seed is reduced by the centrifugal force. The single seed rate was reduced. Besides, when the vibration is added, the single seed rate can be increased. However, when the vibration frequency is too large, the powder wrapped on the surface of the seed easily falls off and settles at the bottom of the coater, resulting in a decrease of single seed rate. As the tilt angle of coater increases, the pelleting qualified rate increases first and then decreases. When the coater angle is too small, the path of the seed rotating with the coater is long, and falls when reaching a higher height in the coater. Since the coater tilt angle is too small, the seed movement path is long, and the seed falls directly from the top to the bottom of the coater to generate a large collision force, so that the powder coated on the surface of the seed falls off under the action of the collision force. The seeds are re-bonded together under the action of the agent, resulting in a decrease in the single seed rate. When the tilt angle of coater is too large, the trajectory of the seed along the coater is small, basically at the bottom of coater, the seed peristalsis effect is not good, and the powder cannot uniformly enter the seed group, resulting in a low single seed rate.

Optimization and test verification

According to the multivariate two-regression equation fitting factor and response value, Design-Expert software was used to get the best parameters.

$$\left\{ \begin{array}{l} MaxJ \\ MaxP \\ 30 \leq A \leq 50 \\ 15 \leq B \leq 25 \\ 30 \leq C \leq 40 \end{array} \right. \quad (4)$$

After the analysis of Design-Expert software, when A=41.74, B=20.28, C=34.89, the optimum value is obtained. That is, when the rotating speed of coating is 41.7 r/min, the vibration frequency of coater is 20.28 Hz, and the coater tilt angle is 34.89°, the pelleting qualified rate is 95.8% and the single seed rate is 83.4%.

CONCLUSIONS

1) Pelleting qualified rate and the single seed rate of Agropyron seeds were significantly increased by introducing vibration.

2) Response surface methodology was applied to analyse the test results. The primary and secondary factors affecting the qualified rate and single seed rate of Agropyron seed pellets were determined as follows: coater rotating speed, coater vibration frequency and coater tilt angle. When coater rotating speed is 41.7 r/min, coater vibration frequency is 20.28 Hz and the coater tilt angle is 34.89°, the pelleting effect and the single seed rate are the best.

3) The optimization results are verified by experiments, and they are basically consistent with the experimental results. The single seed rate and pelleting qualified rate were 83.1% and 94.9% respectively.

ACKNOWLEDGEMENTS

We acknowledge that this work was financially supported by National Natural Science Foundation Project "Research on soil wind erosion monitoring system based on wireless sensor network and its key technologies (41361058)" and "Research on seed pelleting parameters and coating mechanism under the vibration force field (2018MS05023)".

REFERENCES

- [1] Andrew L., Todd E., King Y., Kingsley W., David J., (2016), Flash flaming effectively removes appendages and improves the seed coating potential of grass florets. *Restoration Ecology*, Vol. 24, Issue S2, pp. S98-S105, University of Western Australia / Australia;
- [2] Chi Q., (2015), Experimental design and statistical analysis[M]. *Chongqing University press*, pp. 280-282, Chongqing / China;
- [3] Ge J., Gan D., Meng S., (2016), The research status of seed coating and the necessity of implementing good agricultural practices. *Seed*, Vol 35, Issue 2, pp. 45-49, Beijing/China;
- [4] Gui H., Wuren Q., (2012), Characteristics of *Leymus chinensis* community under different extent of degradation in Hulun Buir Grassland. *Journal of Southern Agriculture*, Vol.43, Issue 12, pp.2035-2039, Inner Mongolia / China;
- [5] Han B., Chen K., Lv X., Lu D., Tang Y., (2018), Development status and existing problems of seed pelletizing coating equipment at home and abroad. *Journal of Chinese agricultural mechanization*, Vol. 39, Issue 11, pp.51-55, Jiangsu / China;
- [6] Hang Y., Sun J., (2012), *Leymus Chinensis* grassland improvements (Review). *Acta Agrestia Sinica*, Vol.20, Issue 4, pp.603-608, Hulun Buir/China;
- [7] Liu J., Zhang X., Jin X., Yang X., Yang L., (2020), Effects of fertilization and seed coating formula on the growth of grass seedlings in sandy land. *Resources and environment in arid area*, Vol. 34, Issue 2, pp.148-153, Hulunbuir / China;
- [8] Masoume A., Anil N. Huang W., Taylor A.G., (2016), Investigation of Soy Protein–based Biostimulant Seed Coating for Broccoli Seedling and Plant Growth Enhancement. *HortScience*, Vol. 51, Issue 9, pp.1121-1126, Cornell University / USA;
- [9] Shen H., Zhu Y., Zhao X., Geng X., Gao S., Fang J., (2016), Analysis of current grassland resources in China (in Chinese). *Chin Sci Bull*, Vol 61, Issue 2, pp.139–154, Inner Mongolia/China;
- [10] Wang J., Xie H., Hu Z., Hu L., Peng B., Liu M., (2017), Parameter optimization on mechanical coating processing of rotary table-roller coating machine for peanut seeds. *Transactions of the Chinese Society of Agricultural Engineering*, Vol 33, Issue 7, pp. 43 – 50, Jiangsu / China;
- [11] Wu F., Zhang H., Xie H., Wang J., Qiu C., (2017), Overview and development of seed coating machine in China [J]. *China Journal of agricultural machinery chemistry*, Vol. 38, Issue 10, pp.116-120, Nanjing / Jiangsu.

EVALUATION OF AN AUTOMATIC CONTROL SYSTEM WITH DRIP IRRIGATION SYSTEM SHOWING POOR HYDRAULIC PERFORMANCE

/

تقييم نظام تحكم أوتوماتيكي مع نظام ري بالتنقيط ذو أداء هيدروليكي ضعيف

Moataz Elnemr

Department of Agricultural Engineering, Faculty of Agriculture, Damietta University / Egypt

Tel: +201062084800; E-mail: moknemr@du.edu.eg

DOI: <https://doi.org/10.35633/inmateh-60-18>

Keywords: automatic control, closed-loop, evaluation, drip irrigation, poor hydraulic performance, real-time

ABSTRACT

A field experiment was conducted with the purpose of testing and evaluating the use of a closed-loop, real-time control system which was developed by (Elnemr M.K., 2017) for application to a poor hydraulic performance drip irrigation system with sandy loam soil cultivated with cucumber crop. This control system collects soil moisture data through three sensors distributed along each third of the lateral. The control system was based on calculating the average soil moisture content (MC) of the three readings and using it as an indicator to start or stop irrigation process according to the requirements of the plant. The control system will start the pump after the depletion of allowed MC percentage of available water which is one of the required inputs to operate the control system. The irrigation process continues until reaching the field capacity (FC) value. The study compared two management methods for the irrigation system. First one was using the proposed control system (Au_m) and the other one was manual operation based on calculating water requirement from climatic data (Cl_m). Using the proposed control system led to increase cucumber crop production by 23.8% of Cl_m productivity. The control system led to save water and seasonal irrigation time. This led to increase water productivity and energy use efficiency of Au_m if compared to Cl_m by 41.71% and 110% respectively. Despite the added cost to the irrigation system because of the control system, the benefit/cost ratio for Au_m was higher by 24.39% due to the decrease in energy and labour costs in addition to the increase in crop production. The study recommended using the researched control system with drip irrigation systems which show poor hydraulic performance to reduce negative effects on crop production and to reach more efficient use for both water and energy with keeping the opportunity to increase benefit/cost ratio. Further studies should be done on the system with drip irrigation system that work under acceptable ranges of hydraulic performance. Also, further studies should be done to investigate the most effective and suitable distribution of the sensors along lateral.

ملخص

تم اجراء تجربة حقلية بغرض اختبار وتقييم استخدام نظام تحكم أوتوماتيكي من نوع الحلقة المغلقة والوقت الحقيقي تم تطويره بواسطة النمر (2017) للتطبيق على نظام ري بالتنقيط ذو أداء هيدروليكي ضعيف في تربة رملية لومية مزروعة بمحصول الخيار. يقوم النظام بتجميع بيانات المحتوى الرطوبي للتربة من خلال توزيع ثلاث حساسات للرطوبة داخل التربة على طول الخط الحقلية بحيث يكون كل منها في أحد اثلاث الخط. يعتمد نظام التحكم على حساب متوسط الرطوبة للقراءات الثلاث واستخدامها كمؤشر لبدء عملية الري أو إيقافها طبقاً لاحتياجات النبات. يقوم النظام بتشغيل طلمبة الري عند استنفاد نسبة الرطوبة المسموح بها من الماء الميسر والتي هي أحد مدخلات تشغيل نظام التحكم وتستمر عملية الري حتى الوصول للسعة الحقلية وهي نقطة إيقاف التشغيل. قارنت الدراسة بين طريقتين لإدارة نظام الري الأولى باستخدام نظام التحكم المقترح والأخرى تشغيل النظام بشكل يدوي اعتماداً على حساب الاحتياجات المائية من خلال البيانات المناخية. أدى استخدام نظام التحكم المقترح إلى زيادة في محصول الخيار بنسبة بلغت 23.8% مقارنة بإنتاجية المعاملة المدارة اعتماداً على البيانات المناخية. كما أدى الاعتماد على نظام التحكم إلى توفير في مياه وزمن الري خلال الموسم. أدى ذلك إلى زيادة إنتاجية المياه بنسبة 41.71% مع زيادة في كفاءة استخدام الطاقة بنسبة 110% مقارنة بالتشغيل اليدوي. بالرغم من زيادة تكاليف نظام الري نتيجة استخدام نظام التحكم إلا أن هناك زيادة في نسبة العائد إلى التكاليف بمقدار 24.39% لمعاملة التحكم الأوتوماتيكي مقارنة بالتشغيل اليدوي نتيجة تقليل تكلفة العمالة والطاقة بالإضافة لزيادة المحصول. أوصت الدراسة باستخدام نظام التحكم المقترح لتجنب الآثار السلبية للأداء الهيدروليكي الضعيف من ناحية الحفاظ على الانتاجية في مستواها الطبيعي واستخدام المياه والطاقة بشكل أكثر كفاءة مع الحفاظ على فرصة زيادة نسبة العائد/ التكاليف. وأوصت الدراسة بإجراء مزيد من التجارب لتحديد التوزيع الأمثل لأجهزة الاستشعار الخاصة بنظام التحكم وعددها الأمثل على طول الخط الحقلية للوصول لأفضل أداء ممكن للنظام المقترح.

INTRODUCTION

Scarcity of water worldwide created a competition between all water resources consumers (FAO, 2013). Agriculture is the main source of people food and one of the main consumers of water resources. Increasing water use efficiency beside energy saving in agriculture has been a big concern. Trickle irrigation systems including drip irrigation are highly recommended for saving water and increase water use efficiency (Luquet et al., 2005). Actual field practices with drip irrigation may affect reaching the goals of improved saving water and crop production (Lankford B., 2012; van der Kooij et al., 2013). Sometimes, drip irrigation system users may suffer from poor hydraulic performance of the system due to poor design or management as well as they may have to use cheaper system components if they can't afford the capital needs. Inexperienced users will also suffer from their inability to operate their irrigation systems in an optimum way in addition to their low skills in system performance monitoring. Using decision support systems and automatic control introduces applicable solutions to avoid the negative impacts which may result from the existence of one or all of poor design, management, and operation. Such improved management utilities when used with different crops as a monitoring tool (Zhang et al., 2013) will be useful for increasing irrigation efficiency (Smarsly K., 2013). Prediction of water needs is a key issue to the automatic control systems to reach success and effective scheduling. Generally, the main two ways of data processing in control systems are open-loop and closed-loop technics. Open-loop control systems miss the feedback data about soil moisture in the root zone which may change the irrigation scheduling strategy. Open-loop control systems technique was used by (Smith M., 2000; Zwart and Bastiaanssen, 2004; Giusti and Marsili-Libelli, 2015) to reduce the prediction of the water needs resulted from climatic data but they were unable to achieve this. Using closed-loop control systems and using sensors to collect data is the key to successive irrigation management in main extensive crops (Ruíz-García et al., 2009). Studies made by (Kim et al, 2008, Kim et al, 2009; Pfitscher et al., 2012), pointed out the importance of using real time, closed-loop automatic control to improve the performance of irrigation systems including efficient water and energy use. Despite the possibility of real time monitoring through the automatic control systems for the soil moisture, the distribution of soil moisture along laterals was not approached in most of the control systems presented. The more accurate data received by soil moisture sensors, the easier to access successful management through the irrigation control system. Hydraulic performance describes how uniform is the distribution of flow rates along the lateral. Irrigation uniformity plays an essential role to increase crop production, water use efficiency, and net profits (Li and Kawano, 1996; López-Mata et al., 2010). If there is a high variation between flow rates along the lateral, it will be hard to choose the point(s) which describe real soil moisture content accurately to decide the right scheduling strategy by the control system. This study aims to evaluate the implication of a real-time, closed-loop control system developed by (Elnemr M.K., 2017) with drip irrigation system working under poor uniformity conditions to investigate the effect of using the mentioned control system on water and energy use efficiency under such conditions besides making an economic evaluation to its use effect on net profits generated by the added cost.

MATERIALS AND METHODS

The field experiment location was 31.41° N, 31.75° E in Kafrelbatikh city, Damietta Governorate, Egypt on cucumber crop (*Sahim F1*) with sandy loam soil. Seeds planting started at 1/3/2019. Seeding rate was 3 seeds/pore then it was reduced to 1 plant/pore after germination. Area dimensions were 20m width, 40m long. 5-share chisel plough was hitched to 60hp tractor to achieve the required soil fragmentation. Amounts of 750-800-600 kg.ha⁻¹ of Ammonium sulphate, Single Superphosphate, and Potassium sulphate, respectively, were scattered on the soil surface on three stages which were vegetative development, flowering, and fruit development. Soil surface levelling was carried out using a scraper to maintain the horizontal level of the soil at zero level. Table 1 illustrates some physical properties of the soil in the experimental site.

Table 1

Physical properties of experiment soil

Depth, cm	Soil particles size distribution			Texture	Field capacity, %	Wilting point, %
	Clay,%	Silt,%	Sand,%			
0-15	18.50	1.50	80.00	Sandy loam	19.48	9.06
15-30	19.13	2.52	78.35	Sandy loam	17.05	8.79
30-45	15.93	1.99	82.08	Sandy loam	16.69	7.05
45-60	17.05	2.01	80.94	Sandy loam	18.29	7.44

Drip irrigation network was divided into two parts, each of them performing one treatment. The difference between the two treatments was managing on/off decision for pumping water. First part was managed using the automatic control system (AU_m), second one was managed basing on climate data and operated by irrigation system operator (CI_m). Three laterals were established to act three replicates of each treatment. As shown in Figure 1, drip irrigation system consisted of 1 HP centrifugal electric pump that suctions water from water basin 0.6 m³ which was always filled with fresh water to assure the existence of water when the control system operates the pump. The pump was connected to the water basin by a PVC pipe with 2.5 cm inner diameter. Manifold was a PVC pipe with 6.3 cm inner diameter. Built in emitters were used in laterals having 16 mm inner diameter and 20m length. Emitters were 50cm spacing along each lateral and the space between laterals was 1.5m. All laterals' inner diameter was 16mm. The pump was connected to the control system through a cable to permit the electric current to switch the pump on. Operating pressure head was measured using a pressure gauge fitted on the manifold.

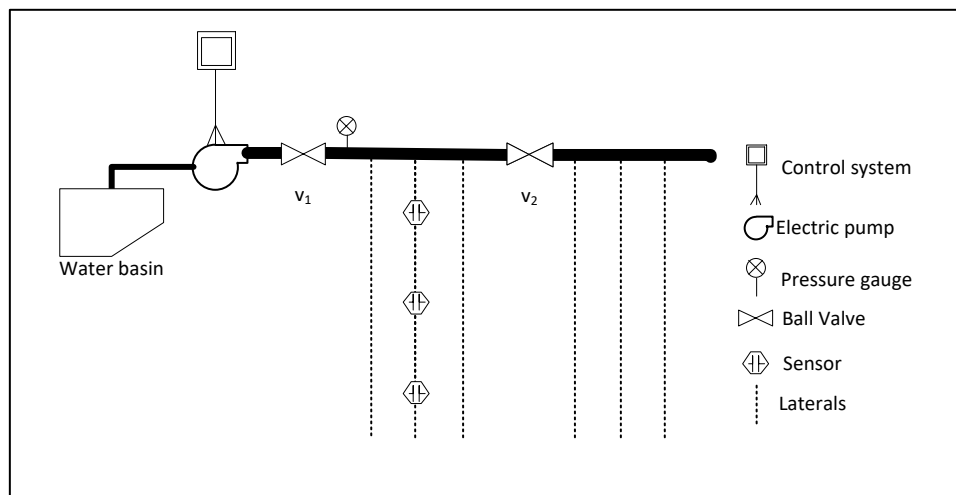


Fig.1 - Irrigation network and field experiment layout

Water inlet to the two parts was controlled by two valves which were marked V_1 and V_2 in Figure 1. V_1 was always open. V_2 was opened just with the need to irrigate (CI_m) treatment. All the laterals started with T-shape valves with the same diameter of the laterals. Water flow to automatically controlled laterals was prevented during the irrigation of the other treatment by closing the T-shape valves. The control system has the ability to operate the pump at any time decided by the user for any required duration. This feature was used to irrigate the (CI_m) treatment. After finishing irrigating the second part, the system was turned to automatic mode to control the first part basing on soil moisture data. Irrigation interval for CI_m was 72h.

The used control system was developed by (Elnemr, M.K., 2017). Control system components, sensors calibration, and design considerations were shown in (Elnemr M., 2019). The designed algorithm of the control system was based on collecting soil moisture content data from the soil under three emission points along each third of lateral length to consider flow rate variation between emitters. The evaluated control system was recommended to be used with the poor hydraulic performance trickle irrigation systems. The average of the three collected values of soil moisture content was used to express the soil moisture content value (MC) which will be used to manage the irrigation system.

The system should be fed at the beginning of irrigation network installation with three values namely soil field capacity (FC), and permanent wilting point (PWP) which are related to soil properties, in addition to moisture allowed depletion (MAD) which is directly related to crop type. All these inputs were entered to the system as percentages with two digits accuracy. The values of FC and PWP used in the experiment were 17.9% and 8.1% respectively. These values are the average of the four values related to these constants as listed in Table 1.

MC_{on} is the soil moisture content at which the control system will give the decision of starting the pump; it will be calculated according to the following equation:

$$MC_{on} = (FC - PWP) \left(1 - \frac{MAD}{100}\right), [\%] \quad (1)$$

The control system was designed to start irrigation process when the soil moisture content reaches the allowed percentage of available water and stop the water pumping after reaching the *FC*. Corresponding values resulted from sensor calibration of *FC* and *PWP* were fed to the system. Values of *FC* and *PWP* shown in Table 1 were used. *MAD* value was 25% for cucumber as a shallow rooted crop (*Phocaides A., 2007*).

The first and second thirds length were 7m and last third was 6m long. Sensors were located under the middle emitter of each third after assuring it is unclogged. Each sensor was put at 20 cm depth as recommended by (*Rivera et al. 2012*). Sensors were connected to the control system through shielded cable which had three ends, two for negative and positive electrodes and the third one for sending the signal.

Primary field experiments were carried out to choose the operating head that would reflect poor hydraulic performance for the irrigation system. Uniformity coefficient parameter (*UC*) was selected to evaluate the system performance with four operating pressure heads which were 5, 8, 10, 20m of water. *UC* values under different pressure heads were calculated using the spread sheet developed by (*El-Nemr M.K., 2012*). Flow rates of 20 emitters from a certain lateral were collected in 250 ml capacity cans. Flow rates were collected at once by operating the system for 2 minutes and the resulted water volume was calculated in l/h. Obtained *UC* values and their evaluation referring to (*ASAE, 1997*) are listed in table 2. Referring to *UC* values, the operating pressure 8m was used during the experiment as the evaluation of uniformity is poor.

Table 2

Values of <i>UC</i> , %		
Pressure head [m]	<i>UC</i> [%]	Evaluation
5	48.14	Unacceptable
8	65.20	Poor
10	85.95	Very good
20	90.27	Excellent

Crop water requirements for the climatic data-based part of the experiment were calculated according to (*FAO, 1998*). CLIMWAT program (*FAO, 1993*) was used to obtain daily reference evapotranspiration (*ET_o*) values from Damietta meteorological station (31.25° N and 31.49° E) which covers the experimental area. The Crop coefficient values were 0.6, 1, and 0.75 for the initial, crop development, mid-season, and late-season growing periods (*Phocaides A., 2007*).

Picking started when cucumber fruit reached the acceptable marketing size (the length of cucumber was 10-14 cm and/or 2 cm diameter). After finishing the growing season, average of three replicates was used to describe the total productivity of each treatment.

Water productivity (*W_p*) has been used to describe the relationship between cucumber crop production and the total amount of water used. It was determined in kg m⁻³ by applying the following equation:

$$W_p = \frac{Y}{W_a} \quad [\text{kg/m}^3] \quad (2)$$

where *Y*= Crop yield, [kg], *W_a*= Amount of applied water, [m³].

Energy use efficiency (*EUE*) indicator was used to express the relationship between crop productivity (kg) and energy consumption (kWh) as follows:

$$EUE = \frac{\text{Crop productivity}}{\text{Energy consumption}} \quad [\text{kg / kWh}] \quad (3)$$

The pump brake power was calculated according to Equation 4.

$$BP = \frac{P_w}{\eta} \quad [\text{kW}] \quad (4)$$

where: *BP*= engine brake power, [kW]; *P_w*= water power, [kW];

η= Pump efficiency which was taken 0.70.

$$P_w = Q \cdot H_t \cdot \omega \quad [\text{kW}] \quad (5)$$

where:

Q= required discharge at the network, [m³/h]; *H_t*= total head, [m]; *ω* = water specific weight, [kg/m³].

$$H_t = H_f + H_s + H_e \quad [\text{m}] \quad (6)$$

where: H_f =friction loss, [m]; H_s =static suction head, [m]; H_e =emitter operating pressure head, [m].

The suction static head was neglected because the water suction level in the water basin and pump water inlet was nearly at the same level. Hazen-Williams formula (Hazen and Williams, 1920) was used to calculate the friction loss for the manifold and laterals.

$$H_f = \frac{10.67 Q^{1.85}}{C^{1.85} \cdot d^{4.87}} L \quad [\text{m}] \quad (7)$$

where: d = inside pipe diameter in m, L = Length of the pipe in m, Q =Total flow rate $\text{m}^3 \cdot \text{h}^{-1}$, C = Formula constant which was 150 for both PVC and PE pipes.

Minor friction losses were assumed 10% of the total friction loss (El-Gindy et al., 2001). Energy consumption was calculated by multiplying the calculated power requirement in the total operation time per season for each treatment. Average of emitters flow rates was used to calculate the operation time for the climatically based part. The control system was provided with a time recorder to record total operation hours done by the system.

The total annual cost per hectare for the growing season was calculated referring to Buchanan, et al. 2002 based on the Egyptian market information for the year 2019. Required cost data were collected in Egyptian pound (EGP) as a unit of price then converted to US\$ which had average price 17.39 EGP during experiment time. Total cost equalled the summation of total annual fixed and variable costs. Fixed costs included depreciation of network components, interest, and taxes and insurance costs. The depreciation costs of the different irrigation network components were calculated according to Equation 9:

$$\text{Depreciation cost} = \frac{\text{Asset cost} - \text{Residual value}}{\text{Useful life of the asset}} \quad [\text{US \$}] \quad (8)$$

The variable costs included energy, labour, repair and maintenance, and additive costs including pesticides, seeds, fertilizers, land rent, and transportation. The residual value of an object was assumed 10% of the price of new object case. The automatic control system cost was 466.06 US\$ with 5 years useful life. Life span of the pump and network components was assumed 10 years. The interest value was 13.5% while taxes and insurance were 2% of the original asset cost of an object. Energy cost (0.04 US\$/ kWh). Labour fees were 5.75 US\$/day/person for 8 hours working day. Repairs and maintenance costs were assumed to equal the depreciation cost. Profit of cucumber crop per kg was 0.29 US\$. The benefits-cost ratio (B/C) was used to describe the final crop profitability for the farmer.

RESULTS

Picking process finished on 11/5/2019. Using automatic control led to increase cucumber production by 23.80% if compared to the production of (Cl_m). Production of (Au_m) reached $15.81 \text{ Mg} \cdot \text{ha}^{-1}$ while production of (Cl_m) was $12.77 \text{ Mg} \cdot \text{ha}^{-1}$. This increase in production reflects the better management achieved by the control system for applying water in the most suitable times. Also, the ability of the control system to use the average MC from three points to make the necessary scheduling strategy shared in avoiding deficit or over irrigation which may result in poor uniformity.

Water productivity of (Au_m) was 9.75 kg m^{-3} while it reached 6.88 kg m^{-3} for (Cl_m). Increase in water productivity was 41.71% of water productivity at (Cl_m) treatment. (Au_m) also led to save 12.63% of water applied to Cl_m . Water productivity was directly impacted by the increase in crop productivity in (Au_m) in addition to saving water.

Using automatic control system led to increase energy use efficiency (EUE) if compared to (Cl_m) treatment. Energy use efficiency (EUE) for the treatment (Au_m) reached $76.09 \text{ kg/kW} \cdot \text{h}$ while it was $36.02 \text{ kg/kW} \cdot \text{h}$ for (Cl_m). Energy use efficiency (EUE) value is mainly related to both productivity and operation time. (Au_m) gave the opportunity to improve energy use efficiency (EUE) by adjusting operation time in addition to the increase in cucumber productivity.

Table 3 shows the costs of cucumber production and the total profits. Total fixed cost of (Au_m) was higher than the (Cl_m) because of the costs of the automatic control system. Labour cost was lower for (Au_m) because there was no need for persons to turn the system on and off. Also, the energy cost was lower for (Au_m) because of the more adjusted operation time which was lower than the seasonal operation time of (Cl_m). The reduction in energy and labour costs led to reduce the total costs of (Au_m) treatment despite the increase in irrigation network costs generated by the costs of the automatic control system.

The total profits of (Au_m) were greater than the profits of Cl_m . These results led to increase in B/C ratio of (Au_m) by 24.39% if compared to (Cl_m) treatment. (Au_m) treatment cost is expected to decrease if the control system manufacturing turned to mass production.

Table 3

Annual costs and benefits/cost ratio of the treatments, US\$/ha

	Cl_m	Au_m
Depreciation	43.90	84.72
Interest	36.22	70.83
Taxes and insurance	9.76	19.08
Total fixed costs	89.88	174.63
Energy	57.02	33.58
Labour	198.70	93.15
Repairs and maintenance	43.90	84.72
Additives	305.03	305.03
Total variable cost	604.66	516.48
Total cost	694.54	691.11
Benefits	3703.30	4584.90
B/C ratio	5.33	6.63

Using the proposed control system led to increase crop productivity, save water, and decrease seasonal operation time. All these effects were followed by increasing water production (W_p) and energy use efficiency (EUE). Despite the poor hydraulic performance of the system which was expected to decrease production, the total productivity with (Au_m) reached the limit of cucumber productivity per hectare in Egypt (*Zaki M., 1992*) and the world average which is 15 Mg/ha. The decrease in crop production in (Cl_m) is mainly related to the poor hydraulic performance and unequal amounts of water applied along laterals. This means that the design considerations of this control system led to avoid over and deficit irrigation of the plants along the lateral. Results also clarified that basing on soil and crop data in the proposed control system led to increase water production (W_p) and helped to reach better scheduling which is in agreement with the studies made by (*Dukes et al. 2007; Elmarzaky et al., 2011; Venkatapur and Nikitha, 2017*) on closed-loop control systems. The proposed control system can be improved to be compatible with renewable energy sources like solar energy to keep real-time monitoring for the soil moisture content to avoid losing data because of any issues related to possible electric current absence. Future experiments should include investigating the introduced control system use with acceptable ranges of hydraulic performance. Also, future work can include choosing the best distribution for the sensors along laterals and the effect of increasing the number of monitoring sensors.

CONCLUSIONS

Field experiment was carried out to investigate the effect of a closed-loop real-time control system which was developed by *Elnemr M.K., 2017* on cucumber crop production, water productivity, and energy use efficiency with poor hydraulic performance drip irrigation system. The control system was designed to manage irrigation system basing on collecting soil moisture data through sensors which were located in each third of the lateral. The average of the three readings was used as the soil moisture content which will decide the irrigation needs. The control system will start the pump when the soil moisture content reaches the allowed depletion of available water. Irrigation process will stop after reaching soil field capacity. The automatic control management was compared to climatic data-based management. Irrigation management with the control system led to increase crop production, water productivity, and energy use efficiency compared to the other management method. Despite the poor hydraulic performance of the irrigation system, the automatic control management kept the productivity of cucumber at the known limits per unit area.

As a result, there was an increase in water production (W_p), and energy use efficiency (EUE) due to the saving in water and operation time. Using the control system also led to increase the B/C ratio compared to (Cl_m) due to increase in crop production with decreasing both labour and energy costs. It is recommended to use the introduced control system with drip irrigation systems which show poor hydraulic performance to reduce negative effects on crop production and to reach more efficient use for both water and energy.

REFERENCES

- [1] ASAE (1997), American Society of Agricultural Engineers, Engineering Practice Standard EP 458: *Evaluation of Micro Irrigation Systems*, St. Joseph, Michigan. USA1997.
- [2] Buchanan R.J., Cross T.L., (2002), *Irrigation Cost Analysis Hand Book*, Agricultural Extension Service, The University of Tennessee. PB1721.
- [3] Dukes M.D., Muñoz-Carpena R., Zotarelli L., Icerman J.; Scholberg J.M., (2007), Soil moisture-based irrigation control to conserve water and nutrients under drip irrigated vegetable production. *Studies of the unsaturated soil Zone (Estudios de la Zona No Saturada del Suelo)*. Vol. 8:229-236.
- [4] El-Gindy, A.M., Abdelaziz A.A., Soliman A.A., (2001), *Irrigation and Drainage Networks Design*, Ain Shams University, Egypt.
- [5] El Marazky M.S., Mohammed F.S, Al-Ghobari H.M., (2011), Evaluation of Soil Moisture Sensors under Intelligent Irrigation Systems for Economical Crops in Arid Regions. *American Journal of Agricultural and Biological Sciences*, vol.6 (2): 287-300.
- [6] El-Nemr M.K., (2012), An Interactive Spreadsheet for Drip Irrigation System Uniformity Parameters Evaluation. *International Journal of Agriculture Sciences*, 4(4):216-220.
- [7] Elnemr M., (2019), Prototype of a control system for trickle irrigation systems considering distributors' flow rate variation. *International Journal of Water Resources and Environmental Engineering*, 11(5): 83-90.
- [8] Elnemr M.K., (2017), Automatic control system for poor hydraulic performance trickle irrigation systems. Egypt patent Dec. 24 2166/2017.
- [9] FAO (1998), Crop Evapotranspiration - Guidelines for Computing Crop Water Requirements, *FAO Irrigation and Drainage Paper 56*.
- [10] FAO (2013), AQUASTAT Database. *Food and Agriculture Organization of the United Nations*, <http://www.fao.org/nr/water/aquastat/data/query/results.html> (accessed 30 December 2013).
- [11] Giusti E., Marsili-Libelli S., (2015), A fuzzy decision support system for irrigation and water conservation in agriculture. *Environmental Modelling and Software*. 63:73–86.
- [12] Hazen A., Williams G.S., (1920), *Hydraulic Tables*, 3rd ed., John Wiley and Sons, New York.
- [13] Kim Y., Evans R.G., (2008), Remote Sensing and Control of an Irrigation System Using a Distributed Wireless Sensor Network. *IEEE Transactions on Instrumentation and Measurement*, 57(7): 1379-1386.
- [14] Kim Y., Evans R.G., Iversen W.M., (2009), Evaluation of Closed-Loop Site Specific Irrigation with Wireless Sensor Network. *Journal of Irrigation and Drainage Engineering*, ASCE, January-February 2009:25-31.
- [15] Lankford B., (2012), Fictions, fractions, factorials and fractures; on the framing of irrigation efficiency. *Agricultural Water Management*. 108:27–38.
- [16] Li J., Kawano H., (1996), The areal distribution of soil moisture under sprinkler irrigation. *Irrigation Sciences*. 32:29-36.
- [17] López-Mata E., Tarjuelo J.M., De Juan J.A., Ballesteros R., Domínguez A., (2010), *Agricultural Water Management*, 98: 190-198.
- [18] Luquet, D., Vidal A. , Smith M., Dauzat J., (2005), More crop per drop: how to make it acceptable for farmers?. *Agricultural Water Management*. 73:108–119.
- [19] Pfitscher L.L., Bernardon D.P., Kopp L.M., Heckler M., Behrens J., Montani P.B, Thome B., (2012), Automatic control of irrigation systems aiming at high energy efficiency in rice crops. Devices, Circuits and Systems (ICDCS), *8th International Caribbean Conference*, pp.1,4, 14-17 March 2012.
- [20] Phocaides A., (2007), *Handbook on pressurized irrigation techniques*. Food and agriculture organization of the United Nations, Rome / Italy.
- [21] Rivera D., Granda S., Arumi J.L., Sndoval M., Billib M., (2012), A methodology to identify representative configurations of sensors for monitoring soil moisture. *Environmental Monitoring and Assessment*. 184:6563–6574.
- [22] Ruíz-García L., Lunadei L.; Barreiro P., Robla J.I, (2009), Review of wireless sensor technologies and applications in agriculture and food industry: State of the art and current trends, *Sensors*, 9: 4728–4750.
- [23] Smarsly K., (2013), Agricultural ecosystem monitoring based on autonomous sensor systems. In: *Second International Conference on Agro-Geoinformatics*, pp.402–407 (IEEE).
- [24] Smith M, (2000). The application of climatic data for planning and management of sustainable rainfed and irrigated crop production. *Agricultural and Forest Meteorology*, 103: 99–108.

- [25] Van der Kooij S, Zwarteveen, M., Boesveld, H., Kuper, M., (2013). The efficiency of drip irrigation unpacked. *Agricultural Water Management*, 123:103–110.
- [26] Venkatapur R.B., Nikitha S., (2017). Review on Closed Loop Automated Irrigation System. *The Asian Review of Civil Engineering*, 6(1):9-14.
- [27] Zaki M, (1992), Production trends for fruit and vegetable crops in Egypt. In: Lauret, F. (ed.). Fruits and vegetables in the Mediterranean economies (Les fruits et légumes dans les économies méditerranéennes). *Proceedings of the Chania conference*. Montpellier: *Mediterranean Options: Series A. Mediterranean Seminars*; n.19 (Options Méditerranéennes: Série A. Séminaires Méditerranéens; n.19), CIHEAM, 1992, p. 147 -150.
- [28] Zhang, X., Zou H., Zhang N., Li Y., Yang Y, (2013), The research and applications of agricultural automation based on Internet of things. *WIT Transactions on Information and Communication Technologies*. 46: 111–119.
- [29] Zwart S.J., Bastiaanssen W.G., (2004), Review of measured crop water productivity values for irrigated wheat, rice, cotton and maize. *Agricultural Water management*, 69:115-133.

RESEARCH ON THE CONTRIBUTION RATIO OF APPLE PEEL PUNCTURE BEHAVIOR TO FRUIT FIRMNESS

苹果果皮穿刺质地对果实硬度贡献率的研究

Juxia Wang ¹⁾, Bingyao Jiang ¹⁾, Shuanghua Xu ²⁾, Qingliang Cui ¹⁾, Decong Zheng ¹⁾ ¹

¹⁾College of Engineering, Shanxi Agriculture University, Taigu/China

²⁾Organization Department, Shanxi Agricultural University, Taigu/China

Tel: +86-0354-6289686; E-mail: zlsqxy_2018@163.com

DOI: <https://doi.org/10.35633/inmateh-60-19>

Keywords: puncture test; peel texture; fruit firmness; peel contribution

ABSTRACT

The texture of apple peel, as an important quality attribute of the fruit, is directly relevant to a fruit's ability to resist mechanical injury. In order to explore the variations in texture of two apple peels under different puncture test conditions and evaluate the relation of apple peel puncture force to whole fruit firmness percentage, at 0.1, 1, 5, 11, and 17 mm/s loading speeds, puncture mechanical measurements were performed using an electronic testing machine mounted with 2, 3.5, 7.9 or 11 mm-diameter probes. For the same probe, the mean values of peel puncture force and stiffness, as well as the fruit puncture force, for Danxia and Fuji cultivars increased firstly and then changed a little with the increase of loading speed. Moreover, at the same loading speed, the puncture measurements of each cultivar increased significantly ($P \leq 0.05$) with increasing probe diameter and the peel puncture force has a significant linear correlation with probe diameter. Among the different cultivars, under the same loading speed, the Fuji peel and fruit samples had the greater puncture force; the Fuji peel contribution change was relatively big with the increasing of loading speed, and Fuji cultivar was more likely to be injured than the other cultivar. The results were expected to serve as a reference for investigating the puncture injury sensitivity of different apple varieties during transportation and storage and to enrich the texture evaluation index of apple peel.

摘要

苹果果皮作为果实的最外层组成部分，其质地特征是评价果实抵抗机械损伤能力的重要指标。为探索不同品种苹果果皮穿刺质地的差异及研究果皮穿刺质地对果实硬度的贡献率，采用直径为 2, 3.5, 7.9, 11 mm 的圆柱体压头，在 0.1, 1, 5, 11, 17 mm/s 的加载速度下对红富士和丹霞苹果果皮及整果果实进行了穿刺力学特性试验，获得果皮及果实的穿刺载荷—位移曲线、破裂抗力与果皮的刚度。试验结果表明：同一品种苹果，在相同压头下随着加载速度的增加，果皮破裂抗力及刚度、果实破裂抗力均呈现先增大后变化幅度不大的趋势；在相同加载速度下随着压头尺寸的增大，果皮及果实的穿刺力学特性参数间存在显著性的差异 ($P \leq 0.05$)，果皮破裂抗力与压头直径之间呈显著正线性相关。不同品种苹果，在相同的加载速度下果皮及果实的破裂抗力均以红富士的为最大；随着加载速度的增加，红富士果皮穿刺质地对果实硬度贡献率的变化相对较大；红富士苹果比丹霞更易损伤。研究结果为不同品种苹果果皮贮运损伤敏感性的评价提供参考依据，丰富苹果果品质地的评价指标。

INTRODUCTION

Peel texture of fruits and vegetables, which is an important index of fruit quality (Ma et al., 2011; Singh et al., 2006; Grimm et al., 2012; Li et al., 2019), is directly relevant to the fruit-resistance ability to mechanical damage (Shao et al., 2009; Tobi et al., 2016; Liu et al., 2018; Chukwutoo et al., 2017) and the injury of puncture between fruits and fruit stems (Allende et al., 2004; Jiang et al., 2009); meanwhile peel texture is one of the main factors affecting fruit firmness (Allende et al., 2004; Jiang et al., 2009; Vanstreels et al., 2005; Wang et al., 2019).

¹ Juxia Wang, A.P. Ph.D. Eng.; Bingyao Jiang, M.S. Eng Stud. Eng.; Shuanghua Xu, M.S. Stud. Eng.; Qingliang Cui, Prof. Ph.D. Eng.; Decong Zheng, Prof. M.S. Eng.

The firmness and compactness of fruit texture, which are closely related to fruit quality (Veringă *et al.*, 2015; Veringă *et al.*, 2018;) could be determined by the puncture strength test, and during postharvest handling, the fruit bears mechanical stress causing peel punctures injuries (Singh *et al.*, 2006; Zhao *et al.*, 2015). Currently, when puncture method is used in assessing peel texture, and when evaluated, research has mainly turned on two sides: direct evaluation of peel texture after peel puncture (Hetzron *et al.*, 2011; Wang *et al.*, 2015) and indirect evaluation of peel texture after the whole fruit and flesh are used to perform puncture tests (Rao *et al.*, 2011; Costa *et al.*, 2012; Costa *et al.*, 2016). Puncture properties of different tomato peels, which were cut from the epidermal segments of each fruit and were made circular in shape, were measured and analysed. It was found that the stiffness and puncture force of various tomato peels were successfully determined using puncture test, and puncture forces were able to represent the resistance of a tomato peel to chewing and peeling satisfactorily (Hetzron *et al.*, 2011). To determine the differences of injury susceptibility of Fuji and Starkrimson apples, two kinds of peel were utilized in puncture tests with 2 mm-diameter punch at 1 mm/s loading speed. The puncture properties of the sunlit-side part were better than those of the shadow-side part, and the puncture resistance ability of Starkrimson peel was superior to that of Fuji peel (Wang *et al.*, 2015).

The whole fruit and flesh without skin were tested under overall puncture load displacement to obtain the mechanical behaviour of various apple skins precisely. Apple skin is important during forced ripening, and the percent contribution of the skin to the overall firmness is greater during cold storage (Grotte *et al.*, 2011). To determine the relation between mechanical properties of two tomato varieties and puncture injury susceptibility, puncture experiments of tomatoes with and without skin were conducted. Fruit elasticity and the toughness of tomato skins affected the susceptibility to fruit puncture injury (Desmet *et al.*, 2002). Puncture tests were executed on Golden Delicious and Red Delicious apple fruits with and without skin. It was discovered that skin is important in puncture properties of apples and that it has a high percent of toughness and rupture force for two apple varieties; but the contribution of skin is higher in Golden Delicious than Red Delicious (Shafiee *et al.*, 2008). Mechanical properties of apple slices with and without skin under puncture tests were examined at a 50 mm/min crosshead speed to a depth of 15 mm. It was indicated that peak puncture force values of Crimson Gala and Honey Crisp were higher than those of McIntosh, Red Delicious, and Empire; the contribution of the skin of Honey Crisp apples to the peak force was the least among all the studied apples (Rao *et al.*, 2011).

To date, the relationship between peel puncture texture and fruit firmness of apples has not been reported under different probe diameters and loading speed test conditions. This study aimed to: (1) examine the variations in texture of two apple peels and whole fruit firmness in two apple cultivars under different puncture test conditions, and (2) determine the relationship between the peel puncture texture and fruit firmness of apples. The results were expected to enhance the objectivity and accuracy of the texture evaluation of apple peel and to serve as a reference for investigating the puncture injury sensitivity of different apple varieties during transportation and storage.

MATERIALS AND METHODS

Apple fruits

Two autumn ripening apple cultivars, Danxia and Fuji, grown in Shanxi Fruit Institute Academy of Agriculture Sciences, were simultaneously picked in October 2017. Sample apples were uniformly shaped and sized, no pests and no mechanical damage. When the fruits were taken to the laboratory on the day of harvest, puncture tests were conducted immediately at room temperature (21°C and 80% RH).

Peel samples

The diameter of puncture circular peel samples is 31 mm (as shown in Fig. 1a). To decrease the influence of peel micro-buckled state on experimental results and consider that the bottom of apples is the main injured part during transportation, peel samples were collected from the flat peridermal segment which was located below equatorial plane of the fruit. On each fruit, two peel samples, which located in the opposite sites, were performed in a one-by-one puncture. The preparation of peel samples used the same method by Wang *et al.* (Wang *et al.*, 2017). Appropriate samples were immediately tested. Ten peel samples originating from five apples were analysed for each cultivar. Sample thickness was checked with a raster thickness gauge (JC010-1, China). The mean and standard deviation of the samples thickness was 0.275 ± 0.026 for Danxia and 0.257 ± 0.028 mm for Fuji.

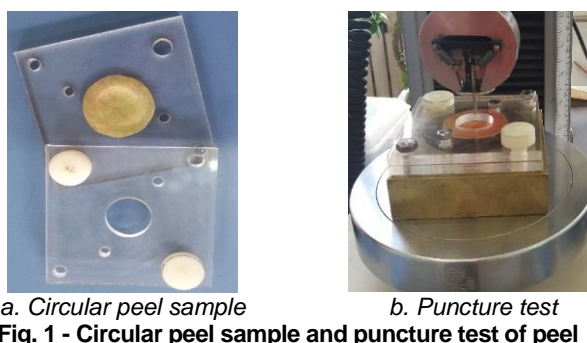


Fig. 1 - Circular peel sample and puncture test of peel

Puncture tests

Five puncture tests were completed on apple peel and whole fruit samples using an electronic testing machine (Instron-5544, USA) at room temperature. The cylindrical probes used were 2, 3.5, 7.9 and 11mm in diameter, and the test speeds were 0.1, 1, 5, 11 and 17 mm/s. A jig comprising an upper and lower film (Wang *et al.*, 2015) was used to fix peel samples (as shown in Fig. 1b).

During the puncture test, apples were placed upon a flat plate, and their stem calyx axis was parallel to the flat plate. The process of acquiring a whole fruit sample was exceptionally simple and efficient. Ten apples were experimented with 10 mm penetration depth for each cultivar, and each fruit was measured at shadow and sunlit sides of the maximum transverse diameter of the fruit. The longitudinal diameters of the fruits were measured using Vernier callipers with a resolution of 0.01 mm. The measured values of the longitudinal diameters ranged from 75.81 ± 1.74 mm and 77.59 ± 2.04 mm for Danxia and Fuji apples, respectively; and transverse diameters ranged from 64.07 ± 1.56 and 65.73 ± 2.35 mm for Danxia and Fuji apples, respectively.

Data analysis

Puncture mechanical parameters were obtained using Duncan's multiple range tests in the ANOVA procedure of SAS, version 8 (SAS Institute, Cary, NC, USA). The differences were assessed with a 95% confidence interval.

RESULTS

Puncture test of peel

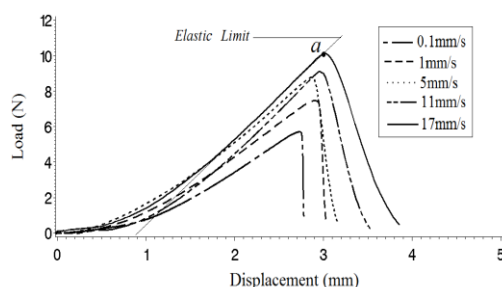


Fig. 2 - Puncture force–displacement curves of peel with different loading speeds under 3.5 mm-diameter probe

Peel puncture force–displacement curves of peel stress-strain curves

In Fig. 2, under 3.5 mm-diameter probe, typical peel puncture force–displacement curves at 0.1, 1, 5, 11 and 17 mm/s loading speeds are shown for the peel of Danxia apple. And at 11 mm/s loading speed, Fuji peel puncture force–displacement curves with 2, 3.5, 7.9, and 11 mm-diameter probes are shown in Fig. 3. As seen with the puncture curves of apples peel, the curves do not have obvious bio-yield point and are composed of two stages, such as that puncture curve subjected to 17 mm/s loading speed. In the initial stage, the load only makes the buckling peel extend gradually, so puncture displacement rapidly increases but the load is significantly small and almost constant. In the second curve stage, when the puncture probe continues to squeeze the sample, the buckling state of peel disappears, and the load raises with increasing puncture displacement until the sample is disrupted at the failure point (a point), however the part curve keeps the maximum slope, which exhibits a linear relation between force and displacement from the upper part of the curve up to the failure point; the curve linear region is known as elastic region and the slope of this portion curve represents the sample elastic modulus that is usually considered as an index of the sample stiffness in material field. Hetzroni *et al.* (2011) considered the part of the curve with the maximum slope to represent the stiffness of the skin sample.

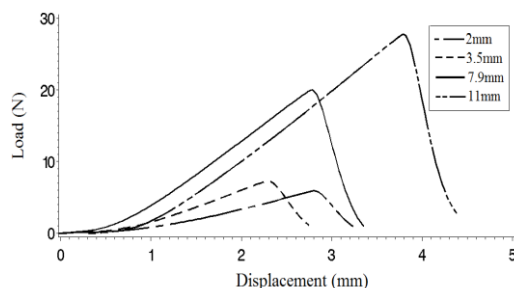


Fig. 3 - Puncture force–displacement curves of peel with different probe diameters at 11 mm/s loading speed

As shown in Fig. 2 and Fig. 3, the portions with the greatest slope were in the top section of the curves until they reached the failure points, which could express the stiffness of peel samples. The measurements of peel puncture force and stiffness extracted from the curves are shown in Table 1. For four parts of peel – i.e. sunlit longitudinal, shadow longitudinal, sunlit transverse and shadow transverse—the results obtained in the maximum load test, tensile strength test, elastic modulus test and failure strain test were as shown in Table 1.

Peel puncture property analysis

Table 1 shows that under the same probe diameter, the means of peel puncture force and stiffness for the same cultivar increased firstly and then changed little with the increase of loading speed. When the loading speed ranged from 0.1 mm/s to 5 mm/s, the puncture force and stiffness of the peel samples increase constantly in the experiment. The reason is that the sample failure takes longer time in the process of the puncture tests, and the deformation of peel sample is based on viscous deformation and grows more slowly. Therefore, under the circumstances, the peel puncture macro-mechanical properties are strongly dependent upon the force action time. As loading speed increased, the puncture force and stiffness of the peel samples show little change compared to those of 5mm/s loading speed. This is because once a certain loading speed has been reached, such as 5mm/s, the deformation of peel sample is on the basis of the elastic deformation and the elastic deformation is elastic wave propagation whose speed is far greater than the loading speed. As a result, the loading speed has almost no influence on elastic deformation in the test. However, for 11 mm/s and 17 mm/s loading speed, the sample fracture period was close to that of 5 mm/s loading speed in Table 1.

With each diameter probe, at 0.1, 1 and 5 mm/s loading speed, the mean values of the peel puncture force had significant differences ($P \leq 0.05$) between each pair of loading speeds for each cultivar. However, the mean values for Danxia and Fuji peel at 5, 11, and 17 mm/s loading speeds did not have a significant difference from each other.

In Table 1, it can be also seen that as probe diameter increased, the puncture force and stiffness of the peel samples increased constantly at the same loading speed; and with each cultivar, the puncture force and stiffness of 2, 3.5, 7.9 and 11 mm-diameter probes had significant differences ($P \leq 0.05$) between each other, except for the Danxia peel stiffness of 2 and 3.5 mm-diameter probes. This could be due to the fact that when the probe diameter is bigger, the larger contact induces between the probe and the sample, and simultaneously, apple peel has the viscous nature, this increases the contact area between liquid layers of peel organizational structure, which causes the increasing friction between liquid layers. These phenomena result in the increasing internal resistance to viscosity of the sample; therefore, the puncture force and stiffness are enlarged with probe diameter increased.

For different cultivars, at the same loading speed, no matter what probes, the Fuji peel samples had greater puncture force than Danxia peel samples; the stiffness of Danxia peel was lower than that of Fuji peel in addition to 2 mm-diameter probe. With the different diameter probe, at 0.1, 1, 5, or 11 mm/s loading speeds, only the Fuji peel puncture force values of 11 mm-diameter probe had a significant difference ($P \leq 0.05$), compared with Danxia peel; and at 1, 5, or 11 mm/s loading speeds, for mean values of peel stiffness, only the Fuji peel stiffness values of 7.9 mm-diameter probe was significantly larger ($P \leq 0.05$), compared with Danxia peel. Based on the above analysis, for the two kinds of peel, the little differences of puncture mechanical parameters could be caused by peel texture. It is observed that the two peels' texture was heavily weighted in elasticity, and contribution rate of viscosity factor in the Danxia and Fuji peel was 24.2% and 29.17% (Wang *et al.*, 2016). These reflected that the resistance ability of puncture rupture was similar for Danxia and Fuji peel.

Table 1

Values of puncture force and stiffness of apple peel at different loading speeds

Breed	Loading speed (mm/s)	Experimental period of sample fracture (s)					Puncture force (N)					Stiffness (N·mm ⁻¹)				
		2 mm in diameter	3.5 mm in diameter	7.9 mm in diameter	11 mm in diameter	11 mm in diameter	2 mm in diameter	3.5 mm in diameter	7.9 mm in diameter	11 mm in diameter	11 mm in diameter	2 mm in diameter	3.5 mm in diameter	7.9 mm in diameter	11 mm in diameter	11 mm in diameter
Danxia	0.1	21.4	26.82	30.58	32.27	3.69±0.63c,D	5.60±0.68c,C	12.29±1.90c,B	14.99±1.29c,A	2.33±0.23c,C	2.87±0.37c,C	4.93±0.42c,B	5.99±1.13cA			
	1	2.328	2.624	3.083	3.435	4.66±0.52b,D	6.91±1.00b,C	14.43±1.59b,B	19.59±2.58b,A	2.87±0.23b,D	3.57±0.23b,C	5.72±0.60b,B	6.82±0.54bA			
	5	0.466	0.591	0.677	0.517	5.38±0.51a,D	8.78±0.71a,C	17.85±1.82a,B	23.82±2.82a,A	3.21±0.34a,D	4.52±0.27a,C	6.83±0.64a,B	8.95±0.71a,A			
	11	0.232	0.27	0.319	0.334	5.31±1.08a,D	9.10±1.23a,C	18.49±1.94a,B	25.13±1.58a,A	3.51±0.32a,D	4.68±0.64a,C	7.13±0.58aB	9.09±0.74a,A			
	17	0.179	0.188	0.22	0.209	5.41±0.85a,D	9.05±0.82a,C	19.00±2.25a,B	25.32±2.46a,A	3.24±0.44a,D	4.71±0.32a,C	7.29±1.00a,B	9.19±1.15a,A			
Fuji	0.1	24.27	27.42	31.6	35.74	4.13±0.56c,D	6.64±1.14c,C	13.89±2.09c,B	19.18±3.89c,A	2.26±0.25c,D	3.13±0.45c,C	5.17±0.87c,B	6.17±0.95c,A			
	1	2.52	2.952	2.864	3.693	4.89±0.56b,D	8.35±1.24b,C	16.75±2.35b,B	24.63±4.45b,A	2.79±0.27b,D	3.76±0.31b,C	6.82±0.64b,B	7.97±0.98b,A			
	5	0.495	0.612	0.661	0.702	5.89±0.44a,D	9.16±1.03a,C	19.82±2.67a,B	27.23±3.25a,A	3.18±0.43a,D	4.69±0.50a,C	8.13±0.62a,B	9.84±1.47a,A			
	11	0.254	0.257	0.308	0.336	5.85±0.59a,D	9.25±1.39a,C	20.38±2.91a,B	28.09±3.14a,A	3.15±0.31a,D	4.83±0.49a,C	8.38±1.05a,B	9.54±1.34a,A			
	17	0.169	0.179	0.216	0.212	5.76±0.77a,D	9.07±1.30a,C	19.68±2.36a,B	27.16±2.37ab,A	3.19±0.32a,D	4.75±0.69a,C	8.02±0.87a,B	10.22±1.20a,A			

Note: Means within rows with a different uppercase letter are significantly different ($p < 0.05$).

Means within columns with a different lowercase letter are significantly different ($p < 0.05$).

Relation between peel puncture force and probe diameter

To determine relation between peel puncture force and probe diameter at the same loading speed, the data of puncture force of all the peel samples was used the procedure of Statistical Analysis System for line regression. Results indicated that the linear line satisfied the chosen function. The fitting equation was:

$$y = \beta x + k \tag{1}$$

where: F is the puncture force, [N];

β is fitting coefficient;

x is the probe diameter, [mm];

k is intercept.

Table 2, respectively, summarizes the fitting coefficients, significance level and determination coefficient ($P \leq 0.0001$) for Danxia and Fuji peel. Results show that at the same loading speed, the puncture force has a significant linear correlation with the probe diameter. In the regression equations, the fitting coefficient reached extremely significant level ($P \leq 0.0001$) for the two cultivars and only the intercept of the regression line has a significant level ($P \leq 0.05$) for Danxia cultivar; moreover, the regression model was better with high determination coefficient which was over 0.88. It is reflected that the measurements have higher accuracy and the puncture force will keep growing when the probe size continues to widen.

Table 2

Linear fitting coefficient, intercept, significance level, determination coefficient of peel

Breed	Loading speed (mm/s)	fitting coefficient		intercept		R ²
		β	Pr > t	k	Pr > t	
Danxia	0.1	1.2962	<0.0001	1.2336	0.0045	0.9297
	1	1.6706	<0.0001	1.2082	0.0191	0.9377
	5	2.0459	<0.0001	1.4755	0.0089	0.9505
	11	2.1843	<0.0001	1.1809	0.0144	0.9673
	17	2.1968	<0.0001	1.2473	0.0108	0.9670
Fuji	0.1	1.6686	<0.0001	0.7813	0.2711	0.8820
	1	2.1465	<0.0001	0.5675	0.4874	0.9024
	5	2.3837	<0.0001	0.9830	0.1476	0.9441
	11	2.4854	<0.0001	0.7293	0.3001	0.9439
	17	2.3879	<0.0001	0.8489	0.1381	0.9598

Puncture test of a whole fruit

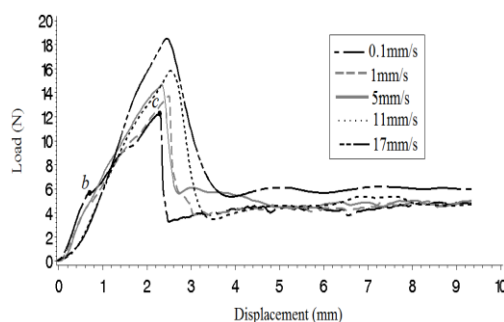


Fig. 4 - Puncture force-displacement curve of whole apples with different loading speeds under 3.5 mm-diameter probe

Relation between peel puncture force and probe diameter

Typical results of puncture load–displacement curves on whole apples of Danxia cultivar, subjected to 3.5 mm-diameter probe puncture at 0.1, 1, 5, 11 and 17 mm/s loading speeds, are shown in Fig. 4. For 0.1, 1 and 5 mm/s loading speeds, such as 0.1 mm/s, b is the yield point and the c -point stands for apple macrostructure failure. But For the 11 and 17 mm/s loading speeds, the curves have no obvious bio-yield points. At 11 mm/s loading speed, typical force vs. displacement curves of whole fruits of Fuji cultivar with 2, 3.5, 7.9, and 11 mm-diameter probes are shown in Fig. 5. In this diagram, with the different probes, the curves have also no obvious bio-yield points in the curves.

Typical results of puncture load–displacement curves on whole apples of Danxia cultivar, subjected to 3.5 mm-diameter probe puncture at 0.1, 1, 5, 11 and 17 mm/s loading speeds, are shown in Fig. 4. For 0.1, 1 and 5 mm/s loading speeds, such as 0.1 mm/s, b is the yield point and the c-point stands for apple macrostructure failure. But For the 11 and 17 mm/s loading speeds, the curves have no obvious bio-yield points. At 11 mm/s loading speed, typical force vs. displacement curves of whole fruits of Fuji cultivar with 2, 3.5, 7.9, and 11 mm-diameter probes are shown in Fig. 5. In this diagram, with the different probes, the curves have also no obvious bio-yield points in the curves.

Apple fruit puncture property analysis

Table 3 shows that the regulation of fruit experimental data change was similar to the peel experimental data. It can be also seen that under the same probe diameter, the means of fruit puncture force for the same cultivar increased first from 0.1mm/s to 5mm/s loading speed, and as loading speed increased, the fruit puncture forces show little change compared to those of 5mm/s loading speed. Moreover, the fruit puncture force means between 0.1 and 5 mm/s loading speeds had a significant difference ($P \leq 0.05$) for Danxia and Fuji fruits. However, at 5, 11, and 17 mm/s loading speeds, no significant effect was observed between any two speeds.

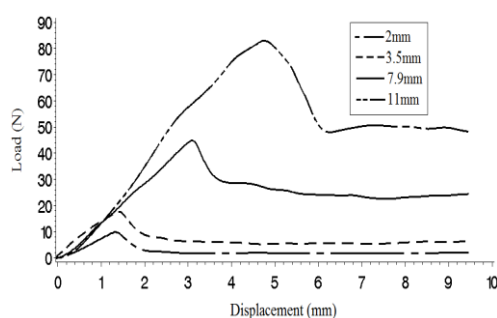


Fig. 5 - Puncture force–displacement curves of whole apples with different probes at 11 mm/s loading speed

Table 3 shows that as probe diameter increased at the same loading speed, the puncture force values of the fruit samples increase constantly; and a significant difference for the fruit puncture force ($P \leq 0.05$) existed between each pair of diameter probes.

Table 3

Values of puncture force of apple fruits at different loading speeds

Breed	Loading speed (mm/s)	Puncture force (N)			
		2 mm in diameter	3.5 mm in diameter	7.9 mm in diameter	11 mm in diameter
Danxia	0.1	7.55±0.65b,D	11.38±0.87c,C	30.62±2.63c,B	51.33±4.95c,A
	1	8.22±0.25b,D	13.15±1.57b,C	37.88±4.95b,B	56.76±2.54b,A
	5	9.25±0.64a,D	16.11±1.32a,C	42.02±2.76a,B	67.42±5.19a,A
	11	9.08±1.01a,D	16.87±1.09a,C	44.03±2.14a,B	71.41±8.19a,A
	17	9.12±1.17a,D	17.26±1.53a,C	45.56±5.23a,B	68.23±0.98a,A
Fuji	0.1	7.51±0.96c,D	13.86±1.41b,C	38.28±4.31b,B	58.26±10.66c,A
	1	8.81±0.99b,D	16.53±2.07a,C	41.83±5.28ab,B	67.76±6.33b,A
	5	10.21±0.67a,D	17.36±1.28a,C	44.43±6.44a,B	70.97±11.68ab,A
	11	10.33±1.10a,D	17.43±2.20a,C	46.73±6.99a,B	74.34±13.42ab,A
	17	10.01±1.23a,D	16.83±1.43a,C	46.95±2.99a,B	78.87±5.46a,A

Note: Means within rows with a different uppercase letter are significantly different ($P \leq 0.05$).

Means within columns with a different lowercase letter are significantly different ($P \leq 0.05$).

Peel contribution percentage

In the process of transporting and storing, the injury between apples was closely related to peel texture. The puncture mechanical characteristics of fruit peel and the puncture injury susceptibility of fruits could be confirmed by the puncture tests (Desmet et al., 2002; Hetzroni et al., 2011). Moreover, fruit firmness is commonly used for puncture test evaluation.

Therefore, contribution percentage of peel to apple fruit firmness could yield information on the evaluation quality and injury susceptibility of fruits; and the contribution percentage was calculated as:

$$\text{Peel contribution percentage} = \frac{\text{Apple peel puncture strength}}{\text{Apple fruit puncture strength}} \times 100 \quad (2)$$

Using the same probe diameter, apple peel puncture force to the whole fruit puncture force percentage at the same speed is shown in Fig. 6. As probe diameter increased, the contribution percentage of the peel kept a downward trend for the two cultivars; and contribution percentage of 0.1 mm/s loading speed reduced from 48.83% to 29.20% for Danxia peel, from 54.94% to 30.04% for Fuji peel, that of 1 mm/s loading speed reduced from 56.67% to 34.50% for Danxia peel, from 55.51% to 36.53% for Fuji peel, that of 5 mm/s loading speed reduced from 58.16% to 35.33% for Danxia peel, from 57.09% to 38.52% for Fuji peel, that of 11 mm/s loading speed reduced from 58.44% to 35.19% for Danxia peel, from 55.27% to 37.03% for Fuji peel, and that of 17 mm/s loading speed reduced from 59.36% to 35.91% for Danxia peel, from 57.58% to 35.71% for Fuji peel; and the contribution percentages of Danxia and Fuji peels were respectively reduced by an average of 39.57% and by an average of 36.61%.

Under the same probe diameter, at 0.1, 1 and 5 mm/s loading speeds, contribution percentages of peel increased constantly. The contribution percentage of 2 mm-diameter probe ranged from 48.83% to 58.16% for Danxia peel, from 54.94% to 57.09% for Fuji peel, that of 3.5 mm-diameter probe ranged from 49.21% to 53.91% for Danxia peel, from 47.36% to 52.75% for Fuji peel, that of 7.9 mm-diameter probe ranged from 37.67% to 42.48% for Danxia peel, from 34.23% to 44.27% for Fuji peel, and that of 11 mm-diameter probe ranged from 29.20% to 35.33% for Danxia peel, from 30.04% to 38.52% for Fuji peel. Along with the increase of loading speed, the contribution percentages of Danxia and Fuji peels were respectively reduced by an average of 15.61% and by an average of 18.21%. But at 11 and 17 mm/s loading speed, the contribution percentages of peel did not change much in comparison with 5mm/s loading speed; and the average of change was no more than 2.77% for Danxia peels and 4.35% for Fuji peels.

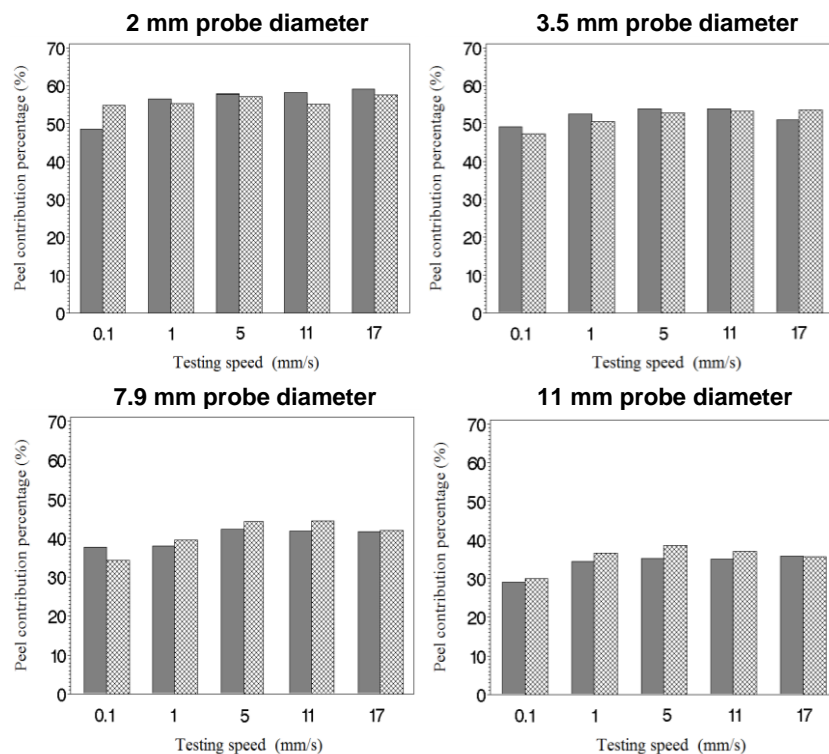


Fig. 6 - Peel contribution percentage to apple fruit firmness at different speeds

In Fig. 6, it shows that under 2, 3.5, 7.9 and 11 mm-diameter probes, the peel contribution percentage for two cultivars remained more than 48%, 47%, 34%, and 29% relatively, and as probe diameter increased, that of peel decreased gradually. These data suggest that peel texture had a lower influence on fruit firmness as probe diameter increased.

At 0.1, 1, 5, 11 and 17 mm/s loading speeds, the contribution percentage of peel remained more than 29%, 34%, 35%, 35%, and 36%, relatively for Danxia and Fuji cultivars and as loading speed increased, that largely remained the same. This result indicates that peel texture had a similar influence on fruit firmness as loading speed increased. Meanwhile, under the same probe diameter, the average of Fuji contribution percentage change was relatively big. This shows that the peel texture of Danxia cultivar had a greater effect on fruit firmness than that of Fuji cultivar and that the peel of Fuji cultivar was more prone to injury than that of Danxia cultivar. Based on whole-fruit test results, the puncture force of a whole Fuji fruit was the larger among the two cultivars. This reflects that cell adhesion of Fuji pulp was larger than that of the other kind of pulp and that Fuji pulp texture had more density than Danxia pulp texture.

Many studies show that the storage period of Fuji apples is longer (Xiao *et al.*, 2016; Wang *et al.*, 2002), and that the character and microstructure of apple peel are closely related to fruit shelf life (Deng *et al.*, 1995; Liu *et al.*, 2012). This also reflects that pulp texture is closely related to storage period of fruits.

CONCLUSIONS

This research evaluated the changes in apple peel and apple fruit puncture properties under different loading speeds and probe diameters. For the same variety, the mean values of peel puncture force and stiffness, and fruit puncture force increased as the probe diameters increased at the same loading speed, and significant difference ($P \leq 0.05$) existed for those puncture parameters between the two probe diameters. With the same probe diameter, as loading speed increased, the above puncture parameters for each cultivar increased firstly then made a few changes and peel texture had a similar influence on fruit firmness. At the same loading speed, under any probe diameter, the Fuji peel and fruit samples had the greatest puncture force in the two varieties, while relating the peel puncture force and fruit firmness, Danxia peel textures had a greater effect on fruit firmness than Fuji. Peel texture had a lower influence on fruit firmness as probe diameter increased and peel puncture force had a significant linear correlation with probe diameter. Based on test results, Fuji cultivar was more likely to obtain injury, compared with Danxia cultivar, and Fuji pulp texture had more density than Danxia. At the same time, the puncture texture of apple peel affected variety difference and fruit maturity, therefore the influence of that will have a better research for the same cultivar of different maturity and different cultivars of same maturity.

ACKNOWLEDGEMENT

This research, titled 'RESERACH ON THE CONTRIBUTION RATIO OF APPLE PEEL PUNCTURE BEHAVIOUR TO FRUIT FIRMNESS', was funded by the National Natural Science Foundation of China (11802167), the applied basic research of Shanxi Province (201801D221297), the Doctor Scientific Research Foundation of Shanxi Agricultural University (2017YJ15) and the Excellent Doctor Scientific Research Foundation the Excellent Doctor Foundation of Work Reward for Shanxi Province (SXVBKY201754). The authors are grateful and honoured to have obtained support from the Key Laboratory of Biomechanics.

REFERENCES

- [1] Allende A., (2004), Micromechanical and geometrical properties of tomato skin related to differences in puncture injury susceptibility. *Postharvest Biology and Technology*, Vol. 59, Issue 1, pp. 80–84, Amsterdam/Netherlands;
- [2] Chukwutoo I.C., (2017), Design for limit stresses of orange fruits (*Citrus sinensis*) under axial and radial compression as related to transportation and storage design. *Journal of the Saudi Society of Agricultural Sciences*, Vol. 16, Issue 1, pp. 72–81, Oxford/England;
- [3] Costa F., (2012), Texture dynamics during postharvest cold storage ripening in apple (*Malus domestica* Borkh.). *Postharvest Biology and Technology*, Vol. 69, pp. 54–63, Amsterdam/Netherlands;
- [4] Costa F., (2016), Mechanical investigation to assess the peel contribution in apple fruit. *Postharvest Biology and Technology*, Vol. 111, pp. 46–47, Amsterdam/Netherlands;
- [5] Deng J.G., (1995), Investigation on the Organization Structure of Apple Fruits. *Journal of fruit trees*, Vol. 12, Issue 2, pp. 71–74, Zhengzhou/P.R.C.;
- [6] Desmet M., (2002), Mechanical properties of tomatoes as related to puncture injury susceptibility. *Journal of Texture Studies*, Vol. 33, Issue 33, pp. 415–429, Malden/U.S.A.;

- [7] Grimm E., (2012), Structural and Physiological Changes Associated with the Skin Spot Disorder in Apple. *Postharvest Biology and Technology*, Vol. 64, Issue 1, pp. 111–118, Amsterdam/Netherlands;
- [8] Grotte, M., (2011), Mechanical properties of the skin and the flesh of apples. *International Journal of Food Properties*, Vol. 4, Issue 1, pp. 149–161, Philadelphia/U.S.A.;
- [9] Hetzronia A., (2011), Biomechanical characteristics of tomato fruit peels. *Postharvest Biology and Technology*, Vol. 59, Issue 1, pp. 80–84, Amsterdam/Netherlands;
- [10] Jiang S., (2009), Study on mechanical parameters of orange at different maturity stages. *Science and Technology of Food Industry*, Vol. 30, Issue 12, pp.117–119, Beijing/P.R.C.;
- [11] Li B.S., (2019), Prediction model of avocado ripening process based on sensory quality at room temperature. *Transactions of the Chinese Society of Agricultural Engineering*, Vol. 35, Issue 13, pp. 285-290, Beijing/P.R.C.;
- [12] Liu G.C., (2012), Research on the Change of 'Hanfu' Apple Fruit Anatomic Structure and Quality During Storage. *Transactions of the Chinese Society of Agricultural Engineering*, Issue 15, pp. 1–4, Haerbin/P.R.C.;
- [13] Liu H.F., (2018), Detection of cracking tomato based on machine vision in greenhouse. *Transactions of the Chinese Society of Agricultural Engineering*, Vol. 34, Issue 16, pp. 170-176, Beijing/P.R.C.;
- [14] Ma Q.H., (2011), Establishment of the Detecting Method on the Fruit Texture of Dongzao by Puncture Test. *Scientia Agricultura Sinica*, Vol. 44, Issue 6, pp. 1210–1217, Beijing/P.R.C.;
- [15] Rao M.A., (2011), Rheological Characteristics of Apple Skin and Apple Firmness. *International Journal of Food Properties*, Vol. 14, Issue 5, pp. 1297-1304, Philadelphia/U.S.A.;
- [16] Singh K.K., (2006), Postharvest physico-mechanical properties of orange peel and fruit. *Journal of Food Engineering*, Vol. 73, Issue 2, pp. 112–120, Oxford/England;
- [17] Shao X.F., (2009), Effect and mechanism of hot air treatment on the fruit texture of Gala apple cultivar. *Journal of Fruit Science*, Vol. 26, Issue 1, pp. 13–18, Zhengzhou/P.R.C.;
- [18] Shafiee S., (2008), Investigation of the effect of skin on mechanical behaviour of apple. *Journal of Food Technology*, Vol. 6, Issue 2, pp. 86–91, Dubai/UAE;
- [19] Tobi F., (2016), Susceptibility of apples to bruising inside ventilated corrugated paperboard packages during simulated transport damage. *Postharvest Biology and Technology*, Vol.118, pp. 111-119, Amsterdam/Netherlands;
- [20] Vanstreels E., (2005), Micromechanical behaviour of onion epidermal tissue. *Postharvest Biology and Technology*, Vol. 37, Issue 2, pp. 163–173, Amsterdam/Netherlands;
- [21] Veringă D., (2015), Determination of the Relaxation Time at Static Compression of Idared Apples Variety. *INMATEH-Agricultural Engineering*, Vol. 47, Issue 3, pp. 75-80, Bucharest/Romania;
- [22] Veringă D., (2018), Determination of the Relaxation Period at Static Compression of Golden Delicious Apples Variety. *INMATEH-Agricultural Engineering*, Vol. 48, Issue 1, pp. 61-66, Bucharest/Romania;
- [23] Wang C.S., (2002), Study on CA Storage Indices of Fuji Apple. *Acta Agriculturae Boreali-sinica*, Vol. 17, Issue 4, pp. 100–103, Beijing/P.R.C.;
- [24] Wang J.X., (2015), Experimental Research on Mechanical Properties of Apple Peels. *Journal of Engineering and Technology Science*, Vol. 47, Issue 6, pp. 688-705, Bandung/Indonesia;
- [25] Wang, J.X., (2016), Evaluation on peels texture of different apple cultivars based on rheological properties. *Transactions of the Chinese Society of Agricultural Engineering*, Vol. 32, Issue 21, pp. 305–314, Beijing/P.R.C.;
- [26] Wang, J.X., (2017), Properties and Microstructure of Apple Peels during Storage. *International Journal of Food Properties*, Vol. 20, Issue 5, pp. 159–1173, Philadelphia/U.S.A.;
- [27] Wang J.X., (2019), Research on tearing properties of apple peels based on microstructure, *INMATEH-Agricultural Engineering*, Vol. 58, Issue 2, pp. 223-230, Bucharest/Romania;
- [28] Xiao Y.P., (1994), Research on Biochemical and Morpho Anatomy of Apple in Natural Storage. *Acta Botanica Boreali-occidentalia Sinica*, Issue 5, pp. 92–95+169, Beijing/P.R.C.;
- [29] Zhao Z.Q., (2015), Vibration modal analysis of Korla pear and establishment of stiffness evaluation index. *Transactions of the Chinese Society of Agricultural Engineering*, Vol. 31, Issue 23, pp. 277-284, Beijing/P.R.C.

DESIGN AND THRESHING OUTPUTS STUDY OF INTERNAL AND EXTERNAL ROTARY ROLLER BUCKWHEAT THRESHER

/

内外滚筒旋转式荞麦脱粒装置设计与脱出物研究

Jiawei Wang, Zhiwei Li*, Saddam Hussain, Qi Lu, Haiyan Song, Decong Zheng ¹

College of Engineering, Shanxi Agriculture University, Taigu/China

Tel: +86-0354-6289384; E-mail: lizhiweitong@163.com

DOI: <https://doi.org/10.35633/inmateh-60-20>

Keywords: buckwheat, internal and external roller, thresher, outputs distribution, test

ABSTRACT

In order to study the distribution of buckwheat threshing outputs, on the self-designed internal and external rotary roller buckwheat threshing device test bench, the feeding amount was 0.5 kg/s, the internal roller speed was 380 r/min, and the external roller speed was +50 r/min (same direction as the internal roller), 0 r/min and -50 r/min (reverse direction compared to the internal roller) for threshing test. By analysing the overall condition of the threshing outputs, the content of each component in the threshing outputs, and the axial distribution of the threshing roller, it was found that the receiving box below the rasp bar roller mainly contained grains and chaff, leaves and petals, and the receiving box below the spike tooth roller mainly contained short stalks. Under the three conditions, the proportion of chaff in the threshing outputs was 40-45%, the proportion of leaves and petals was 23-29%, the proportion of grains was 13-19%, the proportion of short stalks was 14-16%. Grains, chaff, leaves and petals were mainly concentrated at the front, and short stalks were mainly distributed at the rear of the threshing roller, providing a theoretical basis for the design of the cleaning system.

摘要

为研究荞麦脱出物分布情况,在自行设计的内外滚筒旋转式荞麦脱粒装置试验台上,选取喂入量为 0.5 kg/s,内滚筒转速为 380 r/min,外滚筒转速分别为+50 r/min (与内滚筒同向)、0 r/min 和-50 r/min (与内滚筒反向)进行脱粒试验。通过对脱出物整体情况和脱出混合物中各成分含量以及沿脱粒滚筒轴向分布进行分析,纹杆滚筒下方接料盒中主要以籽粒和细小的糠、叶子和花瓣居多,钉齿滚筒下方接料盒中以短茎秆居多,三种条件下脱出物中糠所占比例最大为 40%-45%,叶子和花瓣所占比例次之为 23%-29%,籽粒所占比例为 13%-19%,短茎秆所占比例为 14%-16%,籽粒、糠、叶子和花瓣主要集中在前端位置,短茎秆主要分布在脱粒滚筒后端,因此脱粒装置前端清选负荷较大,而外滚筒不转情况下整体分布优于另外两种情况,外滚筒与内滚筒转向相反时脱出混合物中杂余质量略低于另外两种情况,为后续清选系统的设计提供理论依据。

INTRODUCTION

Buckwheat has an infinite raceme with long flowering period and extremely inconsistent grain maturation time and maturity, which brings some difficulties to its mechanized harvesting (Huang Xiaona et al., 2018). When buckwheat is harvested, there are many withered petals, the stems are brittle and easy to break, and the leaves have not withered. Therefore, there is a large number of things such as chaff, short straws, leaves, and petals in the mixture, which brings some difficulties to the selection of buckwheat (Farooq et al., 2016; Ren Changzhong et al., 2018).

The existing threshing device mainly adopts a form in which the threshing drum is matched with the concave grate. The rubbing, brushing and impacting of the threshing drum complete the separation of grain and straw (Barac et al., 2011; Dhananchezhyan et al., 2013; Chuan-udom et al., 2011). When the threshing drum rotates at a high speed, the kernel crushing rate and kernel loss rate are large, and it is difficult to adapt to the buckwheat mechanized harvesting operation (Govindaraj et al., 2017; Maertens et al., 2000).

¹ Jiawei Wang, As. Ph.D. Stud. Eng.; Zhiwei Li Prof. Ph.D. Eng.; Saddam Hussain, Ph.D. Stud. Eng.; Qi Lu, Haiyan Song, Prof. Ph.D. Eng.; Decong Zheng, Prof. Ph.D. Eng.

In recent years, scholars at home and abroad have conducted a lot of research on the distribution of threshing outputs. *Ni Chen et al. (2013)* and *Bohai Li et al. (2005)* based on the simulation of the spline interpolation method of MATLAB digital signal processing software, a mathematical model of rice threshing outputs was established, which provided a basis for improving the distribution. *Shujuan Yi et al. (2008)* studied the axial distribution of threshing outputs in the nail-type axial flow threshing and separation device, and provided a theoretical basis for further research of the device. *Yaoming Li et al. (2008)* and *Yanhe Zhang et al. (2011)* compared the uniformity of the threshing outputs distribution on the short-rasp-bar tooth cylinder and the spike tooth cylinder; it was found that the short-rasp-bar tooth cylinder can reduce the load of the cleaning device and improve the overall machine quality. *Taibai Xu et al. (2019)* studied the distribution of the extracts after leaving the concave plate in the multi-roller bench test; it was found that the axially-distributed extracts were unevenly distributed in the horizontal roller, and the cleaning loss was serious. *Zhenwei Liang et al. (2019)* studied the distribution of extracts from spiral blade plate-tooth combination and nail-type axial flow separation devices; the axial and circumferential distribution curves and equations of the extracts from the two devices were obtained. *Yaoming Li et al. (2014)* and *Yan Guo et al. (2011)* studied the distribution of the threshing mixture under the shear roller and the longitudinal axial roller; they provided the basis for the design and optimization of the cleaning device. *Liquan Yang et al. (2018)* studied the distribution of corn threshing kernels and provided a scientific basis for the design of the corn kernel harvester threshing system. *Lijun Wang et al. (2015)* analysed the corn exfoliation composition and established the simulation models of different compositions to study the movement law of corn threshing outputs. *Nan Jiang et al. (2013)* with the help of high-speed camera equipment, photographed online the falling process of the ejection from the device; the falling process of the ejection from the nail-type axial flow threshing and separating device was analysed.

Considering the above points, an internal and external rotary roller buckwheat threshing device was designed, and a threshing test was performed on test bench to analyse the distribution of the threshing outputs, which provided a basis for the design of the cleaning device.

MATERIALS AND METHODS

Internal and external rotary roller buckwheat threshing device

The structure of the internal and external rotary roller buckwheat threshing device is shown in Fig. 1. It mainly includes frame, threshing roller, concave grate roller, screw feeding device, top cover, pressing wheel, friction wheel, transmission shaft, reducer and other components, where the concave grate roller is the external roller, the threshing roller is the internal roller, and both of them can rotate independently. During work, the materials from the feeding inlet, enters the concave grate roller under the function of the screw feeding device, and completes the separation of the grain from the stalk under the rubbing and brushing action of the internal and external rollers, and the grain and debris fall through the concave grate roller, straw is discharged from the trash export. The concave grate roller is rotated by the friction wheel, and compacted by the pressing wheel to prevent slipping.

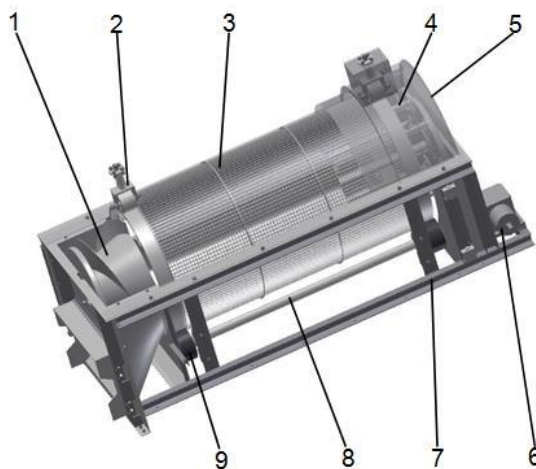


Fig. 1 - Structure of internal and external rotary roller buckwheat threshing device
 1- Screw feeding device; 2- Pressing wheel; 3- Concave grate roller; 4- Threshing roller; 5- Top cover;
 6- Reducer; 7- Frame; 8- Transmission shaft; 9- Friction wheel

The structure of the threshing roller is shown in Fig. 2. It is composed of screw feeding device, rasp bar roller, spike tooth roller and shaft. The screw feeding device adopts the design of double spiral cone blades and cone cylinder, and the material can be pushed into the concave grate roller during the rotation. The rasp bar roller adopts 6 D-shaped left rods with a fully closed design and length of 988 mm, the rubbing effect with the external roller completes the separation of grain and stalk and the backward push of the material. The spike tooth roller uses 6 rows of nails, each row of nails is arranged with 3 spirals and has the length of 494 mm, the grains are further threshed by the action of impacting and combing, the straws are pushed back and thrown out of the machine.

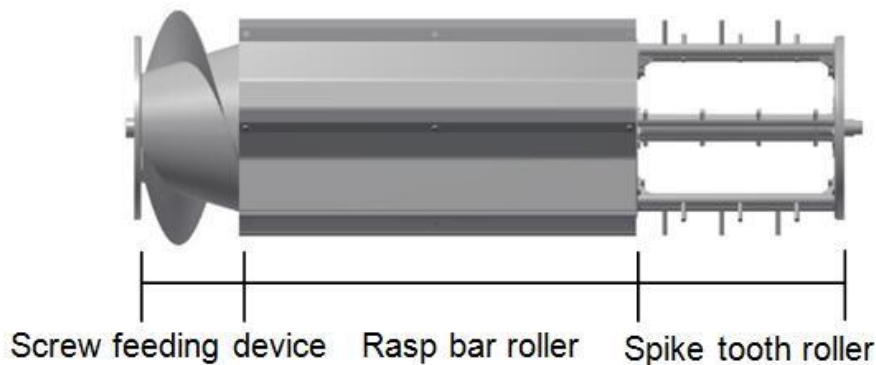


Fig. 2- Structure of threshing roller

The structure of the concave grate roller is shown in Fig. 3. The two ends are support drive plates, and 120 ribs are evenly arranged in the middle circumferential direction; the ribs are reinforced by the ring plate. Wire rings are fixed on the roller longitudinal each 15 mm, and a series of grids with a hole length 14 mm and a hole width 12 mm are formed. The surface of rib is higher than the iron wire 5 mm, in order to block the crop and improve the impact and vibration of the roller on the crop. The working diameter of the concave grate roller is $\text{Ø}636$ mm.

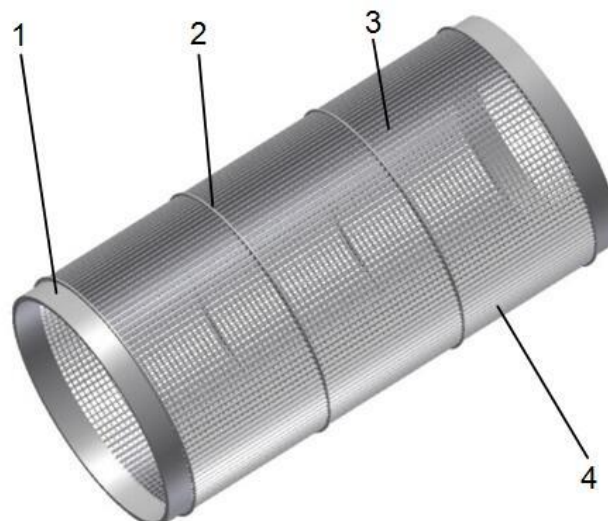


Fig. 3 - Structure of concave grate roller
1- Support drive plate; 2- Ring plate; 3- Rib; 4- Wire ring

Buckwheat threshing device performance test bench

The structure of the buckwheat threshing device performance test bench is shown in Fig. 4. It is mainly composed of conveyor belt, feeding bridge, internal roller reducer, threshing device, external roller reducer, control box, receiving box, motor of 1.5 kW, frame, and motor of 7.5 kW. During work, the material enters the threshing device through the feeding bridge. After threshing, grains and debris fall into the receiving box, and the straw is discharged from the machine.



Fig. 4 - Performance experiment unit of buckwheat threshing device

1- Conveyor belt; 2- Feeding bridge; 3- Internal roller reducer; 4- Threshing device; 5- External roller reducer; 6- Control box; 7- Receiving box; 8- Motor of 1.5 kW; 9- Frame; 10- Motor of 7.5 kW

The conveyor belt is 0.4 m high, 10 m long and 1 m wide, it is driven by a motor of 40 W, and the speed range is 0-60 m/min. The receiving box is placed under the threshing device. The structure is shown in Figure 5. It is divided into five rows along the threshing roller longitudinal, each row is 258 mm wide. The 1-3 rows correspond to the rasp bar roller and 4-5 rows correspond to the spike tooth roller. It is divided into three columns tangential to the threshing roller, and each column is 274 mm wide.

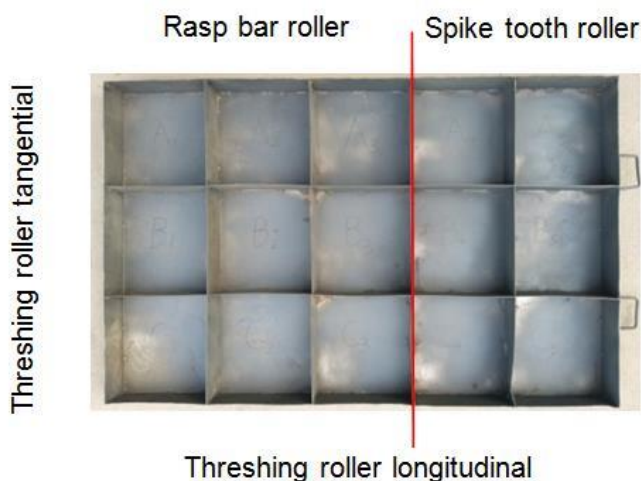


Fig. 5 - Receiving box

Test materials and test methods

The buckwheat used in the experiment is red mountain buckwheat grown in Taigu, Shanxi, 78-92 cm height, the grain moisture content is 10.9%, the stalk moisture content is 45.1%, the grass-valley ratio is 1:2.38, and the thousand-grain weight is 25.4 g, which are harvested manually for testing.

This experiment mainly studied the distribution of threshing outputs under different external roller conditions when the feeding amount was 0.5 kg/s and the rotation speed of the internal roller was 480 r/min. During the test, 6 kg buckwheat were evenly spread on the conveyor belt, the speed of the belt was adjusted to 0.833 m/s and the feeding amount was 0.5 kg/s, the speed of the internal roller was adjusted to 480 r/min by the motor inverter, the rotation speed of the external roller was adjusted to + 50 r/min, 0 r/min, and -50 r/min through the motor inverter (“+” means that the rotation direction of the external roller is the same as that of the internal roller, and “-” means that the rotation direction of the external roller is opposite to that of the internal roller). Three groups of tests were performed, and each group of tests was repeated three times. After the test, we took out the receiving box, manually sorted and weighed the materials in each cell. The threshing outputs mainly consisted of grains, leaves, petals, chaff and short stalks, the size of the short stalks being 10-30 mm, as shown in Fig. 6.

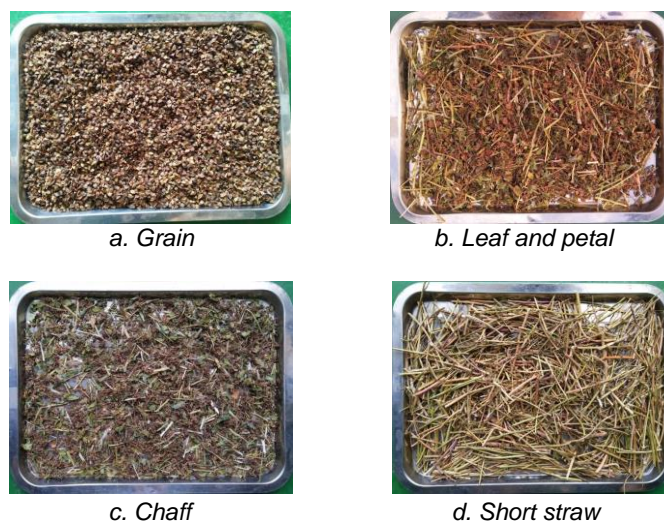


Fig. 6 - Threshing outputs components

RESULTS

Analysis of the overall situation of the threshing outputs

The output mixtures in the receiving box, after the test, are shown in Fig. 7. It can be seen that there are more mixtures in the receiving box below the rasp bar roller, mainly leaves, petals, chaff and grains, mixed with a small number of short straws; there are fewer mixtures in the receiving box below the spike tooth roller, most are short stalks, mixed with a small amount of grains, leaves and petals. It showed that in the buckwheat threshing process, the main grains are threshing under the rubbing effect of the rasp bar roller and the concave grate roller, and with the further impacting of the spike tooth roller and the concave grate roller, the threshing of hard to separated grain is completed, and the straws are more likely to be broken by the spike tooth roller.



Fig. 7 - Overall situation of the threshing outputs

Analysis of threshing outputs components under different external roller rotation conditions

Components weight analysis

Under the three rotating conditions of the external roller, grains, short stalks, chaff, leaves and petals in the threshing outputs and the total mass of the mixtures are shown in Fig. 8. It can be seen the grains weight when the external roller rotates in the same direction with the internal roller is slightly smaller than that when the external roller doesn't rotate or rotates in the reverse direction of the internal roller. The reason is that when the external roller and the internal roller rotate in the same direction, the kneading and squeezing effect of the material between them is small, the threshing is insufficient, and the grain loss is large. The short straws weight when the external roller rotates in the same direction with the internal roller is bigger than that when the external roller doesn't rotate or rotates in the reverse direction of the internal roller. The reason is that when the external roller and the internal roller rotate in the same direction, the movement of the materials between them is more complicated than in the other two cases, and the stems are more likely to be broken and fall into the receiving box.

The chaff weight when the external roller rotates in the reverse direction of the internal roller is slightly smaller than that when the external roller doesn't rotate or rotates in the same direction of the internal roller. The reason is that when the rotation of the internal and external roller is reversed, the relative rotation speed of them increases, the residence time of the materials between the rollers is short, and the number of stalks broken into chaff is reduced. The leaves and petals' weight, when the external roller rotates in the same direction of the internal roller, is bigger than that when the external roller doesn't rotate or rotates in the reverse direction of the internal roller. The reason is that when the external roller and the internal roller turn in the same direction, the relative rotation speed of them decreases, but the movement of the material between them is complicated, and more leaves and petals fall into the receiving box without being broken. The total mass of mixtures is the biggest when the external roller and the internal roller rotate in the same direction; the total mass of the mixtures is the smallest when the external roller and the internal roller rotate in the opposite direction, and the total mass of the mixtures is in the middle when the external roller doesn't rotate. The reason is that when the external roller and the internal roller rotate in the opposite direction, the relative rotation speed of them is the highest, and the materials stay between the rollers for the shortest time, and there are minimal mixtures falling into the receiving box through the external roller. The situation is exactly the opposite when the external roller and the internal roller rotate in the same direction.

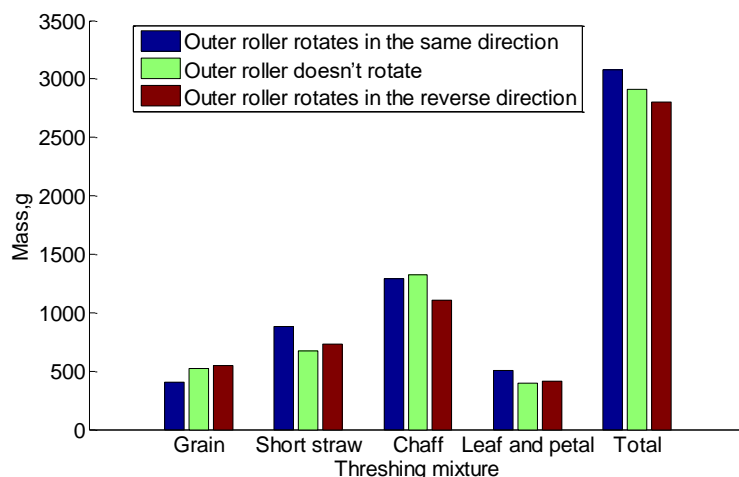


Fig.8 - Mass of components under different outer roller rotation conditions

Components proportion analysis

The proportions of the mass of grains, short stalks, chaff, leaves and petals in the threshing outputs under the three rotation conditions of the external roller are showed in Fig. 9. The maximum proportion of grains is 19% when the external roller and the internal roller rotate in the opposite direction. The minimum proportion of grains is 13% when the external roller and the internal roller rotate in the same direction. The middle proportion of grains is 18% when the external roller doesn't rotate and it is close to the situation of the external roller and the internal roller rotating in the opposite direction. The maximum proportion of short straws is 19% when the external roller and the internal roller rotate in the same direction. The minimum proportion of short straws is 14% when the external roller doesn't rotate. The middle proportion of short straws is 15% when the external roller and the internal roller rotate in the opposite direction. The proportion of short straws is close under the three conditions. The maximum proportion of chaff is 45% when the external roller doesn't rotate. The minimum proportion of short chaff is 40% when the external roller and the internal roller rotate in the opposite direction. The middle proportion of chaff is 42% when the external roller and the internal roller rotate in the same direction. The proportion of chaff is a little different under the three conditions. The maximum proportion of leaves and petals is 29% when the external roller and the internal roller rotate in the same direction. The minimum proportion of leaves and petals is 23% when the external roller doesn't rotate. The middle proportion of leaves and petals is 26% when the external roller and the internal roller rotate in the opposite direction. The proportion of leaves and petals is a little different under the three conditions.

Comprehensive analysis shows that the proportion of chaff in the three conditions is 40%-45%, the proportion of leaves and petals is 23%-29%, the proportion of grains is 13%-19%, and the proportion

of short straws is 14%-16%. This shows that the proportion of grains is close to that of short straws. The reason is related to the physical properties of buckwheat: at buckwheat maturity, the leaves have withered, and there are many withered petals, they are easily broken during the threshing process and mixed with chaff, so the proportion of chaff in the threshing mixtures is the largest. Buckwheat hollow stalks have high moisture content during harvest, they are brittle and easy to be broken, so there are a few short straws in the threshing mixtures, which also brings some difficulties to the cleaning of buckwheat threshing outputs.

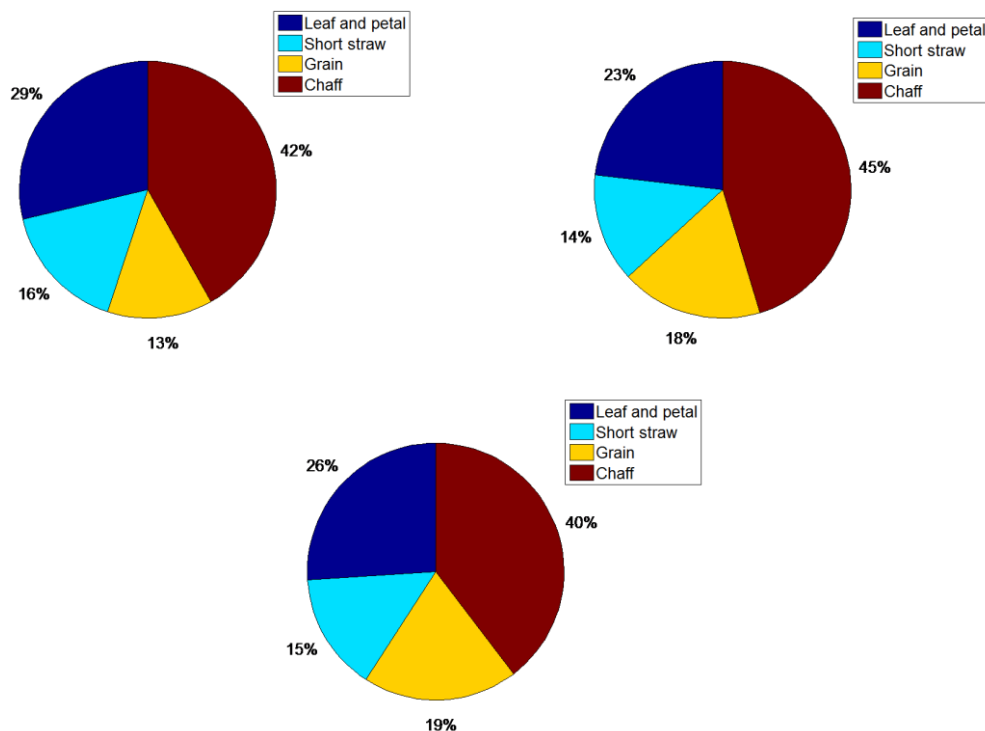


Fig. 9 - The components proportion under different conditions of external roller rotation

Analysis of the components' distribution along longitudinal axis of the threshing roller

The grains' distribution along longitudinal axis of the threshing roller under the three rotation conditions of the external roller is showed in Figure 10(a). Grains gradually decrease along the threshing roller longitudinal, and the decline trend is obvious in 1-3 rows, and the 3-5 rows are gradually flattened, and they are mainly concentrated below the rasp bar roller. It shows that the threshing of the main grains is completed under the rubbing effect of the rasp bar roller and the concave grate roller, and the threshing of the hard to separate grains is further completed under the impact of the spike tooth roller and the concave grate roller. The grains of the first row are the most numerous when the external roller and the internal roller rotate in the opposite direction, and the least numerous when the external roller doesn't rotate. The grains of second and third rows are the most numerous when the external roller doesn't rotate, and the least numerous when the external roller and the internal roller rotate in the same direction. The grains of fourth and fifth rows are the most numerous when the external roller and the internal roller rotate in the opposite direction, and the least numerous when the external roller and the internal roller rotate in the same direction. Comprehensive analysis shows that when the internal and external rollers rotate in the same direction, the grains are quickly dropped into the receiving box, and the grains distribution at rear-end is smaller, and when the external roller doesn't rotate, the overall distribution of the components is relatively good.

The short straws' distribution along longitudinal axis of the threshing roller under three rotation conditions of the external roller is showed in Figure 10(b). The short straws gradually increase along the threshing roller longitudinal, and are mainly concentrated below the spike tooth roller. It shows that the spike tooth roller has a greater impact on the material than the rasp bar roller, and it is easy to break the stalks into the receiving box. The short straws in the first row are the most numerous when the external roller and the internal roller rotate in the opposite direction, and the least numerous when the external

roller doesn't rotate. The short straws in the second row are the most numerous when the external roller and the internal roller rotate in the same direction, and the least numerous when the external roller doesn't rotate; the grains in third to fifth rows are the most numerous when the external roller and the internal roller rotate in the same direction, and the least numerous when the external roller and the internal roller rotate in the opposite direction. Comprehensive analysis shows that when the internal and external rollers rotate, the rasp bar roller and concave grate roller are more likely to break the stalks into the receiving box, and when the external roller and the internal roller rotate in the opposite direction, the distribution of short straws is relatively good.

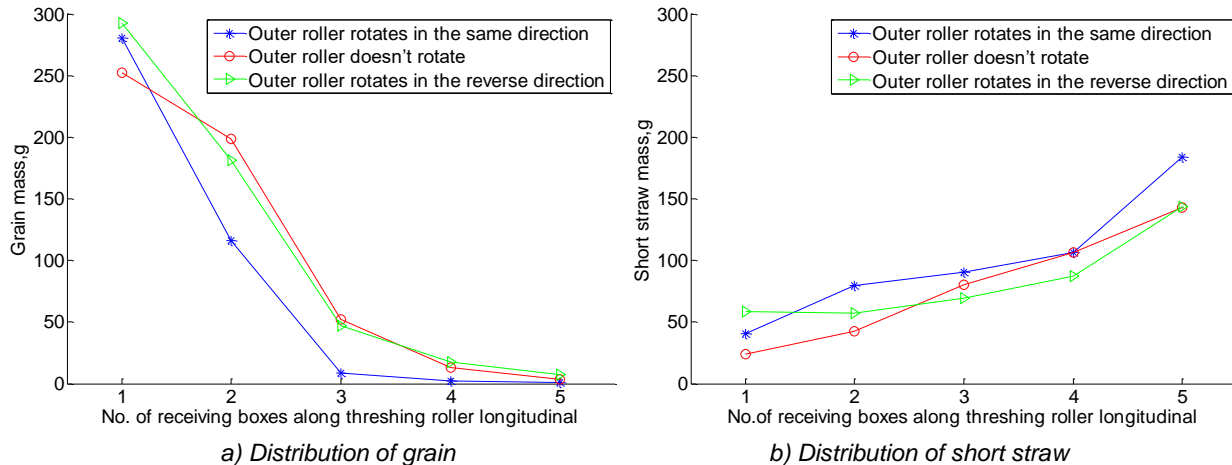


Fig.10 - The components proportion under different conditions of external roller rotate

The chaff distribution along longitudinal axis of the threshing roller under three rotation conditions of the external roller is showed in Figure 11(a). The chaff gradually decreases along the threshing roller longitudinal, and the downward trend of 1-3 rows is obvious, the 3-5 rows are gradually flattened, and they are mainly concentrated in 1-2 rows, and 3-5 rows towards to zero, it shows that during the threshing process, the chaff are easily separated from the crops and fall into the receiving box, and the cleaning pressure of front-end is greater. The chaff of first row are the most when the external roller and the internal roller are rotated in the same direction, and the least when the external roller is not rotated; the chaff of second row are the most when the external roller is not rotated, and the least when the external roller and the internal roller are rotated in the opposite direction; the chaff of third row are the most when the external roller is not rotated, and the least when the external roller and the internal roller are rotated in the same direction; the chaff of fourth and fifth rows are close in three cases, and almost zero. Comprehensive analysis, when the internal and external rollers are rotated, a large amount of chaff are quickly separated and fall into the receiving box, and when the external roller is not rotated, the overall distribution is relatively good.

The leaves and petals distribution along longitudinal axis of the threshing roller under three rotation conditions of the external roller is showed in Figure 11(b). When the external and internal rollers are rotated in the same direction, the leaves and petals increase, then decrease, and then increase, and each row is higher than the other two cases, it shows that when the external roller and the internal roller are rotated in the same direction, the movement of the materials between the rollers is more complicated, the kneading and squeezing effect is more obvious, and a large number of leaves and petals are separated and fall into the receiving box. When the external roller and the internal roller rotated in the opposite direction, the leaves and petals decrease and then increase, it shows that after the materials enter the internal and external rollers, a large number of leaves and petals are separated, and the kneading effect of the rasp bar roller and concave grate roller is small, so the leaves and petals gradually decrease, when they reach the spike tooth roller, due to the large impacting of the spike tooth roller, leaves and petals are knocked down and gradually increasing. Comprehensive analysis shows that the pressure for the selection of leaves and petals is mainly concentrated on the front and back ends, and the distribution of leaves and petals is relatively good when the external roller is not rotated.

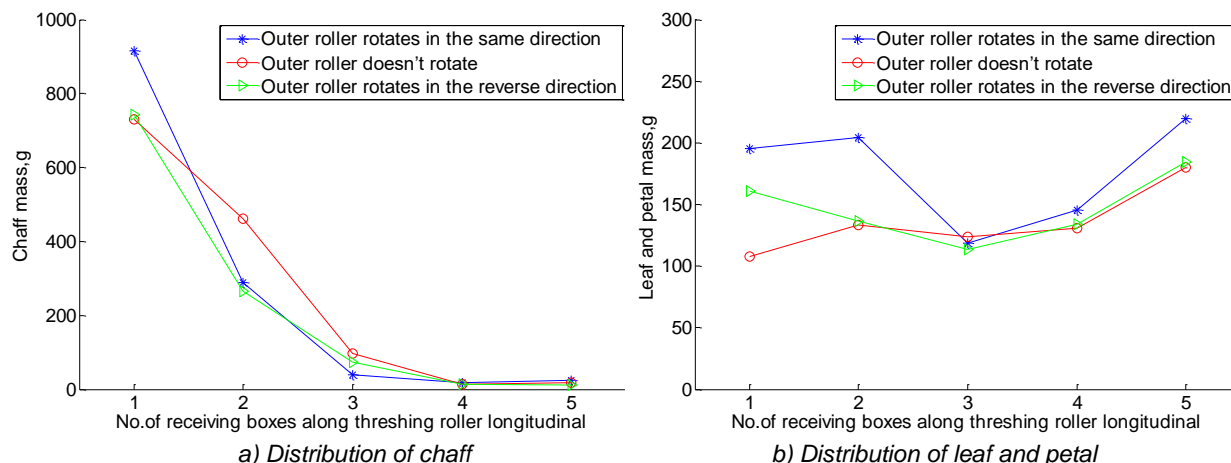


Fig.11 - The components proportion under different conditions of external roller rotate

CONCLUSIONS

(1) The buckwheat threshing test was performed on self-designed internal and external rotary roller buckwheat threshing device test bench. The feeding amount was 0.5 kg/s, the internal roller speed was 480 r/min, and the external roller was +50 r/min (same direction as the internal roller), 0 r/min and -50 r/min (opposite direction of the internal roller), which provided a theoretical basis for the design of subsequent cleaning systems.

(2) Analysing the overall situation of the threshing outputs, it was found that there were more mixtures in the receiving box below the rasp bar roller, mainly leaves, petals, chaff and grains, with a small number of short straws. There were fewer mixtures in the receiving box below the spike tooth roller, most of which were short stalks, mixed with a small amount of grains, leaves and petals.

(3) By analysing the mass of threshing outputs under the three rotation conditions of the external roller, it was found that when the external roller and the internal roller rotated in the opposite direction, the debris mass in the mixtures was slightly smaller than the other two cases, and the grain loss was greater when the external roller and the internal roller rotated in the same direction.

(4) By analysing the proportion of the components of the threshing outputs under the three rotation conditions of the external roller, it was found that the proportion of chaff was 40-45%, and the proportion of leaves and petals was 23-29%, the proportion of grains was 13-19%, the proportion of short straws was 14-16%. The proportion of grains was close to the proportion of short straws.

(5) By analysing the distribution of the threshing outputs along the threshing roller longitudinal under the three rotation conditions of the external roller, it was found that the grains, chaff, leaves and petals were mainly concentrated at the front position, and the short straws were mainly distributed at the rear of the threshing roller, so the cleaning load of the front-end was large, but the overall distribution was better than in the other two cases when the external roller didn't rotate.

ACKNOWLEDGEMENT

This work was supported by the National Key Research and Development Project Plan of China (No. 2016YFD0701804), Major Special Projects for the Construction of China Modern Agricultural Industrial Technology System (No. CARS-07-D-2), Key Research and Development Program of Shanxi Province (No. 201803D221027-2), Youth Science and Technology Innovation Project of Shanxi Agricultural University (No. J141802150).

REFERENCES

- [1] Barać S.R., Biberdžić M., Đikić A., (2011), Result of seeds testing and quality losses of harvested mass depending on the drum-underdrum interspace at buckwheat harvest grain combines. *Research Journal of Agricultural Science*, Vol. 43, Issue 1, pp. 283-288, Timisoara/Romania;
- [2] Chen Ni., (2013), Three-dimensional digital simulation of exudate distribution model of rice and wheat thresher. *Modern Agriculture*, Vol. 2013, Issue 5, pp. 65-66, Jiamusi/China;

- [3] Chuan-udom S., Chinsuwan W., (2011), Effects of operating factors of an axial flow rice combine harvester on grain breakage. *Sonklanakarin Journal of Science and Technology*, Vol. 33, Issue 2, pp. 221–225, Hatyai/Thailand;
- [4] Dhananchezhiyan P., Parveen S., Rangasamy K., et al., (2013), Development of a nylon rasp bar threshing cylinder for portable paddy thresher and its performance evaluation, *Madras Agricultural Journal*, Vol. 2013, Issue 100, pp. 623–626, New Delhi/India;
- [5] Farooq S., Rehman R.U., Pirzadah T., et al., (2016), Cultivation agronomic practices and growth performance of buckwheat. *Molecular breeding and nutritional aspects of buckwheat*, Elsevier, Amsterdam/Netherlands;
- [6] Govindaraj M., Masilamani P., Asokan D., et al., (2017), Effect of different harvesting and threshing methods on seed quality of rice varieties. *International Journal of Current Microbiology and Applied Sciences*, Vol. 2017, Issue 6, pp. 2375–2383, Tamilnadu/India;
- [7] Guo Yan, Li Yaoming, Li Hongchang., et al., (2011), The radial distribution regularities of emerging object with longitudinal axial flow threshing and separating device. *Agricultural Mechanization Research*, Vol. 2011, Issue 12, pp. 110-112, Harbin/China;
- [8] Huang Xiaona, Zhang Weiguo, Dang Weilong., et al., (2018), Research status and development trend of buckwheat harvesting machinery. *Farm Machinery*, Vol. 2018, Issue 10, pp. 84-90, Beijing/China;
- [9] Jiang Nan, Yi Shujuan, Zhang Lili., et al., (2013), High-speed photography analysis on process of mixture of spike type axial flow device. *Agricultural Mechanization Research*, Vol. 2013, Issue 5, pp. 57-59, Harbin/China;
- [10] Liang Zhenwei, Li Yaoming, Baerdemaeker J.D., et al., (2019), Development and testing of a multi-duct cleaning device for tangential-longitudinal flow rice combine harvesters. *Biosystems Engineering*, Vol. 2019, Issue 182, pp. 95-106, San Diego/U.S.A.;
- [11] Li Bohai, Yi Shujuan, Jiang Nan et al., (2005), The tangent distribution of exudates along the roller of axial flow threshing and separating device. *Modern Agriculture*, Vol. 2005, Issue 10, pp. 31-32, Jiamusi/China;
- [12] Li Yaoming, Li Hongchang, Xu Lizhang., (2008), Comparative experiments on threshing performance between short-rasp-bar tooth cylinder and spike tooth cylinder. *Transactions of the Chinese Society of Agricultural Engineering*, Vol. 24, Issue 3, pp. 139-142, Beijing/China;
- [13] Li Yaoming, Wang Chenghong, Xu Lizhang., et al., (2014), Parameter optimization and field test of threshing and separation device in tangential-longitudinal combine. *Transactions of the Chinese Society for Agricultural Machinery*, Vol. 45, Issue 11, pp. 111-116, Beijing/China;
- [14] Maertens K., De Baerdemaeker J., Ramon H., et al., (2000), An analytical grain flow model for a combine harvester, Part I: Design of the Model, *Journal of Agricultural Engineering Research*, Vol. 79, Issue 1, pp. 55-63, Leuven/Belgium;
- [15] Ren Changzhong, Cui Lin, He Feng. et al., (2018), Construction and development of China oat and buckwheat industrial technology system. *Journal of Jilin Agricultural University*, Vol. 40, Issue 4, pp. 524-532, Changchun/China;
- [16] Wang Lijun, Li Yang, Liang Chang., et al., (2015), Motion law of maize mixture in cross air-and-screen cleaning device. *Transactions of the Chinese Society for Agricultural Machinery*, Vol. 46, Issue 9, pp. 122-127, Beijing/China;
- [17] Xu Taibai, Zhou Chenlu., (2019), Experimental Study on the extraction distribution of multi-roller combine harvester. *Modern Agricultural Science and Technology*, Vol. 2019, Issue 4, pp. 144-145, Hefei/China;
- [18] Yang Liquan, Wang Wanzhang, Zhang Hongmei., et al., (2018), Improved design and bench test based on tangential flow-transverse axial flow maize threshing system. *Transactions of the Chinese Society of Agricultural Engineering*, Vol. 34, Issue 1, pp. 35-43, Beijing/China;
- [19] Yi Shujuan, Tao Guixiang, Mao Xin., (2008), Comparative experiment on the distribution regularities of threshed mixtures for two types of axial flow threshing and separating installation. *Transactions of the Chinese Society of Agricultural Engineering*, Vol. 24, Issue 6, pp. 154-156, Beijing/China;
- [20] Zhang Yanhe, Yi Shujuan., (2011), Contrast testing research of rice threshing performance of different threshing device. *Agricultural Mechanization Research*, Vol. 2011, Issue 12, pp. 146-149, Harbin/China;

VIBRATION AND IMPACT DETECTION OF AXIAL- FLOW THRESHING UNIT UNDER DYNAMIC THRESHING CONDITIONS

动态脱粒工况下轴流脱粒装置的振动与冲击检测

Ji Jiangtao^{1,2)}, Hu Jingpeng¹⁾, Wang Shengsheng^{1,2)}, Zhang Ruihong¹⁾, Pang Jing¹⁾ ¹

¹⁾ Henan University of Science and Technology, College of Agricultural Equipment Engineering/ China;

²⁾ Collaborative Innovation Centre of Machinery Equipment Advanced Manufacturing of Henan Province/ China

Tel: +86-379-64877837; E-mail: jjt0907@163.com

DOI: <https://doi.org/10.35633/inmateh-60-21>

Keywords: Axial-flow threshing unit; vibration; impact; acceleration; stress

ABSTRACT

In order to explore the interaction between the axial-flow threshing unit and the agricultural materials, the vibration signal of the axial-flow threshing unit and the stress signal of the internal threshing tooth under the dynamic threshing condition were detected by using the three-way acceleration sensors and the resistance strain gauges. The results show that under the dynamic threshing condition, the amplitude of the vibration signal along the axial direction of the threshing unit experienced a small change, but changed greatly at the feeding direction of materials and vertical direction of fixed bearings, which was mainly caused by the internal impact between the threshing unit and the materials; Under the impact of materials, the threshing element of each measuring point has a continuous peak value of stress signal, and the stress signals gradually decreased along the axial direction. This study further reveals the interaction mechanism between axial-flow threshing unit and materials from the perspective of vibration and impact, and provides new methods for the development of condition detection technology of grain harvesting equipment.

摘要

脱粒装置内部与物料作用情况极其复杂, 为探究轴流脱粒装置与物料之间的相互作用情况, 采用三向加速度传感器和电阻应变片, 实现了动态脱粒工况下轴流脱粒滚筒的振动信号及内部脱粒元件的应力信号的检测。结果表明: 轴流脱粒滚筒由空转变化至脱粒工况, 沿物料轴向运动方向振动幅值变化较小, 沿物料喂入方向和轴承座上下方向的振动幅值变化较为明显; 各测点脱粒元件受冲击载荷作用而出现连续的应力峰值, 且大小沿轴向逐渐降低。本研究从振动和冲击应力的角度进一步揭示了轴流脱粒装置与物料之间的相互作用机理, 为谷物收获装备工况检测技术的发展提供了新的方法和思路。

INTRODUCTION

Axial-flow threshing unit is one of the commonly used threshing forms of the current harvesting equipment (Bello B et al, 2019). Spike tooth is the most widely used threshing element, and it completes the threshing and separating function by impact with the threshed object. The mechanical state of the materials in the threshing unit directly affects the quality of threshing process. Therefore, to improve the threshing quality, it is one of the important contents to develop the mechanism of the interaction between the axial-flow threshing unit and the materials.

Domestic and foreign scholars have focused on the research of the interaction mechanism between the threshing units and materials, mainly about the construction of mathematical models and simulation tests, and most of these works were based on some assumptions, which were quite different from the actual working process of the threshing unit (Chansrakoo and Chuan-Udom, 2018; Steponavicius D et al, 2018; Miu P. and Kutzbach H., 2008). During the actual working process, the threshing unit generated vibration and impact response due to the reaction force of the materials. Tang Zhong et al. reached the conclusion that the unbalanced vibration of the tangential-flow threshing unit was caused by the threshing load by comparing the amplitude of the cutting-flow threshing unit under the condition of idling and threshing (Tang Zhong et al., 2019). Hamed et al carried out dynamic modeling and vibration analysis on the rasp-bar of tangential-flow thresher, and improved the vibration phenomenon by optimizing the structure of the threshing machine (Zare H. et al, 2019).

¹ Ji Jiangtao, Prof. Ph.D. Eng.; Hu Jingpeng, Wang Shengsheng, Ph.D. Eng., Zhang Ruihong, Pang Jing

Therefore, it is necessary to study the vibration phenomenon of the axial-flow threshing unit in threshing process. Wang Yue et al. analysed and calculated the impact frequency and impact stress of the crop in the axial-flow threshing unit, and explained the mechanism of stem and leaf fracture from the perspective of stress (Wang Yue and Ma Ji, 1987). Xie Fangping et al. designed a threshing unit with flexible-spike tooth based on the theory of energy conservation, and simulated the deformation and stress distribution of the flexible-spike tooth under threshing load. The simulation results show that the maximum deformation of the threshing tooth occurred at the free end, and the maximum stress generated at the fixed end (Xie Fangping et al, 2009). The above research shows that it is feasible to use the impact stress of threshing elements to characterize the impact degree of materials, but it is still at the theoretical level, and there is no relevant report on the detection of impact stress at present.

The internal threshing space is complicated and narrow to fix the detection devices in the axial-flow threshing unit. To solve these problems, we set up a vibration and impact detection system on the test bench of axial-flow threshing unit and completed the real-time detection of the vibration signal of the axial-flow threshing unit and the impact stress signal of the spike tooth, which provides new methods for the development of condition detection technology of grain harvesting equipment.

MATERIALS AND METHODS

CONSTRUCTION OF DETECTION SYSTEM OF VIBRATION AND IMPACT

Composition of vibration and impact test bench

The test bench is mainly composed of an axial-flow threshing unit and a detection system, as shown in Fig. 1, which is used to collect the vibration signal of the threshing unit and the stress signal of the spike tooth in real time. The material was fed through the feeding inlet, and it moved in a spiral direction along the threshing cylinder under the impact and friction of the spike tooth. The seeds were continuously removed, collected by the collecting device, and the remaining stalks were discharged from the grass discharge.

The vibration and impact detection system consisted of a three-axis acceleration sensor, resistance strain gauges, Robust DH5902 dynamic signal acquisition instrument and DH5905 wireless telemetry analysis system. The vibration signal was measured by the three-axis accelerometer (356A16). The stress signal was measured by the resistance strain gauges. The performance parameters of the DH5902 dynamic signal acquisition instrument, DH5905 wireless telemetry system and sensors are shown in Tab.1.

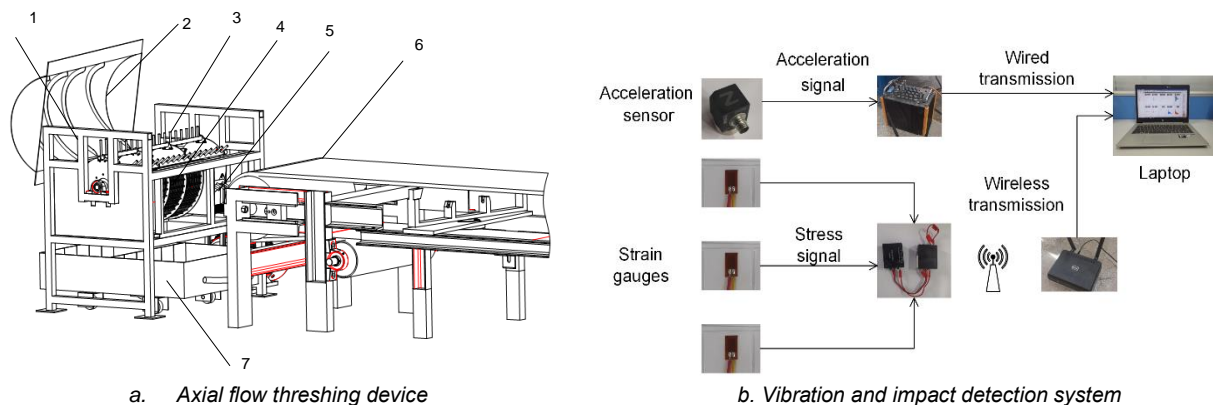


Fig. 1 -Test bench for vibration and impact testing

1. Frame; 2. Top cover; 3. Axial-flow threshing cylinder; 4. Concave plate; 5. Feeding inlet;
6. Conveying device; 7. Collecting device

DETECTION PRINCIPLE OF VIBRATION AND IMPACT

Vibration detection of axial flow threshing drum

When the conveying device works continuously, there is an interaction between the materials and the threshing cylinder. The spike tooth is arranged in the form of spiral along the axial direction, which is in direct contact with the materials. And the reverse force from the materials on each spike tooth is F_i . In every revolution of the threshing process, only some of the spike teeth are in direct contact with the materials, and the whole threshing cylinder is subjected to eccentric load. The force diagram is shown in Fig. 2.

The reverse force F_i can be decomposed into components F_{iy} and F_{iz} in the horizontal and vertical directions, the axial force F_{ix} comes from the axial push of the top cover on the materials. According to the knowledge of mechanical vibration, the reverse force of the material flow on the cylinder can be used as an external excitation force, which can cause the unbalanced vibration of the threshing cylinder. The axial-flow threshing cylinder is matched with the bearing and fixed to the frame by bolts. According to references (Syuhri A et al, 2018), the bearings can be simplified to springs (K_B) and damping (C_B), and the cylinder itself is treated as a spring (K_{EQ}), there by the entire physical model can be simplified and transformed into a series connection of the bearing and the threshing cylinder, as shown in Fig. 2. Therefore, the vibration of the bearing can be used to represent the vibration of the entire threshing cylinder.

Table 1-

Performance parameters of vibration impact detection system		
Name	Performance indicator	Parameter value
Dynamic signal acquisition instrument (DH5902)	Number of channels	16
	Highest sampling frequency [KHz]	100
	Distortion [%FS]	<0.5
Wireless telemetry system (DH5905)	Wireless mode	Wi-Fi
	Highest sampling frequency [KHz]	4
	A/D conversion[system]	16
Accelerometer (356A16)	Range [g]	±50
	Frequency response [Hz]	0.3~6000
	Sensitivity [$mV \cdot g^{-1}$]	100
	Lateral sensitivity [%]	<5
Resistance strain gauge (120-3AA)	Resistance [Ω]	120
	Sensitivity [$mV \cdot V^{-1}$]	2.0
	Base size [mm]	6.9*3.9
	Wire grid size [mm]	3.0*2.3

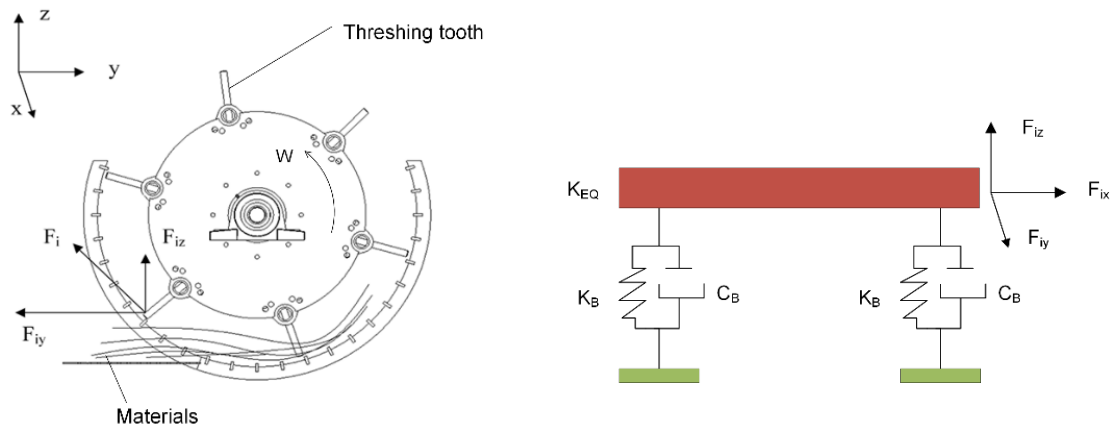


Fig. 2 - Schematic diagram force and vibration model

The amplitude of vibration detected from the bearing of the threshing cylinder in three directions can evaluate the interaction between the axial threshing cylinder and the materials. For easy description of the directions of vibration, a coordinate system is set on the axial-flow threshing cylinder. The X direction indicates the axial direction of the threshing cylinder. The Y direction indicates the tangential direction of the threshing cylinder, and the Z direction indicates the vertical direction of bearing pedestal. The three-axis accelerometer is used to measure the vibration signals in the three directions above, and the sensor is placed above the vertical bearing by the magnetic seat. The actual installation position of the three-axis accelerometer is shown in Figure 3. During the dynamic threshing process, in order to reduce the interference caused by the shaking of the connecting wire during the detection, the connecting wire is fixed by tape.

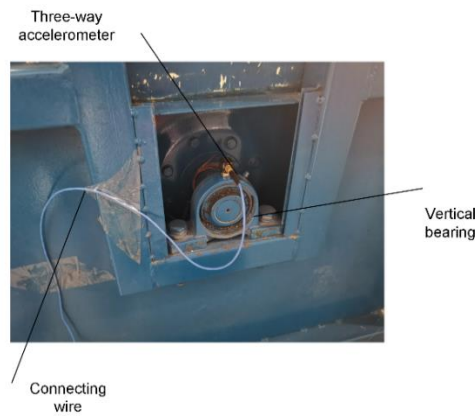


Fig. 3 - Installation position of the accelerometer sensor

Detection of impact stress

The impact load between the materials and the threshing unit causes the unbalanced vibration of the threshing cylinder, which can roughly describe the interaction inside the unit. And the threshing elements, which are in direct contact with the materials, can reflect the interaction mechanism between the material and the spike tooth during the threshing process (*Tang Zhong et al, 2019*). However, there are no measuring reports about the impact stress of threshing elements at present.

Without considering the influence of the interaction force and the friction force among the materials, we suppose the interaction between the spike tooth and the materials conforms to the law of conservation of energy and the theorem of impulse.

$$F^* = \frac{1}{\tau} \int_0^{\tau} F dt = \frac{mg(v_2 - v_1)}{\tau} \tag{1}$$

Where:

V_2 is the speed of the materials, [m/s]; V_1 is the speed of the spike tooth, [m/s]; F is the interaction force between the materials and the spike tooth, [N]; F^* is the average force on the spike tooth from the materials, [N]; τ is the contact time between the materials and the spike tooth, [s].

The spike teeth are all fixed with the gear rod during threshing process, and only the spike tooth interacts with the materials. Based on the theory of cantilever beam in mechanics of materials, each threshing tooth can be simplified as a cantilever beam model, as shown in Fig. 4.

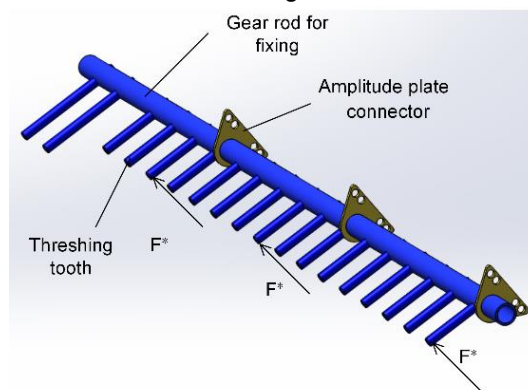


Fig. 4 - Simplified force diagram of the cantilever beam with spike teeth

The spike tooth will generate mechanical stress and strain under the impact load of the materials. The stress signal can be measured by the strain gauge and collected by the DH5905 dynamic signal acquisition instrument. It can be known from the material mechanics that the type of impact stress generated inside the spike teeth belongs to the kind of bending normal stress (*Xie Fangping et al., 2009*), and the formula for calculating the maximum bending normal stress is:

$$\delta_{\max} = \frac{M_{\max}}{W_z} = \frac{F^* l}{W_z} = \frac{mg \cdot \Delta v \cdot l}{\tau \cdot W_z} \tag{2}$$

Where:

δ_{max} is the maximum bending normal stress of the spike tooth, [MPa]; M_{max} is the maximum bending moment generated by the impact load, [MPa]; l is the equivalent length of the spike tooth, [mm]; W_z is the modulus of flexural section of the spike tooth, [mm³]. It can be known from formula (2) that the impact load of the spike tooth is related to the mass, speed and collision position of the materials.

The maximum bending stress of the spike tooth is usually produced near the fixed end. (Xie Fangping et al., 2009). According to the preliminary tests, if the strain gauge was pasted near the top of the spike tooth, the probability of the strain gauge contacting the materials directly would increase, resulting in the abnormal peak value of the impact stress signal. Once the strain gauge was damaged under the impact of materials, the test couldn't be carried out. Therefore, in order to ensure that a reasonable stress signal can be detected and the strain gauge is protected from damage, the strain gauge should be placed close to the root of the spike tooth. To further ensure the normal arrangement of the terminals and leads of the strain gauges, it was finally determined that the strain gauge was attached at a position of 10 mm away from the root of the spike tooth. The sticking method of the strain gauge adopts a 1/2 Wheatstone bridge, that is, two pieces are attached to the front and the back of the spike tooth respectively, and this method is only suitable for measuring the bending strain, eliminating the stretching and the compressive strain, which conforms to the deformation law under the normal stress of the spike tooth (Li Yaoming et al., 2013), as shown in Fig. 5a.

After the sticking was completed, one ohmmeter was used to check the quality of the strain gauges. The unqualified strain gauges should be replaced in time. And finally, the protective rubber was applied on the surface of the strain gauges before the test. In order to obtain the law of the stress signals along the axial direction, three spike teeth were selected as the measuring points, respectively located in the feeding, threshing and separating sections of this threshing cylinder. And strain gauge sensors were installed at the corresponding measuring point. The actual installation positions of each measurement point are shown in Fig.5b. In order to ensure that the signal acquisition module can work normally under the high-speed operation of the threshing cylinder, a fixing device was made using ordinary photosensitive resin material and 3D printing technology, as shown in Fig.5c.

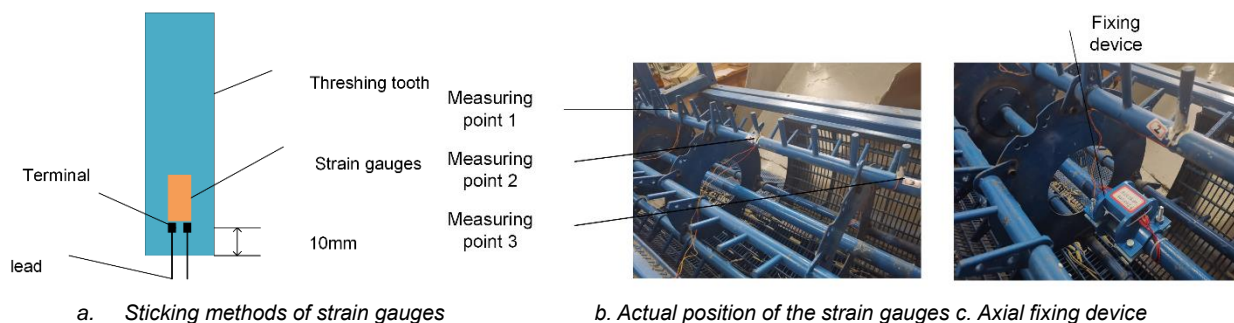


Fig. 5 - Sticking method and measuring points' position of strain gauges

The materials used in the threshing test were ripened Chinese cabbage plants harvested in the Lvyin breeding base of Jiyuan City, Henan Province, and the name of the variety was "Jincai No. 3 F1". The artificially harvested plants were randomly selected in the test field, and the threshing test was completed in time. Since the harvested Chinese cabbage plants were at the later period of the harvest, the test was completed under the condition that the moisture content of the materials was low. Measuring with a rapid moisture meter, the moisture contents of the kernels, pods and stems were 8.39%~10.26%, 13.16%~18.52%, 20.12%~25.32% respectively.

Before the vibration and impact test, the single factor and orthogonal tests of feeding rate, cylinder speed and concave clearance were carried out, and the reasonable range and optimal combination of parameters were obtained. When the feeding rate was 1 Kg/s, the cylinder speed was 750 r/min, and the concave clearance was 20 mm, the threshing unit showed the best threshing performance. With the combination of the above optimal operating parameters, the vibration and impact test bench performed the detection of the vibration and stress signals under the conditions of idling and dynamic threshing.

Before the detection of the dynamic threshing condition, to ensure a constant feeding rate of 1 Kg/s, the Chinese cabbage plants weighting 10 Kg were evenly spread on the conveyor belt with a conveying speed of 1 m/s, and five meters' acceleration adjustment zone was left.

The threshing unit, DH5902 dynamic acquisition instrument and DH5905 wireless telemetry analysis system were started at the same time. After the threshing unit started to operate stably, each channel value of the signal acquisition system was balanced and cleared, and the conveyor belt was activated. Finally, the transportation, feeding, threshing of the materials and the transmission and collection of the signals were completed. The detection under each condition was repeated 5 times, and the average data was statistically analysed to reduce the random test error.



Fig. 6 – Test site of vibration and impact detection

RESULTS

Detection results of the vibration

In the dynamic threshing process, the vibration signal of the axial-flow threshing cylinder was measured by a three-axis accelerometer, and the amplitude change of bearing pedestal was a time-domain process. As shown in Fig.7, it is a time-domain curve of acceleration change in the Y-direction during a complete threshing test of the axial-flow threshing unit, including the static state before the test, the startup state, the stable idling state, the dynamic threshing state, the stall state and the static state of the cylinder. It can be seen from the figure that the vibration amplitude of the bearing pedestal is significantly different under the conditions of stable idling and dynamic threshing. Fig.8 shows the vibration signals of the axial-flow threshing cylinder collected under both idling and dynamic threshing conditions.

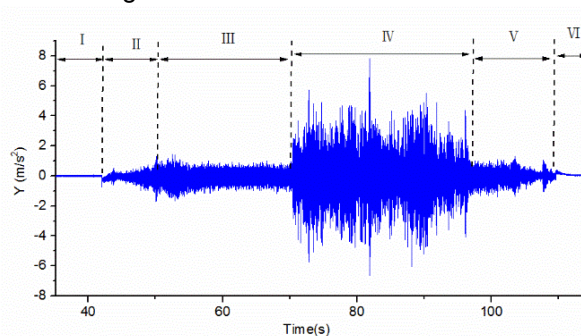


Fig. 7 - Time domain curve of the axial-flow threshing unit in one test process (Y channel)

Note: I. static; II. start; III. stable idling; IV. dynamic threshing; V. stop; VI. Static

According to the statistical results of vibration amplitude, under random vibration, the root mean square values and peak-to-peak values of the threshing process can reflect the impact of the Chinese cabbage plants on the threshing cylinder (Tang Z *et al.*, 2019). With the progress of the threshing process, the root mean square values and peak-to-peak values changed.

Part of the curves of the cylinder after stable operation under idling and threshing conditions were cut off respectively, and the root mean square value and peak-to-peak value were taken as the characteristic quantities to characterize the change of vibration signal. The vibration changes in the three directions of X, Y and Z were compared.

According to Fig. 8a and Fig. 8b, when the axial-flow threshing unit is in the idling state with no-load, the amplitude of the vibration acceleration in the X direction was $-2.426 \sim 2.886 \text{ m/s}^2$, and the root mean square value was 0.757 m/s^2 . The peak-to-peak value was 5.312 m/s^2 . However, when the materials were fed, the amplitude in the X direction increased slightly. The amplitude in X direction was $-3.392 \sim 3.106 \text{ m/s}^2$, the root mean square value was 0.926 m/s^2 , and the peak-to-peak value was 6.498 m/s^2 , increasing by 1.2 times approximately. This state of vibration in the X direction was approximately balanced.

According to Fig. 8c and Fig. 8d, the vibration amplitude significantly increased in the Y direction. The vibration amplitudes of the threshing process under no-load and dynamic threshing conditions were $-1.027 \sim 0.917 \text{ m/s}^2$ and $-3.896 \sim 3.792 \text{ m/s}^2$ respectively, and the root mean square values were 0.313 m/s^2 and 1.232 m/s^2 respectively. The peak-to-peak value was 1.944 m/s^2 and 7.688 m/s^2 respectively, which increased by about 4 times.

According to Fig. 8e and Fig. 8f, the vibration amplitude slightly increased in the Z direction. The vibration amplitudes of the no-load and the dynamic threshing conditions of the threshing process were $-0.708 \sim 0.814 \text{ m/s}^2$ and $-2.919 \sim 2.243 \text{ m/s}^2$ respectively. The root mean square values of the no-load state and the threshing state of the threshing process were 0.236 m/s^2 and 0.616 m/s^2 , and the peak-to-peak values were 1.521 m/s^2 and 5.234 m/s^2 , which increased by 2.6 times and 3.4 times respectively.

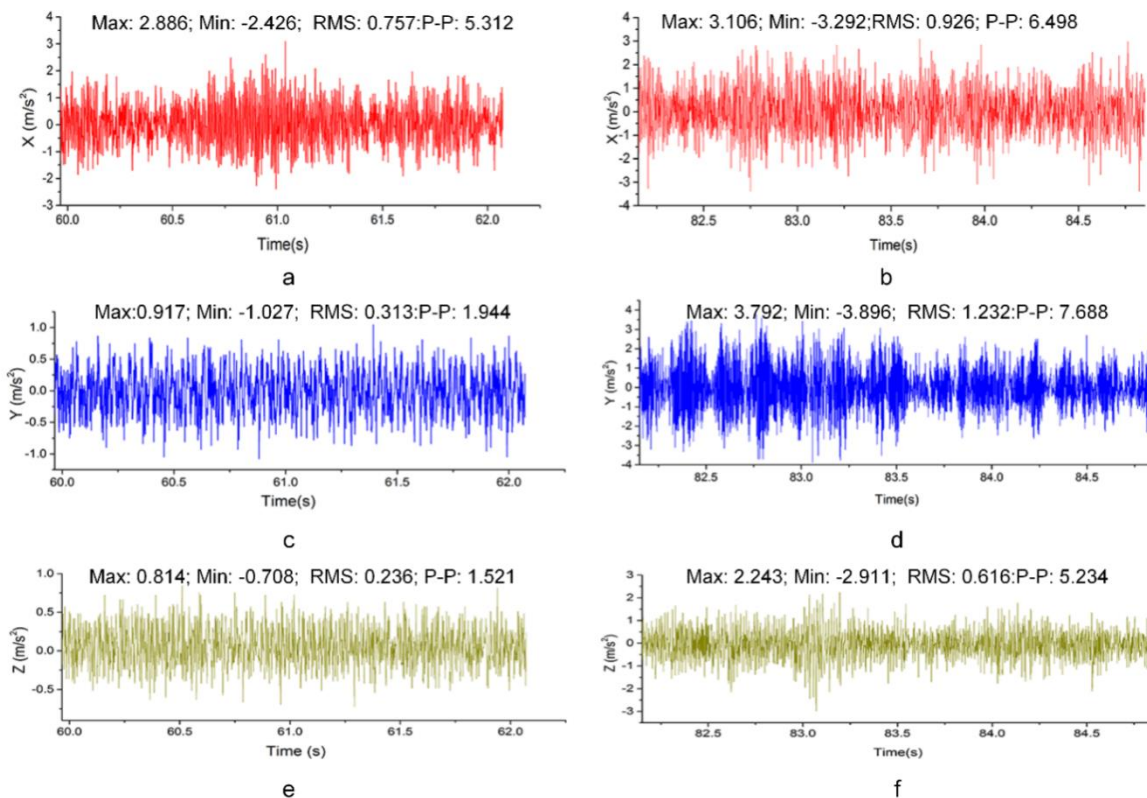


Fig. 8 - Vibration time domain curve under idle conditions and threshing conditions in the X, Y, Z directions

Note: Max- Maximum amplitude; Min- Minimum amplitude; RMS- root mean square; P-P- peak-to-peak

It can be seen from the above results that in the threshing process of Chinese cabbage plants, the amplitude of vibration in the X direction was slightly increased, and the change in vibration was negligible. However, the vibration amplitudes in the Y and Z directions were significantly increased. The reason for this phenomenon was that under the dynamic threshing condition, there was continuous impact and collisions between the materials and the spike teeth. The reaction force of the materials on the cylinder acted as an external excitation force, and the component forces were both in the Y and Z directions, which mainly caused the axial-flow threshing cylinder to generate a relatively strong unbalanced vibration phenomenon in the Y and Z directions, while the X direction vibration was mainly influenced by the axial force of the materials under the push of the spiral deflector and the spike teeth. The vibration in the Y direction was mainly affected by the horizontal component of the materials in the threshing cylinder.

The vibration in the Z direction was mainly caused by the vertical component of the materials in the threshing cylinder. The axial force in the X direction was significantly smaller than the forces in the Y and Z directions, which resulted in different vibration amplitudes of threshing cylinder in different directions.

Detection results of the impact stress

While measuring the vibration of the axial-flow threshing cylinder, the impact stress of the spike teeth in the feeding, threshing and separating sections of the threshing cylinder was detected. The results are shown in Fig.9, Fig.10 and Fig.11.

It can be seen from Fig. 9, Fig.10 and Fig.11 that the time-domain curves of the impact stress of each measuring point included three stages (taking the measuring point 1 of the feeding section as an example): the idling stage before the materials entered the cylinder, the threshing and separating stage after the materials entered the cylinder, and the idling stage after the materials stopped feeding. In the initial idling stage, the threshing cylinder was in an idling state, and the stress of every spike tooth was maintained at a value of 0; In the threshing and separating stage, the materials were continuously fed into the cylinder under the conveying of the conveyor belt. The spike tooth of each section was sequentially subjected to the materials' continuous impact and friction. The bending stress was generated inside the spike tooth, and several peak points appeared on the stress curve. In the dynamic threshing process, although the materials were fed at a constant rate, the basic size, mass, volume of the Chinese cabbage plants differed. Therefore, the spike teeth were subjected to instantaneous impacts and friction at different levels, and the peak points of stress were also at the dynamic change, so the time-domain curve was constantly changing. When the materials stopped feeding, the peak points of stress gradually decreased and eventually stabilized in the initial state or near a certain stress value. The main reason was that the materials in the cylinder were getting less and less until they were completely discharged, and the number of impact and friction of the spike teeth gradually reduced, and finally no interaction appeared anymore. At this time, the time-domain curve tended to be stable.

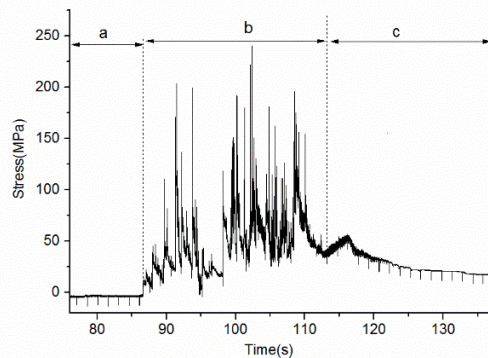


Fig. 9 - Measuring point 1 of the feeding section

Note: Section a represents the idle stage before the material enters the drum, section b represents the threshing and separating stage after the material enters the cylinder, and section c represents the idle stage after the material stops feeding.

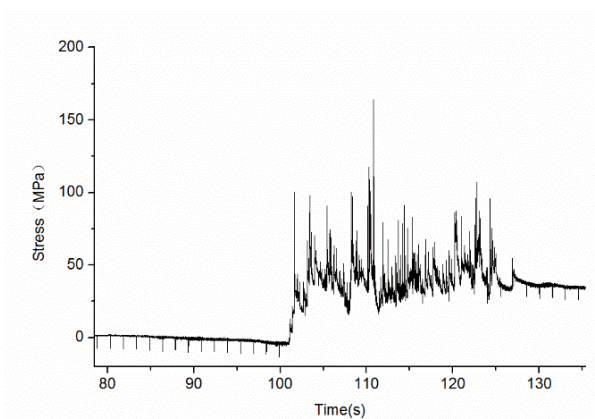


Fig. 10 - Measuring point 2 of the threshing section

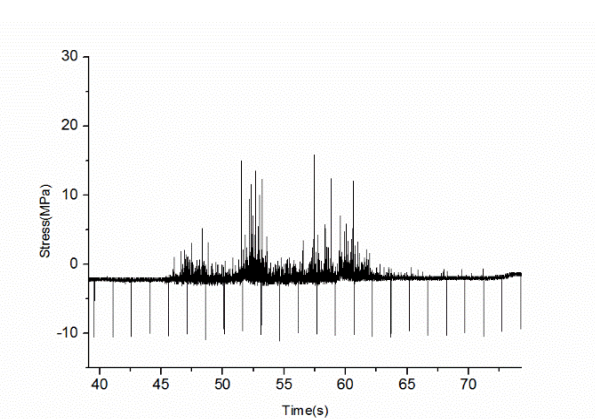


Fig. 11 - Measuring point 3 of the separating section

According to the analysis of the peak values of the time-domain curve of the measuring points, the peak

values of the stress in the feeding section, the threshing section and the separating section decreased in turn. Among them, the stress peak value of the feeding section was the largest and the curve was the most intensive.

The maximum value was 240.575 MPa, and the peak points spread around 200 MPa, as shown in Fig.9. The stress peak value of the threshing section spread around 90 MPa, and the maximum value was 164.128 MPa, as shown in Fig.10. The stress peak value of the separating section was smaller, and the maximum stress peak was only 15.835 MPa, as shown in Fig.11. The reason for this phenomenon was that in the feeding section, the materials were relatively concentrated, which means the volume and weight of the materials were large, so the impact of the spike teeth was strong, resulting in a large internal bending stress. When entering the threshing section, most of the materials were threshed and separated, and some stalks and seeds were removed and separated into the receiving device through the concave sieve. As the material layer became thinner, the volume and mass of the materials decreased, which led to the decrease of the impact on the spike teeth, and the stress generated inside. Similarly, with the process of threshing and separating, there were fewer materials entering the separating area. In addition to the impact of a small amount of materials, there was more friction between the spike tooth and the materials. Therefore, the stress peak value was the lowest, and the time-domain curve was less intensive.

Fig.12 showed the local curve of the dynamic stress of the spike tooth changing from the idling state to the threshing state. It can be seen from the figure that before the materials were fed in, due to the influence of the vibration of the machine, the rotation speed of the cylinder and the self-weight of the spike tooth, the stress peak points of the spike tooth appeared at equal intervals. The values of the three sections were -13.412 MPa, -13.412 MPa, -11.119 MPa respectively. When contacting with the materials, the stress value of the spike tooth instantly rose to the peak, and then gradually decreased until the next collision occurred. And the next peak point appeared. During the time t_i when the material contacted with the spike tooth, because the mass of the materials and the speed difference between them were the largest, the stress generated in the tooth was also the largest. With the contact action, the speed difference between the spike tooth and the materials continuously decreased, and the materials' quality also gradually decreased with the threshing process. After the impact, the friction force decreased gradually, and the bending stress generated by the spike tooth also decreased. This phenomenon is consistent with the derivation of Equation 2. Each subsequent impact is a repetition of the above process.

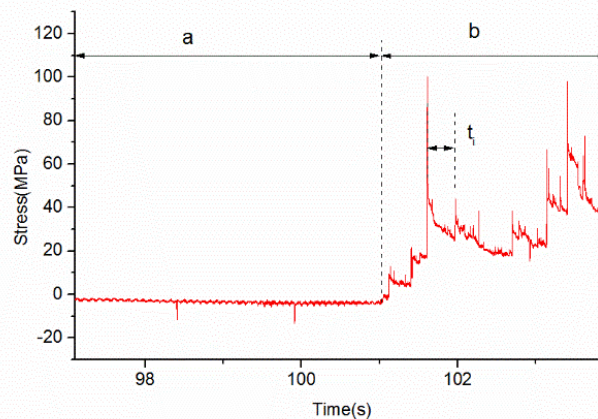


Fig. 12 - Local stress time-domain curve from idling to threshing state.

Note: t_i is the contact time of the materials and the spike tooth during a collision

CONCLUSIONS

1. With the change of axial-flow threshing unit from idling to dynamic threshing condition, the amplitude in the X direction increases from $-2.226\sim 2.86$ m/s² to $-3.392\sim 3.106$ m/s². The root mean square value changes from 0.757 m/s² to 0.926m/s². The peak-to-peak value changes from 5.312 m/s² to 6.498 m/s². The amplitude in the Y direction increased from $-1.027\sim 0.917$ m/s² to $-3.896\sim 3.792$ m/s². The root mean square value increases from 0.313 m/s² to 1.232 m/s². The peak-to-peak value changes from 1.944 m/s² to 7.688m/s².

The amplitude in the Z direction increases from $-0.708\sim 0.814$ m/s² to $-2.919\sim 2.243$ m/s², and the root mean square value increases from 0.236 m/s² to 0.616 m/s², and the peak-to-peak value changes from 1.521 m/s² to 5.234 m/s².

The change of the vibration state in the X direction was so small that can be ignored, but the change of amplitude in the Y and Z directions were obvious, which were mainly caused by the components of the impact load between the threshing cylinder and materials.

2. Under continuous and stable dynamic threshing condition, the values of impact stress of spike teeth in different sections are as follows: the peak value of the stress in the feeding section is the largest, concentrated at about 200 MPa; The threshing section is the second, concentrated at about 90 MPa; The maximum peak value of the separating section is only about 15 MPa. The peak values of impact stress of the separating section are the most intensive, because the stress of the feeding and threshing section is mainly determined by the impact force, while the separating section is affected by a small amount of materials' impact and a large amount of friction.

3. In a very short period of contact between the materials and the spike tooth, the stress values generated by the spike tooth at each measuring point first appears the peak value and then gradually decreases until the next impact point appears. The magnitude and change trend of the stress peak value is mainly determined by the quality and speed of the materials.

ACKNOWLEDGEMENT

This work was sponsored by the National Key Research and Development Program (2017YFD0701204) and National Innovation and Entrepreneurship Training Program for College Students (10464009).

REFERENCES

- [1] Bello B., Tokan A, Jiya D. et al, (2019), Design Model of Automated Groundnut Threshing Machine, *Majlesi Journal of Mechatronic Systems*, Vol.8, Issue1, pp.19-24, Abubakar Tafawa Balewa/Nigeria.
- [2] Chansrakoo W, Chuan-Udom S, (2018), Factors of Operation Affecting Performance of a Short Axial-flow Soybean Threshing Unit, *Engineering Journal*, Vol.22, Issue4, pp.109-120, KhonKaen / Thailand.
- [3] Li Yaoming, Ye Xiaotian, Xu Lizhang et al, (2013), Construction and performance experiment of load test system for half axle of combine harvester, *Transactions of the Chinese Society of Agricultural Engineering (Transactions of the CSAE)*, Vol.29, Issue 6, pp.35-41, Jiangsu /China.
- [4] Miu P., Kutzbach H., (2008), Modeling and simulation of grain threshing and separation in threshing units-Part I, *Computers and Electronics in Agriculture*, Vol.60, Issue 1, pp.96-104, Tennessee/ United States.
- [5] Syuhri A, Sholahuddin I, Syuhri S., et al, (2018), Modeling and evaluation of a threshing drum under vertical vibration, *Journal of Mechanical Engineering and Sciences*, Vol.12, Issue 2, pp. 3750-3758, Jember/Indonesia.
- [6] Steponavicius D, Puzauskas E, Spokas L, et al, (2018), Concave Design for High-Moisture Corm Ear Threshing. Mechanics, *Design and Optimization of Mechanical Systems*, Vol.24, Issue 1, pp. 80-91, Akademija/Lithuania.
- [7] Tang Zhong, Zhang Haotian, Zhou Yuepeng, et al, (2019), Mutual Interference and Coupling Response of Multi-cylinder Vibration among Combine Harvester Co-Frame, *Impact and Vibration*, Vol.2019, pp.1-14, Jiangsu/China.
- [8] Tang Zhong, Li Yaoming, Wang Chenghong, (2013), Experiments on Variable-mass Threshing of Rice in the Tangential-longitudinal-flow Combine Harvester, *Jomo Kenyatta University of Agriculture and Technology*, Vol.15, pp.1319-1334, Jiangsu/China.
- [9] Wang Yue, Ma Ji, (1987), Research on principle of grain threshing and straw breaking in the axial-flow threshing apparatus, *Transactions of the Chinese Society for Agricultural Machinery*, Issue 1, pp. 57-91, Beijing/China.
- [10] Xie Fangfei, Luo Xiwen, Lu Xiangyang, et al, (2009), Kinetic analysis of flexible threshing under law of conservation of energy. *Journal of Hunan Agricultural University (Natural Sciences)*, Vol.35, Issue 2, pp.181-184, Hunan/China.
- [11] Zare H., Maleki A., Rahaghi M., et al, (2019), Vibration modelling and structural modification of combine harvester thresher using operational modal analysis and finite element method, *Structural Monitoring and Maintenance*, Vol.6, Issue 1, pp. 33-46, Islamic/Iran.

ASSESSMENT INDICES FOR THE EFFICIENCY OF THE SEPARATION PROCESS ON A SIEVE WITH CONICAL SEPARATION SURFACE

INDICI DE APRECIERE A EFICIENȚEI PROCESULUI DE SEPARARE PE O SITĂ CU SUPRAFAȚA DE SEPARARE CONICĂ

Dorel Stoica ¹⁾, Gheorghe Voicu ¹⁾, Lucreția Popa ²⁾, Gabriel Constantin ¹⁾, Paula Tudor ¹⁾ ¹

¹⁾ POLITEHNICA University of Bucharest, Faculty of Biotechnical Systems Engineering / Romania;

²⁾ INMA Bucharest / Romania

Tel: 0724.715585; E-mail: ghvoicu_2005@yahoo.com

DOI: <https://doi.org/10.35633/inmateh-60-22>

Keywords: separation process efficiency, conical sieve, separation curves, index of appreciation

ABSTRACT

The objective of this paper is to present the efficiency of the separation process on a sieve with a conical separation surface, with a vertical shaft and having vibrational motion. Separation intensity curves of rape seeds through circular sieve apertures were drawn by regression analysis of the quantities of material separated at different distances from the central axis of the sieve, using the Gaussian distribution law. The coefficients of the regression equation and the correlation coefficient of the distribution function with experimental data show a high degree of correlation between them. The movement of the material on the sieve and the separation process, in general, was assessed by the position of the distribution curve maximum, depending on the material flow rate.

REZUMAT

Obiectivul acestei lucrări este acela de a prezenta eficiența procesului de separare pe o sită cu suprafața de separare conică cu ax verticală având mișcare vibratorie. Curbele intensității de separare a semințelor de rapiță prin ochiurile circulare ale sitei au fost trasate prin analiza de regresie a cantităților de material separat la diferite distanțe de axa centrală a sitei, utilizând legea de distribuție Gauss. Coeficienții ecuației de regresie și coeficientul de corelație a funcției de distribuție cu datele experimentale arată un grad ridicat de corelație între acestea. Mișcarea materialului pe sită și procesul de separare, în general, a fost apreciat prin poziția maximului curbei de distribuție, în funcție de debitul de alimentare cu material.

INTRODUCTION

Nationally, the concerns of designers and builders to make machines and plants for seed cleaning and sorting are very high, due to the need to increase the quality used for both sowing and consumption, (Casandroi, 1993; German R.F. and Lee J.H.A., 1969; Stoica D., 2011, Constantin et al, 2019).

The particles of raw materials contain different impurities that cannot be admitted into the products (grist, semolina, flour, etc.), because they negatively influence both the separation process and the quality of the finished products, (Casandroi, 1993; Stoica D., 2011; Tucu D., 1994, Dal-Pastro et al., 2016).

The processing capacity is influenced by the size of the useful surface of the perforated sheet with which the upper sieve frame is equipped and the characteristics of the seed mixture (moisture, content of impurities etc.).

Removing the hazardous impurities from the mass of stored seeds and reducing or preventing damage caused by impurities on the quality of agricultural crop seeds lead to an increase in the storage period and a reduction in storage losses. In the paper of (Zhou XianQing et al., 2009), the influence of impurities on microbial activity and storage quality was analyzed, at a temperature of 30°C and relative humidity 80-90%, under simulated storage conditions. The results showed that the remaining impurities in the wheat seeds had a negative effect on their storage quality. Microbial activity was faster, and the storage quality of the wheat suffered. That's why the impurities must be separated, as much as possible, before storing wheat, to reduce the negative effects on wheat quality during storage.

¹ Stoica Dorel, Ph.D. Eng.; Voicu Gh., Prof. Ph.D.Eng.; Popa L., Ph.D.Eng.; Constantin G.A., Ph.D.Eng.; Tudor P., Ph.D.Eng.

On the sieves of the machines intended for cleaning and sorting the seeds of agricultural crops, the seeds are separated due to the sifting state generated by the oscillation movement of the sieves and, eventually, of a stream of air running through the material layer on the sieve, bottom up. Material separation is a complex process influenced by many factors, as: the physical properties of the components subject to separation, the geometry of the separation surface, the kinematic and functional parameters of the sieve (Jun-xia Yan, 2010; Pruteanu et. al, 2018; Constantin G.A., 2014; Constantin G.A. et al, 2014).

The shape and geometrical characteristics of the sieve are chosen according to the particle size of the material to be separated. Feeding mode and thickness of the material layer on the sieve must be provided by a uniform supply flow; at a flow too high there is the danger to find, in the refusal of the sieve, undersized particles which did not meet the necessary conditions for separation (to get in touch with the sieve and to have the time required to train through the apertures). Also, the length of the particle path on the sieve is a factor that directly influences the quality of separation. The inclination angle of the sieves and the shape of the material particles subjected to the sifting are also the factors that indicate (show) the efficiency of the sifting process, (Voicu Gh., 2011; Casandroi, 1993).

The geometric dimensions of the particles and their distribution, as well as the ratio between the average particle size and the characteristic size of the sieve apertures influences the separation process, so: for values of average particle size d smaller than $0.7 \cdot a$ (a – diameter of sieve apertures or small side of elongated holes), the particles pass easily through the aperture, and for values d greater than $1.5 \cdot a$, the particles pass quickly along the sieve and it does not prevent the passage of small particles through the apertures. For particle size d , between $0.7 \cdot a$ – $1.5 \cdot a$, these tend to clog the apertures in the sieve, in this case it is necessary that the sieves have apertures with size a bigger by 10–15%, for proper separation (Casandroi, 1993; Voicu Gh and Casandroi T, 1995).

The temperature of the products should be as close to or below the ambient temperature, because this influences the separation capacity inversely, in this sense the products are cooled to separate (Casandroi, 1993; Voicu Gh and Casandroi T, 1995). Electric conductivity and static electricity negatively affect the sifting capacity of the sieves (Casandroi, 1993; Voicu Gh and Casandroi T, 1995). The speed of movement and the character of the material movement on the sieve directly influence the process of material separation, these being given by the kinematic regime of the sieve separation block. In the case of fixed sieves, particle displacement occurs due to the slope of the sieve and only small impurities can be separated, without proper separation by the width or thickness of the particles (Casandroi, 1993; Voicu Gh and Casandroi T, 1995).

The description of seed separation on sieve with oscillation motion and the vibrational movement of sieves was made by different authors in two different ways (Bracacescu et al., 2014; Casandroi et al., 2009; Constantin, 2014; Jun-xia et al., 2010; Kharchenko et al., 2019; Simonyan & Yiljep, 2008; Szymański T., Wodziński P., 2003).

Some approach the stochastic description of the separation process, through mathematical models that result from the correlation with the results obtained in the experiments of some functions or laws of distribution existing in mathematical statistics (Voicu Gh. et. al, 2006). Stochastic models can describe both the intensity of material separation along the length of the sieve, as well as the cumulative separation of the material at various distances from the feed end of the sieve along its length (Voicu Gh. et. al, 2006).

The second way of describing the process of separation on the sieve, is the deterministic model, that takes into account the main parameters, which characterizes the process of separation, mathematical model that is determined by applying the theory of dimensional analysis, based on the results of experimental research to determine the values of the dimensionality criteria and the coefficients of the mathematical model.

The paper presents the influence of the material feed flow on the material movement and the separation process for a sieve with outer vertical conical work surface, with horizontal oscillating motion, for a preset oscillation frequency and four values of the amplitude of the sieve oscillation.

MATERIALS AND METHODS

The experimental stand, presented in detail in the paper (Stoica D. et. al, 2012; Stoica D., 2011), has a conical sieve suspended with the separation surface of perforated sheet with holes ϕ 4.2 mm, having a horizontal inclination of 8° , driven in oscillating motion by a mechanism with an eccentric arranged tangentially at the distance d (variable), from the centre of the sieve. The sieve is suspended at the top and bottom by means of three metal cables with a diameter 1.5 mm arranged circularly at 120° .

The experiments were performed with rape seeds having dimensions between $\phi 1.25\text{--}2.5$ mm (at over 95% percentage) and moisture content of 8.05%. In the mixture of seeds subjected to separation were introduced straw particles with dimensions between 3-4 mm at approx. 3% percentage.

The eccentric drive system allowed the three-stage oscillation frequency to be changed (500, 520 and 790 min^{-1}) and the amplitude of the four-stage oscillations. The diameter at the base of the cone was $\phi 430$ mm, and the specific number of circular apertures on the separation surface was $2.25\text{ apertures/cm}^2$ (the active surface of the sieve was approx. 31%), diameter of the funnel hole for feeding the sieve was $\phi 25$ mm. The simplified scheme of the experimental installation is shown in Figure 1.

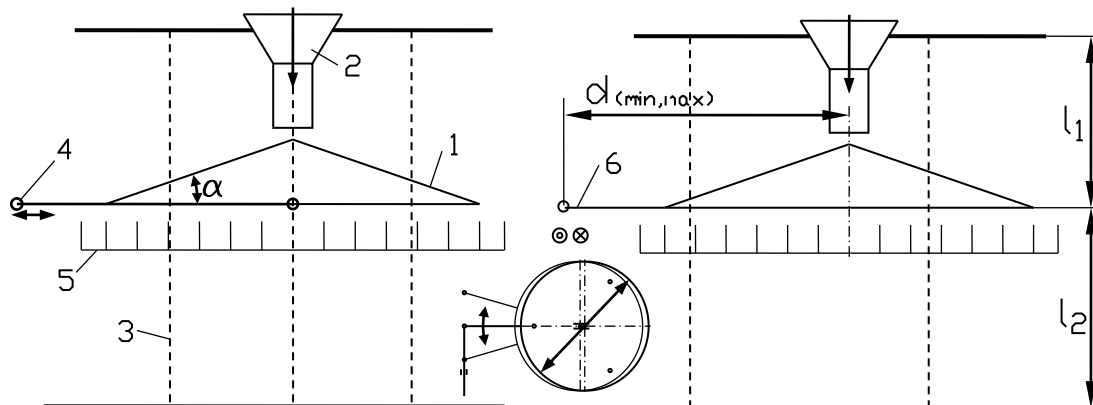


Fig. 1 - Scheme of the suspended conical sieve used for experiments (views to 90°)

1) conical sieve with apertures $\phi 4.2$ mm; 2) height adjustable feed funnel; 3) elastic cables made of steel wire; 4) drive mechanism with oscillating slide; 5) collection box with concentric compartments; 6) lever linking to the connecting rod of the drive mechanism

The amplitude of the sieve oscillation was measured horizontally at the connection point of the sieve with the arm 6, for maximum opening of the drive mechanism connecting rod.

To express the influence of the feed flow on the separation process on the conical sieve, the seeds separated by the apertures of the sieve were collected in a box with several concentric collecting compartments. The mass of seeds collected in each compartment was compared to the initial mass of the sample (that was of 0.500 kg), the results being presented as a percentage compared to this. The feed rate was calculated by reporting the seed mass of the sample at the drain time of the funnel material, which could be adjusted by the distance between the outlet and the sieve.

It is worth mentioning that, during experimental determinations, it was found that the seed impurities in the seed mass were completely separated beyond the bottom edge of the sieve, in all the tests carried out, so that the separation process is presented by the distribution of the separated material along the radius of the sieve cone base.

The experimental results are presented in Table 1.

They were drawn, comparatively (on the same graph), distribution curves of seed separation frequency on the mesh generatrix for three feed rate values used in experiments, under the conditions in which the other parameters of the working regime (amplitude of oscillations A and frequency of oscillation F) were kept constant. Based on the experimental data, the separation curves were plotted by nonlinear regression analysis, using the Gaussian law, expressed by equation 1:

$$p_x(\%) = A_o \cdot \exp\left(-\frac{(x - x_c)^2}{2 \cdot w^2}\right) \quad (1)$$

where: $p_x(\%)$ represents the percentage weight of the separated material over a length interval (radius) of sieve.

According to mathematical statistics, in relation (1) „ A_o ” represents the maximum percentage of material collected in the boxes below the sieve, „ x_c ” represents the radius of the sieve corresponding to the maximum percentage of separated seeds (or the average of the Gaussian distribution function), and „ w ” represents the dispersion to the maximum position. These coefficients depend on the parameters of the sieve working regime and are determined from the regression analysis, together with the correlation coefficient R^2 .

RESULTS AND DISCUSSIONS

The data presented centrally in Table 1 were processed and synthetically ordered according to the values of the feed flow and after the amplitude of the oscillation at one of the three oscillation frequencies used in the experiments ($F = 520 \text{ min}^{-1}$).

Table 1

Variation of the amount of material collected under the sieve (%), for the oscillation frequency $F = 520 \text{ min}^{-1}$ and four amplitudes of the sieve oscillation, at three feed rates

Den No.	$F = 520 \text{ min}^{-1}$. $M_p = 0.500 \text{ kg}$		The sieve interval from which seeds are collected (m)								
	Amplitude of the oscillations	Feed rate	Separated seeds	0	0.04	0.07	0.10	0.13	0.16	0.205	Over sieve
1	$A_1 = 3.58 \text{ mm}$	$Q_1 = 0.02 \text{ kg/s}$	g	0	113	120	140	125	2	0	0
			%	0	22.6	24	28	25	0.4	0	0
$Q_2 = 0.033 \text{ kg/s}$		g	0	104	131	108	99	56	2	0	
		%	0	20.8	26.2	21.6	19.8	11.2	0.40	0	
3		$Q_3 = 0.042 \text{ kg/s}$	g	0	104	131	108	99	56	2	0
			%	0	20.8	26.2	21.6	19.8	11.2	0.40	0
4	$A_2 = 3.74 \text{ mm}$	$Q_1 = 0.02 \text{ kg/s}$	g	0	201	215	84	0	0	0	0
			%	0	40.2	43	16.8	0	0	0	0
$Q_2 = 0.033 \text{ kg/s}$		g	0	104	131	108	99	56	2	0	
		%	0	20.8	26.2	21.6	19.8	11.2	0.40	0	
6		$Q_3 = 0.042 \text{ kg/s}$	g	0	114	141	90	70	39	21	25
			%	0	22.8	28.2	18	14	7.80	4.20	5
7	$A_3 = 3.91 \text{ mm}$	$Q_1 = 0.02 \text{ kg/s}$	g	0	195	210	94	1	0	0	0
			%	0	39	42	18.8	0.2	0	0	0
$Q_2 = 0.033 \text{ kg/s}$		g	0	127	138	107	56	53	19	0	
		%	0	25.4	27.6	21.4	11.2	10.6	3.8	0	
9		$Q_3 = 0.042 \text{ kg/s}$	g	0	115	150	88	65	36	20	26
			%	0	23	30	17.6	13	7.2	4	5.2
10	$A_4 = 4.10 \text{ mm}$	$Q_1 = 0.02 \text{ kg/s}$	g	0	187	208	102	3	0	0	0
			%	0	28	36.6	19	12	4	0.4	0
$Q_2 = 0.033 \text{ kg/s}$		g	0	140	183	95	60	20	2	0	
		%	0	28	36.6	19	12	4	0.40	0	
12		$Q_3 = 0.042 \text{ kg/s}$	g	0	134	176	81	48	26	12	23
			%	0	26.8	35.2	16.2	9.60	5.20	2.40	4.60

Based on the percentages of the material collected under the sieve at different distances from the vertical axis of oscillation, the graphs presented in fig. 2 were drawn, for the four amplitudes.

Each of the four graphs shows three distribution curves of the material on the collection radius of the sieve, representing the variation of separated seeds percentage according to the preset feed rate and used for experiments.

These separation curves were plotted by regression analysis of the experimental data with the Gaussian distribution function (relation 2), allure of these curves being about the same, but with more or less significant differences, depending on the parameters of the working regime used in experiments, respectively with the feeding flow.

The values of the coefficients of the regression equation (equation 2, A_0 , x_c , w), as well as the values of the correlation coefficients χ^2 and R^2 for the four amplitudes of the oscillation at each of the three feed rates are presented in table 2.

Analyzing the data in tables 1 and 2 and the graphs in fig. 2, it is found that the position of the maximum separation curves for the three feed rates, $Q_1 = 0.020 \text{ kg/s}$, $Q_2 = 0.033 \text{ kg/s}$, $Q_3 = 0.042 \text{ kg/s}$, changes at each of the four amplitudes of the oscillation.

Thus, if the point of the separation curve's maximum position is at 0.078 m from the center of sieve oscillation vertical axis for oscillation amplitude $A_1 = 3.58 \text{ mm}$ and flow Q_1 , for higher material flows (Q_2 , Q_3), this point approaches even more the vertical axis of the sieve, values that are influenced, we suppose, also by sieve apertures dimension.

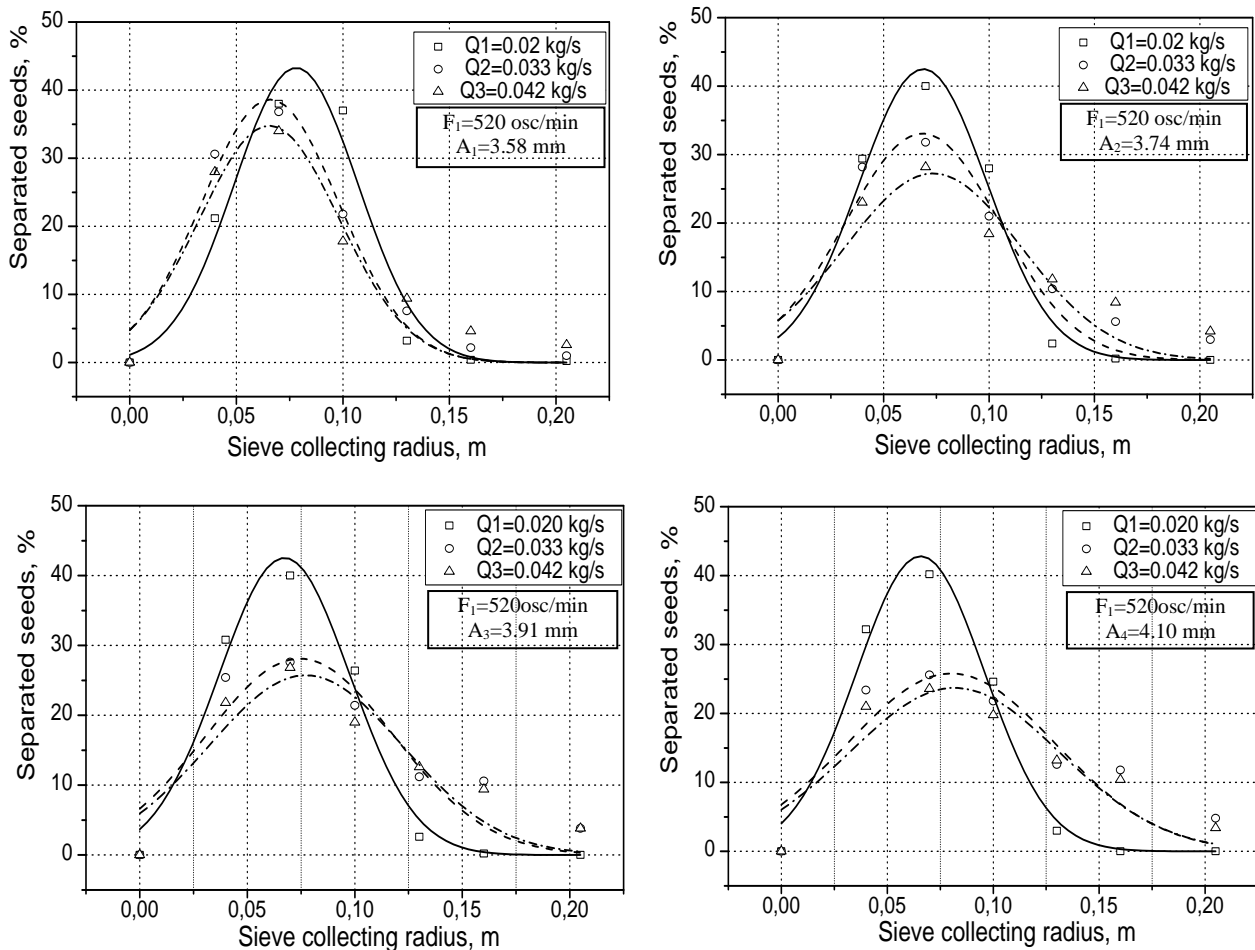


Fig. 2 - The influence of the feed flow on the seed separation process on the conical sieve generatrix, at the oscillation frequency $F = 520 \text{ min}^{-1}$ and four amplitudes of the oscillation

However, there is a slight increase in the dispersion of the material on the sieve, represented by the coefficient values w from table 2, for the flow Q_1 .

If the amplitude of the oscillation increases to $A_2 = 3.74 \text{ mm}$ or $A_3 = 3.91 \text{ mm}$ and then to $A_4=4.10 \text{ mm}$ for higher feed rates, respectively $Q_2 = 0.033 \text{ kg/s}$ or $Q_3 = 0.042 \text{ kg/s}$, it is found that the dispersion of the material on the sieve also increases.

Table 2

The coefficients of the regression equation (eq. 2) A_0 , x_c , w and the correlation coefficients χ^2 and R^2 with experimental data, for three material feed rates at the oscillation frequency $F = 520 \text{ min}^{-1}$ and four amplitudes of the sieve oscillation

Sample No	Working regime	Gaussian type function	A	x_c	w	χ^2	R^2
1	$A_1 = 3.58 \text{ mm}$	$Q_1=0.02 \text{ kg/s}$	49.979	0.063	0.029	14.104	0.973
2		$Q_2=0.033\text{kg/s}$	40.581	0.067	0.033	28.420	0.937
3		$Q_3=0.042 \text{ kg/s}$	35.972	0.071	0.036	11.543	0.916
4	$A_2 = 3.74\text{mm}$	$Q_1=0.02 \text{ kg/s}$	49.746	0.056	0.0263	11.892	0.980
5		$Q_2=0.033\text{kg/s}$	38.010	0.067	0.034	14.614	0.960
6		$Q_3=0.042 \text{ kg/s}$	33.278	0.068	0.034	16.587	0.931
7	$A_3 = 3.91 \text{ mm}$	$Q_1=0.02 \text{ kg/s}$	49.370	0.059	0.026	7.483	0.987
8		$Q_2=0.033\text{kg/s}$	37.400	0.066	0.033	15.012	0.954
9		$Q_3=0.042 \text{ kg/s}$	34.065	0.067	0.033	18.308	0.926
10	$A_4 = 4.10 \text{ mm}$	$Q_1=0.02 \text{ kg/s}$	49.143	0.061	0.026	4.899	0.991
11		$Q_2=0.033\text{kg/s}$	37.613	0.065	0.032	19.482	0.938
12		$Q_3=0.042 \text{ kg/s}$	35.283	0.065	0.031	21.235	0.919

If at feed rates Q_1 and Q_2 , for the amplitude of oscillation $A_2 = 3.74$ mm, the position of the separation curve maximum does not change significantly, at the feed rate $Q_3 = 0.042$ kg/s, the maximum of the separation curve moves towards the edge of the sieve, at $x_c = 0.074$ m instead of 0.069 m, as in the case of the feed rate Q_1 .

In the same conditions by increasing the dispersion of the material on the surface of the sieve, the percentage of material separated at the maximum point of the separation curve decreases with the increase of the feed rate (see fig. 2,b).

From the analysis of the separation curves in fig. 2,c, at the same frequency of oscillation $F = 520 \text{ min}^{-1}$, but at slightly greater amplitude of oscillation, $A_3 = 3.91$ mm, the dispersion of the material over the sieve collection area increases with increasing feed flow, the percentages of separated material at the maximum point decrease insignificantly, but the maximum of the separation curve moves significantly from the vertical axis of the screen to its edge. Thus, if at the feed rate $Q_1 = 0.02$ kg/s, the position of the separation curve maximum is at $x_c = 0.067$ m relative to the axis of sieve oscillation, at the feed rate $Q_2 = 0.033$ kg/s the separation curve maximum moves from 0.074 m, at $x_c = 0.077$ m for the feeding flow $Q_3 = 0.042$ kg/s, from where it can be assumed that the sieve can work at a much larger load of material at this oscillation amplitude for the analyzed oscillation frequency ($F = 520 \text{ min}^{-1}$).

The same phenomenon can be observed from the analysis of the separation curves in fig. 2,d for the amplitude of the oscillation $A_4 = 4.10$ mm.

We find that the position of the separation curve maximum with respect to the collecting radius of the sieve, moves from the axis of oscillation to the edge of the sieve as the feed flow increases from 0.066 m (for $Q_1 = 0.02$ kg/s) at $x_c = 0.082$ m (for $Q_3 = 0.042$ kg/s). It is worth mentioning that, (as well as amplitude A_3) the percentages of separated material at higher feed rates decrease significantly, with the increase of the separated material dispersion on the generatrix of the sieve.

The synthetic representation of those presented above can be seen from the analysis of the curves in fig. 3, which shows the position of the separation curve maximum in relation to the collection radius of the sieve according to the material flow rate.

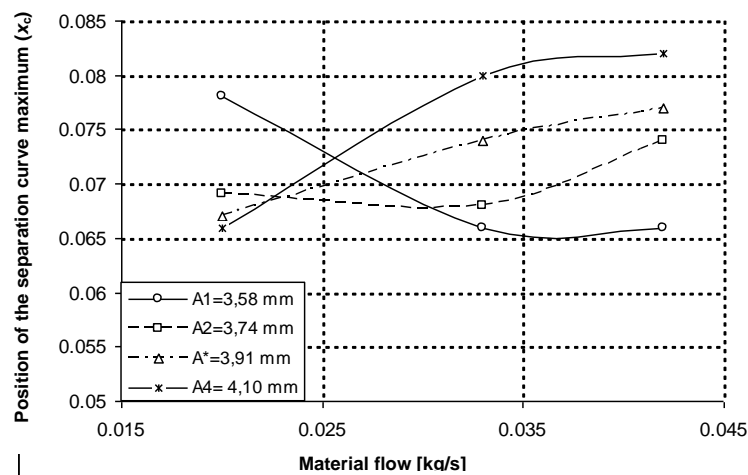


Fig. 3 - at the frequency $F = 520 \text{ min}^{-1}$ and four amplitudes of the sieve oscillation, depending on the material flow rate

CONCLUSIONS

A vertical conical sieve with circular apertures and a horizontal oscillating motion was used to analyze the sifting process and the separation of rape seeds through the apertures, for three different feed rates and four amplitudes of the sieve oscillation.

From the data presented in the paper, it was found that the position of the maximum distribution curve of the separation changes with the change of the feed rate and the amplitude of the sieve oscillation. At low feed rates ($Q_1=0.02$ kg/s), the maximum of the separation curve approaches the axis of oscillation of the sieve as the amplitude of oscillation increases, while for higher feed rates, this point departs from the axis of oscillation when the amplitude of oscillation increases.

Separation curves were plotted by regression analysis of experimental data with Gaussian distribution function, aspect of these curves being about the same, but with more or less significant differences, depending on the parameters of the working regime used in experiments, respectively with the feeding flow.

We can say that at low feed rates ($Q_1 = 0.02$ kg/s, $Q_2 = 0.033$ kg/s) and low oscillation frequencies (like the one I presented earlier, $F = 520$ min⁻¹) under the experimental conditions performed in the present paper, material losses over the outer edge of the sieve are minimal (in table 2 they have zero value for the flows Q_1 and Q_2).

The data presented in the paper can be a reference base for the specialists (designers and users of machines) in the field of seed processing of agricultural crops and, especially, of those in the field of cleaning and conditioning before storage and industrial processing.

ACKNOWLEDGEMENT

The work has been funded by Ministry of National Education and Research through the Executive Agency for Higher Education, Research, Development and Innovation Funding, within the project entitled “Ensure the sustainable development of the base of agro-mechanical practical applications in gardens, solariums, vineyards and orchards (PRAGRODEZ)”, CNFIS-FDI-2019-0288.

REFERENCES

- [1] Bracacescu C., Sorica C., Manea D., Yao Guanxin, Constantin G.A., (2014), Theoretical contributions to the drive of cereal cleaning technical equipment endowed with non-balanced vibration generating systems, *INMATEH – Agricultural Engineering*, 42(1), pp.69-74;
- [2] Casandroi T., David L., (1994), Equipment for primary processing and preservation of agricultural products. (Echipamente pentru procesarea primară și conservarea produselor). *Guidelines for laboratory work*, ch.4, University Politehnica of Bucharest Publishing House, Bucharest/Romania;
- [3] Casandroi T., Popescu M., Voicu Gh., (2009), Developing a mathematical model for simulating the seeds separation process on plane sieves, *U.P.B. Sci. Bull.*, Series D, Vol. 71, Iss. 3, pp.17-28;
- [4] Constantin G.A., Voicu Gh., Ipate G., Mușuroi G., Stefan E.M., Munteanu M.G., Stoica D. (2019), Influence of motion type on granulometric distribution of grist obtained from some varieties of wheat and corn, *Proceedings of the 47th International Symposium “Actual Tasks on Agricultural Engineering”*, Croatia, Opatija, p.409-417;
- [5] Constantin G.A., (2014). Researches on the sifting and sorting process of grist fractions in an industrial milling plant, Doctoral thesis, University “Politehnica” of Bucharest;
- [6] Constantin G.A., Voicu Gh., Ștefan E.M., (2014), Influence of kinematic regime and quantity of material on efficiency of sifting process, *3rd International Conference on Thermal Equipment, Renewable Energy and Rural Development*, pp. 199-204;
- [7] Dal-PAstro F., Facco P., Bezzo F., Zamprogna E., Barolo M., (2016), Data-driven modeling of milling and sieving operations in a wheat milling process, *Food and Bioproducts Processing*, Issue 99, pp. 99-108;
- [8] German R.F., Lee J.H.A., (1969), Grain separation on oscillating combine sieves as affected by air volume and frequency, *Transactions of the ASAE*, 12 (6);
- [9] Jun-xia Yan, Chu-sheng Liu, La-la Zhao, (2010), Dynamic characteristics of vibrating screen with determinate structure and statistically indeterminate structure, *Applied mechanics and materials*, vols.34-35, pp.1850-1854;
- [10] Kharchenko S., Kovalyshyn S., Zavgorodniy A., Kharchenko F., Mikhaylov Y., (2019), Effective sifting of flat seeds through sieve, *INMATEH – Agricultural Engineering*, 58(2), pp.17-26;
- [11] Pruteanu A., David L., Matache M., Nitu M., (2018), Particle size distribution of some chopped medicinal plants, *17th International Scientific Conference Engineering for Rural Development Proceedings*, Volume 17 May 23-25, 2018, Jelgava, Latvia, pp. 640-645, DOI: 10.22616/ERDev2018.17. N304;
- [12] Simonyan K.J., Yiljep Y.D., (2008), Investigating Grain Separation and Cleaning Efficiency Distribution of a Conventional Stationary Rasp-bar Sorghum Thresher, *Agricultural Engineering International: the CIGR Ejournal Manuscript PM 07 028*. Vol. X, pp.1-13;

- [13] Stoica D., Voicu G., Ungureanu N., Voicu P., Orasanu N., (2012), Research on the working process and efficiency of a conical suspended sieve with pendulum movement, *Proceedings of the 40. International Symposium on Agricultural Engineering. Actual Tasks on Agricultural Engineering*, Opatija, Croatia, pp.463-473;
- [14] Stoica D., (2011), *Contributions to the study of the vibrational phenomena regarding the machines in the field of processing agricultural products (Contribuții la studiul fenomenelor vibratorii privind utilajele din domeniul prelucrării produselor agricole)*, Doctoral thesis, University “Politehnica” of Bucharest, Romania;
- [15] Szymański T., Wodziński P., (2003), Screening on a screen with a vibrating sieve, *Physicochemical Problems of Mineral Processing*, 37, pp.27-36;
- [16] Tucu D., (1994), *Milling. Technological systems and productive structures*, Ed. Mirton, Timișoara, 1994
- [17] Voicu Gh., Casandroi T., (1995), *Milling and baking equipment*, Course, vol.I. *Milling processes and equipment*, U.P.B. Lithography, Bucharest / Romania;
- [18] Voicu Gh., Căsăndroi T., Toma L., (2006), A multiple logistic regression static model to estimate grain losses on sieve cleaning system from combine, In *Proceedings Actual Task on Agricultural Engineering, of the 34th International Symposium on agricultural engineering*, Opatija, Croatia, pp. 481–491, 2006;
- [19] Voicu Gh., Stoica D., Ungureanu N., (2011), Influence of oscillation frequency of a sieve on the screening process for a conical sieve with oscillatory circular motion, *Journal of Agricultural Science and Technology B1*, pp.1224-1231;
- [20] Zhou XianQing, Zhang YuRong, Wang JunLi, Yu LinPing, Liu XueJun, (2009), Influence of sieve-through impurities on wheat microbe activity and storage quality, *Transactions of the Chinese Society of Agricultural Engineering*, 25(6), pp.274-279.

SHADOW PROCESSING TECHNOLOGY OF AGRICULTURAL PLANT VIDEO IMAGE BASED ON PROBABLE LEARNING PIXEL CLASSIFICATION

基于概率学习像素分类法的农业植物视频图像阴影处理技术研究

Cheng Yang¹⁾, Ping Wang¹⁾, Yan Bao^{**1)} 1

¹⁾ College of Electronic Information and Electrical Engineering, Changsha University, Changsha, 410022 / China

<https://doi.org/10.35633/inmateh-60-23>

Keywords: *probability learning; pixel classification; agricultural plants; video images*

ABSTRACT

In order to solve the problem of difficult pre-processing of crop video image shadows, a probable learning pixel classification method is proposed to study its processing technology. The algorithm effectively detects the shadow area by performing intelligent video collaborative detection on the shaded parts of the crop video sequence. Firstly, the cloud collaborative detection algorithm that can be widely used in agriculture was proposed. The video key frame was obtained and the background modeling algorithm with strong adaptability to crop illumination was applied to realize real-time detection of the target, so as to construct the crop pixel model. Finally, the proposed algorithm and the constructed model are applied to the processing of shadows of agricultural plant video images for experimental verification. The results show that in video frames 47, 194 and 258, the probable learning pixel classification method can be used to determine the shaded part of each frame, which can greatly improve the detection accuracy of crop shadows. The research in this paper shows that the probability learning pixel classification method can better enhance the shadow robustness and accuracy of crop video images.

摘要

为了解决作物视频图像阴影预处理困难的问题，提出了一种概率学习像素分类方法来研究其处理技术。该算法通过对作物视频序列的阴影部分进行智能视频协同检测，有效地检测出阴影区域。首先，提出了可广泛应用于农业领域的云协同检测算法。获取视频关键帧，采用对作物光照适应性强的背景建模算法实现对目标的实时检测，从而构建作物像素模型。最后，将所提出的算法和所构建的模型应用于农业植物视频图像的阴影处理并进行实验验证。结果表明，在 47 帧、194 帧和 258 帧中，采用概率学习像素分类方法可以确定每帧的阴影部分，大大提高了作物阴影的检测精度。本文的研究表明，基于概率学习的像素分类方法能够更好地加强作物视频图像阴影的稳定性和准确性。

INTRODUCTION

Recently, the use of information technology to bring data from different sources into decision-making related to agricultural production is the popular management strategy—precision agriculture (PA). An example of a PA application is the measurement and management of the number and space utilization of cultivated land (Rashno A, Nazari B, Sadri S., 2017). Due to the development of computer technology and digital video technology, and the economic benefits of pursuing the image acquisition process, the range of video cameras used in real-time fields is gradually expanding (Windrim L, Ramakrishnan R, Melkumyan A., 2018). The traditional method of regional segmentation has the method of regional growth and regional division (Xu M, Zhu J., Lv P., 2017). This kind of method can segment images with a priori knowledge such as complex scenes or natural scenes without a priori knowledge, and can also achieve better performance. However, this type of method is an iterative method with large spatial and temporal overhead (Tatar N., Saadatseresht M., Arefi H., 2018). In this paper, a shadow processing technique based on probable learning pixel classification method is proposed, which can effectively segment the shadow region of agricultural plant video images, which has important practical significance.

The presence of shadow will affect many subsequent agricultural image processing operations, and then affect the researchers in agriculture related research. The purpose and requirements for processing shadows in images vary from application to application (Nan M, Zhu R., Li Y., 2018). In order to improve the shadow processing technology of agricultural plant video images, a *probable learning pixel classification*

¹⁾ Cheng Yang, As. Lec. Stud., Ping Wang, Lec. Stud.; Yan Bao, Assoc. Prof. Ph.D.

method is proposed based on real-time intelligent video capture, and a crop pixel model is constructed based on cloud collaborative detection. The probability learning pixel classification method based on real-time intelligent video capture is realized by calling the interface provided by Haikang through the process of capturing video frames into images on the video server. The crop pixel model based on cloud collaborative detection algorithm estimates the value of model parameters under the condition of giving the initial value of missing data, and then estimates the missing value of crop data according to the parameters. According to the estimated crop missing data, the parameter value was updated, and repeated iterations were carried out until the convergence and the end of the iteration.

The pre-processing operations for image shading include two steps of shadow detection and shadow elimination. The innovation of this paper is to propose a video sequence processing method for shadow detection and removal. A probability learning pixel classification algorithm for the shadow distribution model is established for a pixel and sometimes a crop shadow. By combining the algorithm to store all observed image pixel values for real-time applications, real-time applied probabilistic reasoning unsupervised pixel classification is implemented, which solves the problem of difficult to handle shadow regions in the traditional image classification method.

This article applies the computer technology in the agricultural production, makes every effort to innovate the present agricultural production pattern. The probability learning pixel classification method is used to explore the agricultural plant shadow processing technology, and a crop pixel model is built based on cloud collaborative detection. Based on the video image capture, a real-time intelligent video capture algorithm is proposed, and the main model and algorithm are applied. The principle and implementation process are analyzed. Finally, the algorithm proposed in this paper is tested and the results are summarized and analyzed.

Related work

In agriculture-related early satellite remote sensing technology, images obtained from satellites or aircraft could effectively provide relevant agricultural information such as forests, cultivated land, soil and plant density. The next stage after the image was obtained was that the vegetation was segmented from the background. *Hadiuzzaman M.* used a standardized different index and morphological operations to segment plants, and found that the method was feasible (*Hadiuzzaman M., Haque N., Rahman F., 2017*). *Argandacarreras I.* designed a robust segmentation algorithm, and found that the algorithm could obtain good segmentation results under outdoor light changes (*Argandacarreras I., Kaynig V., Rueden C., 2017*). *Yang S.* classified broadleaf grasses and grasses using Gabor filters and artificial neural networks. The study found that this method had certain advantages (*Yang S, Feng Z., Wang M., 2018*). *Arun P.V.* took the colour image of sugar beet field in seedling stage as the research object, and proposed a real-time agricultural image pixel-by-pixel classification method based on depth separable convolution. Compared with the existing pixel-by-pixel classification method, it was found that the method obtains high classification accuracy. (*Arun P.V., Buddhiraju K.M., Porwal A., 2018*). *Li J.* proposed a KmeansNet model for the classification and recognition of plant image sets. It was found that this method was a variant of the SPCANet model, except that the convolution kernel of the convolutional layer was obtained by the Kmeans algorithm (*Li J, Khodadadzadeh M., Plaza A., 2017*). *Majdar R.S.* proposed a plant image set classification method based on deep learning. The research showed that the deep learning model with the smallest set of reconstruction errors could get the category label of the test set (*Majdar R.S., Ghassemian H., 2017*). However, various vegetation segmentation studies did nothing to the shadows. So far, many scholars have analyzed the shadow features, established a model of shadow generation, and proposed a number of related algorithms for detecting shadow regions. *Hou B.* proposed image processing and support vector machine methods. Experiments showed that the method adapts to different illumination intensities and could reduce the influence of noise, plant shadows and debris on image segmentation, and obtain a complete segmentation image (*Hou B, Kou H., Jiao L., 2017*). *Sharma A.* used a variety of typical colour constancy algorithms to compare the effects of colour restoration in grape leaf images. The results showed that various algorithms had a certain effect on the consistency of leaf colour in the image (*Sharma A, Liu X., Yang X., 2018*). *Yan X.* had many assumptions and low detection efficiency for general colour shadow detection. Based on the shadow analysis, the bottom-up method was used to detect the shadow using gradient and colour information. The simulation results showed that the shadow detection rate of this method was optimal in most cases, the average shadow discrimination rate was as high as 0.92, and the total average was 0.73. The detection effect was better than other methods (*Yan X, Lu Y., Liu L., 2018*). *Groot H.G.J.* proposed a colour image shadow detection method. It was found that this method could effectively detect shadow areas

of various intensities under complex background conditions. It had the advantages of accurate detection, fast processing speed and no need for manual intervention. It was suitable for practical applications (Groot H.G.J., Oostdijk A., Van Persie M., 2017). In summary, most scholars verified the effectiveness of the algorithm through experiments. However, for image shading, some scholars have also proposed many shadow detection algorithms, and have achieved certain results. Therefore, based on the previous studies, this paper has important practical significance for the research of agricultural plant video image shadow processing technology based on probability learning pixel classification.

MATERIALS AND METHODS

Shadow processing technology of agricultural plant video image, based on probable learning pixel classification

Probable learning pixel classification based on real-time intelligent video capture

The multi-channel fast detection mechanism refers to the function of pedestrian detection when the system is deployed. It is divided into two steps when testing pedestrians. The first step is to quickly detect pedestrians in the system. The method of fast detection is a background modeling method. When the current video is larger than the background model, the video frame may be initially identified as having a potential abnormality (Wang P, Hu X, Li Y. 2016). The reason why the video frame is first detected in one step is because no part of the camera deployment area will occur for most of the time, such as military management areas or warehouses where pedestrians are prohibited from entering or leaving. If the video stream data in the response time of the timer is captured for a complete detection, it will waste more time to affect the video data to be forwarded to the client (Girard F, Kavalec C, Cheriet F., 2019). So, the first step is to quickly detect the video data, capture the valuable video data, and then use the trained machine learning model for more accurate detection. The video data is captured and the trained machine learning model is used for more accurate detection (Xiao-Bing H.U., Rong-Fang Z., Xing Y.E., 2017). After the video streaming server starts running, the main thread will establish two sockets, which are the data port and the control port (Yang J., Wang C., Cai G., 2016). The video stream obtained by the server from the NVR (Network Video Recorder) is sent from the data port to the client, and the client requests the server. Both are sent from the control port to the server (Yang J., Wang C., Xie C., 2017). The socket created by the main thread will always be in the listening state, listening to the client's connection request (Tolstik T., Marquardt C., Matth Us C., 2014). When the connection request of the client is monitored, a connection is established with the client, and the client also sends a video request to the server through the control port. The server main thread checks its permissions according to the client's request, determines whether the client can view the video of the channel, and then the server establishes the corresponding channel (Skakun S, Kussul N, Shelestov A.Y., 2016). Each channel has a ring buffer and is independent of each other. Each channel reads the configuration information such as the IP (intellectual property) address, port number, user name, and password of the NVR in the database, and logs in to the NVR using the NET_DVR_Login_V30 interface. After the login is completed, the main thread will start two sub-threads, one is the forwarding sub-thread responsible for the video stream forwarding view, and the other is the capture sub-thread responsible for acquiring the key frames in the video stream.

Next, the main thread will use the NET_DVR_Real Play_V30 interface to obtain the video stream of a certain channel according to the channel number, stream type, stream taking mode, callback function and other parameters of the client request channel (Xiao-Hong W., Yu-Qian Z., Miao L., 2015). The callback function is an execution function for obtaining a video stream, and the main line can obtain the code stream type and size of the video stream and the User ID of the code stream through the callback function. Through these attribute information of the code stream the main thread distributes the video stream of each channel to its own ring buffer, and then the sub thread responsible for forwarding uses the optimal forwarding algorithm in Chapter 3 to send the video stream in the buffer to the client. The sub-thread responsible for forwarding then uses the optimal forwarding algorithm in Chapter 3 to send the video stream in the buffer to the client. After the main thread obtains the callback function and the video stream is mounted on the ring buffer according to the channel number of the video frame, the same video frame is also placed in the playback buffer constructed by the server in the callback function. The capture sub-thread will set the timer at the beginning of the startup. The response interval of the timer is 1 second. During the response time, the sub-thread will obtain the video dump from the playback buffer through the above-mentioned Player Buf-based capture scheme. And then check the value of flag bit. In the case where the flag value is 1, the image is quickly detected. If the detected key frame image is dynamically changed based on the detection

background, the risk of potential abnormality is considered, and the image is saved locally or continues to utilize the cloud-based machine learning model. Perform a second test.

Crop pixel model based on cloud collaborative detection algorithm

The Histogram of Oriented Gradient (HOG) is a feature of statistically analyzing the gradient direction of a local region of an image. It is commonly used for object detection in computer vision and image processing. Compared to other features, HOG has many advantages. First, the HOG operates on the local square of the image, maintaining a good invariance to both image geometry and optical distortion. Secondly, under the conditions of spatial and directional space sampling and normalization, pedestrians are allowed to have some subtle actions that do not affect the detection effect. In an image, the shape of the local target can be described by the statistical information of the gradient, so that each image is extracted by HOG, and the generated vector is used to represent the gradient statistical information. Using a 64*128 image to extract the HOG feature's practice flow: After completing the first three steps of the above process, a 16*16 pixel block and an 8*8 pixel cell are created in the 64*128 image window. Each block has 4 cells, and the number of directions of the gradient is bins=9. Histogram statistics are performed on the gradient direction of all pixels in each cell to obtain a 9-dimensional feature vector; thus, a 36-dimensional vector is obtained in each block. The sample image window is scanned with overlapping blocks, with 7 scanning areas in the horizontal direction and 15 scanning areas in the vertical direction, and all the block features are connected. Finally, a feature of 36*7*15=3780 dimensions is obtained. SVM (Support Vector Machine) is a VC (Vapnik–Chervonenkis) learning theory based on statistical learning theory and a machine learning algorithm that minimizes structural risk to deal with the classification problem of binary samples. Based on the limited sample information, it seeks a balance between the complexity of the model and the learning ability. Get the best promotion (generalization) ability. The nonlinear SVM adopts the kernel function mapping method to map the original sample space to the dimensional space, and finds a hyperplane to correctly classify the samples, so that the interval between the positive and negative samples is the largest.

For crop video images, the distribution of individual pixels and their values is continually evaluated.

Sometimes it will be in a general background state: sometimes it may be the shadow of a swinging plant; sometimes it can be part of the plant itself. Therefore, we can give the pixel (x, y) the value of $i_{x,y}$ is the weight of crop $c_{x,y}$, field $f_{x,y}$ and shadow $s_{x,y}$ and:

$$i_{x,y} = w_{x,y} \cdot (c_{x,y}, f_{x,y}, s_{x,y}) \tag{1}$$

These distributions are labelled subscripts and are emphasized as they differ from other pixels. For example, some parts of the image correspond to plants, and other parts are dark stripes between plants. $\Theta = \{\omega_l, \mu_l, \sum_l; l \in \{c, f, s\}\}$ is defined as a parameter of the pixel (x, y) model, such as $w_{x,y} = (\omega_c, \omega_f, \omega_s)$, $f_{x,y} \sim N(\mu_f, \sum_f)$, and the like. For the sake of clarity, we will ignore the subscript x, y of these parameters below. However, it should be clear that there are different sets of parameters for the pixels at position x, y. i is a pixel value and L is a random variable representing the pixel number in the image. Our model defines this probability as:

$$P(L = l, I(x, y, t) = i | \Theta) = \omega_l \cdot (2\pi)^{\frac{2}{d}} \left| \sum_l \right|^{-\frac{1}{2}} \exp\left\{-\frac{1}{2}(i - \mu_l)^T \sum_l^{-1}(i - \mu_l)\right\} \tag{2}$$

Among them, $I(x, y, t)$ is the instantaneous pixel value of the pixel (x, y) at time t. Assuming these probabilities, we can classify the pixel values, i.e. we choose class l with the highest posterior probability of $I(x, y, t)$.

RESULTS

Experimental design and analysis

Experimental environment

Table 1

Hardware Configuration Table

Model	To configure	Number	Remarks
Inter(R)Core(TM)i5-4000U	<ul style="list-style-type: none"> · CPU Main Frequency 1.6GHZ · 8GB Memory*1 · 500GB Hard Disk · 64-bit operating system 	1	nothing

Application of probability learning pixel classification in shadow processing of agricultural plant video images

The concept of online learning is part of incremental learning. The basic idea is to learn the image features of the newly added samples, so that the model perceives the environmental changes in the device deployment area, solves the disadvantages of the algorithm model in the previous system, and improves the accuracy and robustness of the algorithm. Online learning is ideal for applications where the sample continues to grow and is used for iterative updates of the model. Most organizations now apply offline trained models and deploy them online for prediction or classification. The model trains and learns the new data on the line. After collecting the new data in the background, the new data is integrated with the previous data before training. Updating the model in this way not only wastes the storage space of the machine, but also wastes a lot of training time compared to the incremental training method. In the online learning phase of the system, the video server sends the detected image to the client for Alarm information, and the client user determines the result. If the server determines that there is no pedestrian image as a pedestrian, it is a false check. The client marks this image as a negative sample and sends it to the cloud server. When the cloud model is trained again, the information of the new sample set can be learnt, enhancing the model's effect on pedestrian detection in this context in continuous learning.

The offline training module is a model that is pre-trained and generated by the sample set before the model goes online. The model generated by the pre-training is not specific to the detection scenario. Before offline training of the algorithm, it is needed to build an initial version of the sample library, including video frames (positive samples) containing pedestrians or other targets and video frames (negative samples) that do not contain people or other targets. In order to obtain a good classifier, a certain number and quality of sample sets representing the environmental characteristics of the subordinate areas of the monitoring equipment are required. These sample sets include states in various situations as much as possible. For example, negative samples are used to capture images of different illuminations and angles in the same region, while positive samples should be collected from pedestrian images of different ages, genders, and regions.

In the collaborative training mechanism offline training module, this paper adopts the INRIA pedestrian detection data set with more comprehensive illumination conditions and human gestures in the picture, including 1218 negative sample images and 614 positive sample images. Each picture in this dataset is calibrated for the pedestrian area, and a rectangular frame is drawn, and the fixed point coordinates, the length and width of the rectangle on the rectangular frame are recorded. In order to get better results when using INRIA dataset, this paper pre-processes the original data, that is, 10 images of 64*128 size are randomly cut out from each original image, which increases the number of images. The number of original training sets also increases the diversity of the original training set.

The model training process is as shown in the following figure: Firstly, the training sample is cut to the appropriate size, and the image is selected by the histogram of oriented gradients (HOG). When the feature selection is performed, the detection sub-parameter file is generated according to the specific sample set, and the training is performed.

The model is saved locally. According to the HOG feature extraction process, each picture in the sample set is extracted into a one-dimensional vector, and all the images generated by the image are involved in the training of the SVM. Before the SVM is trained, the corresponding parameters are selected according to actual needs, and the parameters are set and then started. Perform SVM model training. To test the work of the shadow removal method, a continuous crop video stream is taken. This video stream is processed on the Windows operating platform of memory 1G and CPU 2.8GHZ using MATLAB 7.5. Processing data indicates that the pixels of the shadows and fields are relatively concentrated, while the pixels of the plants are relatively discrete. In order to distinguish the shadow from the plant, the pixel model and the incremental EM are determined.

In Figure 1, 47 frames, 194 frames, and 258 frames of the video, respectively, the shadow portion in each frame is determined by the probability learning pixel classification method, and then replaced with the corresponding field pixel value. From the examples, it can be seen that our real-time method has a good shadow removal capability, which paves the way for more sophisticated processing in various farmland applications.

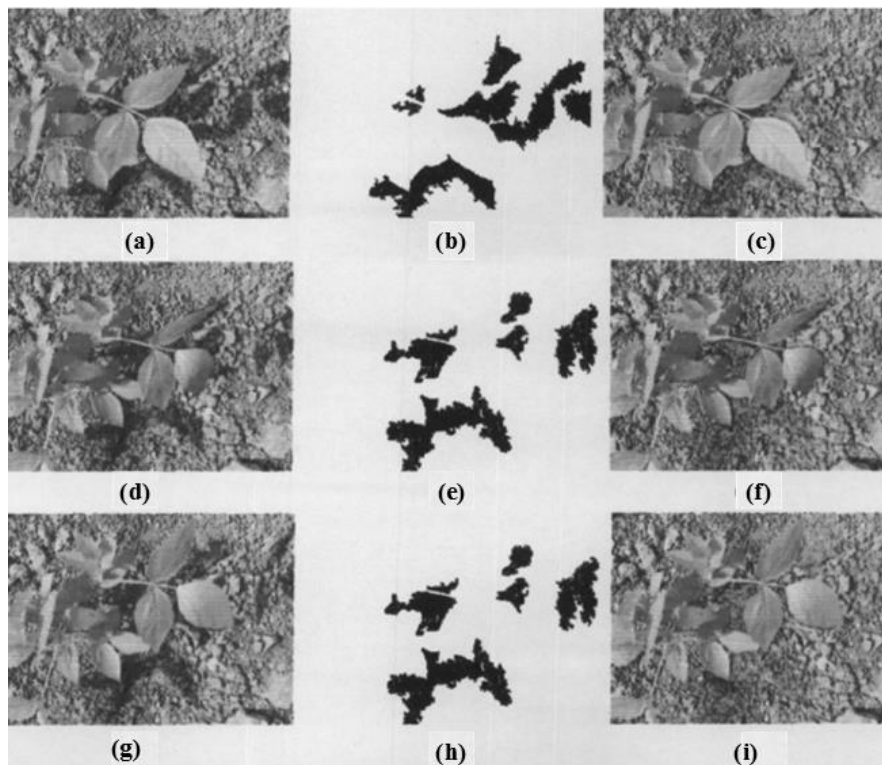


Fig. 1 - (a) Shadow detection (c) Shadow removal image (d) Shadow detection (f) Shadow removal image (g) Shadow removal image (h) detection of 258 frame (h) Shadow removal image (i)

Algorithm and model performance experiment and result analysis

Transaction response time: The time interval after the thread requests a video frame from the NVR to return to the video frame and write to the local disk.

The experimental results of Scheme 1 are analyzed as follows:

Table 2

Number of concurrent threads and corresponding time

	1	2	3	4
Transaction Maximum Response Time (ms)	874	1403	2334	2868
Transaction minimum response time (ms)	130	284	392	573
Transaction average response time (ms)	502	843.5	1363	1720.5

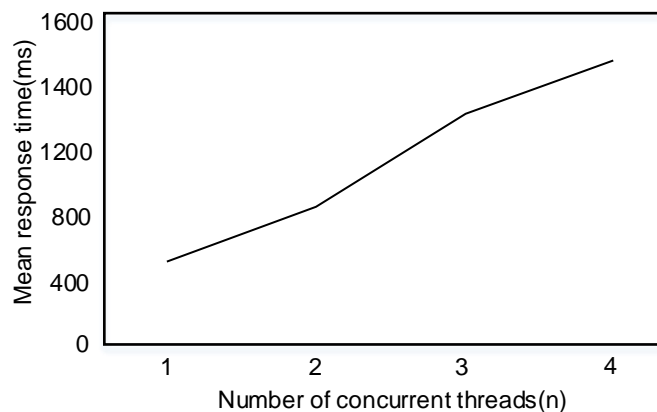


Fig. 2 - The relationship between the average response time and the number of concurrent threads

As can be seen from Figure 2, the average response time of a transaction has a tendency to increase as the number of concurrent threads increases. Analysis: Since the Haikang SDK (Software Development Kit) function interacts with the NYR to obtain images, when the number of concurrent threads increases, the degree of concurrency supported by the NVR is insufficient to cope with multiple threads requesting video frames at the same time, that is, the NVR delays when processing these requests.

There is the phenomenon that the operation of capturing a picture cannot be completed within a prescribed time interval of the program, and an error occurs. Limiting program capture performance is the degree of parallelism supported by the NVR. The experimental results of Scheme 2 are analyzed as follows:

Table 3

Number of concurrent threads and response time				
	1	2	3	4
Transaction Maximum Response Time (ms)	532	590	658	730
Transaction minimum response time (ms)	50	68	79	106
Transaction average response time (ms)	291	329	368.5	418

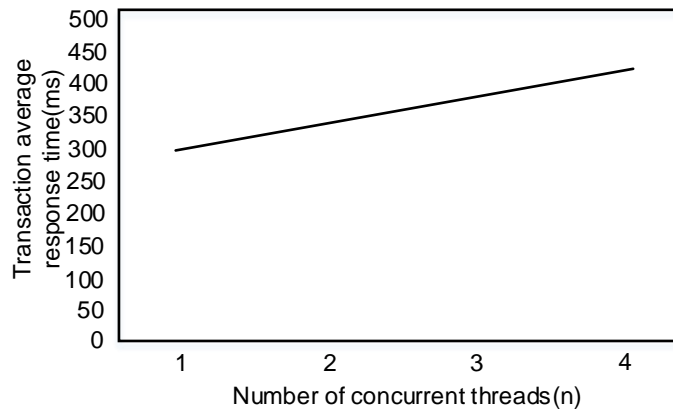


Fig. 3 - The relationship between the average response time and the number of concurrent threads

As shown in Figure 3, it can be seen that the transaction response time is increasing with the increase of the capture sub-thread. Analysis: In this scheme, the second callback is set in the callback function of the main thread, and the video stream obtained by the main thread from the NVR is decoded and stored locally, and the decoding process is also obtained from the NVR. The video stream is decoded into the YUV format. The process of initial decoding is also dependent on the NVR, and the NVR performs linear execution internally when it is converted to the YUV format. As the number of channel threads increases, the time interval for data snooping on each thread increases. Therefore, when the number of server-side channels is greatly expanded, the capture scheme based on the decoding callback will generate a long delay. This method cannot be applied to a specific system. The results of the third experiment are analyzed as follows:

Table 4

Number of concurrent threads and response time				
	1	2	3	4
Transaction Maximum Response Time (ms)	28	29	29	30
Transaction minimum response time (ms)	13	14	19	15
Transaction average response time (ms)	20	23	24	23

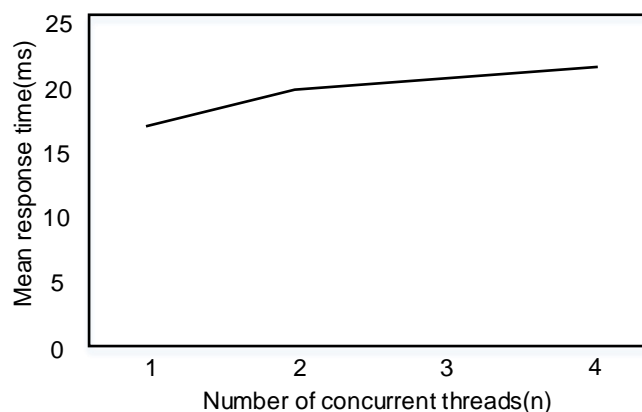


Fig.4 - The relationship between the average response time and the number of concurrent threads

The experiment shows that the average capture time does not fluctuate randomly with the increase of the number of channels, and the response time of the transaction is stable.

This experiment is simulated on VS2010IDE. By comparing the effects of traditional SVM training model and incremental SVM training model, the performance of incremental SVM training results for pedestrian detection is verified and suitable for use in the system. In this experiment, the model is based on offline training. The support vector set is set to SA_SV. Then, during the running of the system, the image of the pedestrian appears in the picture as the new sample B.

The experimental results of the distribution of samples and the number of iterations are as follows:

Table 5

Comparison Table of Detection Accuracy between Traditional Algorithms and Online Learning Algorithms

Classification number	training set	New Sample Set	traditional algorithm		Online Learning Algorithms	
			Time/s	accuracy rate	Time/s	accuracy rate
2	Initial sample set	1832	976.5	83%		
	New Sample Set 1	100	1024.6	83.3%	18.3	83.3%
	New Sample Set 2	200	1119.1	84.2%	32.3	85.2%
	New Sample Set 3	200	1203.5	85.4%	31.2	85.9%
	New Sample Set 4	200	1312.3	85.6%	33.2	86.5%
	New Sample Set 5	200	1429.6	86.1%	34.3	86.7%

The number of iterations of the algorithm can be adjusted according to the needs of the online training. According to the experimental observation, the number of iterations will affect the accuracy of the algorithm to some extent. The relationship is as shown below:

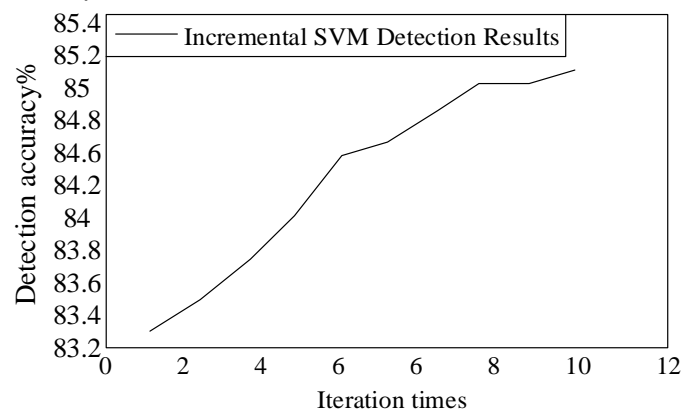


Fig. 5 - The relationship between the detection effect of incremental SVM and the number of iterations

The above results are analyzed as follows: Online learning can greatly shorten the training time, and can also effectively improve the accuracy of the training model detection. As the number of online training iterations increases, it can help to improve the detection accuracy of the generated model.

CONCLUSIONS

Scientific observation of crops is the basis of agricultural production and the application of computer technology in agricultural production can further improve the current situation of agricultural production. Therefore, this paper proposes a pixel classification based on the probability of real-time intelligent video learning, build the crops pixel model based on the cloud detection algorithm together, this algorithm to achieve HOG+SVM agriculture detection algorithm for the premise, the application of the idea of online learning system, that are related to the agricultural production, in turn, online update iteration model, enhance the model to improve the adaptability and agricultural environment detection accuracy.

A cloud collaborative detection mechanism is proposed to solve the problem of inaccurate offline model detection. The detected images are combined with the opinions of the client experts to form a new training sample and it is sent to the cloud model training server again.

The incremental training method is used to strengthen the detection model, which enhances the detection effect of the video server and dynamically improves the detection accuracy of the model in a specific scene.

This paper systematically studies intelligent video surveillance, and has achieved certain research results. However, there are still some shortcomings. In this paper, when online training of the model on the server, the online training requires continuous adjustment of the expert opinion of the test sample and then returns to the sample set on the remote server. Therefore, the experimental process of this part is carried out under the experimental environment of simulation.

REFERENCES

- [1] Argandacarreras I, Kaynig V, Rueden C., (2017), Trainable Weka Segmentation: a machine learning tool for microscopy pixel classification. *Bioinformatics*, Vol.33, Issue 15, pp.2424;
- [2] Arun P V, Buddhiraju K M, Porwal A., (2018), Integration of Contextual Knowledge in Unsupervised Subpixel Classification: Semivariogram and Pixel-Affinity Based Approaches. *IEEE Geoscience & Remote Sensing Letters*, Vol.29, Issue 99, pp.1-5;
- [3] Girard F, Kavalec C, Cheriet F., (2019), Joint segmentation and classification of retinal arteries/veins from fundus images. *Artificial Intelligence in Medicine*, Vol.5, Issue 21, pp.4-7;
- [4] Groot H G J, Oostdijk A, Van Persie M., (2017), Cloud and Shadow Detection using Sequential Characteristics on Multi-Spectral Satellite Images. *Electronic Imaging*, Vol.2017, Issue 13, pp.87-94.
- [5] Hadiuzzaman M, Haque N, Rahman F., (2017), Pixel-based heterogeneous traffic measurement considering shadow and illumination variation. *Signal Image & Video Processing*, Vol.11, Issue 3, pp.1-8;
- [6] Hou B, Kou H, Jiao L., (2017), Classification of Polarimetric SAR Images Using Multilayer Autoencoders and Superpixels. *IEEE Journal of Selected Topics in Applied Earth Observations & Remote Sensing*, Vol.9, Issue 7, pp.3072-3081;
- [7] Li J, Khodadadzadeh M, Plaza A., (2017), A Discontinuity Preserving Relaxation Scheme for Spectral-Spatial Hyperspectral Image Classification. *IEEE Journal of Selected Topics in Applied Earth Observations & Remote Sensing*, Vol.9, Issue 2, pp.625-639.
- [8] Majdar R S, Ghassemian H., (2017), A probabilistic SVM approach for hyperspectral image classification using spectral and texture features. *International Journal of Remote Sensing*, Vol.38, Issue 15, pp.4265-4284;
- [9] Nan M, Zhu R, Li Y., (2018), Deshadowing of Urban Airborne Imagery Based on Object-Oriented Automatic Shadow Detection and Regional Matching Compensation. *IEEE Journal of Selected Topics in Applied Earth Observations & Remote Sensing*, Vol.11, Issue 99, pp.1-21;
- [10] Rashno A, Nazari B, Sadri S., (2017), Effective pixel classification of Mars images based on ant colony optimization feature selection and extreme learning machine. *Neurocomputing*, Vol.226, Issue 89, pp.66-79;
- [11] Sharma A, Liu X, Yang X., (2018), Land cover classification from multi-temporal, multi-spectral remotely sensed imagery using patch-based recurrent neural networks. *Neural Networks the Official Journal of the International Neural Network Society*, Vol.10, Issue 5, pp.346;
- [12] Skakun S, Kussul N, Shelestov A Y., (2016), Efficiency Assessment of Multitemporal C-Band Radarsat-2 Intensity and Landsat-8 Surface Reflectance Satellite Imagery for Crop Classification in Ukraine. *IEEE Journal of Selected Topics in Applied Earth Observations and Remote Sensing*, Vol.9, Issue 8, pp.3712-3719;
- [13] Tatar N, Saadatseresht M, Arefi H., (2018), A Robust Object-Based Shadow Detection Method for Cloud-Free High Resolution Satellite Images Over Urban Areas and Water Bodies. *Advances in Space Research*, Vol.7, Issue 8, pp.77-98;
- [14] Tegolo D, Tegolo D., (2016), A multiscale approach to automatic and unsupervised retinal vessel segmentation using Self-Organizing Maps. *International Conference on Computer Systems & Technologies*. ACM, Vol.47, Issue 13, pp.26-52;
- [15] Tolstik T, Marquardt C, Matth?Us C., (2014), Discrimination and classification of liver cancer cells and proliferation states by Raman spectroscopic imaging. *The Analyst*, Vol.139, Issue 22, pp.6036-6043;

- [16] Wan S, Gong C, Zhong P., (2019), Multiscale Dynamic Graph Convolutional Network for Hyperspectral Image Classification. *IEEE Transactions on Geoscience and Remote Sensing*, Issue 99, pp.1-16;
- [17] Wang P, Hu X, Li Y., (2016), *Automatic cell nuclei segmentation and classification of breast cancer histopathology images. signal processing*, Vol.122, Issue 9-10, pp.1-13;
- [18] Wang W, Zhang J, Wu W., (2018), *An Automatic Approach for Retinal Vessel Segmentation by Multi-Scale Morphology and Seed Point Tracking. Journal of Medical Imaging and Health Informatics*, Vol.77, Issue 12, pp.26-52;
- [19] Windrim L, Ramakrishnan R, Melkumyan A., (2018), A Physics-Based Deep Learning Approach to Shadow Invariant Representations of Hyperspectral Images. *IEEE Trans Image Process*, Vol.21, Issue 99, pp.665-677;
- [20] Xiao-Bing H U, Rong-Fang Z, Xing Y E., (2017), Characteristic indexes of floc structure in activated sludge based on dimensionality reduction methods. *China Environmental Science*, Vol.37, Issue 5, pp.1759-1768;
- [21] Xiao-Hong W, Yu-Qian Z, Miao L., (2015), Automatic Segmentation for Retinal Vessel Based on Multi-scale 2D Gabor Wavelet. *Acta Automatica Sinica*, Vol.41, Issue 5, pp.970-980;
- [22] Xu M, Zhu J, Lv P., (2017), Learning-based Shadow Recognition and Removal from Monochromatic Natural Images. *IEEE Transactions on Image Processing*, Vol.26, Issue 12, pp.5811-5824.
- [23] Yan X, Lu Y, Liu L., (2018), General Meaningful Shadow Construction in Secret Image Sharing. *IEEE Access*, Vol.6, Issue 99, pp.1-1;
- [24] Yang J, Wang C, Cai G., (2016), Discrimination of liver cancer in cellular level based on backscatter micro-spectrum with PCA algorithm and BP neural network // SPIE/COS Photonics Asia. *International Society for Optics and Photonics*, Vol.22, Issue 31, pp.42-71;
- [25] Yang S, Feng Z, Wang M., (2018), Self-Paced Learning-Based Probability Subspace Projection for Hyperspectral Image Classification. *IEEE Transactions on Neural Networks & Learning Systems*, Vol.24, Issue 99, pp.1-6.

CONTROL METHOD FOR PARAMETERS COORDINATE MATCH OF FLUTED ROLLER FERTILIZER APPARATUS

/

外槽轮施肥参数协调匹配控制方法

Huimin Feng^{1, 2)}, Nana Gao²⁾, You Li²⁾, Weiqiang Fu³⁾, Yuming Guo^{*1)} ¹

¹⁾ College of Engineering, Shanxi Agricultural University, Taigu /China;

²⁾ Beijing Research Centre for Information Technology in Agriculture, Beijing /China;

³⁾ Beijing Research Centre of Intelligent Equipment for Agriculture, Beijing /China

Tel: +86-0354-6286869; E-mail: guoyuming99@sina.com

<https://doi.org/10.35633/inmateh-60-24>

Keywords: Control method, nearly-optimal set, exposure length, rotational speed, fluted roller apparatus

ABSTRACT

To improve the fertilization accuracy and distribution uniformity of nitrogen fertilizer, control method of working parameters coordinate match was proposed in this paper. Take minimum coefficient of variation as criterion, the nearly-optimal set of exposure length and rotational speed was solved based on regression models with known values of target fertilizer amount and operating speed, the interfaces were built to rapidly calculate related parameters. The static and dynamic experiments were conducted to verify the reliability and accuracy of regression models and control method; the results showed that under static conditions, the biggest difference value of fertilizer amount is 0.22g per revolution; under dynamic conditions, the deviation of fertilizer amount is less than 4.01%, the maximum deviation of rotational speed is 2.74%. Those results indicate that the control method is practical and feasible for fertilization operation.

摘要

为提高施肥作业精度和肥料分布均匀性,提出了一种基于目标施肥量和作业速度的排肥器开度和转速协调匹配控制方法。以各行排肥量一致性变异系数最小为优化准则,根据回归模型求解已知目标施肥量和作业速度下近优的排肥器开度和转速组合,并搭建了静态和动态测试界面。通过静态和动态试验对回归模型和控制方法进行了验证,静态条件下,最大排肥器单转排量偏差为0.22g;动态条件下,施肥量偏差均小于4.01%,马达实际平均转速与模型计算转速最大偏差为2.74%。结果表明本控制方法实用可行。

INTRODUCTION

Topdressing fertilizer application of a certain amount of nitrogen is essential for winter wheat. Nitrogen fertilizer plays an important role in nutrient accumulation and yield improvement for winter wheat during growing period (Efretuei A et al, 2016), adequate and uniform distribution of nitrogen topdressing fertilizer is the key to balance nutrients absorption for crops.

As the core implement mechanism of fertilization machinery, fluted roller fertilizer apparatus (Botao Wang et al, 2017; Qingzhen Zhu et al, 2018) is being widely used to achieve variable fertilization by adjusting the rotational speed or exposure length of fluted roller. Extensive variable rate fertilization (VRF) studies on rotational speed control method was reported, electric motor (Rui Zhang et al, 2012), hydraulic motor (Liping Chen et al, 2008) and mechanical continuous variable transmission (Chunying Liang et al, 2013, Ning Su et al, 2015) were studied to replace chain transmission and precisely control the rotational speed. The optimal adjustment of parameters to obtained the minimum coefficient of variation (Gómez-Gil J. et al, 2009; Benjamin E. et al, 2019) is still a major challenge, bivariate real-time adjustment algorithm was carried out based on the fuzzy-PID control technology, to control exposure length and rotational speed simultaneously (Man Chen et al, 2016). Control algorithm based on fuzzy system was conducted to generate nearly-optimal bivariate control parameters of exposure length and rotational speed (Yuxue Gu et al, 2011).

¹ Huimin Feng, Ph.D.; Nana Gao, Ph.D.; You Li, Eng.; Weiqiang Fu, Ph.D.; Yuming Guo, Prof.

Nevertheless, in practical fertilization, with a certain fertilization requirement, the exposure length is normally pre-set, the fertilizer discharge rate is calibrated under fixed rotational speed, which apparently ignores the deviation caused by the difference between the fixed rotational speed and actual rotational speed.

Research on coordinate matching control method of exposure length and rotational speed of fluted roller was proposed in this paper, the relationship of those two factors with target fertilizer amount and operating speed was discussed, the flowchart was embedded in a vehicle terminal to verify the reliability of control method. The static and dynamic experiments based on this method were conducted to evaluate the consistency of fertilizer distribution.

MATERIALS AND METHODS

Precision fertilization system

The topdressing fertilizer applicator (Huimin Feng et al, 2018) for winter wheat was taken as research object. Working principle of precision fertilization system is shown in fig.1, tractor position information is real-time acquired and calculated by high precision Global Navigation Satellite System (GNSS) receiver. Then, the information is sent to vehicle terminal. The target speed of hydraulic motor is calculated by the terminal according to the operating speed and machine parameters, the real-time speed of motor is monitored by hall sensor and then the controller realizes closed-loop control of hydraulic motor speed through Proportional–Integral–Derivative (PID) algorithm, thus precisely controlling the rotational speed of distributing shaft.

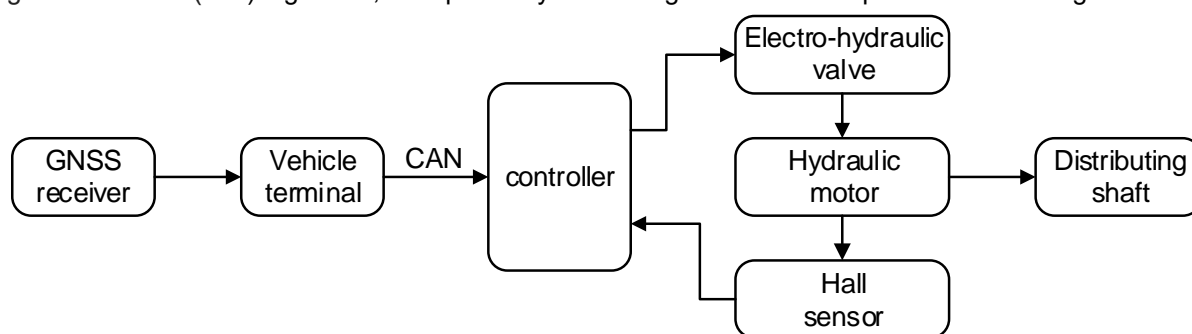


Fig. 1 - Schematic diagram of precision topdressing fertilization system

Structure of fertilizer apparatus

Circular-arc straight fluted roller fertilizer apparatus was taken as search object, as showed in fig.2, the number of grooves is 6, the radius of fluted roller is 25mm, the exposure length is the effective working length which is adjusted by spiral screw and adjustable wheel.

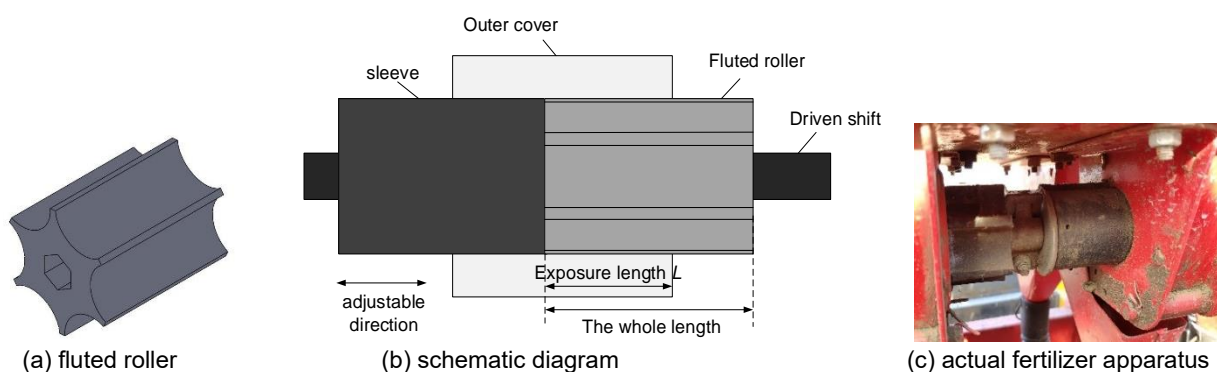


Fig. 2 - structure of fluted roller fertilizer apparatus

Fertilization model

Distributing shaft is connected with the hydraulic motor by a hexagonal shaft, so the speed of fluted roller is equal to the speed of hydraulic motor; the rotational speed of fluted roller was calculated according to formula (1), to realize real-time matching between the theoretical rotational speed R_0 of fluted roller and operating speed V of tractor.

$$R_0 = \frac{10 \cdot V \cdot W \cdot Q_0}{6 \cdot n \cdot q} \quad [\text{r/min}] \quad (1)$$

Where:

- W is operating width of applicator, [m];
- Q_0 is fertilizer amount per unit, [kg/hm²];
- n is number of rows;
- q is fertilizer discharge rate, [g/r].

Calibration of fertilizer discharge rate

The topdressing fertilizer amount of winter wheat is basically within the range of 80~350 kg/hm² (Zhongyang Huo et al, 2004), the settable range of exposure length L is 0~40 mm and 5~120 r/min for rotational speed R . The range of L and R in our study was decided based on previous tests and also the fertilization amount, which were 10~24 mm and 10~40 r/min, respectively.

The fertilizer discharge rate q is one of the key parameters for the fertilization models (Shiqiang Pan et al, 2016), static tests based on uniform fertilization were carried out to test the fertilization performance. Urea was selected as experimental material; the granularity scope of urea particles is 0.85~2.80 mm. The exposure length L was set at 10, 12, 15, 18, 20 and 24 mm with various rotational speed R of 10, 15, 20, 25, 30 and 40 r/min, the fertilizer discharged amount P by 7 synchronous fertilizer apparatus in one min interval was collected and weighed, respectively, and each test was measured with 3 replications.

The fertilizer discharge rate q and the coefficient of variation CV were calculated according to formula (2).

$$\left\{ \begin{aligned} q &= \frac{\sum_{i=1}^n P_i / n}{R} \\ S &= \sqrt{\frac{\sum_{i=1}^n (q_i - q)^2}{n-1}} \\ CV &= \frac{S}{q} \times 100\% \end{aligned} \right. \quad (2)$$

Control method

For fertilizer operating system, the variation of target fertilizer amount Q , fertilizer discharge rate q and coefficient of variation CV are all closely related to the change of exposure length L and rotational speed R . The relationship based on calibration data was analysed, as shown in fig.3; any fertilizer discharge rate q corresponds to infinite sets of exposure length L and rotational speed R along with various coefficients of variation CV , and for the target fertilizer amount Q as well, so the nearly-optimal set with minimum coefficient of variation can improve the fertilization accuracy.

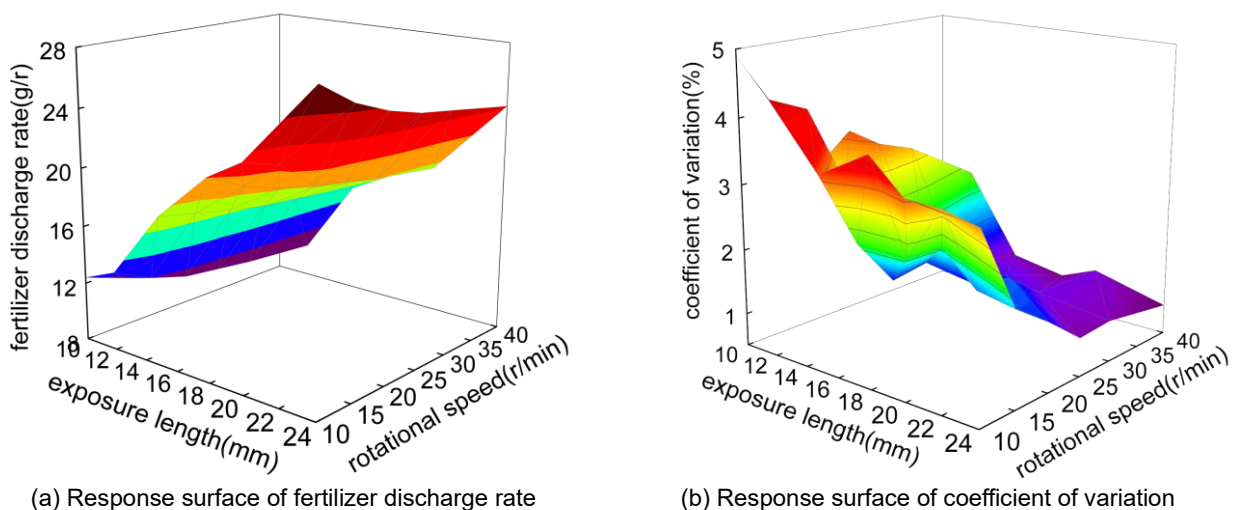


Fig.3 - Response surface based on calibration data

To find the nearly-optimal set of exposure length L and rotational speed R , the control method based on target fertilizer amount Q and operating speed V was proposed, this method consists of two parts: establish the models of fertilizer discharge rate q , coefficient of variation CV and target fertilizer amount Q with exposure length L and rotational speed R , then obtain the nearly-optimal set of exposure length L and rotational speed R by solving those models.

Method for solving nearly-optimal set

The flowchart of solving nearly-optimal set was shown in fig.4. In fig.4(a), the unique rotational speed was solved based on regression model $Q=F(L, R, V)$ with known values of target fertilizer amount Q , operating speed V and exposure length L ; in fig.4(b), the function of solving root was called as a sub-process to calculate the coefficient of variation CV and fertilizer discharge rate q based on regression models $CV=F(L, R)$ and $q=F(L, R)$. The nearly-optimal set was decided by the loop flowchart when the coefficient of variation CV had the minimum value.

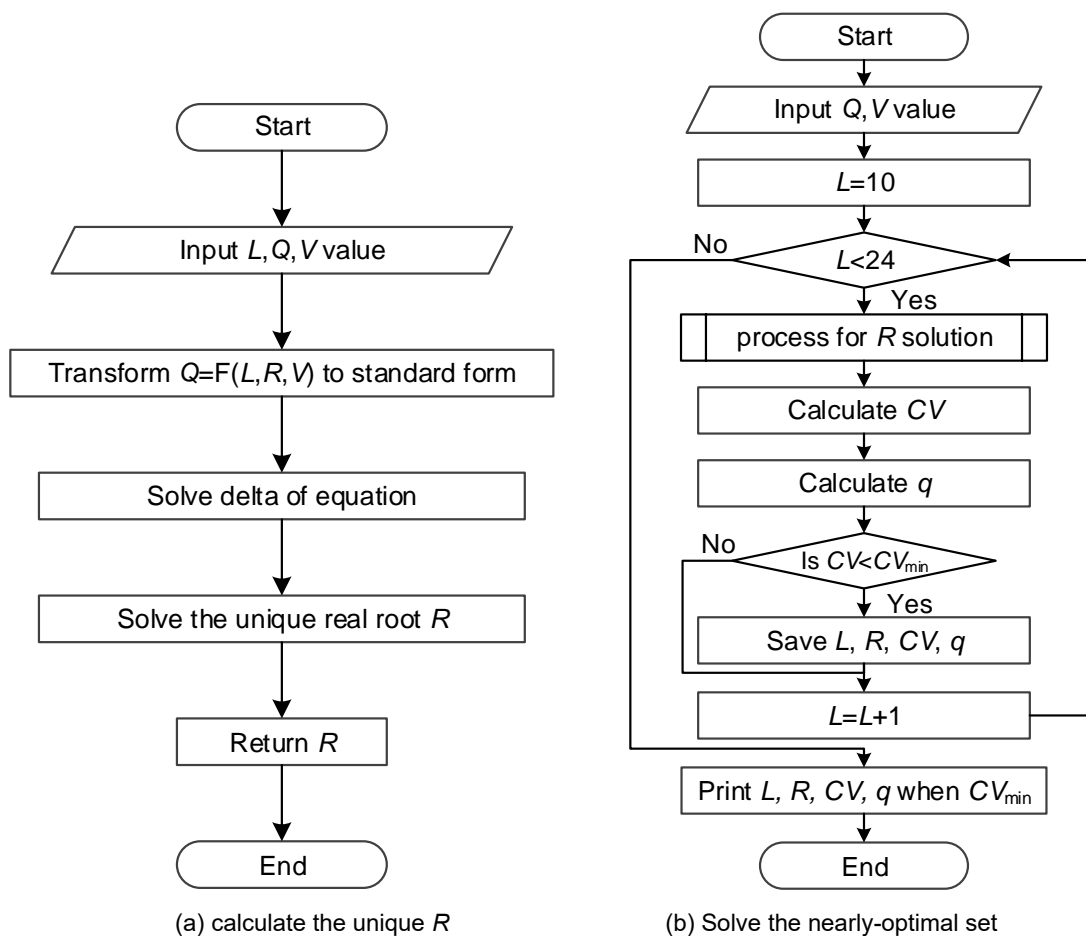


Fig. 4 - Flowchart for nearly-optimal set solution of exposure length and rotational speed

Regression models

Based on the calibration results and formula (1), the fertilizer amount per unit area Q at different operating speed can be calculated. The practical operating speed of topdressing fertilization for wheat is 3 ~ 6 km/h, a part of the related results at the operating speed of 3, 4, 5 and 6 km/h were summarized in table 1.

The range of Q is 40 ~ 600 kg/hm², which completely covers the range of topdressing fertilizer amount for winter wheat.

Table 1

Results of target fertilizer amount at different operating speed

L	R	q	CV	V ₃	Q ₃	V ₄	Q ₄	V ₅	Q ₅	V ₆	Q ₆
[mm]	[r/min]	[g/r]	[%]	[km/h]	[kg/hm ²]						
10	20	10.75	2.95	3	143.33	4	107.5	5	86	6	71.67
12	20	11.35	2.84	3	151.33	4	113.5	5	90.8	6	75.67
15	20	17.05	1.49	3	227.33	4	170.5	5	136.4	6	113.67
18	20	19.3	2.21	3	257.33	4	193.0	5	154.4	6	128.67
20	20	20.05	1.71	3	267.33	4	200.5	5	160.4	6	133.67
24	20	25.60	1.55	3	341.33	4	256.0	5	204.8	6	170.67
10	25	10.40	3.42	3	173.33	4	130.0	5	104	6	86.67
12	25	11.04	3.31	3	184.00	4	138.0	5	110.4	6	92.00
15	25	16.52	1.58	3	275.33	4	206.5	5	165.2	6	137.67
18	25	18.64	1.45	3	310.67	4	233.0	5	186.4	6	155.33
20	25	19.56	1.69	3	326.00	4	244.5	5	195.6	6	163.00
24	25	24.92	1.09	3	415.33	4	311.5	5	249.2	6	207.67

Note: V₃ mean operating speed at 3km/h, Q₃ mean target fertilizer amount at 3km/h, and so on.

ANOVA analysis was performed to obtain the functional relationship between the exposure length L and the rotation speed R and their influence on the fertilizer distribution work, by analyzing the data in table 1.

According to fig.3, the response of fertilizer discharge rate q and coefficient of variation CV to exposure length L and rotational speed R showed a quadratic relationship, respectively. The factors which have significant impact on fertilizer discharge rate q will be taken as variables in the model of target fertilizer amount Q based on formula 1.

The factors effect on target fertilizer amount Q is consistent except that the coefficients in the models are inversely proportional to the operating speed; the regression analysis results at the operation speed of 3 km/h are shown in table 2.

Table 2

ANOVA of fertilization regression models

Responses	Sources	DF	SS	F value	Pr>F
q	model	5	974.63	279.31	<.0001**
	L	1	16.54	23.69	<.0001**
	R	1	3.94	5.64	0.0241*
	L*R	1	2.01	2.88	0.1
	L*L	1	0.005	0.01	0.9362
	R*R	1	4.370	6.26	0.018*
CV	model	5	36.00	35.93	<.0001**
	L	1	2.400	11.98	0.0016**
	R	1	5.130	25.59	<.0001**
	L*R	1	0.0034	0.02	0.8968
	L*L	1	1.39	6.92	0.0133*
	R*R	1	3.53	17.62	0.0002**
Q ₃	model	5	585050.6	516.26	<.0001**
	L	1	316.61	1.4	0.2465
	R	1	15.46	0.07	0.7957
	L*R	1	31206.48	137.69	<.0001**
	R*R	1	18.4	0.08	0.7776
	R*R*R	1	12.27	0.05	0.8176

Note: ** is extremely significant, P<0.01; * is significant, P<0.05.

Quadratic term R^2 has a significant effect on q and CV , Quadratic term L^2 has a significant effect on CV . The regression models were obtained based on the ANOVA analysis results, as shown in table 3; the determination coefficient of regression models for q , CV and Q were 0.979, 0.8569 and 0.9885, respectively.

Table 3

Regression models	
Regression models	R^2
$q = 2.2536 + 1.2033L - 0.2143R - 0.0006L^2 - 0.005LR + 0.0037R^2$	0.979
$CV = 10.5153 - 0.4584L - 0.2446R + 0.0098L^2 + 2.0822 \times 10^{-4}LR + 3.3476 \times 10^{-3}R^2$	0.8569
$Q = (-31.6916 + 4.8096L + 5.2035R + 1.885LR - 0.246R^2 + 0.0027R^3) / V$	0.9885

Model solution

As shown in table 3, the model of target fertilizer amount Q can be considered as a cubic equation for rotational speed which involves known variables of exposure length L and operating speed V . The model can be solved by using Shengjin discriminant function and Shengjin equation.

The solving procedure of Shengjin equation is the following: for cubic equation $aX^3 + bX^2 + cX + d = 0$ ($a, b, c, d \in R$, and $a \neq 0$), the multiple root discriminant function is $A = b^2 - 3ac$, $B = bc - 9ad$, $C = c^2 - 3bd$, the final discriminant function is $\Delta = B^2 - 4AC$.

The roots of equation were decided by the positive or negative value of discriminant function.

According to Shengjin equation, the general form of cubic equation for rotational speed is expressed as follows:

$$0.0027R^3 - 0.246R^2 + 5.2035R + 1.885LR + 4.8096L - 31.6916 - QV = 0 \tag{3}$$

The simplified discriminant function is expressed as follows:

$$\Delta = 5.9049 \times 10^{-4} Q^2 V^2 + 0.217L^3 + 1.4909L^2 + 0.0294QV - 0.0733QVL - 0.8847L - 0.0109 \tag{4}$$

The discriminant function is a ternary quartic polynomial, of which is difficult to judge the monotonicity by taking the partial derivatives method. Traversal algorithm was used to calculate the value of discriminant function, the range of target fertilizer amount Q , operating speed V and exposure length L is 80~400kg/hm², 3~6 km/h and 10 ~24 cm, respectively. The step of each variable was 0.1, the flowchart was showed in fig. 5.

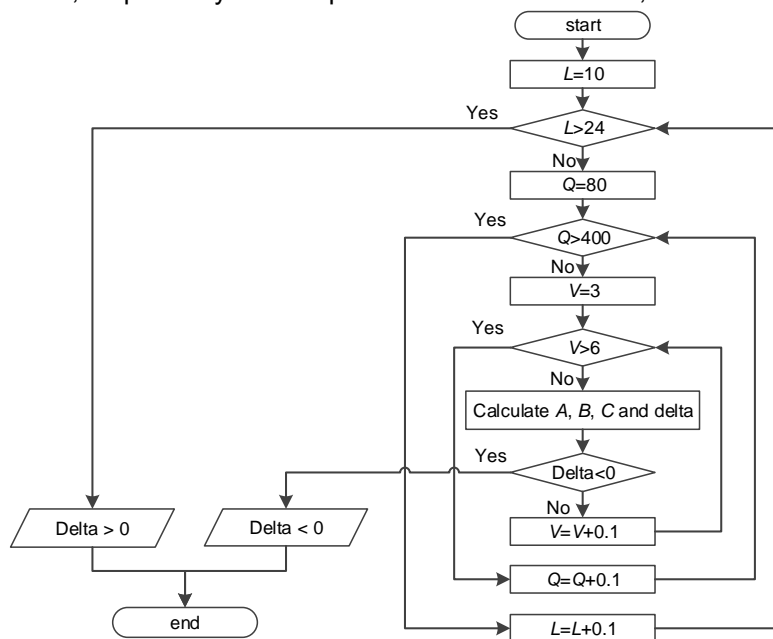


Fig. 5 - Traversal algorithm flowchart for delta discriminant

The results indicated that the value of discriminant is always greater than 0 within the given range, which means there is only one real root for the cubic equation. The root is expressed as follows:

$$X_1 = \frac{-b - (\sqrt[3]{Y_1} + \sqrt[3]{Y_2})}{3a} \tag{5}$$

of which, $Y_{1,2} = Ab + 3a \left(\frac{-B \pm \sqrt{B^2 - 4AC}}{2} \right)$.

The calculation results proved that within the given range, when target fertilizer amount Q and operating speed V is given, the equation has unique solution of rotational speed R at any given exposure length L .

Interfaces for static calibration tests and solving nearly-optimal set

The interfaces based on the flowchart of control method in fig.4 were embedded in the vehicle terminal, which can be used for static calibration tests and dynamic operation tests, as showed in fig.6. for static tests in 6(a), the fertilizer discharge rate q and coefficient of variation CV can be solved with given exposure length L and rotational speed R , for the dynamic operation tests in 6(b), with given operating speed V and target fertilizer amount Q , the nearly-optimal set of exposure length L and rotational speed R was solved, meanwhile, the related fertilizer discharge rate q and coefficient of variation CV was solved.

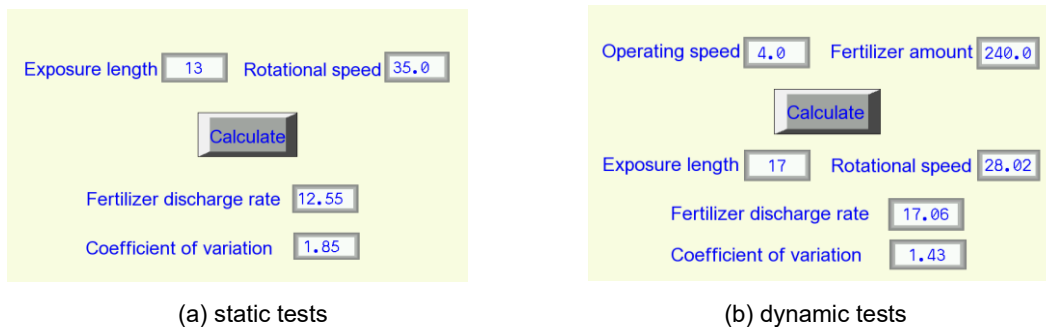


Fig. 4 - Interfaces for control method

Verification experiments design

The experiments under static and dynamic condition were conducted to verify the reliability and accuracy of models and control method.

The regression models of fertilizer discharge rate q and coefficient of variation CV was verified under static condition; 9 groups data were collected when exposure length L set at 14, 18 and 22 mm, rotational speed set at 22, 30 and 35 r/min.

The control method for nearly-optimal set was verified under dynamic condition. The experiment field is 100×3m², 5 groups of selected operating speed [km/h] and target fertilizer amount [kg/hm²] (5, 200), (3, 200), (3, 120), (5, 120) and (4, 200) were conducted with the recommended set of exposure length L and rotational speed R calculated by interface 4(b), the rotational speeds were measured by CAN bus recorder in real time. 2 groups of (5, 200) and (5, 120) were conducted with practical exposure length as control group; the fertilizer applicator and field experiments were shown in fig.5.



Fig. 5 - Experiments under dynamic condition

RESULTS

Regression models verification under static condition

The data of fertilizer discharge rate and coefficient of variation tested under static condition was compared to the data calculated by the interface 4(a), the results were analysed in table 4.

Table 4

Experimental results under static condition

L [mm]	R [r/min]	q [g/r]			CV [%]		
		C-value	T-value	D-value	C-value	T-value	D-value
14	22	14.52	14.32	-0.2	2.32	2.93	0.61
14	30	13.78	13.79	0.01	1.78	2.59	0.81
14	35	13.56	13.48	-0.08	1.66	2.04	0.38
18	22	18.81	18.66	-0.15	1.76	2.23	0.47
18	30	17.92	17.9	-0.02	1.23	1.76	0.53
18	35	17.6	17.55	-0.05	1.11	1.66	0.55
22	22	23.09	23.31	0.22	1.51	3.79	2.28
22	30	22.04	21.99	-0.05	0.99	2.07	1.08
22	35	21.62	21.56	-0.06	0.87	1.83	0.96

Note: C-value is calculated value; T-value is tested value; D-value is difference value.

As shown in table 4, under static condition, the fertilizer discharge rate obtained from experiments are basically uniform compared with the values calculated by regression models. The largest difference value is 0.22g per revolution, the difference values of q were less than 0.1g per revolution in 6 groups. The CV values obtained from experiments has the same trend as the CV values calculated by the models, the CV values decreased with the increase of rotational speed at the same opening length level. The biggest difference value is 2.28% at the opening length of 22mm with the rotational speed of 22r/min. The difference values of CV values in 7 groups are less than 1.

The results showed that regression models have good prediction accuracy for fertilizer discharge rate q and coefficient of variation CV.

Control method of nearly-optimal set verification

Under dynamic condition, the applied fertilizer amount Q_t , deviation of applied fertilizer amount D_t , coefficient of variation CV, average rotational speed R_A and deviation of rotational speed D_R were analysed, the deviation of applied fertilizer amount was compared to the control group and the results were shown in table 5.

Table 5

Experimental results under dynamic condition

groups	V	Q	L	q	Q_t	D_Q	CV[%]		R_A [r/min]		D_R
	[km/h]	[kg/hm ²]	[mm]	[g/r]	[kg/hm ²]	[%]	C-value	T-value	C-value	T-value	%
E-group	5	200	18	18.2	207.67	3.83	1.38	3.89	27.46	27.35	-0.44
	3	200	13	13.44	200	0	2.51	4.17	22.26	21.64	-2.74
	3	120	15	17.64	124.8	4.01	3.76	5.01	10.23	10.11	-1.17
	5	120	13	13.44	118.52	1.23	2.51	3.53	22.26	22.64	1.75
	4	200	16	16.42	193.57	3.21	1.82	5.78	24.37	23.77	-2.46
C-group	5	120	12	12.56	128.42	7.02	-	4.07	-	-	-
	5	200	15	15.02	211.06	5.53	-	4.81	-	-	-

Note: E-group means experimental group; C-group means the control group.

For 5-group experiments conducted by using control method, the deviation of applied fertilizer amount is less than 4.01%, the coefficient of variation is within 3.53 to 5.78%, which could meet the fertilizing accuracy requirements of JB/T7864—2013 *Cultivator-fertilizer*.

The CV values obtained from experiments are larger than the CV values calculated by the control method, which is caused by applicator vibration under dynamic condition. Tested CV values are less than the CV values in control group. The largest deviation of rotational speed is 2.74%, which means the control method has high reliability for rotational speed controlling.

When operating speed is 5 km/h, target fertilizer amount is 120 kg/hm² and 200 kg/hm², the deviations of applied fertilizer amount calculated by the control method are 1.23% and 3.83%, which decreased by 5.79% and 1.71% compared to the control groups, respectively. In control groups, the fertilizer discharge rate q is obtained from static calibration, in which case, there is a difference value because of the uncertain operating rotational speed, which it will cause a larger fertilizer amount deviation. The fertilizer discharge rate q obtained from the control method is calculated based on the practical rotational speed, which highly improved the fertilization accuracy.

CONCLUSIONS

The control method for fertilizer parameters coordinate match was proposed to improve the fertilizer accuracy during topdressing process for winter wheat. Take coefficient of variation as criterion, the nearly-optimal set of exposure length and rotational speed was solved based on target fertilizer amount and operating speed.

The interfaces were built to rapidly calculate the parameters' values, the experiments were carried out to verify the reliability of the regression models and control method. The results showed that the regression models have great prediction for fertilizer discharge rate and coefficient of variation under static conditions, the largest difference value for fertilizer discharge rate being 0.22g per revolution. Under dynamic conditions, fertilization accuracy is highly improved by using the control method, the fertilizer deviations are less than 4.01%, the largest deviation for rotational speed is 2.74%; compared with the control groups at the same experimental condition, the fertilizer deviations are decreased by 5.79% and 1.71%, respectively.

This control method provides nearly-optimal set of exposure length and rotational speed and corresponding fertilizer discharge rate of fluted roller fertilizer apparatus. Meanwhile, it avoids tedious calibration tests before each fertilizing operation. This control method is practical and feasible for fertilizer parameters settings, which can be extended to other types of fertilizer apparatus.

ACKNOWLEDGEMENT

The research is founded by National Key Research and Development Program of China (2016YFD0200600). I would like to express my gratitude to my colleagues from Beijing Research Centre for Information Technology in Agriculture for helping me to conduct the experiments.

REFERENCES

- [1] Benjamin E., Anatha Krishnan D., Kavitha R., (2019), Development of Fertilizer Broadcaster with Electronically Controlled Fluted Roller Metering Mechanism for Paddy Crop. *International Journal of Current Microbiology and Applied Sciences*, Vol.8, Issue.4, pp.2694-2703, Tamil Nadu/India;
- [2] Botao Wang, Lu Bai, Shangpeng Ding et al, (2017), Simulation and experimental study on impact of fluted-roller fertilizer key parameters on fertilizer amount. *Journal of Chinese Agricultural Mechanization*, Vol.38, Issue.10, pp.1-6,23, Beijing/China;
- [3] Chunying Liang, Peng Lv, Jianwei Ji et al, (2013), Application of fuzzy self-tuning PID algorithm in variable rate fertilization system. *Journal of Shenyang Agricultural University*, Vol.44, Issue.4, pp.461-466, Shenyang/China;
- [4] Efreteui A., Gooding M., White E. et al, (2016), Effect of nitrogen fertilizer application timing on nitrogen use efficiency and grain yield of winter wheat in Ireland[J]. *Irish Journal of Agricultural and Food Research*, Vol.55, Issue.1, pp.63-73, Dublin/Ireland;
- [5] Gómez-Gil J., de-Lózar-Escudero A., Navas-Gracia L et al, (2009), Analytical estimation of optimal operation variables of a centrifugal fertilizer distributor, using the gradient method on multiple seeds. *Agrociencia*, Vol.43, Issue.5, pp.497-509, Montecillo/Mexico;
- [6] Huimin Feng, Nana Gao, Zhijun Meng et al, (2018), Design and experiment of deep fertilizer applicator based on autonomous navigation for precise row-following. *Transactions of the Chinese Society for Agricultural Machinery*, Vol.49, Issue.4, pp.60-67, Beijing/China;
- [7] Liping Chen, Wenqian Huang, Zhijun Meng et al, (2008), Design of variable rate fertilization controller based on CAN bus. *Transactions of the Chinese Society for Agricultural Machinery*, Vol.39, Issue.8, pp.101-104, Beijing/China;

- [8] Man Chen, Wei Lu, Xiaochan Wang et al, (2016), Design and experiment of optimization control system for variable fertilization in winter wheat field based on fuzzy PID. *Transactions of the Chinese Society for Agricultural Machinery*, Vol.47, Issue.2, pp.71-76, Beijing/China;
- [9] Ning Su, Taosheng Xu, Liangtu Song et al, (2015), Variable rate fertilization system with adjustable active feed-roll length. *International Journal of Agricultural and Biological Engineering*, Vol.8, Issue.4, pp.19-26, Beijing/China;
- [10] Qingzhen Zhu, Guangwei Wu, Liping Chen et al, (2018), Influences of structure parameters of straight flute wheel on fertilizing performance of fertilizer apparatus. *Transactions of the CSAE*, Vol.34, Issue.18, pp.12-20, Beijing/China.
- [11] Rui Zhang, Chunjiang Zhao, Xiu Wang et al, (2012), A Variable-Rate Fertilizer Control System for Disc Fertilizer Spreaders. *Intelligent Automation & Soft Computing*, Vol.18, Issue.5, pp.461-467, London/U.K.;
- [12] Shiqiang Pan, Yaxiang Zhao, Liang JIN et al, (2016), Design and experimental research of external grooved wheel fertilizer apparatus of 2BFJ-6 type variable rate fertilizer applicator. *Journal of Chinese Agricultural Mechanization*, Vol.37, Issue.1, pp.40-42, Nanjing/China;
- [13] Yuxue Gu, Jin Yuan, Chengliang Liu, (2011), FIS-based method to generate bivariate control parameters regulation sequence for fertilization. *Transactions of the CSAE*, Vol.27, Issue.11, pp.134-139, Beijing/China;
- [14] Zhongyang Huo, Xin Ge, Hongcheng Zhang et al, (2004), Effect of different nitrogen application types on N-absorption and N-utilization rate of specific use cultivars of wheat. *Acta Agronomica Sinica*, Vol.30, Issue.5, pp.449-454, Beijing/China.

IMPROVING THE OPERATING COMFORT OF THE ELECTRIC MINI-TILLER BASED ON SIMULATION ANALYSIS AND FIELD TEST

/

基于仿真分析和田间试验的电动微耕机操作舒适性提高

Po Niu, Jian Chen, Chenjun Hu, Jindou Zhao

Southwest University, College of Engineering and Technology/P.R China

Tel: 8613628384705; E-mail: jianchen@swu.edu.cn

DOI: <https://doi.org/10.35633/inmateh-60-25>

Keywords: electric mini-tiller, operating comfort, simulation analysis, field test

ABSTRACT

Now the engine mini-tiller has become indispensable agricultural machinery in vast hilly and mountainous areas of Southwest China. Many researches have been made to improve its operating comfort, but little effects have been obtained. As an alternative, a new type of electric mini-tiller was developed. For further improvement of its operating comfort, simulation analysis and field test were integrated to decrease the vertical force and vibration RMS values at the handle. The results showed that when the position of centre of gravity moved 19.78 cm, the vertical force was reduced from 154.24 N to 0 N, and vibration RMS values decreased by 20.16% under working condition.

摘要

目前, 微耕机已经成为中国西南广大丘陵山区不可缺少的农业机械。为了改善其操作舒适性, 做了许多研究, 但是效果很小。因此, 开发了一种新型电动微耕机, 为了进一步改善其操作舒适性, 采用仿真分析和田间试验相结合的方法来减小扶手处的垂向力和振动加速度值。结果表明, 在正常工作条件下, 当重心位置移动 19.78 cm 时, 垂向力由 154.24 N 减小到 0 N, 振动加速度值减小 20.16%。

INTRODUCTION

Being small volume, light weight, simple structure and easy transfer in the farm land, the internal combustion engine mini-tiller has become the main and indispensable agricultural machinery in the hilly and mountainous area of Southwest China (Chen J. et al, 2014). However, there have been urgent needs of improvement of its operating comfort, especially nowadays, for most tiller operators are women and aging people in the area.

The mini-tiller is a kind of walking machinery and its operating comfort mainly relies on the vibration acceleration and the force applied to the operator's two hands through the tiller's handles. Therefore, decreasing the both can make the operating comfort increase.

The tiller's engine vibration is mainly caused by two coupling effects of cycling movement of the piston-connecting rod of the engine and periodical rotary blades cutting soils. The vibration acceleration at the handle can be reduced from two aspects: reducing vibration or obstructing vibration transmission from its resources to the operator's hands (Ying Y.B. et al, 1994; Ragni L, 1999; Dong X.Q. et al, 2012; Xu L.Z. et al, 2014). Bini and Kathirvel deals with machine vibration, hand transmitted vibration of walking and riding type power tillers during rototilling in untilled and tilled fields and in transport mode on farm and bitumen roads. The results indicate that machine vibration increased with the increase in engine speed and major excitation of the power tiller vibration was the unbalanced inertial force of the engine (Bini and Kathirvel, 2006). Tewari and Dewangan pointed that the operators of hand tractors experience high levels of vibration in the hand and arm, which cause early fatigue and result in shorter working hours. Suitable isolators were designed and installed in different strategic locations in the hand tractor in order to reduce the effect of vibration level, and hence reduce work stress. The results indicated that the engine mounting and the handle isolators reduced the vibration acceleration by more than 50% (Tewari and Dewangan, 2009). Liang Xincheng et al. selected 1Z-105 diesel mini tiller as a prototype, its vibration characteristics were analysed in the time and frequency domains and the effects on the human body were explored, and suggestion was made regarding the handling comfort of the mini tiller (Liang X.C. et al, 2018). But these researches have little effect; the main reasons lie in implementation of measures stated above being difficult without a substantial increase in size, weight and price of the tiller (Thomas H.L. et al, 2015; Caffaro F. et al, 2016; Niu P. et al, 2017), which is unacceptable for local the farmers.

As a countermeasure, a new type of electric mini-tiller was developed, which can achieve a tillage depth of 10 cm or more and replace the engine tiller for farming operations in dry land tillage and land preparation in vast hilly and mountainous areas of Southwest China. Because its power is a group of lithium battery and a brushless DC motor instead of combustion engine, its vibration resulting from the power is decreased, but the vibration caused by periodical rotary blades cutting soils still exists, further efforts are needed. Until now, vibration of electric mini-tillers has not captured much researchers' attentions, perhaps because unlike the one mentioned above, the majority of existing ones were only suitable for shallow tillage, in other words, they can get a tillage depth of about 5 cm (Cai K. et al, 2013; Gao H.S. et al, 2012; Zhao R.H. et al, 2015). Therefore, vibration produced by these kinds of electric mini-tillers is not so intense.

The other factor that influences tiller's operating comfort is the force applied to operator's hands. It can be decomposed into three components along three directions, namely, top-bottom, left-right and front-back. Under normal circumstances, the latter two components are small and uncontrollable compared with the first one (Hu C.J., 2018). So, the component of the force in the direction top-bottom, i.e. the vertical force should be carefully considered to increase the operating comfort. When cultivating clay soil, a certain vertical force is necessary to ensure adequate tillage depth. However, under some soil conditions, a small force is sufficient. Therefore, the determination of the best vertical force for different soils is a problem worth exploring, but so far there are few reports about it.

In this study, the newly developed electric mini-tiller mentioned above was taken as the research object, the method of combining three-dimensional modelling, force analysis, simulation analysis and field test was adopted to decrease its vibration and vertical force at the handles and improve its operating comfort by changing the position of the tiller centre of gravity, so as to provide available theory and reference to improve the operating comfort of tillers.

MATERIALS AND METHODS

Electric mini-tiller

The electric mini-tiller is mainly composed of handrail, motor controller, electric motor (brushless DC motor, rated power, 0.75 kW), battery pack (60V20Ah lithium battery), rotary blade roller (type of blade, machete; no. of blades, 4x3), transmission system (direct drive), frame, and depth-limiting device, as shown in fig.1. The transmission system consists of power input shaft, one pair of straight bevel gears and power output shaft. The significant parameters of the tiller are listed in table 1, and the material properties of its primary components are delineated in table 2.

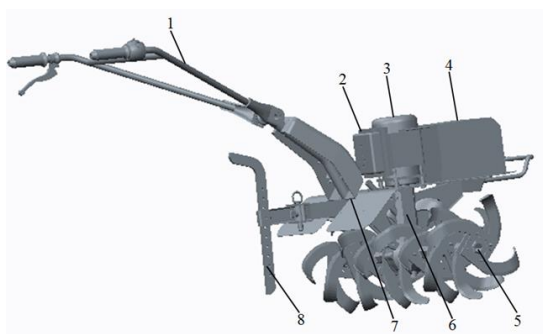


Fig. 1 - Electric mini-tiller
 1 –Handrail; 2 –Motor controller; 3 –Electric motor; 4 –Battery pack; 5 –Rotary blade roller;
 6 –Transmission system; 7 –Frame; 8 –Depth limiting device

Table 1

Parameters						
Item	Mass [kg]	Tillage width [cm]	Tillage depth [cm]	Forward speeds		
				Slow	Medium	Rapid
				[m/s]	[m/s]	[m/s]
Parameter	50	70	≥10	0.1 (only used for field transfer)	0.3 (mainly used for field transfer, rarely for tilling)	0.5 (used for tilling)

Table 2

Material parameters							
Component	Handrail	Frame	Gearbox housing	Power input/output shaft	Straight bevel gear	Rotary blade shaft	Rotary blade
Material	E235B (ISO 630)	E235B (ISO 630)	Cr20 (ISO/R 185)	18CrMo4 (ISO 683)	18CrMo4 (ISO 683)	18CrMo4 (ISO 683)	Type SC; Type DC (ISO 630)
Density [g/cm ³]	7.85	7.85	7.00	7.86	7.86	7.86	7.82

Because the electric motor and battery pack consist of many kinds of materials, their densities were obtained by measuring their mass and volume and then performing a simple calculation. The results were 2.14 g/cm³ and 8.90 g/cm³, respectively.

Test instruments and software

The key performance indices of SC900 soil firmness tester (Spectrum Technologies, Inc., United States, fig.2 [a]), 356A16 three-dimensional acceleration sensor (PCB Piezotronics, Inc., United States, fig.2 [b]), and LMS SCADAS Mobile (Siemens, Germany, fig.2 [c]) are listed in table 3-table 5.



[a] SC900 soil firmness tester

[b] Three-dimensional acceleration sensor

[c] LMS SCADAS Mobile

Fig. 2 - Test instruments

Table 3

Key performance indices of SC900 soil firmness tester

Index	Pressure range	Depth range	Resolution	Depth precision
	[kPa]	[mm]	[kPa]	[mm]
Index	0–7000	0–450	35	12.5

Table 4

Key performance indices of 356A16 three-dimensional acceleration sensor

Index	Range	Frequency	Transverse sensitivity	Mass	Sensitivity		
					X	Y	Z
	[g]	[kHz]	[%]	[g]	[mV/g]	[mV/g]	[mV/g]
Index	±50	0.3–6	<5	7.4	96.1	98.6	100.4

Table 5

Key performance indices of LMS SCADAS Mobile

Index	Dynamic range	Operation temperature	Input voltage	Digital signal rate
	[dB]	[°C]	[V]	[kHz]
Index	150	-20–50	±10	51.2

The LMS Test.Lab (LMS International NV, Belgium, fig.3) was used as the analysis software for the field testing of the tiller, mainly for vibration signal acquisition, processing, and analysis.

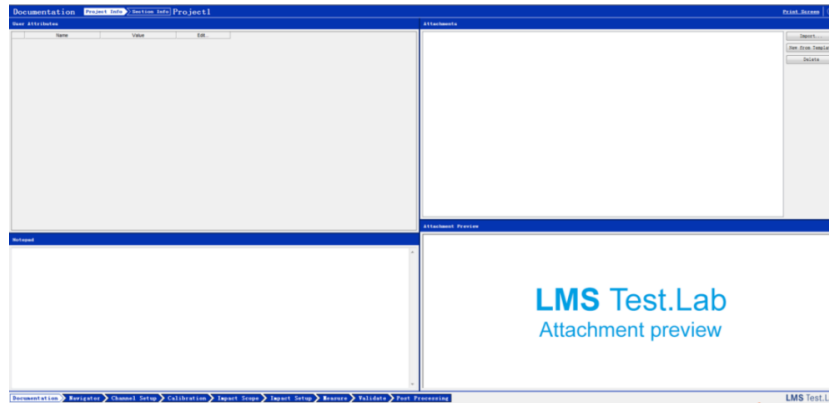


Fig. 3 - LMS Test.Lab

In the field test, the sampling frequency was set to 2 kHz and the Hann window was selected as the window function of the system.

Soil parameters

Five soil samples of the test farm plot were collected using a cutting ring. The soil moisture rate *c* was calculated using equation (1):

$$c = \frac{m_a - m_b}{m_a} \cdot 100\% \quad [\%] \quad (1)$$

Where:

m_a is the soil sample mass before drying, g; and *m_b* is the soil sample mass after drying, [g].

The soil sample mass before and after drying, as well as the moisture rate, are listed in table 6.

Table 6

Soil moisture rate			
Soil sample mass before drying	Soil sample mass after drying	Moisture rate	Average value
[g]	[g]	[%]	[%]
98.9665	80.8651	18.29	18.89
92.0825	74.1260	19.50	
98.1202	82.6903	15.72	
105.3226	84.4531	19.81	
106.3432	83.5563	21.14	

The soil density ρ can be calculated using equation (2):

$$\rho = \frac{m_a}{v} \quad [g/cm^3] \quad (2)$$

Where:

v is the soil sample volume, [cm³].

The soil density values are listed in table 7.

Table 7

Soil density			
Soil sample mass before drying	Soil sample volume	Soil density	Average value
[g]	[cm ³]	[g/cm ³]	[g/cm ³]
98.9665	59.41	1.96	1.74
92.0825	59.41	1.54	
98.1202	59.41	1.65	
105.3226	59.41	1.77	
106.3432	59.41	1.79	

When measuring the soil firmness, an SC900 soil firmness tester was inserted into the soil at a uniform speed (< 25 mm/s) in the vertical direction, and the soil firmness data were recorded once every 25 mm. The soil firmness values are listed in table 8.

Table 8

Soil firmness			
Soil depths [mm]	0–50	50–100	100–150
Parameter value [kPa]	0–0.165	0.165–0.355	0.355–0.480

Methods

Fig.4 illustrates the research procedure. First, a three-dimensional model of the tiller was established and its centre of gravity determined using Creo/E software (Parametric Technology Corp., United States). The relationship between the centre of gravity position and the vertical force at the handles was determined using force analysis. Then, based on the relationship of the installation position and force among each part of the tiller, the vibration dynamic model and its balance equation were developed. The vibration simulation program of the electric mini-tiller-soil system was created based on the balance equation using MATLAB/Simulink software (MathWorks, Inc., United States). The vibration acceleration values at the handles obtained by the simulation analysis were then compared with those from the field test, so as to confirm whether three-dimensional modeling and simulation analysis could be used to analyse and improve the operating comfort of the electric mini-tiller. Finally, the centre of gravity position was adjusted by shifting the position of the battery pack, in order to reduce the vertical force at the handles to its minimum value of 0 N. The three-dimensional model and the vibration dynamic model of the tiller after the centre of gravity adjustment were developed, and the vibration acceleration values at the handles were obtained from the simulation analysis, which were then compared with those determined before the centre of gravity adjustment.

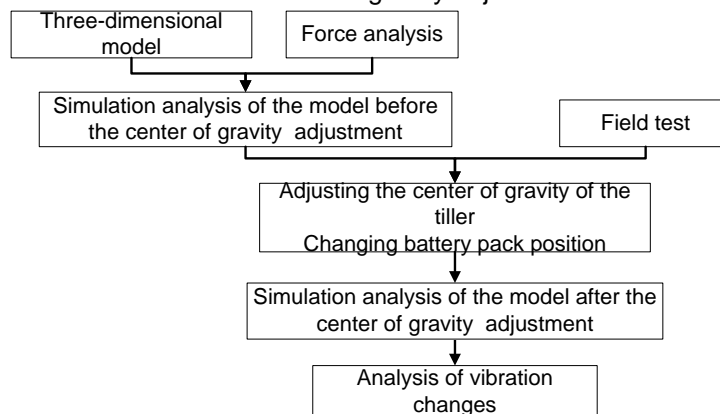


Fig. 4 - Research procedure

Field test

The test was conducted from 9:00 a.m. to 4:00 p.m. on December 19, 2018 on a farm plot (sandy loam), with a length of 50 m and a width of 35 m, located in the Hechuan District, Chongqing, China (29°39'45" N, 106°23'45" E; 210 m above mean sea level).

The three-dimensional acceleration sensor was fixed on the handle, according to ISO 5349-a. The X, Y, and Z directions of the sensor correspond to the vertical, forward-and-reverse, and left-to-right directions, respectively (fig.5). The field test is shown in fig.6; the tiller was progressing at a forward speed of 0.5 m/s.



Fig. 5 - Corresponding relation of X, Y, and Z directions



Fig. 6 - Field test

Mini-tiller vibration is a type of random vibration and can be described using statistical characteristic values. This study compared vibration acceleration values via the root mean square (RMS) values. The RMS values in the vertical direction (X direction) were selected as the research object, since vertical vibrations have the greatest impact on operating comfort (Li G., et al, 2016; Hu C.J., 2018).

The vibration acceleration signals obtained from the field test were processed using LMS Test.Lab Signature Acquisition software. The vibration acceleration curve and the RMS values were then determined.

Determination of the centre of gravity of the three-dimensional model

Three-dimensional models of the main components of the tiller were established based on prototype size. Their masses were attained by defining the material parameters (table 2) of the models, and were then compared with the corresponding measured values of the prototype, as shown in table 9.

Table 9

Comparison of the masses of the three-dimensional model components with those of the prototype

Component	Mass of model	Mass of prototype	Relative error
	[kg]	[kg]	[%]
Handrail	3.21	3.27	1.87
Frame	13.32	13.56	1.80
Electric motor	6.59	6.68	1.37
Battery pack	8.38	8.52	1.67
Gearbox housing	4.78	4.85	1.46
Power input shaft	0.28	0.28	0
Power output shaft	0.36	0.36	0
Rotary blade shaft	0.95	0.96	1.05
Single rotary blade	0.44	0.44	0
Rotary blade roller	12.44	12.48	0.32

As can be seen from table 9, the model masses of the main components were in good agreement with those of the prototype, with all of the relative errors < 2.0%. Therefore, the three-dimensional model of the tiller was obtained by assembling the main model components in terms of their assembly relationship (fig.7). The total model mass was 49.36 kg, exhibiting a relative error of 0.13% compared with the prototype mass of 50 kg.



Fig. 7 - Three-dimensional model of the electric mini-tiller

As shown in fig.7, the coordinate system was established, with point O (the intersection point of the centre line of the power input shaft and the centre line of the power output shaft) as the origin, and the X, Y, and Z directions of the sensor corresponding to the forward-and-reverse, vertical, and left-to-right directions, respectively. Point C (-3.52 cm, 20.616 cm, and -0.042 cm), the centre of gravity of the three-dimensional model, was determined using Creo/E software.

Relationship between the centre of gravity and the vertical force at the handles

The force diagram of the rotary blade roller tilling soil is illustrated in fig.8. The angle β between OA and OC is 20° and the radius of the resultant force R' is $0.9 R$ (Asl and Singh, 2009).

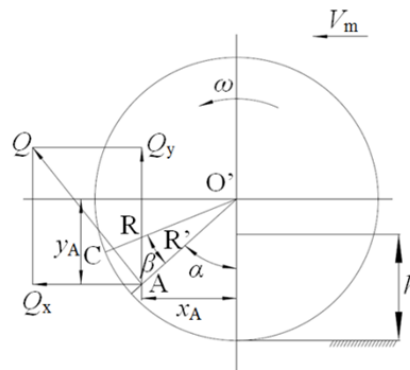


Fig. 8 - Force diagram of the rotary blade roller

Where:

R is the turning radius of the rotary blade roller, 160 mm; Q is the cutting resistance; Q_x and Q_y are the horizontal component force and vertical component force, [N] respectively; point A is the action point; and x_A and y_A are the horizontal distance and vertical distance, respectively, [cm].

From fig.8, the geometric relationship of the parameters is shown in equation (3):

$$\begin{cases} \alpha = \cos^{-1} \left[\frac{(R - h)}{R} \right] - 20^\circ \\ Q_x = Q \cos \alpha \\ Q_y = Q \sin \alpha \\ x_A = R \sin \alpha \\ y_A = R \cos \alpha \end{cases} \quad (3)$$

Where:

Q can be calculated from $Q = T/R'$; T is the torque of rotary blade roller, and it can be calculated from $T = 9550 P/n$; P is the power of the rotary blade roller, which is calculated from $P = P_n \cdot \eta_T$ (P_n is the rated power, 0.75 kW and η_T is the transmission efficiency, 0.97); n is the rotational speed of the rotary blade roller, 145 r/min; and h is the tillage depth, 10 cm.

According to Eq. (3), $\alpha = 48^\circ$, $Q = 331$ N, $Q_x = 221$ N, $Q_y = 246$ N, $x_A = 10.7$ cm, and $y_A = 9.6$ cm.

When the electric tiller was progressing at a forward speed of 0.5 m/s, the coordinate system was established consistent with fig.7. The forces on each part of the tiller are shown in fig.9.

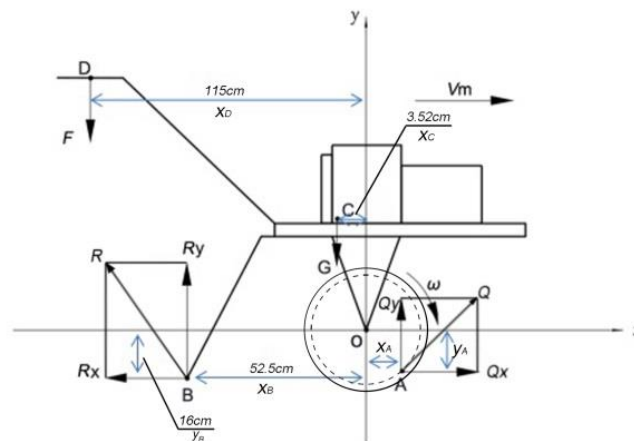


Fig. 9 - Force analysis of the electric mini-tiller

Where:

G is the gravity of the electric mini-tiller, $G = mg$, 484 [N]; U is the soil reaction force received by the depth-limiting device; U_x and U_y are the horizontal component force and vertical component force, respectively, [N]; point B is the action point; x_B and y_B are the horizontal distance and vertical distance, respectively, [cm]; C is the centre of gravity of the tiller; x_C is the horizontal distance, [cm]; F is the vertical force at the handles,

[N]; D is the action point; x_D is the horizontal distance, [cm]; and v_m is the tiller's forward speed, 0.5 m/s. The respective measured values of x_A , x_B , x_C , and x_D were 52.5 cm, 16 cm, 3.52 cm, and 115 cm.

Equation (4) can be obtained from the force balance:

$$\begin{cases} Q_y + U_y - F - G = 0 \\ Q_y x_A + Q_x y_A + G x_C + F x_D - U_x y_B - U_y x_B = 0 \\ Q_x - U_x = 0 \end{cases} \quad (4)$$

When the acquired data (G , Q_x , Q_y , x_A , y_A , x_B and x_D) were input into equation (4), the relationship between F and x_C could be calculated:

$$7.744x_C + F = 180.44 \quad (5)$$

Before the centre of gravity adjustment, x_C was 3.52 cm and F was 154.24 N.

Simulation analysis

Since the deformations of the handrail, battery pack, electric motor, frame, and rotary blade roller can be neglected during the tilling process, their three-dimensional models can be simplified as rigid bodies, and the dynamic transmission process of the tiller can be simplified as a spring system without damping mass.

In addition, since the rotational speed of the rotary blade roller during the tilling process was relatively low, and the fluctuation of the cutting resistance was small, the cutting resistance can be simplified as a vertical constant force, allowing the dynamic interaction process between the rotary blade roller and the soil to be simplified as a forced vibration of a single-degree-of-freedom mass-spring-damper.

The construction of the vibration dynamic model of the tiller took into consideration the relationship of the installation position and force among each part (fig.9), as shown in fig.10.

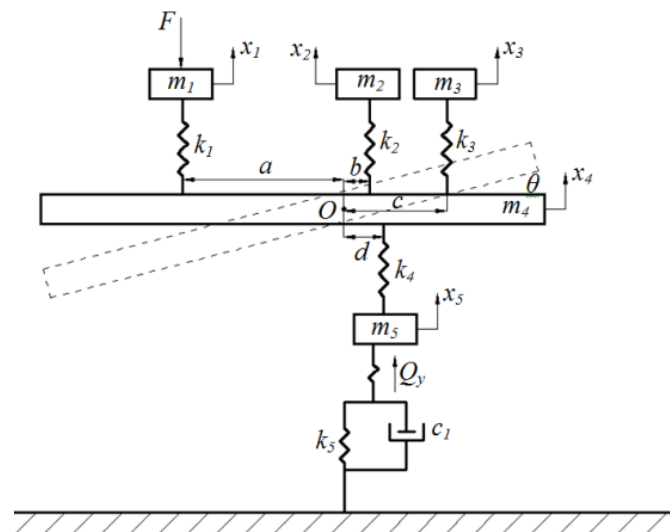


Fig. 10 - Vibration dynamic model

Where:

m_1 , m_2 , m_3 , m_4 , and m_5 are the masses of the handrail, electric motor, battery pack, frame, and rotary blade roller, respectively, [kg]; x_1 , x_2 , x_3 , x_4 , and x_5 are the vertical displacements of the centroid of the handrail, electric motor, battery pack, frame, and rotary blade roller, respectively, [cm]; k_1 , k_2 , k_3 , and k_4 are the structural stiffness values between the frame and the handrail, electric motor, battery pack, and frame, respectively, 5.5×10^7 N/m; k_5 is the soil equivalent stiffness, 4.5×10^6 N/m; O is the centroid of frame; θ is the maximum pitch angle (the frame moving around its centroid), 0.03 rad; c_1 is the soil equivalent damping, 4.5×10^3 N-s/m; a , b , c , and d are the horizontal distances from the action point of the handrail, electric motor, battery pack, and rotary blade roller to point O , which can be obtained by measuring, m; F is the vertical force at the handles, 152.24 N; and Q_y is the vertical component force of the tilling resistance of the soil to the rotary blade roller, 246 N.

The balance equation of the vibration dynamic system is shown in equation (6):

$$\begin{cases}
 m_1 \ddot{x}_1 = F - k_1 [x_1 - (x_4 - a \tan \theta)] \\
 m_2 \ddot{x}_2 = -k_2 [x_2 - (x_4 + b \tan \theta)] \\
 m_3 \ddot{x}_3 = -k_3 [x_3 - (x_4 + c \tan \theta)] \\
 m_4 \ddot{x}_4 = k_1 [x_1 - (x_4 - a \tan \theta)] + k_2 [x_2 - (x_4 + b \tan \theta)] \\
 \quad + k_3 [x_3 - (x_4 + c \tan \theta)] - k_4 [(x_4 + d \tan \theta) - x_5] \\
 m_5 \ddot{x}_5 = k_4 [(x_4 + d \tan \theta) - x_5] - Q_y - k_5 x_5 - c_1 \dot{x}_5 \\
 J \ddot{\theta} = bk_2 [x_2 - (x_4 + b \tan \theta)] + ck_3 [x_3 - (x_4 + c \tan \theta)] \\
 \quad - ak_1 [x_1 - (x_4 - a \tan \theta)] - dk_4 [(x_4 + d \tan \theta) - x_5]
 \end{cases} \tag{6}$$

Where:

J is the rotational inertia of the frame rotation around its centroid, [kg·m²].

Based on equation (6), the vibration simulation program of the tiller was constructed, as shown in fig.11.

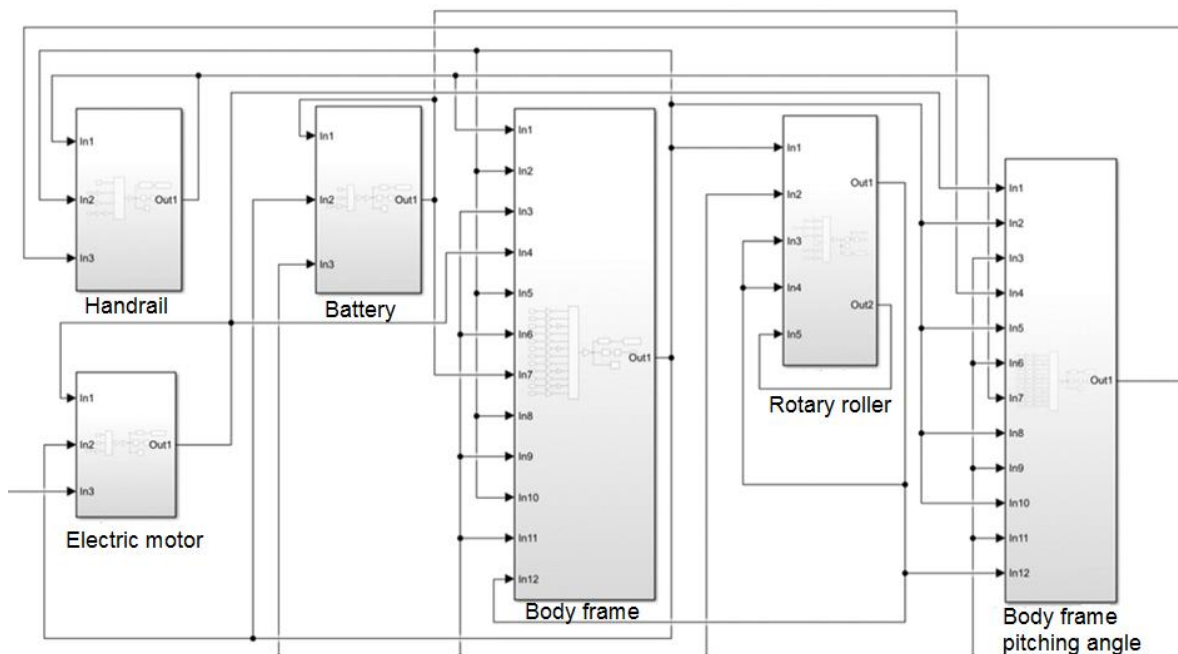


Fig. 12 - Vibration simulation program of the tiller in Simulink

The relevant parameter values (table 10) obtained from 2.2.2 and 2.2.3 were input into the vibration simulation program of the tiller.

Table 10

Parameter values in the balance equation of the vibration dynamic system			
Parameter	Value	Parameter	Value
F [N]	154.24	b [m]	0.061
Q_y [N]	246	c [m]	0.242
m_1 [kg]	3.21	d [m]	0.093
m_2 [kg]	6.59	k_1 [N/m]	5.5×10^7
m_3 [kg]	8.38	k_2 [N/m]	5.5×10^7
m_4 [kg]	13.32	k_3 [N/m]	5.5×10^7
m_5 [kg]	12.44	k_4 [N/m]	5.5×10^7
J [kg·m ²]	240	k_5 [N/m]	4.5×10^6
a [m]	0.378	c_1 [N·s/m]	4.5×10^3

The system simulation time was set to 10 s.

RESULTS

Comparison of RMS values obtained by simulation analysis and field test

The vibration acceleration curves and RMS values in X direction obtained by the field test and simulation analysis are shown in figs.12 and 13, respectively, as well as table 11.

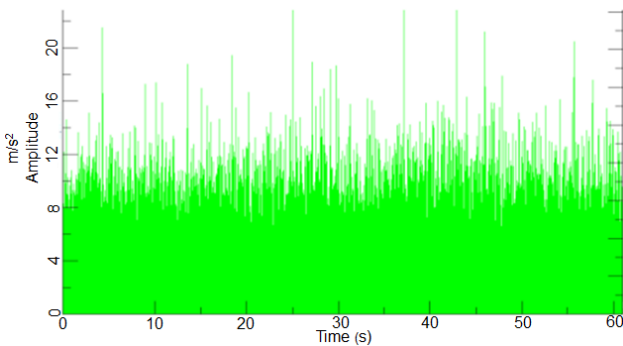


Fig.12 - Vibration acceleration curve from the field test

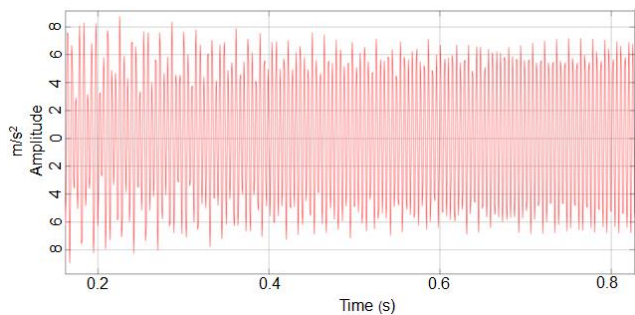


Fig.13 - Vibration acceleration curve from the simulation analysis

Table 11

Position	RMS values		
	Field test [m/s ²]	Simulation analysis [m/s ²]	Relative error [%]
Handle	8.12	7.69	5.30

As seen from Table 11, the RMS values obtained by the simulation analysis were in good agreement with those from the field test (relative error of 5.3%). Therefore, simulation analysis can be used to analyse and improve the operating comfort of the electric mini-tiller.

Centre of gravity adjustment

For the electric tiller, the electric motor and rotary blade roller are installed on its frame by bolts and pins, respectively, and are directly connected with the transmission system, making position adjustment relatively difficult. However, the battery pack is placed on the frame and fixed with elastic rope, which is easy to assemble and disassemble, as well as reposition. Therefore, the position of the battery pack was adjusted to change the position of the centre of gravity.

According to equation (5), when the centre of gravity of the tiller is moved 19.78 cm toward the handrail, and its horizontal distance to the origin increases from 3.52 cm to 23.3 cm, the vertical force at the handles attains its minimum value of 0 N. In order to meet this centre of gravity adjustment requirement, the battery pack was shifted 39.6 cm toward the handrail, to a position between the electric motor and the handrail.

After the centre of gravity adjustment, the three-dimensional model of the tiller was established (fig.14) with point C' (-23.3 cm, 20.616 cm, and -0.042 cm). The vibration dynamic model was then constructed (fig.15), with a balance equation and vibration simulation program identical to those used before the centre of gravity adjustment.



Fig.14 - Three-dimensional model

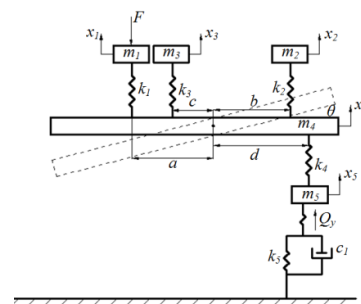


Fig.15 - Vibration dynamic model

The vertical force at the handle F is 0 N, a , b , c , and d are 0.180 m, 0.532 m, 0.154 m, and 0.615 m, respectively. The remaining parameter values are the same as those before the centre of gravity adjustment.

Vibration comparison before and after the centre of gravity adjustment

The RMS values at the handles were obtained by inputting the parameter values after the centre of gravity adjustment into the vibration simulation program of the tiller.

The RMS values before and after the centre of gravity adjustment are listed in table 12.

Table 12

RMS values before and after the centre of gravity adjustment			
Position	Before adjustment	After adjustment	Reduction rate
	[m/s ²]	[m/s ²]	[%]
Handle	7.69	6.14	20.16

From table 12, it can be seen that the RMS value at the handles decreased by 20.16% compared with the value before the centre of gravity adjustment, from 7.69 m/s² to 6.14 m/s².

CONCLUSIONS

1) The RMS values obtained by the simulation analysis were in good agreement with those from the field test (relative error of 5.3%). Therefore, simulation analysis can be used to analyse and improve the operating comfort of the electric mini-tiller.

2) According to the relationship between the centre of gravity and the vertical force at the handles, when the centre of gravity of the tiller was shifted 19.78 cm toward the handrail, and the horizontal distance of the centre of gravity to the origin increased from 3.52 cm to 23.3 cm, the vertical force decreased from 154.24 N to 0 N.

3) Based on the requirement of the centre of gravity adjustment, the layout of the electric mini-tiller was adjusted by shifting the position of the battery pack 39.6 cm toward the handrail, to a position between the electric motor and the handrail. The RMS value then decreased by 20.16%, compared with the value before the centre of gravity adjustment, from 7.81 m/s² to 6.14 m/s².

4) After the centre of gravity adjustment, when the electric mini-tiller progresses at a forward speed of 0.5 m/s, both the vertical force and the vibration at the handles are reduced, thereby improving operating comfort.

ACKNOWLEDGEMENT

This work was financially supported by the Special Projects of Generic Key Technology Innovation in Chongqing's Major Industries (csct2015zdcy-ztxx80003) and the Scientific Research Innovation Projects for Graduate Student of Chongqing (CYB17071).

REFERENCES

- [1] Asl J.H., Singh S., (2009), Optimization and evaluation of rotary tiller blades: Computer solution of mathematical relations. *Soil & Tillage Research*, vol.106, issue 1, ISSN:0167-1987, pp.1-7, London/U.K.;
- [2] Bini, S., Kathirvel K., (2006), Vibration characteristics of walking and riding type power tillers. *Biosystems Engineering*, vol.95, issue 12, ISSN:1537-5110, pp.517-528, London/U.K.;
- [3] Caffaro F., Cremasco M.M., Preti C. et al., (2016), Ergonomic analysis of the effects of a telehandler's active suspended cab on whole body vibration level and operator comfort. *International Journal of Industrial Ergonomics*, vol.53, ISSN:0619-8141, pp.19-26, London/U.K.;
- [4] Cai K., Zhang J.L., Ke X.R. et al., (2013), Research on the control system of dual-driven electric rotary tiller (两轮独立驱动电动微耕机的控制系统研究). *Guangdong Agricultural Sciences*, vol.40, issue 14, ISSN:1004-874X, pp.179-181, Guangzhou/China;
- [5] Gao H.S., Zhang S.H., Shi J.L. et al., (2012), Development of electric micro-farming machines for greenhouses (温室大棚用电动微耕机研制). *Journal of Machine Design*, vol.29, issue 11, ISSN:1001-2354, pp.83-87, Beijing/China;
- [6] Chen J., Chen C., Chen H., (2014), Three new challenges micro tillers face in southwest China and study of countermeasures. *Journal of Agricultural Mechanization Research*, vol.36, issue 10, ISSN:1003-188X, pp.245-248, Haerbin/China;

- [7] Dong X.Q., Song J.N., Wang J.C. et al., (2012), Vibration frequencies optimization and movement characteristics analysis of vibration shovel for meadow (草地振动松土机运动特性分析与振动频率优化). *Transactions of the Chinese Society of Agricultural Engineering*, ISSN:1002-6819, vol.28, issue 12, pp.44-49, Beijing/China;
- [8] Hu C.J., (2018), Structural Optimization Design and Vibration Analysis of Electric Mini-tiller (电动微耕机整机结构优化设计及振动分析). *Master Dissertation of Southwest University*, Chongqing/China;
- [9] ISO Copyright Office, (2001), *ISO 5349-a. Mechanical vibration-measurement and evaluation of human exposure to hand transmitted vibration, part 1: general requirements*, Geneva, Switzerland;
- [10] Li G., Chen J., Xie H.J. et al., (2016), Vibration test and analysis of mini-tiller. *International Journal of Agricultural and Biological Engineering*, vol.9, issue 3, ISSN:1394-6344, pp.97-10, Beijing/China;
- [11] Liang X.C., Chen J., Wang Z., (2018), Research on the vibration of mini-tiller. *INMATEH-Agricultural Engineering*, vol.56, issue 3, ISSN:2068-4215, pp.17-24, Bucharest/Romania;
- [12] Niu P., Yang M.J., Chen J. et al., (2017), Structural optimization of handrail of a handheld tiller by vibration modal analysis. *INMATEH-Agricultural Engineering*, vol.52, issue 2, ISSN:2068-4215, pp.91-98, Bucharest/Romania;
- [13] Ragni L., Vassalini G., Xu F. et al., (1999), Vibration and noise of small implements for soil tillage. *Journal of Agricultural Engineering Researches*, vol.74, issue 4, ISSN:0021-8643, pp.403-409, London/U.K.;
- [14] Servadio P., Marsili A., Belfiore N.P., (2007), Analysis of driving seat vibrations in high forward speed tractors. *Biosystems Engineering*, vol.97, issue 2, ISSN:1537-5110, pp.171-180, London/U.K.;
- [15] Tewari V.K., Dewangan K.N., (2009). Effect of vibration isolators in reduction of work stress during field operation of hand tractor. *Biosystems Engineering*, vol.103, issue 4, ISSN:1537-5110, pp.146-158, London/U.K.;
- [16] Thomas H.L., Morten K.E., Ario K., (2015), Experimental analysis of occupational whole-body vibration exposure of agricultural tractor with large square baler. *International Journal of Industrial Ergonomics*, vol.47, issue 5, ISSN:0619-8141, pp.79-83, London/U.K.;
- [17] Xu L.Z., Li Y.M., Sun P.P. et al., (2014), Vibration measurement and analysis of tracked-whole feeding rice combine harvester (履带式全喂入水稻联合收获机振动测试与分析). *Transactions of the Chinese Society of Agricultural Engineering*, vol.30, issue 8, ISSN:1002-6819, pp.49-55, Beijing/China;
- [18] Ying Y.B., Zhang L.B., Dong M.D. et al., (1994), Study on absorber of vibration transmitted by walking tractor handles (手扶拖拉机手把减振装置的研究). *Transactions of the Chinese Society of Agricultural Engineering*, vol.10, issue 4, ISSN:1002-6819, pp.74-79, Beijing/China;
- [19] Zhao R.H., Wu Y.Q., Liu Z.Z. et al., (2015), Design of electric micro rotary tiller (温室电动微耕机的设计). *Shandong Agricultural Sciences*, vol.47, issue 2, ISSN:1001-4942, pp.129-131, Jinan/China.

NEAR-INFRARED SPECTROSCOPY AS A RAPID AND SIMULTANEOUS ASSESSMENT OF AGRICULTURAL GROUNDWATER QUALITY PARAMETERS

/

NEAR INFRARED SPECTROSCOPY SEBAGAI METODE CEPAT DAN SIMULTAN UNTUK PREDIKSI KUALITAS AIR TANAH LAHAN PERTANIAN

Ichwana Ichwana¹⁾, Zulkifli Nasution²⁾, Agus Arip Munawar*¹⁾

¹⁾ Syiah Kuala University, Department of Agricultural Engineering / Indonesia;

²⁾ North Sumatera University, Faculty of Agriculture / Indonesia;

*Corresponding author: Tel: +6281220743572; E-mail: aamunawar@unsyiah.ac.id

DOI: <https://doi.org/10.35633/inmateh-60-26>

Keywords: groundwater, FT-NIRS, spectroscopy, agriculture, environment.

ABSTRACT

Groundwater quality in agricultural area is highly affected by human activities. To determine groundwater quality, several methods are widely applied. Yet, most of them are based on standard laboratory analysis which is normally time consuming, expensive, and involve chemical materials from which may cause another environmental pollution. Thus, a rapid, effective and simple alternative method is required to assess groundwater quality. Fourier transform near-infrared spectroscopy (FT-NIRS) is considered to be employed due to its advantages. The main purpose of the present study, is to evaluate the feasibility of FT-NIRS technology in assessing groundwater quality parameters: total dissolved solids (TDS) and Sulfate concentration (SC). Transmission spectra data were acquired for groundwater samples from 8 different wells in wavelength range from 1000 to 2500 nm. Spectra data were corrected by multiplicative signal correction (MSC), while TDS and SC prediction models were established by using partial least squares regression (PLSR) and validated by full cross validation method. Obtained results showed that FTIR is able to detect and predict TDS and SC rapidly. Achieved maximum correlation coefficient (r) and RPD index were 0.86; 1.82 for TDS and 0.83; 1.76 for SC prediction respectively. It may be concluded that FT-NIRS combined with proper multivariate approach, can be used to assess groundwater quality parameters rapidly and simultaneously.

ABSTRAK

Studi ini bertujuan untuk menerapkan metode teknologi inframerah sebagai metode alternatif baru yang cepat dan simultan untuk prediksi dan penentuan kualitas air tanah lahan pertanian di area Banda Aceh dan Aceh Besar. Data spektrum untuk sampel air tanah direkam dalam bentuk transmisi dengan panjang gelombang 1000 – 2500 nm. Spektrum diperbaiki dengan metode MSC, sedangkan model prediksi TDS dan SC dibangun dengan metode PLSR. Hasil studi menunjukkan bahwa teknologi inframerah dapat memprediksi secara cepat dan simultan kadar TDS dan SC dengan koefisien korelasi dan indeks kehandalan: 0.86; 1.82 untuk TDS dan 0.83; 1.76 untuk SC. Dapat disimpulkan bahwa teknologi sinar inframerah dapat diterapkan sebagai metode alternatif yang cepat dan akurat untuk penentuan kualitas air tanah di lahan pertanian.

INTRODUCTION

Water is one of the most important natural resources to all living matters. Besides being used for drinking, water is also used for washing, building, irrigating, cleaning and many other activities. Water descends from clouds as rain and drops onto the earth (Fritzsche *et al.*, 2019). Water beneath the earth surface is called groundwater. It is defined as the water found underground in the cracks and spaces in soil, sand and rock (Serranti *et al.*, 2018). It is stored in and moves slowly through geologic formations of soil, sand and rocks that are called aquifers. Generally speaking, groundwater is normally treated and processed by filtering so that it can be used as drinking water. It plays important roles in maintaining human race. It is used by more than 80 percent of the people worldwide, including almost everyone who lives in rural areas.

Groundwater is mostly used for irrigation, fertilization, etc. (Gandariasbeitia *et al.*, 2017; Sahamishirazi *et al.*, 2017).

Furthermore, groundwater can normally be found in almost any place. The water table can be deep or shallow, and may rise or fall depending on many factors.

Heavy and strong rains or snow melting can cause the rise of water table, or heavy pumping of groundwater supplies may cause the water table to fall (Fritzsche *et al.*, 2019). Water in aquifers is brought to the surface naturally through a spring or can be discharged into lakes and streams. Groundwater can also be extracted through a well drilled into the aquifer. A well is a pipe in the ground that fills with groundwater. This water can be brought to the surface by a pump. Shallow wells may go dry if the water table falls below the bottom of the well. Some wells, called artesian wells, do not need a pump because of natural pressures that force the water up and out of the well (Fritzsche *et al.*, 2019; Zhu *et al.*, 2018).

Aquifers normally consist of gravel, sandstone, sand, and fractured rock or stone, Water can move and deliver through these subsequent materials. The speed at which groundwater flows depends on the size of the spaces in the soil or rock and how well the spaces are connected (Lu *et al.*, 2018; Sano *et al.*, 2018). People need to be ensured that they are provided with pure, healthy and non-toxic water for daily used, especially for drinking. Groundwater quality is quite related to soil conditions since groundwater flows inside beneath porous rocks and soil or aquifers. Thus, groundwater needs to be analysed as it acts as water resource. Groundwater quality is highly affected by many factors, including human activities.

The chemical, biological, and physical unbalance caused by soil contamination by hazardous materials may be detrimental to plant, animal, and human health. For example, the symptoms of reduced root growth, reduced seed sprouting, and seedling stunting, necrosis, and chlorosis may affect plant growth in soils contaminated with heavy metals (Chakraborty *et al.*, 2017; Soriano-Disla *et al.*, 2019).

Agricultural crops (fruits, grains, and vegetables) for livestock for human consumption, growing on contaminated soil, can potentially uptake and accumulate toxic materials in their edible plant parts, and may be affected by groundwater quality, and thus, be harmful to animal and human health through the food chains. From this point of view, it is necessary to determine groundwater quality, monitor its condition and further take preventative actions to avoid any harmful impacts. A reliable and environmentally friendly method is therefore needed to rapidly detect and determine groundwater quality (Fritzsche *et al.*, 2019).

The conventional and standard methods for determining groundwater quality are based on regular field data samplings and followed by reinforced chemical analyses in the laboratory or known as wet chemical analysis. It sometimes also involves complicated procedures. However, this method may be costly and time-consuming as a result of the intensive groundwater samplings in-situ and the analyses in the laboratory. Moreover, such investigations can only provide limited information on specific locations and moments in time (Munawar *et al.*, 2016; Pasquini, 2018).

During the last few decades, infrared technology has been widely used and has become the most promising method of analysis in many field areas including soil science and agriculture due to its advantage; simple sample preparation, fast, and environmentally friendly since no chemicals are used (Deng *et al.*, 2018; Munawar *et al.*, 2016; Pasquini, 2018; Samadi *et al.*, 2018; Yusmanizar *et al.*, 2019). More importantly, it has the potential ability to determine multiple parameters simultaneously (Agussabti *et al.*, 2020; Agus Arip *et al.*, 2019). Therefore, the main purpose of this present study is to investigate the feasibility and apply infrared spectroscopy based on Fourier transform in determining groundwater quality parameters in terms of total dissolved solids (TDS) and sulfate concentration (SC). Prediction models were established by performing calibration and full cross validation using partial least squares regression (PLSR) with enhanced and corrected spectra data using multiplicative scatter correction (MSC) robustness.

MATERIALS AND METHODS

Spectra data acquisitions

Infrared spectra data for groundwater samples were taken by irradiation halogen lamp onto a 40 mL of water samples derived from different locations in Banda Aceh and Aceh Besar areas. Groundwater samples cover different land-use type and acceptable locations. Spectra data were recorded in form of transmission data in wavelength range from 1000 to 2500 nm or in wavenumbers 4000 – 10000 cm^{-1} (A A Munawar *et al.*, 2019; Yunus *et al.*, 2019). Spectra data were saved in two different file formats (*.SPA and *.CSV) that were used for further analysis (Saputri *et al.*, 2019; Sudarjat *et al.*, 2019).

Total dissolved solids (TDS) and sulfate concentration (SC) measurements

Actual TDS and SC data were measured and collected using standard laboratory analysis. TDS data were obtained by using gravimetric analysis according to SNI 06-6989, 27 – 2005, whilst SC data were measured based on SNI 06-6989, 20 – 2004.

Outlier removal

Spectra data were firstly projected on principal component analysis (PCA) followed by *Hotelling T²* ellipse for outlier detection. If there are any data outside the ellipse, then these spectra data are noted as outlier and removed prior to further analysis (Arendse et al., 2018; Cozzolino, 2014).

Spectra data enhancement

Once outlier data were removed, spectra data were corrected and enhanced using multiplicative scatter correction (MSC) in order to eliminate noises due to light scattering, sensor curvature and inside temperature (Ma et al., 2018).

TDS and SC prediction models

Both these groundwater quality parameters were predicted using partial least squares regression (PLSR) models and validated using full cross validation. Spectra data used for models were raw un-corrected spectra and enhanced spectra data by MSC (Darusman et al., 2019; Munawar et al., 2019; Suci et al., 2019). Obtained results were then compared. The prediction accuracy and robustness were judged by the following statistical parameters: coefficient of determination (R^2), correlation coefficient (r), root-mean-square error (RMSE) and residual prediction deviation (RPD) (Ghosh et al., 2019).

Relevant and optimum wavelength

Relevant wavelength for TDS and SC parameters prediction were inspected and observed using regression coefficient plot derived from the best and the most accurate PLSR model. Optimum wavelengths were located in the highest peak and lowest valley of the respective spectra plot dataset.

RESULTS

Groundwater spectra features

Typical spectra data features of groundwater samples are given in Fig 1. As shown in these figures, the strong absorbance and transmittance bands are located at around 1460 nm and 1920 nm. TDS and SC are chemical parameters and bond with C-H-O or S-O, O-H structures. Thus, it is possible for FTIRS to predict them since these structured chemical bonds are vibrated in IR wavelength region.

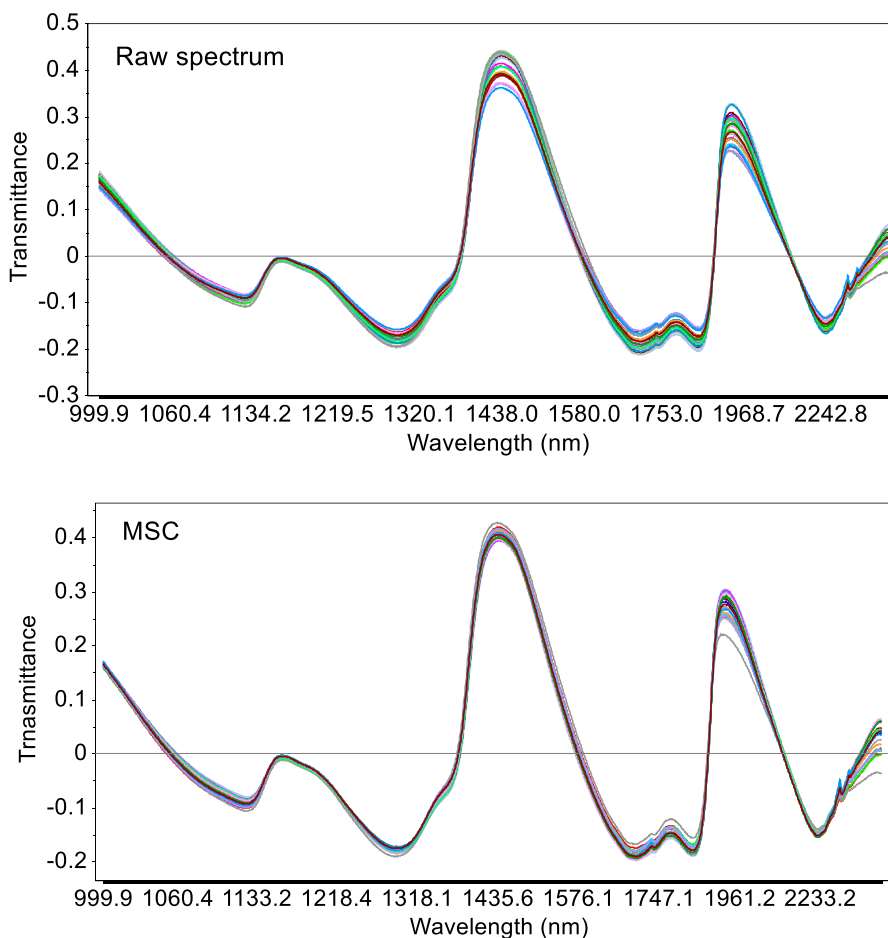


Fig. 1 - Typical raw and MSC spectrum of groundwater samples

All spectra data were projected onto principal component analysis (PCA) followed by Hotelling T² ellipse for outlier detection as shown in Fig.2. Some data are noted and removed because they are potential outliers. Thus, remaining data were 23 spectra data and also TDS and SC parameters.

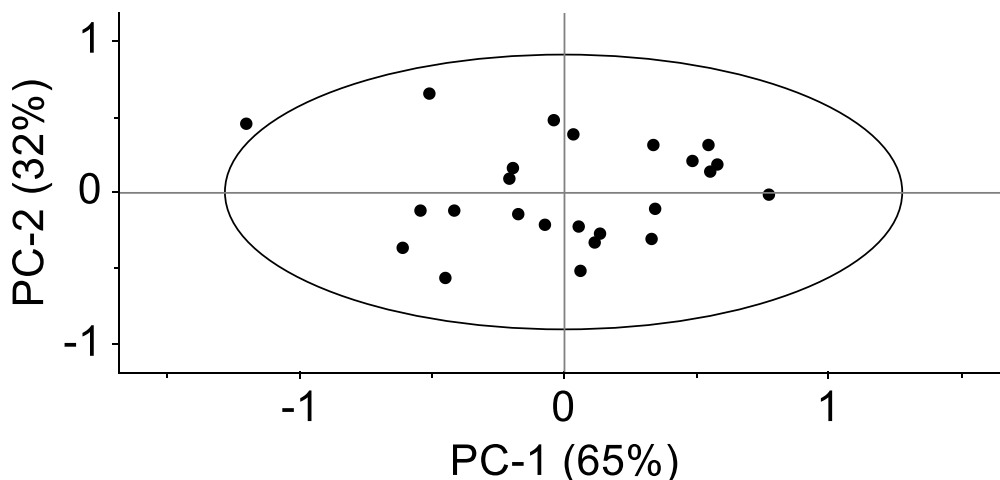


Fig. 2 - PCA projection and Hotelling T² ellipse for outlier detection

TDS and SC prediction

Actual TDS and SC parameters derived from standard laboratory measurements are presented in Table 1. As shown in the table below, the maximum TDS and Sulfate content of respective site locations are maximum 681.16 and 22.09 mg/L respectively. They were still under allowed maximum concentration based on SNI standard for groundwater quality parameters. The allowed TDS maximum is 1500 mg/L and allowed Sulfate is 400 mg/L respectively.

Table 1

Descriptive statistics for actual TDS and SC parameter		
Descriptive Statistic	Sulfate SO ₄ (mg/L)	TDS (mg/L)
Mean	12.32	332.71
Max	22.09	681.16
Min	3.86	122.83
Range	18.22	558.33
Std. Deviation	4.27	162.10
Variance	18.26	26277.34
RMS	13.05	368.55
Skewness	0.55	0.69
Kurtosis	0.60	-0.08
Median	11.63	341.18
Q1	9.77	186.61
Q3	14.31	421.10

Based on the descriptive table above, it can be seen from Skewness value, that both TDS and SC contents are in the range -1.69 - +1.69 which are inferred as normally distributed data. Yet, for multivariate analysis, this indicator was not obligatory. Thus, partial least squares regression still can be employed to develop prediction models. At first, raw un-corrected spectra data were used to develop prediction model for TDS and SC prediction. Then, MSC corrected spectra were used also to develop models for both groundwater quality parameters. Prediction result for TDS prediction is presented in Table 2, while for SC prediction is presented in Table 3.

Table 2

Prediction result for TDS parameter

Spectrum	Statistical parameters			
	R ²	r	RMSE	RPD
Raw	0.89	0.94	50.15	3.23
MSC	0.95	0.97	33.46	4.84

Table 3

Prediction result for Sulfate parameter

Spectrum	Statistical parameters			
	R ²	r	RMSE	RPD
Raw	0.60	0.77	2.67	1.60
MSC	0.63	0.79	2.52	1.70

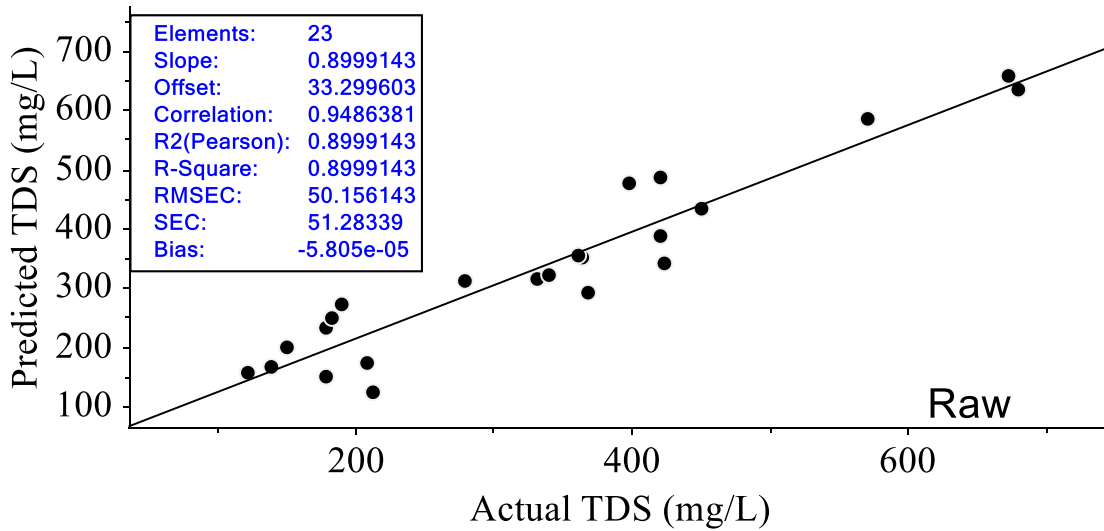


Fig. 3 - TDS Prediction results based on Raw spectrum

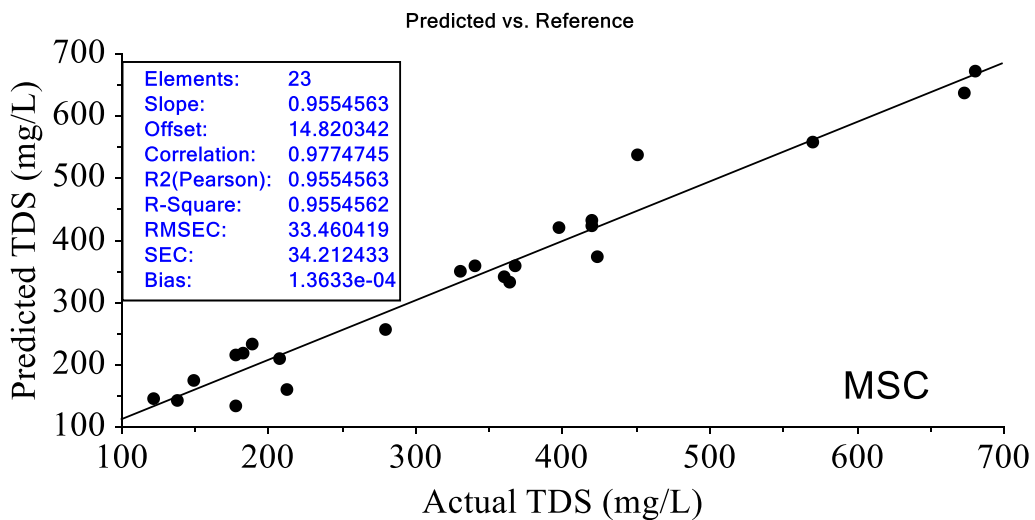


Fig. 4 - TDS Prediction results based on MSC spectrum

Based on prediction results, it can be seen that even using raw un-corrected spectra data, TDS can be predicted very well with coefficient correlation of 0.94 and the coefficient of determination is 0.89. Moreover, the residual prediction deviation (RPD) index achieved was 3.23. It can be inferred that TDS can be predicted accurately and robustly. Prediction results for TDS parameter was increased when spectra data were corrected using MSC method. The coefficient of determination and correlation were improved to 0.95 and 0.97 respectively. Moreover, the RPD index was also increased to 4.84 which can be categorized as excellent model performance.

Similar findings were also obtained for Sulfate content, when spectra data were corrected using MSC spectra correction method. As shown in Figure 5, the maximum achieved correlation and determination coefficient were 0.79 and 0.63 respectively. However, the maximum RPD index is 1.70 which can be inferred as a coarse prediction performance.

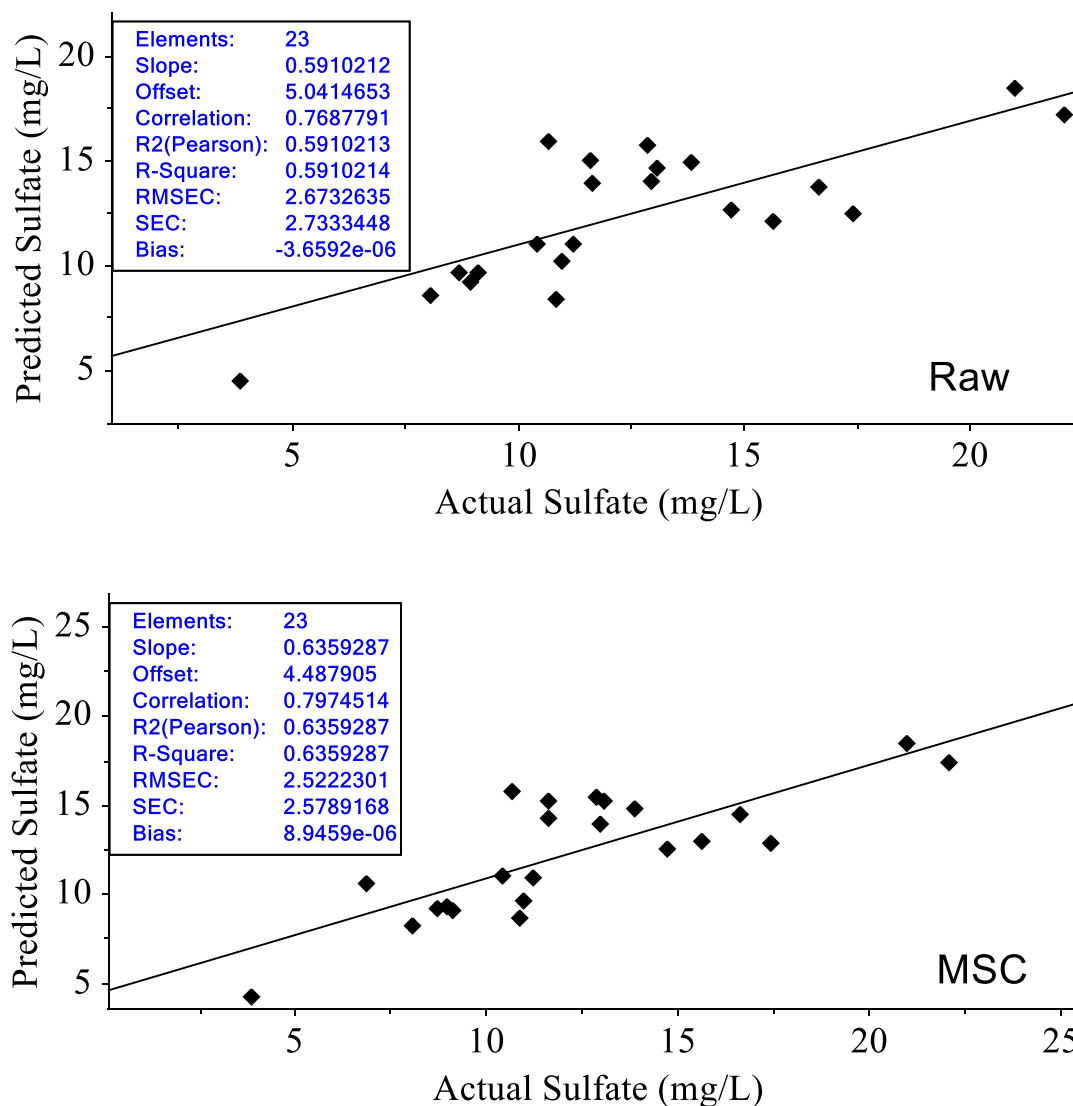


Fig. 5 - Sulfate prediction results based on Raw and MSC spectrum

Judging from YDS and SC prediction performances, it seems that Fourier transform infrared spectroscopy can be used and applied as an alternative method to predict groundwater quality indices on agricultural area. However, some improvements are still needed to enhance and improve prediction accuracy and robustness of those models. Nevertheless, infrared technology based on spectra data of FTIR can be employed as alternative fast and simultaneous method to predict groundwater quality parameters in agricultural areas and other environmental area as well.

CONCLUSIONS

In this work, we researched the FTIR technique as a rapid and non-destructive method for groundwater quality prediction in terms of TDS and Sulfate contents. We employed MSC spectra correction and PLSR method to develop prediction models. Based on the obtained results, we may conclude that FTIR is able to predict TDS of groundwater with excellent performance (RPD = 4.86) and coarse and sufficient prediction model performance (RPD = 1.70).

ACKNOWLEDGEMENT

We thank to LPPM *Universitas Syiah Kuala* for providing research grant and funding through Penelitian Lektor Kepala scheme 2019. We also express our sincere gratitude to the reviewers for their valuable and positive suggestions.

REFERENCES

- [1] Agussabti, Rahmaddiansyah, Satriyo, P., & Munawar, A. A. (2020). Data analysis on near infrared spectroscopy as a part of technology adoption for cocoa farmer in Aceh Province, Indonesia. *Data in Brief*, 29, 105251. <https://doi.org/10.1016/j.dib.2020.105251>
- [2] Arendse, E., Fawole, O. A., Magwaza, L. S., & Opara, U. L. (2018). Non-destructive prediction of internal and external quality attributes of fruit with thick rind: A review. *Journal of Food Engineering*, 217, 11–23. <https://doi.org/10.1016/j.jfoodeng.2017.08.009>
- [3] Chakraborty, S., Li, B., Deb, S., Paul, S., Weindorf, D. C., & Das, B. S. (2017). Predicting soil arsenic pools by visible near infrared diffuse reflectance spectroscopy. *Geoderma*, 296, 30–37. <https://doi.org/10.1016/j.geoderma.2017.02.015>
- [4] Cozzolino, D., (2014). An overview of the use of infrared spectroscopy and chemometrics in authenticity and traceability of cereals. *FRIN*, 60, 262–265. <https://doi.org/10.1016/j.foodres.2013.08.034>
- [5] Darusman, D., Zulfahizal, Z., Yunus, Y., & Munawar, A. A. (2019). Soil Quality Assessment By Near Infrared Spectroscopy : Predicting Ph And Soil Organic Carbon. *International Journal of Scientific and Technology Research*, 8(10). Retrieved from <http://www.ijstr.org/paper-references.php?ref=IJSTR-1019-23953>
- [6] Deng, Y., Wang, Y., Zhong, G., & Yu, X. (2018). Simultaneous quantitative analysis of protein, carbohydrate and fat in nutritionally complete formulas of medical foods by near-infrared spectroscopy. *Infrared Physics and Technology*, 93 (July), 124–129. <https://doi.org/10.1016/j.infrared.2018.07.027>
- [7] Fritzsche, A., Ritschel, T., Schneider, L., & Totsche, K. U. (2019). Identification and quantification of single constituents in groundwater with Fourier-transform infrared spectroscopy and Positive Matrix Factorization. *Vibrational Spectroscopy*, 100 (August 2018), 152–158. <https://doi.org/10.1016/j.vibspec.2018.09.008>
- [8] Gandariasbeitia, M., Besga, G., Albizu, I., Larregla, S., & Mendarte, S. (2017). Prediction of chemical and biological variables of soil in grazing areas with visible- and near-infrared spectroscopy. *Geoderma*, 305 (June), 228–235. <https://doi.org/10.1016/j.geoderma.2017.05.045>
- [9] Ghosh (Nath), S., Debsarkar, A., & Dutta, A. (2019). Technology alternatives for decontamination of arsenic-rich groundwater—A critical review. *Environmental Technology and Innovation*, 13, 277–303. <https://doi.org/10.1016/j.eti.2018.12.003>
- [10] Lu, G., Haes, A. J., & Forbes, T. Z. (2018). Detection and identification of solids, surfaces, and solutions of uranium using vibrational spectroscopy. *Coordination Chemistry Reviews*, 374, 314–344. <https://doi.org/10.1016/j.ccr.2018.07.010>
- [11] Ma, Y., Liu, Z. H., Xi, B. D., He, X. S., Li, Q. L., Qi, Y. J., ... Guo, Y. (2018). Characteristics of groundwater pollution in a vegetable cultivation area of typical facility agriculture in a developed city. *Ecological Indicators*, (May), 1–8. <https://doi.org/10.1016/j.ecolind.2018.10.056>
- [12] Munawar, A.A., von Hörsten, D., Wegener, J. K., Pawelzik, E., & Mörlein, D. (2016). Rapid and non-destructive prediction of mango quality attributes using Fourier transform near infrared spectroscopy and chemometrics. *Engineering in Agriculture, Environment and Food*, 9 (3). <https://doi.org/10.1016/j.eaef.2015.12.004>
- [13] Munawar, A A, Syah, H., & Yusmanizar. (2019). Fast and robust quality assessment of honeys using near infrared spectroscopy. *IOP Conference Series: Earth and Environmental Science*, 365, 012053.

- <https://doi.org/10.1088/1755-1315/365/1/012053>
- [14] Munawar, Agus Arip, Kusumiyati, Hafidh, Hayati, R., & Wahyuni, D. (2019). The application of near infrared technology as a rapid and non-destructive method to determine vitamin C content of intact mango fruit. *INMATEH - Agricultural Engineering*, 58 (2), 1–12. <https://doi.org/10.35633/INMATEH-58-31>
- [15] Munawar, Agus Arip, Kusumiyati, & Wahyuni, D. (2019). Near infrared spectroscopic data for rapid and simultaneous prediction of quality attributes in intact mango fruits. *Data in Brief*, 27. <https://doi.org/10.1016/j.dib.2019.104789>
- [16] Pasquini, C. (2018). Near infrared spectroscopy: A mature analytical technique with new perspectives – A review. *Analytica Chimica Acta*, 1026, 8–36. <https://doi.org/10.1016/j.aca.2018.04.004>
- [17] Sahamishirazi, S., Zikeli, S., Fleck, M., Claupein, W., & Graeff-Hoenninger, S. (2017). Development of a near-infrared spectroscopy method (NIRS) for fast analysis of total, indolic, aliphatic and individual glucosinolates in new bred open pollinating genotypes of broccoli (*Brassica oleracea* convar. botrytis var. italica). *Food Chemistry*, 232, 272–277. <https://doi.org/10.1016/j.foodchem.2017.04.025>
- [18] Samadi, Wajizah, S., & Munawar, A. A. (2018). Fast and simultaneous prediction of animal feed nutritive values using near infrared reflectance spectroscopy. *IOP Conference Series: Earth and Environmental Science*, 122 (1). <https://doi.org/10.1088/1755-1315/122/1/012112>
- [19] Sano, H., Omine, K., Prabhakaran, M., Darchen, A., & Sivasankar, V. (2018). Groundwater fluoride removal using modified mesoporous dung carbon and the impact of hydrogen-carbonate in borehole samples. *Ecotoxicology and Environmental Safety*, 165 (August), 232–242. <https://doi.org/10.1016/j.ecoenv.2018.09.001>
- [20] Saputri, Y., Yusriana, & Munawar, A. A. (2019). Infrared Spectroscopic Features of Turmeric Powder. *IOP Conference Series: Earth and Environmental Science*, 365, 012051. <https://doi.org/10.1088/1755-1315/365/1/012051>
- [21] Serranti, S., Trella, A., Bonifazi, G., & Izquierdo, C. G. (2018). Production of an innovative biowaste-derived fertilizer: Rapid monitoring of physical-chemical parameters by hyperspectral imaging. *Waste Management*, 75, 141–148. <https://doi.org/10.1016/j.wasman.2018.02.013>
- [22] Soriano-Disla, J. M., Janik, L. J., Forrester, S. T., Grocke, S. F., Fitzpatrick, R. W., & McLaughlin, M. J. (2019). The use of mid-infrared diffuse reflectance spectroscopy for acid sulfate soil analysis. *Science of the Total Environment*, 646, 1489–1502. <https://doi.org/10.1016/j.scitotenv.2018.07.383>
- [23] Suci, R. H., Zufahrzal, Z., & Munawar, A. A. (2019). Applying LIBS-QCL Spectrum Coupled With Principal Component Analysis To Distinguish Gayo Arabica And Robusta Coffee. *International Journal of Scientific and Technology Research Technology Research*, 8 (10), 919–924. Retrieved from <http://www.ijstr.org/paper-references.php?ref=IJSTR-1019-23310>
- [24] Sudarjat, Kusumiyati, Hasanuddin, & Munawar, A. A. (2019). Rapid and non-destructive detection of insect infestations on intact mango by means of near infrared spectroscopy. *IOP Conference Series: Earth and Environmental Science*, 365, 012037. <https://doi.org/10.1088/1755-1315/365/1/012037>
- [25] [Yunus, Y., Devianti, Satriyo, P., & Munawar, A. A. (2019). Rapid Prediction of Soil Quality Indices Using Near Infrared Spectroscopy. *IOP Conference Series: Earth and Environmental Science*, 365, 012043. <https://doi.org/10.1088/1755-1315/365/1/012043>
- [26] Yusmanizar, Setiasih, I. S., Nurjanah, S., Muhaemin, M., Nurhadi, B., Rosniawaty, S., & Munawar, A. A. (2019). Fast and Non-Destructive Prediction of Moisture Content and Chologenic Acid of Intact Coffee Beans Using Near Infrared Reflectance Spectroscopy. *IOP Conference Series: Materials Science and Engineering*, 506, 012033. <https://doi.org/10.1088/1757-899X/506/1/012033>
- [27] Zhu, F., Ma, S., Liu, T., & Deng, X. (2018). Green synthesis of nano zero-valent iron/Cu by green tea to remove hexavalent chromium from groundwater. *Journal of Cleaner Production*, 174, 184–190. <https://doi.org/10.1016/j.jclepro.2017.10.302>

FAULT ANALYSIS METHOD FOR LIQUID LEVEL CONTROL CIRCUIT OF A WATER SUPPLY SYSTEM

/

某型供水系统液位控制电路的故障分析方法

Wang Ling ¹

Shaanxi Vocational & Technical College, Shaanxi, Xi'an, 710038 / China

*Tel: +8615886493548; E-mail: txdzwl@163.com

DOI: <https://doi.org/10.35633/inmateh-60-27>

Keywords: water supply system, liquid level control circuit, fault analysis

ABSTRACT

Agricultural irrigation is a very important link in agricultural production, but in the current situation of water shortage, reasonable control of agricultural water supply can not only achieve the purpose of irrigation, but also save water resources to the maximum extent. Therefore, this paper studies the agricultural water supply control system and its related circuits. According to the actual situation of agricultural irrigation, based on the nine-point controller in logic control, a control system of agricultural water supply based on nine-point controller is designed, and also the corresponding control circuit. The control system is verified by experiments. The results show that the control system circuit can meet the operation requirements under extreme conditions and has high stability. The experimental results of the control system show that the whole control system is obviously superior to the traditional PID control system, while the actual application results show that the whole control system has a good response and can control the water supply system in real time according to the actual situation of agricultural irrigation.

摘要

农业灌溉是农业生产中一个非常重要的步骤，但是在水资源逐渐短缺的今天，合理的控制农业供水既可以达到灌溉的目的，同时也能够尽可能的节约水资源，因此这里对农业供水系统中的控制系统及其相关电路进行研究。本研究根据农业灌溉的实际情况，以逻辑控制中的九点控制器为基础，设计了一个基于九点控制器的农业供水控制系统，并对其相应的控制电路进行了设计。然后通过实验的方式对该控制系统进行验证，验证结果表明控制系统的电路能够适应极端条件的运行需求，有较高的运行稳定性。而对控制系统的实验结果则证明了整个控制系统明显优于传统的PID控制系统，而实际的应用效果则表明整个控制系统具有良好的响应性，能够根据农业灌溉的实际情况对供水系统进行实时的控制。

INTRODUCTION

China is a country with a large population, but the corresponding cultivated land is very scarce, so it is very important to improve the efficiency of cultivated land planting, in which ensuring sufficient irrigation and water supply is an important way to improve the efficiency of planting. The national conditions determine the special importance of water supply in economic and social development (Roy P., Kar B., and Roy B K., 2017). Correspondingly, China's water resources are not abundant, so we must improve the utilization rate of water resources. At this time, the only way to meet the dual requirements of irrigation and water conservation is to use automation technology to realize the precise control of agricultural water supply (İsmail Bayram and Hapoglu H., Aldemir A., 2018). In agricultural automatic water supply control, liquid level control is one of the common control systems in agricultural production process. The liquid level control system has the characteristics of nonlinearity, time lag and inertia (Tao J., Fan Q. and Ma L., 2017). However, the conventional control methods are sometimes difficult to meet the control requirements. On the one hand, the response time of water supply system control is relatively slow, on the other hand, it is the problem of frequent system failure caused by the longer operation time of water supply system (Zhang B., Wei Y.J. and Liu W.Y., 2017). Therefore, it is necessary to design a water supply control system which can not only adapt to the harsh working environment, but also respond positively to the demand of agricultural water supply (Kim S.W., Choi H.S. and Park D.U., 2018).

¹ Wang Ling, As. Ph.D. Stud.

According to the requirements of water saving, agricultural irrigation control and system safety in the current agricultural irrigation, this paper proposes a nine-point controller based agricultural water supply level control system, and the water supply system adopts the coaxial phase method of temperature resistance circuit to improve the safety of the whole system circuit. First of all, the agricultural liquid level control system based on nine-point controller can make real-time response to the whole water supply system according to the response curve of agricultural irrigation water, and adjust the size of water flow in the water supply system. Secondly, the temperature resistance circuit of coaxial phase method improves the adaptability of the whole system to the environment, and ensures that the system can reduce the failure rate under the continuous high temperature and long-time operation conditions.

The agricultural liquid level control water supply system based on the nine-point controller and the coaxial phase method temperature resistant circuit designed in this study overcomes the problem of water resource utilization efficiency in the process of agricultural irrigation on the one hand, and the problem of slow response speed in the traditional control method on the other hand; it also overcomes the system operation problem brought by the surrounding environment under the long-term continuous work security issues. That is to say, the design of the whole circuit can not only meet the needs of irrigation, but also ensure the stability of the system operation, so it has a certain degree of innovation.

The fault analysis method of the liquid level control circuit of a certain type of agricultural water supply system is studied by using the theory of agricultural irrigation coaxial phase method. The nine-point controller model based on the farmland water supply level system is constructed based on the liquid level circuit. The analysis of control faults proposed a temperature-resistant circuit control method based on the coaxial phase method water finder, and analysed the main principles and implementation flow of the model and method. Finally, the effectiveness of the system and model designed is verified by experiments.

In recent years, as liquid level control has been widely used in water supply systems, more and more scholars have conducted a lot of related research on their circuit control failures. Ye X designed a new automatic water level measurement and control system. The results show that the system has the characteristics of reasonable structure, fast response, stable and reliable, wide range of use, etc. It can carry out online real-time monitoring of liquid level of various conductive media (Ye X. and Chen B., 2018). Singh S combined with a large-scale new pumping station to design a variable-frequency constant-pressure water supply control system using PLC. The research results show that the system works stably, can meet the demand of constant pressure variables, and maintain the constant pressure at the end of the water supply pipe network, so that the water supply system is always in high efficiency and energy saving the best state (Singh S. and Mohanty A.R., 2018). Paul R used a simple water tank and corresponding equipment to conduct a water supply test on a test water supply system in an agricultural park. The study found that the method is feasible, but it lacks a wide range of practicalities (Paul R. and Sengupta A., 2017).

Byrdin V.M. designed the living water supply system of a living quarter in Kundulun District of Baotou City. It was found that the system realized the groundwater injected into the water tank of the residential pump house by the submersible pump, and then the water in the water tank was converted to constant pressure by the water pump. It was then available to the residents with effectiveness (Byrdin V.M., 2017). Maurye P. analysed the liquid level control logic of the condenser vacuum pumping system, solved the fault, and proposed an improved method, which can be used for reference to solve the same problem (Maurye P., Basu A. and Bandyopadhyay T.K., 2017). Gutiérrez E. designed a liquid level control system of the utility model. It was found that the system could generate control signals through the monitoring machine, control the water pump and valve of the water source well, and improve the efficiency and accuracy of the water level control without manual telephone notification (Gutiérrez E., Balcázar N. and Bartrons E., 2017).

Agrawal A proposed a multi-boiler steam drum liquid level control energy-saving water supply control system and its control method. The research results show that the method can not only make the water supply control valve open the maximum boiler by dynamically adjusting the water supply to the mother pipe. It poses a safety hazard problem and enables the feed pump in a multi-boiler system to operate at optimum energy efficiency (Agrawal A., Kothari A.K. and Rao K.R., 2019). Takahashi T. proposed a comprehensive evaluation model for the vulnerability of water supply subsystem based on the catastrophe progression method, and a case study of a water distribution subsystem. The results show that the method has theoretical and practical feasibility and overcomes the subjectivity of previous vulnerability assessment methods (Takahashi T, Ito T and Kim S Y. 2017).

Mandlate J.S. established a mathematical model of the logical structure of the urban water supply system to solve the systematic problem of water system risk assessment (Mandlate J.S, Soares B.M. and Seeger T.S., 2017). Chen WL established a multi-objective simulation model for large-scale irrigation district water supply system based on system simulation technology. The research results show that this method can greatly improve the utilization of water resources in irrigation districts and give full play to the economic and social benefits of irrigation water resources (Chen WL, Ho T.Y. and Huang J.W., 2018).

It can be seen from the above studies that many scholars have established different methods for liquid level control water supply systems for different occasions, and verified the practicability and effectiveness of the system through experiments. However, most of these studies focus on the design and temperature control of centralized water supply systems, and there are few research results on the analysis of circuit control failures (Pawlak M., 2018). Therefore, this paper has important significance for the research of fault analysis methods for the liquid level control circuit of a certain type of water supply system.

MATERIALS AND METHODS

NINE-POINT CONTROLLER MODEL BASED ON WATER SUPPLY LEVEL SYSTEM

In the current system control, PID control represented by proportional, integral and differential control is the most common control method, but the realization of this control is based on the engineers' full understanding of the system, and it also takes a long time to determine the parameters. Therefore, this study decided to adopt another kind of control, which is different from PID control. It is a logic science generated by simulating the human brain's transactional thinking mode. Therefore, this control method is also called logic control, and this control mode is similar to the current computer's arithmetic models such as addition and carry operation. This study adopts nine-point control. It is a logic control mode.

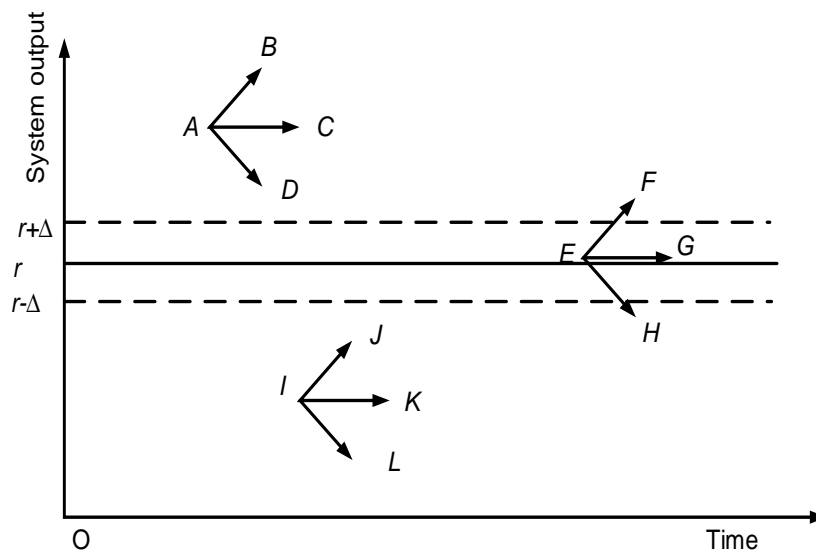


Fig. 1 - Nine-point controller system principle

The so-called nine-point controller refers to nine rules in the system control. Here, take Figure 1 as an example to illustrate. The first rule is that when the curve moves toward *AB* direction, the response curve is above the zero error band, which causes the negative deviation of the system to increase, the system needs to apply a strong reducing force to change the direction of the system movement; the second rule is that the curve moves toward *AC* direction, and the response curve is still above the zero error band, so that the negative deviation of the system remains unchanged, and the system needs to apply a "reducing" action. The third rule is that the curve moves toward the *AD* direction, and the response curve is still above the zero error band, so that the negative deviation of the system is gradually reduced. At this time, the system needs to exert a "slightly reduced" force to ensure that the system enters the zero error band; the fourth rule is that the curve moves toward the *EF* direction, and the response curve is in the zero error band, so that the system gradually crosses the zero error. At this time, the system needs to exert a "micro reduction" force to ensure that the system does not cross the zero error band; the fifth rule, the curve moves toward the *EG* direction, the response curve is in the zero error band, and remains in the zero error band; at this time, the system needs to exert a "hold" force to ensure that the system does not cross the zero error band; the sixth rule, the curve moves toward the *EH*

direction, and the response curve is in the zero error band, but it will cross the zero error band. At this time, the system needs to exert a "micro plus" force to ensure that the system does not cross the zero error band. In the seventh rule, the curve moves towards the IJ direction, and the response curve is under the zero error band, and moves towards the zero error band. In this case, the system needs to exert a "slight" force to ensure that the system enters the zero error band. In the eighth rule, the curve moves toward the IK direction, the response curve is under the zero error band, and maintains the current state. At this time, the system needs to apply "plus" force to ensure that the system enters the zero error band. In the ninth rule, the curve moves toward IL direction, and the response curve is under the zero error band, and gradually away from it. At this time, the system needs to apply "strong plus" force to change the system direction and make it enter the zero error band. The above nine rules are the basic principle of nine-point controller.

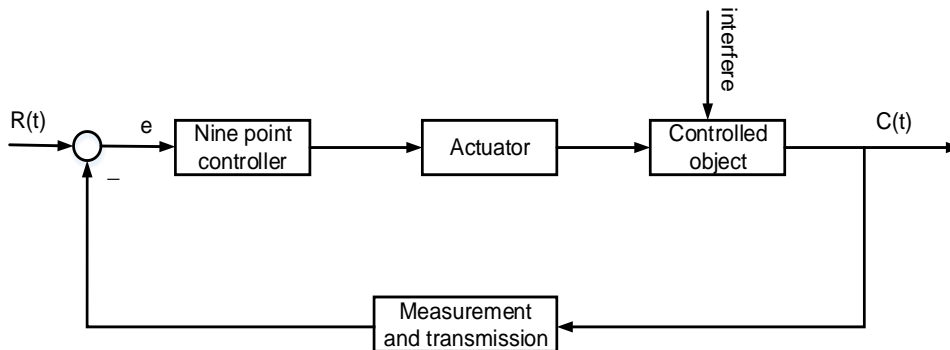


Fig. 2 - Schematic diagram of nine-point controller system

In order to play an effective control role, the nine-point controller must be in a closed-loop control loop. The control loop used in this study is shown in Figure 2. In Figure 2, T represents the sampling period, R represents the expected value of the system, C represents the measured value of the system, and $E = R(T) - C(T)$ represents the deviation of the control system. $E' = (E_i - e_{i-1}) / T$ represents the rate of change of deviation, I represents the number of adoption times. Then, according to the basic principle of nine-point controller, deviation and parameter change of deviation change rate, it can be divided into three categories as shown in Figure 3, and the whole nine-point controller design can be realized in nine cases. The modeling method of hybrid modeling is selected, and the mathematical model of the controlled object is constructed by using the open-loop step response curve method. Using a single-phase circulation pump to supply water to the water tank, in the manual control mode, adjusting the opening degree of the electric regulating valve, changing the water supply amount of the water tank, an interference signal is applied to the controlled water tank, and recording the system under the condition of step interference, level change data (Bhuyan S K., Hota P K. and Panda B., 2018). The opening of the electric control valve is adjusted manually. The initial stage valve opening is 35%, waiting for the system to reach equilibrium. At this time, the liquid level is stable at 8mm. Adjusting the electric adjustment opening to 45% is equivalent to adding a step signal into the system to break the original level balance. The system needs to be adjusted for a period of time, and the liquid level reaches a new equilibrium state to a height of 25 mm. After the test is completed, the data of the experiment is exported from the ACCESS database to EXCEL (Manikandan P. and Khan F A., 2019). The results are shown in Figure 4 below.

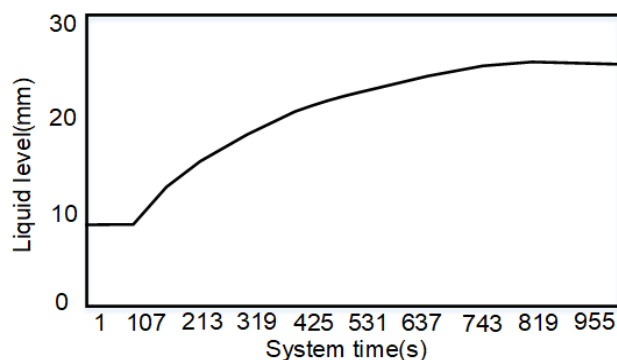


Fig. 3 - Drawing curves in EXCELL

By analysing the data in the graph, the two constants can be obtained, and the transfer function of the first-order liquid level control system composed of the single-capacity water tank is obtained.

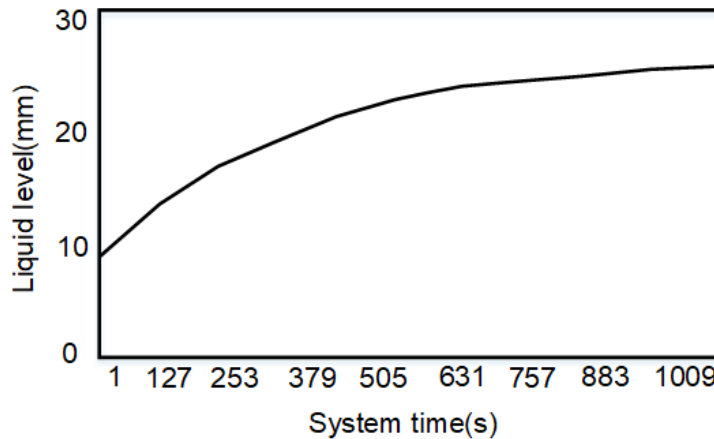


Fig. 4 - Rising section of response curve

Using the above calculation and analysis method, the transfer function of the obtained water tank is:

$$G(s) = \frac{K}{TS+1} \text{ Where } k = 173; t = 190.$$

TEMPERATURE-RESISTANT CIRCUIT CONTROL METHOD BASED ON COAXIAL LINE PHASE METHOD

In order to realize the nine-point controller mentioned in this study, we need to design a corresponding control circuit to cooperate with the whole controller to complete the operation and control of the water supply system. The basic principle of the phase detector is to compare the phase of the input signal with the output signal of the phase-locked loop. The ideal phase detector frame is shown in Figure 5. It produces an error voltage V_e corresponding to the phase difference between the two signals. The stable output of the phase-locked loop circuit is guaranteed.

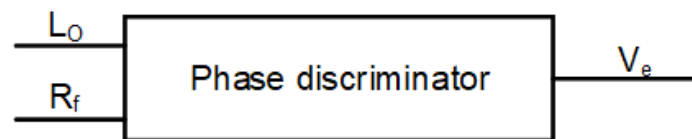


Fig. 5 - Principle block diagram of ideal phase discriminator

Phase detectors can be divided into two main categories, namely analog phase detectors and digital phase detectors. Both have their own advantages and disadvantages. The analog phase detector has a higher operating frequency, but there is zero drift and the sensitivity is not high. The digital phase detector has a faster operating frequency, and the main disadvantages are phase-detection dead zone and low operating frequency, but the high integration and stability of the digital phase detector are not available in the analog phase detector, and the phase detector requires that the input signal and the output signal remain fully synchronized, that is, the input signal and the output signal have the same frequency and the same phase (Diao K., Sweetapple C. and Farmani R., 2016). Analog phase detectors have a wide range of applications in areas such as automatic control, radar signal scanning and communications. According to the different circuit structure, it can be divided into sample-and-hold phase detector and mixing type phase detector. According to the different devices, it can be divided into passive phase detector and active phase detector. The waveforms of the phase detectors of the analog phase detector are also different, such as triangular wave type, sawtooth wave type and sine wave type (Singh J., Singh S. and Singh A., 2019). The diode balance phase detector is a common analog phase detector, which respectively applies the sum and difference of two input sinusoidal signals to the detection diode, and then the potential difference generated after the detection is the output voltage of the phase detector. In the coaxial phase method moisture meter, the mixer is the core part of the circuit. Based on the working environment requirements of the coaxial phase method water detector, high frequency signals are used to prevent interference, but the phase difference error of the direct measurement of the chirp frequency signal is relatively large, because the period of the high frequency signal is short and the resolution is relatively low. The measurement error is relatively large.

In order to solve this problem, the principle of integration and difference is used to preserve the difference frequency, which greatly reduces the measurement error of water content caused by the phase difference measurement (Roy P. and Roy B K., 2016). Let the phase-shifted signal input to the mixer be the signal sent by the local oscillator:

$$S_t = A_1 \cos(2\pi f_i t + \Delta\phi) \quad (1)$$

$$S_i = A_2 \cos 2\pi f_i t \quad (2)$$

The performance of the mixer circuit is mainly considered from the following aspects: frequency conversion gain, noise figure, distortion and interference, and selectivity. The conversion gain can be mainly divided into variable frequency voltage gain and variable frequency power gain. The noise figure is the ratio of the noise power ratio of the input signal to the noise power ratio of the IF signal at the output. The distortion of the mixer is mainly the frequency distortion. In the mixer, various external factors will always be mixed into some interference signals that are close to the frequency of the intermediate frequency signal. In order to reduce the external interference, the intermediate frequency output loop should be better. The mixer circuit mainly includes a mixing part and a filter circuit (Wee S Y. and Aris A Z., 2017). The transistor mixer is used to convert the high frequency signal of 75MHz into the intermediate frequency signal of 20KHz. The circuit of the transistor mixer has many types, and the frequency conversion circuit is mainly used to convert the nonlinear input characteristics of the transistor.

Common transistor mixers have a common emitter mixing configuration and a common base mixing configuration. The common-emitter mixing configuration may include the local oscillator voltage and the signal voltage is injected from the base and the local oscillator voltage is injected from the transmitter, and the signal voltage is injected by the base, and the common-base mixing configuration mainly includes the local oscillator voltage and the signal voltage. Both are injected from the transmitter. The designed mixer uses a transistor common emitter mixer. The measured signal voltage is input from the base and the local oscillator signal voltage is injected from the emitter. The advantage is mainly to suppress the traction phenomenon caused by mutual interference between the local oscillator signal and the input signal, and reduce the traction phenomenon. The reliability of the circuit (Du J., Yang H. and Shen Z., 2017), the realization of the moisture meter circuit of the coaxial phase method water finder is designed by combining the discrete component circuits. In addition to the turbine flowmeter being a separate component, the five separate components are combined and the circuit board is used with each other, connected together to form a circuit system.

The first component is a 75.00MHz oscillating circuit assembly, the external dimensions are $30 \times 12 \times 0.8\text{mm}^3$ Max, the working voltage is +12VDC, the operating current is $\leq 40\text{mA}$, the operating temperature is $0-140^\circ\text{C}$, the nominal frequency is At 75.00MHz, the allowable frequency difference is $\pm 0.5\text{KHz}$ at room temperature, the output waveform is sine wave, and the output amplitude is $\geq 10\text{dm}/50\Omega$. The circuit uses a double panel structure (Abraham E. and Stoianov I., 2016).

The second component is the 75.02MHz oscillator circuit component, the external dimensions are $40 \times 12 \times 0.8\text{mm}^3$ Max, the working voltage is +12VDC, the operating current is $\leq 40\text{mA}$, the operating temperature is $0-140^\circ\text{C}$, the nominal frequency is at 75.00MHz, the allowable frequency difference is $\pm 0.5\text{KHz}$ at room temperature, the output waveform is a quasi-sine wave, and the output amplitude is $>0.8\text{V}/\text{IKfl}$. The circuit is designed in a double-panel structure.

The third component is a mixer circuit component. There are two groups. The external dimensions are $30 \times 12 \times 1.5\text{mm}^3$ Max, the working voltage is +12VDC, the working current is $\leq 30\text{mA}$, and the working temperature is $0-140^\circ\text{C}$. The allowed frequency difference is $\pm 1.0\text{KHz}$ at room temperature, the output waveform is square wave, the output amplitude is low level $\leq 1\text{V}$, and the high level is $5\text{V} \pm 0.5\text{V}$. The circuit is designed in a double-panel structure. The fourth component is the phase detector circuit component, the external dimensions are $30 \times 12 \times 0.8\text{mm}^3$ Max, the working voltage is +12VDC, the operating temperature is $0-140^\circ\text{C}$, the circuit is designed with double panel structure (Chen G., Ren L. and Xu Y., 2019). The fifth component is the voltage-frequency converter circuit component, the external dimensions are $30 \times 12 \times 0.8\text{mm}^3$ Max, the operating voltage is +12VDC, the operating temperature is $0-140^\circ\text{C}$, the phase amplitude is in the range of $60^\circ \sim 180^\circ$. When changing, the output amplitude varies from 1000 to 4000 Hz. The circuit is designed with a double panel structure.

RESULT ANALYSIS

EXPERIMENTAL ENVIRONMENT

This paper uses the ae2000 and cs4000 experimental devices produced by Zhejiang Zhongkong Company for laboratory verification simulation. The experimental device has three upper, middle and lower water tanks, stainless steel water storage tank, forced convection heat exchange system and three-phase 4.5kW electricity. Heat the boiler. There are two power circuits: one is composed of single-phase circulating pump, electromagnetic flow meter, electric regulating valve and related components; the other is composed of inverter, small flow pump, turbine flow meter and other components (Wang S., Zhang H. and Wang S., 2016).

TEMPERATURE TEST AND FAULT ANALYSIS OF CONTROL CIRCUIT

The main purpose of agricultural water supply system is to protect the irrigation of agricultural crops, especially in the high temperature weather, which is more frequent. In addition, the long-term operation of the whole system will inevitably lead to the phenomenon of system heating. Therefore, whether the designed circuit can meet the requirements of high temperature environment in the underground, temperature testing is the most important link. Temperature test on the circuit board is to test whether the circuit can reach the temperature resistance of the high temperature environment in the well, and whether the design of the test circuit is reasonable, and finally whether the function can be realized. Therefore, it is very important to carry out high temperature experiments on the circuit. Temperature experiments are performed on each component of the circuit. The advantage of this is that it is convenient to modify each circuit, reduce the workload, and improve the overall temperature resistance of the circuit. At room temperature (from 30°C in winter), the data was tested every 10°C increase and continued to rise to 140°C (Although the temperature of the working environment will not be higher than 80°C, in order to ensure the safety of the whole circuit, it is still necessary to verify the safety of the circuit in some extreme cases). The temperature test was carried out using an incubator, and the wires were directly led out for testing. Temperature test on the oscillating circuit and the mixing circuit, starting from 30°C, every 10°C increase in temperature, test the data once, up to 140°C, record the experimental data, observe the two-way mixer circuit through the oscilloscope. The output frequency is obtained, and the experimental data as shown in Table 1 is obtained.

Table 1

Temperature(°C)	30	40	50	60	80	100	120	140
Mixer 1 Frequency (KHz)	19.49	19.51	19.58	19.62	19.81	20.11	20.35	21.03
Mixer 2 Frequency (KHz)	19.49	19.52	19.57	19.62	19.82	20.10	20.34	21.05

It can be seen from the temperature experimental data that as the experimental temperature increases, the frequency of the mixer 1 and the mixer 2 are substantially the same, and the magnitude of the change is substantially the same. It can be seen from the data in the table that the designed mixer circuit can almost eliminate the influence of temperature change on the phase measurement and reach the temperature resistance condition of 140°C. When the temperature continues to rise above 150°C, the measurement effect is distorted and the output is unstable. Temperature test on the phase detector circuit, starting from 30°C, every 10°C increase, tests the data once, up to 140°C, observes the output voltage value through the oscilloscope and records the experimental data. The experimental data obtained are shown in Table 2.

Table 2

Temperature(°C)	30	40	50	60	70	80
Voltage(V)	3.83	3.83	3.84	3.84	3.85	3.86
Temperature (°C)	90	100	110	120	130	140
Voltage(V)	3.87	3.90	3.85	3.82	3.73	3.65

It can be seen from the data in the table that the magnitude of the voltage value remains basically constant. When the temperature rises to 100°C, the voltage gradually decreases. When the temperature rises to 150°C, the output voltage is unstable, so it can be satisfied the requirements for temperature measurement at 140°C in a downhole environment. Finally, the temperature test of the voltage-frequency conversion circuit is carried out. Starting from 30°C, the data is tested once every 10°C, and it is raised to 140°C. The output pulse signal frequency is observed by an oscilloscope and the experimental data is recorded. The experimental data is shown in Table 3.

Table 3

Experimental data of voltage-frequency conversion circuit temperature

Temperature (°C)	30	40	50	60	70	80
Frequency (Hz)	4169	4172	4183	4200	4215	4219
Temperature (°C)	90	100	110	120	130	140
Frequency (Hz)	4227	4188	4106	4003	3986	3942

It can be seen from table 3 that with the increase of temperature, the pulse signal frequency of the circuit increases slowly. When the temperature is 90°C, the pulse signal frequency reaches the maximum value of 4227Hz. When the temperature continues to increase, the pulse signal frequency tends to decrease. When the temperature reaches 140°C, the pulse signal frequency drops to 3942Hz, so within 150°C, the pulse signal frequency of the circuit. The maximum temperature drift is: $4227-3942=285\text{Hz}=0.285\text{KHz}$. When the temperature exceeds 150°C, the output is unstable, so it can meet the requirements of 140°C temperature measurement. The turbine flowmeter is a separate part. A square wave signal with a frequency of 20 Hz and 3.5V is applied to the signal generator. Starting from 30°C, the data is tested once every 10°C, and it is raised to 140°C. The frequency of the pulse signal output by the oscilloscope is basically unchanged. Perform temperature experiment on the whole circuit, put it into the incubator, lead the wire, and energize the circuit. Starting from 30°C, every one degree (TC, test data) always rise to 140°C. Observe the record through the oscilloscope and obtain experimental data. It can be seen that the output of the two mixers is basically the same, the phase-detection circuit and the voltage-frequency conversion circuit have an increasing trend at 30~90 °C, and at 90~140°C. The output of C is declining. The maximum temperature drift is: $4221-3896=325\text{Hz}=0.325\text{KHz}$. When the temperature rises to 150°C, the output frequency is unstable. Therefore, the circuit can work normally at 140°C. The temperature requirement of the coaxial line phase method is that the sub-module is designed and finally packaged. Each circuit is an independent unit, which is connected to each other through lines to realize the overall function. The circuit is on the experiment board. After the performance and temperature test, each part of the circuit is packaged in blocks, the bottom plate is installed, and the outer casing is purchased. The function of the outer casing is to isolate the circuit from the outside and reduce the interference of the external circuit. The size of the package must be selected according to the size of the circuit. Overall physical map is as shown in Fig.6.

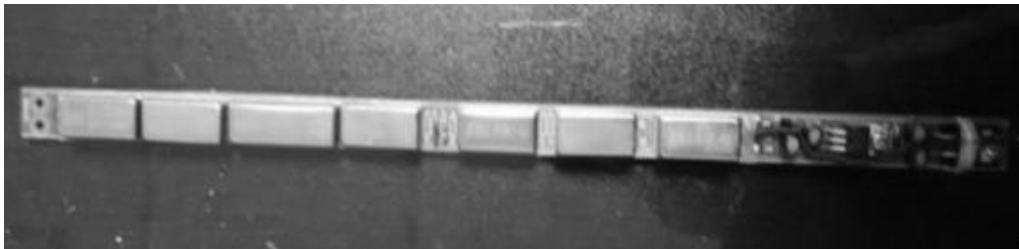


Fig. 6 - Circuit physical diagram

The peak period of the system test water supply is mainly concentrated in several time periods during the day. The water consumption at night decreases rapidly. The water supply is basically zero during the time from 1:00 to 4:00, and the liquid level of the water tank is basically maintained. At the high liquid level h2, the measurement accuracy of the pressure gauge is low, and the water injection port of the water tank is at the top of the water tank. Even if the submersible pump stops water injection, the water surface will maintain long-term fluctuation. All of the above result in a high on-off frequency when the contact signal of the high liquid level h2 is entered. When designing the circuit, only the relay ka3 is considered to be the pump stop relay of the submersible pump at the high level h2 of the inlet water. In the theoretical analysis, when the liquid level reaches the high liquid level h2, the relay ka3 only needs to send a pump stop signal to release the ka4. After the self-locking, the water injection is stopped, and the control requirement can be satisfied. Therefore, the design of the self-locking circuit is not performed, and the phenomenon that the contact signals of the relay ka3 with the high liquid level h2 of the inlet water is shaken, so that the long-term frequency of the relay ka3 coil occurs. The higher on and off level eventually ablates its coils and contacts.

PERFORMANCE TEST OF THE APPLICATION OF LIQUID LEVEL CONTROLLER IN A WATER SUPPLY SYSTEM

After the modeling work in the above chapters, it is now necessary to discuss and study the control performance of the nine-point controller in the liquid level control system. The unit positive step signal is applied to the control loop where the nine-point controller and the conventional PID control module are located, and the corresponding graph is obtained during the simulation time of 50s. The graph of the conventional PID is shown in Figure 7. The simulation curve of the nine-point controller is shown in Figure 8. In all of the following simulations, the abscissa is the time axis (unit: second) and the ordinate is the liquid level height (unit: cm).

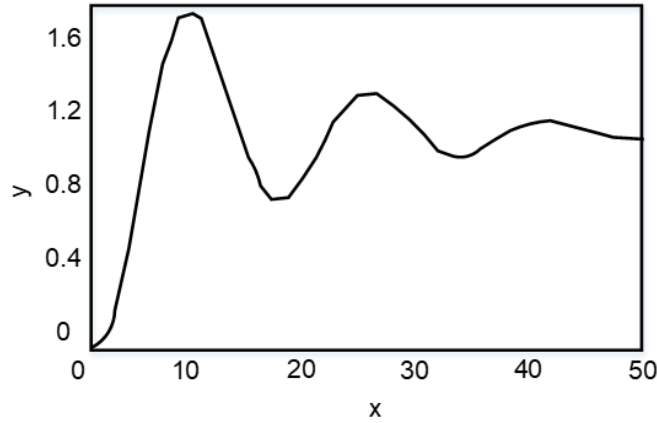


Fig. 7 - Conventional PID simulation curve

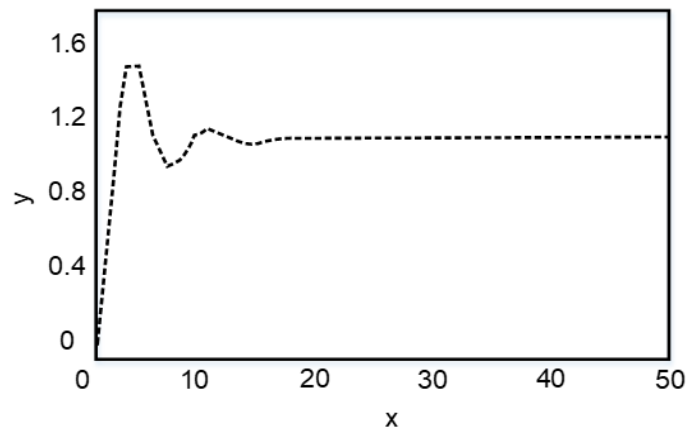


Fig. 8 - Nine-point controller simulation curve

From the overall shape of the above two simulation diagrams, the conventional PID control is not much different from the nine-point controller control, but the two curves are put into a graph from the system's rise time. The control time of the system is compared in three aspects, as shown in Figure 9.

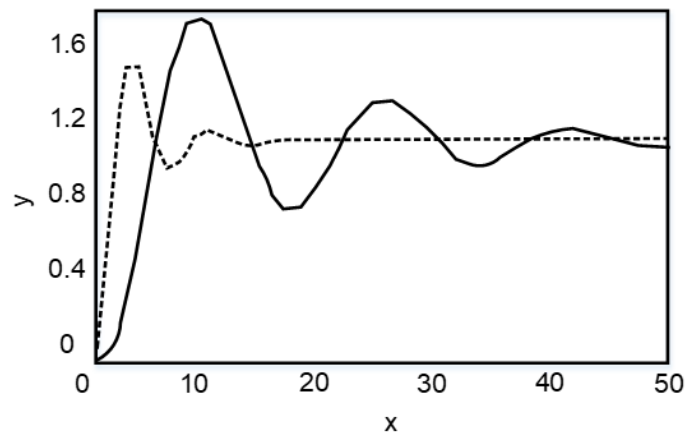


Fig. 9 - Contrast charts of control schemes

For the nine-point controller parameter tuning process, the attenuation ratio of the system response curve can be adjusted to between 1/4 and 1/10 by referring to the tuning mode of the conventional PID parameter. After that, consider what kind of interference you may encounter when the system is running, and what its strength is. Based on these analysis conclusions, according to the function of the nine-point controller parameters and the correlation between them, the corresponding parameter adjustment scheme is taken out. This not only greatly shortens the time for parameter setting, but also makes it possible to adjust the parameters more rationally when encountering complex conditions.

Table 4

Practical application of agricultural water supply control system

Time	Weather condition	System traffic (L/min)
13:00	Rain	0.00
13:30	Rain	0.00
14:00	Rain	0.00
14:30	Fine	42.54
15:00	Fine	42.66
15:30	Fine	36.24
16:00	Fine	35.16
16:30	Fine	30.12
17:00	Fine	24.06

The above table is the specific application results in agricultural irrigation. It can be seen from the table that when the weather is rainy, the whole water supply system has been completely closed because agricultural irrigation can be completed by relying on rainwater under natural conditions. After the weather turns sunny, the evaporation caused by the sun intensifies, so the water supply system begins to supply water to the irrigation system. However, as the time gradually approaches the evening, the natural environment temperature begins to decline, the evaporation decreases, and the water required for irrigation also decreases. The water supply control system gradually controls the water supply according to the irrigation demand, so the flow, appearing on the flow A, gradually decreases over time. From the perspective of the whole application, the response of the whole control system is very timely, and the whole water supply system can be controlled in real time and accurately according to the surrounding environment changes.

CONCLUSIONS

In the rapid development of agricultural modernization, there are many ambiguities in the understanding of the water supply system of large-scale facility agricultural parks and their use, and the liquid level is one of the common controlled objects in the agricultural production process, and its control sometimes happens. It affects the final agricultural production and sometimes even the safety of the entire agricultural production process. Therefore, this paper discusses the fault analysis method of the agricultural irrigation liquid level control circuit of a water supply system by establishing a nine-point controller model and using the temperature-resistant circuit design method based on the coaxial line hemotoxic method.

The implementation of the circuit adopts the PCB method, and the designed circuit is realized by Altium Designer software, and the circuit is reasonably wired, which improves its ability to resist high frequency interference. Temperature test is carried out for each circuit and the whole circuit, which satisfies the temperature resistance requirement that the circuit can work normally at 140°C, does not produce distortion, and improves the temperature resistance of the coaxial line phase water detector. Through the simulation comparison between the nine-point controller and the conventional PID controller on the MATLAB platform, it can be seen that the nine-point controller can better complete the industrial control task, and can make the overshoot and adjustment time of the agricultural water supply system of optimization. After a period of optimization, the control effect can even ensure that the system can control the phenomenon when the control parameters are adjusted in a small range, so that the system can transition to a new control state more smoothly. In the design of the circuit, there is room for improvement.

The selection of components in the agricultural irrigation system and the wiring of the high-frequency circuit PCB can also have a better solution, which is one of the directions of future research.

REFERENCES

- [1] Abraham E., Stoianov I., (2016), Sparse null space algorithms for hydraulic analysis of large-scale water supply networks, *Journal of Hydraulic Engineering*, vol. 142, no. 3, pp. 04015058;
- [2] Agrawal A., Kothari A.K., Rao K.R., (2019), Effect of hearth liquid level on the productivity of blast furnace, *Transactions of the Indian Institute of Metals*, vol. 78, no. 88, pp. 11-21;
- [3] Bhuyan S K., Hota P K., Panda B., (2018), Modeling and simulation of grid connected hybrid energy system and its fault analysis, *International Journal of Power Electronics and Drive Systems*, vol. 9, no. 2, pp. 775;
- [4] Byrdin V.M., (2017), Normal wave diffraction on a plate submerged in a liquid: Level gauge model, factorization method modification, and waveguide quasiresonances, *Mechanics of Solids*, vol. 52, no. 3, pp. 299-314;
- [5] Chen G., Ren L., Xu Y., (2019), Failure analysis of YBCO tapes considering the amplitude and duration of sinusoidal overcurrent, *IEEE Transactions on Applied Superconductivity*, vol. 29, no. 5, pp. 1-5;
- [6] Chen W.L., Ho T.Y., Huang J.W., (2018), Continuous monitoring of pH level in flow aqueous system by using liquid crystal-based sensor device, *Microchemical Journal*, vol. 26, no. 8, pp. 155-164;
- [7] Diao K., Sweetapple C., Farmani R., (2016), Global resilience analysis of water distribution systems, *Water research*, vol. 106, pp. 383-393;
- [8] Du J., Yang H., Shen Z., (2017), Micro hydro power generation from water supply system in high rise buildings using pump as turbines, *Energy*, vol. 137, pp. 431-440;
- [9] Gutiérrez E., Balcázar N., Bartrons E., (2017), Numerical study of Taylor bubbles rising in a stagnant liquid using a Level-Set / Moving-Mesh method, *Chemical Engineering Science*, vol. 164, no. 11, pp. 158-177;
- [10] İsmail Bayram, Hapoglu H, Aldemir A., (2018), Distributed Wireless Liquid Level Control of a Process Simulator Over a Network, *Wireless Personal Communications*, vol. 28, no. 2, pp. 1-18;
- [11] Kim S.W., Choi H.S., Park D.U., (2018), Water level response measurement in a steel cylindrical liquid storage tank using image filter processing under seismic excitation, *Mechanical Systems & Signal Processing*, vol. 10, no. 1, pp. 274-291;
- [12] Mandlate J.S, Soares B.M., Seeger T.S., (2017), Determination of cadmium and lead at sub-ppt level in soft drinks: An efficient combination between dispersive liquid-liquid microextraction and graphite furnace atomic absorption spectrometry, *Food Chemistry*, vol. 2, no. 21, pp. 907-912;
- [13] Manikandan P., Khan F A., (2019), Determination of stress on turbine generator shaft due to subsynchronous resonance using finite element method, *Acta Technica Corviniensis-Bulletin of Engineering*, vol. 12, no.1, pp. 21-24;
- [14] Maurye P., Basu A., Bandyopadhyay T.K., (2017), Multi-gel casting apparatus for vertical polyacrylamide gels with in - built solution flow system and liquid level detectors, *Electrophoresis*, vol. 38, no. 16, pp. 289-301;
- [15] Paul R., Sengupta A., (2017), Design and application of discrete wavelet packet transform based multiresolution controller for liquid level system, *Isa Transactions*, Vol. 71, no. 2, pp. 29-39;
- [16] Pawlak M., (2018), Active fault tolerant control system for the measurement circuit in a drum boiler feed-water control system, *Measurement and Control*, vol. 51, no. 1-2, pp. 4-15;
- [17] Roy P., Kar B., Roy B.K., (2017), Fractional Order PI-PD Control of Liquid Level in Coupled Two Tank System and its Experimental Validation, *Asian Journal of Control*, vol. 19, no. 5, pp. 75-86;
- [18] Roy P., Roy B K., (2016), Fractional order PI control applied to level control in coupled two tank MIMO system with experimental validation, *Control Engineering Practice*, Vol. 48, pp. 119-135;
- [19] Singh J., Singh S., Singh A., (2019), Distribution transformer failure modes, effects and criticality analysis (FMECA), *Engineering Failure Analysis*, vol. 99, pp. 180-191;
- [20] Singh S., Mohanty A.R., (2018), Measurement of boiling liquid levels by decomposition of sound waves in a waveguide, *Applied Acoustics*, vol. 1, no. 29, pp. 248-257;
- [21] Takahashi T., Ito T, Kim S.Y., (2017), Extraction Behaviour of Sr (II) from High-Level Liquid Waste using Ionic Liquid Extraction System with DtBuCH18C6, *Energy Procedia*, vol. 1, no. 31, pp. 170-177;
- [22] Tao J., Fan Q., Ma L., (2017), Improved linear quadratic and proportional control system for improved liquid level system regulation in a coke fractionation tower, *Isa Transactions*, vol. 6, no. 9, pp. 29-35;

- [23] Wang S., Zhang H., Wang S., (2016), Cumulative deformation analysis for transformer winding under short-circuit fault using magnetic–structural coupling model, *IEEE Transactions on Applied Superconductivity*, vol. 26, no. 7, pp. 0-5;
- [24] Wee S Y., Aris A Z., (2017), Endocrine disrupting compounds in drinking water supply system and human health risk implication, *Environment international*, vol. 106, pp. 07-233;
- [25] Ye X., Chen B., (2018), Condition Assessment of Bridge Structures Based on a Liquid Level Sensing System: Theory, Verification and Application, *Arabian Journal for Science & Engineering*, vol. 3, no. 5, pp. 1-20;
- [26] Zhang B., Wei Y.J., Liu W.Y., (2017), A Novel Ultrasonic Method for Liquid Level Measurement Based on the Balance of Echo Energy, *Sensors*, vol. 17, no. 4, pp. 706.

DESIGN AND TEST OF HYDRAULIC DEVICE FOR ELECTRO-HYDRAULIC CONTROLLED HITCH SYSTEM OF A HORTICULTURAL TRACTOR

园艺电液控制系统液压装置的设计与试验

Qiang GAO, Zhixiong LU, Jinlin XUE ^{*)}, Huisong GAO ¹

College of Engineering, Nanjing Agricultural University, Nanjing, 210031, China

Tel: 086+13813902501; E-mail: xuejinlin@njau.edu.cn

DOI: <https://doi.org/10.35633/inmateh-60-28>

Keywords: horticultural tractor, electronic control, hydraulic suspension, hydraulic device

ABSTRACT

This paper proposed a structural design scheme of the hydraulic device of the electro-hydraulic controlled hitch system of a YM554A horticultural tractor with hydraulic device model, and the designed hydraulic device was simulated and tested to verify its performance. Results show that the motion of hydraulic actuator is stable with good response for tillage depth control, while the maximum lifting force of 10.62kN and the static settlement value of 13mm all meet the standard requirements. And the oil pressure changes rapidly with a large fluctuation with the plough position changed from transportation state to tillage state, but it quickly stabilizes, and as the tillage depth becomes larger, the oil pressure drops but remains basically stable with the maximum oil pressure change of 0.35MPa.

摘要

本文提出了 YM554A 园艺拖拉机电液悬挂控制系统所用液压装置的结构设计方案,建立了液压装置模型,进行了液压执行器运动仿真和耕作深度控制,测量了系统的提升力和静沉降值,并在田间测量了不同耕作深度下液压执行机构从运输状态到耕作状态的油压。仿真结果表明,液压执行机构的运动是稳定的,对耕作深度控制有良好的响应,特别是在耕作深度变化时,液压执行机构的响应速度快。台架试验结果表明,最大提升力为 10.62kN,半小时内的静沉降值为 13mm,均满足标准要求。田间试验的结果表明,当从运输状态变化到耕作状态时,油压波动大,但是很快稳定下来,而且随着耕作深度变大,油压下降但仍基本稳定,最大油压变化为 0.35MPa。所设计的液压装置静沉降小,起升力大,响应速度快。

INTRODUCTION

The hydraulic hitch device of a tractor is an important device to control the agricultural machinery operation, which determines the power performance, operation quality, fuel consumption, exhaust emissions, operation efficiency and so on (Ranjbarian et al, 2017; Eltom et al, 2015). The horticultural tractor based on the traditional tractor platform, which equipped hydraulic controlled hitch system, cannot meet the needs of production and management of modern horticulture operations and facility agriculture in terms of overall structure, energy saving and emission reduction, power transmission and so on. Therefore, modern hydraulic technology, sensing technology, electronic technology and control technology can be adopted to improve efficiency and quality by accurate and rapid adjustment of the hitch system (Wang et al, 2017; Soren et al, 2017; Soren et al, 2018; Suomi et al, 2015; Anthonis et al, 2004).

In 1970s, electronic technology has been applied to farm vehicles to realize the electronic control of tractor's hydraulic hitch mechanism (Lee et al. 1996, and Jiang et al. 1992). Anthonis et al. (2004) established a mathematical model based on the relationship between traction force and three factors such as speed, tillage depth and soil resistance. The dynamic characteristics of the three models were studied respectively, which laid a foundation for the design of the electro-hydraulic controlled hitch system. Later, BOSCH Company and some famous tractor manufacturers such as New Holland and John Deere have already developed their own tillage control system, which makes the technology of electro-hydraulic controlled hitch system more mature. Since the 1990s, some researchers have focused on the research of control algorithm, control system design, core component design of the electro-hydraulic controlled hitch system (Shafaei et al, 2019; Hua et al. 2019; Kang et al, 2015; Chen et al, 2014; Chen et al. 2018; Zhao et al, 2014).

¹ Qiang GAO, M.S.; Zhixiong LU, Prof. Ph.D.; Jinlin XUE, Prof. Ph.D.; Huisong GAO, Ph.D.

However, the researches and application of the electro-hydraulic controlled hitch system are mainly aimed at heavy tractors. The researches on electro-hydraulic controlled hitch system are very few for small and middle size tractors, especially for horticultural tractors, and there is a lack of detailed design and in-depth theoretical analysis of the hydraulic devices of electro-hydraulic controlled hitch system.

Therefore, the objective of this paper is to aim at horticultural tractor to put forward the design scheme of hydraulic device suitable for electro-hydraulic controlled hitch system, carry out structural design of the hydraulic device and build the hydraulic device model. The designed hydraulic device was simulated and tested to verify its performance.

MATERIAL AND METHODS

Design Scheme of Hydraulic Device of Electro-hydraulic Controlled Hitch system

Retaining the raw three-point hitch mechanism, the hydraulic device of an electro-hydraulic controlled hitch system is used to replace the raw mechanical hydraulic device for a YM554Y horticultural tractor. The design requirements are: ① Electrically operated hydraulic valve(s) is (are) used to replace the original distributor. ② Operation panel is used to replace the original control handle. ③ Some sensors for force, displacement or angle measurement are installed. ④ The system has small settlement, sufficient lifting force and rapid response.

The electro-hydraulic controlled hitch system is mainly composed of hydraulic device, hitch mechanism and control system, as shown in Fig. 1. The hydraulic device is electronically controlled by an ECU in the control system, where the electromagnetic proportional valve can change the flow rate and flow direction of the hydraulic oil according to the control signal, so as to drive the hitch mechanism to realize lifting and dropping of farm implements. It is mainly composed of a hydraulic pump, a hydraulic control valve, and a hydraulic actuator. The hydraulic control valve is a combined valve which includes electrically operated 2-position 3-port hydraulic valves, electrically operated 2-position 2-port hydraulic valve, relief valve and check valve in the valve body, as shown in Fig. 2. By combining all kinds of valves above, it can simplify the system structure and reduce the installation space.

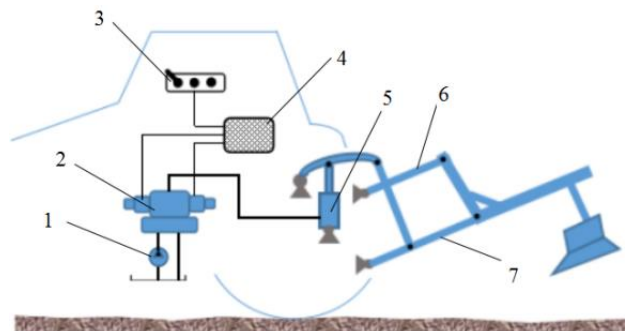


Fig. 1 - Schematic diagram of electro-hydraulic controlled hitch system

1- Hydraulic pump; 2-Hydraulic control valve; 3-Control panel; 4-ECU;
5-Hydraulic actuator; 6-Upper pull rod; 7-Lower pull rod

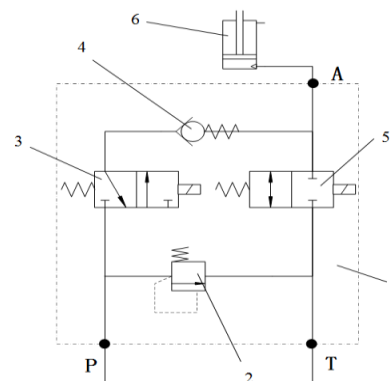


Fig. 2 - Hydraulic control valve

1-Valve body; 2-Relief valve; 3-Electrically operated 2-position 3-port hydraulic valve;
4-Check valve; 5-Electrically operated 2-position 2-port hydraulic valve; 6-Hydraulic actuator

The two electrically operated valves are controlled by the ECU, which can automatically control lifting and dropping of the hydraulic actuator. Here the YM554Y horticultural tractor adopts three-point hitch mechanism, mainly composed of upper pull rod, lower pull rod, lifting rod and so on. The hydraulic actuator provides power to drive the left and right pull rods, thus to control lifting and dropping of farm implements.

The working principle of the hydraulic control valve is that the 2-position 2-port valves and the 2-position 3-port valves are all closed when the ECU does not output the control signal. The oil from the hydraulic pump goes through the port *P* into the valve body, and then flows directly through the relief valve and the port *T* to the oil tank. Meanwhile, because the check valve closes and the 2-position 3-port valve closes, the oil in the hydraulic actuator at the port *A* is cut off, the piston rod of the actuator remains at a certain height, and the farm implements suspended are in a certain position. When the ECU outputs control signal to 2-position 3-port valve, instead of 2-position 2-port valve, the oil passage between the 2-position 3-port valve and the hydraulic actuator is opened, while the oil passage via 2-position 2-port valve is still closed. So, the oil from the hydraulic pump flows into the actuator through the port *P*, the 2-position 3-port valve, the check valve and the port *A*. Therefore, the piston rod extends outwards and the farm implement is lifted.

When the ECU outputs control signal to the 2-position 2-port valve, instead of the 2-position 3-port valve, the oil passage between the 2-position 2-port valve and the actuator is opened, while the oil passage via the 2-position 3-port valve is closed. So, the oil from the hydraulic pump flows back to the oil tank through the port *P*, the relief valve and the port *T*. At the same time, the oil passage between the 2-position 2-port valves and the actuator is opened. Then the oil in the actuator flows back to the oil tank through the 2-position 2-port valves and the port *T*. The piston rod retracts and the farm implement is dropped.

Design of the Hydraulic Device

Here, the original hydraulic pump remained with the flow rate of 35 L/min, the pump pressure of 20MPa and the pump speed of 2200r/min. But a hydraulic cylinder with single shaft and single flow port is chosen as the hydraulic actuator with the inner diameter of 75mm, the diameter of the piston rod of 35mm and its stroke of 200mm. Then the components of the hydraulic control valve are designed as follows.

The relief valve is a kind of direct-acting threaded cartridge valve (Fig. 3). When the pressure at the RO1 port does not reach 85% of the set pressure of the valve spring, RO1 to RO2 will not pass through. When the pressure at the RO1 port exceeds 85% and continues to rise, RO1 to RO2 will relief until the maximum set pressure of the spring is reached. And the structure of check is shown in Fig. 4. When the pressure of OO1 port is large enough to overcome the spring force, the liquid flow flows from OO1 port to OO2 port with a very low pressure drop, which prevents the liquid flow from OO2 port to OO1 port.

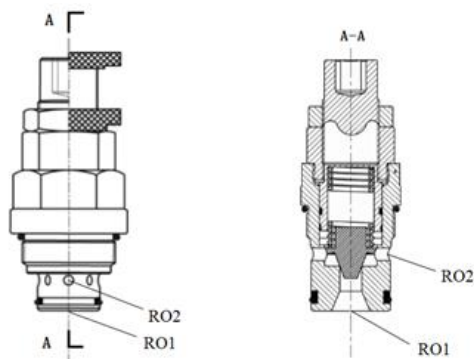


Fig. 3 - Relief valve

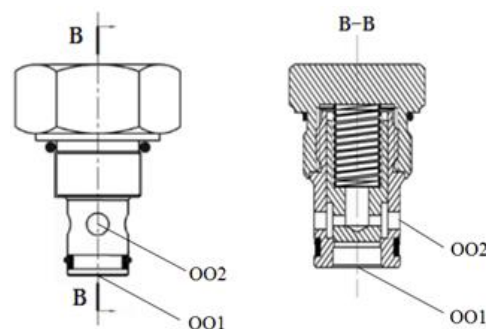


Fig. 4 - Check valve

The electrically operated 2-position 2-port valve is a kind of normally closed threaded cartridge valve powered with a 12 V DC voltage (Fig. 5). When it is not electrified, the oil passage will be closed between VO1 port and the VO2 port; otherwise the oil passage will be opened between the VO1 port and the VO2 port. And the electrically operated 2-position 2-port valves is a sliding valve powered with a 12 V DC voltage (Fig. 6), which controls the flow direction by changing the position of the inlet and outlet passage of the fluid. When it is not electrified, the oil passage between the VO2 port and the VO3 port is closed, while the oil passage between the VO2 port and the VO1 port is opened. When it is electrified, the oil passage between the VO2 port and the VO3 port is opened, while the oil passage between the VO2 port and the VO1 port is closed.

Model of Electro-hydraulic Controlled Hitch system

Model of Hydraulic Components

According to the design scheme above and the design of the main hydraulic components, the hydraulic components were modelled by using AMESim software, as shown in Fig. 7, where the mass block was used to replace the farm implement, the resistance force block provided the tillage resistance force, the displacement sensor outputs the displacement signal of the hydraulic actuator, the pressure sensor outputs the oil pressure signal, and the sensor signals above were input into the interface icon Simulink control. Then one of its outputs loaded to the mass block by converting the resistance force of the actuator into the tillage resistance force via a gain, and the other output were current signals, which controlled the action of the two electrically operated valves.

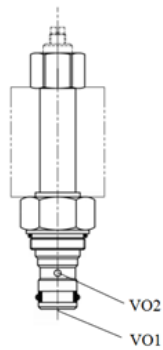


Fig. 5 - Electrically operated 2-position 2-port valves

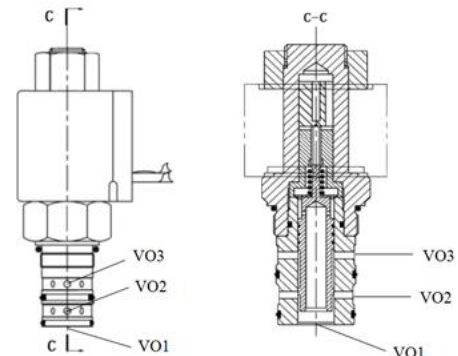


Fig. 6 - Electrically operated 2-position 3-port valve

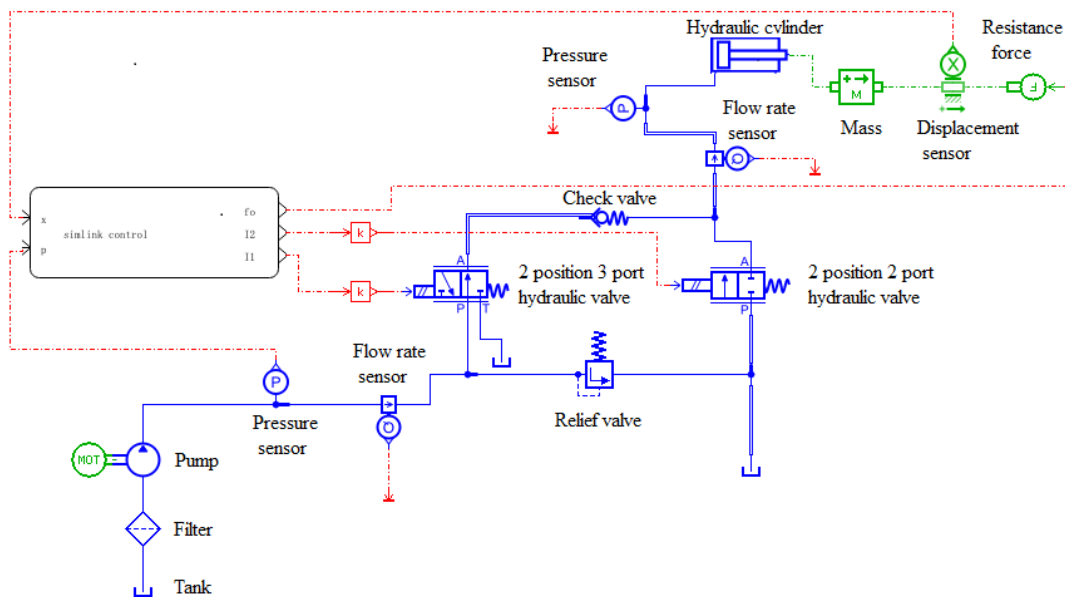


Fig. 7- Model of hydraulic components

Model Parameters

Taking a plough implement as an example, its weight is 200kg and the width of single plough is 30cm. The tillage depth is set to 20cm, while the specific resistance of soil is 5N/cm². The equivalent mass *M* of the load acting on the piston is expressed as:

$$M = k \cdot m \cdot i_g^2 \tag{1}$$

In the formula, *k* is the correction coefficient, it is set to 1.05 here; *m* is the mass of farm tool, it is set to 200 kg here; *i_g* is the lifting speed ratio at the centre of gravity of the farm implements, and the lifting speed ratio is 6.

According to the above formula, the equivalent mass *M* can be calculated to be 7560 kg. The model parameters are shown in Table 1.

Table 1

Parameters of the model		
Name	Number	Unit
Flow rate of hydraulic pump	35	L/min
Hydraulic pump pressure	18	MPa
Hydraulic actuator diameter	75	mm
Hydraulic actuator rod diameter	35	mm
Piston stroke	200	mm
Voltage of electrically operated valve	12	V
Oil pressure of Electrically operated valve	20	MPa
Gain	6	
Mass of mass block	7560	kg

Model of Control System

An interface icon S-Function in Matlab Simulink was used to import the build AMESim model of the hydraulic components, while a PID controller was established to verify performances of the designed hydraulic device. The established model of the control system is shown in Fig. 8.

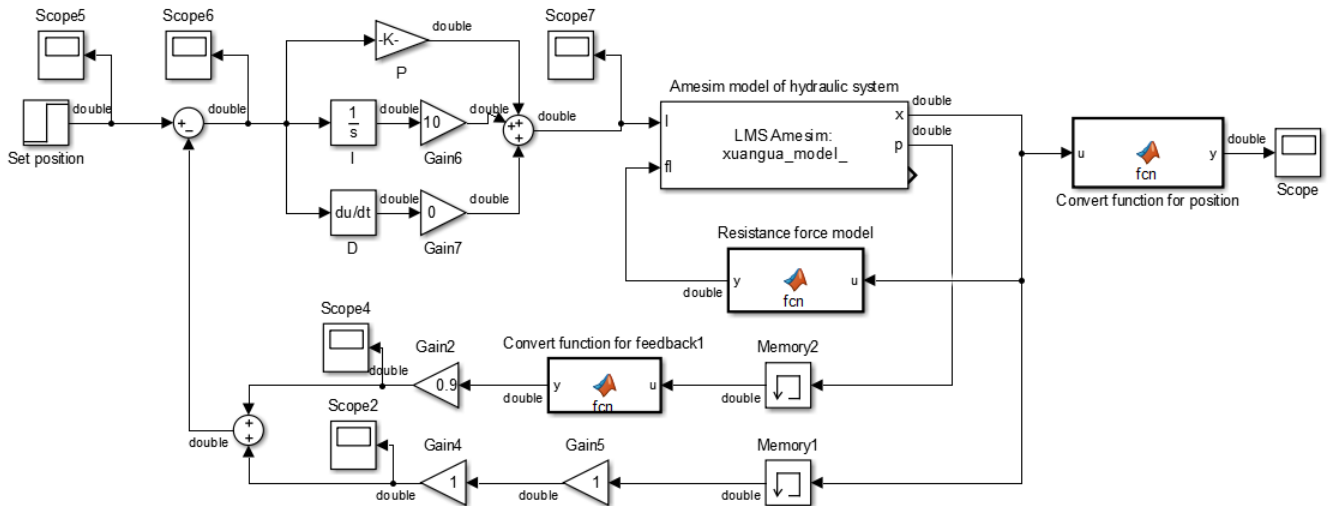


Fig. 8 - Model of control system

RESULTS

Simulation of Hydraulic Actuator Motion

The initial piston displacement is set to 0, and the preset piston displacement is set to 0.2 m to observe the piston movement (Fig. 9 and Fig. 10) and the flow of piston orifice (Fig. 11).

From Fig. 9 and Fig. 10, it takes piston displacement about 6.3 s from 0 to 0.2 m. At the same time, the piston's beginning speed reaches the maximum at 0.186 m/s, then its speed gradually decreases, and the piston moves smoothly after about 1.8 s.

From Fig. 11, the piston flow rate increases at first and then tends to stabilize after about 1.8s. Therefore, it shows that the hydraulic device has good stability through the piston displacement, velocity and flow chart.

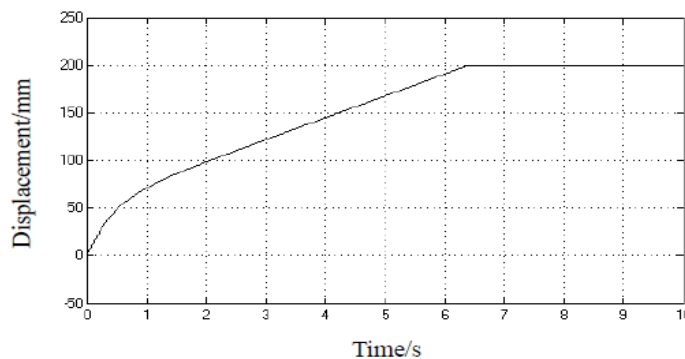


Fig. 9 - Displacement of piston in hydraulic actuator

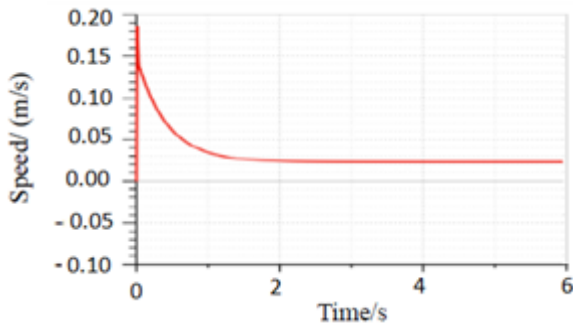


Fig. 10 - Motion speed of piston

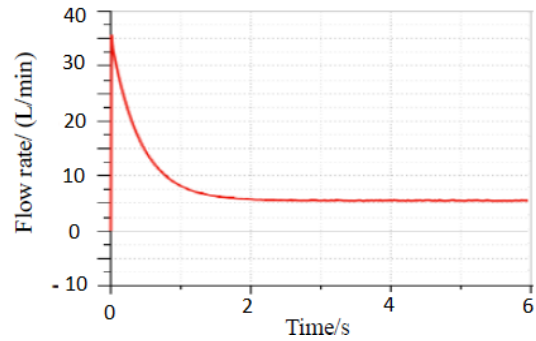


Fig. 11 - Flow rate of piston port

Simulation of Tillage Depth Control

The simulation of tillage depth control is to test the responsiveness of the model when the tillage depth changes according to Fig. 8. Firstly, the target value of tillage depth is set to 30cm with the simulation time of 6s. The simulation result (Fig.12) shows that the set tillage depth can be achieved after about 1.8s, and the lifting curve is very smooth with no significant oscillation.

Then the responsiveness of the system is verified. The set tillage depth is changed to 48 cm at a certain time after reaching the set tillage depth of 30 cm. The response result of the change of the set tillage depth is shown in Fig. 13.

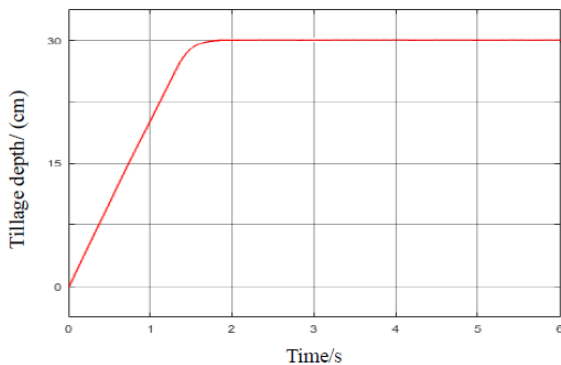


Fig. 12 - Curve of tillage depth

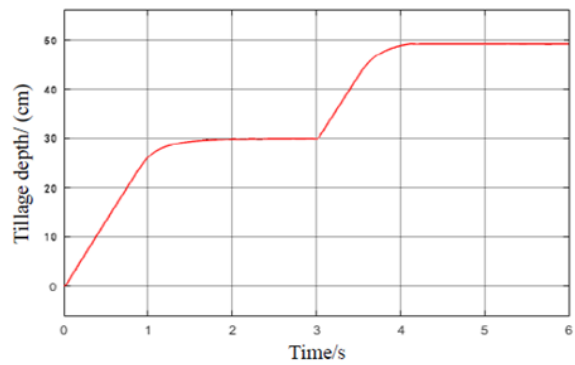


Fig. 13 - Curve at the change of tillage depth

It shows that it takes about 1.8s to reach the set tillage depth of 30cm with no significant oscillation. Then it takes about 3s to convert to the tillage depth of 48 cm, and it reaches the set tillage depth of 48cm after 1s. It shows that the system has good transient response characteristics.

Test Bench Experiments

The designed hydraulic control valve (Fig. 14 (a)) was installed on the tractor electro-hydraulic control test bench (Fig. 14 (b)). According to the test standard in China (GB/T 3871.4-2006, 2006), the lifting force and static settlement value were tested at the loading point of the lifting frame mounted on the three-point linkages with the specified pressure value of 16MPa±0.5MPa (see Fig. 14 (b)). The experimental results are shown in Table 2.



(a) Hydraulic control valves



(b) Tractor electro-hydraulic control test bench

Fig. 14 - Test of hydraulic control valve

According to the data in Table 2, the maximum lifting force of the hydraulic hitch mechanism is 10.62kN, which is calculated according to the calculation equation of the maximum lifting force in the test standard (GB/T 3871.4-2006, 2006), and the total static settlement value is 13mm in half an hour, which are in accordance with the standard requirements. Therefore, the designed hydraulic device meets the requirements through the test bench experiments.

Table 2

Test location number	Lifting force test		Static settlement test
	Lifting force at loading point (kN)	Relief valve opening pressure (MPa)	Height(mm)
Test location 1	16.04	16.5	823
Test location 2	15.42	16.3	820
Test location 3	14.69	16.3	819
Test location 4	13.86	16.3	816
Test location 5	13.07	16.2	812
Test location 6	12.33	16.2	810

Field Experiments

To further verify the performance of the designed hydraulic control valve, it was installed on a YM554 tractor with a XL-425 plough. An oil pressure sensor was installed in the oil tube connected to the hydraulic actuator. The oil pressure was measured during the period from transport state to the tillage state with different tillage depth of 80mm, 120mm and 180mm, respectively. During the whole process, the tractor speed is basically stable at 1 km/h. The variation of the oil pressure and the tractor speed are recorded in Fig. 15.

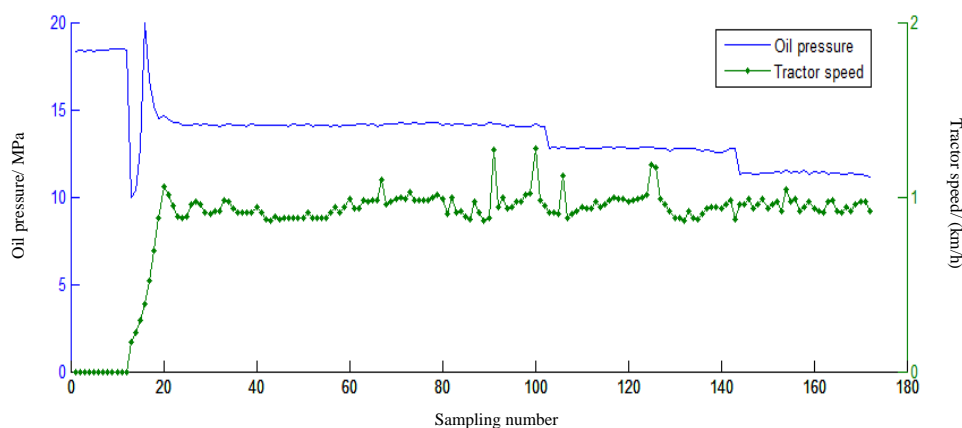


Fig. 15 - The change of the oil pressure in hydraulic actuator and tractor speed

From Fig.15, the tractor speed is basically stable at about 1km/h with the maximum speed of 1.28km/h and the minimum speed of 0.88km/h in the process of tractor farming. As to the oil pressure, it is larger at the transportation state and drops rapidly when the plow changes from the transportation state to the tillage state, then it fluctuates to a certain extent and it stabilizes quickly to 14.1MPa with small fluctuation of 0.31MPa after the tillage depth reaches 80 mm. With the increase of tillage depth, the oil pressure drops, but it keeps stable basically to 12.7MPa and 11.3MPa with small fluctuation of 0.28MPa and 0.35MPa at the tillage depth of 120mm and 180mm respectively. Therefore, the designed control valve has quick response to adapt the changes from transportation state to tillage state with large fluctuation of oil pressure and changes of tillage depth without significant fluctuation and the oil pressure remain basically stable at a certain tillage depth.

CONCLUSIONS

Aiming at YM554Y tractor, this paper puts forward the structural design scheme of the hydraulic device of the electro-hydraulic controlled hitch system, carries out the structural design of the hydraulic device, then builds the hydraulic device model based on AMESI and Simulink software, and finally carries out the simulation of hydraulic actuator motion and the simulation of tillage depth control and the test bench test.

The results of hydraulic actuator motion simulation and tillage depth control simulation show that the hydraulic actuator motion is stable and the response of tillage depth control is good, especially when the tillage depth changes, the hydraulic device can respond quickly.

The lifting force and static settlement test of the system on the test bench show that the hydraulic device designed meets the requirements. And the designed control valve has quick response to adapt the changes of operating states of the farm implement according to the field experiments, with basically stable oil pressure at a certain tillage depth. This study can provide reference for the development of electro-hydraulic controlled hitch system of tractors.

ACKNOWLEDGEMENT

The study is supported by “National Key R&D Program (2016YEF0700904)”, “Jiangsu three new projects of agricultural machinery (NJ2018-11)”, “Jiangsu projects of independent innovation in agriculture (CX(18)1007)”, and “Jiangsu University Qinglan Project”.

REFERENCES

- [1] Anthonis A., Mouazen M., Saeys W., and Ramon H., (2004), An automatic depth control system for online measurement of spatial variation in soil compaction, Part3: Design of depth control system, *Biosystems Engineering*, Vol.89, pp.253-253.
- [2] Chen Z., Wu H., Zhang Y., Peng B., Gu F., Hu Z., (2018), Development of automatic depth control device for semi-feeding four-row peanut combine harvester, *Transactions of the Chinese Society of Agricultural Engineering*, Vol.34, issue 15, pp.10-18.
- [3] Chen, J.S., and Cheng W.B., (2014), Linear analysis of hydraulic control system of an electric-hydraulic proportion, *Advanced Materials Research*, Vol.898, pp.582-585.
- [4] Eltom A.E.F., Ding W., Ding Q, Tagar A., (2015), Field investigation of a trash-board, tillage depth and low speed effect on the displacement and burial of straw, *CATENA*, Vol.133, pp.385-393.
- [5] GB/T 3871.4-2006, (2006), *Agricultural tractors - Test procedures - Part 4: Rear three-point linkage lifting capacity*, Beijing: China Standard Press. (in Chinese) GB/T3871.4-2006. Beijing/China
- [6] Hua B., Zhao J., Liu C., Du Y., Mao E., Song Z., (2019), Performance simulation and test of plug-in proportional raising valve of electro-hydraulic hitch for heavy tractor, *Transactions of the Chinese Society of Agricultural Engineering*, Vol.35, Issue 8, pp.109-117.
- [7] Jiang Y., Honami N. and Umeda S., (1992), Microcomputer control system for tractor implements, *JSAM*, Vol.54, Issue 3, pp.5-13.
- [8] Kang J., He P., Nie Y., He J., (2015), Design of auxiliary depth-control system for micro-tiller, *Engineering in Agriculture Environment and Food*, Vol.8, Issue 2, pp.101-105.
- [9] Lee J., Yamazaki M., Oida A., Nakashima H., Shimizu H., (1996), Non-contact sensors for distance measurement from ground surface, *Journal of Terramechanics*, Vol.33, Issue 3, pp.155-165.
- [10] Ranjbarian S., Askari M., Jannatkhah J., (2017), Performance of tractor and tillage implements in clay soil, *Journal of the Saudi Society of Agricultural Sciences*, Vol.16, Issue 2, pp.154-162.
- [11] Shafaei S.M., Loghavi M., Kamgar S., (2019), A practical effort to equip tractor-implement with fuzzy depth and draft control system. *Engineering in Agriculture, Environment and Food*, Vol.12, Issue 2, pp.191-203.
- [12] Soren K. N., Munkholm, L. J., Mathieu L., Michael N., and Green, O., (2017), Seed drill instrumentation for spatial coulter depth measurements, *Computers and Electronics in Agriculture*, Vol.141, pp.207-214.
- [13] Soren K. N., Munkholm, L. J., Mathieu L., Michael N., and Green, O., (2018), Seed drill depth control system for precision seeding, *Computers and Electronics in Agriculture*, Vol.144, pp.174-180.
- [14] Suomi P., and Oksanen T., (2015), Automatic working depth control for seed drill using ISO 11783 remote control messages, *Computers and Electronics in Agriculture*, Vol.116, pp.30-35.
- [15] Wang Y., Jing H., Zhang D., Cui T., Yang L., (2018), Development and performance evaluation of an electric-hydraulic control system for subsoiler with flexible tines, *Computers and Electronics in Agriculture*, Vol.151, pp.249-257.
- [16] Zhao J., Zhu Z., Song Z., Zhou R., Wang R., Mao E., (2014), Proportional controller for electro-hydraulic hitch system in heavy tractor, *Transactions of the Chinese Society of Agricultural Machinery*, Vol.45, Issue S, pp.10-16. (in Chinese with English abstract)

RESEARCH OF THE OF BULK MATERIAL MOVEMENT PROCESS IN THE INACTIVE ZONE BETWEEN SCREW SECTIONS

ДОСЛІДЖЕННЯ ПРОЦЕСУ ПЕРЕМІЩЕННЯ СИПКОГО МАТЕРІАЛУ В НЕАКТИВНІЙ ЗОНІ МІЖ ГВИНТОВИМИ СЕКЦІЯМИ

Trokhaniak O.M.^{*1)}, Hevko R.B.²⁾, Lyashuk O.L.²⁾, Dovbush T.A.²⁾, Pohrishchuk B.V.³⁾, Dobizha N.V.³⁾

¹⁾National University of Life and Environmental Sciences of Ukraine;

²⁾Ternopil Ivan Puluj National Technical University / Ukraine;

³⁾Ternopil National Economical University / Ukraine;

E-mail: klendii_o@ukr.net

DOI: <https://doi.org/10.35633/inmateh-60-29>

Keywords: screw, sections, material, curved tracks, material flight angle

ABSTRACT

The article presents the results of theoretical and experimental studies of the process of moving bulk material in the inactive zone between hinged screw sections of a flexible screw conveyor. The influence of the gap between the edges of adjacent screw sections and the magnitude of their circular displacement on the process of continuous transportation of bulk material is presented. The results of theoretical and experimental studies are compared. This will allow choosing the optimal design, kinematic and technological parameters of the developed sectional screw working body when transporting bulk agricultural materials along curved paths, both in horizontal and inclined directions, as well as along curved paths.

РЕЗЮМЕ

В статті представлені результати теоретичних і експериментальних досліджень процесу переміщення сипкого матеріалу в неактивній зоні між шарнірно з'єднаними гвинтовими секціями гнучкого гвинтового конвеєра. Наведено вплив величини зазору між краями сусідніх гвинтових секцій та величини їх колового зміщення на процес неперервного транспортування сипкого матеріалу. Проведено порівняння результатів теоретичних і експериментальних досліджень. Це дозволить вибрати раціональні конструктивні, кінематичні та технологічні параметри розробленого секційного гвинтового робочого органу при транспортуванні сипких сільськогосподарських матеріалів по криволінійних трасах, як у горизонтальному та похилому напрямках, а також по криволінійних трасах.

INTRODUCTION

Screw conveyors are widely used in the movement of various bulk materials, mainly agricultural products, which include: grain, granular seeds, fodder flour, chaff, bran, compound feed, cereal, granules of fertilizers, etc. The results of studies on the contact interaction of such bulk materials with working surfaces of screw conveyors are described in (Loveikin V. and Rogatynska L., 2011; Lyashuk O.L., et al., 2015; Rogovskii I.L., et al., 2019; Wang D.-X., 2012, Pylypaka S.F., et al., 2019).

Research on mechanical and technological properties of agricultural materials is given in the works (Tsarenko O.M., et al., 2003; Rogovskii I.L., et al., 2019).

Mainly for transportation of such cargoes rigid auger conveyors installed at different angles to the horizon are used, as well as flexible screw conveyors, the determination of the parameters and modes of which are described in the works (Hevko B.M., et al., 2018; Haydl H.M., 1986; Mondal D., 2018; Owen Philip J., 2010, Qi J., et al., 2017, Roberts Alan W., and Bulk Solids, 2015, Tian Y. et al., 2018).

Pneumatic conveyors, which can transport various loads of curved tracks, have been widely used. The main disadvantage of these types of conveyors is significant energy costs and price, which limits their use. The study of these types of conveyors, as well as screw feeders for feeding bulk materials are in the works of (Baranovsky V.M., et al., 2018, Hevko R.B., et al., 2018; Lech M., 2001; Manjula E.V.P.J., et al., 2017; Naveen T. et al., 2015).

The combination of technological operations, such as transportation and mixing of feed mixtures, is possible with the use of conveyor washers that can work on different routes, but only stationary.

The results of studies on such conveyors are given in (Hevko R.B., et.al., 2017; Hevko R.B., et.al., 2018; Lyashuk O.L., et.al., 2018; Yao Y.P., et.al., 2014).

The results of theoretical and experimental developments, which are presented in this article, are a continuation of previous studies and are aimed at improving the efficiency of the work of screw conveyors, the constructive schemes and the working bodies of which are given in the studies (Hevko B.M., et.al., 2018; Hevko R.B., et.al., 2014, 2016, 2019).

MATERIALS AND METHODS

In order to increase the reliability of the flexible screw conveyor functioning, it is proposed that its working body is made of separate screw sections that are hinged to each other. Fig.1a shows the location of the edges of adjacent sections, the screw ribs 1 and 2 which are located in the axial direction with a gap δ (inactive zone). The screw sections are interconnected using a hinge mechanism 3, made on the principle of a universal joint with spaced axes that are mutually perpendicular and located in an elastic casing 4. In the circumferential direction, the edges of adjacent helical ribs are offset from each other by an angle α . The idea of the design of such a working body is that when the bulk material ascends from the edge of the screw rib 1, the distance δ must fly through after some time t_1 . At the same time, the edge of the screw rib 2 is the least (it is necessary to take into account the angle of the material flight) for a time t_2 and it must be rotated through an angle α in order to capture the transported material.

A general view of the sections of the working body located on the curvilinear region and its individual elements are presented in Fig.1b.

The purpose of these studies is to establish rational parameters and operating modes of the developed working body, which will ensure stable transportation of bulk materials on various technological routes.

Let's consider the movement of bulk cargo through a fixed casing using the screw sector of the screw spiral. Let us single out its elementary volume, which simultaneously contacts the fixed casing and the rotating section of the screw spiral. From the side of the casing, a reaction acts on it, perpendicular to its surface and the corresponding friction force. The reaction from the side of the gutter is determined by the vector sum of the gravity efforts of the selected elementary volume and centripetal force.

The elementary volume is also affected by the reaction from the surface of the screw rib directed perpendicular to the surface of the screw at the contact point and the corresponding friction force. Fig.1c shows the forces acting on the elementary volume of bulk material moving in the casing.

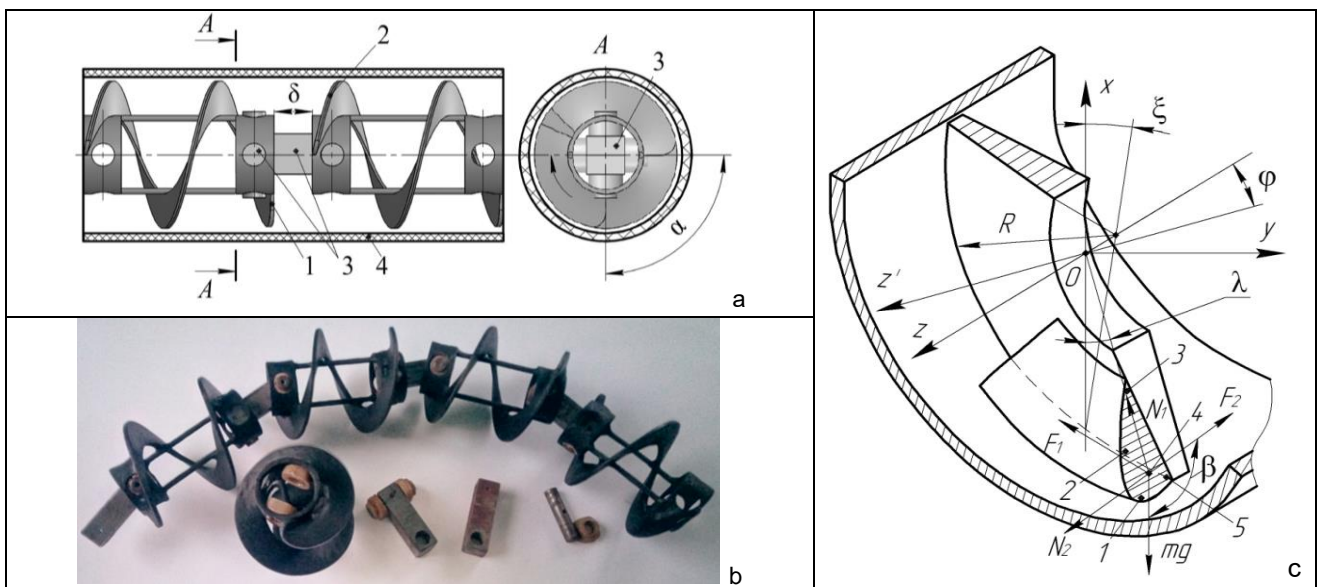


Fig. 1 - Design and calculation scheme of the screw working body, the sections of which are hinged

a - the image of two sections; b - is a general view of sections of a working body located on a curved section and its individual elements; c - scheme for determining the forces acting on the elementary volume of bulk material that moves inseparably in the casing

We will assume that the friction forces between the particles of the material (grains, maize, or other bulk material) significantly exceed their friction forces over the surface of the auger and casing.

This assumption makes it possible to consider the motion of particles as a whole with the same angular velocity. The actual movement of the material differs from the ideal, so points 1 and 2, which are at the edge of the cross-section of the bulk material flow are slightly behind points 3, 4 and 5, which are near the edges of the auger.

A significant lag will be observed only in the case of transport of material having a low coefficient of friction between individual particles (grains). However, for the transport of grain material, the intermixing of the individual particles is negligible, the particles almost stick together and move in a continuous stream, especially at high speeds. This statement is experimentally confirmed in the works (Hevko R.B., et al., 2018, Tsarenko O.M., et al., 2003).

The speed of movement of point 1, which is at the edge of the stream cross section, is maximum due to the maximum distance from the centre of the casing.

The same will be the linear velocity of point 5. The velocity of points 2 and 4 decreases in proportion to the radius at which they move. The lowest speed is characteristic of point 3, which is closest to the centre of rotation.

The equation of motion of a single elementary volume of bulk material that is unrelated to the flow can be written as a system of two differential equations:

$$m(d^2z/dt^2) = N_1 \cos \xi - F_1 \sin \xi - F_2 \sin \beta - mg \sin \varphi \quad (1)$$

$$mR(d^2\lambda/dt^2) = N_1 \sin \xi + F_1 \cos \xi - F_2 \cos \beta - mg \sin \lambda \cos \varphi \quad (2)$$

where m is the mass of the material particle; R is the radius of the casing; N_1 - the reaction of the screw on the material; F_1 - friction force from reaction N_1 ; N_2 is the reaction of the casing to the material; F_2 - friction force from reaction N_2 ; ξ - is the angle of elevation of the screw surface; φ is the angle of inclination of the auger section axis to the horizon; β is the direction of the material particle motion relative to the casing; λ is the angular position of a material particle in its rotational motion; z is the longitudinal coordinate of the particle along the casing axis.

The N_2 reaction is determined by the condition:

$$N_2 = mg \cos \lambda \cos \varphi + mR \cdot (d\lambda/dt)^2 \quad (3)$$

The friction forces are determined accordingly:

$$F_1 = f_1 N_1; \quad F_2 = f_2 N_2 \quad (4)$$

where f_1 is the coefficient of friction of the material on the helical rib surface; f_2 is the coefficient of friction of the material on the casing surface.

Between the directions of motion of a material particle and the geometry of a helical edge, when rotating it at an angular velocity ω , it is possible to write such geometric dependences:

$$\operatorname{tg} \beta = \dot{z} / R \dot{\lambda}; \quad \operatorname{tg} \xi = \dot{z} / R(\omega - \dot{\lambda}) \quad (5)$$

If we consider the movement of the selected element of material in the stream, then from the equation (2) last addition can be excluded, because its weight is offset by the support of the bulk material below. The rest of the effort is still ongoing. Then equation (2) takes the form:

$$mR(d^2\lambda/dt^2) = N_1 \sin \xi + F_1 \cos \xi - F_2 \cos \beta \quad (6)$$

To solve the system of equations (1) - (5), we apply the transformation to get rid of the unknown force N_1 and express the parameters through the magnitude of the angle λ . First, this system takes the form:

$$m\ddot{z} = N_1(\cos \xi - f_1 \sin \xi) - f_2(mg \cos \lambda \cos \varphi + mR\dot{\lambda}^2) \sin \beta - mg \sin \varphi \quad (7)$$

$$mR\ddot{\lambda} = N_1(\sin \xi + f_1 \cos \xi) - f_2(mg \cos \lambda \cos \varphi + mR\dot{\lambda}^2) \cos \beta - mg \sin \lambda \cos \varphi \quad (8)$$

In the final form, the differential equation of motion for the variable λ takes the form:

$$\ddot{\lambda} + \dot{\lambda}^2 A + B_c \cos \lambda - B_s \sin \lambda - C = 0 \quad (9)$$

In this equation, the coefficients are determined by the following dependencies:

$$A = f_2[\cos(\beta + \xi) - f_1 \sin(\beta + \xi)] \quad B = (f_2 g / R) \cdot [\cos(\beta + \xi) - f_1 \sin(\beta + \xi)] \cos \varphi \cos \xi$$

$$B_s = (g / R) \cdot (\cos \xi - f_1 \sin \xi) \cos \varphi \cos \xi; \quad C = (g / R) \cdot (\sin \xi + f_1 \cos \xi) \cos \varphi \cos \xi \quad (10)$$

In the case of flow movement, when applying formula (6), the coefficient $B_s = 0$.

During the flow, it is necessary that the centripetal force is greater than the force of gravity. Otherwise, the particles of bulk material will not be in continuous mode, which significantly distorts the picture of stream transportation. This is achieved under the condition $\dot{\lambda} > \sqrt{g/R}$ (Hevko R.B., et al., 2014).

An important moment of movement is the separation of the flow particles from the spiral rib and their free flight inside the casing to a halt or until the next section comes into contact with the screw rib.

The free movement of cargo particles on the surface of the casing in case of separation from the blade is written in the form of two differential equations of the second order:

$$m(d^2z/dt^2) = -F_2 \sin \beta - mg \sin \varphi \quad (11)$$

$$mR(d^2\lambda/dt^2) = -F_2 \cos \beta - mg \sin \lambda \cos \varphi \quad (12)$$

After the conversion we get:

$$m\ddot{z} = -f_2(mg \cos \lambda \cos \varphi + mR\dot{\lambda}^2) \sin \beta - mg \sin \varphi \quad (13)$$

$$mR\ddot{\lambda} = -f_2(mg \cos \lambda \cos \varphi + mR\dot{\lambda}^2) \cos \beta - mg \sin \lambda \cos \varphi \quad (14)$$

The third stage of motion may be the free flight of the flow particles at separation from the casing surface if the calculated value of the pressure force on the chute is $N_2 < 0$. Then, the equation of particles' motion can be described by a system of three independent differential equations of motion on three mutually perpendicular axes, and x, y, z :

$$\ddot{x} = -g \cos \varphi; \quad \ddot{y} = 0; \quad \ddot{z} = -g \sin \varphi \quad (15)$$

Free-fall body movement will end if contact with the casing occurs, that is, inequality $x^2 + y^2 \geq R^2$. The relation between velocities in Cartesian and cylindrical coordinate systems when separating material particles from a helical edge will be written in the form:

$$\dot{x} = R\dot{\lambda} \sin \lambda \quad \dot{y} = -R\dot{\lambda} \cos \lambda \quad (16)$$

When a material particle falls on the casing surface, the angular velocity of rotation is written as the sum of the projections of velocity vectors tangent to the circle at the point of contact:

$$\dot{\lambda} = (\dot{x} \sin \lambda - \dot{y} \cos \lambda) / R \quad (17)$$

Equation (9) is a second-order nonlinear differential equation, an analytical solution is impossible, and therefore we apply a numerical method for integrating such equations, the Runge-Kutta method.

Let's consider the flow of bulk material at different points in its cross section. The characteristic points of the flow cross-section are shown in Fig.1c.

The presence of different linear velocities for individual points of intersection of the material flow leads to different trajectories of their flight at separation from the auger edge. The linear velocity of separation of the particle:

$$v_i = R_i \dot{\lambda} \quad (18)$$

where R_i is the radius of rotation of the i particle.

The velocity v_i is directed tangential to the circle of the appropriate radius and directed along a vector that makes up the angle β_i with the circle in the XOY plane. It follows from (5) that:

$$\operatorname{tg} \beta_i = \dot{z} / (R_i \dot{\lambda}) \quad (19)$$

Moreover, both the longitudinal (axial) \dot{z} and angular velocities $\dot{\lambda}$ of all elements of the section, according to assumptions, are the same. An analysis of formula (19) shows that particles that are at smaller radii have a larger exit angle β_i , and accordingly, have a smaller component of the peripheral velocity in a plane perpendicular to the z axis.

In order to determine the maximum possible distance of flight of particles from different points of the cross section, we consider the free motion of each of the particles in a circle of the corresponding radius. We assume that individual particles interact with each other during free motion, that is, there are friction forces between them, and each of them moves in a circle of a preliminary radius. This assumption is justified by the fact that the lower particles cannot rise up due to the presence of upper particles there. The lag or advance of the lower particles relative to the upper is practically absent because of the significant friction forces between them. Therefore, at small distances, the motion of particles can be considered as the motion of a connected mass.

The smaller the radius of rotation of the particle R_i , the smaller the centripetal acceleration is:

$$a_{ni} = R_i \dot{\lambda}^2 \quad (20)$$

In the case of a decrease in angular velocity due to braking, the centripetal acceleration will become smaller than the acceleration of gravity g and the particles begin to fall freely onto the lower surface of the casing. Fall begins with the lower layers, gradually spreading to the upper layers.

The maximum flight length should be considered such a distance along the z axis, when the particle moves over the surface of the casing in contact with it. Such a study must be carried out for an arbitrary moment of separation of the particle from the blade ($0 \leq \lambda \leq 2\pi$) and from that to determine the shortest flight length. In this case, it is necessary to calculate the angular displacement of the particle in the direction of the angle λ in order to determine the coordinates of the point that the particle reaches at the maximum flight length. Knowing the corresponding final coordinate, we can calculate the axial distance between the ends of the adjacent helical ribs δ and the necessary angular displacement α between them.

The motion of each particle is determined from equations (13) and (14), in which it is necessary to set the corresponding radii R_i , angles β_i and friction coefficients f_i . When solving systems of differential equations (9), (13) and (14) and (15), it is necessary that the final conditions at the previous stage automatically become the initial ones for the following. To analyse the motion of a particle in the flow and in the separation zone, a program in Delphi was created using the Runge-Kutta method which has the ability to graphically display the results.

The experimental research procedure is as follows. A transfer pipe was adopted as the basis, the structure description and operation principle of which are given in the work (Hevko R.B., et al., 2016). As bulk material was selected grain mixed with granules of plastic material of different colours. Directly under the discharge pipe was a tray on which the material was unloaded and, using filming, the flight range of the bulk material was fixed, fixing the trajectory of multi-coloured granules. The angle of departure of the material was fixed at $\lambda = 90^\circ, 180^\circ, 270^\circ$. According to theoretical studies at an angle $\lambda = 270^\circ$, the flight length L of the material is minimal, therefore, to ensure continuous movement of material between adjacent screw sections, the most unfavourable option must be taken into account. The rotation frequency of the working body n and its angle of inclination to the horizon φ , according to the results of theoretical studies, were chosen at the following values $n = 450, 600, 750$ rev/min; $\varphi = 10^\circ, 20^\circ, 30^\circ$.

RESULTS

Based on the results of the calculations, graphical dependences (Fig. 2) of the free flight length L of the material particles on the rotational speed n of the working body $L = f(n)$, (Fig. 2a) and the inclination angle φ of the screw section axis to the horizon $L = f(\varphi)$, (Fig. 2b) at different angular positions of the material particle at the moment of its separation from the helical rib λ are presented.

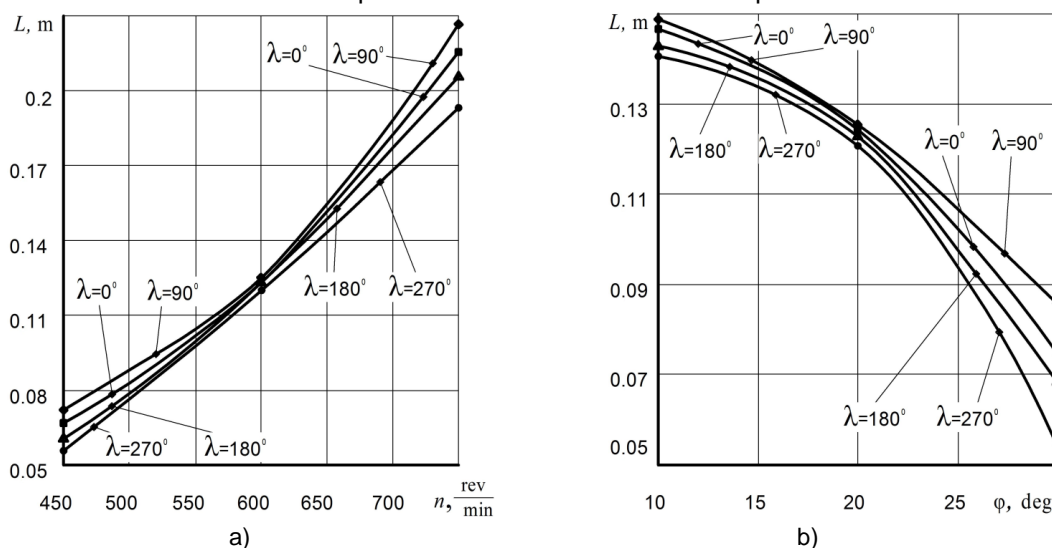


Fig. 2 - Graphical dependences of the free flight range of the material particle L on the rotation speed of the working body n (a) and the angle of inclination of the screw section axis to the horizon (b) at different angular positions λ of the particle at the time of separation from the screw edge to contact with the lower surface of the casing

When making calculations and studying the influence of one of the parameters on the value of L , the others were assumed constant and the value of their parameters was: $\xi = 22.6^\circ$; $\varphi = 20^\circ$; $R = 50$ mm; $n = 600$ rev/min.

From the analysis of the graphic dependences $L = f(n)$ we can conclude that the maximum value of L corresponds to the separation angle of the material particle from the helical rib $\lambda = 90^\circ$, ($\lambda = 0^\circ$ corresponds to the lower horizontal point of the casing) and will be $L = 0,228$ m for $n = 750$ rev/min (Fig. 2a). The minimum value of L will be $L = 0.193$ m for $\lambda = 270^\circ$.

At $n = 450$ rev/min the values of L for various values of λ are in the range $L = 0.056...0.072$ m, and at $n = 600$ rev/min the minimum range of variation is $L = 0.119...0.125$ m at various values of λ .

From the analysis of the graphical dependencies $L = f(\varphi)$, we can conclude that the maximum value of L corresponds to the minimum angle $\varphi = 10^\circ$ and will be $L = 0.144...0.148$ m (Fig. 2b) for various values of λ . With increasing angle φ , the value of L decreases, and at $\varphi = 30^\circ$ it is $L = 0.054...0.086$ m.

With an increase in the elevation angle ξ , the range of L values also increases for various angular positions λ at the moment of separation of the material particle from the helical rib.

A multivariate experiment was also performed. The range of parameters changes had the following limits: $450 \leq n \leq 750$ rev/min; $0 \leq \lambda \leq 270$ deg; $10 \leq \varphi \leq 30$ deg.

Based on the statistical processing of the regression equation to establish the change, L has the form:

$$L = -0.06384 + 0.304 \cdot 10^{-3} \cdot n + 0.1783 \cdot 10^{-2} \cdot \varphi - 0.1853 \cdot 10^{-4} \cdot \lambda + 0.715 \cdot 10^{-7} \cdot n^2 - 0.377 \cdot 10^{-5} \cdot n \cdot \varphi - 0.86 \cdot 10^{-7} \cdot n \cdot \lambda - 0.455 \cdot 10^{-4} \cdot \varphi^2 + 0.194 \cdot 10^{-5} \cdot \varphi \cdot \lambda - 0.48 \cdot 10^{-7} \cdot \lambda^2 \quad (21)$$

When establishing the influence of two factors on the value of L , the third is assumed to be unchanged with its average value. The average values of the factors are as follows: $n = 600$ rev/min; $\lambda \leq 270$ deg; $10 \leq \varphi \leq 30$ deg.

The surface response range of flight of the wheat grain L with a bulk weight of 720 kg/m³, is shown in Fig. 3.

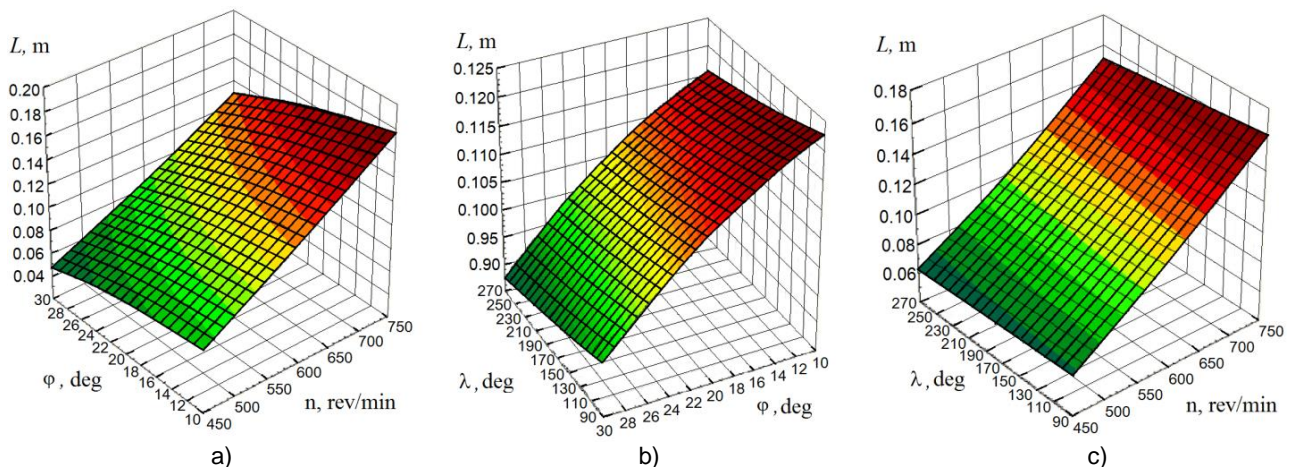


Fig. 3 – Response surfaces of the flight range of the material L : a - $L = f(\varphi; n)$; b - $L = f(\lambda; \varphi)$; c - $L = f(\lambda; \varphi)$

Based on the analysis of the regression equation and response surfaces, it was found that the maximum speed on the value of L has the rotation frequency of the working body n . So, for average values of λ and φ of growth of n from 450 to 750 rev/min, L increases by 0.092 m. The next in intensity of influence on the value of L is the angle of inclination of the screw section axis to the horizon φ . Its increase from 10° to 30° at average values of λ and n leads to a decrease in L by 0.028 m. The angle λ has a minimal effect on L , whose growth from 90° to 270° for average values of φ and n leads to a decrease in L by 0.009 m.

The data obtained must be taken into account when designing such a sectional screw working body. Based on the most unfavourable option in this range of parameters, the distance between the ends of adjacent screw ribs δ should not exceed 0.04 m.

Experimental studies to determine the power for the transportation of grain material also shown that for $n = 600$ rev/min with a gap of $\delta = 14$ mm the power is about $N = 1.2$ kW; at $\delta = 28$ mm - $N = 1.7$ kW; at $\delta = 42$ mm - $N = 3.2$ kW. Therefore, it is rational to choose a gap value δ within 0.01...0.03 mm.

The maximum productivity of the flexible screw conveyor was within the speed of rotation of the working body 600... 700 rev/min respectively 6.5... 7.7 m³/h.

A comparison of the results of theoretical and experimental studies showed that at $n = 600$ rev/min; $\varphi = 20^\circ$ and various λ values, the discrepancy between the obtained data is 3.8%...14.7%.

Therefore, theoretical studies that can be applied to a wider range of changes in the structural and kinematic parameters of the working body with articulated sections have been carried out.

CONCLUSIONS

The article presents the results of theoretical and experimental studies of the working body of a flexible screw conveyor made of separate sections, which are hinged to each other.

Based on the derived equations of a particle motion of material between adjacent screw sections was found the dependence of their flight distance L from the rotational speed of the working body n , its angle to the horizon φ and different angular positions of the particle λ on the helical rib which moves in the flow of grain material at the moment of its separation from the helical rib.

Based on the proposed methodology, experimental studies were carried out, the results of which show that for the factor field the parameter changes are $450 \leq n \leq 750$ rev/min; $0 \leq \lambda \leq 270$ deg; $10 \leq \varphi \leq 30$ deg, the value of L varies in the range from 0.042 to 0.188 mm.

Taking into consideration the sharp increase in power costs for the material transportation process at $\delta > 0.032$, the gap value δ should be chosen within 0.01...0.03 mm.

Based on comparisons of the results of theoretical and experimental studies at $n = 600$ rev/min; $\varphi = 20^\circ$ and various values of λ , their divergence is 3.8%...14.7%.

REFERENCES

- [1] Baranovsky V.M., Hevko R.B., Dzyura V.O., Klendii O.M., Klendii M.B., Romanovsky R.M., (2018), Justification of rational parameters of a pneumoconveyor screw feeder, *INMATEH-Agricultural engineering*, vol.54, no.1, pp.15-24, ISSN 2068 – 2239, Bucharest / Romania;
- [2] Haydl H.M., (1986), Design aspects of large-diameter tubular conveyor galleries, *Proceedings of the institution of civil engineers, Part 1 – Design and construction*, vol.80, pp. 633-639, ISSN 0307-8353, London / England;
- [3] Hevko B.M., Hevko R.B., Klendii O.M., Buriak M.V., Dzyadykevych Y.V., Rozum R.I., (2018), Improvement of machine safety devices, *Acta Polytechnica, Journal of Advanced Engineering*, Vol.58, no.1, pp.17-25, ISSN 1805-2363, Prague / Czech Republic;
- [4] Hevko R.B., Yazlyuk B.O., Liubin M.V., Tokarchuk O.A., Klendii O.M., Pankiv V.R., (2017), Feasibility study of mixture transportation and stirring process in continuous-flow conveyors, *INMATEH: Agricultural Engineering*, vol.51, no.1, pp.49-59, ISSN 2068 – 2239, Bucharest / Romania;
- [5] Hevko R.B., Liubin M.V., Tokarchuk O.A., Lyashuk O.L., Pohrishchuk B.V., Klendii O.M., (2018), Determination of the parameters of transporting and mixing feed mixtures along the curvilinear paths of tubular conveyors, *INMATEH: Agricultural Engineering*, vol.55, no.2, pp.97-104, ISSN 2068 – 2239, Bucharest / Romania;
- [6] Hevko R.B., Strishenets O.M., Lyashuk O.L., Tkachenko I.G., Klendii O.M., Dzyura V.O., (2018), Development of a pneumatic screw conveyor design and substantiation of its parameters, *INMATEH: Agricultural Engineering*, vol.54, no.1, pp.153-160, ISSN 2068 – 2239, Bucharest / Romania;
- [7] Hevko R.B., Zalutskyi S.Z., Hevko M.R. (2014), Design development and manufacturing technology of a screw working body with an elastic surface (Розробка конструкції та технологія виготовлення шнекового робочого органу з еластичною поверхнею), *Bulletin of the Engineering Academy of Ukraine (Вісник інженерної академії України)*, vol. 1, pp.152-159, Kiev / Ukraine;
- [8] Hevko R.B., Zalutskyi S.Z., Hladyo Y.B., Tkachenko I.G., Lyashuk O.L., Pavlova O.M., Pohrishchuk B.V., Trokhaniak O.M., Dobizha N.V., (2019), Determination of interaction parameters and grain material flow motion on screw conveyor elastic section surface, *INMATEH: Agricultural Engineering*, vol.57, no.1, pp. 123-134, ISSN 2068 – 2239, Bucharest / Romania;
- [9] Hevko R.B., Klendii M.B., Klendii O.M. (2016), Investigation of a transfer branch of a flexible screw conveyor, *INMATEH: Agricultural Engineering*, vol. 48, no.1, pp. 29-34, ISSN 2068 – 2239, Bucharest / Romania.

- [10] Lech M., (2001), Mass flow rate measurement in vertical pneumatic conveying of solid, *Powder Technology*, Vol.114, Issues 1–3, pp. 55-58, ISSN: 0032-5910;
- [11] Loveikin V., Rogatynska L., (2011), A Model of Loose Material Transportation by Means of High-Speed Conveyers with Elastic Operating Devices (Модель транспортування сипкого вантажу швидкохідними гвинтовими конвеєрами з еластичними робочими органами), *Bulletin of I. Puluji Ternopil National Technical University (Вісник ТНТУ ім. І. Пулюя)*, vol.16, pp.66-70, ISSN 2522-4433, Ternopil / Ukraine;
- [12] Lyashuk O.L., Rogatynska O.R., Serilko D.L., (2015), Modelling of the vertical screw conveyor loading, *INMATEH Agricultural Engineering*, vol.45, no.1, pp.87-94, ISSN 2068 – 2239, Bucharest / Romania;
- [13] Lyashuk O.L., Sokil M.B., Klendiy V.M., Skyba O.P., Tretiakov O.L., Slobodian L.M., Slobodian N.O., (2018), Mathematical model of bending vibrations of a horizontal feeder-mixer along the flow of grain mixture, *INMATEH Agricultural Engineering*, vol.55, no.2, pp.35-44, ISSN 2068 – 2239, Bucharest / Romania;
- [14] Lyashuk O.L., Vovk Y.Y., Sokil M.B., Klendii V.M., Ivasechko R.R., Dovbush T.A., (2019), Mathematical Model of a Dynamic Process of Transporting a Bulk Material by Means of a Tube Scraping Conveyor, *Agricultural Engineering International: CIGR Journal*, vol. 21, no. 1, pp. 74-81;
- [15] Manjula E.V.P.J., Hiromi W.K. Ariyaratne, Ratnayake Chandana, Morten C. Melaaen, (2017), A review of CFD modelling studies on pneumatic conveying and challenges in modelling offshore drill cuttings transport, *Powder Technology*, Vol.305, pp.782-793, ISSN 0032-5910;
- [16] Mondal D., (2018) - Study on filling factor of short length screw conveyor with flood-feeding condition, *Mater. Today Proc.*, vol.5, pp.1286–1291, ISSN: 2214-7853;
- [17] Naveen Tripathi, Atul Sharma, S.S. Mallick, P.W. Wypych, (2015), Energy loss at bends in the pneumatic conveying of fly ash, *Particuology*, vol.21, pp. 65-73, ISSN 1674-2001;
- [18] Owen Philip J., Cleary Paul W., (2010), Screw conveyor performance: comparison of discrete element modelling with laboratory experiments. *Progress in computational fluid dynamics*, vol.10, Issue 5-6, pp.327-333, ISSN 1741-5233, Geneva / Switzerland;
- [19] Qi J., Meng H., Kan Z., Li C., Li Y., (2017), Analysis and test of feeding performance of dual-spiral cow feeding device based on EDEM, *Trans. Chin. Soc. Agric. Eng.*, vol.33, pp.65–71, ISSN 1002-6819;
- [20] Pylypaka S.F., Nesvidomin, V.M., Klendii M.B., Rogovskii I.L., Kresan T.A., Trokhaniak V.I., (2019), Conveyance of a particle by a vertical screw, which is limited by a coaxial fixed cylinder, *Bulletin of the Karaganda University. «Mathematics» series*. vol. 95, no. 3, pp. 129-139, ISSN: 2518-7929;
- [21] Rogovskii I.L., Titova L.L., Davydenko O.O., Trokhaniak V.I., Trokhaniak O.M., (2019), Technology of Producing Reinforced Concrete Columns of Circular Cross-Sectional and Investigation of Their Strain-Stress State at Transverse-Longitudinal Bending, *Acta Polytechnica, Journal of Advanced Engineering*, 59(5), pp.510-517, ISSN 1805-23, Prague / Czech Republic;
- [22] Rogovskii I.L., Titova L.L., Trokhaniak V.I., Rosamaha Yu.O., Blesnyuk O.V., Ohienko A.V., (2019), Engineering management of two-phase coulter systems of seeding machines for implementing precision farming technologies, *INMATEH: Agricultural Engineering*, vol. 58, issue 2, pp. 137-146, ISSN 2068 – 2239, Bucharest / Romania;
- [23] Roberts Alan W., Bulk Solids, (2015), Optimizing Screw Conveyors, *Chemical engineering*. vol.122(2), pp.62-67, New York / USA;
- [24] Tsarenko O.M., Voityuk L.M., Shvayko M.V. and others, (2003), Mechanical-technological properties of agricultural materials: course-book (Механіко-технологічні властивості сільськогосподарських матеріалів: підручник), *published by Meta (видавництво Мета)*, 448p., Kiev / Ukraine;
- [25] Tian Y., Yuan P., Yang F., Gu J., Chen M., Tang J., Su Y., Ding T., Zhang K., Cheng Q., (2018), Research on the Principle of a New Flexible Screw Conveyor and Its Power Consumption, *Applied Sciences*, vol.8, no.7, ISSN 2076-3417;
- [26] Yao Y.P., Kou Z.M., Meng W.J., Han G., (2014), Overall Performance Evaluation of Tubular Scraper Conveyors Using a TOPSIS-Based Multiattribute Decision-Making Method, *Scientific World Journal*, New York / USA;
- [27] Wang D.-X., (2012), Research on Numerical Analysis and Optimal Design of the Screw Conveyor, *Univ. Technol.*, vol.27, pp.32–36.

RESULTS OF THE NUTRITIONAL PRESERVATION RESEARCH OF THE ALFALFA LAYING ON STORAGE WITH TWO-PHASE COMPACTION

/

РЕЗУЛЬТАТИ ДОСЛІДЖЕННЯ ЗБЕРЕЖЕНОСТІ ПОЖИВНИХ РЕЧОВИН ЛЮЦЕРНИ ПРИ ЗАКЛАДЦІ НА ЗБЕРІГАННЯ МЕТОДОМ ДВОСТАДІЙНОГО УЩІЛЬНЕННЯ

Milko D.O.¹⁾, Sclyar O.H.¹⁾, Sclyar R.V.¹⁾, Pedchenko G.P.¹⁾,
Zhuravel D.P.¹⁾, Bratishko V.V.²⁾

¹⁾ Dmytro Motornyi Tavria State Agrotechnological University / Ukraine

²⁾ National University of Life and Environmental Sciences of Ukraine / Ukraine

*E-mail: milkodmitry@gmail.com

DOI: <https://doi.org/10.35633/inmateh-60-30>

Keywords: *coefficients of nutrients preservation, procurement of fodder, storing of alfalfa, cost of fodder procurement.*

Abbreviations: *CP.CFi – crude fibre preservation coefficient; CP.CP – crude protein preservation coefficient; CP.NFE – nitrogen-free extracts preservation coefficient; CP.CF – crude fat preservation coefficient.*

ABSTRACT

In modern manufacturing of livestock production, the outstanding value is allocated for a food supply. The main criterion for evaluating the quality of feed components is the nutrient content of the feed ration. However, in the process of the storage, the maintenance of the nutritious substances decreases for various reasons that are leading to decreasing livestock efficiency and increasing the cost. The results of the use of a two-phase compaction of the forage vegetable components on the example of the alfalfa are given in the article. The dependence coefficient of the nutritional preservation on density of the alfalfa put on storage are also presented in this article.

The applied method and the results obtained can be used in the development and design offices to create new equipment based on the two-phase compaction of the fodder vegetable component mixes by preparing them for storage.

The application of this method brings to decreasing losses of nutrients in the storage process which reduces the components cost in total with increasing additional weights and the milk productivity.

АНОТАЦІЯ

У сучасному промисловому виробництві продукції тваринництва видатне значення відводиться на кормову базу. Основним критерієм оцінки якості кормових компонентів є вміст поживних речовин у кормовому раціоні. Однак в процесі зберігання вміст поживних речовин знижується з різних причин, що призводить до зниження продуктивності тварини і підвищення собівартості продукції. У статті наведені результати використання двохстадійного ущільнення рослинних компонентів кормів на прикладі люцерни. Також представлені залежності коефіцієнтів збереження поживних речовин від щільності закладеної на зберігання люцерни. Використаний метод і отримані результати можуть бути використані в розробках конструкторських бюро для створення нової техніки заснованої на двохстадійному ущільненні рослинних компонентів кормових сумішей при заготівлі їх до зберігання. Застосування даного методу призводить до зниження втрат поживних речовин в процесі зберігання, що зменшує витрати на заготівлю компонентів в сукупності з підвищенням приростів і надоїв.

INTRODUCTION

The preservation of nutrients in feed crops in the storage process is of great importance affecting the vital functions of the livestock, their productivity and the quality of the obtained products (*Liu et al., 2018; Mikula et al., 2018; Katsande et. al., 2019*). To a large extent the preservation of the feed components depends on the conditions of their storage and compacting (*Wang et al., 2010; Santos et al., 2016*).

Taking into account the peculiarities of the voluminous fodder structure, it should be noted that in order to achieve the high-quality plant raw materials indices when laying in storage the degree of the compaction is of particular importance. It is also necessary to take note of the effect of the residual relaxation which occurs after the removal of the load and, as a result, a retraction of the oxygen in the air mixtures which leads to the negative consequences namely to the oxidative processes that increase in general the nutritional value of canned food (McCormick *et al.*, 2011; Maraldi *et al.*, 2016; Coblenz *et al.*, 2015, 1996; Stoškus *et al.*, 2019). As a result of the dairy cows activity, alcohols and other oxygen-containing forms are released as well. Lower concentrations of highly reactive alkenes and aldehydes were also detected (Malkina *et al.*, 2011).

MATERIAL AND METHODS

The technology of a two-phase compaction is realized by a constructive technological line which is shown in Fig.1, a. It allows to decrease the relaxation effect after removal and find the way out from a current situation. Two-phase compaction technology increases the quality of the feed preservation and declines its cost. An experimental installation of the two-phase compaction line is shown in Fig.1, b.

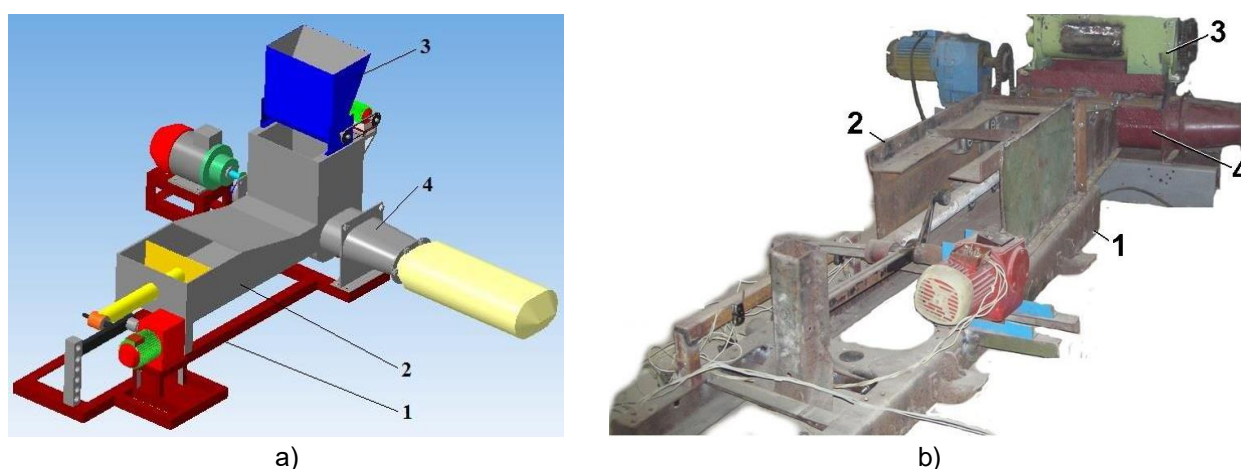


Fig.1 – Laboratory unit

a) Structural diagram b) Main view

1 – frame; 2 – squeezer of preliminary compaction of plant mass; 3 – dozer of preservatives; 4 – twin-screw compactor

The research is based on revealing the influence of the constructive and technological parameter line on the quality indicators of the preserved plant raw materials and on comparing them with the traditional harvesting and storage methods.

The laboratory installation consists of the squeezer of a preliminary compaction, 2, (first phase of compaction) and a two-screw compactor 4, which are mounted on the frame 1. At the same time on the two-screw compactor is mounted a dozer of free-flowing preservatives, 3. The installation will be started by the asynchronous electric motors. The drive mechanism of the preliminary compaction squeezer is a screw, a dozer of preservatives and the two-screw compactor are positioned catenary. The piston sizes of the preliminary compaction squeezer were 300x400 mm, with the stroke of the piston 700 mm. The diameter of the screws was 150 mm, the length was 800 mm and the overlap value was 50 mm. The diameter of the dosing drum was 200 mm, with a cell diameter of 3 mm and a depth of 1.5 mm. The alfalfa in the flowering phase was used during the experiment.

The preservation quality of plant materials after two months of storage was investigated. The combustion heat, total nitrogen and crude fibre were measured.

RESULTS AND DISCUSSION

The ash-content research solution is presented in Fig. 2 and the results are given in Table 1. As a result of carrying out the chemical analyses, combustion heat of vegetable raw material samples was defined and the results are given in Table 2.

According to the Kjeldahl method, the presented samples of plant materials were analyzed for the content of crude fat, crude fiber and total nitrogen.

Table 1

The results of carrying out chemical analyses on the determination of vegetable raw materials ash-content

Sample no.	Mass of crucible [g]	Mass of crucible with hitch [g]	Mass of crucible with hitch after desiccation [g]	Mass of hitch [g]	Mass of ash [g]	Ash-content [%]	Average ash-content [%]
Medick condensed after storage							
1	87.7602	90.8674	88.4526	3.1072	0.6924	22.28	18.97
2	90.4581	93.4624	91.0020	3.0043	0.5439	18.10	
3	78.4418	81.6450	78.9714	3.2032	0.5296	16.53	

The results of the experiments proved that the crude fat content in the samples made up 2.25% as it was determined by the Soxhlet method.

Table 2

The results of carrying out chemical analyses on the plant materials combustion heat definition

Sample no.	Hitch, n [g]	Normal of Mohr's salt, K	Control, [ml]	Volume of solution of Mohr's salt for the sample [ml]	Heat of combustion, Q [kcal/g]	Heat of combustion. Average value Q_{ave} [kcal/g]
1	0.0250	24.6	51.4	24.3	4.05	4.047
2	0.0227			24.6	4.01	
3	0.0212			25.5	4.08	



a)



b)



c)

Fig. 2 – Carrying out chemical researches on ash-content measurements

a) drying of samples; b) burning of samples in the muffle furnace; c) cinder remains

The results of the vegetable raw materials researches on the crude cellulose content are presented in Table 3.

Table 3

The results of carrying out chemical analyses on the crude cellulose content determination

Sample no.	Hitch, n [g]	Normal of Mohr's salt, K	Control, [ml]	Volume of solution of Mohr's salt for the sample [ml]	Content of crude fibre [%]	Average value [%]
1	0.0510	24.6	48.5	36.4	16.01	20.22
2	0.0511			31.0	23.12	
3	0.0552			30.9	21.52	

Due to chemical expertise, the content of total nitrogen was determined, and the results of these tests are given in Table 4.

Table 4

The results of carrying out chemical analyses on the total nitrogen content determination

Sample no.	Variant 1	Variant 2	Variant 3	Average value	Delta	Content of nitrogen [%]	Average content of nitrogen [%]
Alfalfa condensed after harvesting							
1	2.8	2.6	2.7	2.70	3.13	2.44	2.45
2	2.6	2.8	2.8	2.73	3.10	2.41	
3	2.6	2.6	2.7	2.63	3.20	2.49	
Control	5.8	5.8	5.9	5.83	-	-	-

Process of carrying out the titration of the surplus of the sulfuric acid alkali solution is presented in Fig. 3.



Fig. 3 – The process of determining the total nitrogen content by titration

CONCLUSIONS

The chemical composition analysis of the fodder material was carried out in the Dmytro Motornyi Tavria State Agrotechnological University chemical laboratory. The results of the nutrient preservation depending on feed density (extent of compaction) are presented in Fig.4.

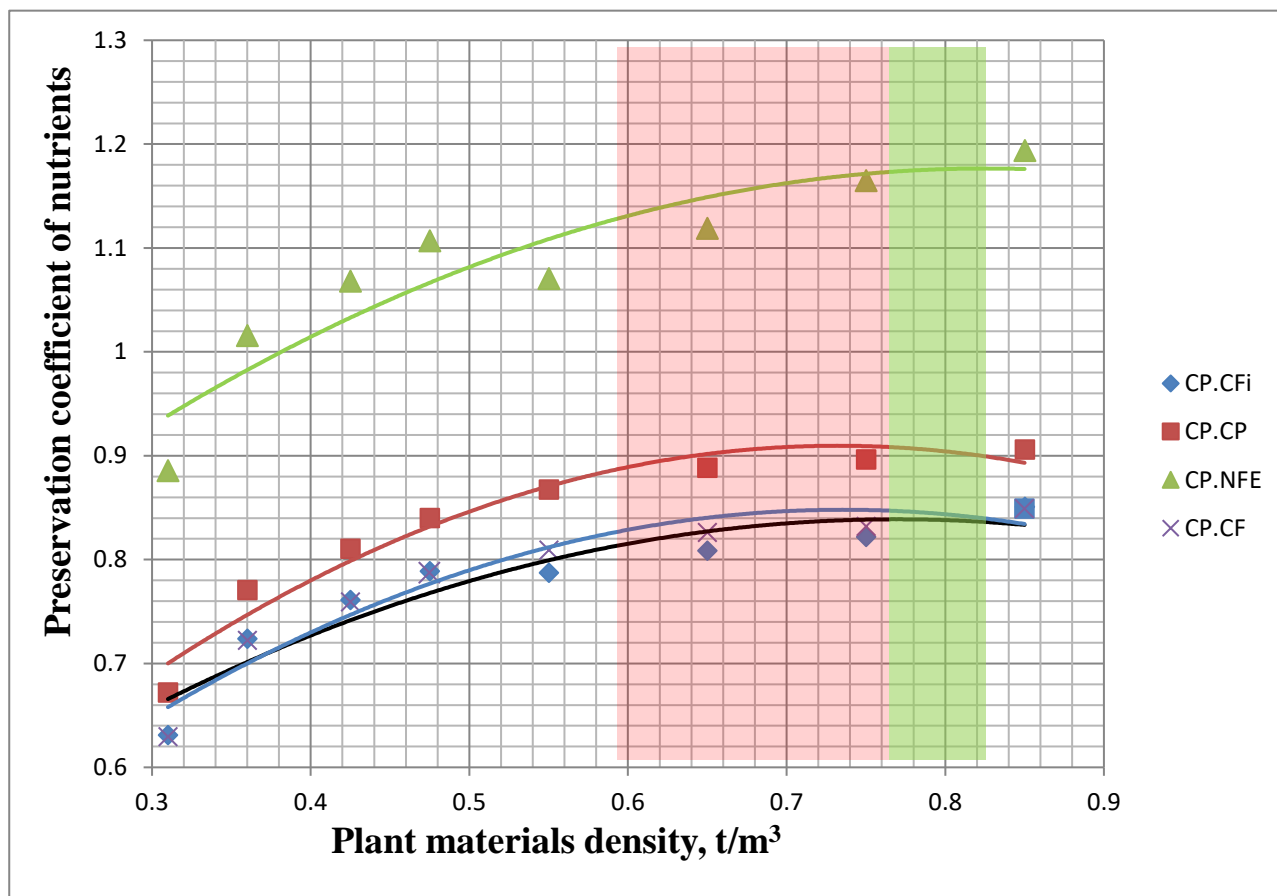


Fig. 4 – Results of determination of plant materials safety coefficients

On the basis of the vegetable raw materials chemical analysis put in the polymeric storages on the offered technology, the following data were obtained: the content of the crude fat (CF) was 2.25% by definition of the Soxhlet extractor, the crude fibre content (CFi) was 20.22%, the crude protein content (CP) was 14.5%. The submitted data confirm a high quality of the received fodder weight. Also, the high quality confirmed the production tests in the farms of the Zaporizhia and Kherson regions.

The data obtained show, that the degree of compaction of plant materials has an optimum, being at the level of 0.78 - 0.82 t/m³. As the density of plant materials increases during packing, there is a destruction of its cellular structure, which means disintegration and oxidation of nutrients. On the contrary, at the insufficient compaction, a considerable development of the pathogenic micro flora occurs which leads to the development of putrefactive and other anaerobic bacteria.

ACKNOWLEDGMENTS

The authors thank the chemical laboratory staff of the University of the Dmytro Motornyi Tavria State Agrotechnological University for assistance with plant materials preparing and chemical analysis.

REFERENCES

- [1] Coblenz W.K., Fritz J.O. and others, (1996), Quality Changes in Alfalfa Hay During Storage in Bales. *Journal of Dairy Science*, Vol. 79, No. 5, pp. 873-885.
- [2] Coblenz, W.K., Coffey K.P. and others, (2015), Storage characteristics, nutritive value, and fermentation characteristics of alfalfa packaged in large-round bale sand wrapped in stretch film after extended time delays. *Journal of Dairy Science*, Vol. 99, No. 5, pp. 1-15.

- [3] Katsande S., Baloyi J.J. and others, (2019), Rumen degradability of selected forage legumes using the in Sacco nylon bag technique. *Animal Nutrition and Feed Technology*, Vol. 19, No. 1, pp. 57-63.
- [4] Liu Q., Wang C. and others, (2018) Effects of dietary protein level and rumen-protected pantothenate on nutrient digestibility, nitrogen balance, blood metabolites and growth performance in beef calves. *Journal of Animal and Feed Sciences*, Vol. 27, No. 3, pp. 202-210.
- [5] Malkina I.L., Kumar A. and others, (2011), Identification and quantitation of volatile organic compounds emitted from dairy silages and other feedstuffs. *Journal of Environmental Quality*, Vol. 40, pp. 28-36.
- [6] Maraldi M., Molari L. and others, (2016), Method for the characterization of the mechanical behaviour of straw bales. *Bio systems engineering*, Vol. 151, pp. 141 -151.
- [7] McCormick M.E., Han K.J. and others, (2011), Forage conservation efficiency and lactation response to bahia grass conserved as barn-stored hay, outdoor-stored hay, or baleage. *Journal of Dairy Science*, Vol. 94 No. 5, pp. 2500-2507.
- [8] Mikuła R., Pruszyńska-Oszmałek E. and others, (2018), Effect of different pre-calving feeding strategies on the metabolic status and lactation performance of dairy cows. *Journal of Animal and Feed Sciences*, Vol. 27, No. 4, pp. 292-300.
- [9] Stoškus R., Jatkauskas J. and others, (2019), The effect of mixed bacterial inoculant on the microbial population and aerobic stability of lucerne and maize baleage. *Journal of Animal and Feed Sciences*, Vol. 28, No. 4, 383-391.
- [10] Santos M.C., L. Kung Jr. (2016), The effects of dry matter and length of storage on the composition and nutritive value of alfalfa silage. *Journal of Dairy Science*, Vol. 99 no. 7, pp. 1-4.
- [11] Wang J., Wang, J.Q. and others, (2010), Effect of storing total mixed rations anaerobically in bales on feed quality. *Animal Feed Science and Technology*, Vol 161, pp. 94-102.

OPTIMIZATION RESEARCH OF FERTILIZER GUIDING MECHANISM BASED ON THE DISCRETE ELEMENT METHOD

基于离散元法的导肥装置优化研究

Hong Jian Zhang¹⁾, Yu Feng Li¹⁾, Chun Bao Xu¹⁾, Shuang Xi Liu^{1,2)}, Ze Kun Quan¹⁾, Jin Xing Wang^{*1,2)} ¹

¹⁾ College of Mechanical and Electronic Engineering, Shandong Agricultural University, Taian 271000, China;

²⁾ Shandong Provincial Key Laboratory of Horticultural Machinery and Equipment, Taian 271000, China;

Tel: +86 05388246826; E-mail: jinxingw@163.com

DOI: <https://doi.org/10.35633/inmateh-60-31>

Keywords: fertilizer guiding mechanism, DEM, simulation optimization, discrete coefficient, uniformity

ABSTRACT

Discrete Element Method was used to study the fertilizer guiding mechanism of double-row orchard ditching fertilizer to solve certain problems, such as the low uniformity of fertilization in orchard. Firstly, on the basis of studying the existing B fertilizer guiding mechanism, A and C fertilizer guiding mechanisms were proposed, and three virtual simulation models of the fertilizer guiding mechanism were established. Secondly, the physical parameters of the fertilizer particles were analysed, combined with the dynamic analysis of the falling process of the fertilizer particles, the dynamic model of the fertilizer particles in the three fertilizer guiding mechanisms was established. Finally, three kinds of fertilizer guiding mechanisms A, B and C were analyzed by the discrete element simulation experiment, and the C fertilizer guiding mechanism was the best. Then, the C fertilizer guiding mechanisms under different curvature radius were simulated, the discrete coefficients of the edge region and the middle region were used to evaluate the fertilizer uniformity, and the optimal curvature radius of the C fertilizer guiding mechanism was obtained. The results of simulation and prototype orchard experiments show that the dispersion coefficients of the edge region and the middle region of the C fertilizer guiding mechanism are the smallest, the uniformity of fertilization is the highest, the A fertilizer guiding mechanism is the second, the B fertilizer guiding mechanism is the lowest; in the C fertilizer guiding mechanism under different radius of curvature, when the radius of curvature is 600mm, the dispersion coefficients of the edge region and the middle region of the C fertilizer guiding mechanism are the smallest, and the fertilization uniformity is the highest; after the optimization, the discrete coefficient is reduced from 0.51 to 0.26, and the fertilization uniformity is increased by 49.02%. This study has significant potential to design and processing of orchard ditching fertilizer applicator.

摘要

针对果园开沟施肥不均匀的问题, 采用离散元仿真设计对果园开沟施肥机的导肥机构进行优化。首先, 在研究现有 B 型导肥机构基础上, 提出 A 型和 C 型导肥机构, 建立三种导肥机构的虚拟仿真模型。其次, 分析肥料颗粒的物理参数, 结合肥料颗粒下落过程中的动力学分析, 建立肥料颗粒在三种导肥机构中的动力学模型。最后, 先对 A 型、B 型、C 型三种导肥机构进行离散元仿真试验, 分析优化出最佳 C 型导肥机构; 后对不同曲率半径下的 C 型导肥机构进行施肥均匀度仿真试验, 利用边缘区域与中间区域的变异系数评价施肥均匀度, 分析优化出 C 型导肥机构的最佳曲率半径。仿真与样机果园试验结果表明: C 型导肥机构边缘区域与中间区域离散系数最小, 施肥均匀度最高, A 型导肥机构次之, B 型导肥机构最低; 在不同曲率半径的 C 型导肥机构中, 曲率半径为 600mm 时, C 型导肥机构边缘区域与中间区域离散系数最小, 施肥均匀度最高; 优化后变异系数由 0.51 减小到 0.26, 施肥均匀度提高 49.02%。为果园开沟施肥机设计加工提供科学依据。

INTRODUCTION

Fertilizer is the food of fruit trees. Fertilization of fruit trees is the key operation link in fruit tree production. The quality of fertilization directly affects the absorption of nutrients in fruit trees. Rational fertilization is the basis for high quality and high yield of fruit trees (Yin Yan Shi et al, 2018; Xiao Chun Zheng et al, 2011; Da Yong Han et al, 2010). Fruit trees fertilizers predominantly are inorganic fertilizer and organic fertilizer. Inorganic fertilizer is mainly chemical fertilizer, characterized by strong fertility and fast fertilizer efficiency, but it can easily cause soil structure change, soil organic matter content decline, tree growth and fruit quality reduction.

¹ HongJian Zhang, Ph.D. Stud. Eng.; YuFeng Li, M.S. Stud. Eng.; ChunBao Xu, M.S. Stud. Eng.; ShuangXi Liu, As. Ph.D. Eng.; ZeKun Quan, M.S. Stud. Eng.; JinXing Wang, Prof. Ph.D. Eng.

The application of organic fertilizer can help improve soil physicochemical properties, improve leaf physiology, increase fruit yield and improve fruit quality (Chen Ma et al, 2017; JuSheng Gao et al, 2005; Ning Wu et al, 2016). Fertilization uniformity is a key factor affecting the effect of fertilization operations, and it is an important indicator for evaluating the performance and effectiveness of working tools (Jing Ma et al, 2016; Zhou et al, 2009; Ming Li et al, 2016; LiYe Zhao et al, 2002). Patterson et al (1962) studied the theoretical motion model and motion mechanism of various fertilizer granules, simulated and tested the fertilizer granule distribution and fertilization uniformity, and analysed the average error between the theoretical value and the actual measured value, which laid the foundation for the mathematical theoretical model of the fertilizer application machine. P. Van Liedekerke et al (2009) used the discrete element method to start the flow of granules from the container, and the plate and the inclined disk were used to simulate the flow of granules affected by the rotating disk. Artur Przywara et al (2015) studied the influence of the structure and operating parameters of the centrifugal disc spreader on the spatial distribution of the fertilizer, determined the rotational speed of the disc, the feed position of the fertilizer on the disc, the blade angle on the disc and the type of fertilizer had affected the spatial distribution of the fertilizer. Villette et al (2010) proposed a new method for simultaneously measuring the horizontal flow and vertical flow distribution of a disc-type fertilizer, paving the way for studying the distribution of fertilizer granules and testing the uniformity of fertilization. Aphale et al (2003) calculated and tested the trajectories of various fertilizer granules, and obtained the average error between the theoretical value and the actual measured value under different disk rotational speed conditions, which provided a theoretical basis for the test. Zhang Tao et al (2015) simulated the fertilization process of the fertilizer-discharging mechanism through discrete elements, formulated design variables and optimization targets, developed motion simulation software and parameterized platform, optimized the structural parameters of the fertilizer-discharging mechanism, and improved the uniformity of fertilization. Chen Xiongfei et al (2015) designed a two-stage spiral fertilizer device, and established a mathematical model of the single-circle discharge amount of the fertilizer-fertilizing spiral. It was determined through experiments that the two-stage spiral fertilizer-removing device had better fertilizer-removing effects for various forms and better adaptability with fertilizer. Yang Xinlun et al (2015) established the mathematical model of the blade type fertilizer mechanism, formulated the design variables and optimization objectives, developed the motion simulation software and the parameterization platform, and optimized the structural parameters of the blade type fertilizer removal mechanism. Yuan Wensheng et al (2018) designed a scoop wheel fertilizer discharge device and established the three-dimensional model for simulation of fertilizer, tested cavitation resistance and uniformity of the amount of fertilizer per entire fertilizer apparatus, and studied the fertilizer discharge effect of the fertilizer discharger under different rotation speeds of the fertilizer components. Lv Jinqing et al (2015) carried out simulation tests on the screw-type fertilizer discharge mechanism under different working speed conditions, accurately analysed the mathematical relationship between the rotational speed and the displacement, realized the optimal design of the screw-type fertilizer discharge mechanism, and improved the uniformity of fertilization.

After a comprehensive analysis of research status, and the effect of fertilizer-discharging mechanism on fertilization uniformity, a conclusion was reached that, at present, the research on the effect of fertilizer-dispensing mechanism on fertilization uniformity is mature, but the research on the influence of fertilizer guiding mechanism on fertilization uniformity is still in its infancy. Based on the study of the influence of the fertilizer guiding mechanism on fertilization uniformity, this paper optimizes the existing fertilizer guiding mechanism and provides a theoretical basis for the design and processing of the orchard ditching fertilizer machine.

MATERIALS AND METHODS

Machine Structure

Double-row orchard ditching fertilizer overall structure is shown in Fig.1 and Fig.2, mainly configured by the rack, fertilizer box, transmission, ditching mechanism, fertilizer mechanism, fertilizer guiding mechanism, soil covering machine and the technical parameters of the whole machine are shown in Table 1.

Main technical parameters		
Item	Parameters	Units
Supporting power	≥58	Kw
Outline size	3820×2040×2510	mm
Fertilization depth	0~500	mm
Fertilizer application amount	0.5~2	kg.m ⁻¹
Base fertilizer application amount	3~5	kg.m ⁻¹
Fertilizer box volume	650	L
Base fertilizer box volume	2500	L

Table 1

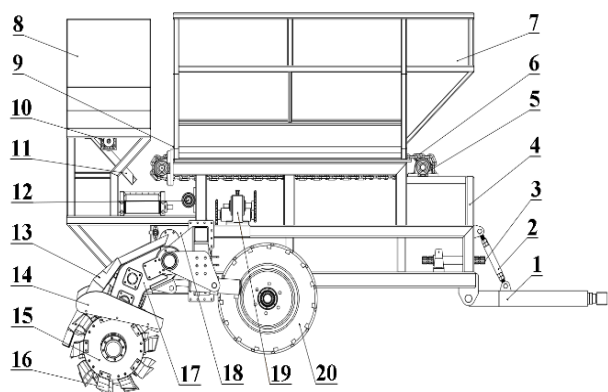


Fig. 1 - Main view of the machine

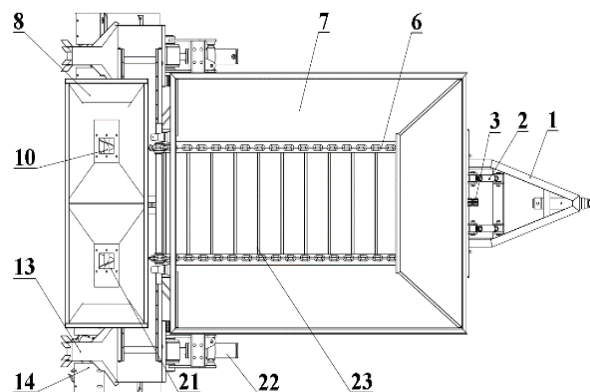


Fig. 2 - Vertical view of the machine

- 1) traction rack; 2) adjusting pull pipe; 3) drive shaft; 4) rack; 5) base fertilizer sprocket; 6) O-chain; 7) base fertilizer box; 8) fertilizer box; 9) base fertilizer outlet; 10) auger; 11) conveyor board; 12) side transmission box; 13) fertilizer guiding mechanism; 14) soil cover; 15) trench cutter disc; 16) trench cutter; 17) trench transmission box; 18) main transmission box; 19) middle transmission box; 20) wheel; 21) fertilizer outlet; 22) hydraulic cylinder; 23) base fertilizer scraper

Fertilizer Guiding Mechanism

The fertilization methods in the orchard mainly include the general application on the whole orchard, the application on the crown, the application on the ring ditch, the application on the strip ditch, the application on the radial ditch and the application in the holes. For new orchards with wide line spacing and wide plant spacing, strip-shaped furrow fertilization is often used. The strip-shaped furrow fertilization method requires strips of 1000~2000mm long, 300~400mm wide and 300~500mm deep between the rows of fruit trees, then fertilize and cover the soil (Biao Liu *et al*, 2017; WuZhen Qi *et al*, 2019).

Because the amount of fertilization in the orchard is large, in order to ensure the smooth fall of the fertilizer, the fertilizer guiding mechanism of the existing orchard trenching and fertilizing machine is mostly a trough-shaped structure, as shown in Fig. 3. Among them, the fertilizer-in port of the fertilizer guiding mechanism is connected with the fertilizer-out port of the fertilizer-discharging mechanism, and the fertilizer-out port of the fertilizer guiding mechanism is equal to the groove width. The fertilizer plug-in plate in the fertilizer guiding mechanism divides the fertilizer-transfer port and the fertilizer-out port into three parts.

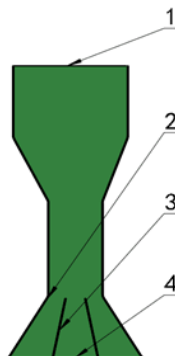


Fig. 3 - Diagrammatic sketch of fertilizer guiding mechanism

- 1) Fertilizer-in port; 2) Fertilizer-transfer port; 3) Fertilizer plug-in plate; 4) Fertilizer-out port

Parameters Determination of Fertilizer Granules Characteristics

The fertilizer granules used in the experiment were granular organic fertilizers. 100 granular organic fertilizers were randomly selected as the parameter measurement samples, which were placed on blank A4 paper and measured by image processing technology to obtain the accurate size of the granular organic fertilizer.

First, a black square of 10mm×10mm was fabricated on the red A4 paper as an area calibration, and blank A4 paper with area calibration was used as the background plate. Next, the parameter measurement was randomly scattered on the background board, and the original image of granular organic fertilizers was obtained. The colour difference between the test sample and the background plate was used, and a single original image was divided to obtain the threshold value of the other image, as shown in Fig. 4.

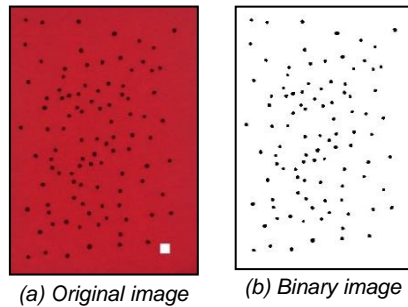


Fig. 4 - Original image and binary image of granular organic fertilizer

Finally, according to the area calibration on the background plate in the binary image, the equivalent diameter and circularity of the granular organic fertilizer were calculated. Also, the minimum equivalent diameter, the minimum circularity, the maximum equivalent diameter and the maximum circularity, the average equivalent diameter and the average circularity of the statistical parameter measurement sample were calculated, as shown in Table 2.

Table 2

Granular organic fertilizer	Parameter of granular organic fertilizer		
	Circumference C (mm)	Equivalent diameter \bar{D} (mm)	Circularity ϕ
Average value	9.16	2.92	0.93
Minimum value	7.60	2.42	0.90
Maximum value	11.92	3.79	0.97

It can be seen from Table 2 and Fig. 4 that the circularity of the 100-parameter measurement samples is 0.93, and the concentration is between 0.90 and 0.97. As the circularity of parameter measurement sample gets closer to 1, the closer the parameter measurement sample is to the sphere (Jin Yuan et al, 2014). Since the parameter measurement sample has a high circularity distribution, the granular organic fertilizer is assumed to be spherical during the simulation.

The granular organic fertilizer circularity distribution diagram was drawn, as shown in Fig. 5.

$$\text{Circularity: } \phi = 4\pi S/C^2 \tag{1}$$

$$\text{Equivalent diameter: } d = C/\pi \tag{2}$$

$$\text{The average diameter: } \bar{D} = D/N \tag{3}$$

$$D = \sum_{i=1}^N d_i \tag{4}$$

In equations (1), (2), (3), (4): S -the area of granular organic fertilizer; C - the circumference of granular organic fertilizer; N -the amount of granular organic fertilizer

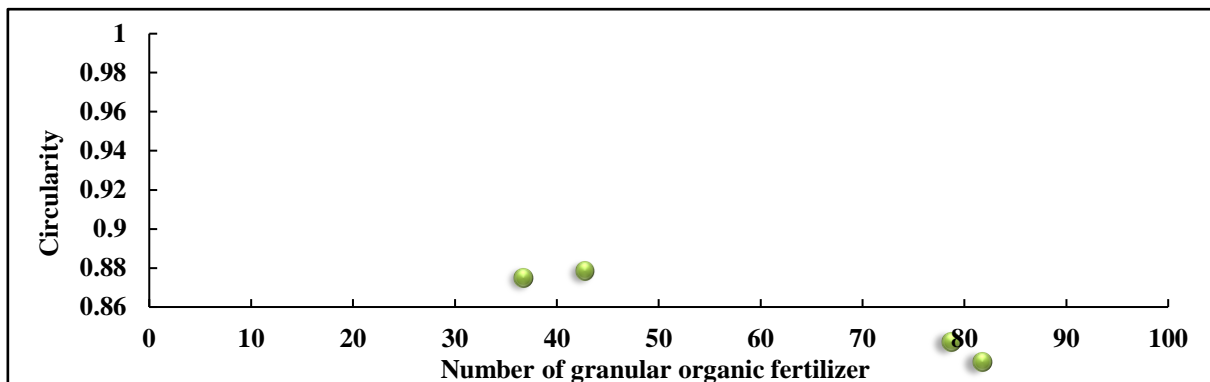


Fig. 5 - Circularity distribution of granular organic fertilizer

The Equation of Motion of Fertilizer Granules in the Fertilizer Guiding Mechanism

Granular organic fertilizers fall into the fertilizer guiding mechanism by means of fertilizer discharge mechanism, with a certain initial velocity v_p . After the granular organic fertilizer enters the fertilizer guiding mechanism, it is subjected to gravity G_p , buoyancy F_{fp} , and air resistance F_{zp} . After the interaction, it finally falls into the ditch of the orchard trenching and fertilizing machine. The specific process is shown in the Fig. 6 (INNS F.M. et al, 1962).

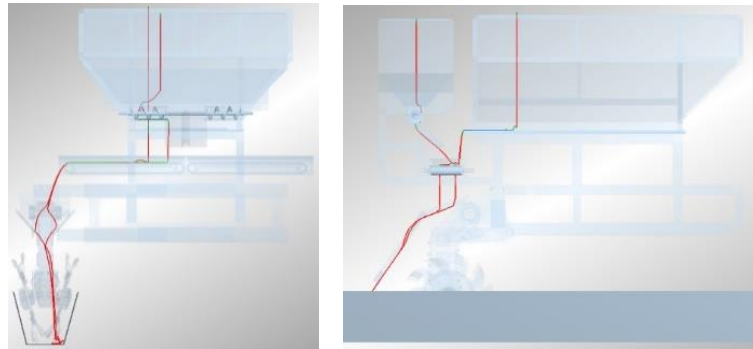


Fig. 6 - Falling process of fertilizer

Gravity: $G_p = \rho_p V_p g$ (5)

Buoyancy: $F_{fp} = \rho_a V_p g$ (6)

Air resistance: $F_{zp} = \frac{1}{2} K \rho_a S_p V_p^2$ (7)

Air resistance coefficient: $K = \frac{3}{8} C_D \rho_a \frac{1}{\rho_p r_p}$ (8)

There is a correlation between drag coefficient C_D and Reynolds number R_e :

$$R_e = 2 \frac{r_p v_p \rho_p}{\eta_a} \quad (9)$$

In equations (5), (6), (7), (8), (9):

ρ_p -granular organic fertilizer density; V_p -volume of granular organic fertilizer; ρ_a -air density;

η_a -aerodynamic viscosity; v_p -granular organic fertilizer velocity;

S_p -granular organic fertilizer frontal area; r_p -granular organic fertilizer radius; g -gravity acceleration;

Assuming that the positive direction of the Z axis is opposite to the direction of gravity of the granular organic fertilizer, the equation of motion of the granular organic fertilizer in the X, Y, and Z directions (Cunningham, F. M, 1963; Pitt, R. E., 1982) is:

X direction: $\frac{d^2x}{dt^2} = -K v_{Px} \sqrt{v_{Px}^2 + v_{Py}^2 + v_{Pz}^2}$ (10)

Y direction: $\frac{d^2y}{dt^2} = -K v_{Py} \sqrt{v_{Px}^2 + v_{Py}^2 + v_{Pz}^2}$ (11)

Z direction: $\frac{d^2z}{dt^2} = -K v_{Pz} \sqrt{v_{Px}^2 + v_{Py}^2 + v_{Pz}^2}$ (12)

In equations (10), (11), (12):

v_{Px} -the velocity component in the X direction;

v_{Py} -the velocity component in the Y direction;

v_{Pz} -the velocity component in the Z direction;

Fertilization Uniformity Evaluation

The granular organic fertilizer passes through the fertilizer guiding mechanism and finally falls into the ditch of the orchard ditching fertilizing machine. In order to evaluate the uniformity of fertilization, the distribution range of fertilizer in a ditch is selected as the sampling area, and meshing is performed according to 15 rows and 15 columns, as shown in Fig. 7. Among them, the width of the sampling area is the groove width, and the cell grid size is 20mmx20mm.

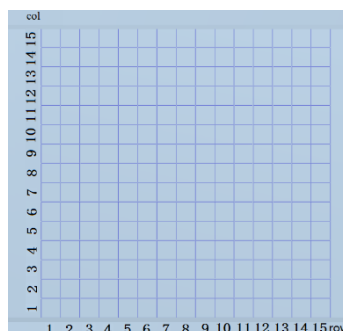


Fig. 7 - Mesh partition of sampling regions

The discrete coefficient CV is used as a measure of the uniformity of fertilizer distribution.

The equations for calculating the discrete coefficient is:

$$CV = \frac{S}{\bar{q}} \tag{13}$$

$$S = \sqrt{\frac{\sum_{i=1}^n (q_i - \bar{q})^2}{n-1}} \tag{14}$$

$$\bar{q} = \sqrt{\frac{\sum_{i=1}^n (q_i)^2}{n}} \tag{15}$$

In equations (13), (14), (15): S - standard deviation; \bar{q} - the average number of samples in the unit area of the mesh granular organic fertilizer; n - total number of cell grids in the entire sampling area; q_i - the number of samples in the i -th unit lattice region granular organic fertilizer;

To better reflect the distribution of granular organic fertilizer in the entire sampling area, the discrete coefficients of the 1th row, and the 15th row are selected as a reflection of the edge area of the organic fertilizer distribution, discrete coefficients of 5th row, 8th row, 11th row are used as a parameter to reflect the uniformity of granular organic fertilizer distribution in the middle region.

Experiment and Analysis

Firstly, the fertilizer guiding mechanism was introduced into the EDEM simulation software and the relevant parameters were set. In order to obtain the effect of the granular organic fertilizer passing through the fertilizer guiding mechanism into the ditch, an open groove of 1000mm in length, 300mm in width and 400mm in depth was set to simulate the ditching of the ditching and fertilizing machine. The open groove was located directly below the export of the fertilizer guiding mechanism, wherein the axis was in the same vertical plane as the central axis of the fertilizer guiding mechanism, and the bottom of the opening groove was 200mm away from the export of the fertilizer guiding mechanism. Secondly, the fertilizer guiding mechanism was set as a random granules’ generator, so that granular organic fertilizer was randomly generated at the opening port in the simulation process. Among them, the granular organic fertilizer was randomly generated with an average equivalent diameter of 2.92mm as the mean value, a minimum equivalent diameter of 2.42mm, and a maximum equivalent diameter of 3.79mm. Finally, the motion characteristics of the assembly was set up. According to the principle of relative motion, the motion of the assembly was converted into the relative motion of the geometry, that is, the open groove moved in a reverse direction with respect to the fertilizer guiding mechanism at a speed of 0.25m/s (*Jin Yuan et al, 2014*).

In the simulation experiment, in order to ensure the accuracy of the test data under different structural parameters, the total simulation time was set to 2s, the fixed time step was set to 20%, and the target storage interval was set to 0.04s. The material of the mechanism was set to steel, and the relevant material parameters in the test were shown in Table 3. The dynamic friction coefficient and the static friction factor between the material granules and the different materials were determined by the shear box method and the bevel method respectively. The dynamic and static friction factor measurement test of the material granules and each material was repeated three times, and the test results were averaged. The free fall was utilized. The method was used to determine the collision recovery coefficient between material granules and different materials. The collision recovery coefficient determination test of material granules and the same material was repeated three times, and the test results were averaged. The contact mechanical parameters between different materials are shown in Table 4.

Parameter of material			Table 3
Parameter	Granular organic fertilizer	Fertilizer guiding mechanism	Land
Poisson ratio	0.25	0.45	0.50
Shear modulus [Pa]	1×10 ⁷	1×10 ⁶	1×10 ⁸
Density [kg·m ⁻³]	1300	3500	1200

Parameter of contact mechanics between materials			Table 4
Parameter	Granular organic fertilizer—Granular organic fertilizer	Granular organic fertilizer—Fertilizer guiding mechanism	Granular organic fertilizer—Land
Recovery coefficient	0.10	0.45	0.02
Static friction factor	0.30	0.30	1.25
Dynamic friction factor	0.25	0.20	1.25

Test and Analysis of Different Shapes of Fertilizer Plug-in Plate

In the fertilizer guiding mechanism, the fertilizer plug-in plate was one of the important factors affecting the uniformity of fertilization. The fertilizer plug-in plate of the existing linear fertilizer guiding mechanism was a linear type, and on this basis, a concave and a convex fertilizer guiding mechanism are proposed. Among them, the fertilizer plug-in plate of the concave fertilizer guiding mechanism was a concave curve type, and the fertilizer plug-in plate of the convex fertilizer guiding mechanism was a convex curved type, and the three fertilizer plug-in plates basically covered most guiding fertilizer insertion boards, which covered the main possible types of fertilizer plug-in plates, namely the concave, linear, and convex fertilizer guiding mechanisms, shown in Fig. 8.

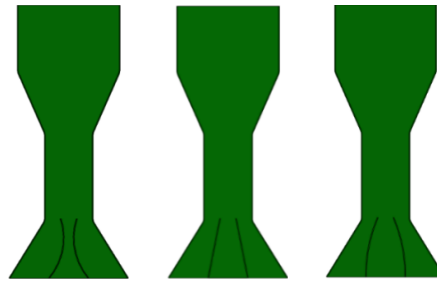


Fig. 8 - Diagrammatic sketch of three fertilizer guiding mechanisms

The shape of the fertilizer plug-in plate in the fertilizer guiding mechanism was taken as a single factor variable, and other parameters were unchanged. The simulation tests were carried out on the concave, linear and convex fertilizer guiding mechanisms respectively. Among them, the radius of curvature of the fertilizer plug-in plate of the concave and the linear fertilizer guiding mechanism was set to 350mm.

At 1s, the velocity directions of 330 granular organic fertilizers at the fertilizer outlets of the concave, linear and convex types were measured, as shown in Table 5. Among them, the range of the velocity direction is -1~1 in the EDEM simulation software. Based on the horizontal speed, the entire speed plane was equally divided into six parts at intervals of 30°, as shown in Fig. 9.

The speed direction in Table 5 through $\angle\alpha = \frac{v_{fi}}{2} \times 180^\circ$ was converted to the speed plane of Fig. 9, and the amount of granular organic fertilizer in each part was counted.

" $\angle\alpha$ " is the angle between the velocity direction of the granular organic fertilizer and the horizontal velocity direction; " v_{fi} " - the speed direction of the i -th granular organic fertilizer.

The velocity distribution map of different parts of granular organic fertilizer was drawn, as shown in Fig. 10.

Velocity direction of granular organic fertilizer

Table 5

Item	Velocity direction of granular organic fertilizer in concave fertilizer guiding mechanism	Velocity direction of granular organic fertilizer in linear fertilizer guiding mechanism	Velocity direction of granular organic fertilizer in convex fertilizer guiding mechanism
Minimum value	-0.98	-0.98	-0.98
Maximum value	0.99	0.99	0.99
Average value	0.18	0.34	0.13
Variance	0.35	0.40	0.30

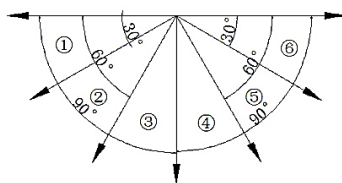


Fig. 9 - Partition of velocity direction

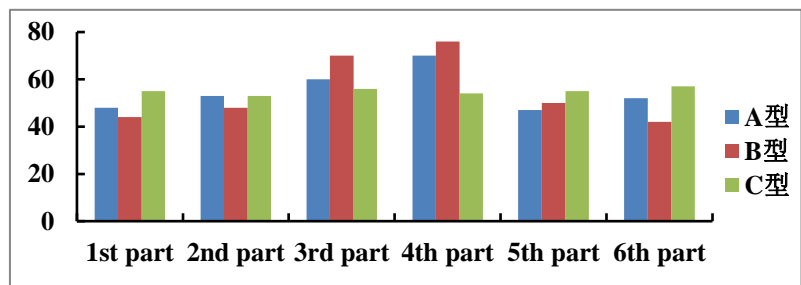


Fig. 10 Distribution of velocity direction in different parts

It can be seen from Fig.10 that in the concave and linear fertilizer guiding mechanism, the granule direction of the granular organic fertilizer is distributed in the third and fourth parts, and the number of granules is higher than the first, second, fifth and sixth parts.

In the convex fertilizer guiding mechanism, the granule direction distribution of the granular organic fertilizer is almost equal in the number of granules in each part. The granular organic fertilizer in the first and sixth parts of the velocity direction is concentrated on both sides of the bottom of the ditch when falling into the bottom of the ditch; the granular organic fertilizer in the third and fourth parts of the velocity direction is concentrated in the bottom of the ditch when falling into the middle part of the bottom of the ditch; the granular organic fertilizer in the second and fifth parts of the velocity direction is concentrated in the middle of the ditch when falling into the bottom of the ditch. In the concave and linear fertilizer guiding mechanism, when the granular organic fertilizer falls into the bottom of the ditch, it is concentrated in the middle part of the ditch, and the distribution on both sides is less, resulting in uneven distribution of granular organic fertilizer; in the convex fertilizer guiding mechanism, the velocity direction of the granular organic fertilizer is distributed evenly in all parts, and the distribution after falling into the bottom of the groove is relatively uniform.

In order to further evaluate the uniformity of fertilization, the discrete coefficients of the edge region and the middle region in the sampling area were calculated and counted. The results of the discrete coefficients of the edge regions of different fertilizer guiding mechanisms are shown in Table 6. The discrete coefficients of the middle regions of different fertilizer guiding mechanism are shown in Table 7.

Table 6

CV of different fertilizer guiding mechanisms in edge region			
Edge region	CV of concave fertilizer guiding mechanism	CV of linear fertilizer guiding mechanism	CV of convex fertilizer guiding mechanism
1 st row	0.57	0.43	0.36
15 th row	0.50	0.54	0.43

Table 7

CV of different fertilizer guiding mechanisms in middle region			
Middle region	CV of concave fertilizer guiding mechanism	CV of linear fertilizer guiding mechanism	CV of convex fertilizer guiding mechanism
5 th row	0.43	0.50	0.29
8 th row	0.42	0.52	0.32
11 th row	0.42	0.49	0.28

From the discrete coefficients of each region in the sampling area, it can be seen that in the three concave, linear and convex fertilizer guiding mechanisms, the discrete coefficients of the edge region and the middle region of the convex fertilizer guiding mechanism are lower than the concave and linear guides. The discrete coefficient of each part of the fertilizer guiding mechanism has the highest uniformity of fertilization.

The shape of the fertilizer plug-in plate changes the speed direction of the granular organic fertilizer, thereby affecting the uniformity of fertilization. The convex fertilizer plug-in plate is superior to the linear and concave fertilizer plug-in plate, and the convex fertilizer guiding mechanism is optimal.

Test and Analysis of the Fertilizer Plug-in Plate with Different Curvature Radius

In order to further determine the influence of the fertilizer plug-in plate with different curvature radius on the fertilization uniformity in the convex fertilizer guiding mechanism, the radius of curvature of the fertilizer plug-in plate was taken as a single factor variable, with a radius of curvature of 150mm~800mm at intervals of 50mm. The simulation experiment was carried out on the fertilizer plug-in plate, and the simulation results are shown in Fig. 11, 12.

The discrete coefficients of the edge region and the middle region under different curvature radius were analyzed, as shown in Table 8.

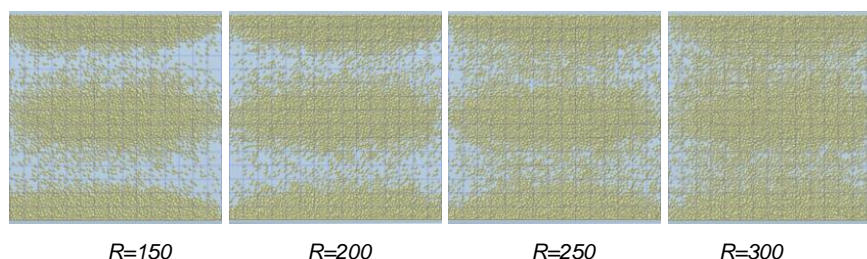


Fig. 11 Simulation result under different curvature radius

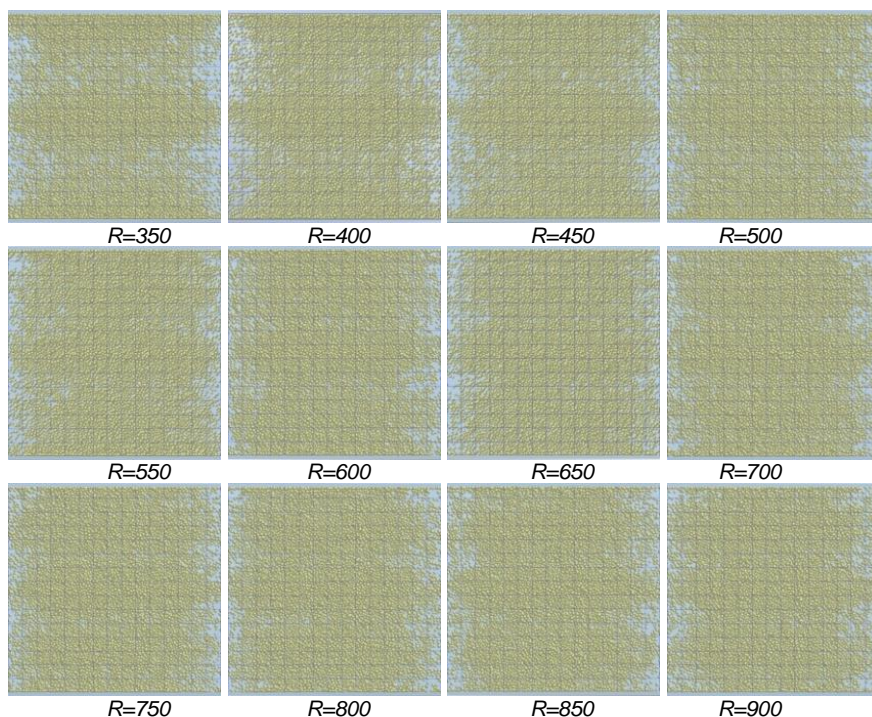


Fig. 12 - Simulation result under different curvature radius

Table 8

CV under different curvature radius					
Curvature radius	Edge region			Middle region	
	1st row	15th row	5th row	8th row	11th row
150	0.99	1.02	0.81	0.82	0.86
200	0.73	0.82	0.67	0.66	0.67
250	0.64	0.54	0.52	0.54	0.54
300	0.53	0.50	0.44	0.39	0.44
350	0.36	0.44	0.29	0.32	0.28
400	0.30	0.32	0.25	0.24	0.30
450	0.21	0.38	0.25	0.21	0.23
500	0.23	0.37	0.19	0.16	0.19
550	0.18	0.31	0.15	0.21	0.16
600	0.19	0.29	0.20	0.18	0.15
650	0.21	0.39	0.16	0.15	0.19
700	0.24	0.36	0.21	0.19	0.17
750	0.28	0.28	0.17	0.20	0.21
800	0.25	0.37	0.14	0.18	0.17

It can be seen from Table 8 that when the radius of curvature is in the range of 150mm~550mm, the discrete coefficient of the edge region and the middle region is gradually decreased; when the radius of curvature is in the range of 550mm~800mm, the discrete coefficient of the edge region and the middle region does not change much; the radius of curvature of the fertilizer plug-in plate affects the uniformity of fertilization within a certain range.

To further describe the relationship between the radius of curvature and the uniformity of fertilization, a cubic polynomial was used to fit the discrete coefficient curves of the edge region and the middle region.

First, at different radius of curvature, the average of the discrete coefficients of the first row and the 15th row is taken as the feature point of the discrete coefficient of the edge region; secondly, at the different radius of curvature, the discrete coefficient of the fifth row, the eighth row, the 11th row is averaged and used as the feature point of the middle region discrete coefficient. Finally, the cubic polynomial fitting is performed on the feature points of the edge region and the middle region to obtain the discrete coefficient fitting curve between the edge region and the middle region.

The results of the discrete coefficient fitting are shown in Fig. 13.

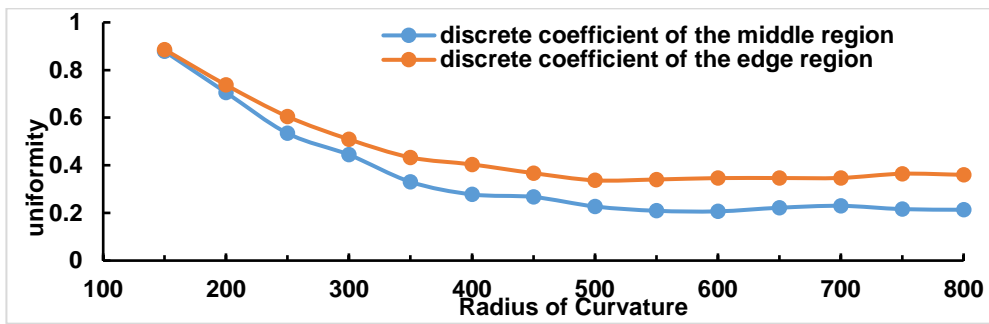


Fig. 13 - Fitting curve of CV

It can be seen that the edge region fitting discrete coefficient obtains a minimum value when the radius of curvature is 566mm, and the middle region fitting discrete coefficient obtains a minimum value when the radius of curvature is 596mm. In order to ensure that the discrete coefficients of edge and middle regions are minimized, and combined with processing technology and cost, the optimal curvature radius is finally determined to be 600 mm.

In the convex fertilizer guiding mechanism, the radius of curvature of the fertilizer plug-in plate affects the uniformity of fertilization. Under the processing conditions, when the radius of curvature of the fertilizer plug-in plate is 600mm, the cost is low and the uniformity of fertilization is high.

Field Trials

In mid-June 2017, a field trial was conducted in the experimental farm of Henghe in Shandong Province, as shown in Fig. 14. The farm was a large-scale standardized planting of orchard, with a row spacing of 2.5m and a plant spacing of 1m. The Plant was 3 years old and grew well. The test site was loam, the soil had an absolute moisture content of 23.3%, the soil firmness was 76.0kPa, and the terrain was flat, which provided favourable conditions for the smooth progress of the test. The test prototype was a two-row ditching and fertilizing machine for the orchard. The fertilizer guiding mechanism was a linear fertilizer guiding mechanism before optimization and an external convex fertilizer guiding mechanism with a radius of curvature of 600mm. In order to ensure the accuracy of the experimental data, three regions were randomly selected, and repeated verification tests of three discrete coefficient measurements were performed for each region, and the discrete coefficient curves before and after optimization were plotted, as shown in Fig. 15.



(a). Field operation (b). Fertilization effect in sampling area before and after optimization

Fig. 14 - Field Test

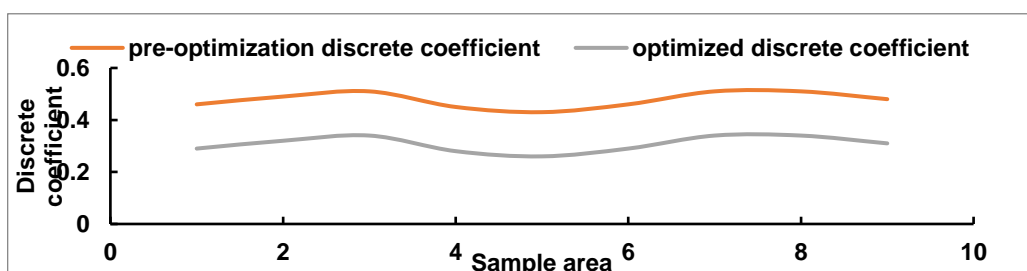


Fig. 15 - CV curve before and after optimization in different regions

The experimental results show that the optimized discrete coefficient curve is below the pre-optimization discrete coefficient curve. The optimized discrete coefficient is significantly smaller than the pre-optimization discrete coefficient. The average value of the discrete coefficient of the sampled area before optimization is 0.51. The average value of the discrete coefficient of the sampled area after optimization is 0.26. Fertilization uniformity increased by 49.02%.

After optimizing the parameters of the fertilizer guiding mechanism, under the conditions of the same ditch depth and speed, the discrete coefficient of the sampling area is reduced, the uniformity of fertilization is improved, and the technical requirements for the ditching and fertilization of the orchard are satisfied.

CONCLUSIONS

(1) Based on the existing linear fertilizer guiding mechanism, two other fertilizer guiding mechanisms, a concave fertilizer guiding mechanism and a convex fertilizer guiding mechanism are proposed.

(2) By using the shape of the fertilizer plug-in plate as a single factor variable, the three kinds of fertilizer guiding mechanisms of concave, linear and convex type are simulated respectively to determine that the convex fertilizer plug-in plate of the convex fertilizer guiding mechanism has the best shape and its uniformity of fertilization is the highest. Among them, the shape of the fertilizer plug-in plate affects the uniformity of fertilization by changing the velocity direction of the granular organic fertilizer.

(3) By using the radius of curvature of the fertilizer plug-in plate as a single factor variable, the simulation experiment is carried out on the convex fertilizer guiding mechanism with the radius of curvature of 150mm~800mm, and the polynomial is used to fit the discrete coefficient of the edge region and the middle region to determine the curve. The convex fertilizer guiding mechanism has an optimum radius of curvature of 600 mm. According to the field test, the discrete coefficient after optimization was reduced from 0.51 to 0.26, and the uniformity of fertilization was increased by 49.02%.

ACKNOWLEDGEMENT

This work was supported in part by "13th Five-Year" national key research and development plan (2016YFD0201104), "Double first class" award subsidy fund (SYL2017XTTD14), Shandong modern agricultural industry technology system, Shandong province key research and development plan (2017CXGC0211).

REFERENCES

- [1] Aphale A., Bolander N., Park J., Shaw L., Svec J., Wassgren C., (2003), Granular fertilizer particle dynamics on and off a spinner spreader. *Biosystems Engineering*, pp.319-329;
- [2] Chen X.F., Luo X.W., Wang Z.M., Zhang M.H., Hu L., Yang W.W., Zeng S., Zang Y., Wei H.D., Zheng. L., (2015), Design and experiment of fertilizer distribution apparatus with double-level screws. *Transactions of the Chinese Society of Agricultural Engineering*, issue 31, pp.10-16;
- [3] Cunningham F.M., (1963), Performance characteristics of bulk spreaders for granular fertilizer. *Transactions of the ASAE*, issue 6, pp.108-114;
- [4] Gao J.S., Xu M.G., Wang B.R., Qin D.Z., Wen S.L., Shen H.P., (2005), Combined fertilization of chemical and organic fertilizers in a long-term position experiment, *Chinese Agricultural Science Bulletin*, vol.21, issue 9, pp.211-214;
- [5] Han D.Y., Lv Z.Q., Cui F.F., Shen X., (2010), Design of the Fertilizing Machine for Fruit Trees, *Journal of Agricultural Mechanization Research*, vol.32, issue 12, pp.65-68;
- [6] Inns F.M., Reece A. R., (1962), The theory of the centrifugal distributor II: motion on the disc, off-centre feed. *Journal of Agricultural Engineering Research*, issue 7, pp.345-353;
- [7] Liedekerke P. Van., Tijskens E., Dintwa E., Rioual F., Vangeyte J., Ramon H., (2009), *Powder Technology*, issue 190, pp.348-360;
- [8] Li M., Zhang T., Dong X.H., Wang C., Niu Z.J., Ge C., Wei L.J., (2016), Parameter optimization on scraper fertilizer feed unit of 3ZSP-2 type sugarcane intertillage fertilizer applicator-cum-hiller. *Transactions of the Chinese Society of Agricultural Engineering*, issue 32, pp.36-42;
- [9] Liu B., Xiao H.R., Song Z.Y., Mei S., (2017), Present State and Trends of Fertilizing Machine in Orchard. *Journal of Agricultural Mechanization Research*, issue 39, pp.263-268;
- [10] Lv J.Q., Wang Z.M., Sun X.S., Li Z.H., Guo Z.P., (2015), Design and Experimental Study of Feed Screw Potato Planter Propulsion. *Journal of Agricultural Mechanization Research*, issue 6, 194-196;

- [11] Ma C., Meng H.W., Kan Z., Qi J.T., (2017), Design of Jujube Harvest Test Device Based on Self-excited Vibration and Force Compensation, *Journal of Agricultural Mechanization Research*, vol.39, issue10 , pp.12-17;
- [12] Ma J., Yan H.J., Wang, C.Y., (2016), Effect of end gun on/off on variable rate fertigation uniformity and its improvement for centre pivot irrigation system, *Journal of Hydraulic Engineering*, issue 12, pp.1577-1584;
- [13] Patterson D.E., Reece A.R. The theory of the centrifugal distributor. I: Motion on the disc, near-centre feed., (1962), *Journal of Agricultural Engineering Research*, issue 7, pp.232-240;
- [14] Pitt R.E., Farmer G.S., Walker L.P., (1982), Approximating equations for rotary distributor spread patterns. *Transactions of the ASAE* , issue 25, pp.1544-1552;
- [15] Przywara Artur., (2015), The Impact of Structural and Operational Parameters of the Centrifugal Disc spreader on the Spatial Distribution of Fertilizer. *Agriculture and Agricultural Science Procedia*, issue 7, pp.215~222;
- [16] Qi W.Z., Wang J.X., Liu. S.X., Wang Y.L., Wang Z., Zhao G.X., (2019), Design and Experiment of Control System for Rice and Wheat Variable Rate Fertilizer Applicator. *Journal of Agricultural Mechanization Research* , issue 41, pp.72-79;
- [17] Shi Y.Y., Chen M., Wang X.C., Morice, O., Li C.G., Ding, W M., (2018), Design and Experiment of Variable-rate Fertilizer Spreader with Centrifugal Distribution Cover for Rice Paddy Surface Fertilization, *Transactions of the Chinese Society for Agricultural Machinery*, vol.49, issue 3, pp.86-93+113;
- [18] Villette S., Piron E., Martin R., Courreau D., Miclet D., Gée C., (2010), Impact recording system to characterize centrifugal spreading. *Book of Abstracts*;
- [19] Zhang T., Liu F., Liu Y.Q., Zhao M.Q., Zhang S., Li N., Li L.F., Lv B., (2015), Discrete Element Simulation of Outer Groove Wheel Type Fertilizer Discharging Device Capacity Analysis. *Journal of Agricultural Mechanization Research* , issue 9, pp.198-201;
- [20] Zhao L.Y., (2002), Study on the Text System of Virtual Instrument for Precision Seed-Metering Device, MS Thesis, Nanjing: Nanjing Agricultural University;
- [21] Zheng X.C., Lu H.J., Che J.X., Zhai B.N., Zhao Z.Y., Wang, Y.L., (2011), Investigation of present yield and fertilization on Fuji apple in Baishui County, *Journal of Northwest A&F University*, vol.39, issue 9, pp.145-151;
- [22] Zhou Z., Fu Z.T., Wang X., Zheng L.J., (2009), Experiment of fertigation uniformity of drip fertigation machine. *Transactions of the Chinese Society of Agricultural Engineering* , issue 25, pp.7-13;
- [23] Wu N., Wu D.S., Li H., Liang H., (2016), Calibration of Manure Spreaders. *Journal of Agricultural Mechanization Research*, vol.38, issue 9 , pp.255-259;
- [24] Yuan J., Liu Q.H., Liu X.M., Zhang T., Zhang X.H., (2014), Simulation of Multi-fertilizers Blending Process and Optimization of Blending Cavity Structure in Nutrient Proportion of Variable Rate Fertilization. *Transactions of the Chinese Society for Agricultural Machinery* , issue 45, pp.125-132;
- [25] Yuan J., Liu Q.H., Liu X.M., Zhang T., Zhang X.H., (2014), Granular Multi-flows Fertilization Process Simulation and Tube Structure Optimization in Nutrient Proportion of Variable Rate Fertilization. *Transactions of the Chinese Society for Agricultural Machinery*, issue 11, pp.81-87;
- [26] Yang X.L., Wang J.W., Wang J.F., Zhou W., (2015), Parameters Optimization Design and Analysis of Vaned Fertilizer Distributing Device. *Journal of Agricultural Mechanization Research*, issue 7, pp.160-163;
- [27] Yuan W.S., Li K., Jin C.Q., Hu M.J., Zhang W.Y., (2018), Design and Experiment of Hill Placement Fertilizer Applicator. *Journal of Agricultural Mechanization Research*, issue 40, pp.145-149.

EXPERIMENTAL MODEL OF A COMBINED THERMAL SYSTEM FOR EFFICIENT USE OF RENEWABLE ENERGIES**MODEL EXPERIMENTAL DE SISTEM TERMIC COMBINAT PENTRU UTILIZAREA EFICIENTĂ A ENERGIILOR REGENERABILE**Dumitrescu C.¹⁾, Rădoi R.^{*1)}, Cristescu C.¹⁾, Dumitrescu L.¹⁾ ¹¹⁾ Hydraulics and Pneumatics Research Institute INOE 2000-IHP / Romania;

Tel: 0721253787; E-mail: radoi.ihp@fluidas.ro

DOI: <https://doi.org/10.35633/inmateh-60-32>**Keywords:** *renewable energy; efficiency; solar; biomass; thermal system***ABSTRACT**

The article presents an experimental model of a modular structure system for the production of thermal energy and the results of conducting specific tests. The experimental model uses two renewable energy sources - solar energy and energy generated by burning biomass - to provide thermal energy for an increased duration, regardless of the atmospheric factors. Properly sized, the system can be designed as a series product, in a variety of powers, to be used by heat suppliers, and also by individuals, especially the ones from remote areas, who want to ensure their thermal energy independence by using renewable energy.

REZUMAT

Articolul prezintă un model experimental de sistem destinat producerii de energie termică, în construcție modulară, precum și rezultatele obținute în urma realizării experimentărilor specifice. Modelul experimental utilizează două surse regenerabile de energie, energia solară și energia generată prin arderea biomasei, în scopul furnizării de energie termică pentru o durată crescută, indiferent de factorii atmosferici. Printr-o dimensionare adecvată, sistemul poate fi conceput la nivel de produs de serie, într-o gamă variată de puteri, pentru utilizarea de către furnizorii de energie termică, precum și de către persoane private, mai ales din zonele izolate, care vor să-și asigure independența energetică termică prin utilizarea energiilor regenerabile.

INTRODUCTION

Currently, the functioning of the world economy is largely based on energy from non-renewable resources (coal, oil, natural gas). A number of negative aspects, such as greenhouse gas emissions, which favour global warming, pollution, acid rain, are due to the use of these conventional resources, which, moreover, are close to depletion. This has triggered a significant investment process globally to make the most of renewable energy resources, which come from natural resources that are constantly renewed in relatively short intervals or are inexhaustible in the medium or long term. According to the latest reports, they contributed more than 22% to the production of electricity and accounted for 19% of total energy consumption globally (Maican E., 2015).

Compared to the trend of continuous growth of the capacity of renewable energy conversion systems, and so of the energy production from these sources, a current but also future problem is on the one hand, increasing the efficiency of clean energy production systems, and on the other hand, optimizing associated consumption (***, 2018). What is important for the consumer is the amount of energy delivered, the form of useful energy needed, how high the energy losses are, and how much he/she has to pay for the delivered energy (Bostan et al, 2017). For energy-efficient generation and use of renewable energy, one of the modern trends is to develop hybrid or combined systems, which use two or more renewable energy sources (Guo et al, 2018). Nowadays, a lot of technologies and equipment for the capture, storage and use of renewable energy have been developed (Cristescu et al, 2016).

As to the thermal energy - used to obtain domestic hot water and to heat the house - one of the modern solutions is combining solar energy with energy from burning of plant biomass (Anvari et al, 2019; Dumitrescu et al, 2018). Significant quantities of thermal energy can be produced by high efficiency biomass recovery processes, such as gasification followed by combustion (Kozlov et al, 2019; Srinivas and Reddy, 2014).

¹ Dumitrescu C., Ph.D. Eng.; Rădoi R., Ph.D. Eng.; Cristescu C., Ph.D. Eng.; Dumitrescu L., Ph.D. Stud. Eng.

Such a combined thermal system that uses solar thermal energy and the thermal energy generated by the burning of plant biomass has been designed and developed in the Institute INOE 2000-IHP. This combined thermal system was developed as an experimental model and was subjected to experimental tests, according to a special methodology, to maximize results. In the following, the experimental model of combined thermal system is presented, as well as several experimental results obtained from testing it.

MATERIALS AND METHODS

Presentation / description of the combined thermal model

The development of the experimental model of combined thermal system was imposed by the need to test the constructive solutions adopted, the feasibility of the idea of obtaining and using thermal energy from two renewable sources, and also the way to control the related processes, in order to experimentally validate them. For the physical development of the experimental model of the combined thermal system, an execution project was first developed, based on which the main components were acquired and the main subassemblies were executed. Considering the target group addressed throughout this research project, that is individual consumers, usually from remote areas, several minimum requirements were put at the base of the project, namely:

- The two types of combined renewable energy sources are: solar energy and biomass energy (pellets), since both are accessible to isolated consumers;
- The experimental model will have a modular design, with minimal costs;
- the main components of the system must have a performance / price balance that will be the basis of marketing them; thus, the solar panels will be of evacuated tube type, and the energy module will be based on a TLUD (top-lit-up-draft) type gasifier (*Mukunda et al, 2010*).

On the whole, according to figure 1, the experimental model of the combined thermal system consists of several main parts, presented in the lines below.

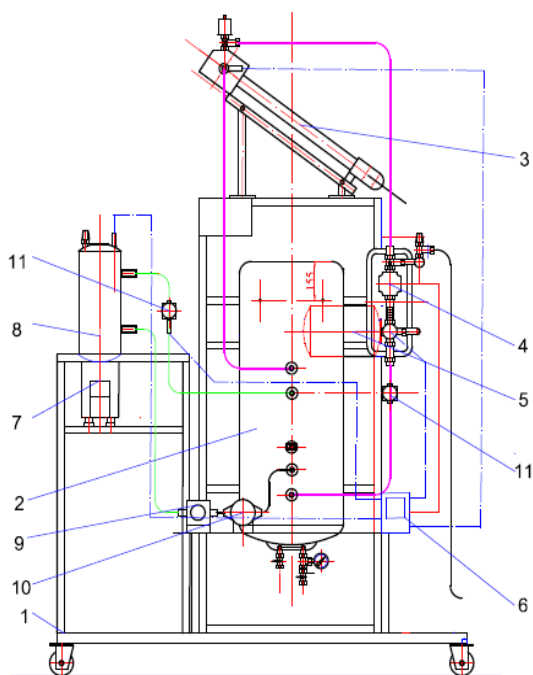


Fig. 1 - Draft of the combined thermal system



Fig. 2 - Physical development of the combined thermal system experimental model

On a frame (1), welded from laminated profiles, the main parts of the system are installed, namely: a boiler with two serpentine and electrical resistor (2), provided with pressure valve, pressure gauge and taps required for connection to the cold water source and to the consumer, respectively; a solar thermal panel (3), equipped with pressure valve and temperature sensor; a pumping group (4) for the solar thermal panel, which includes the recirculation pump, visual flow meter, visual thermometer, pressure gauge and safety valve, to which an expansion vessel is connected (5); a solar controller (6), which ensures automatic control of pump operation depending on the temperature in the boiler and the solar panel; an energy module with TLUD type gasifier, based on the burning of biomass (pellets) that heats the water which is in a well-insulated thermally

tank (8), equipped with safety valve and temperature sensor; a recirculation pump (9) of hot water to the boiler and return, controlled by the solar controller depending on the temperature of the boiler and the water tank; a water volume meter (10) with electrical signal; two volumetric flow meters (11), located on the circuits of the hot water recirculation pumps.

The tests were performed on the basis of a methodology elaborated previously, which includes the description of the main operations, in chronological order necessary for the testing, referring to the (physical) means of testing and testing schemes, the nomenclature of tests and specific responsibilities.

Before carrying out the tests, it was necessary to carry out preparatory, preliminary activities, to achieve the appropriate conditions in order to maximize the results obtained experimentally. First, an operational testing scheme - presented below - has been developed.

Testing scheme of the combined thermal model

The operational testing scheme developed is shown in Figure 3 below. It includes the mechanical-hydraulic assembly of the combined thermal system, as well as the sensors and transducers necessary for the appropriate operation, and also the computer-based system for acquisition and recording of the experimental data regarding the evolution of the thermal parameters of interest.

The functional scheme of the combined thermal system has as its central element a bivalent boiler (1) with 2 serpentes (SERP1 and SERP2) and an electrical resistor (RE), equipped with the necessary elements for pressure control (safety valve SS2, pressure gauge M2). The boiler performs heating of domestic water from two renewable energy sources (solar thermal energy and thermal energy obtained from burning of plant biomass), and, for safety reasons, from electrical energy.

Solar thermal energy is captured using a solar thermal mini-panel (2) (PST), equipped with a solar station (3) (ST), which provides the fluid for taking over and conveying heat through a circulation pump (P1), supervised by a safety valve (SS1) and a pressure gauge (M1), which sends the hot fluid into a serpentine (SERP1) of the bivalent boiler (B2S) to dispose the captured solar heat; the temperature is measured visually with a dial thermometer (T), and the fluid flow is measured with a volumetric flow meter (4) (DV1). Fluid temperatures at the solar thermal panel (PST) outlet and at the panel inlet are measured and taken via thermal sensors (S1 and S5).

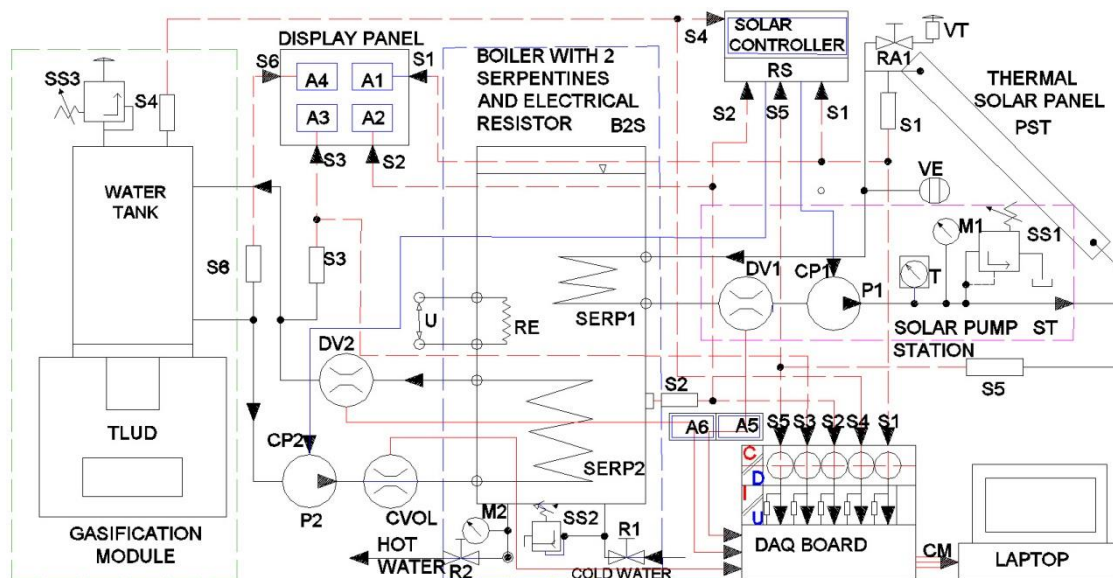


Fig. 3 - Test diagram of the combined thermal model

Thermal energy from biomass is captured by combustion, using a gasifier (TLUD) type oven (5) where combustion and gasification of pellets of vegetal nature take place; the heat is taken up by a water tank (REZ) (6), which can operate under pressure, assisted by a safety valve (SS3), the temperature of the fluid in the tank being measured by a thermal detector (S4). The captured heat is taken up by a fluid (water) conveyed by a circulation pump (P2), through a serpentine (SERP2), the flow being measured with a volumetric flow meter (DV2) (7), and the volume of fluid being evaluated with a volumetric meter (CVOL). Fluid temperatures at the tank inlet and outlet are measured by means of temperature detectors (S3 and S6).

Equipping the combined thermal system with sensors and transducers

To perform the experimental testing on the combined thermal system, in order to assess its thermal efficiency, the acquisition of the evolution of the process parameters (temperatures, flows, volumes of fluid, etc.) was considered. To capture these parameters, the system was equipped with a series of thermal sensors, flow meters, pressure gauges, thermometers, fluid volume meter. The correct location / installation of the thermal sensors on the indicated circuits, including the flow meters, was carefully taken care of, and on the other hand the installation of elements to adapt their signals, usually continuous, by converting these signals into digital signals, compatible with the acquisition board on the processing computer. The installation of the main sensors can be seen in figures 4 ... 11 below.



Fig.4 - Solar thermal panel with thermal sensor (S1)



Fig. 5 - Installation of thermal detector to the boiler inlet (S2)



Fig. 6 - Installation of thermal detector to the boiler outlet (S3)



Fig. 7 - Installation of thermal detector to the tank (S4)



Fig. 8 – Installation of volumetric flow meter to the panel (DV1)



Fig. 9 - Installation of volumetric flow meter to the gasifier (DV2)



Fig. 10 - Measuring water consumption at the TLUD gasifier

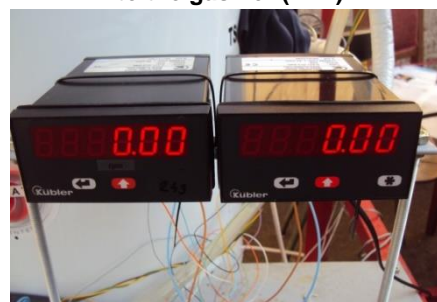


Fig. 11 - Circulation pumps flow display

Computer system for data acquisition and functioning control

For acquisition of the experimental data regarding the evolution of the parameters of interest, a data acquisition system has been designed which consists mainly of hardware components: electrical and electronic circuits, acquisition board, continuous to digital (C/D) signal converters, (I/U) elements transforming current (I) units to voltage (U) units, including elements displaying parameters of interest (A1, A2, A3, A4, A5 and A6), and also original software components, installed on a laptop computer, through which recording and processing of experimental data describing the evolution of the parameters is done.

Consideration was given to the correct implementation of the electrical circuits in order to acquire signals, adapt and process information, and also register the files of interest.



Fig. 12 - Bench with signal adaptation circuits



Fig. 13 - Power supply



Fig. 14 - Data acquisition subsystem

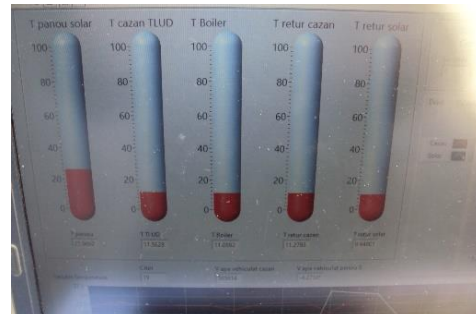


Fig. 15 - Computer display

The main thermal parameters measured for the evolution of the combined system are as follows:

- hot water temperature at the solar thermal panel outlet (S1), as displayed on the panel;
- hot water temperature inside the boiler (S2), as displayed on the panel;
- water temperature at the boiler outlet and gasifier inlet (S3), as displayed on the panel;
- water temperature inside the solid fuel / pellet gasifier (S4/S6), as displayed on the panel.

The secondary thermal parameters measured, of functional interest, are as follows:

- water temperature at the solar panel let (S5);
- water temperature at the solid fuel gasifier outlet (S6);
- ambient temperature (Tmed).

The main quantitative parameters measured are as follows:

- flow pumped by the pump P1 into the solar thermal panel PST (Q1);
- flow pumped by the pump P2, from the solid fuel gasifier REZ (Q2);
- volume flow pumped by the pump P2, during operation, CVOL.

In the end, the operation of the main components of the combined thermal system - the circulation pump of hot fluid generated by the gas module, the circulation pump within the solar thermal panel circuit, the fluid volume meter - was verified; the correct wiring of electrical circuits and signals of the sensors was also verified, including testing of the acquisition and calibrating the signals on the computer.

RESULTS

The functional behaviour of the combined thermal system experimental model was monitored, by simultaneous use of the two renewable energy sources: biomass energy and solar thermal energy.

Consideration was given to creating the conditions for the two subsystems to work at normal parameters, and the measurement instrumentation and data acquisition subsystem to produce significant data records.

The experiments have been conducted in the open air, in the yard of the Institute INOE 2000-IHP, (figure 16). Ambient temperature was measured by using a HANNA type digital thermometer.



Fig. 16 - The combined thermal model experimental test bench



Fig. 17 - Exposing the solar thermal panel to the sun

Following the conducting of experimental tests, according to the test methodology, a number of numerical results and also graphs regarding the evolution of the parameters of interest were obtained. The experimental results regarding the parameters of interest were visually tracked and monitored by means of the computer. Two types of records resulted, namely:

Written visual records of experimental data

The main parameters of interest are the temperatures which influence the thermal process, namely: ambient temperature, water temperature in the gasifier, water temperature in the solar panel and water temperature in the boiler.

The following table records the parameters mentioned above, depending on the time at which they were read visually, using the available equipment / instrumentation.

Table 1

Recorded values of the main parameters

Time of recording	Symbol	11:20	11:30	11:50	12:05	12:15	12:30
Ambient temperature (°C)	T_{med}	7.3	7.5	7.9	8.1	8.2	8.6
Temperature in the TLUD gasifier (°C)	T_{TLUD}	15	14	22	38	50	40
Temperature in the solar panel (°C)	T_{PST}	25	23	25	35	40	50
Temperature in the boiler (°C)	T_{boiler}	10	11	12	12	14	18
Pressure in the boiler (bar)	P_{boiler}	1.2 ... 1.3					

From the analysis of the tabular numerical data regarding the system temperatures, one can notice a higher increase of water temperature in the boiler, due to the contribution of both thermal subsystems.

Computer records of experimental data

During the experiments, computer data recordings were made, mostly in graphical form, but also as numerical data. In the following, some examples of graphs are given, which are completely in line with the numerical data presented above. The computer screen shows the increase of the temperatures of interest, through the variable vertical bars for: temperature in the solar thermal panel T_{PST} , temperature in the TLUD gasifier T_{TLUD} , temperature in the boiler T_{boiler} , and also the return temperatures of gasifier and solar panel.

The computer screen is shown in figure 18 below, and the variation graph of the flow rates of the circulation pumps for gasifier (red) and solar panel (blue) is shown, in detail, in figure 19.

For the acquisition, registration and processing of experimental data, a Virtual Instrument application was created in the LabVIEW platform, 2014 version.

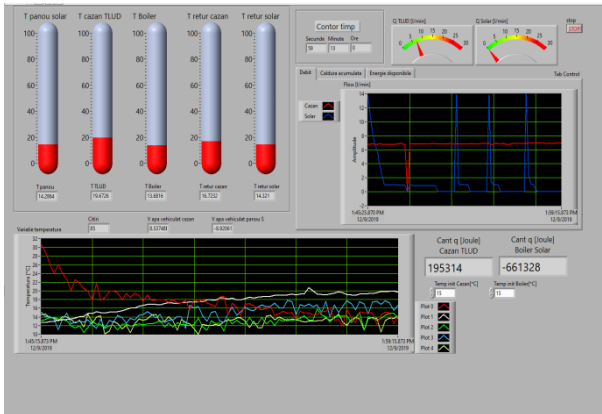


Fig. 18 - Computer screen capture

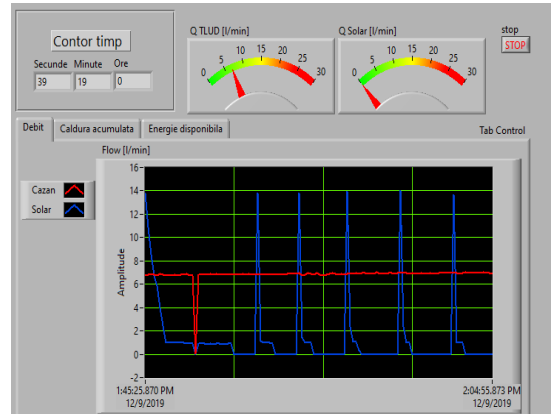


Fig. 19 - Graph of variation of flow rates of circulation pumps

Figure 19 shows, in addition to the flow variation at the circulation pump of the TLUD gasifier, which can be read both on the graph (red colour) and on the clock above the graph (6.6 l/min), frequent discharging taking place in the solar thermal panel, a fact illustrated by the blue graph. To reduce the frequency of hot water discharge in the solar thermal panel one should add more panels or increase their dimensions.

From the analysis of the complex graph in figure 20, below, one can notice the red graph (Plot 0) indicating discharge of hot water in the solar panel, while the TLUD gasifier is still accumulating heat, even above 20°C, which can be seen on the white graph (Plot 1), then it begins to descend due to the action of the circulation pump, which leads to the increase in temperature in the boiler, from about 11-12°C, to about 16-17°C, as shown in the green graph (Plot 2), somewhat in line with the data read visually, presented in the table above.

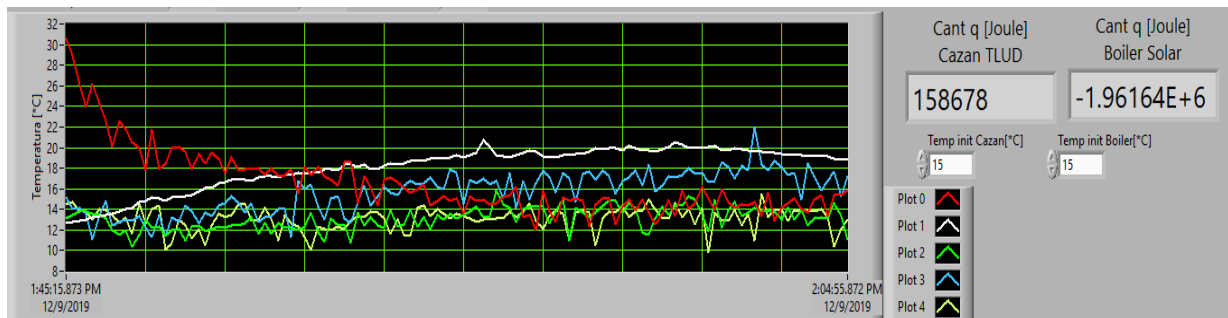


Fig.20 - The complex graph of temperature variation in the combined thermal system

The blue graph (Plot 3) shows the evolution of the water temperature upon return to the gasifier, showing that the circulation speed is too high; there is not enough time for the heat exchange in the gasifier to occur, that is, the water returns to the gasifier at a fairly high temperature. As an immediate measure it is necessary to reduce the circulation pump flow for the water in the gasifier, which is achievable if the pump speed were variable. The orange graph (Plot 4) shows that the discharge of hot water from the solar panel is done at high flow rates, almost double compared to the ones in the gasifier, but also at high frequency, which keeps the water on return to a relatively low temperature.

CONCLUSIONS

Testing of the experimental model of the combined thermal system revealed some important conclusions regarding the functional behaviour, as follows:

- The experimental model of combined thermal system functionally corresponds to the requirements of the technical documentation, achieving the purpose for which it was designed;

- The ratio of the heat sources (the biomass-based thermal generator and the solar thermal panel) size and the boiler size must be optimized, in the sense of increasing the power of the former. In other words, the capacity of the boiler is too high compared to the heat sources;
- This disproportionate situation is due to the impossibility of purchasing a smaller boiler with two serpentines, its volume of water (about 120 l) being too large, situation that we have accepted since an experimental model was in discussion;
- The biomass / pellet based thermal generator, although functionally appropriate, turned out to be too small, so for a prototype one has to think something bigger, i.e. for a power of about 10-12 kW;
- In conclusion, to develop a prototype, it is necessary to increase the powers of both thermal subsystems, to make a greater contribution to the increase in water temperature inside the boiler, on a larger range, in a much smaller time. In this way, an optimal consumption of hot water can be provided and guaranteed to the beneficiary.

ACKNOWLEDGEMENT

This paper has been funded under Programme I – Development of national R&D system, Subprogramme 1.2 – Institutional performance – Projects financing excellence in RD&I, Financial Agreement no. 19PFE/17.10.2018, while the scientific results have been obtained in the framework of a project co-financed by the European Union through the European Regional Development Fund, under Competitiveness Operational Programme 2014-2020, Priority Axis 1: Research, technological development and innovation (RD&I) to support economic competitiveness and business development, Action 1.1.4 - Attracting high-level personnel from abroad in order to enhance the RD capacity, project title: *Establishing a high level proficiency nucleus in the field of increasing renewable energy conversion efficiency and energy independence by using combined resources*, project acronym: CONVENER, Financial Agreement no. 37/02.09.2016.

REFERENCES

- [1] Anvari S., Khalilarya S., Zare V., (2019), Power generation enhancement in a biomass-based combined cycle using solar energy: Thermodynamic and environmental analysis, *Applied Thermal Engineering*, Vol.153, pp.128-141, Ed. Elsevier, London/U.K.;
- [2] Bostan I., Dulgheru V., Sobor I., Bostan V., Sochireanu A., (2017), *Renewable energy conversion systems. Wind, Solar, Hydraulic Energy (Sisteme de conversie a energiilor regenerabile. Eoliană, Solară, Hidraulică)*. Tehnica-Info Publishing House, Chişinău/Republic of Moldova;
- [3] Cristescu C., Dumitrescu C., Drumea P., Dulgheru V., Kedzia K., (2016), Technologies of capture and storage of energy from renewable sources, *Proceedings of 22nd International Conference on Hydraulics and Pneumatics HERVEX 2016*, ISSN 1454 – 8003, pp.368-382, Baile Govora/Romania;
- [4] Dumitrescu L., Cristescu C., Barbu V., Mateescu M., (2018), Combined system for the production of thermal energy using solar and biomass energy, *Proceedings of International Symposium ISB-INMA TEH' 2018*, ISSN-L 2344 - 4118, pp. 965-970, Bucharest/Romania;
- [5] Guo S., Liu Q., Sun J., Jin H., (2018), A review on the utilization of hybrid renewable energy, *Renewable and Sustainable Energy Reviews*, Vol.91, pp.1121-1147, Ed. Elsevier, London/U.K.;
- [6] Kozlov A., Marchenko O., Solomin S., (2019), The modern state of wood biomass gasification technologies and their economic efficiency, *Energy Procedia*, Vol.158, pp.1004-1008, Ed. Elsevier, London/U.K.;
- [7] Maican E., (2015), *Renewable energy systems (Sisteme de energii regenerabile)*. Printech Publishing House, Bucharest/Romania;
- [8] Mukunda H.S., Dasappa S., Paul P.J., Rajan N.K.S., Yagnaraman M., Kumar D.R., Deogaonkar M., (2010), Gasifier stoves—Science, technology and field outreach, *Current Science*, Vol.98, Issue 5, pp.627–638, Bengaluru/India;
- [9] Srinivas T., Reddy B.V., (2014), Hybrid solar–biomass power plant without energy storage, *Case Studies in Thermal Engineering*, Vol. 2, pp.75–81;
- [10] ***(2018), *Renewables 2018. Global Status Report*, ISBN 978-3-9818911-3-3, https://www.ren21.net/wp-content/uploads/2019/05/GSR2018_Full-Report_English.pdf.

KINETOSTATIC ANALYSIS OF THE PRECOMPACTION MECHANISM IN MUNICIPAL SOLID WASTE COLLECTING EQUIPMENT

/

ANALIZA CINETOSTATICĂ A MECANISMULUI DE PRECOMPACTARE LA MAȘINILE DE COLECTAT DEȘEURI MENAJERE

Moise V.¹⁾, Voicu Gh.*¹⁾, Lazea M.²⁾, Stoica D.¹⁾, Popa L.³⁾, Tudor P.¹⁾, Ungureanu L.¹⁾ ¹

¹⁾ University Politehnica of Bucharest / Romania; ²⁾ CCR Romania; ³⁾ INMA Bucharest / Romania

*) Corresponding author: Tel: 0724715585; E-mail: ghvoicu_2005@yahoo.com

DOI: <https://doi.org/10.35633/inmateh-60-33>

Keywords: municipal waste, garbage truck, precompacting mechanism, kinetostatic analysis

ABSTRACT

In the paper is done the kinetic analysis of the mechanism for municipal solid waste takeover and precompaction, of specific equipment for its collection and transport.

The corresponding dimensioning of the actuation mechanism elements shall be made only after the determination of the forces and moments acting on them. The determination of the forces and moments acting on the elements of the mechanism is done by kinetostatic analysis. For the kinetostatic analysis of the mechanism, the applied and inertial forces in the centres of gravity of the elements are reduced, after which the procedures made for each structural group in the composition of the mechanism are applied. Finally, the driving forces are obtained to be applied in the translational couplings (hydraulic cylinders) for setting the mechanism in motion. For the accuracy of the calculation, the driving forces are determined by the virtual exponents' method too.

REZUMAT

În lucrare se face analiza cinetostatică a mecanismului de preluare și precompactare a reziduurilor menajere, de la o mașină specifică pentru colectarea și transportul acestora. Dimensionarea corespunzătoare a elementelor mecanismului de acționare se face numai după stabilirea forțelor și momentelor care acționează asupra acestora. Determinarea forțelor și momentelor care acționează asupra elementelor mecanismului se face prin analiza cinetostatică. Pentru analiza cinetostatică a mecanismului se procedează la reducerea forțelor aplicate și a forțelor de inerție în centrele de greutate ale elementelor, după care se apelează procedurile realizate pentru fiecare grupă structurală din componența mecanismului. În final se obțin forțele motoare care trebuie aplicate în cuplele de translație (cilindrii hidraulici), pentru punerea în mișcare a mecanismului. Pentru corectitudinea calculului se determină forțele motoare și prin metoda puterilor virtuale.

INTRODUCTION

Garbage trucks for collecting municipal solid waste shall be equipped with mechanisms to retrieve and pre-compact the residues discharged from the special pre-collection containers. Most mechanisms of this kind are located at the back of the machines, realizing, together with the compaction plate inside the equipment collection container, the compaction of the loaded residues. This compaction occurs progressively as the pickup mechanism brings material to the loading area. Most of the pickup and pre-compacting mechanisms are flat mechanisms with articulated bars, the elements of which are operated with hydraulic cylinders. In figure 1, the kinematic scheme of the system for collecting and pre-compacting the household material introduced into the takeover tank in the pre-collection containers is presented (Voicu Gh., Lazea M., Zabava B.S., Tudor P., Moise V., 2019; Voicu Gh., Lazea M., Tudor P., Zabava B.St., Moise V., 2019).

¹ Moise V., Prof. Ph.D. Eng.; Voicu Gh., Prof. Ph.D. Eng.; Lazea M., Ph.D. Stud.; Popa L., Ph.D. Eng.; Tudor P., Lect. Ph.D. Eng.; Dugășescu I., Lect. Ph.D. Eng.; Ungureanu L., Lect. Ph.D. Eng.

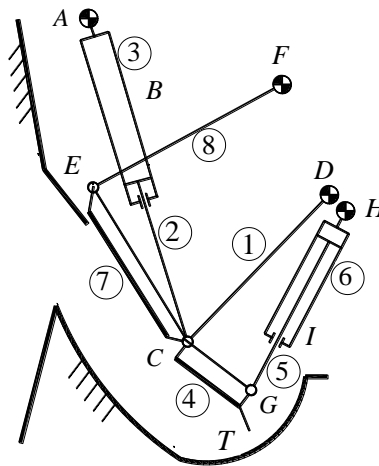


Fig. 1 – Kinematic scheme of waste pre-compaction mechanism

After the structural and kinematic analysis of the mechanism, we pass to the kinetostatic analysis, that is, the determination of the forces and moments acting on the kinematic elements.

The kinetostatic analysis of the mechanism comprises several stages, namely:

- Kinetostatic study of each modular group in part;
- Elaborating the calculation program for determining the reactions of all kinematic joints of the mechanism, as well as the driving forces in *B* and *I* active couplings (Demidovitch B., Maron I., 1987; Dorn W.S., Mc Cracken D.D., 1976; Moise V., Maican E., Moise Șt. I., 2003; Moise V., Maican E., Moise Șt.I., 2016).
- Drawing the corresponding reaction hodographs of joints *A* and *D*;
- Drawing the driving forces diagrams of the *B* and *I* translation kinematic coupling;
- The tabular presentation of the shares in the joints *A*, *D* and *H* for 81 positions of the mechanism elements.

MATERIAL AND METHODS

1. Kinetostatic analysis of the mechanism

The kinetostatic analysis of the mechanism starts from the initial position, that is, the position in which hydraulic cylinders 2-3 and 5-6 are in initial position (Fig. 2).

For the kinetic analysis of the mechanism, proceed to reduce the applied and inertial forces in the centres of gravity of the elements, after which the functions corresponding to each structural group are used. It is noted that the kinetostatic analysis is done in inverse kinematic analysis, i.e. from the last kinematic analyzed structural group (RRTaR motor dyad (4, 5, 6)) and ending with the first group (RRTaR motor group (1, 2,3)), (Artobolevski I.I., 1977; et al, 2003; Moise V., Simionescu I., Ene M. et al, 2008; Moise V., Simionescu I., Ene M. et al, 2015; Moise V., Simionescu I., Ene M., 2018; Pelecudi Chr., Maroș D., Merticaru V., et al, 1985; Simionescu I., Moise V., 1999).

Motor group RRTaR (4,5,6)

On the elements of the motor dyad RRTaR(4,5,6) act (Fig.3,a):

- Gravity forces:

$$\bar{G}_4 = -m_4 \bar{g}, \bar{G}_5 = -m_5 \bar{g}, \bar{G}_6 = -m_6 \bar{g}$$

- Inertial forces:

$$\bar{F}_{i4} = -m_4 \bar{a}_{G4}, \bar{F}_{i5} = -m_5 \bar{a}_{G5}; \bar{F}_{i6} = -m_6 \bar{a}_{G6}$$

- The resultant moments of the inertial forces:

$$\bar{M}_{i4} = -IG_4 \cdot \bar{\varepsilon}_4, \bar{M}_{i5} = -IG_5 \cdot \bar{\varepsilon}_5, \bar{M}_{i6} = -IG_6 \cdot \bar{\varepsilon}_6 \tag{3}$$

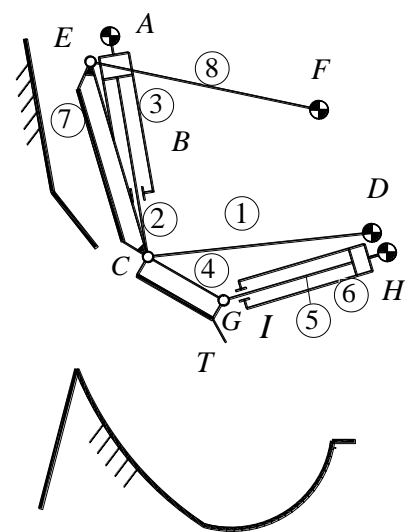


Fig. 2 – Kinematic scheme of the mechanism in the initial position

- Technological forces: \bar{Q} .

The points of reduction of force systems shall be considered in the centres of gravity G_4 , G_5 , and G_6 , corresponding to the elements 4, 5 and 6. The kinematic parameters of the points G_4 , G_5 , and G_6 are calculated using the procedure **A1R**, (Pelecudi Chr., 1975; Pelecudi Chr., Simionescu I., Moise V., Ene M., 1981).

The resulting inertial, gravity and reaction forces have the following form (Fig.3,b):

$$\bar{F}_{R4} = \bar{F}_{4X} + \bar{F}_{4Y}, \bar{F}_{R5} = \bar{F}_{5X} + \bar{F}_{5Y}, \bar{F}_{R6} = \bar{F}_{6X} + \bar{F}_{6Y} \tag{4}$$

where:

$$\bar{F}_{4X} = -m_4 \cdot \bar{a}_{G4X} + \bar{Q}_X ; \bar{F}_{4Y} = -m_4 \cdot (\bar{a}_{G4Y} + \bar{g}) + \bar{Q}_Y \tag{5}$$

$$\bar{F}_{5X} = -m_5 \cdot \bar{a}_{G5X}; \bar{F}_{5Y} = -m_5 \cdot (\bar{a}_{G5Y} + \bar{g}) \tag{6}$$

$$\bar{F}_{6X} = -m_6 \cdot \bar{a}_{G6X}; \bar{F}_{6Y} = -m_6 \cdot (\bar{a}_{G6Y} + \bar{g}) \tag{7}$$

In relation to the reduction points, the resulting moments are:

$$\bar{CM}_4 = -IG_4 \cdot \bar{\varepsilon}_4; \bar{CM}_5 = -IG_5 \cdot \bar{\varepsilon}_5; \bar{CM}_6 = -IG_6 \cdot \bar{\varepsilon}_6 \tag{8}$$

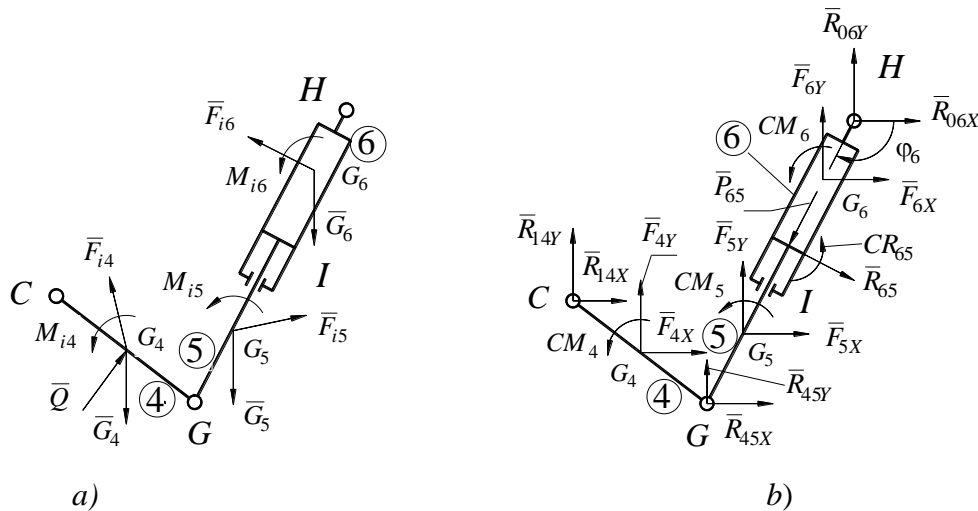


Fig. 3 – Motor groups RRTaR (4,5,6)

a) highlight of the forces and moments acting on the elements of the structural group
 b) kinetostatic scheme of the motor group RRTaR (4,5,6)

The reactions in the kinematic couplings of the motor groups, together with the acting force in the hydraulic cylinder, form the output data of the procedure **A2RC**.

Dyad RRR (7,8)

On the elements of the dyad RRR(7,8) act (Fig. 4,a):

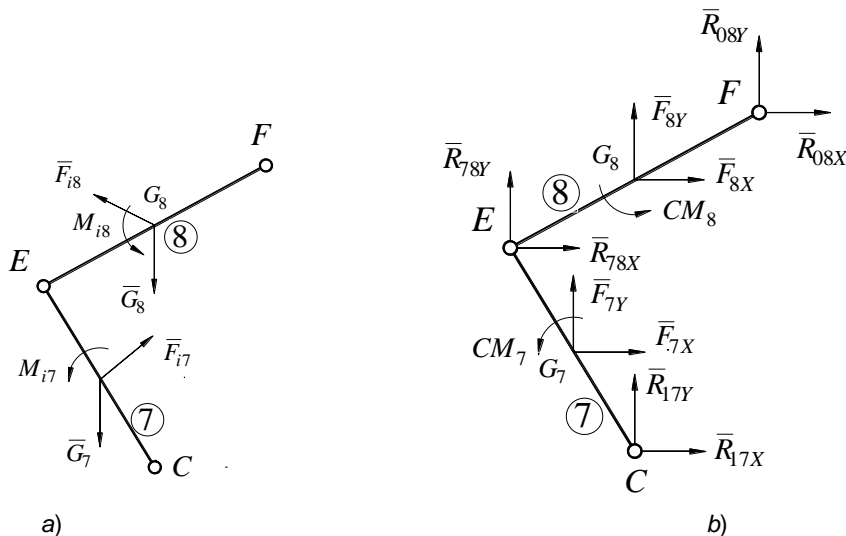


Fig. 4 - Dyad RRR (7,8)

a) highlighting the forces and moments acting on the elements of the structural group;
 b) kinetostatic scheme of the dyad RRR(7,8)

- gravity forces:

$$\bar{G}_7 = -m_7 \bar{g}, \bar{G}_8 = -m_8 \bar{g} \quad (9)$$

- inertial forces:

$$\bar{F}_{i7} = -m_7 \bar{a}_{G7}, \bar{F}_{i8} = -m_8 \bar{a}_{G8} \quad (10)$$

- the resultant moments of the inertial forces:

$$\bar{M}_{i7} = -IG_7 \cdot \bar{\varepsilon}_7, \bar{M}_{i8} = -IG_8 \cdot \bar{\varepsilon}_8 \quad (11)$$

The reduction points of the force systems shall be considered in the G_7 and G_8 gravity centres of elements 7 and 8. The kinematic parameters of these points are calculated using the **A1R** procedure.

The accelerations of the G_7 and G_8 reduction points of the force systems being known by the components on the coordinate axes, the inertial forces are:

$$\bar{F}_{i7} = F_{i7X} \bar{i} + F_{i7Y} \bar{j}, \bar{F}_{i8} = F_{i8X} \bar{i} + F_{i8Y} \bar{j} \quad (12)$$

The results of the applied, inertial and gravity forces are:

$$\bar{F}_{R7} = \bar{F}_{7X} + \bar{F}_{7Y}, \bar{F}_{R8} = \bar{F}_{8X} + \bar{F}_{8Y} \text{ (Fig. 3.6.9.b)} \quad (13)$$

where:

$$\bar{F}_{7X} = -m_7 \cdot \bar{a}_{G7X}; \bar{F}_{8Y} = -m_8 \cdot (\bar{a}_{G8Y} + \bar{g}) \quad (14)$$

$$\bar{F}_{8X} = -m_8 \cdot \bar{a}_{G8X}; \bar{F}_{8Y} = -m_8 \cdot (\bar{a}_{G8Y} + \bar{g}) \quad (15)$$

In relation to the reduction points, the resulting moments are:

$$\bar{CM}_7 = -IG_7 \cdot \bar{\varepsilon}_7, \bar{CM}_8 = -IG_8 \cdot \bar{\varepsilon}_8 \quad (16)$$

The reactions in the C, E and F kinematic couplings form the output data of the **D1RC** procedure.

Motor group RRTaR (1,2,3)

On the elements of the motor dyad $RRTaR (1,2,3)$ act (Fig. 5.a):

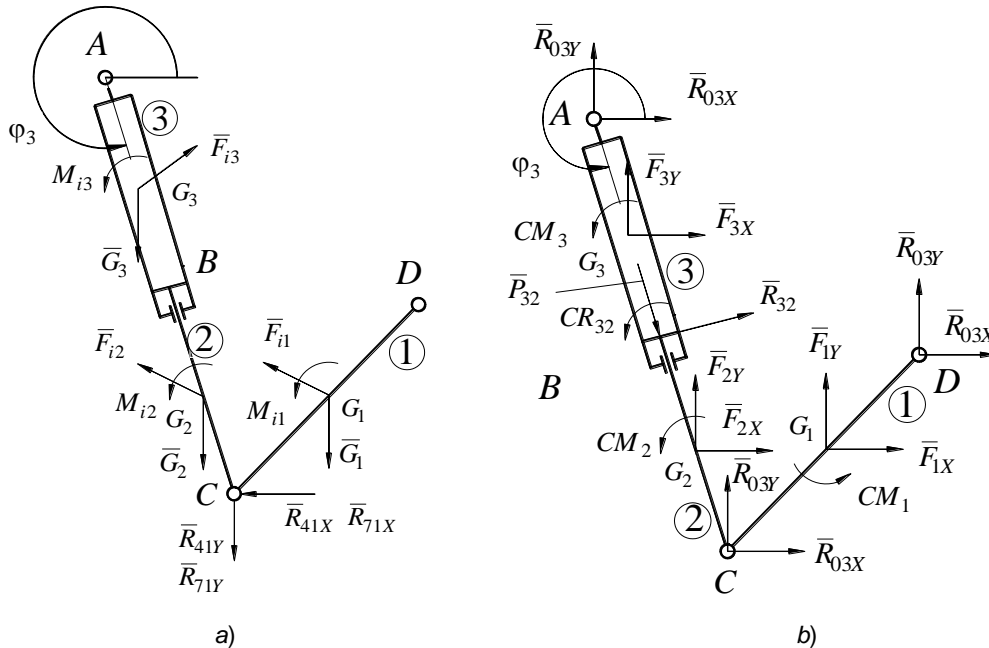


Fig. 5 - Motor group RRTaR (1,2,3)

a) highlight of the forces and moments acting on the elements of the structural group;

b) kinetostatic scheme of the motor dyad $RRTaR (1,2,3)$

- gravity forces:

$$\bar{G}_1 = -m_1 \bar{g}, \bar{G}_2 = -m_2 \bar{g}, \bar{G}_3 = -m_3 \bar{g} \quad (17)$$

- inertial forces:

$$\bar{F}_{i1} = -m_1 \bar{a}_{G1}, \bar{F}_{i2} = -m_2 \bar{a}_{G2}, \bar{F}_{i3} = -m_3 \bar{a}_{G3} \quad (18)$$

- the resultant moments of the inertial forces:

$$\bar{M}_{i1} = -IG_1 \cdot \bar{\varepsilon}_1, \bar{M}_{i2} = -IG_2 \cdot \bar{\varepsilon}_2, \bar{M}_{i3} = -IG_3 \cdot \bar{\varepsilon}_3 \quad (19)$$

- reactions of elements 4 and 7 on element 1 of the motor group $RRTaR(1,2,3)$, namely :
 $\bar{R}_{41X} = -\bar{R}_{14X}$, $\bar{R}_{41Y} = -\bar{R}_{14Y}$, $\bar{R}_{71X} = -\bar{R}_{17X}$, $\bar{R}_{71Y} = -\bar{R}_{17Y}$.

Points of reduction of system forces are considered in the centres of gravity G_1 , G_2 and G_3 , corresponding to the elements 1, 2 and 3.

Kinematic parameters of the points G_1 , G_2 and G_3 shall be calculated using the procedures **A1R** and **A1RALFA**.

The resultant inertial, gravity and reaction forces have the following form:

$$\bar{F}_{R1} = \bar{F}_{1X} + \bar{F}_{1Y}, \bar{F}_{R2} = \bar{F}_{2X} + \bar{F}_{2Y}, \bar{F}_{R3} = \bar{F}_{3X} + \bar{F}_{3Y} \quad (20)$$

where:

$$\bar{F}_{1X} = -m_1 \cdot \bar{a}_{G1X} + \bar{R}_{41X} + \bar{R}_{71X}; \bar{F}_{1Y} = -m_1 \cdot (\bar{a}_{G1Y} + \bar{g}) + \bar{R}_{41Y} + \bar{R}_{71Y} \quad (21)$$

$$\bar{F}_{2X} = -m_2 \cdot \bar{a}_{G2X}; \bar{F}_{2Y} = -m_2 \cdot (\bar{a}_{G2Y} + \bar{g}) \quad (22)$$

$$\bar{F}_{3X} = -m_3 \cdot \bar{a}_{G3X}; \bar{F}_{3Y} = -m_3 \cdot (\bar{a}_{G3Y} + \bar{g}) \quad (23)$$

In relation to the reduction points, the resulting moments are:

$$\bar{CM}_1 = -IG_1 \cdot \bar{\varepsilon}_1 + \bar{G}_1 C \times (\bar{R}_{41X} + \bar{R}_{41Y}) + \bar{G}_1 C \times (\bar{R}_{71X} + \bar{R}_{71Y}) \quad (24)$$

$$\bar{CM}_2 = -IG_2 \cdot \bar{\varepsilon}_2; \bar{CM}_3 = -IG_3 \cdot \bar{\varepsilon}_3 \quad (25)$$

The reactions in the kinematic couplings of the motor groups, together with the driving force in the hydraulic cylinder, form the existing data of procedure **A2RC**.

For the phases in which the hydraulic cylinder consisting of elements 2 and 3 is in action, the balancing force (driving force) in the active coupling B can also be calculated using the virtual exponent equation, namely:

$$\begin{aligned} \sum \bar{P} \cdot \bar{v} = & \bar{FE}_{32} \times \bar{v}_{32} + (\bar{F}_{i1} + \bar{G}_1) \cdot \bar{v}_{G1} + (\bar{F}_{i2} + \bar{G}_2) \cdot \bar{v}_{G2} + \\ & + (\bar{F}_{i3} + \bar{G}_3) \cdot \bar{v}_{G3} + (\bar{F}_{i4} + \bar{G}_4) \cdot \bar{v}_{G4} + (\bar{F}_{i5} + \bar{G}_5) \cdot \bar{v}_{G5} + \\ & + (\bar{F}_{i6} + \bar{G}_6) \cdot \bar{v}_{G6} + (\bar{F}_{i7} + \bar{G}_7) \cdot \bar{v}_{G7} + (\bar{F}_{i8} + \bar{G}_8) \cdot \bar{v}_{G8} + \\ & + \bar{M}_{i1} \cdot \bar{\omega}_1 + \bar{M}_{i2} \cdot \bar{\omega}_2 + \bar{M}_{i3} \cdot \bar{\omega}_3 + \bar{M}_{i4} \cdot \bar{\omega}_4 + \bar{M}_{i5} \cdot \bar{\omega}_5 + \\ & + \bar{M}_{i6} \cdot \bar{\omega}_6 + \bar{M}_{i7} \cdot \bar{\omega}_7 + \bar{M}_{i8} \cdot \bar{\omega}_8 = \bar{0} \end{aligned} \quad (26)$$

Using the above relationship, it results:

$$\begin{aligned} FE_{32} = & (m_1(a_{G1X} \cdot v_{G1X} + (a_{G1Y} + g) \cdot v_{G1Y} + IG_1 \cdot \omega_1 \cdot \varepsilon_1 + \\ & + m_2(a_{G2X} \cdot v_{G2X} + (a_{G2Y} + g) \cdot v_{G2Y} + IG_2 \cdot \omega_2 \cdot \varepsilon_2 + \\ & + m_3(a_{G3X} \cdot v_{G3X} + (a_{G3Y} + g) \cdot v_{G3Y} + IG_3 \cdot \omega_3 \cdot \varepsilon_3 + \\ & + m_4(a_{G4X} \cdot v_{G4X} + (a_{G4Y} + g) \cdot v_{G4Y} + IG_4 \cdot \omega_4 \cdot \varepsilon_4 + \\ & + m_5(a_{G5X} \cdot v_{G5X} + (a_{G5Y} + g) \cdot v_{G5Y} + IG_5 \cdot \omega_5 \cdot \varepsilon_5 + \\ & + m_6(a_{G6X} \cdot v_{G6X} + (a_{G6Y} + g) \cdot v_{G6Y} + IG_6 \cdot \omega_6 \cdot \varepsilon_6 + \\ & + m_7(a_{G7X} \cdot v_{G7X} + (a_{G7Y} + g) \cdot v_{G7Y} + IG_7 \cdot \omega_7 \cdot \varepsilon_7 + \\ & + m_8(a_{G8X} \cdot v_{G8X} + (a_{G8Y} + g) \cdot v_{G8Y} + IG_8 \cdot \omega_8 \cdot \varepsilon_8 - \\ & - Q \cdot \cos(\varphi_4 + \pi/2) \cdot v_{G4X} - Q \cdot \sin(\varphi_4 + \pi/2) \cdot v_{G4Y}) / v_{32}. \end{aligned} \quad (27)$$

For phases in which the hydraulic cylinder consisting of elements 5 and 6 is in action, the balancing force (driving force) in the active coupling may be calculated using the relationship:

$$\begin{aligned} \sum \bar{P} \cdot \bar{v} = & \bar{FE}_{65} \times \bar{v}_{65} + (\bar{F}_{i1} + \bar{G}_1) \cdot \bar{v}_{G1} + (\bar{F}_{i2} + \bar{G}_2) \cdot \bar{v}_{G2} + \\ & + (\bar{F}_{i3} + \bar{G}_3) \cdot \bar{v}_{G3} + (\bar{F}_{i4} + \bar{G}_4) \cdot \bar{v}_{G4} + (\bar{F}_{i5} + \bar{G}_5) \cdot \bar{v}_{G5} + \\ & + (\bar{F}_{i6} + \bar{G}_6) \cdot \bar{v}_{G6} + (\bar{F}_{i7} + \bar{G}_7) \cdot \bar{v}_{G7} + (\bar{F}_{i8} + \bar{G}_8) \cdot \bar{v}_{G8} + \\ & + \bar{M}_{i1} \cdot \bar{\omega}_1 + \bar{M}_{i2} \cdot \bar{\omega}_2 + \bar{M}_{i3} \cdot \bar{\omega}_3 + \bar{M}_{i4} \cdot \bar{\omega}_4 + \bar{M}_{i5} \cdot \bar{\omega}_5 + \\ & + \bar{M}_{i6} \cdot \bar{\omega}_6 + \bar{M}_{i7} \cdot \bar{\omega}_7 + \bar{M}_{i8} \cdot \bar{\omega}_8 = \bar{0} \end{aligned} \quad (28)$$

Using the above relationship, it results:

$$\begin{aligned}
 FE_{65} = & (m_1(a_{G1X} \cdot v_{G1X} + (a_{G1Y} + g) \cdot v_{G1Y} + IG_1 \cdot \omega_1 \cdot \varepsilon_1 + \\
 & + m_2(a_{G2X} \cdot v_{G2X} + (a_{G2Y} + g) \cdot v_{G2Y} + IG_2 \cdot \omega_2 \cdot \varepsilon_2 + \\
 & + m_3(a_{G3X} \cdot v_{G3X} + (a_{G3Y} + g) \cdot v_{G3Y} + IG_3 \cdot \omega_3 \cdot \varepsilon_3 + \\
 & + m_4(a_{G4X} \cdot v_{G4X} + (a_{G4Y} + g) \cdot v_{G4Y} + IG_4 \cdot \omega_4 \cdot \varepsilon_4 + \\
 & + m_5(a_{G5X} \cdot v_{G5X} + (a_{G5Y} + g) \cdot v_{G5Y} + IG_5 \cdot \omega_5 \cdot \varepsilon_5 + \\
 & + m_6(a_{G6X} \cdot v_{G6X} + (a_{G6Y} + g) \cdot v_{G6Y} + IG_6 \cdot \omega_6 \cdot \varepsilon_6 + \\
 & + m_7(a_{G7X} \cdot v_{G7X} + (a_{G7Y} + g) \cdot v_{G7Y} + IG_7 \cdot \omega_7 \cdot \varepsilon_7 + \\
 & + m_8(a_{G8X} \cdot v_{G8X} + (a_{G8Y} + g) \cdot v_{G8Y} + IG_8 \cdot \omega_8 \cdot \varepsilon_8 - \\
 & - Q \cdot \cos(\phi_4 + \pi/2) \cdot v_{G4X} - Q \cdot \sin(\phi_4 + \pi/2) \cdot v_{G4Y})) / v_{65}.
 \end{aligned}
 \tag{29}$$

RESULTS

Applying the theoretical method described below, by simulating the working process of a machine, designed to collect the municipal waste, for appropriate constructive dimensions, the results obtained are presented.

For the kinetostatic analysis of the mechanism we used:

- a) The kinematic scheme of the mechanism (Fig.1);
- b) The positions of the coupling adjacent to the base and dimensions of the elements as follows: $XA = 0$ m, $YA = 0$ m, $XD = 1.000$ m, $YD = -0.733$ m, $XF = 0.800$ m, $YF = -0.270$ m, $XH = 1.100$ m, $YH = -0.800$ m, $CE = 0.770$ m, $CD = 0.870$ m, $EF = 0.900$ m; $CG = 0.330$ m;
- c) Phase working times: $t_1 = 5$ sec, $t_2 = 5$ sec, $t_3 = 5$ sec, $t_4 = 5$ sec,
- d) Initial position of the mechanism: $S_{230} = 0.833$ m, $S_{560} = 0.667$ m;
- e) Hydraulic cylinder piston work: $stroke_{23} = 0.600$ m, $stroke_{56} = 0.400$ m;
- f) Hydraulic cylinder piston road lengths: $d_2 = 0.700$ m, $d_5 = 0.550$ m;
- g) Transmission function used for hydraulic cylinder actuation: sinusoidal function $l \sin$;
- h) The masses of the mechanism elements: $m_1 = 10.0$ kg, $m_2 = 5.0$ kg, $m_3 = 10.0$ kg, $m_4 = 20.0$ kg, $m_5 = 5.0$ kg, $m_6 = 10.0$ kg, $m_7 = 20$ kg; $m_8 = 20$ kg;
- i) Position of the mass centres: $DG_1 = CD/2$, $CG_2 = d_2/2$ m, $AG_3 = 0.4$ m, $CG_4 = CG/2$ m, $CG_5 = d_5 / 2$ m, $AG_6 = AD/2$ m, $FG_7 = 0.3$ m, $EG_8 = 0.3$ m;
- j) Inertial moments of elements: $I_{G1} = 0.6$ kgm², $I_{G2} = 0.2$ kgm², $I_{G3} = 1.1$ kgm², $I_{G4} = 0.2$ kgm², $I_{G5} = 0.3$ kg m²; $I_{G6} = 0.35$ kg, $I_{G7} = 1.0$ kg; $I_{G8} = 0.9$ kg;
- k) Technological strength:
 - $Q = 1000$ N, for branches *cb* and *cd* of the diagram in figure 2;
 - $Q = 0$ N, for branches *ab* and *da* of the diagram in figure 2.

In figures 6 and 7, the hodographs of the reactions in the *D* and *A* joints are presented.

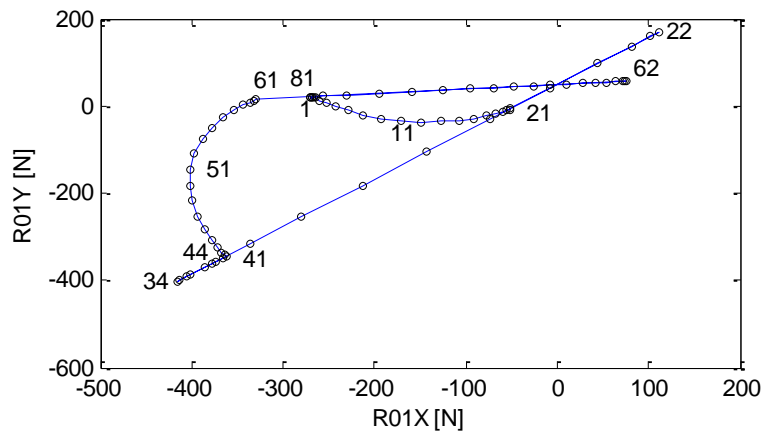


Fig. 6 – The hodograph of reactions in *D* joint

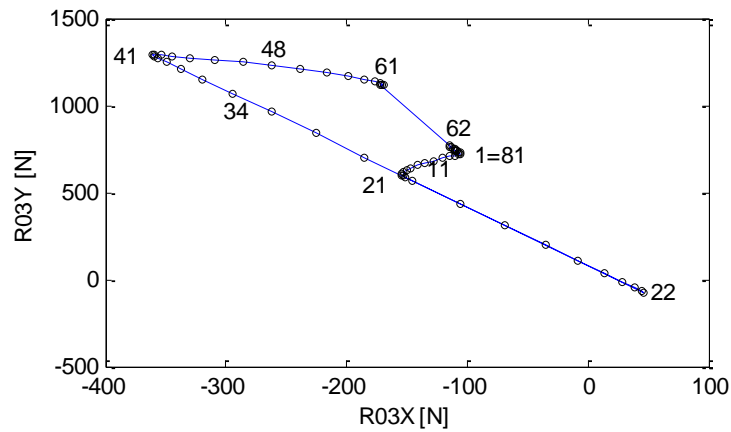


Fig. 7 – The hodograph of reactions in A joint

The diagrams of the driving forces in the hydraulic cylinders formed with elements 2 and 3, respectively 5 and 6, depending on the position of the mechanism, are shown in figures 8a and 8b.

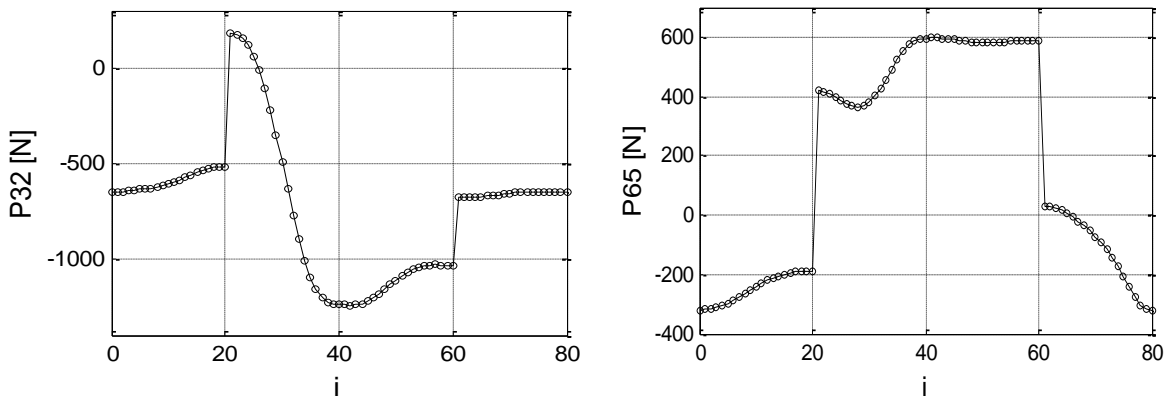


Fig. 8 – Driving force diagram

(a) from the hydraulic cylinder 2-3 ; (b) – from the hydraulic cylinder 5-6

Table 1 shows the size of the components on the coordinate axes of the reactions in the *D* and *H* kinematic couplings, depending on the position of the mechanism.

Table 1

Poz	R03X	R03Y	R01X	R01Y	R06X	R06Y
0	-109.94	741.26	-270.33	21.23	319.51	133.34
1	-109.47	738.49	-269.12	21.12	318.27	133.21
2	-108.83	735.68	-267.31	20.18	316.04	134.08
3	-107.95	732.80	-264.33	17.71	311.97	136.80
4	-106.91	729.80	-259.54	13.26	305.42	141.96
5	-106.03	726.56	-252.32	6.71	296.07	149.74
6	-105.84	722.86	-242.13	-1.57	283.88	159.90
7	-106.92	718.33	-228.63	-10.84	269.10	171.86
8	-109.70	712.50	-211.86	-20.03	252.22	184.80
9	-114.27	704.89	-192.29	-27.98	233.84	197.85
10	-120.37	695.14	-170.84	-33.67	214.68	210.20
11	-127.38	683.21	-148.70	-36.45	195.53	221.19
.....						
59	-171.60	1118.15	-329.85	14.84	-550.33	-111.01
60	-172.11	1121.07	-329.41	15.15	-550.80	-110.73
61	-114.07	766.47	75.80	56.85	-21.98	72.42
62	-114.00	766.04	74.42	56.71	-20.20	72.94
.....						
79	-109.81	740.44	-267.56	21.52	316.33	132.87
80	-109.94	741.26	-270.33	21.23	319.51	133.34

CONCLUSIONS

The values obtained for the reaction forces, through the kinematic analysis of the mechanism, allow proceeding to the next stage, i.e. the real design of the kinematic elements.

To verify the results obtained by kinematic analysis, the driving forces in the hydraulic cylinders and the method of virtual exponents were determined and the results were identical to those in the kinetostatic calculations. Depending on the driving forces in the hydraulic cylinders, we can choose the cylinders from the producers' constructive offer.

For collecting and compacting waste, the constructive form of the kinematic elements can be chosen by machine designers.

ACKNOWLEDGEMENT

Part of this paper was funded by the European Social Fund from the Sectoral Operational Programme Human Capital 2014-2020, through the Financial Agreement with the title "Scholarships for entrepreneurial education among doctoral students and postdoctoral researchers (Be Entrepreneur!)", Contract no. 51680/09.07.2019 - SMIS code: 124539.

REFERENCES

- [1] Artobolevski I.I., (1977), *Theory of mechanisms and machines (Theorie des mecanismes et des machines)*, 453 p., Mir Publishing House, Moscow / Russia;
- [2] Demidovitch B., Maron I., (1987), *Elements of numerical calculation (Elements de calcul numerique)*. 717 p., Mir Publishing House, Moscow / Russia;
- [3] Dorn W.S., Mc Cracken D.D., (1976), *Numerical methods with Fortran*, 468 p., Technical Publishing House, Bucharest / Romania;
- [4] Duca C., Buium Fl., Părăoanu G., (2003), *Mechanisms*, 481 p., Gh. Asachi Publ. House, Iasi/ Romania;
- [5] Moise V., Maican E., Moise Șt. I., (2003), *Numerical method in engineering*, 305 p., Bren Publishing House, Bucharest / Romania;
- [6] Moise V., Simionescu I., Ene M., Neacșa M., Tabără I.A., (2008), *Analysis of applied mechanisms*, 282 p., Printech Publishing House, Bucharest / Romania;
- [7] Moise V., Simionescu I., Ene M., Rotaru Al., (2015), *Analysis of plane mechanisms with articulated bars. Applications in MATLAB*, Printech Publishing House, Bucharest / Romania;
- [8] Moise V., Maican E., Moise Șt.I., (2016), *Numerical methods. Applications in MATLAB*, Printech Publishing House, Bucharest / Romania;
- [9] Moise V., Simionescu I., Ene M., (2018), *Optimal synthesis of flat cam mechanisms*, Printech Publishing House, Bucharest / Romania;
- [10] Pelecudi Chr., (1975), *Precision of the mechanism*, 398 p., Publishing House of the Academy of the Socialist Republic of Romania, Bucharest / Romania;
- [11] Pelecudi Chr., Simionescu I., Moise V., Ene M., (1981), *Design of mechanism*. Polytechnic Institute of Bucharest / Romania;
- [12] Pelecudi Chr., Maroș D., Merticaru V., Pandrea N., Simionescu I., (1985), *Mechanisms*, 394 p., Didactic and Pedagogical Publishing House Bucharest / Romania;
- [13] Simionescu I., Moise V., (1999), *Mechanisms*, 238 p., Technical Publishing House, Bucharest / Romania;
- [14] Voicu Gh., Lazea M., Zabava B.S., Tudor P., Moise V., (2019), Kinematic analysis of the pre-taking and pre-compacting mechanisms of some garbage trucks, *Journal of Engineering Studies and Research*, Vol. 25, No. 2, pp.56-62, Bacau / Romania;
- [15] Voicu Gh., Lazea M., Tudor P., Zabava B.St., Moise V., (2019), Comparative analysis of the municipal waste collection and pre-compacting systems, *Sixth International Conference Research people and actual tasks on multidisciplinary sciences*, pp.354-359, Lozenec / Bulgaria.

MODELING HERBICIDE INSTALLATION FOR THE TREATMENT OF PEACH PLANTATIONS

МОДЕЛИРАНЕ НА ХЕРБИЦИДНА УРЕДБА ЗА ТРЕТИРАНЕ НА НАСАЖДЕНИЯ ОТ ПРАСКОВИ

Dimitar Kehajov^{*1}; *Atanas Atanasov*² ¹

Agricultural University, Plovdiv, University of Ruse / Bulgaria

Tel: +359 87 817 2059; E-mail: dkehajov@mail.bg

DOI: <https://doi.org/10.35633/inmateh-60-34>

Keywords: modelling, herbicide installation, spraying, peaches

ABSTRACT

An approach to modeling herbicide installation for the treatment of peach plantations is proposed. The height of the stem was determined for 4 varieties of peaches. Considering this parameter, the maximum height of the herbicide system and the nozzles on it are indicated. Simulated modelling of the sprayed fluid along the working width of each nozzle was performed. The irregularity of spraying was determined depending on the distance between the nozzles. On the basis of the analysis, the optimal parameters of the spreader system were determined: height - 0.35 m, distance between the spreaders - 0.40 m.

РЕЗЮМЕ

Предложен е подход за моделиране на хербицидна уредба за третиране на прасковени насаждения. Определена е височината на стъблото при 4 сорта праскови. Съблюдавайки този параметър е посочена максималната височина на хербицидната уредба и на разпръсквачите, разположени върху нея. Извършено е имитационно моделиране на изпръсканата течност по работната ширина на всеки разпръсквач. Установена е неравномерността на пръскане в зависимост от разстоянието между разпръсквачите. Въз основа на направения анализ са определени оптималните параметри на разпръсквателната уредба: височина – 0,35 m, разстояние между разпръсквачите – 0,40 m.

INTRODUCTION

The problem with pesticide spraying in agriculture is in the conflict of increasing their deposition on the target crops on the one hand and reducing losses beyond the targets on the other (*Escolà A. et al., 2013*). Very often, treatment conditions impede both. Environmental pollution due to the deposition of pesticide droplets outside the target can be minimized by using optimum design and operating parameters of the sprayers (*Delele M. et al., 2007*). A three-dimensional model has been developed that is used to adjust the spread in orchards to reduce drift without reducing bio-efficiency. It has been established that the spatter quality is influenced by the steady speed, fan speed (airflow rate), number, type, size, position and orientation of the nozzles and the fluid pressure. The authors (*Ramsdale B. and C. Massersmith, 2001*) conducted field experiments to determine the effect of sprayer type, spray rate and additives in herbicide efficacy.

Herbicide applications are complex processes, and as such, few studies have been conducted that consider multiple variables that affect the droplet spectrum of herbicide sprays (*Creech C. et al., 2015*). The objective of this study was to evaluate the effects of nozzle type, orifice size, herbicide active ingredient, pressure, and carrier volume on the droplet spectra of the herbicide spray. The laboratory study was conducted using a Sympatec laser diffraction instrument to determine the droplet spectrum characteristics of each treatment combination. When averaged over each main effect, nozzle type had the greatest effect on droplet size. The effect on droplet size of the variables examined in this study from greatest effect to least effect were nozzle, operating pressure, herbicide, nozzle orifice size, and carrier volume.

¹ *Dimitar Kehajov, Assoc. Prof. Ph.D.; Atanas Atanasov, Assoc. Prof. Ph.D.*

In 2008 and 2009, *Kempenaar C. et al. (2011)* tested 11 machines from three categories of herbicide application technology: weed wipers, controlled droplet applicators (CDA) and sensor sprayers. Weed wipers used the least amount of herbicide, less than 0.05 L product ha⁻¹. Sensor sprayers applied between 0.1 and 0.4 L product ha⁻¹ depending on level of weed presence and configuration of the machine. The double number of nozzles and sensors on the spray bar reduced herbicide use by about 50%.

To control weeds, a pneumatic sprayer was developed to apply herbicides dissolved in oil or water with a volume of 2.3 L/ha (*McWhorter Ch. et al., 1988*). The working fluid is fed through a tube into an air stream that sprays it. The number of drops varies from 16 to 54 drops/cm² at an air jet pressure of 3.4 to 62 kPa and an outlet diameter of 2 mm. The number of droplets obtained at 34 kPa increased from 7 droplets/cm² at 0.8 mm of the hole to 48 droplets/cm² at the 2.4 mm diameter hole. The sprayer is designed primarily for treatment with oil-dissolved herbicides at rates of 2.3 to 4.7 L/ha.

Novel spray nozzles with high penetration efficiency and low drifting rates have been developed in recent years and exists on nozzle market (*Bolat A. et al., 2018*). To determine efficiencies of these new products on weed control the authors tested standard flat fan nozzle, air induction nozzle, with standard flat fan nozzle at three different herbicide application volume of 200 l/ha, 300 l/ha and 400 l/ha. Efficiency levels of each method was determined via pesticide coverage rates, weed control efficiency. Wiper applicators allow herbicides to be directly transferred onto the surface of target plants, thereby avoiding application to nearby desirable plants of shorter stature (*Harrington K. and H. Ghanizadeh, 2017*). This form of herbicide application can greatly reduce costs of weed control and risks of environmental contamination. The risk of drift to susceptible plants in areas adjacent to the weed control operations can also be eliminated by using wiper applicators. Despite the huge potential for using wiper applicators to improve weed control in agricultural and non-agricultural sectors, there has been only limited research into the factors that might affect their performance and efficacy. These factors include the growth stage of weeds at the time of application, types of herbicide used, design of wiper applicator and the quantity of herbicide deposited on plants.

An interesting field study was conducted in 2015 and 2016 to compare particle drift of glyphosate using a fluorescent tracer dye applied with hooded and open sprayers at four spray qualities (*Foster H. et al., 2018*). It is current agronomic practice to estimate the average weed density throughout the field and to use this information to decide whether or not to spray and at what dose to apply the herbicide used (*Paice M., P. Miller, W. Day, 1996*). Significant long-term economic and environmental benefits are expected to accrue if the herbicide dose changes according to spatial variations in weed density. The high availability and relatively low cost of information technology and electronic control systems make this concept more practical, but its implementation places a number of limitations on the specification of the sprayer. Chemical weed control is, and will continue to be, essential in high-yield agriculture (*Biller R., 1998*). However, economic and environmental considerations call for a further reduction in herbicide use in the future. One method of achieving this is the localized application of herbicides to weeds. The detection of weeds against the background of soil or plant debris is possible using optoelectronic sensors. The application of such a system results in herbicide saving between 30 and 70%, with a weed control efficiency of 100%.

Precise weed control uses ultrasound recognition and guidance (*Andújar D. et al., 2012*). Site-specific weed management requires sensing of the actual weed infestation levels in agricultural fields to adapt the management accordingly. However, sophisticated sensor systems are not yet in wider practical use, since they are not easily available for the farmers and their handling as well as the management practice requires additional efforts. The ultrasonic readings permitted the separation between weed infested zones and non-infested areas with up to 92.8% of success. This system will potentially reduce the cost of weed detection and offers an opportunity to its use in non-selective methods for weed control.

An aggregated distribution pattern of weed populations provides opportunity to reduce the herbicide application if site-specific weed management is adopted (*Hamouz P. et al., 2013*). The weed infestation was estimated immediately before the post-emergence herbicide application. Treatment maps for every weed group were created based on the weed abundance data and relevant treatment thresholds. The herbicides were applied using a sprayer equipped with boom section control. The herbicide savings were calculated for every treatment and the differences in the grain yield between the treatments were tested using the analysis of variance. The site-specific applications provided herbicide savings ranging from 15.6% to 100% according to the herbicide and application threshold used.

The author *Lei Tian (2002)* develops and tests an intelligent sprayer for accurate pesticide application based on local vision. The aim is to develop new technologies to evaluate the density and size of weeds in real time and to effectively reduce the amount of herbicide applied to crops. The machine vision system is specially designed to operate under variable outdoor lighting conditions. Multiple vision sensors have been used to cover the target area. Weed infestation conditions in each control zone (control area) were detected instead of trying to identify each individual plant in the field. To increase the accuracy of delivery, each individual spray nozzle is controlled separately. The integrated system was tested to evaluate performance and productivity under different conditions.

Site-specific application of pesticides has so far focused mainly on herbicides (*Ørum J.E. et al, 2017*). The purpose of precision farming technologies in relation to herbicide use is to reduce herbicide cost and environmental impact from spraying, but at the same time to achieve acceptable weed control. Another purpose is to increase the spraying capacity, to reduce the number of sprayer refills, and finally to minimize time spent on weed monitoring.

The authors *Beckie H., K. Harker (2017)* recommend several effective practices for weed control with reducing herbicide treatment. Another way to control weeds is to apply alternative methods (*Rifai M., M.Bartošová, P.Brunclik, 2000*). The authors compare 3 alternative methods with traditional chemical in terms of efficiency and cost. 1) Gas treatment is carried out at 7-day intervals, 3 times. Low speed gives good results in the early stages of growth. In order to achieve higher efficacy in emergent weeds, perennials, weeds in later stages of growth and weeds with higher germination intensity, repetition of treatments is required. 2) Hot steam treatment at a travel speed of 1 km/h over an interval of 7 days. This technology is less effective in perennial weeds. For greater reduction of emergent weeds and for a longer period of time, re-treatment is required, maximum 2 weeks after the first one. 3) Mulching with sawdust results in 99.4% reduction of weeds. Only one treatment with chemical preparations was performed. The results are extremely good 2-3 weeks after treatment. Later, new weeds emerge and emerge, and repeating the treatment is inevitable.

The analysis shows that the chemical method is fundamental in the control of weeds in cultivated crops. The purpose of the presented study is to propose an approach for modeling an herbicide installation for the treatment of peach plantations under specific conditions.

MATERIALS AND METHODS

The observations in this work were carried out in a young peach plantation established 5 years ago with a total area of 1.0 ha. The field is of irregular geometric shape conditionally divided into 2 parts: a rectangle 80x75 m in size and a trapeze with a large base 80 m, a small base - 30 m and a height of 75 m. Four varieties are grown: Laskava, Ufo, Femina and Cassiopeia. Each of the varieties has an area of 0.25 ha. The trees are planted 5 m between rows, and inside the row the step is 4 m. 50 trees are grown in 0.1 ha, with a distance of 3 m from the adjacent fields.

The problem with this planting is the presence of many weeds. Attempts to mechanically destroy them by cultivation do not produce the desired effect. Destroying them requires spraying with an herbicidal bar spraying system, as treatment with a fan sprayer can cause stress or destruction of the trees by inaccurately directing the jet from the working solution.

An important condition for herbicide spraying is not to treat the leaves of fruit trees. The spraying system must be below the crowns of the trees, at a certain distance from their lowest spaced parts. The height of the stem and the limits of its variation have a significant influence on this limitation. Taking this into account, this determines the height at which the spraying system is to be positioned without the risk of spraying on the leaf mass of the trees grown. This data shows us the overall height of the spraying system. During spraying, the movement takes place in pre-treated row spacing. This implies a lot of bumps along the way. There is a danger that its frame will come into contact with some of the lower branches of the trees and damage or destroy them.

For the correct selection of the working height of the spraying system, a dimensional characteristic of the peach tree varieties from the observed plantation is made. For this purpose, 10 seedlings from each of the cultivated varieties are randomly selected and the height of the stem of each of them is measured. The data obtained from the measurements are processed with the software Statistica version 13.3.

By working with bar spraying system, they are required to provide very good transverse uniformity throughout the working width.

The simulation of the bar spraying system at a certain height is performed by varying the distance between the nozzles. The main objective of the changed distances is to determine the optimum distance, with the smallest transverse irregularity in the amount of fluid sprayed (the smallest CV coefficient).

The experimental studies were performed with a Lechler IDK 120-03 injector nozzle at the Department of Agricultural Mechanization at the Agrarian University, Plovdiv at the stand (*Trifonov A. et al., 2000*) shown in Figure 1.

The stand consists of a tank, a piston diaphragm pump with a flow rate of 105 l / min and a pressure of 2 MPa, a boom spray system composed of 5 separate sections with 3 nozzles each. In the first section it is possible to change the height of the nozzles above the collecting platform in the range from 0.20 to 1.00 m and the distance between them from 0.30 to 0.70 m. Below the sections is a collecting platform measuring 1.20 x 2.00 m and consisting of 40 channels with a width of 0.05 m, 0.07 m depth and a slope of 5°. Below each channel is a measuring cylinder with a volume of 200 cm³.

The stand is controlled by the onboard controller for controlling the TeeJet 884-E sprayers. Under its control are the main shut-off valve, 5 section shut-off valves, the pressure regulator. The controller allows selecting the proper sprayer operating mode and controlling this mode by displaying the solution pressure, speed, nozzle size, solution consumption rate and spray area up to date.

The stand has a flowmeter, a turbine type with a magnetic induction sensor and a speed simulator consisting of a pneumatic wheel and an induction sensor. The speed of the wheel is steadily controlled by an induction motor and a frequency converter.

Changing the managed variables involves the following basic steps: adjusting the height above the collecting plane 0.35 m; distance between the tips of the triangular chutes from the collecting plane 0.05 m; pressure in the discharge line 0.3 MPa; The experiment was carried out in 3 repetitions, measuring the amount of fluid entering the collecting chutes by measuring cylinders.



Fig. 1 - Experimental stand of spreader boom system

The amount of working fluid in each measuring cylinder is equal to the amount sprayed at 0.05 m from the working width of the nozzle, depending on the distance to its axis. The results of the experiment are given in the first row in an Excel table. In the next row, the same data is plotted, offset by 0.35 m (from 8 columns to the right). In the third row, the same data is offset by another 0.35 m (from 15 columns). In this way the work of 3 adjacent nozzles is imitated. The results of the three rows are collected by columns (each corresponds to the amount of spray solution from the nozzle 0.05 m from its working width). A histogram for the distribution of the working fluid is constructed. A variational analysis of the obtained results was made - average, variance, root mean square deviation and coefficient of variation were found. Using the obtained values for the coefficient of variation, a curve is constructed and, by its nature, the distance between the nozzles is determined, where the agrotechnical requirements ($CV \leq 10\%$) are maximum satisfied.

The second series of calculations is made at a displacement of 0.40 m, and the third - at a displacement of 0.45 m.

RESULTS

- Stem height

In this indicator, the results are strongly grouped. The average value for all varieties is about 0.63 m. Almost complete overlap of stem height scattering was observed in the individual varieties (Figure 2).

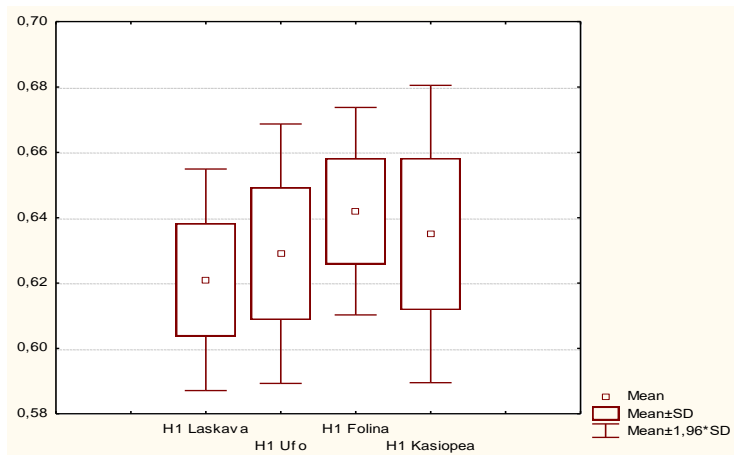


Fig. 2 - Stem height

This leads to the claim that this indicator has no proven statistical difference between the cultivated peach varieties.

Table 1

Stem height						
Descriptive Statistics						
	Valid N	Mean	Minimum	Maximum	Variance	Std.Dev.
H1 Laskava	10	0,621000	0,600000	0,650000	0,000299	0,017288
H1 Ufo	10	0,629000	0,600000	0,660000	0,000410	0,020248
H1 Folina	10	0,642000	0,620000	0,660000	0,000262	0,016193
H1 Kasiopea	10	0,635000	0,600000	0,660000	0,000539	0,023214

The expected lowest placement of twigs and leaves on them may be about 0.59 m. Between the nozzles, the machine frame on the one hand and these twigs on the other, a buffer zone of about 0.25 m is required. It follows that the height of the frame and the spraying system cannot be more than 0.35 m.

σ

- Unevenness in working width

The following results were obtained for the distribution of the working fluid spread over the width of the torch (Table 2)

Table 2

Indicators	Distribution of the working fluid along the width of the torch, ml																
	Distance from the nozzle axis, m																
	0.4	0.35	0.3	0.25	0.2	0.15	0.1	0.05	0	0.05	0.1	0.15	0.2	0.25	0.3	0.35	0.4
Amount of working fluid	6	12	17	27	45	63	76	88	110	88	76	63	45	27	17	12	6

The results obtained are plotted in an Excel table and processed according to the procedure described in the Materials and methods section.

The results for each distance between the bar nozzles are statistically processed and presented in the following figures:

- for a distance of 0.35 m

Figure 3 shows that there is a rather large unevenness in the working width. As a rule, two adjacent nozzles must 100% overlap (with their left and right half torches) the torch of the nozzle located between them. When the distance is not optimal (small spread height or small / large distance between the nozzles) there is no possibility to provide this overlap and the distribution of the sprayed liquid is obtained with large irregularities as is the case here.

- for a distance of 0.40 m

Figure 4 shows that as the distance between the nozzles increases, the irregularity observed above (Figure 3) decreases substantially, being below the standard threshold of 10% for the coefficient of variation.

The results obtained in this embodiment are better than the previous one with deviations along the axis and at a distance of 0.35 m to the left and right of the axis. In the other positions, a relatively good levelling of the sprayed liquid is observed.

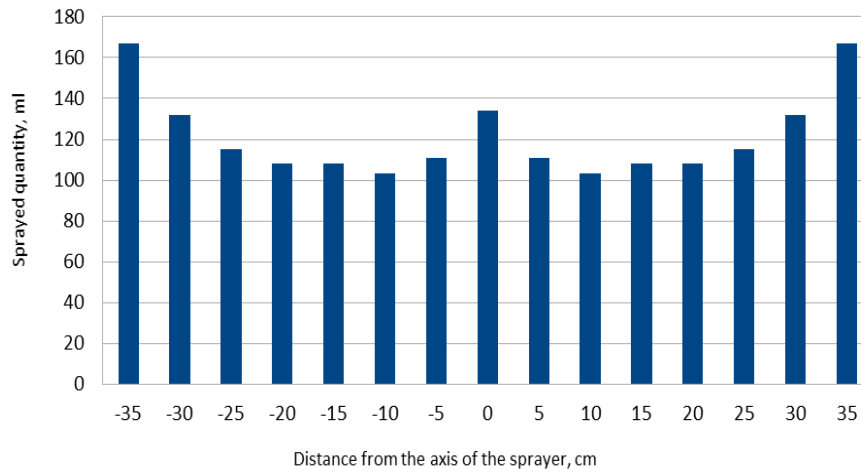


Fig. 3 - for a distance of 0.35 m between the nozzles

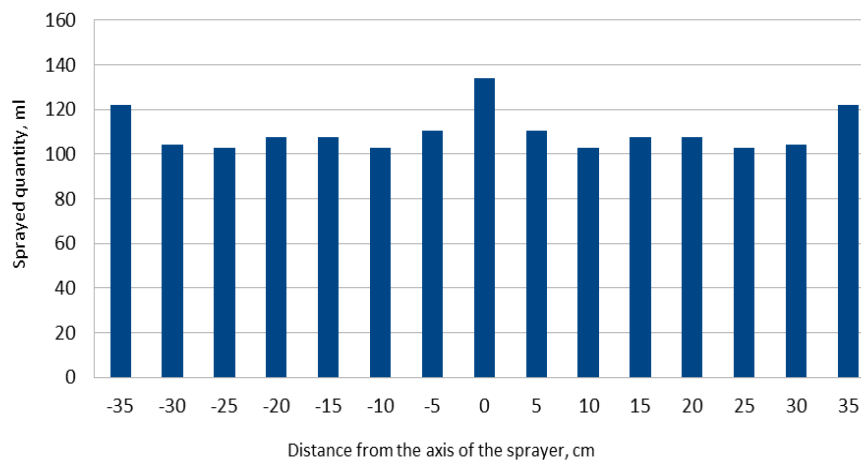


Fig. 4 - for a distance of 0.40 m between the nozzles

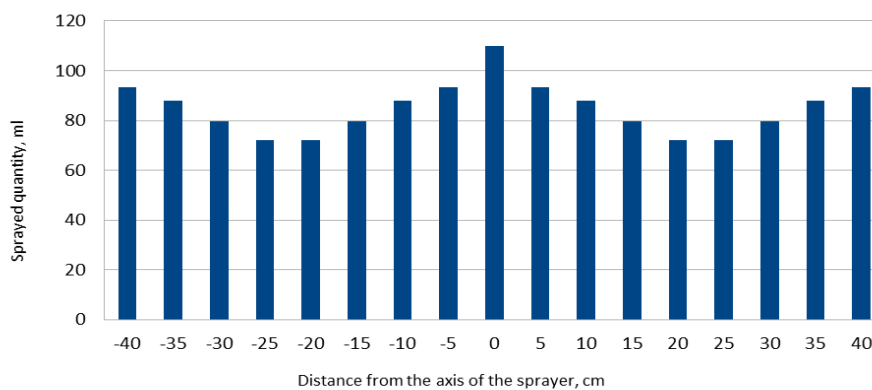


Fig. 5 - for a distance of 0.45 m between the nozzles

At this distance between the nozzles, there is an increase in unevenness. To determine the optimum distance of the bar at which there will be minimal unevenness in the working width, a variational analysis was performed with the data obtained for the sprayed amount of fluid across the bar width.

The end result of this analysis is to obtain the so-called coefficient of variation. A regression curve is constructed with the coefficient of variation data. The minimum in this curve gives us the answer for the optimum distance between the nozzles at a fixed spray height of 0.35 m

Table 3

Indicators	Spacing between nozzles, [m]		
	0.35	0.40	0.45
Average value, \bar{X}	137	110	91
Dispersion, σ^2	717	82,9	130
RMS, σ	26.77	9.05	11.38
Coefficient of variation, CV %	19.49	8.22	12.68

The limit on the coefficient of variation must not exceed 10%. To determine the limits of variation of the spray height at which this condition is met, the graph of Figure 6 is plotted.

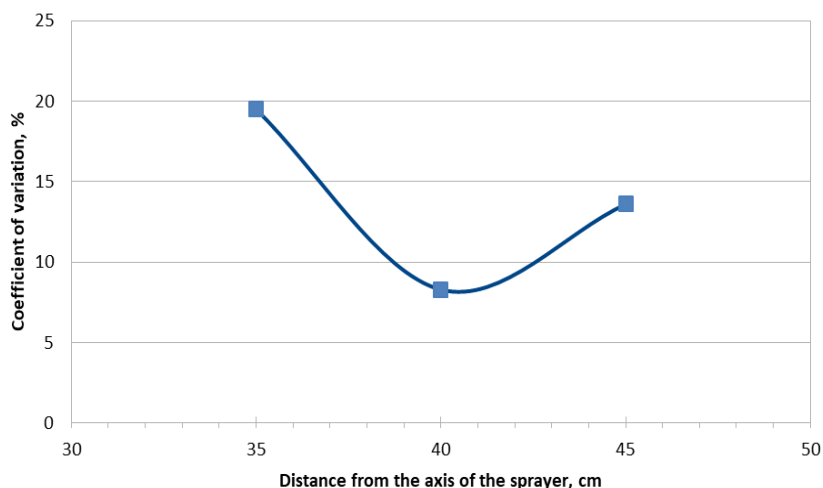


Fig. 6 - Coefficient of variation

The graph shows that the (CV) % coefficient of variation with the nozzle of 0.40 m has the lowest value and meets the agro-technical requirements as follows:

The width of the frame will be 3.5 m so that the treated trees will not be damaged during the movement. It will be pivotally secured with 2 deflecting sections each 1 m long for interior space treatment. At the ends of the deflection sections, 2 free rotating wheels with rubber sheath are mounted. On contact with the stem, they push the sections back and forth in the aisle so that there is no damage. After passing the obstacle, the sections return to the starting position under the influence of springs attached to the frame and each section.

CONCLUSIONS

An approach to modelling the herbicide installation for the treatment of peach plantations is proposed, including the following herbicide spraying parameters for a particular plantation: 1) height of the spraying system and the frame – 0.35 m; 2) distance between nozzles – 0.40 m; 3) frame width – 3.5 m.

ACKNOWLEDGEMENT

The article reflects the results of the work on the project 2020-AIF-01.

REFERENCES

- [1] Andújar D., Weis M., Gerhards R., (2012), An Ultrasonic System for Weed Detection in Cereal Crops, *Sensors*, 12, pp.17343-17357, Sensors (Basel);
- [2] Beckie H., Harker K., (2017), Our top 10 herbicide-resistant weed management practices, *Pest Management Science*, 73 (6), pp.1045-1052, SCI (Society of Chemical Industry);
- [3] Biller R., (1998), Reduced Input of Herbicides by Use of Optoelectronic Sensors, *Computers and Electronics in Agriculture*, Vol.71 (4), pp.357-362, Ed. Elsevier B.V. London/U.K.;
- [4] Bolat A., Bayat A., Tetik O., Karaagac A., Cerit I., Sevelmis U., (2018), Performance of Herbicide Spraying Methods at Different Application Volumes in Maize, *Frezenius Enviromental Bulletin*, vol.27 (5), pp.2963-2967, Germany;
- [5] Crech C., Henry R., Fritz B., Kruger G., (2015), Influence of Herbicide Active Ingredient, Nozzle Type, Orifice Size, Spray Pressure, and Carrier Volume Rate on Spray Droplet Size Characteristics, *Weed Technology*, 29 (2), pp. 298-310, Cambridge University Press;
- [6] Delele M. et al., (2007), CFD prototyping of an air-assisted orchard sprayer aimed at drift reduction, *Computers and Electronics in Agriculture*, 55: pp. 16–27, Ed. Elsevier B.V., London/U.K.;
- [7] Escolà A., Rosell-Polo J.R., Planas S., Gil E., Pomar J., Camp F., Llorens J., Solanelles F., (2013), *Computers and Electronics in Agriculture*, Vol.95, pp.122-135, Ed. Elsevier B.V., London/U.K.;
- [8] Foster H., Sperry B., Reynolds D., Kruger G. and Claussen S., (2018), Reducing Herbicide Particle Drift: Effect of Hooded Sprayer and Spray Quality, *Weed Technology*, 32 (6), pp.714-721, Cambridge University Press;
- [9] Hamouz P., Hamouzová K., Holec J., Tyšer L., (2013), Impact of site-specific weed management on herbicide savings and winter wheat yield, *Plant Soil Environ.*, 59, pp.101-107, Czech Academy of Agricultural Sciences;
- [10] Harrington K., Ghanizadeh H., (2017), Herbicide application using wiper applicators - A review, *Crop Protection*, Vol.102, pp.56-62 Elsevier B.V. , London/U.K.;
- [11] Kempenaar, C., Michielssen J., Dijk C., (2011), Herbicide weed control on pavements: advances in application technology, *Aspects of Applied Biology*, 114, pp.105-112, Association of Applied Biologists, Warwick/U.K.;
- [12] Lei Tian, (2002), Development of a sensor-based precision herbicide application system, *Computers and Electronics in Agriculture*, 36 (2-3), pp.133-149, Ed. Elsevier B.V., London/U.K.;
- [13] McWhorter Ch., F.Fulgham and W.Barrentine, 1988, An Air-Assist Spray Nozzle for Applying Herbicides in Ultralow, *Weed Science*, Vol. 36 (1), pp. 118-121, Cambridge University Press;
- [14] Ørum J.E., Kudsk P., Jensen P.K., (2017), Economics of Site-Specific and Variable-Dose Herbicide Application. In: Pedersen S., Lind K. (eds) *Precision Agriculture: Technology and Economic Perspectives*. *Progress in Precision Agriculture*. Springer, Cham;
- [15] Paice M., Miller P., Day W., (1996), Control requirements for spatially selective herbicide sprayers, *Computers and Electronics in Agriculture*, Vol.14 (2–3), pp.163-177, Ed. Elsevier B.V. , London/U.K.;
- [16] Ramsdale B. and Messersmith C., (2001), Nozzle, Spray Volume, and Adjuvant Effects on Carfentrazone and Imazamox Efficacy, *Weed Technology*, 15 (3), pp.485-491, Cambridge University Press.;
- [17] Rifai M., Bartošová M., Brunclík P., (2000), Alternative Methods of Weed Control in Apple Orchards, *Pakistan Journal of Biological Sciences* 3 (6): pp.933-938, Asian Network for Scientific Information, Pakistan;
- [18] Trifonov A. et al, (2000), Stand simulator of the work of plant protection sprayers; *Agricultural Machinery*, XXVII, 4, pp. 20-24 (Трифонов А. и др.; 2000, Стенд-симулатор на работата на пръскачки за растителна защита; *Селскостопанска техника*, XXXVII, 4, с.20-24), Scientific-Technical Union of Mechanical Engineering INDUSTRY 4.0, Bulgaria.

EFFECTS OF DOUBLE V-SHAPED OPENERS WITH FURROW COMPACTION FUNCTION ON SEEDBED CHARACTERISTICS AND SOYBEAN EMERGENCE UNDER DOUBLE ROW RIDGE CULTIVATION TECHNIQUE

垄上双行种植技术下具有种沟镇压功能的双 V 型筑沟器对种床特性和大豆出苗的影响

Jiaxin Zheng, Jiameng Fang, Yuqing Zhao, Yong Zhao,
Zhi Yang, Rong Chen*)¹

School of Mechanical and Electrical Engineering, Yunnan Agricultural University, Kunming 650201, China
Tel: 15808841895; E-mail: 15808841895@163.com
DOI: <https://doi.org/10.35633/inmateh-60-35>

Keywords: double V-shaped opener, soybean, seedbed characteristics, furrow compaction

ABSTRACT

Based on the technical characteristics of double-row ridge planting, a double V-shaped opener with the furrow compaction function was designed. This opener with the sliding knife and profiling mechanism was capable of furrow opening, compacting and profiling, and thereby created excellent seedbeds with tight bottom and soft soils. Through sunlight greenhouse tests, the effects of the double V-shaped opener on seedbed characteristics and soybean emergence were studied under the compaction forces of T1 (0 N), T2 (500 N), T3 (600 N) and T4 (700 N). The furrow compaction planting significantly affected the seedbed characteristics and soybean emergence and could preserve soil moisture in seedbeds. Under the semiarid condition, the average emergence time under T2 was 0.79 day earlier than under T1, and the emergence rates under T2, T3 and T4 were significantly raised. The seedling height uniformity under T2 was 5.34% higher than under T1. The average emergence time ranked from early to later as T3<T4<T2. The deep seeding uniformity, the emergence uniformity and the average seedling height were all improved as the furrow compaction force was enlarged within 500-700 N. Furrow compaction could preserve soil moisture in seedbeds, and the seedbed soil physical properties and soybean seedling emergence were optimized under the furrow compaction force of 600-700 N.

摘要

本文根据垄上双行的种植技术特点, 设计了具有种沟镇压功能的双 V 型筑沟器, 该筑沟器具有滑刀和仿形机构, 可实现开沟、压沟和仿形功能, 进而构建底部紧实, 覆盖土壤松软的优良种床。

通过日光温室试验, 研究分别在 T1 (0N)、T2 (500N)、T3 (600N)、T4 (700N) 镇压力下, 双 V 型筑沟器对种床特性和大豆出苗的影响。结果表明, 种沟镇压播种对种床特性和大豆出苗的影响是显著的。在半干旱环境下, T2 的平均出苗时间比 T1 提前 0.79 天, T2、T3、T4 的出苗率显著提高, 苗高一致性 T2 比 T1 提高了 5.34%, 平均出苗时间由短到长依次为: T3<T4<T2。在 500-700N 镇压力范围内, 随着种沟镇压力的增大, 播深一致性越好, 出苗一致性越好, 平均苗高随镇压力的增大而增大。试验表明, 种沟镇压对种床土壤具有保墒作用, 种沟镇压力为 600-700N 时, 种床土壤物理特性及大豆出苗情况最佳。

INTRODUCTION

Soybean is one of the three major crops in Northeast China (Wei et al., 2015). The annual yield of soybean in the spring sowing areas of Northeast China accounts for 40% of total annual yield in China. The total soybean planting area in Northeast China is the largest and most productive in the country (Xue, 2013). The double row ridge cultivation technique is one of the commonly-used planting techniques in the soybean planting areas of Northeast China (Jia et al., 2016; Jia et al., 2017). The technique is defined as the way of planting two rows of soybeans in 60- to 65-cm-wide routine ridges at the between-row distance of 10 to-15 cm as well as the auxiliary advanced cultivation techniques. Compared with the single-row ridge planting at the same variety and density, the double row ridge cultivation raises the crop yield by 15%-20% and the water and fertilizer utilization rate by 10% (Liu et al., 2010). This technique is illustrated in Fig. 1.

¹ Jiaxin Zheng, Lect. Ph.D.; Jiameng Fang, Stud.; Yuqing Zhao, A.P.; Yong Zhao, Stud.; Zhi Yang, Stud.; Rong Chen, Lect. Ph.D.

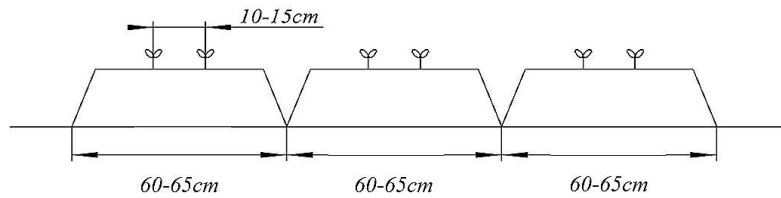


Fig. 1 - Schematic diagram of the double row ridge cultivation technique

During furrow compaction, the soils of the planting layers are crushed and compacted prior to planting so as to eliminate gaps between soil clods. This procedure prevents moisture evaporation and loss (preservation of soil moisture) and is favourable for the elevation of soil moisture from deep layers through capillary pores, so that moisture can gather in the planting layers. This procedure promotes seed germination. Planting via agricultural mechanization depends on seed furrow compaction, which ensures seeding depth conformity and below-seed soil consolidation that are favourable for seedling emergence. Practice proves that loose seedbeds are favourable for soil moisture conservation, and compacted root beds contribute to raising humidity and to the root growth and development of crops (Jia et al., 2015; Zhao et al., 2017; Li et al., 2019). As reported, too large or too low soil compactness is unfavourable for crop growth (Nawaz et al., 2013). At the soil depth 0-200 mm, the threshold soil compactness for crop growth is 2-3 MPa, and soil compactness beyond this threshold will decelerate root growth (Shah et al., 2017). The task of farmers is to create a "loose top and compact bottom" plowed soil layer for crops (Pulkrabek et al., 2015), but this task cannot be accomplished only by the use of press wheels.

Furrow compaction can crush the large soil aggregates and makes the soil aggregates around the seedbeds uniform and tight (Neto and Angelo, 2012; Song et al., 2009). Theoretically, furrow compaction can crush seedbed soil macroaggregates, makes the peripheral soils uniform and compact and significantly enhances crown dry weight, root length and seedling height, which are all favourable for raising soybean emergence rate and shortening the emergence time.

MATERIALS AND METHODS

Design of double V-shaped opener

The structure of the double V-shaped opener (China Patent, CN 104584732 B) is illustrated in Fig. 2.

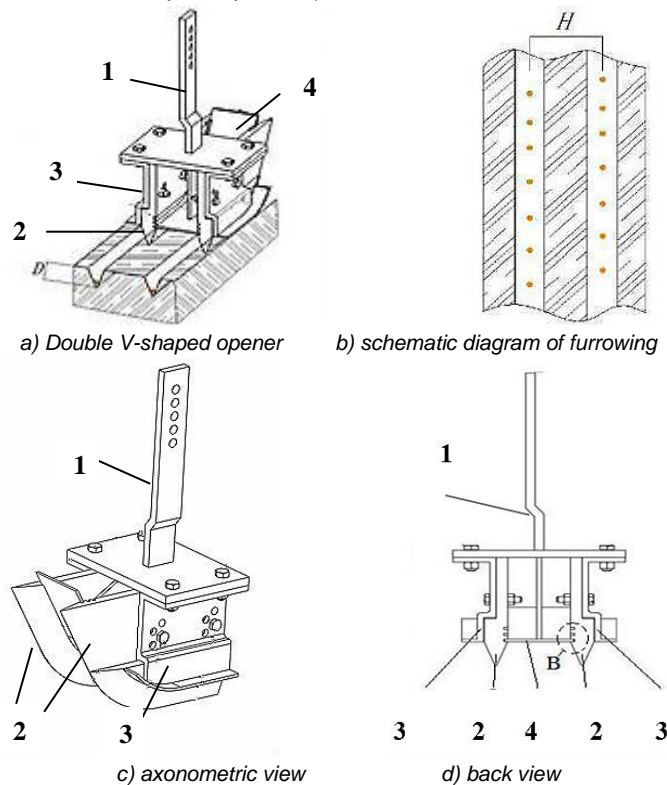


Fig. 2 - Double V-shaped opener

1 - shovel-handle connection frame 2 - squeezing knife 3 - profiling pressing plate 4 - central plate

Note: D is furrowing depth, mm; H is space between two adjacent furrows, mm.

According to the agronomic requirement of soybean ridge double-row precision planting, we designed a double V-shaped opener with furrow creating blades. It mainly consisted of a shovel-handle connection frame, two symmetrical profiling pressing plates, a central pressing plate, and two symmetrical V-shaped squeeze knives. This can opener creates two seed furrows with V-shaped sections. The seeds falling into the furrows will be retained at the bottom, which ensured the seeds will be linearly distributed. The furrow row space H was 100-150 mm according to agronomic requirements, and the furrowing depth D can be adjusted to 40, 50 or 60 mm. The seed furrows featured with smooth walls, compact soils, uniform shapes and consistent depth ensured the uniformity of planting depth, improved seeding quality, protected moisture and decreased water loss.

The profiling pressing plate, the central plate of the handle connection frame, and the lateral walls of the V-shaped squeeze knives functioned together, which imposed pressure on the side walls of the seed furrows, thereby tightening the furrow shape and creating smooth furrows. The large furrow compactness decreased moisture loss and wall coarseness, avoided wall soil glide, and reduced the probability of seeds being retained on walls or being brought out of furrows. The resulting furrows were smooth-surfaced and uniformly-shaped with consistent depth, which ensured the uniformity of planting depth (Murray and Chen, 2019).

Experimental field

Experiments were conducted in the sunlight greenhouse of College of Biological and Agricultural Engineering, Jilin University (N43.86°, E125.34°, 200 m altitude). This area was located in the cold temperate zone and enjoyed the continental monsoon climate in the north temperate zone, with frequent winds in spring and autumn. The average annual rainfall was 450-550 mm, sunshine duration was 2350-2450 h, and effective accumulated temperature was 2300-2700°C. The sunlight greenhouse was provided with the typical black soil in Northeast China and located in a flat terrain with fertile soils. In the past 30 years, the average summer temperature (June to August) was 20.9-22.8°C, and the precipitation in this period was 300-350 mm, accounting for about 60% of total annual precipitation. In dry and cold winters, the average precipitation was less than 30 mm, which accounted for only 5% of annual precipitation. The soil physical and chemical properties before the experiments are shown in Table 1.

Table 1

Some physical and chemical properties of the soil from the experimental field at 0–100 mm depth range

Properties	Values
Cone index (MPa)	0.920
Bulk density (g/cm ³)	1.233
Water content (% d. b.)	21.4
Soil temperature (°C)	14.3
pH	7.06
Organic matter (%)	2.56
Total nitrogen (%)	0.14
Available Potassium (K ₂ O, mg/kg)	172.2
Available phosphorus (P ₂ O ₅ , mg/kg)	16.5

Experimental design and processing method

During the experiments from August to September 2017, weeding and irrigation were conducted in the period 6-11 August. When the soil moisture content at 0-100 mm deep reached 10%-11%, soil preparation, ridging and suppression were started. Soybeans were sowed manually and equidistantly on August 11 and completed the same day. The experiments lasted 30 days and the tilling way was ridge tillage.

Four ridges were created in the experimental field. After the ridges were compacted, the height from the platform to the furrow was 180 mm-(with error of 20 mm), the ridge length was 10 m, and the upper surface of the platform was 200-300 mm wide. At both ends of each ridge, a 0.5-m-long adjusting zone was reserved. The 9-m-long central part was divided into three 3-m-long segments, which were the data acquisition areas under stable working. Two furrows were opened on each ridge, and the space between the furrows was 110 mm. The notations were T1 to T4: furrowing with total compaction force of 0, 500, 600 and 700 N respectively.

Subsidiary tests were conducted by using the parts that can create two V-shaped furrows on the seedbed and can compact furrows by increasing the counterweight (Fig. 3a). Bionic press wheels in diameter of 300 mm and width of 210 mm were used to compact the soils after covering (Fig. 3b).



a) Parts of supplementary tests



b) Bionic press roller

Fig. 3 - Test materials

The variety of the tested soybean seeds was Hefeng50. The average soil temperature on the ridges during the test period was 19.1°C, which met the requirement for sowing. The seeding method is manual seeding at equal distance. The double V-shaped opener with furrow compaction ability was used to create two furrows on each ridge. On each ridge, 60 seeds were sowed, with 30 seeds in each furrow. The space between rows was 110 mm, the row distance was 110 mm, and the seeding depth was 50 mm. Theoretical research shows the crop yield is significantly related to the optical energy per unit area. The ideal planting way for higher soybean yield is the equal distance between rows. Under this planting mode, the between-plant competition is the smallest, and it creates the canopy that receives the largest irradiation energy (Celik *et al.*, 2007) (Fig. 4a). Soil covering with shovels was conducted to avoid disturbance of soils. Profiling press rollers were used in soil compaction throughout (Fig. 4b).



a) Manual sowing



b) Design sketch after sowing

Fig. 4 - Furrowing, sowing and compaction in the sunlight greenhouse

To simulate field mechanized sowing and avoid effects of fertilization on soybean seedling emergence, we did not apply watering or fertilization at the emergence stage.

Soil physical properties

From the start to the end of emergence, soil volumetric moisture contents were measured by a soil moisture analyzer (TDR300 Soil Moisture Meter, USA). Each ridge was divided equally into 3 segments. In each segment, measurement was conducted 10 times and the average was conducted. Before and after operations, soil compactness was measured using an SC900 soil compaction meter. Measurement was conducted every 50 mm at the depth of 0-100 mm by using a 3/4"-diameter cone head.

Status of seedling emergence

From the start to the end of seedling emergence, the seedlings in each segment were counted every two days. The emergence rate (PE) and mean emergence time (MET) were calculated. The average days when the PE and MET stabilized were computed as follows (Jia *et al.*, 2016):

$$PE = \frac{S_{te}}{m} \times 100\% \quad (1)$$

$$MET = \frac{N_1 T_1 + N_2 T_2 + \dots + N_n T_n}{N_1 + N_2 + \dots + N_n} \quad (2)$$

where S_{te} is the total number of emerging seedlings per 5 m; m is number of seeds sown per 5 m; N_1, \dots, n is the number of emerging seedlings since the time of previous count;

T_1, \dots, n is number of days after planting.

The conformity of seedling heights was measured since the 20th day after planting when all seedlings emerged. After that, the height of each seedling was recorded. Seedling height conformity is a key influence factor on crop yield. Seedling height conformity was computed as follows:

$$PC = \frac{\bar{X}}{\sqrt{\left[\sum X^2 - \frac{(\sum X)^2}{N} \right] / (N-1)}} \tag{3}$$

Where: X is the seedling height, cm; N is the number of seedlings.

On the 20th day after emergence, roots at the seedling stage were sampled. From each stable measurement zone in the four ridges, 5 plants that represented the local conditions were selected, or namely 15 plants were chosen from each ridge. The plants were stubbed out and immersed in water. After the earth pillars became loose, the roots were washed to leave the complete roots. Then the roots were spread onto glass plates and stretched out gently by using tweezers. When the roots were unoverlapped, the main root lengths, the lateral root length at the longest upper part, the lateral root length at the shortest upper part, the lateral root length at the longest lower part, and the lateral root length at the shortest lower part (the lateral roots growing at the hypocotyl were considered as the upper-part lateral roots, the lateral roots growing on the main root were regarded as the lower-part lateral roots) were measured using tapelines (Zhu et al., 2018). The total length of lateral roots and total root length were calculated as follows:

$$L_c = 0.618 \times n \times \frac{(L_{max} + L_{min})}{2} \tag{4}$$

$$L = L_z + L_c \tag{5}$$

where, L_c is the total length of lateral roots, cm; L_{max} is the longest lateral root length, cm; L_{min} is the shortest lateral root length, cm; L is the total root length, cm; L_z is the main root length, cm; n is the number of lateral roots.

Crown dry weight: Each sample was oven-dried first at 105°C for 2 h and then at 75°C until reaching constant weight, which was the dry weight. The leaf area was measured using a Li-201 leaf area meter.

RESULTS AND DISCUSSION

Through comparative tests with the compacted furrows, the water contents, soil compactness, average emergence time, emergence rate, total root length, dry root weight, and leaf area were measured. The measured data were qualitatively and quantitatively analyzed to clarify the effects of furrow compaction on the seedbed characteristics and soybean seedling emergence.

Soil moisture content

Figures 5, 6, 7 shows the variation of water contents at the depth of 0-50 mm, >50-100 mm, and >100-150 mm from planting to emergence (11 to 20 August) on the furrows with or without compaction. The soil moisture contents under different treatments changed generally as follows: the water contents increased with the enlargement of soil depth within a certain range.

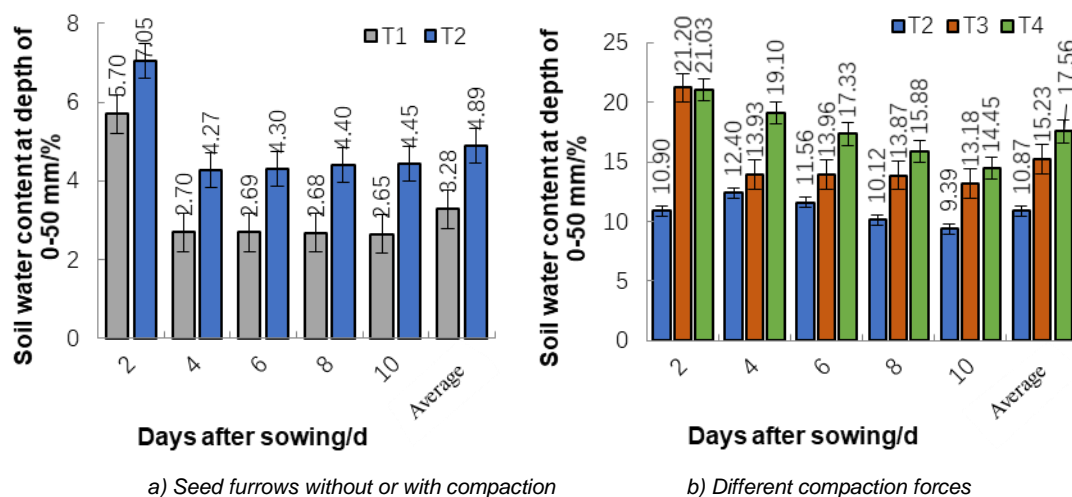


Fig. 5 - Effects of different operating method on soil moisture content at the depth of 0-50 mm

The operating methods significantly affected the soil moisture contents at the depth of 0-50 mm. Comparison between furrows without and with compaction showed the soil moisture contents were significantly affected by compaction and by the compaction forces.

At the soil depth of 0-50 mm, the average water content under T1 was significantly lower than that under T2, and the soil moisture contents under T1 and T2 both significantly declined since the 4th day, but stabilized within 4-10 days (Fig. 5a). The water content under T1 at the depth of 0-50 mm gradually declined with the increase of days, as it significantly dropped from the maximum of 5.7% to 2.7% on the 4th day and then slowly dropped to 2.65%. The water content under T2 significantly declined from the maximum of 7.05% to 4.27% on the 4th day, and rose within 4-10 days to 4.45%. The reason was that the soils around the seedbed under T2 were compacted and thereby the soil particle density and soil capillary porosity (equivalent pore size was 0.02-0.002 mm) rose. The evaporation rate was controlled by water conductivity when the water content was below the saturated level. With the decline of water content, the capillary water conductivity dropped; under the isothermal condition, the water vapors were affected by soil grain surface force and capillary force and slowly gathered at the soil compact surface, forming membranous water, namely aggregating around the compacted seeds. Thus, minor recovery of water content occurred in the seedbed under T2 at the depth of 0-50 mm. Though the humidity raising effect was not evident, it could preserve soil moisture at the depth of 0-50 mm to some extent.

The effects of compaction force on the seedbed water content within the depth of 0-50 mm were illustrated in Fig. 5b. As the compaction force was enhanced, the water contents under T3 and T4 within the depth of 0-50 mm significantly surpassed those under T2, and the average water content under T4 was higher than that under T3, but not significantly. The changing trends of soil moisture content in Fig. 5b are similar to those in Fig. 5a, but significantly declined on the 4th day, and stabilized within 4-10 days.

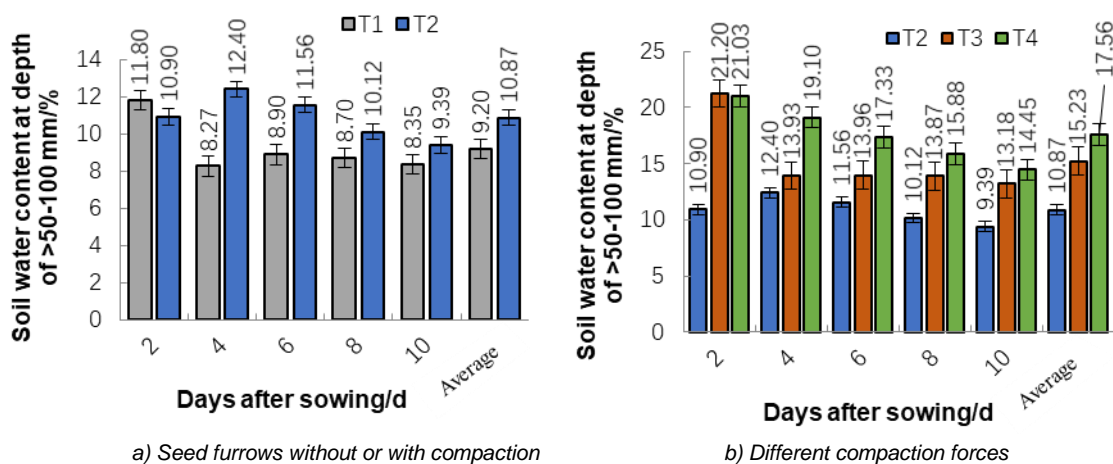
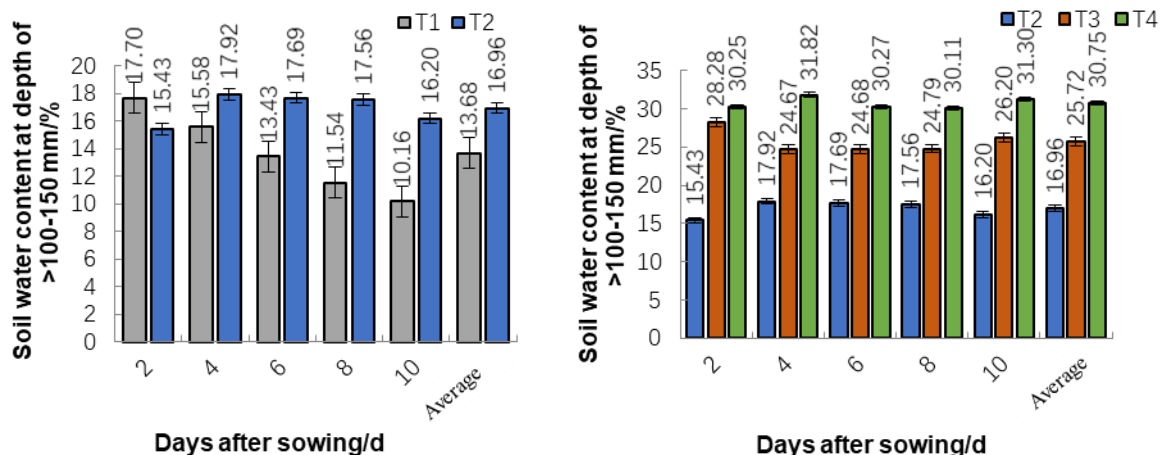


Fig. 6 - Effects of different operating method on soil moisture content at the depth of >50-100 mm

At the depth >50-100 mm, the average water content under T2 surpassed that under T1 (Fig. 6a). On the 2nd day, the water content under T1 was larger than that under T2. The water loss due to evaporation under T1 was more than that under T2. It was suggested that seed furrow compaction contributed to soil moisture preservation in the depth >50-100 mm to some extent. On the 4th day under T2, the soil water content did not significantly decline, but rose slightly. It was deduced that furrow compaction promoted water contents at the depth >50-100 mm to some extent.

The effects of furrow compaction force on the soil moisture content at the depth >50-100 mm were illustrated in Fig. 6b. The average soil water content was positively correlated with the compaction force, as the soil moisture preservation effect was improved at higher compaction force.

The soil moisture content at the depth >100-150 mm under T2 was higher than that under T1 (Fig. 7a). The soil moisture content under T1 gradually declined with the increase of days, and the seedbed soil moisture content under T2 did not drop significantly, indicating the seed furrow compaction could preserve soil moisture at the depth >100-150 mm.



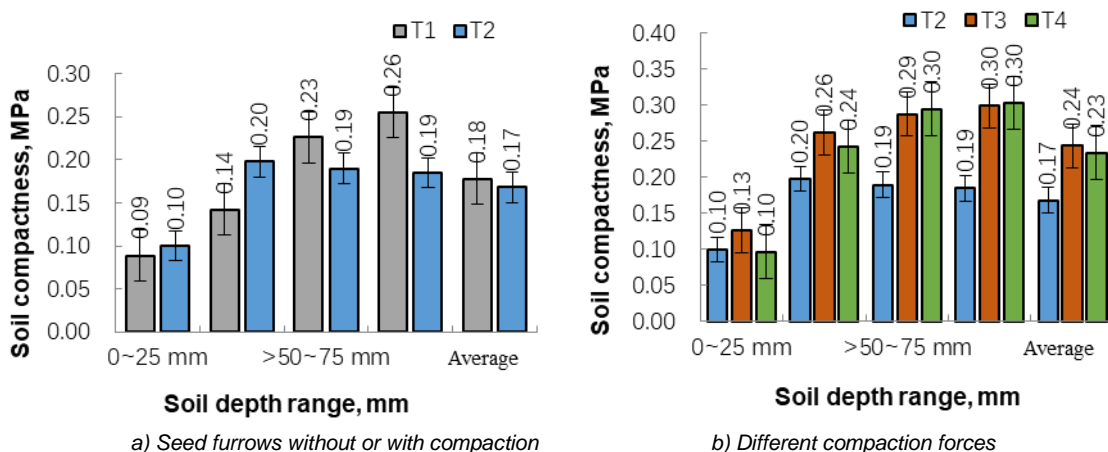
a) Seed furrows without or with compaction
 b) Different compaction forces
Fig. 7 - Effects of different operating method on soil moisture content at the depth >100-150 mm

The effects of furrow compaction forces on soil moisture contents at the depth >100-150 mm are illustrated in Fig. 7b. Clearly, the soil moisture content rose and the soil moisture preservation efficiency was higher at larger compaction force. Moreover, within the first 10 days of seedling emergence, the water content did not drop obviously, indicating that furrow compaction can well preserve soil moisture.

The above experimental results imply that furrow compaction can preserve soil moisture, which is consistent with the existing studies (Pulkrabek et al., 2015). Our results also suggest soil moisture and volume weight both affect the water use efficiency of plants and interact, but the effect of soil moisture is more significant. Moreover, the spatial variation of soil bulk density is favourable for enhancing water use efficiency (Li et al., 2019).

Soil compactness

The furrow compaction compared with no compaction significantly affected the soil compactness at different layers (P<0.05), and the soil compactness at different layers changed to different extents along with the enhancement of compaction force. The furrow compaction experiments were conducted from 11 to 20 August, 2017. The soil compactness at a specific depth was measured every 2 days (Fig. 8). The soil compactness significantly varied with the furrow compaction compared with T1. The soil compactness under T1 was enlarged with the increase of soil depth. The soil compactness under T2 maximized at the depth >25-50 mm, and declined slowly with the increment of soil depth, forming a false or true interphase soil layer environment (Fig. 8a). In conclusion, the soil compactness increased abruptly at a certain depth and was higher than that at upper or lower layers, so that the water content at this depth range increased.



a) Seed furrows without or with compaction
 b) Different compaction forces
Fig. 8 - Effects of different treatments on soil compactness

The effects of compaction forces on the soil compactness at different layers are shown in Fig. 8b. As the furrow compaction force was enlarged, the soil compactness under T3 or T4 was strengthened with the increase of soil depth, and such changes were more evident than under T2. The soil compactness degrees

were not significantly different between T3 and T4. In our experiments, the soil compactness at any soil depth was below 2-3 MPa, so the soil compactness after any treatment obeyed agronomic requirement.

Mean emergence time

Table 2 lists the daily seedling numbers within the first 15 days of seedling emergence under T1, T2, T3, and T4. Seedling emerged the earliest under T3 and the latest under T1. The seed furrow compaction significantly affected the emergence time ($P < 0.05$) (Fig. 9). The average emergence time under T2 was 0.79 day earlier compared with T1.

The average emergence time under different furrow compaction forces ranked as $T3 < T4 < T2$. On the 2nd day of planting, the water contents at the depth of 0-50 mm and 50-100 mm both maximized under T3 and ranked as $T3 > T4 > T2$. The compaction under T2, T3 or T4 compared with T1 relatively well reserved water contents, and the water content was inversely proportional to the seedling emergence time.

Table 2

The seedling numbers under different treatments within the first 15 days of planting

Date	Days of planting	Total number of seedlings			
		T1	T2	T3	T4
14 Aug.	4	0	0	3	0
15 Aug.	5	0	4	21	9
16 Aug.	6	4	10	27	18
17 Aug.	7	6	17	29	29
18 Aug.	8	7	24	30	32
19 Aug.	9	10	25	36	42
20 Aug.	10	13	26	39	43
21 Aug.	11	14	27	40	43
22 Aug.	12	14	29	41	45
23 Aug.	13	14	30	42	46
24 Aug.	14	14	31	42	46
25 Aug.	15	15	31	43	46

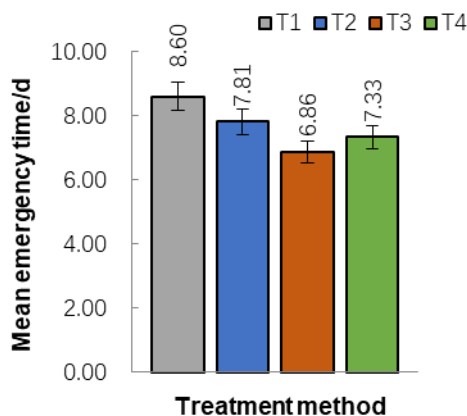


Fig. 9 - Average emergence time under different treatments

Soybean emergence rate

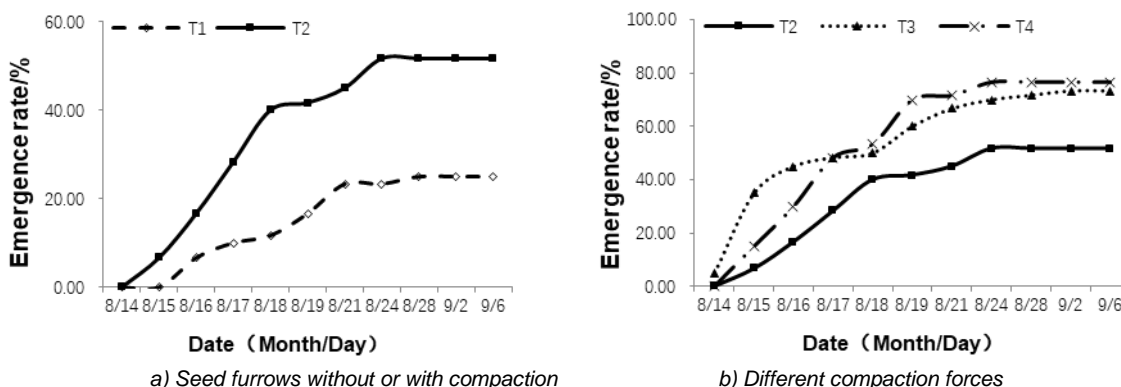


Fig. 10 - Effects of furrow compaction on soybean emergence rate

Results showed under the same conditions, the furrow compaction affected soil moisture content, as the soybean seed emergence rate rose at higher soil moisture content, and the emergence rates after furrow compaction were higher than that without compaction. The emergence rates ranked as T4 > T3 > T2. The furrow compaction and the compacting forces both significantly affected the emergence rates (Fig. 10). The emergence rate under T2 was significantly higher than that under T1 ($P < 0.05$) (Fig. 10a). The emergence rates under T3 and T4 were both higher than that under T2 (Fig. 10b). The emergence rate under T3 from planting to the 4th day of emergence was higher than that under T4, and the emergence rate beyond the 4th day was higher under T4 than under T3. According to the variation of water content at different depths, the water content on the 2nd day at the depth of 0-100 mm was higher than T3 than under T4. Beyond the 4th day after planting, the seedling emergence rates and soil moisture contents both declined abruptly. At this moment, the water content under T4 decreased at lower rate than under T3. The water content beyond the 4th day was higher than under T3, indicating the seed emergence rate was positively correlated with the soil moisture content. The furrow compaction significantly affected water contents and directly impacted the seed emergence rate. Under the same conditions, the emergence rate under larger soil moisture content was higher. The seedling numbers ranked as T4>T3>T2. The seed furrow compaction by the opener crushed the soils around the seedbed and made the seeds and seedbed soils fully contact, which increased the seed emergence rates.

Conformity of seedling height

The seedling height conformity is a key influence factor on crop yield. The seedling height conformity was significantly affected by furrow compaction ($P < 0.05$) and by the compaction force. The seedling height conformity under furrow compaction compared with no compaction was 3.56, with an increase of 5.34%. The seedling height conformity was the highest under the largest compaction force of T4, and ranked as T4>T3>T2>T1. The reason was that during furrow compaction by using the opener, the compaction efficiency was higher under a larger compaction force, so the variation coefficient of seed deep seeding minimized and the compaction force during the compaction was uniform, leading to the conformity of emergence time (Jia et al., 2015; Zhao et al., 2017). The seeds with high consistency of deep seeding can absorb moisture and nutrient consistently, which increased the seedling emergence conformity and the regularity of crop growth. Thus, the seedling emergence conformity was higher under the treatment of T4.

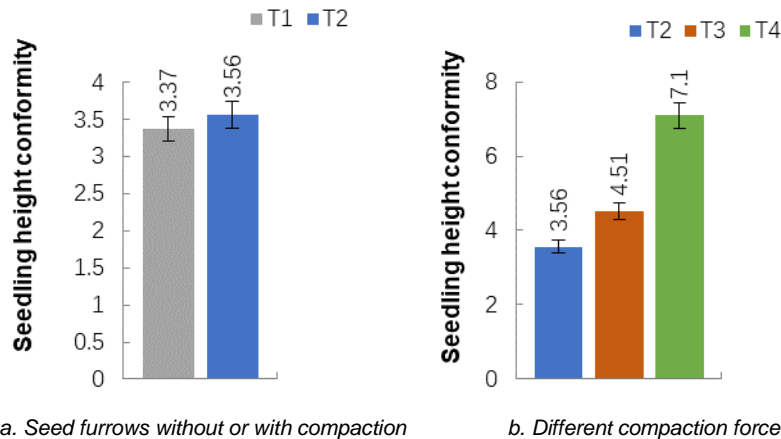


Fig. 11 - Effects of treatments on seedling height conformity

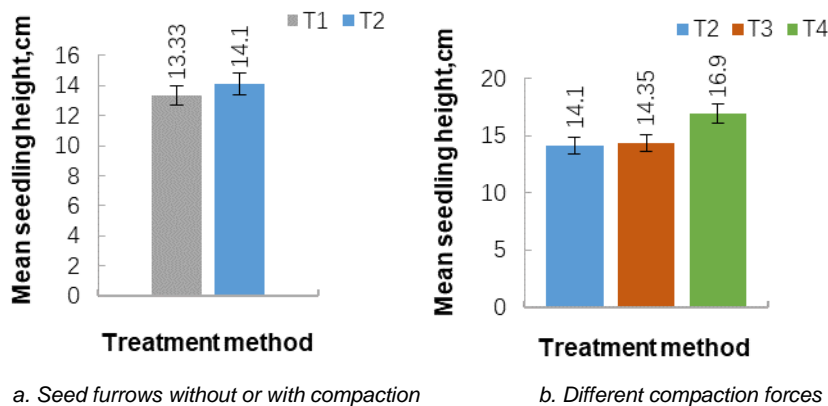


Fig. 12 - Effects of treatments on mean seedling height

Figure 12 shows the average height of soybean seedlings on the 20th day after different treatments. Clearly, the seedlings under T2 were higher than those under T1. The average seedling height under T4 was significantly larger than that under T2 and T3. This was because seed furrow compaction ensured the relatively high water content around seeds, so that the seeds can germinate quickly. As the compaction force was enhanced, the field moisture capacity also increased and at late stage of seedling emergence, continually supported seed growth. Furthermore, as the compaction force was strengthened, the deep seeding consistency and the seedling emergence conformity both increased. As for T1, however, the seedling emergence conformity was low, and the soil moisture loss was accelerated, so the seedlings became irregular. Thus, the average seedling height maximized under T4 and minimized under T1.

The seedling height conformity under T4 was higher than under T3 and T2 (Fig. 13). Missing seedling or seedling height unevenness occurred in the plots treated by T1. The seedling heights under T2 were irregular; the seedling heights under T3 were non-uniform. However, the emergence rate under T2 was high, and the seedling heights under T4 were relatively uniform.

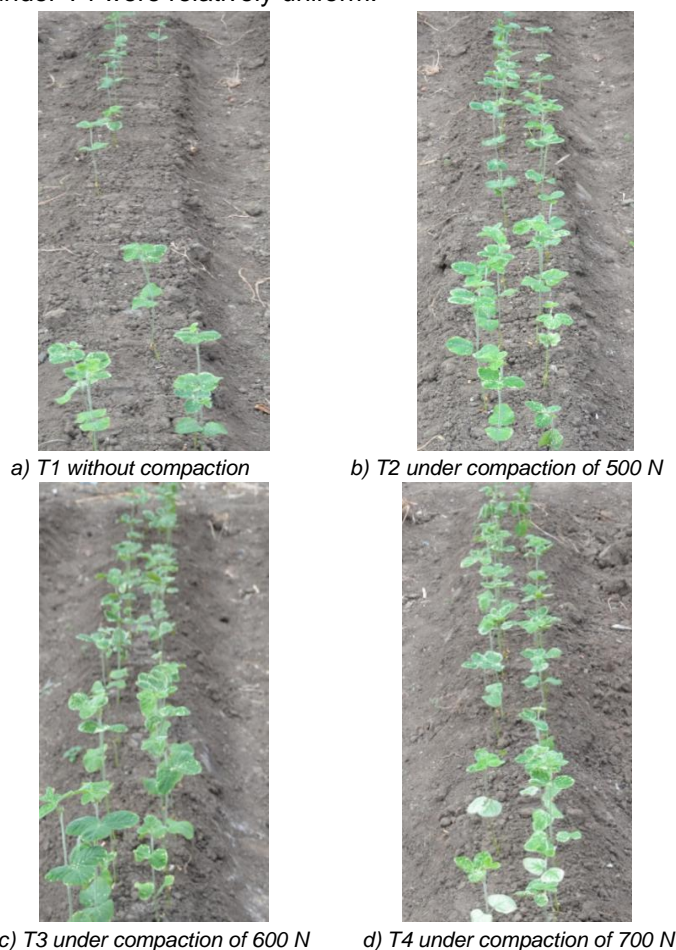


Fig. 13 - Seedling heights on the 20th day after different treatments

Roots and crown

The compaction force larger than 600 N can significantly increase the crown dry weight, seedling height, leaf areas, main root length and total root length.

Table 3

Effects of pre-planting compaction on soybean roots

Processing method	Root number	Main root length cm	Root length cm
T1 (no compaction)	9.9±0.9 a	16.8±1.6 a	50.5±3.1 a
T2 (500N compaction)	11.1±1.1 a	16.6±1.5 a	57.5±4.6 a
T3 (600 N compaction)	12.6±1.2 a	19.5±2.1 b	66.2±4.8 b
T4 (700 N compaction)	12.9±1.3 a	21.2±2.7 c	75.4±5.1 c

Note: letters denote significant differences ($P < 0.05$); the same below.

Table 4

Effects of furrow compaction on soybean crown

Processing method	Crown dry weight g/pot	Seedling height cm	Leaf area cm ² /pot
T1 (no compaction)	0.48±0.12 a	13.33±2.3 a	162±15 a
T2 (500N compaction)	0.53±0.10 a	14.10±2.2 a	165±15 a
T3 (600N compaction)	0.62±0.11 b	14.35±2.8 b	175±18 b
T4 (700N compaction)	0.58±0.12 b	16.90±1.2 b	172±16 b

Compared with T1, the average root number after treatment by T2 increased by 1.2, with an amplitude of 12.12% (Table 3). The average root length rose by 7 cm, with an amplitude of 13.9%. The soybean root length maximized after treatment of T4, with an amplitude of 31.10% from the treatment of T2. The soybean root length was enlarged with the rise of compaction force within 500-700 N. The compaction force larger than 600 N can significantly increase the crown dry weight, seedling height and leaf area compared with T1 (Table 4).

Furrow compaction can refine and tighten furrow soils and decrease the aggregate size. When the compaction force surpassed 600 N, the total root length was the largest and significantly larger than that under T1 ($P < 0.05$). As reported, total root length and root surface area both significantly increased with the decrease of aggregate size, and under low soil moisture content (*Song et al., 2009*). The small-size aggregates (especially the size of 1-2 mm) compared with large-size aggregates and the unscreened soils can largely shorten the emergence time, and significantly increase, soybean emergence rate crown dry weight, seedling height, leaf area, total root length and root surface area. These findings are consistent with our results.

CONCLUSIONS

Through sunlight greenhouse tests, the effects of the double V-shaped opener on seedbed characteristics and soybean emergence were studied under the compaction forces of T1 (0 N), T2 (500 N), T3 (600 N) and T4 (700 N). The furrow compaction planting significantly affected the seedbed characteristics and soybean emergence and could preserve soil moisture in seedbeds. The furrow compaction significantly affected soil moisture content at different soil depths. Thus, furrow compaction could preserve soil moisture at shallow soil layers. Under the semiarid condition, the average emergence time under T2 was 0.79 day earlier than under T1, and the emergence rates under T2, T3 and T4 were significantly raised. The seedling height uniformity under T2 was 5.34% higher than under T1. The average emergence time ranked from early to later as $T3 < T4 < T2$. The deep seeding uniformity, the emergence uniformity, and the average seedling height were all improved as the furrow compaction force was enlarged within 500-700 N. The compaction force larger than 600 N can significantly increase the crown dry weight, seedling height, leaf areas, main root length, and total root length. Furrow compaction can preserve soil moisture in seedbeds, and the seedbed soil physical properties and soybean seedling emergence were optimized under the furrow compaction force of 600-700 N.

ACKNOWLEDGEMENT

This work is supported by Polygonatum kingianum Coll. et Hemsl Adaptive Seedbed Establishment Technology for High-Altitude Hilly Areas, 2018 Yunnan Education Department Scientific Research Fund (2018JS272), Yunnan Youth Fund (2017FD080), Yunnan Agricultural Joint Youth Fund (2018FG001-091).

REFERENCES

- [1] Celik A., Ozturk L., Way T.R., (2007), Effects of various planters on emergence and seed distribution uniformity of sunflower, *Applied Engineering in Agriculture*, Vol. 23, Issue 1, pp. 57-61;
- [2] Jia H.L., Wang W.J., Luo X.F., Zheng J.X., Guo M.Z., Zhuang J., (2016), Effects of profiling elastic press roller on seedbed properties and soybean emergence under double row ridge cultivation, *Soil & Tillage Research*, Vol. 162, pp. 34-40;
- [3] Jia H.L., Wang W.J., Zhuang J., Luo X.F., Yao P.F., Li Y., (2015), Design and experiment of profiling elastic press roller, *Transactions of the Chinese Society for Agricultural Machinery*, Vol. 46, Issue 6, pp. 28-34;

- [4] Jia H.L., Zheng J.X., Yuan H.F., Guo M.Z., Wang W.J., Yu L.L., (2017), Design and experiment of a Double-V-shaped furrow opener of soybean seeder, *Journal of Jilin University (Engineering and Technology Edition)*, Issue 1, pp. 323-331;
- [5] Li Y., Li Z., Cui S., Jagadamma S., Zhang Q.P., (2019), Residue retention and minimum tillage improve physical environment of the soil in croplands: A global meta-analysis, *Soil & tillage research*, Vol. 194, pp. 104292;
- [6] Liu L.H., Zheng G.P., Qian Y.D., Lv Y.D., (2010), Influence of single or double row ridge and fertilizer quantity on yield and quality of hybrid sweet sorghum, *Henan Agricultural*, Vol. 3, pp. 15-17.
- [7] Murray S.E., Chen Y., (2019), Discrete element modeling of soil displacement resulting from hoe openers, *Transactions of the ASABE*, Vol. 62, Issue 2, pp. 253-262;
- [8] Nawaz M.F., Bourrié G., Trolard F., (2013), Soil compaction impact and modelling. A review, *Agronomy for sustainable development*, Vol. 33, Issue 2, pp. 291-309;
- [9] Neto W.P.H., Angelo R.C., (2012), Emergence of corn according to the sowing depth of the seed and loads on press wheels, *Agricultural Engineering (Engenharia Agrícola)*, Vol. 32, Issue 2, pp. 326-332, Brasil;
- [10] Pulkrabek J., Urban J., Jedlickova M., (2015), Effect of Autumn Tillage on Soil Compaction in the Beginning of Sugar Beet Vegetation, *Sugar and Sugar Beet Journal (Listy cukrovarnické a reparské)*, Vol. 131, Issue 9-10, pp. 272-278, ISSN 1210-3306 (Print), 1805-9708 (Online), Czech Republic;
- [11] Shah A.N., Tanveer M., Shahzad B., Yang G.Z., Fahad S., Ali S., Bukhari M.A., Tung S.A., Hafeez A., Souliyanonh B., (2017), Soil compaction effects on soil health and crop productivity: an overview, *Environmental science and pollution research*, Vol. 24, Issue 11, pp. 10056-10067;
- [12] Song R., Liu L., Wu C.S., Ma L.Y., (2009), Effect of soil aggregate size on emergence and seedling growth of soybean, *Chinese Journal of Oil Crop Sciences*, Vol. 31, Issue 2, pp. 223-227;
- [13] Wei W., Xu Y.L., Li S.X., Zhu L., Song J., (2015), Developing suppressive soil for root diseases of soybean with continuous long-term cropping of soybean in black soil of Northeast China, *Acta agriculturae scandinavica section B-Soil and plant science*, Vol. 65, Issue 3, pp. 279-285;
- [14] Xue Q.X., (2013), Analysis on the change of 30 year's soybean area, production and yield in China and northeast China, *Chinese Agricultural Science Bulletin*, Vol. 29, Issue 35, pp. 102-106;
- [15] Zhao S.H., Liu H.J., Tan H.W., Yang Y.Q., Zhang X.M., (2017), Design and experiment of bidirectional profiling press device for hilly area, *Transactions of the Chinese Society for Agricultural Machinery*, Vol. 48, Issue 4, pp. 82-89;
- [16] Zhu Q., Kong L.J., Xie F.T., Zhang H.J., Wang H.Y., Ao X., (2018), Effects of biochar on seedling root growth of soybeans, *Chilean journal of agricultural research*, Vol. 78, Issue 4, pp. 549-558.

WRITING NORMS

Article Types

Three types of manuscripts may be submitted:

1. **Regular articles:** These should describe new and carefully confirmed findings, and experimental procedures should be given in sufficient detail for others to verify the work. The length of a full paper should be the minimum required to describe and interpret the work clearly (max.10 pages, even number);
2. **Short Communications:** A Short Communication is suitable for recording the results of complete small investigations or giving details of new models or hypotheses, innovative methods, techniques or apparatus. The style of main sections has not necessarily to be in accordance with that of full-length papers (max. 6 pages, even number);
3. **Reviews:** Submissions of reviews and perspectives covering topics of current interest are welcome and encouraged (max.10 pages, even number).

Manuscripts should be written in English (American or British usage is accepted, but not a mixture of these) and submitted **electronically** at the following e-mail addresses: ***inmatehjournal@gmail.com***

Please be sure to include your full affiliation and e-mail address (see Sample manuscript)

The authors are responsible for the accuracy of the whole paper and references.

There are allowed 2 papers by each first author.

The text layout should be in single-column format. To avoid unnecessary errors it is strongly advised to use the "spell-check" and "grammar check" functions of your word processor.

Review Process

All manuscripts are reviewed by 2 members of the Scientifically Review Office. Decisions will be made as rapidly as possible and the journal strives to return reviewers' comments to authors in approx.3 weeks.

The editorial board will re-review manuscripts that are accepted pending revision.

NOTE:

Submission of a manuscript implies: that the work described has not been published before (excepting as an abstract or as part of a published lecture or thesis) that it is not under consideration for publication elsewhere.

1. REGULAR ARTICLES

- Manuscripts should be concise, in **1.15 line spacing**, and should have 2 cm all over margins. The font should be **Arial 10 pt.** Ensure that each new paragraph is clearly indicated, using **TAB at 1 cm.**
- Title will be **Arial 12 pt.** and explicit figures will be **Arial 9 pt.**
- Text will be written in English.
- Chapters' titles are written by **Arial 10 pt, Bold, Uppercase** (e.g. **INTRODUCTION, MATERIALS AND METHODS**), between chapters is left a space for 10 pt. At the beginning of each paragraph, TAB of 1 cm.
- The paper body will be written in **Arial 10 pt., Justify alignment.**

TITLE **Arial 12 pt., Uppercase, Bold, Center** (in English language) and **Bold Italic** (in native language).

Should be a brief phrase describing the contents of the paper. Avoid long titles; a running title of no more than 100 characters is encouraged (without spaces).

AUTHORS **ARIAL 9, Bold, Centre alignment**

Under the paper's title, after a space (enter) 9 pt., write **authors' names** and **affiliations (Arial 8 pt.-Regular)**

When the paper has more than one author, their name will be followed by a mark (Arabic numeral) as superscript if their affiliation is different. **Less than 6 authors.**

Corresponding author's name (next row), **(Arial 8 pt.)**. Should be added also: phone, fax and e-mail information, for the paper corresponding author (**font: 8 pt., Italic**).

KEYWORDS **(In English)** about 4 to 7 words that will provide indexing references should be listed (**title: Arial 10pt, bold italic, text Arial 10 pt., italic**).

A list of non-standard **Abbreviations** should be added. In general, non-standard abbreviations should be used only when the full term is very long and used often. Each abbreviation should be spelled out and introduced in parentheses the first time it is used in the text. Standard abbreviations (such as ATP and DNA) need not to be defined.

ABSTRACT **(in English and Native language, Arial 10 pt.)**, the title **bold**; the text of abstract: **italic** should be informative and completely self-explanatory, briefly present the topic, state the scope of the experiments, indicate significant data, and point out major findings and conclusions. The Abstract should be max.250 words. Complete sentences, active verbs, and the third person should be used, and the abstract should be written in the past tense. Standard nomenclature should be used and abbreviations should be avoided. No literature should be cited.

INTRODUCTION (*Arial 10 pt.*) should provide a clear statement of the problem, the relevant literature on the subject, and the proposed approach or solution. It should be understandable to colleagues from a broad range of scientific subjects. We should refer to the current stage of researches performed in the field of the paper to be published, by quoting up-to-date specialty studies, preferably published after 2006, excepting certain referential specialty books/studies, especially papers issued in magazines/journals/conferences/ISI quoted symposia or in other international data bases, which are well known and available.

MATERIALS AND METHODS (*Arial 10 pt.*) should be complete enough to allow experiments to be reproduced. However, only truly new procedures should be described in detail; previously published procedures should be cited, and important modifications of published procedures should be mentioned briefly. Methods in general use need not be described in detail.

RESULTS (*Arial 10 pt.*) should be clearly presented. The results should be written in the past tense when describing findings in the authors' experiments. Results should be explained, but largely, without referring to the literature. Discussion, speculation and detailed interpretation of data should not be included in the Results, but should be put into the Conclusions section.

CONCLUSIONS (*Arial 10 pt.*) The main conclusions drawn from results should be presented in a short Conclusions section. Do not include citations in this section.

Formulae, symbols and abbreviations: Formulae will be typeset in Italics (preferable with the Equation Editor of Microsoft Office 2003) and should be written or marked as such in the manuscript, unless they require a different styling. They should be referred to in the text as Equation (4) or e.g. (4). The formulae should be numbered on the right side, between brackets (*Arial 10 pt.*):

$$P = F \cdot v \quad (1)$$

Terms of the equation and the unit measure should be explained, e.g.

P is the power, [W];

F – force, [N];

v – speed, [m/s]

SI units must be used throughout.

Tables should be self-explanatory without reference to the text. The details of the methods used in the experiments should preferably be described in the legend instead of in the text. [The same data should not be presented both in table and graph form or repeated in the text.](#)

Table's title will be typed *Arial 9 pt, Bold, Centered*

In the table, each row will be written Arial 9 pt, single-spaced throughout, including headings and footnotes.

The table should be numbered on the right side, *Arial 10 pt.*

Figure (*Arial 9 pt., Bold, Center*) should be typed in numerical order (Arabic numerals). Graphics should be high resolution (e.g.JPEG).Figure number is followed by what represent the figure or graph e.g.:

Fig.1 – Test stand

Legend: *Arial 8 pt, Italic, Center, e.g.:*

1 - plansifter compartments; 2- break rolls; 3 – semolina machines; 4 – reduction rolls; 5 – flour

ACKNOWLEDGMENTS (*Arial 10 pt.*) of people, grants, funds etc should be brief (*if necessarily*).

REFERENCES (*Arial 10 pt.*)

(In alphabetical order, in English and in the original publication language).

Minimum 10 references, last 10 years, minimum 3 references from the last 2 years

References must be from all over the world, not only from the authors' country.

It can be used "References" tool from the *Word Editor*.

References should be cited in the text in brackets as in the following examples:

(Babiciu P., Scripciu V., 2000)

All references must be provided in English with a specification of original language in round brackets.

Authors are fully responsible for the accuracy of the references.

References should be alphabetically, with complete details, as follows:

Examples:

Books: Names and initials of authors, year (between brackets), title of the book (Italic), volume number, publisher, place, pages number or chapter, ISSN/ISBN:

[1] Vlăduț V., (2009), *Study of threshing process in axial flow apparatus (Studiul procesului de treier la aparatele cu flux axial)*, vol.1, ISSN/ISBN, "Terra Nostra" Publishing House, Iași/Romania;

Journal Article: Names and initials of authors, year (between brackets), full title of the paper, full name of the journal (Italic), volume number, publisher, place, ISSN, page numbers:

[1] Lizhi Wu, Yan Di., (2005), *Demonstrational study on the land consolidation and rehabilitation (LCR) project of saline-alkali soil in arid areas: a case study of Lubotan LCR project in Pucheng County, Shaanxi Province (干旱区盐碱化土地整理工程实证研究-以陕西蒲城县卤泊滩土地整理项目为例)*, *Transactions of the Chinese Society of Agricultural Engineering*, vol.21, no.1, pp.179-182, Madison/Wisconsin;

[2] Leonov I.P., (1973), *Basic machine theory for tobacco stringing. Post-harvest care of tobacco and rustic tobacco (Основы теории машин для закрепления табака на шнуры. Послеуборочная обработка табака и махорки)*, *Collection of scientific articles (сборник научно-исследовательских работ)*, pp.37-45;

Conference or Symposium: Names and initials of authors, year (between brackets), full title of the paper (Regular), full name of the conference/symposium (Italic), volume number, publisher, place, ISSN, page numbers

[1] Bungescu S., Stahli W., Biriș S., Vlăduț V., Imbrea F., Petroman C., (2009), *Cosmos program used for the strength calculus of the nozzles from the sprayers (Program Cosmos folosit pentru calculul de rezistență la zgomot al aparatelor de distribuție)*, *Proceedings of the 35 International Symposium on Agricultural Engineering "Actual Tasks on Agricultural Engineering"*, pp.177-184, Opatija / Croatia;

Dissertation / Thesis: Names and initials of authors, year (between brackets), full name of the thesis (Italic), specification (PhD Thesis, MSc Thesis), institution, place;

[1] Popa L., (2004), *Research on the influence of structural and functional parameters of the braking system on the braking performance of agricultural trailers (Cercetări privind influența caracteristicilor constructive și funcționale ale sistemelor de frânare asupra performanțelor de frânare ale remorcilor agricole)*, PhD dissertation, Transylvania University of Brașov, Brașov / Romania.

Patents: Names and initials of authors, year (between brackets), patent title (Italic), patent number, country:

[1] Grant P., (1989), *Device for Elementary Analyses*. Patent, No.123456, USA.

Legal regulations and laws, organizations: Abbreviated name, year (between brackets), full name of the referred text, document title/type (Italic), author, place:

[1] *** EC Directive, (2000), *Directive 2000/76/EC of the European Parliament and of the Council of 4 December 2000, on the incineration of waste, Annex V*, *Official Journal of the European Communities*, L332/91, 28.12.2000, Brussels.

Web references: The full URL should be given in text as a citation, if no other data are known. If the authors, year, and title of the documents are known and the reference is taken from a website, the URL address has to be mentioned after these data:

The title of the book, journal and conference must be written in Italic, the title of the article, chapter of the book, must be written Regular.

Citation in text

Please ensure that every reference cited in the text is also present in the reference list (and vice versa). Do not cite references in the abstract and conclusions. Unpublished results, personal communications as well as URL addresses are not recommended in the references list.

Making personal quotations (one, at most) should not be allowed, unless the paper proposed to be published is a sequel of the cited paper. Articles in preparation or articles submitted for publication, unpublished, personal communications etc. should not be included in the references list.

Citations style

Text: All citations in the text may be made directly (or parenthetically) and should refer to:

- **single author:** the author's name (without initials, unless there is ambiguity) and the year of publication:

"as previously demonstrated (*Brown, 2010*)".

- **two authors:** both authors' names and the year of publication: (*Adam and Brown, 2008; Smith and Hansel, 2006; Stern and Lars, 2009*)

- **three or more authors:** first author's name followed by "et al." and the year of publication: "As has recently been shown (*Werner et al., 2005; Kramer et al., 2000*) have recently shown"

Citations of groups of references should be listed first alphabetically, then chronologically.

Units, Abbreviations, Acronyms

- Units should be metric, generally SI, and expressed in standard abbreviated form.
- Acronyms may be acceptable, but must be defined at first usage.



Edited by: INMA Bucharest

6, Ion Ionescu de la Brad Blvd., sect. 1, Bucharest, ROMANIA

Tel: +4021.269.32.60; Fax: +4021.269.32.73

[https:// inmateh.eu](https://inmateh.eu)

e-mail: inmatehjournal@gmail.com